Thèse en cotutelle présentée

Pour obtenir le grade de

Docteur de
l'Université de Bordeaux
et de l'Université de Salamanque

École doctorale Sciences Physiques et de l'Ingénieur

Doctorado en Física Fundamental y Matemáticas

Specialité Astrophysique, Plasmas, Nucléaire

Par Valeria Ospina-Bohórquez

Sous la direction de **João Jorge SANTOS**
de **Laurent GREMILLET**
et de **Luca VOLPE**

Experimental and numerical investigations on ion acceleration from near-critical gas targets

Soutenue le 14 décembre 2022 à l'Université de Bordeaux
devant un jury composé de :

M. Emmanuel d'Humières	Professeur	Université de Bordeaux	Président
M. Victor Malka	Professeur	Weizmann Institute of Science	Rapporteur
M. Luis O. Silva	Professeur	Instituto Superior Técnico	Rapporteur
Mme. Livia Lancia	Chargée de recherche	LULI, École Polytechnique	Examinatrice
Mme. Anna Grassi	Maîtresse de conférences	LULI, Sorbonne Univ.	Examinatrice
M. João Jorge Santos	Professeur	Université de Bordeaux	Directeur de thèse
M. Laurent Gremillet	Ingénieur de recherche	CEA-DAM	Encadrant de thèse
M. Luca Volpe	Professeur	Universidad de Salamanca	Co-directeur de thèse

Experimental and numerical investigations on ion acceleration from near-critical gas targets

Experimental and numerical investigations on ion acceleration from near-critical gas targets

Experimental and numerical investigations on ion acceleration from near-critical gas targets

Fdo. Prof. João Jorge Santos   Fdo. Dr. Laurent Gremillet   Fdo. Prof. Luca Volpe

Resumé

Les sources d'ions rapides générées par des lasers intenses constituent un sujet d'étude prometteur pour de multiples domaines de la recherche. Alors que l'accélération d'ions par interaction laser-solide a été étudiée de manière exhaustive, les plasmas de densité quasi critique (soit une densité électronique de l'ordre de $10^{21}\,\mathrm{cm}^{-3}$ pour une longueur d'onde laser d'environ $1\,\mu\mathrm{m}$) ont été peu abordés, en raison des difficultés liées à la génération contrôlée de densités critiques (à partir d'une cible solide, liquide ou gazeuse). De tels plasmas pourraient cependant donner lieu à plusieurs mécanismes d'accélération, tels que le « target normal sheath acceleration » ou l'accélération par choc non-collisionnel, ainsi qu'à la génération de populations d'électrons chauds dits super-pondéromoteurs.

Cette thèsee s'inscrit dans le cadre du développement de sources d'ions produites par un laser intense à haut taux de répétition (HTR), nécessaires aux besoins de la plupart des applications. Les nouvelles installations lasers fs de très haute puissance (de l'ordre du pétawatt) et intensité ($I_L \gtrsim 10^20\,\mathrm{Wcm}^{-2}$) comme VEGA-3, Apollon, L4 Aton ou BELLA PW, capables de délivrer une impulsion de quelques fs par seconde, sont ainsi parfaitement adaptées à cet objectif. Par ailleurs, des buses à gaz de type « shock nozzle » nouvellement développées, connectées à des systèmes de gaz à haute pression, sont choisies pour leur compatibilité avec ces HTR et le fort couplage laser-gaz attendu.

Une étude paramétrique basée sur des simulations 1-D de type « particle-in-cell » (PIC) a d'abord été effectuée pour comprendre l'interaction entre un laser intense et un jet de gaz quasi-critique et non-uniforme. Nous avons ainsi cherché à déterminer un jeu optimal de paramètres expérimentaux concernant l'interaction d'une impulsion laser $\lambda_L = 0.8\,\mu\mathrm{m}$, $\tau_L = 100$ fs, $I = 10^{20}$ W/cm^2, avec un jet de gaz quasi critique similaire à celui produit par une buse à gaz non commerciale, développée au sein de notre groupe de collaboration. Nous avons utilisé pour cela le code PIC CALDER développé au CEA.

Les données expérimentales analysées pendant cette thèse ont été obtenues lors de deux campagnes sur les installations laser VEGA-2 (200 TW) et VEGA-3 (1 PW), au CLPU, Univ. Salamanque. La première visait à étudier le potentiel, en matière d'accélération ionique, d'une impulsion laser fs ultra intense interagissant avec un jet de gaz supersonique. La seconde, qui a constitué la campagne principale de cette thèse, a permis de mettre en évidence, par l'intermédiaire de mesures de temps de vol, l'accélération vers l'avant de particules α d'énergie 0.6 MeV/amu à un taux de répétition modéré, présentant des dispersions en énergie et angulaire relativement modérées. Elle a également confirmé la génération abondante d'électrons chauds telle que prédite par les simulations numériques, jusqu'à des énergies d'environ 50 MeV. Par ailleurs, la formation d'un canal plasma, s'étendant de part et d'autre du pic de densité du gaz, a été révélée par interférométrie. Plusieurs simulations 2-D, effectuées pour expliquer certains de ces résultats, sont en accord qualitatif avec les mesures, permettant d'identifier les mécanismes d'accélération d'ions et d'électrons, ainsi que de décrire le phénomène de formation du canal laser.

Le travail effectué lors de cet thèse a permis d'éclairer la physique de l'interaction entre une impulsion laser ultra intense et un gaz dense - une configuration encore peu explorée en régime femtoseconde - mais aussi d'en relever les nombreux défis techniques. Nous avons pu développer une méthodologie expérimentale adaptée ainsi qu'un ensemble de diagnostics compatibles avec un fonctionnement à HTR. Si les performances obtenues en matière d'énergie ionique restent modestes, elles n'en sont pas moins encourageantes et invitent à persévérer car les applications de l'interaction laser-gaz sont nombreuses, allant de la production de radio-isotopes médicaux

à des études de physique fondamentale. Du point de vue numérique, notre étude des conditions les plus propices à l'accélération ionique par choc électrostatique par une impulsion fs donne des conditions optimales d'interaction laser-jet de gaz, propices à la production de chocs électrostatiques, donne des objectifs expérimentaux clairs pour des travaux futurs et souligne l'importance des améliorations à apporter sur le développement de buses à gaz.

Mots clés : Cibles laser à haut taux de répétition, Interaction laser-plasma relativiste, Accélération d'ions par laser

Abstract

Fast ion sources driven by ultraintense lasers are promising in many fields of fundamental and applied science. While laser-based ion acceleration from solids has been extensively studied, near-critical-density plasmas (i.e. with free electron density of the order of $10^{21}\,\mathrm{cm}^{-3}$ for a $\sim 1\,\mu\mathrm{m}$ laser wavelength) have been little addressed so far due to difficulties in achieving well-controlled near-critical densities (from a solid, liquid or gas target). Such plasmas are predicted to give rise to a mix of acceleration mechanisms combining target normal sheath and collisionless shock acceleration, as well as hot-electron production beyond the standard ponderomotive scaling. The work carried out during this thesis lays within the framework of developing laser-driven ion sources that can operate at high repetition rate (HHR) as is needed for most applications. The recently commissioned petawatt-level facilities like VEGA-3, L4 Aton, Apollon or BELLA PW, which can deliver one ultrahigh-intensity ($I_L \gtrsim 10^{20}\,\mathrm{Wcm}^{-2}$) few-fs laser pulse per second, are perfectly suited for this purpose. At the same time, state-of-the-art shock nozzles connected to high-pressure gas systems are chosen due to their HRR compatibility. Furthermore, a strong laser-gas energy coupling is expected by interacting at near-critical densities.

As a first approach to the problem, we have conducted a parametric numerical study, based on 1-D particle-in-cell (PIC) simulations, with the objective of illuminating the physics of the interaction of ultraintense fs laser pulses with strongly nonuniform, dense gas targets. Specifically, we aimed at obtaining an optimal set of experimental parameters regarding the interaction of the a $\lambda_L = 0.8\,\mu\mathrm{m}$, $\tau_L = 100$ fs, $I = 10^{20}$ W/cm^2 laser pulse with a nitrogen gas jet shaped as that produced by a non-commercial nozzle developed within our collaboration group. The PIC code Calder developed at CEA was used.

The experimental data analysed in this thesis have been obtained during two campaigns that took place at the 200 TW VEGA-2 and 1 PW VEGA-3 laser systems located at CLPU, Univ. of Salamanca. The first aimed at studying the potential for ion acceleration of a state-of-the-art gas jet coupled with shock nozzles. The second experiment, at the core of this thesis, which was the main experimental task of this thesis work revealed, through time-of-flight measurements, the forward generation at a moderately high repetition rate of $\approx$0.6 MeV/amu α particles, with relatively low energy dispersion and divergence. It also confirmed the copious hot electron generation predicted by numerical simulations, up to energies of $\sim 50\,\mathrm{MeV}$, measuring maximum electron energies of $\approx$50 MeV. Optical probe interferograms evidenced channel formation across the gas density peak. These measurements have been found in qualitative agreement with the results of 2-D PIC simulations, which served to identify the main processes of laser-driven particle acceleration and plasma dynamics.

The experimental and numerical work conducted during this thesis has shed light on the relatively unexplored problem of ultraintense fs laser pulses interacting with dense gases. On the experimental side, after overcoming various technical challenges, we have developed a methodology and a suite of diagnostics, both suitable for HHR operation. Although still modest in terms of energy, the ions source tested at the VEGA-3 facility is encouraging and thus motivates further developments. These should be guided by our numerical results, notably those of our parametric study, which, despite its reduced 1-D geometry, provided helpful guidelines on how to design gas targets prone to electrostatic shock formation when exposed to femtosecond laser pulses. This study highlights the importance of advances in supersonic gaz nozzle development in the years to come.

Resumen

Las fuentes de iones rápidos generados por láseres intensos son un tema de estudio prometedor para múltiples campos de la investigación. Si bien la aceleración de iones por interacción láser-sólido se ha estudiado exhaustivamente, los plasmas de densidad cuasicrítica (es decir, una densidad de electrones del orden de $10^{21}\,\mathrm{cm}^{-3}$ para una longitud de onda láser de aproximadamente $1\,\mu\mathrm{m}$) han sido poco discutidos, debido a las dificultades relacionadas con la generación controlada de densidades críticas (a partir de un blanco sólido, líquido o gaseoso). Sin embargo, estos plasmas podrían dar lugar a varios mecanismos de aceleración, como la *target normal sheath acceleration* o la aceleración por choques electrotáticos no colisionales (*collisionless shock acceleration* - CSA), así como a la generación de poblaciones de electrones energéticos, llamados superponderomotores.

Esta tesis se enmarca en el desarrollo de fuentes de iones producidas por un láser intenso con una alta tasa de repetición (HTR, por sus siglas en inglés), necesaria para la mayoría de las aplicaciones. Las nuevas instalaciones láser con pulsos del orden del femtosegundo producidos cada segundo, y de muy alta potencia (del orden de un petavatio) e intensidad ($I_L \gtrsim 10^{2}0\,\mathrm{Wcm}^{-2}$) como VEGA-3, Apollon, L4 Aton o BELLA, se adaptan perfectamente a este objetivo. Además, las boquillas de gas de tipo choque (*shock nozzle*) recientemente desarrolladas, conectadas a sistemas de gas de alta presión, se eligen por su compatibilidad con los sistemas láser HTR y debido al fuerte acoplamiento láser-gas al que pueden dar lugar.

En primer lugar, se realizó un estudio paramétrico basado en simulaciones 1-D de tipo *particle-in-cell* (PIC) para comprender la interacción entre un láser intenso y un jet de gas cuasicrítico y no uniforme. Se buscó determinar un conjunto óptimo de parámetros experimentales relacionados con la interacción de un pulso láser $\lambda_L = 0.8\,\mu\mathrm{m}$, $\tau_L = 100$ fs, $I = 10^{20}$ W/cm^2, con un jet de gas cuasicrítico similar al producido por una boquilla de choque no comercial, desarrollada dentro de nuestro grupo de colaboración. Para ello se utilizó el código PIC CALDER desarrollado por el CEA.

Los datos experimentales analizados en esta tesis se obtuvieron durante dos campañas en las instalaciones láser VEGA-2 (200 TW) y VEGA-3 (1 PW), en el CLPU, Univ. Salamanca. La primera tenía como objetivo estudiar el potencial de aceleración de iones de un pulso láser ultraintenso con una duración de femtosegundo interactuando con un jet de gas supersónico. La segunda, que constituyó la campaña principal, permitió destacar, a través de medidas de tiempo de vuelo, la aceleración frontal de partículas α de energía ≈ 0.6 MeV/amu a una tasa de repetición moderada, exhibiendo una energía y una dispersión angular relativamente moderadas. También confirmó la abundante generación de electrones energéticos predicha por simulaciones numéricas, hasta energías de alrededor de 50 MeV. Además, la interferometría reveló la formación de un canal de plasma, que se extendía a ambos lados del pico de densidad del jet de gas. Varias simulaciones en 2-D, realizadas para explicar algunos de estos resultados, están en concordancia cualitativa con las mediciones, lo que permite identificar los mecanismos de aceleración de iones y de electrones, así como describir el fenómeno de formación del canal láser.

El trabajo realizado durante la elaboración de esta tesis ha arrojado luz sobre la física de la interacción entre un pulso láser ultraintenso y un gas denso, una configuración aún poco explorada en el régimen de femtosegundo. Al mismo tiempo, se debieron afrontar numerosos retos técnicos, como el desarrollo de una metodología experimental adaptada, así como de

un conjunto de diagnósticos compatibles con la operación a alta tasa de repetición. Aunque los rendimientos obtenidos en términos de energía iónica pueden considerarse modestos, son alentadores e invitan a perseverar en esta línea de investigación, teniendo en cuenta que las aplicaciones de la interacción láser-gas son numerosas y van desde la producción de radioisótopos médicos hasta estudios de física fundamental. Desde el punto de vista numérico, nuestro estudio de las condiciones más favorables a la aceleración de iones por choque electrostático mediante un pulso de femtosegundo proporciona condiciones óptimas de la interacción láser-gas para la producción de choques electrostáticos, de tal forma que se dejan claros los objetivos experimentales para trabajos futuros con énfasis en la importancia de mejorar las técnicas de fabricación de las boquillas de gas.

Palabras clave: Blanco láser a alta tasa de repetición, Interacción láser-plasma relativista, Aceleración de iones por láser

Contents

Introduction

Scientific context

Plasma physics

In the solid state atoms are located inside a rigid matrix, like an ice cube. By heating solid matter, we obtain a liquid were the atoms can slide over each other, which allows water to fit inside a cup. By heating even more we achieve the gaseous state where the atoms or molecules are independent from one another, e.g. water vapor. If we transfer enough energy to this system, for example by heating it up to tens of thousands of degrees, the electrons separate from the atom nucleus and we obtain a mix of negative and positive charges. This is frequently referred to as the fourth state of matter: a *plasma*. Over 99.9% of the known Universe is composed of matter in the plasma state. At night, we can have a glimpse of our plasma Universe looking at the sky stars and nebulas. The Sun, the source of everything living on our planet, is a sphere of plasma. Plasmas are scarcely found naturally on Earth in lightning storms or polar auroras. The latter are the trace of highly energetic particles coming from the Sun interacting with the Earth's magnetosphere. However, human-created plasmas are constantly around us: from the flat screens of the TVs of the 2000s to tattoo erasing and clinical disinfection devices and neon tubes, as well as in industrial machines used for cutting or welding. Importantly, the search for a clean and inexhaustible source of energy is focused on sustaining, in a controlled way, thermonuclear reactions in deuterium-tritium (DT) plasmas. Two approaches are currently being studied: magnetic confinement fusion (MCF) in which a low-density, hot plasma is confined by magnetic fields inside tokamaks or stellarator devices, and inertial confinement fusion (ICF) whereby a DT capsule is compressed to more than a hundred times the solid density and heated by high-energy lasers.

Plasma physics is the branch of physical studies that investigates the dynamics of systems made of charged particles interacting with self-consistent electric and magnetic fields. The discipline itself has many areas of applications, including space and astrophysics, controlled fusion and accelerator physics.

Laser

The word *laser* is an acronym for Light Amplification by Stimulated Emission of Radiation. A laser is created when a material, such as a gas or a crystal (called the amplifying medium), absorbs energy from an external light or electric current, exciting the electrons to a higher energetic level within the atom. The first laser emitting light in the optical domain ($\lambda = 694.3\,\text{nm}$) was built in 1960 by T. Maiman using a ruby crystal, which is naturally doped with chromium atoms, as an amplifying medium. After being excited, electrons decay to a lower energy state while releasing light particles called photons. The energy of the latter is determined by their wavelength, $\mathcal{E}_X$ and λ_X (where h is the Plank constant and c is the speed of light). Such a deexcitation can occur spontaneously or in an stimulated manner. Stimulated emission is achieved by seeding the gain medium with photons of the desired laser wavelength λ_x. The polarization, frequency, phase and traveling direction of the emitted photons are the same as the seed photon ones, a laser can then be viewed as a light amplifier. The emitted light is described as temporally and spatially coherent.

Coherence allows lasers to be tightly focused and travel large distances while remaining collimated. The latter property is used in lidars to measure distances with high accuracy and create high-resolution 3-D maps that have guided, for example, the helicopter Ingenuity on its flights across Mars [1]. Temporal coherence is exploited to produce femtosecond (10^{-15} s) pulse lasers with a broad frequency spectrum. As plasmas, lasers have invaded our day-to-day life and can be found in printers, optical communication systems, eye surgery devices (to correct myopia), bar code scanners in supermarkets or laser pointers.

In a nutshell, this thesis work is centered on the study of laser-created plasmas from dense gases and one of their main applications nowadays: the production of energetic ion beams.

Ion acceleration by ultra-high intensity (UHI) lasers

The generation of energetic ion sources, with energies in the 10-100 MeV range, is one of the major applications of laser-plasma interactions using ultra-intense short-pulse lasers. The latter were made available thanks to the development of the *chirped pulse amplification* (CPA) technique by D. Strickland and G. Mourou [2] in 1985. As sketched in Fig. 1, the CPA technique is based on temporally stretching the laser pulse using a double-grating system or the group velocity dispersion (GVD) in an optical fiber. The so-called *chirped* pulse has a lower intensity than the original pulse, which allows it to be amplified without damaging the amplifier. The last step consists of re-compressing the temporally-stretched pulse by means of an additional pair of double gratings. Thus, the frequencies that arrive first to the compressor are forced to transit a larger spatial length than those arriving afterwards. This leads the frequencies to overlap spatially, thereby yielding a very intense pulse, temporally compressed down to femtosecond durations.
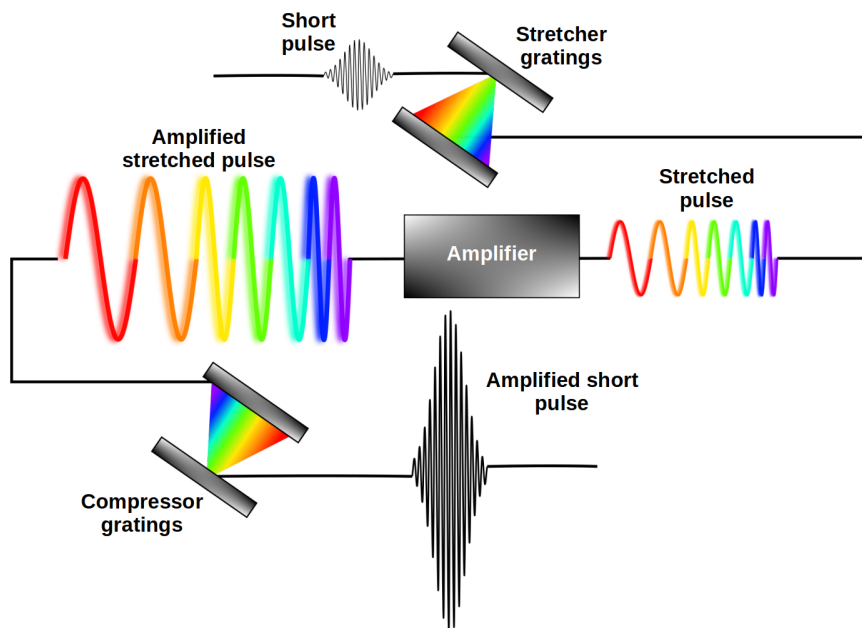
Fig. 1: Chirped pulse amplification (CPA) technique for amplifying short laser pulses.

Nowadays, energetic ion sources are produced using particle accelerators (PAs) that employ electromagnetic fields to drive particles to very high energies. Their accelerating field strength is limited by the breakdown between the electrodes, which obliges these facilities to be quite large and expensive. One of the most famous PAs is the Large Hadron Collider (LHC) [3] located at the European Organization for Nuclear Research (CERN, the french acronym for *Centre Européen pour la Recherche Nucléaire*), at the border between France and Switzerland. However, this PA is huge (it is a 27 km ring) and mostly targeted at fundamental high energy

particle physics research. Most PAs are much smaller and, besides fundamental research, can serve for a large array of applications, including cancer treatment as, for example, the Proton Therapy Center [4] in Orsay, France. Electric fields driven by plasmas can be orders of magnitude higher than those available in conventional PAs, up to TV/m, which could be translated into more compact and cheaper medium scale accelerator facilities.

This thesis is part of a roadmap to develop experimental laser-based platforms for high-repetition-rate (HHR) ion acceleration. Such ion sources can be employed as ultra-fast probing tools in science and industry, such as proton radiography [5] and time-resolved probing of laser-created transient states [6–8]. They can also be used in the creation of warm dense matter [9], the isochoric heating of dense plasmas [11], or the production of radioisotopes and intense neutron sources production, with possible medical spinoffs [10–12]. Most of these applications exploit the unique properties of laser-driven ion beams, notably their short duration, high number density, low emittance, high laminarity and compactness. Some of them (notably in medicine and nuclear physics) nonetheless require substantial progress in terms of repetition rate, which should at least approach that of the laser system being used. The ultimate goal will then to build ion plasma accelerators making the most of the 1 Hz HHR that is envisioned on upcoming petawatt (or multi-petawatt) femtosecond lasers, a repetition rate much higher than that (one shot per hour) accessible on existing higher-energy, subpicosecond systems.

Ion acceleration mechanisms: interaction of a short laser pulse with a near-critical plasma

The search for for ever more energetic and efficient particle sources motivates the investigation of novel acceleration schemes involving new states of matter, target shapes and compositions. The physics of laser-matter interaction is divided into two regimes depending on the transparency or opacity of the irradiated (and ionized) medium. The transition between transparency and opacity occurs at the so-called *critical density* $n_c = 1.11 \times 10^{21}/\lambda_L^2$ [cm^{-3}] where λ_L is the laser wavelength in µm. A medium with a free electron density (once ionized) $n > n_c = 1.74 \times 10^{21}$ cm^{-3} with be opaque to a moderate-intensity laser pulse with wavelength $\lambda_L = 0.8$ µm. This density level is about a hundred times denser than the air that we breathe. Opaque plasmas are know as *overdense plasmas* ($n \gg n_c$) while transparent ones are given the name of *underdense plasmas* ($n \ll n_c$). Solid and liquid targets are typically opaque to the laser. However, the laser interaction with the outer layer of the material can allow for a $1-50\%$ energy transfer to the target electrons accelerating them to $\approx$MeV energies. These fast electrons induce strong ($\approx$ TV/m) charge separation fields over µm scales after propagating through the target and exiting into vacuum. Ions with the higher charge-to-mass ratios, typically protons present as surface organic contaminants, are preferentially accelerated by the sheath electric fields that are set up at the plasma-vacuum interfaces, a process known as Target Normal Sheath Acceleration (TNSA) [13,14].

Solid thin-foil targets are widely used in laser-matter interaction experiments due to their simple fabrication process. A downside of such targets, however, is the production of debris during the interaction, which can damage the optical elements and make HHR operation difficult.

When the medium's density drops strongly below n_c the laser is allowed to propagate inside the material while exciting nonlinear wakefields capable of accelerating electrons to relativistic velocities [15]. These wakefields originate from the strong ponderomotive force exerted, both in the longitudinal and transverse directions, by the laser pulse on the plasma electrons. In particular, the transverse expulsion of the electrons out of the laser's path generates a positively charged plasma channel, in which the ions can be transversely accelerated by a form of Coulomb

explosion [16]. Moreover, the interplay of the laser-induced electron currents inside and outside the channel can give rise to a strong magnetostatic field, which can act as a piston in a decreasing plasma density gradient [17–20]. The experimental generation of multi-MeV ion beams has been reported in this interaction regime, using picosecond lasers [21].

Fewer studies have addressed the case of *near-critical plasmas*, i.e. of electron density approaching the critical density, $n \approx n_c$, due to the technical difficulty of achieving such densities in a controlled and repetitive manner. When $n_e \approx n_c$ UHI laser pulses can propagate significant distances while volumetrically heating the plasma electrons to relativistic temperatures. Near-critical plasmas are predicted to give rise to new ion acceleration regimes combining TNSA and collisionless shock acceleration (CSA) [22–29], as well as enhanced conversion efficiency into hot electrons [30].

This thesis is centered on the study of ion acceleration from UHI lasers interacting with near-critical plasmas. Hereafter, we present the main ion acceleration mechanisms operating during the interaction of an UHI laser pulse with a transparent near-critical target: TNSA, Coulomb explosion, magnetic vortex acceleration (MVA) and collisionless shock acceleration (CSA).

Target normal sheath acceleration (TNSA)

In the late 1980s the generation of protons from solid foils irradiated by ns laser pulses was already linked to the surface electrostatic fields produced by the hot electrons exiting the target [31, 32]. The CPA technique [2] (1985) unveiled the era of terawatt and petawatt lasers reaching on-target intensities $I_L > 10^{18}$ W cm^{-2}. By 1986 proton energies up to a few MeVs were already measured with maximum laser intensities of 10^{18} W cm^{-2} [31], mainly originating from the (non-irradiated) backside of the target. Energy is transported there by the MeV-electrons energized by the laser at the target's front side. In 1997 protons of up to 10 MeV, issued from the interaction of a 10^{19} W cm^{-2} intensity, ps duration laser pulse with a solid target, were successfully characterized [33]. In the early 2000s the term Target Normal Sheath Acceleration (TNSA) [13, 14] was coined to refer to this (not-so new) ion acceleration scheme linked to the general and long-known process of plasma expansion driven by hot electrons [34, 35]. When exiting into vacuum, hot electrons can induce strong charge-separation fields at the target-vacuum interfaces, capable of accelerating the surface ions (mainly protons present as organic impurities at the surfaces of the target) to energies of a few tens of MeV [36, 37]. The adjective *normal* comes from the fact that ions are accelerated perpendicularly to the target rear surface [38, 39].

Figure 2 is a sketch of TNSA occurring at the rear plasma-vacuum interface of a near-critical non-uniform plasma slab. In this case, the laser has transferred part of its energy to the up-ramp electrons through a non-linear wakefield process described in Chapter 3. The energized electrons have then crossed the plasma slab and exited into vacuum, giving rise to the longitudinal electrostatic field E_x, that subsequently accelerates the local ions in the forward direction (see orange arrow).

The simplest description of TNSA can be obtained considering a semi-infinite plasma slab, such as the one in the inset of Fig. 2, expanding into vacuum in a self-similar way [34, 35]. The cold ions are modeled as a fluid (see Chapter 1) that exhibits, at $t = 0$, a sharp boundary at $x = 0$ and a constant density n_i at $x \leq 0$. The plasma is supposed to expand after the electrons have thermalized, and thus obey a Boltzmann distribution

$$n_e(\phi) = n_{e,0} \exp\left(\frac{e\phi}{k_B T_e}\right), \tag{0.1}$$

where ϕ is the electrostatic potential, n_e the electron density, $n_{e,0}$ the unperturbed electron
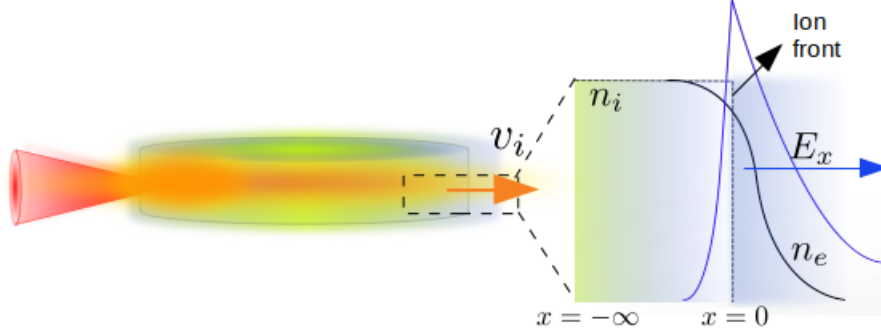
Fig. 2: Sketch of TNSA in a near-critical plasma slab. The orange arrow shows the preferential direction for ion acceleration (hereafter, v_i stands for ion velocity).

density, k_B the Boltzmann constant and T_e the electron temperature. Assuming quasineutrality, i.e. $n_e \approx Z^* n_i$, one can obtain expressions for the electron density n_e, the ion velocity v_i and the electric field E_x with respect to space and time

$$
\begin{aligned}
\frac{\partial \phi}{\partial x} &= \frac{k_B T_e}{e} \frac{\nabla n_e}{n_e} \\
n_\alpha &\approx n_{\alpha,0} \exp\left(-\frac{x}{C_s t} - 1\right), \alpha = e,i \\
v_i &= C_s + \frac{x}{t} \\
E_x &= -\frac{\partial \phi}{\partial x} = \frac{k_B T_e}{e C_s t},
\end{aligned}
\tag{0.2}
$$

where $C_s = \sqrt{Z^* k_B T_e / m_i}$ is the ion sound speed. Quasineutrality breaks down at the ion front, see inset of Fig. 2, where the density scale length $L_n = (\partial n / \partial x)/n$ becomes equal to the Debye length $\lambda_{De} = \lambda_0 (n_{e,0}/n_e)^{1/2}$, the distance at which the plasma can not efficiently screen the charge separation field (see Chapter 1). Here $\lambda_0 = \sqrt{k_B T_e/(4\pi n_{e,0} e^2)}$ is the unperturbed electron Debye length. The ion velocity and electrostatic field at the ion front write

$$
\begin{aligned}
v_f(t) &\approx 2C_s \ln\left(2\omega_{pi} t\right), \\
E_f(t) &\approx 2\sqrt{\frac{n_{e,0} k_B T_e}{\epsilon_0}} \left(\omega_{pi} t\right)^{-1}.
\end{aligned}
\tag{0.3}
$$

where $\omega_{pi} = C_s/\lambda_{De,0}$ is the ion plasma frequency (see Chapter 1).

Mora [40] obtained more accurate expressions based on Lagrangian simulations of the same system composed of Boltzmannian electrons, electron and ion densities coupled by the Poisson equation and the fluid equations of continuity and motion for the ions:

$$
\begin{aligned}
v_f(\tau) &= 2C_s \ln\left(\tau + \sqrt{\tau^2 + 1}\right), \\
E_f(t) &\approx \frac{2E_0}{(2e_N + \omega_{pi}^2 t^2)^{1/2}},
\end{aligned}
\tag{0.4}
$$

where $\tau = \omega_{pi} t/\sqrt{2e_N}$, $e_N \approx 2.7182$ is Euler's number and $E_0 = \sqrt{n_{e,0} k_B T_e/\epsilon_0}$. Fig. 3a shows the corresponding structure of the ion front at times $\omega_{pi} t = 50$ and $\omega_{pi} t = 100$. For comparison, the dotted line is the self-similar solution obtained using Eqs. 0.2. Figure 3b shows the electric field at $\omega_{pi} t = 50$. The electric field peaks at $x/C_s t \approx 5.59$, that is, at the location of the ion front. The dotted line corresponds again to the self-similar solution. Note that, at late times $\omega_{pi} t \gg 1$, E_f is twice the self-similar field given in Eq. 0.2.
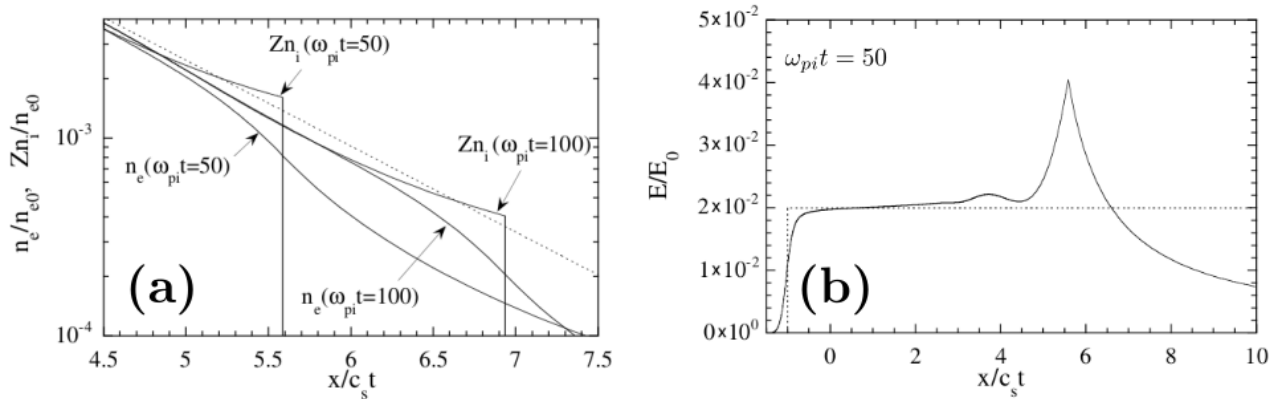
Fig. 3: (a) Structure of the ion front at times $\omega_{pi}t = 50$ and $\omega_{pi}t = 100$. The dotted line is the usual self-similar solution obtained using Eqs. 0.2. (b) Electric field at $\omega_{pi}t = 50$, the ion front is located at $x/C_s t \approx 5.59$. Figures extracted from Ref. [40].

Up to now proton beams with broad energy spectra and cutoff energy up to 85 MeV [36] have been produced via TNSA. Unlike the near-critical target sketched in Fig. 2, TNSA is generally associated with laser-solid interactions, as a result of the hot electron cloud traveling across the entire target and exiting into vacuum through the sharp plasma boundary. However, one must bear in mind that any strong density discontinuity within the plasma will cause the energized electrons to induce charge-separation fields capable of accelerating ions. Therefore, TNSA in non-uniform plasmas can arise both from the charge separation field at the plasma-vacuum interface as well as from the electron density discontinuities within the ionized plasma. Note also that the proton-rich contaminant layers which often provide the source of the fastest ions in solid targets do not exist in gas targets. Although protons can be present as impurities (e.g. from the ablated gas nozzle), the ions experiencing acceleration are those making up the whole gas target.

Coulomb explosion

The transverse ponderomotive force of the laser pulse can create a channel partially depleted of electrons. The resulting charge-separation field tends to pull back the electrons while setting to transverse outward motion the local ions. This process, similar to Coulomb explosion, is sketched in Fig. 4.
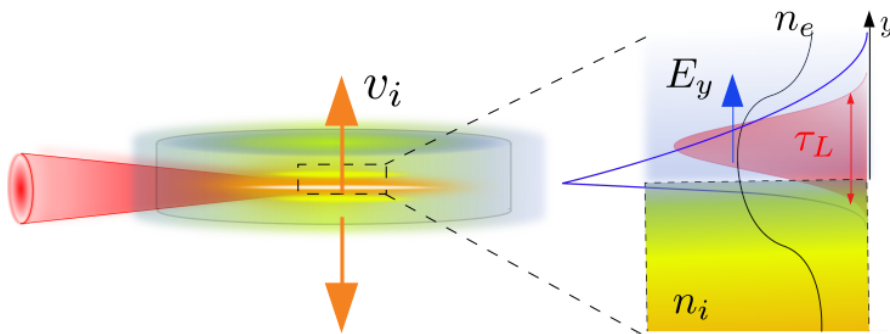
Fig. 4: Sketch of CE in a near-critical plasma slab.

A simple estimate of the ion energy gain can be obtained upon assuming that the laser pulse is long enough that a steady-state channel is formed. The transverse electrostatic field,

$\mathbf{E}_\perp$, that acts on the electron fluid is then given by (see Chapter 1):

$$e\mathbf{E}_\perp = \mathbf{f}_{\text{pond}} = -\partial_\perp \gamma_e m_e c^2 \,, \tag{0.5}$$

where $\gamma_e = \sqrt{1 + a(y)^2/2}$ is the mean electron Lorentz factor, $a = eE_L/m_e c\omega$, $\mathbf{f}_{\text{pond}}$ the laser's transverse ponderomotive force, ω_0 the laser frequency, c the velocity of light, m_e the electron mass and e the elementary charge. The maximum ion energy gain is then given by

$$\mathcal{E}_{i,\max} = Z^* e \int_0^\infty dy E_\perp = Z^*[\gamma_e(0) - 1]m_e c^2 \simeq Z^* \frac{a_0}{\sqrt{2}} m_e c^2 \,, \tag{0.6}$$

where Z^* is the ion charge state. It has been assumed that the laser amplitude $a_0 \gg 1$ and that the accelerating field is sustained over the channel-crossing time of the ions.

Magnetic vortex acceleration (MVA)

The electrons accelerated in the forward direction within a plasma channel create an azimuthal magnetostatic field that is shielded by a backward electron stream flowing along the channel walls. When reaching a region of decreasing density, the plasma channel tends to increase in transverse size, creating a an increasingly large magnetic cavity, commonly referred to as a magnetic vortex. The magnetic pressure experienced by the plasma electrons at the longitudinal front of the cavity generates an electrostatic field that, in turn, accelerates the ions located on axis, a process known as *magnetic vortex acceleration* (MVA, see Fig. 5).
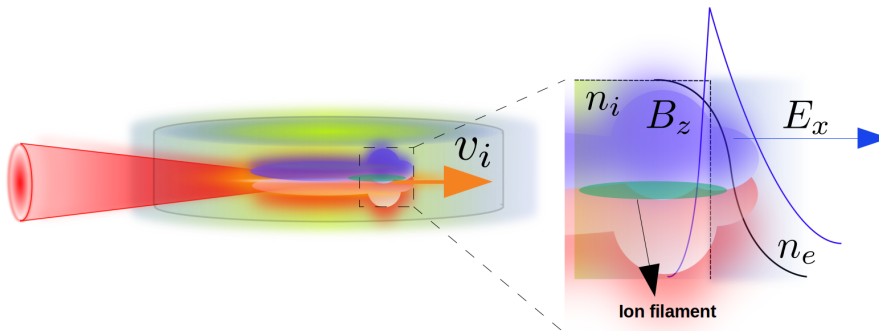
Fig. 5: Sketch of MVA in a near-critical plasma slab.

Bulanov [18] obtained, using particle-in-cell (PIC) simulations (see Chapter 3), an optimum near-critical plasma profile regarding proton acceleration with a TW laser. The latter is a micrometric near-critical plasma slab surrounded by low density wings which could be obtained by exploding a solid foil with a secondary laser or with the laser pedestal (see Appendix A) [41].

Optimum acceleration via the MVA scheme is achieved when matching the laser focal spot size with the channel diameter, in order to avoid laser filamentation (see Chapter 1). The laser pulse energy should also be completely absorbed near the rear side of the target [20, 42]. The optimum laser pulse amplitude a_0^* after self-focusing (see Chapter 1) and the self-focusing channel diameter D_{sf}^* write [42]:

$$a_0^* = \left(8\pi \frac{P_L}{P_c} \frac{n_e}{n_c}\right)^{1/3,}$$
$$D_{sf}^* = \frac{2c}{\omega_{pe}} \sqrt{a_0^*} = \frac{\lambda_L}{\pi} \sqrt{a_0^* \frac{n_c}{n_e}} \,, \tag{0.7}$$

where ω_{pe} is the electron plasma frequency, P_L is the laser power and $P_c \approx 17 n_c/n_e \approx 170$ GW [43] is the critical power above which laser self-focusing can occur and ω_{pe} is the electron plasma

frequency (see Chapter 1). Note that if the laser focal spot is fixed, one could still tune the electron density to reach the optimum self-focusing channel diameter. In general, the tightest laser focus and the shortest pulse duration provide the highest proton energies, according to numerical and (scarce) experimental results [14]. Considering our experimental parameters: $P_L = 1\,\mathrm{PW}$, $n_e = 10^{20}\ \mathrm{cm^{-3}}$ and $n_c = 1.73 \times 10^{21}\ \mathrm{cm^{-3}}$ for a $\lambda_L = 0.8\,\mathrm{\mu m}$ one obtains $a_0^* = 1.74$ and $D_{sf}^* = 1.3\,\mathrm{\mu m}$, ten times smaller than the minimum focal spot diameter that can be achieved $D_L \approx 15\,\mathrm{\mu m}$ FWHM (see Chapter 4). The laser is then likely to filament unlike what occurs in the optimum MVA scenario.

Collisionless shock acceleration (CSA)

This ion acceleration mechanism relies on the electrostatic potential barrier that is created at the boundary between two plasma regions with different temperatures, densities or velocities, called a *collisionless electrostatic shock* [44–47]. Our experimental scenario (as reproduced by PIC simulation) is better described by a density discontinuity (since the hot electrons can generally extend, to some degree, beyond the density gradient). Figure 6 depicts the case of two the shock wave triggered at the interface of two plasmas of different densities.
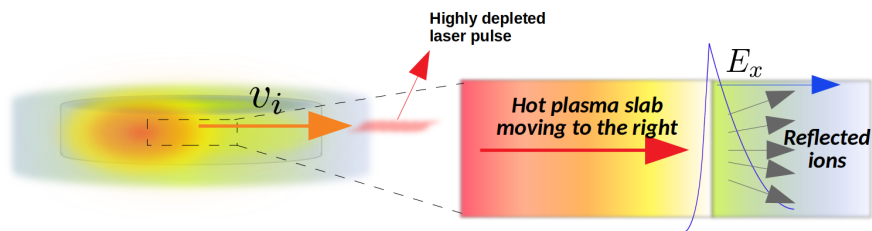
Fig. 6: Sketch of CSA in a near-critical plasma slab.

In this example, the expansion of the left plasma into the right one at velocity v_s can give rise to forward ion reflection at a velocity equal to twice the shock velocity expressed as $2v_s - v_0$ in the lab frame. Here v_s and v_0 are the lab frame shock and incoming ion velocities, respectively. These shocks can be triggered in several ways: by applying a laser piston to the overcritical boundary of a uniform overcritical plasma [48, 49]; or in partially transparent plasmas where strong electron pressure gradients, with scale lengths comparable with the local Debye length λ_{De}, and/or laser-driven ion acceleration can trigger shock formation. This thesis work is particularly interested in the shocks triggered in plasmas (partially) transparent to the laser light, as a result of the strong electron pressure gradients and laser-driven ion pre-acceleration [30, 44–47]. CSA is expected to generate ion energy spectra relatively more peaked than those, typically exponentially decaying, produced through TNSA [50].

Figures 7a and b illustrate an electrostatic shock wave triggered in a decreasing plasma density profile of experimental relevance, as described by a 1-D PIC simulation (see Chapter 3). Figure 7a plots the (x, p_x) ion phase space while Fig. 7b plots the spatial profile of the electrostatic potential at the same time. The shock front, located at $x \simeq 1200\,\mathrm{\mu m}$, is associated with a sharp increase in the electrostatic potential. It propagates at $v_s \simeq 0.15c$ in the laboratory frame and reflects part of the upstream ions to $v_r \simeq 0.25c$. The far-upstream ions have a finite velocity ($v_0 \sim 0.05c$) because of the large-scale, relatively uniform TNSA-type field induced in the decreasing density profile. The velocity of the reflected ions is consistent with the prediction $v_r = 2v_s - v_0 \simeq 0.3 - 0.05 \simeq 0.25c$.
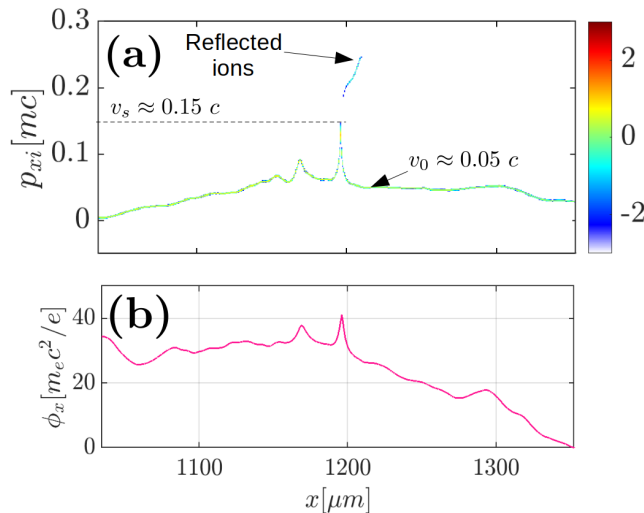
Fig. 7: (a) Electrostatic shock formation as seen in the ion (x,p_x) phase space obtained by numerically solving the Vlasov equation. (b) Corresponding electrostatic potential ϕ_x.

Quest for producing near-critical targets: recent experimental results

The use of near-critical plasmas in the laboratory is made difficult by the need to achieve well controlled, reproducible density profiles that do not lead to a premature absorption of the laser pulse. The experiments referred to hereafter are summarized in Table 1.

Previous experimental attempts in this direction have resorted to the use of double-layer targets composed of a near-critical layer (e.g. carbon nanotubes) and a thin diamond-like solid layer [51–54] with $\lambda_L = 0.8\,\mu m$ fs lasers. The ion acceleration mechanism was identified to be a mix of radiation pressure acceleration (RPA) [55] and TNSA. In 2015 Bin *et al.,* [51] measured C^{6+} ion spectra, which exhibited a peak at 15 MeV/amu when using a circularly polarized laser pulse, at the Gemini laser ($E = 4\,J$, $\tau_L = 50\,fs$) located at the Rutherford Appleton Laboratory (RAL) [56]. Afterwards, in 2018, the same experimental group measured protons up to 30 MeV and C^{6+} ions up to 13 MeV/amu with monotonically decaying spectra using, this time, the linearly polarized Gemini laser [52]. Finally, Ma *et al.,* [53] measured protons up to 60 MeV and C^{6+} ions up to 50 MeV/amu at the Corels laser ($E = 9\,J$, $\tau_L = 33\,fs$) facility in Korea [57].

In 2008 Romagnani *et al.,* [22] captured, for the first time, the expanding front of a collisionless shock using proton radiography. The experiment was performed at the LULI2000 facility ($E = 60\,J$, $\tau_L = 470\,ps$) with a pulse duration $\tau_L \approx 470\,ps$ and a maximum on-target intensity $I \approx 10^{15}\,W\,cm^{-2}$. The target was a $25\,\mu m$ thick tungsten foil and the expanding plasma had an approximate electron density $n_e \approx 10^{15}\,cm^{-3}$.

Near-critical targets have also been obtained by exploding solid foils by a ns pulse before the arrival of the ps pulse with $\lambda_L \approx 1\,\mu m$ [58, 59, 66]. Using 100 nm mylar foils Antici *et al.,* [58] (2017) measured protons up to 45 MeV, exhibiting a monotonically decaying spectra, and found low density CSA (LDCSA) [67] to be the main ion acceleration mechanism. The experiment was performed at the TITAN laser facility ($E = 180\,J$, $\tau_L = 700\,fs$) located at the Lawrence Livermore National Laboratory (LLNL). In 2018, Pak *et al.,* [59] reported, for the first time, the measurement of proton and C^{6+} ion beams with narrow energy spreads $\Delta E/E \approx 10\% - 20\%$ with $\approx 10^9$ particles per sr. This experiment was also conducted at the TITAN laser facility where exploded 500 nm mylar foils were used as targets and CSA was found to be the main acceleration mechanism.

Moderate-density gas jets irradiated by CO_2 ($\lambda_L = 10\,\mu m$) laser pulses [60, 68, 69], where the

Author	Date	Facility	Laser characteristics	Target	Observations
Bin *et al.* [51]	2015	Gemini	$\lambda_L = 800\,\mathrm{nm}$, $I_{max} = 2 \times 10^{20}\,\mathrm{W.cm^{-2}}$ ($a_0 = 9.6$) $E = 4\,\mathrm{J}$, $\tau_L = 50\,\mathrm{fs}$ $D_L = 3.5\,\mu\mathrm{m}$, circular polarization	Double layer target: C nanotubes + diamond-like solid layer	C^{6+} ions up to $20\,\mathrm{MeV/amu}$ Slightly peaked spectra RPA
Bin *et al.* [52]	2018	Gemini	$\lambda_L = 800\,\mathrm{nm}$, $I_{max} = 2 \times 10^{20}\,\mathrm{W.cm^{-2}}$ ($a_0 = 9.6$) $E = 4\,\mathrm{J}$, $\tau_L = 50\,\mathrm{fs}$ $D_L = 3.5\,\mu\mathrm{m}$, linear polarization	Double layer target: C nanotubes + diamond-like solid layer	Protons up to $30\,\mathrm{MeV/amu}$ C^{6+} ions up to $60\,\mathrm{MeV/amu}$ Mononically decaying spectra RPA + TNSA
Ma *et al.* [53]	2019	Corels	$\lambda_L = 800\,\mathrm{nm}$, $I_{max} = 5 \times 10^{20}\,\mathrm{W.cm^{-2}}$ ($a_0 = 15.2$) $E = 9\,\mathrm{J}$, $\tau_L = 33\,\mathrm{fs}$ $D_L = 4.5\,\mu\mathrm{m}$, linear polarization	Double layer target: C nanotubes + diamond-like solid layer	Protons up to $60\,\mathrm{MeV}$ C^{6+} ions up to $50\,\mathrm{MeV/amu}$ Mononically decaying spectra RPA + TNSA
Romagnani *et al.* [22]	2008	LULI PICO2000	$\lambda_L = 1054\,\mathrm{nm}$, $I_{max} = 5 \times 10^{15}\,\mathrm{W.cm^{-2}}$ ($a_0 = 0.02$) $E = 60\,\mathrm{J}$, $\tau_L = 470\,\mathrm{ps}$ $D_L = 15\,\mu\mathrm{m}$	$25\,\mu\mathrm{m}$ tungsten foils	Shock structures in an expanding plasma via proton radiography ($n_e \approx 10^{15}\,\mathrm{cm^{-3}}$)
Antici *et al.* [58]	2017	TITAN	$\lambda_L = 1054\,\mathrm{nm}$, $I_{max} = 2 \times 10^{20}\,\mathrm{W.cm^{-2}}$ ($a_0 = 12.7$) $E = 180\,\mathrm{J}$, $\tau_L = 700\,\mathrm{fs}$ $D_L = 7\,\mu\mathrm{m}$, linear polarization + LP beam	$100\,\mathrm{nm}$ mylar foil	Protons up to $45\,\mathrm{MeV}$ (Spectrometer) Monotonically decaying spectra Forward LDCSA
Pak *et al.* [59]	2018	TITAN	$\lambda_L = 1054\,\mathrm{nm}$, $I_{max} = 2 \times 10^{20}\,\mathrm{W.cm^{-2}}$ ($a_0 = 12.7$) $E = 180\,\mathrm{J}$, $\tau_L = 700\,\mathrm{fs}$ $D_L = 7\,\mu\mathrm{m}$, linear polarization + LP beam	$500\,\mathrm{nm}$ mylar foil	Protons and C^{6+} ions (ToF) $\Delta E/E \simeq 10 - 20\%$ Forward CSA
Habergerger *et al.* [60]	2012	Neptune	$\lambda_L = 10\,\mu\mathrm{m}$, $I_{max} < 6.5 \times 10^{16}\,\mathrm{W.cm^{-2}}$ ($a_0 = 2.1$) $E = 60\,\mathrm{J}$, $\tau_L = 100\,\mathrm{ps}$ (train of 3 ps pulses) $D_L = 60\,\mu\mathrm{m}$, linear polarization	Laval gas nozzle H_2 gas jet, $n_e \simeq 4n_c$	Protons up to $20\,\mathrm{MeV}$ (CR-39) $\Delta E/E \simeq 1\%$, low emittance Forward CSA
Sylla *et al.* [61]	2013	LOA *Salle Jaune*	$\lambda_L = 800\,\mathrm{nm}$, $I_{max} = 10^{19}\,\mathrm{W.cm^{-2}}$ ($a_0 = 2.1$) $E = 810\,\mathrm{mJ}$, $\tau_L = 35\,\mathrm{fs}$ $D_L = 20\,\mu\mathrm{m}$, linear polarization	Laval gas nozzle He and a small fraction of H_2 $n_e \approx 0.2\,n_c$	He^+ ions up to $250\,\mathrm{keV}$ measured in the transverse direction
Chen *et al.* [62]	2017	TITAN	$\lambda_L = 1054\,\mathrm{nm}$, $I_{max} = 2.2 \times 10^{19}\,\mathrm{W.cm^{-2}}$ ($a_0 = 4.2$) $E = 210\,\mathrm{J}$, $\tau_L = 5\,\mathrm{ps}$ $D_L = 10\,\mu\mathrm{m}$	Laval gas nozzle H_2 gas jet, $n_e \simeq 0.2n_c$	Protons up to $600\,\mathrm{keV}$ (ToF) $\Delta E/E \simeq 2\%$ Forward CSA
Puyuelo-Valdés *et al.* [63]	2019	LULI PICO2000	$\lambda_L = 1054\,\mathrm{nm}$, $I_{max} = 5 \times 10^{19}\,\mathrm{W.cm^{-2}}$ ($a_0 = 6.3$) $E = 60\,\mathrm{J}$, $\tau_L = 250\,\mathrm{ps}$ $D_L = 12\,\mu\mathrm{m}$	Laval gas nozzle H_2 gas jet, $n_e \simeq 2.3\,n_c$ Modified by the laser ASE	Protons up to $6\,\mathrm{MeV}$ (TP + IP TR) Slightly peaked spectra Forward HB [64]
Singh *et al.* [65]	2020	Corels	$\lambda_L = 800\,\mathrm{nm}$, $I_{max} = 10^{20}\,\mathrm{W.cm^{-2}}$ ($a_0 = 6.8$) $\tau_L = 30\,\mathrm{fs}$, linear polarization	Laval gas nozzle He + small fraction of H_2, $n_e \simeq 0.2\,n_c$	First experiment in the PW regime He^{2+} ions up to $750\,\mathrm{keV}$ (TP) measured in the transverse direction Exponential decaying spectra Transverse CSA

Tab. 1: Published experimental works on ion acceleration from near-critical plasma targets. The acronyms used in the table are: time of flight (ToF), Thomson parabola (TP), long pulse (LP), imaging plate of the type TR (IP TR), amplified spontaneous emission (ASE) and hole boring (HB).

critical density constraint is eased ($n_c \propto \lambda_L^{-2}$), have also been employed and the laser pedestal has been used to sculpt the gas up-ramp into a steep density front [62,63]. In 2012 Haberberger *et al.,* [60] demonstrated CSA-produced proton beams up to 20 MeV with an extremely narrow energy spread $\Delta E/E \approx 1\%$ as well as a low emittance. A pure H_2 gas jet with $n_e \approx 4\ n_c$ was used as target and the experiment was carried out at UCLA's Neptune laser, using a train of 3 ps long laser pulses.

The advent of new high-intensity high-repetition-rate (HRR) facilities like Apollon (France), VEGA-3 (Spain), L4 Aton (ELI Beamlines, Czech Republic) or BELLA iP2 (USA) drives the application of this ion acceleration scheme using high-density gas-jets, a debris-free targetry compatible to HHR operation. Pioneer experiments have been conducted both in the TW [61,70] and the PW [65] regimes. In 2013 Sylla [61] reported on the transverse acceleration of He^+ ions up to 250 keV from a pure He gas with $n_e \simeq 0.2 n_c$ delivered by a supersonic conical nozzle and irradiated by LOA's Salle Jaune laser ($E_L = 0.8\,J$, $\tau_L = 35\,fs$). Chen *et al.,* [62] measured protons up to 600 keV using the TITAN laser and a Laval nozzle with pure hydrogen gas ($n_e \approx 2.5\ n_c$). The fast protons were measured in the forward direction and had a low energy spread $\Delta E/E \approx 2\%$. CSA was pointed out as the ion acceleration mechanism at place. Puyuelo-Valdés *et al.,* [63] measured protons up to 6 MeV with an slightly peaked spectra in the PICO2000 laser facility located at LULI. They used a pure hydrogen gas jet with and a Laval nozzle and $n_e \approx 2.3\ n_c$. Hole boring [64] was identified as the main acceleration mechanism. Finally, Singh *et al.,* [65] performed the first experiment in the PW regime at the Corels laser facility using as well a Laval nozzle and a gas mixture composed of He and a small fraction of H_2 with $n_e \approx 0.2\ n_c$. They measured protons and He^{2+} ions up to 750 keV, characterized by an exponentially decaying spectra, accelerated in the transverse direction through mass-dependent radial CSA.

This thesis work is centered on the development of an experimental platform for laser-driven HRR production of ion beams from high-density gas targets. We chose gases since they are a naturally debris-free targetry and can be rapidly replenished at the laser focus before each shot. Femtosecond laser facilities were chosen to drive the plasma fields owing to their possibly HRR. Finally, to ensure a strong laser-gas coupling we worked with high-density near-critical gas targets with $n_e \approx 0.1\ n_c$. Such near-critical gas targets were produced by connecting a high-pressure gas system to a shock nozzle (see Chapter 2).

Presentation of the manuscript

This thesis manuscript is organized as follows.

Chapter 1 introduces the theoretical concepts involved in the interaction of a high-intensity laser pulse with a near-critical density target. It also presents the main numerical tool used during this thesis, the Particle-in-Cell (PIC) method, as well a description of solitary waves and electrostatic shock structures.

Chapter 2 discusses the operation and characterization of high pressure gas targetry systems and the shock nozzles that were used during the experiments detailed in Chapter 4. Since current nozzle fabrication techniques cannot produce identical nozzle batches, each nozzle needs to be characterized thoroughly to select its experimental working points. This Chapter presents two nozzle characterization campaigns performed in preparation for the experiments. Finally, we describe the performance of the high pressure gas system during high-intensity laser shots. The shot-to-shot laser induced nozzle damage is discussed in detail, shedding light on the advantages, as well the operational difficulties that these new targetry systems entail. The author performed and analyzed both nozzle characterization campaigns described in this Chapter.

Chapter 3 presents a 1-D numerical PIC study which aims at understanding collisionless

electrostatic shock (CES) formation in transparent plasmas with density profiles akin to those explored experimentally. Such CES result from the strong electron pressure gradients together with laser-driven ion pre-acceleration. We tackle the problem under our experimental conditions [a] considering a pure nitrogen gas jet produced from a shock nozzle. The author conducted and analyzed all the simulations detailed in this Chapter.

Chapter 4 summarizes the results from two experimental campaigns on ion acceleration from near-critical gaseous targets: i) the VEGA-2 200 TW (CLPU, Spain) laser campaign (2018), which was the first experiment conducted by our research group in such subject and ii) the VEGA-3 laser (CLPU, Spain) campaign conducted in the PW regime in 2021. The VEGA-2 experiment was performed before this thesis work started. However, the author was already strongly involved in all the experimental activities including fielding of diagnostics and data analysis. During the VEGA-3 experiment, at the core of this thesis work, the author took the leading role in coordinating the design, realization and data analysis, which was conducted together with an international group of collaborators.

Chapter 5 details a 2-D PIC simulation performed to explain the experimental observations in pure He targets during the VEGA-3 campaign. Specifically, we succeeded in reproducing the experimental laser channeling through the gas target as well as the angular distribution of low energy electrons and off-axis ions (up to $\approx 6\,\text{MeV}$ α particles), deviation linked to the magnetic field produced by the electron return current in the plasma-vacuum interface. Finally, we also observed radial CES from the transverse expansion of the PIC channel, which accelerates α particles up to $\approx 7\,\text{MeV}$. The author performed and analyzed all the 2-D simulations discussed in this Chapter.

Finally, a series of conclusions and perspectives drawn from the thesis global outcomes are summarized at the end of the manuscript.

For a reader who is specifically interested in the operation of novel gaseous targets and their experimental realization, the author recommends centering its first reading in **Chapter 2**, to have a general idea of the technical advantages and difficulties of these targets. Afterwards, **Chapter 4** could shed some light on the experimental possibilities of these high density gas systems, as well as on the challenges that experimentalists must overcome in the near future.

If the reader is more keen on the physics of ultra-high intensity lasers interacting with near-critical targets, the author recommends to first read **Chapter 1**, where are reviewed the theoretical concepts involved in the cited physics, and then dive into **Chapter 3** to understand the parameters that play a key role in the laser-target interaction, in a simplified 1-D geometry. Afterwards, a brief reading of the summary of experimental results given in **Chapter 4** is needed to comprehend the experimental conditions that were replicated in the 2-D PIC simulations discussed in **Chapter 5**.

---

[a] $\lambda_L = 800\,\text{nm}$, $I_{max.} \approx 10^{20}\ \text{W}\,\text{cm}^{-2}$ ($a_0 \approx 7$), $E \approx 18\,\text{J}$, $\tau_L \approx 100\,\text{fs}$ and $D_L \approx 15\,\text{µm}$ FHWM

Chapter 1

<div style="text-align: right">

Theoretical framework

</div>

1.1   Introduction

This chapter briefly introduces the theoretical concepts and numerical tools needed to describe the interaction of a high-intensity laser pulse with a target of near-critical density.

Section 1.2 discusses the collective phenomena occurring in plasmas that are governed by the long range interactions of Coulomb electric forces between charged particles. Sections 1.3 and 1.4 summarize the kinetic and fluid plasma descriptions, respectively, as well as an introduction to the generation of non-magnetized waves in plasmas. Section 1.5 recapitulates a selection of laser-plasma interaction physics notions including the main laser-plasma interaction simulation tool used along this thesis: the Particle-in-Cell (PIC) method. Finally, Section 1.6 describes the propagation of solitary waves in plasmas, also called *solitons*, considering initially cold ions and hot electrons in equilibrium as well as the transition of the system into an electrostatic shock structure by considering particle trapping. The Section finishes with the description of the so-called *supercritical shocks* where particle reflection acts as an extra energy dissipation mechanism.

1.2   Collective behavior in plasmas

1.2.1   Debye shielding

A plasma is an ionized medium where atoms are partially or completely ionized and coexist with free electrons and ions of various degrees of charge. A plasma behaves, essentially, in a collective manner in which the charged particles create long-range fields which in turn govern their dynamics. In a (non-relativistic) plasma, charged particles mainly interact through long-range Coulomb electric forces, scaling as $\mathcal{F}_{\mathcal{C}} \propto 1/r^2$, while small scale charge fluctuations are effectively screened. Considering a test particle with charge $q_T > 0$ and infinite mass located at $r = 0$ within an infinite uniform plasma. The test particle will repel all other ions and attract electrons creating a shielding cloud that tends to cancel its own charge [71]. After a certain time electrons and ions will reach the equilibrium within their same species and can be described by Boltzmann distributions: $n_e = n_0\exp(-e\phi/T_e)$ and $n_i = n_0\exp(-e\phi/T_i)$ where each density becomes n_0 at large distances from the test particle. We can then define the electron and ion Debye lengths as

$$\lambda_{De,i} = \sqrt{\frac{k_B T_{e,i}}{4\pi n_0 e^2}} \, .$$ (1.1)

A plasma therefore only tolerates small variations from electrical neutrality expressed as:

$$-n_e e + \sum_i n_i q_i \approx 0.$$ (1.2)

defining the final range of the test particle potential. Departing from a non-equilibrium state the electrons will move and shield the ion potential. Electrons can ensure charge quasineutrality only at distances larger than the *Debye length* λ_{De}. The sphere with a radius equal to λ_{De} is called the *Debye sphere*. The number of electrons inside the *Debye sphere* is:

$$N_{De} = \frac{4}{3}\pi n_e \lambda_{De}^3,$$ (1.3)

where $n_e \lambda_{De}^3 \propto T_e^{3/2}/n_e^{1/2}$ is the so-called *plasma parameter*. The time scale for plasma neutrality is ω_{pe}^{-1}, where $\omega_{pe} = \sqrt{\frac{4\pi n_e e^2}{m_e}}$ is the electron plasma frequency, which is discussed in Section 1.4. Supposing a plasma in equilibrium described following a fluid approach the Debye length and

electron plasma frequency are linked through the so-called thermal electron velocity: $\lambda_{De}\omega_{pe}^{-1} = v_{Te}$.

1.2.2 Plasma coupling and degeneracy parameters

The coupling parameter Γ is defined as the ratio of the Coulomb energy over the kinetic energy:

$$\Gamma = \frac{<E_p>}{<E_k>} = \frac{e^2}{4\pi\epsilon_0 k_B T_e}\sqrt[3]{\frac{4\pi n_e}{3}}. \tag{1.4}$$

It measures the strength of *ee* correlations or *coupling* in the plasma medium. When $\Gamma << 1$ the plasma is labeled as *weakly coupled*, since the kinetic energy dominates over the electrostatic potential energy. This is the case of the plasmas studied during this thesis' work.

The plasma degeneracy parameter is described as:

$$\Theta = \frac{k_B T_e}{E_F}, \tag{1.5}$$

where $k_B T_e$ is the thermal energy and E_F is the Fermi energy. A plasma is said to be *degenerate* is $\Theta \ll 1$. In this case quantum effects need to be taken into account to describe the dynamics of the electrons.

1.3 The Vlasov-Landau description of a plasma

The plasmas encountered during this thesis work satisfy $n_e\lambda_{De}^3 >> 1$ and $\Gamma \ll 1$ for both electrons and ions. Hence, the charged particles' trajectories are governed by the collective electromagnetic fields together with small-angle (or large impact parameter) collisions inside the Debye sphere. Such uncorrelated plasmas can be described by a one-particle distribution function $f_\alpha(\mathbf{r},\mathbf{p},t)$ for each α species.

The latter specifies the probability of finding a particle within the $\Delta\mathbf{r}\Delta\mathbf{p}$ volume around $(\mathbf{r},\mathbf{p})$ at a given time t. The evolution of f_α is governed by the Vlasov-Landau equation

$$\frac{\partial f_\alpha}{\partial t} + \mathbf{v} \cdot \frac{\partial f_\alpha}{\partial \mathbf{r}} + q_\alpha\left(\mathbf{E} + \frac{\mathbf{v} \times \mathbf{B}}{c}\right)\frac{\partial f_\alpha}{\partial \mathbf{p}} = \left(\frac{\partial f}{\partial t}\right)_c. \tag{1.6}$$

The right hand side (r.h.s.) stands for the small-angle elastic collisions. Other processes can be added such as inelastic collisions and field ionization. The macroscopic electric field $\mathbf{E}$ and magnetic field $\mathbf{B}$ are described by the Maxwell's equations:

$$\nabla \cdot \mathbf{E} = 4\pi\rho, \tag{1.7}$$

$$\nabla \cdot \mathbf{B} = 0, \tag{1.8}$$

$$\nabla \times \mathbf{E} = -\frac{1}{c}\frac{\partial \mathbf{B}}{\partial t}, \tag{1.9}$$

$$\nabla \times \mathbf{B} = \frac{4\pi}{c}\mathbf{J} + \frac{1}{c}\frac{\partial \mathbf{E}}{\partial t}, \tag{1.10}$$

where c is the speed of light in vacuum, ρ_α is the charge density and $\mathbf{J}_\alpha$ the current density of the α species. We introduce the charge $\rho_\alpha(\mathbf{r},t)$ and charge density $\mathbf{J}_\alpha(\mathbf{r},t)$ calculated from the distribution function f_α:

$$\rho_\alpha(\mathbf{r},t) = q_\alpha \int f_\alpha(\mathbf{r},\mathbf{p},t) d^3 p, \tag{1.11}$$

$$\mathbf{J}_\alpha(\mathbf{r},t) = q_\alpha \int \mathbf{v} f_\alpha(\mathbf{r},\mathbf{p},t) d^3 p. \tag{1.12}$$

The collisions of particles within a plasma are characterized by the *mean free path* λ_c of particles and their *collisional frequency* ν_c. These parameters can be obtained for electron-electron (*ee*), ion-ion (*ii*) or electron-ion (*ei*) collisions [72, 73]. A plasma is considered to be highly collisional if the *mean free path* is much smaller than the characteristic length of the problem $\lambda_c << L$ which van vary based on whether we are interested in the whole system or a specific region within it.

In the case of an electrostatic shock propagating in a medium, L would be the shock precursor distance at which the upstream plasma is already perturbed by the shock. This distance can range from $10\lambda_{De} \lesssim L \lesssim 100\lambda_{De}$. If one would be interest in studying the probability of *ee* collisions we would then extend L to the entire plasma medium comparing it with the profile's density scale length L_n, for example.

The plasmas created by the interaction of an ultra-high intensity (UHI) laser pulse with a dense gas jet have a high electron density n_e close to the critical density n_c and reach high electron temperatures T_e. In this regime *ei* collisions are inefficient since their *mean free path* $\lambda_{ei} >> \lambda_{De}$. Consequently, collisional effects are of the second order, the plasmas are considered collisionless.

1.3.1 The Particle-in-Cell (PIC) method

A Particle-in-Cell (PIC) code is a Monte Carlo method [74] to solve Vlasov-Landau equations for both ions and electrons (even without collisions). The distribution function of the α species f_α is decomposed into a shape function $\mathcal{S}_\alpha^l$ of order l in the position space and a Dirac function in the momentum space as

$$f_\alpha(\mathbf{R_i},\mathbf{P_i},t) = \sum_{j=1}^{N_\alpha} \mathcal{W}_{j,\alpha}(t)\mathcal{S}_\alpha^l[\mathbf{R_i} - \mathbf{r_j}(t)]\delta[\mathbf{P_i} - \mathbf{p_j}(t)]. \tag{1.13}$$

where $\mathbf{R_i}$ and $\mathbf{P_i}$ are the position and momentum vectors of the *ith* mesh, $\mathbf{r_j}$ and $\mathbf{p_j}$ the position and momentum of the *jth* particle, α the index of the charged particle, $\mathcal{W}_{j,\alpha}(t)$ the statistical weight of the *jth* particle of the α species at the instant t and $\mathcal{S}_\alpha^l$ is the shape function of order l.

Each *macroparticle* represents a finite and large number of physical particles as measured by $\mathcal{W}_{j,\alpha}(t)$ and is characterized by the same Z^*/A ratio and charge density as the physical particles that it represents. Note that the numerical convergence is reached when the number of *macroparticles* tends to infinity [74]. The PIC method solves the Vlasov-Landau equation where the one-particle distribution function is continuous in the phase space. It must not be confused by the Klimontovitch equation solved by a molecular dynamic code. The method operates by integrating the Newton equation along the *macroparticles* trajectories $(\mathbf{r_j}(t),\mathbf{p_j}(t))$. Looping over all N_α *macroparticles* in the simulation, the charge and current density at a given instant are

$$\rho(\mathbf{R_i},t) = \sum_{\alpha} \sum_{j=1}^{N_\alpha} q_\alpha \mathcal{W}_{j,\alpha}(t)\mathcal{S}_\alpha^l[\mathbf{R_i} - \mathbf{r_j}(t)], \tag{1.14}$$

$$\mathbf{J}(\mathbf{R_i},t) = \sum_\alpha \sum_{j=1}^{N_\alpha} q_\alpha v_{j,\alpha}(t) \mathcal{W}_{j,\alpha}(t) \mathcal{S}_\alpha^l[\mathbf{R_i} - \mathbf{r_j}(t)], \tag{1.15}$$

where q_α is the electric charge of the α species and $v_{j,\alpha}$ is the *jth* macroparticle's velocity at the instant t. The quantities projected to the mesh points are then used to compute the discrete $\mathbf{E}(\mathbf{R_i})$ and $\mathbf{B}(\mathbf{R_i})$ fields at the next time step using a charge conservation scheme. External fields can also be considered either injected from the domain's boundaries or immersed in the plasma from the initial time. Once the mesh-point fields are calculated they are interpolated back to the *macroparticles* $(\mathbf{r_j}(t),\mathbf{p_j}(t))$. Their new momenta and position are calculated by a *particle-pusher*. Finally, both ρ_α and $\mathbf{J}_\alpha$ are projected to the mesh nodes, thereby closing the system. This is the calculation loop at the center of the PIC method.

The intrinsic noise of PIC codes, issued from the coarse-grained *macroparticles* can be reduced by using high order shape functions. Fig. 1.1a shows the shape functions $\mathcal{S}_\alpha$ of orders 0, 1 and 2.
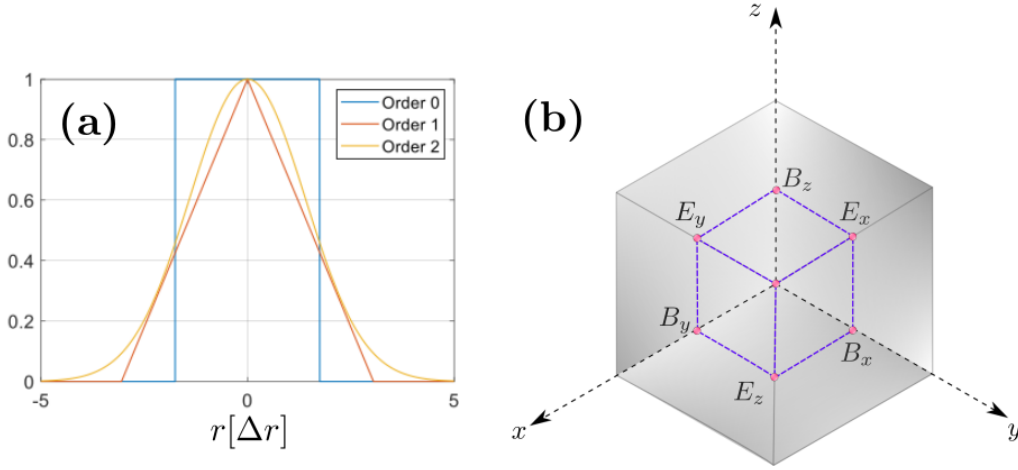
Fig. 1.1:   (a) Shape functions $\mathcal{S}_\alpha$ of orders 0, 1 and 2. (b) Scheme of a simulation *cell* with the 3-D mesh for the electric (at the axes centers) and magnetic (at the center of each face) fields.

Esirkepov's current deposition method (2001) [75] relies on inverting the divergence operator in the continuity equation to compute $\mathbf{J}$. In this way $\mathbf{E}$ is determined by the Maxwell-Ampère equation only (i.e. without the need of solving the Maxwell-Gauss equation) while $\mathbf{B}$ is advanced by the Maxwell-Faraday equation. This is done following the *finite-difference* time domain scheme developed by Yee (1996) [76]. The evolution of the electromagnetic fields is solved every half time step on a Cartesian grid with nodes located at $(x,y,z = i\Delta x, j\Delta y,k\Delta z)$, where i, j and k are integers. In a 3-D geometry the fields are advanced as

$$\frac{E_x\big|_{i+\frac{1}{2},j,k}^{n+1} - E_x\big|_{i+\frac{1}{2},j,k}^{n}}{c^2\Delta t} = \frac{B_z\big|_{i+\frac{1}{2},j+\frac{1}{2},k}^{n+\frac{1}{2}} - B_z\big|_{i+\frac{1}{2},j-\frac{1}{2},k}^{n+\frac{1}{2}}}{\Delta y} - \frac{B_y\big|_{i+\frac{1}{2},j,k+\frac{1}{2}}^{n+\frac{1}{2}} - B_y\big|_{i+\frac{1}{2},j,k-\frac{1}{2}}^{n+\frac{1}{2}}}{\Delta z} - \mu_0 J_x\big|_{i+\frac{1}{2},j,k}^{n+\frac{1}{2}}, \tag{1.16}$$

$$\frac{E_y\big|_{i,j+\frac{1}{2},k}^{n+1} - E_y\big|_{i,j+\frac{1}{2},k}^{n}}{c^2\Delta t} = \frac{B_x\big|_{i,j+\frac{1}{2},k+\frac{1}{2}}^{n+\frac{1}{2}} - B_x\big|_{i,j-\frac{1}{2},k-\frac{1}{2}}^{n+\frac{1}{2}}}{\Delta z} - \frac{B_z\big|_{i+\frac{1}{2},j,k+\frac{1}{2}}^{n+\frac{1}{2}} - B_z\big|_{i-\frac{1}{2},j+\frac{1}{2},k}^{n+\frac{1}{2}}}{\Delta x} - \mu_0 J_y\big|_{i,j+\frac{1}{2},k}^{n+\frac{1}{2}}, \tag{1.17}$$

$$\frac{E_z|_{i,j,k+\frac{1}{2}}^{n+1} - E_z|_{i,j,k+\frac{1}{2}}^{n}}{c^2\Delta t} = \frac{B_y|_{i+\frac{1}{2},j,k+\frac{1}{2}}^{n+\frac{1}{2}} - B_y|_{i-\frac{1}{2},j,k+\frac{1}{2}}^{n+\frac{1}{2}}}{\Delta x} - \frac{B_x|_{i,j+\frac{1}{2},k+\frac{1}{2}}^{n+\frac{1}{2}} - B_x|_{i,j-\frac{1}{2},k+\frac{1}{2}}^{n+\frac{1}{2}}}{\Delta y} - \mu_0 J_z|_{i,j,k+\frac{1}{2}}^{n+\frac{1}{2}},$$

(1.18)

$$\frac{B_x|_{i,j+\frac{1}{2},k+\frac{1}{2}}^{n+\frac{1}{2}} - B_x|_{i,j+\frac{1}{2},k+\frac{1}{2}}^{n-\frac{1}{2}}}{\Delta t} = -\frac{E_z|_{i,j+1,k+\frac{1}{2}}^{n} - E_z|_{i,j,k+\frac{1}{2}}^{n}}{\Delta y} + \frac{E_y|_{i,j+\frac{1}{2},k+1}^{n} - E_y|_{i,j+\frac{1}{2},k}^{n}}{\Delta z},$$

(1.19)

$$\frac{B_y|_{i+\frac{1}{2},j,k+\frac{1}{2}}^{n+\frac{1}{2}} - B_y|_{i+\frac{1}{2},j,k+\frac{1}{2}}^{n-\frac{1}{2}}}{\Delta t} = -\frac{E_x|_{i+\frac{1}{2},j,k+1}^{n} - E_x|_{i+\frac{1}{2},j,k}^{n}}{\Delta z} + \frac{E_z|_{i+1,j,k+\frac{1}{2}}^{n} - E_z|_{i,j,k+\frac{1}{2}}^{n}}{\Delta x},$$

(1.20)

$$\frac{B_z|_{i+\frac{1}{2},j+\frac{1}{2},k}^{n+\frac{1}{2}} - B_z|_{i+\frac{1}{2},j+\frac{1}{2},k}^{n-\frac{1}{2}}}{\Delta t} = -\frac{E_y|_{i+1,j+\frac{1}{2},k}^{n} - E_y|_{i,j+\frac{1}{2},k}^{n}}{\Delta x} + \frac{E_x|_{i+\frac{1}{2},j+1,k}^{n} - E_x|_{i+\frac{1}{2},j+1,k}^{n}}{\Delta y}.$$

(1.21)

Note that the spatial derivatives of the **E** and **B** fields are of the second order and centered. Fig. 1.1b shows the scheme of a simulation *cell* with the 3-D mesh for the electric (at the axes centers) and magnetic (at the center of each face) fields. The *Courant Friedrichs Lewy* (CFL) condition that ensures the convergence of this scheme reads

$$\left(\frac{1}{\Delta x^2} + \frac{1}{\Delta y^2} + \frac{1}{\Delta z^2}\right) \leq \frac{1}{c^2\Delta t^2}.$$

(1.22)

The $\mathbf{E}(\mathbf{R_i})$ and $\mathbf{B}(\mathbf{R_i})$ fields at the mesh nodes N_m are interpolated to the *macroparticle's* position using the shape function $\mathcal{S}_\alpha^l$

$$\mathbf{E}(\mathbf{r_j}) = \sum_{i=1}^{N_m} \mathbf{E}(\mathbf{R_i})\mathcal{W}_{j,\alpha}\mathcal{S}_\alpha^l[\mathbf{R_i} - \mathbf{r_j}],$$

(1.23)

$$\mathbf{B}(\mathbf{r_j}) = \sum_{i=1}^{N_m} \mathbf{B}(\mathbf{R_i})\mathcal{W}_{j,\alpha}\mathcal{S}_\alpha^l[\mathbf{R_i} - \mathbf{r_j}].$$

(1.24)

The new *macroparticle's* momenta and positions are advanced using the relativistic equation of motion

$$\frac{d\mathbf{p}}{dt} = q_\alpha\left(\mathbf{E} + \frac{\mathbf{p}}{\gamma m_\alpha} \times \mathbf{B}\right),$$

(1.25)

$$\frac{d\mathbf{r}}{dt} = \frac{\mathbf{p}}{\gamma m_\alpha},$$

(1.26)

applying a leap-frog scheme.

The PIC code used during this thesis work, called CALDER [77], has been developed at CEA-DAM during the past twenty years. It is massively parallelized using the Message Passing Interface (MPI) library [78] which allows it to run in a large amount of CPUs. The simulations presented in this thesis work were run each one on the supercalculators of the *Très Grand Centre de Calcul* (TGCC). To give an order of magnitude, the 1-D simulations that will be presented in Chapter 3 were run on 4000 processors during 24 hours corresponding to eleven years of computation in a single CPU.

`CALDER` has been enriched during the previous years by including diverse physical processes that improve the simulations of laser-matter interactions. In particular, in this thesis we have made use of the field-induced ionization module as well as the elastic and inelastic collisions' description.

The field-induced ionization module developed by R. Nuter [79] is based on the ionization rates calculation proposed in Ref. [80]. It allows to create the distribution function of the free (ionized) electrons. The ionization event is determined through a Monte Carlo approach. In case of success, a *macroelectron* with a certain statistical weight $\mathcal{W}_e$ is produced and the electric field is corrected introducing an ionization current so as to conserve the total energy.

The elastic collisions' module is described in Ref. [81] and it is based on the cross sections calculation of Ref. [82] which was adapted to *macroparticles* of different statistical weights in Ref. [83]. Finally, the impact-induced ionization module also presented in Ref. [81] is based in the cross sections calculation described in Ref. [84] which is adapted to the interaction of *macroelectrons* and *macroions* of different statistical weights. The method relies on the random pairing of *macroparticles* at every time step in every *cell* to perform *macrocollisions*. The scattering or energy loss/gain of the *macroparticles* is determined from cross-sections that are sampled with the inversion of the cumulative distribution, a usual Monte Carlo sampling method. The cross-sections depend of the conditions of each *cell* (e.g. density, temperature, ionization degree of the different ionic species,...) as well as on the relative velocity of the two *macroparticles*.

1.4 Fluid description of a plasma

Considering the electron distribution function f_e to follow locally a Maxwell-Boltzmann distribution at time scales $t \gg \nu_{ei}^{-1}$, a plasma can also be characterized following a macroscopic approach that describes the evolution of its average values (i.e. density, velocity and temperature), an approximation called *Local Thermodynamic Equilibrium*. The so-called hydrodynamic plasma description is precise at large scales, and allows to reduce the dimensionality of the physics from the six dimensions of the phase space to three dimensions in space. Taking the first two moments of the Vlasov Eq. 1.6 leads to the density and momentum continuity equations of the fluids with charge q_α and mass m_α [85]:

$$\frac{\partial n_\alpha}{\partial t} + \nabla \cdot (n_\alpha \mathbf{u}_\alpha) = 0, \tag{1.27}$$

$$m_\alpha n_\alpha \left(\frac{\partial \mathbf{u}_\alpha}{\partial t} + \mathbf{u}_\alpha \cdot \nabla \mathbf{u}_\alpha \right) = q_\alpha n_\alpha \left(\mathbf{E} + \frac{\mathbf{u}_\alpha \times \mathbf{B}}{c} \right) - \nabla P_\alpha. \tag{1.28}$$

The pressure of each fluid is related to its density by an *equation of state* (EoS) which depends on the frequency ω and wavenumber k of the process that is being considered. When $w/k >> v_j$ the adiabatic EoS is valid:

$$\frac{T_\alpha}{n_\alpha^{\gamma_\alpha - 1}} = \text{const or } \frac{p_\alpha}{n_\alpha^{\gamma_\alpha}} = \text{const}, \tag{1.29}$$

where $\gamma_\alpha = (d+2)/d$ is the adiabatic index and d is the dimension number. The value $\gamma_\alpha = 5/3$, obtained for perfect neutral monoatomic gases, is applicable in plasmas for three-dimensional flows, $\gamma_\alpha = 3$ for uni-dimensional flows and $\gamma_\alpha = 1$ for isothermal flows.

A plasma can then be considered as a mixture of two fluids composed of electrons ($q_e = -e$) with density n_e and average velocity $\mathbf{u}_e$ and a fluid of ions ($q_i = Z^*e$) with density n_i and

average velocity $\mathbf{u}_i$. Without a magnetic field, both fluids are coupled by the Poisson equation:

$$-\nabla^2\phi = 4\pi e(n_e - Z^* n_i), \tag{1.30}$$

referred to as the *two-fluid* model.

1.4.1 Electrostatic plasma waves in hot plasma

The following derivations are based on the ones performed in Ref. [85]. Using the previously described two-fluid model, one can investigate the linear waves excited in an homogeneous plasma. These are low-amplitude waves that can be linked to a small disturbance in the plasma initial state. Each wave is governed by its *dispersion relation* between the wave's angular frequency ω and the wave vector $\mathbf{k}$. In a non-magnetized plasma there are two types of electrostatic waves: high-frequency electron plasma waves, and low-frequency ion acoustic waves, both having their polarization parallel to $\mathbf{k}$.

1.4.1.1 Electronic plasma waves

Let us take a look at the high frequency charge density fluctuations associated to the motion of electrons. The ions here are considered as a immobile neutralizing background. Within the adiabatic limit $\omega/k \gg v_{Te}$ a one-dimensional $\gamma_\alpha = 3$ adiabatic index can be considered. An electron fluid can then be described by Eqs. 1.27, 1.28 and 1.29. The fluid description is closed by relating the electric field to the density via the Poisson equation 1.30. Linearizing the mentioned equations for small perturbations in the electron density, velocity, pressure and electric field, we can obtain a wave equation that describes such small amplitude fluctuations:

$$\left(\frac{\partial^2}{\partial t^2} - 3v_{Te}^2 \frac{\partial^2}{\partial x^2} + \omega_{pe}^2 \right) \delta n_e = 0, \tag{1.31}$$

where ω_{pe} is the *electron plasma frequency* defined by $\omega_{pe} = \sqrt{\frac{4\pi n_e e^2}{m_e}}$ and δn_e a small perturbation of the electron density. Looking for a wave-like solution of Eq. 1.31, one obtains:

$$\omega^2 = \omega_{pe}^2 + 3k^2 v_{Te}^2, \tag{1.32}$$

which is the dispersion relation for electron plasma waves. The frequency of these waves is roughly ω_{pe} plus a small thermal correction that depends on the wavenumber k. ω_{pe}^{-1} is the characteristic time at which the electrons will respond to the charge separation disruption. An analog quantity can be found for ions:

$$\omega_{pi} = \sqrt{\frac{4\pi n_i Z^{*2} e^2}{m_i}}, \tag{1.33}$$

called the *ion plasma frequency* and orders of magnitude smaller than ω_{pe}.

1.4.1.2 Ion acoustic waves

A plasma also supports oscillations at a much lower frequency than the characteristic inertia of the electrons. There, both the ion and electron motions must be considered with appropriate closures of the pressure. As $v_{Ti} \ll \omega/k \ll v_{Te}$, the electrons (ions) can be described by an isothermal (adiabatic) EoS with $\gamma_\alpha = 1$ ($\gamma_\alpha = 3$). We again describe the ion fluid with a three equations set composed of Eqs. 1.27, 1.28 and 1.29, considering that the ion charge is $q_i = Z^* e$. Considering small perturbations in the ion density, velocity, pressure and electric field we can

obtain a wave equation for the fluctuations on the ion density supposing that $\delta n_e \approx Z^* \delta n_i$ since the electrons follow closely the slow motion of the massive ions:

$$\left(\frac{\partial^2}{\partial t^2} - \frac{Z k_B T_e + 3 k_B T_i}{m_i} \times \frac{\partial^2}{\partial x^2} \right) \delta n_i = 0, \tag{1.34}$$

where δn_i is a small perturbation of the ion density. Searching for wave-like solutions of Eq. 1.34, we obtain the dispersion relation for ion acoustic waves:

$$\omega = \pm k v_s, \tag{1.35}$$

where $v_s = \sqrt{C_s^2 + 3v_{Ti}^2}$ and $C_s = \sqrt{(Z T_e + 3 T_i)/m_i}$ is the ion acoustic speed. This dispersion resembles the dispersion of an acoustic wave in a gaseous medium and the velocity v_s acts as the speed of sound.

1.5   Basics of laser-plasma physics

The propagation of an electromagnetic wave, such as the one associated to a high-intensity laser pulse, is described by Maxwell's equations (see Eqs 1.7-1.10). Note that $\mathbf{E}$ and $\mathbf{B}$ can also be described with respect to the vector potential $\mathbf{A}$ and the scalar potential Φ:

$$\mathbf{E} = -\Delta\Phi - \frac{\partial \mathbf{A}}{\partial t}, \tag{1.36}$$

$$\mathbf{B} = \nabla \times \mathbf{A}. \tag{1.37}$$

1.5.1   Normalized vector potential

In the paraxial approximation in vacuum (valid as long as the beam is not tightly focused), the vector potential of a Gaussian beam envelop with a Gaussian temporal profile can be written as:

$$\mathbf{A_0}(x,r,t) = A_0 \exp\left(-2\ln 2 \frac{(x-ct)^2}{c^2 \tau_0^2} \right) \frac{W_0}{W(x)} \exp\left(-\frac{r^2}{W(x)^2} - i\frac{k_0 r^2}{2R(x)} \right) \exp(i\phi(x)) \tag{1.38}$$

where A_0 is the maximum value of the vector potential and τ_0 the pulse duration at the full width at half maximum (FWHM). $W(x) = W_0(1 + x^2/Z_r^2)^{1/2}$ describes the transverse size of the pulse at $1/e$ of the electric field maximum, $\phi(x)$ is the Gouy phase and $R(x) = x(1 + Z_r^2/x^2)$ is the curvature of the wave front with respect to x, see Fig. 1.2. Here W_0 taken at $x = 0$ is the beam waist and $Z_r = \pi W_0^2/\lambda_0$ is the Rayleigh length, with $\lambda_0 = 2\pi c/\omega_0$ the laser wavelength linked with the wave number k_0 through the dispersion relation equal to $k_0 = \omega_0/c$ in vacuum (ω_0 is the laser angular frequency, $T = 2\pi/\omega_0$ the laser period and $f = \omega_0/(2\pi)$ the laser frequency).

We usually define the transverse size of a focused laser pulse by the so-called focal spot w_0 which is taken at the FWHM of the laser pulse intensity profile and can be linked to the beam waist: $w_0 = \sqrt{2\ln 2} W_0$. Making use of the Gaussian approximation, we can also define the maximum intensity of the laser pulse:

$$I_0 = \frac{2P_0}{\pi W_0^2}, \tag{1.39}$$
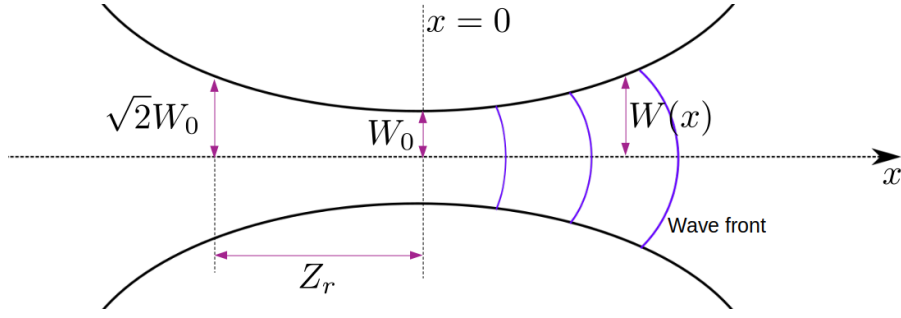
Fig. 1.2: Evolution of a Gaussian laser pulse seen in the transverse size of the laser pulse (black curves) taken at $1/e$ of the electric field maximum. The purple curves represent the evolution of the wave front.

with $P_0 = 2\sqrt{\ln 2 E_0/(\pi \tau_0)}$ the power of the laser pulse and E_0 the laser energy. We can finally express the maximum of the potential vector A_0 for a linear polarization as:

$$A_0 = \sqrt{\frac{I_0 \lambda_0^2}{2\pi^2 \epsilon_0 c^3}}. \tag{1.40}$$

The normalized vector potential a_0 is defined as:

$$a_0 = \frac{e A_0}{m_e c}. \tag{1.41}$$

Note that in non-relativistic cases $a_0 \propto v_e/c$, where v_e is the oscillatory velocity of the electron. We can rewrite Eq. 1.41 with Eq. 1.40 to obtain an expression based on usual quantities:

$$a_0 = 0.85\sqrt{I_0[10^{18}\mathrm{W\,cm^{-2}}]}\,\lambda_0[\mathrm{\mu m}] \tag{1.42}$$

Once normalized the a_0 value is very useful to characterize the regime of the laser-plasma interaction. If $a_0 << 1$, the interaction is non-relativistic and the electrons will mainly move in the laser polarization direction. In this thesis $a_0 > 1$ and the relativistic regime prevails.

1.5.2   Single electron motion in a laser field

The motion of a single electron due to an incident laser pulse characterized by the electromagnetic fields $\mathbf{E}$ and $\mathbf{B}$ is ruled by the Lorentz force:

$$\frac{d\mathbf{p}}{dt} = -e\left(\mathbf{E} + \frac{\mathbf{p}}{m_e \gamma_e} \times \mathbf{B}\right), \tag{1.43}$$

where $\gamma_e = \sqrt{1 + p^2/m_e^2 c^2}$ is the Lorentz factor. The electric and magnetic fields can be written as a function of the vector potential $\mathbf{A}$, see Eqs. 1.36 and 1.37. Using the Lagrangian derivative along the electron velcity:

$$\frac{\partial \mathbf{A}}{\partial t} = \frac{d\mathbf{A}}{dt} - (\mathbf{v} \cdot \nabla)\mathbf{A}, \tag{1.44}$$

we obtain

$$\frac{d}{dt}(\mathbf{p} - e\mathbf{A}) = -e\left[(\mathbf{v} \cdot \nabla)\mathbf{A} + \mathbf{v} \times (\nabla \times \mathbf{A})\right]. \tag{1.45}$$

The vector relation

$$\mathbf{v} \times (\nabla \times \mathbf{A}) = (\nabla \mathbf{A}) \cdot \mathbf{v} - (\mathbf{v} \cdot \nabla)\mathbf{A} \tag{1.46}$$

allows to transform Eq. 1.45 in:

$$\frac{d}{dt}(\mathbf{p} - e\mathbf{A}) = -e(\nabla \mathbf{A}) \cdot \mathbf{v}. \tag{1.47}$$

Additionally, the equation of the conservation of energy writes:

$$\frac{d}{dt}\gamma_e m_e c^2 = -e\mathbf{v} \cdot \mathbf{E} = e\mathbf{v} \cdot \frac{\partial \mathbf{A}}{\partial t} \tag{1.48}$$

In the case of a plane wave only depends on x and it is polarized in the yz plane:

$$\frac{d}{dt}p_x = -e\mathbf{v}_\perp \cdot \frac{\partial \mathbf{A}}{\partial t}, \tag{1.49}$$

$$\frac{d}{dt}(\mathbf{p}_\perp - e\mathbf{A}) = 0. \tag{1.50}$$

Since the electron is supposed to be initially at rest we deduce:

$$\mathbf{p}_\perp = e\mathbf{A}, \tag{1.51}$$

an equality that results from the conservation of the transverse canonical momentum valid in 1-D (planar wave). Substituting the expression for the transverse velocity $\mathbf{v}_\perp = e\mathbf{A}/m_e\gamma_e$ in Eq. 1.48 and 1.49 we obtain

$$\frac{d}{dt}\gamma_e m_e c^2 = \frac{e^2}{2m_e\gamma_e}\frac{\partial A^2}{\partial t}, \tag{1.52}$$

$$\frac{d}{dt}p_x = -\frac{e^2}{2m_e\gamma_e}\frac{\partial A^2}{\partial x}. \tag{1.53}$$

Note that the term $-(e^2/2m_e\gamma_e)/\partial A^2/\partial x$ is the relativistic expression of the *ponderomotive force*. Considering a diluted plasma and moderately relativistic particles we can obtain an analytical expression for this non-linear force from Eq. 1.53, valid in a 3-D geometry [86]:

$$\mathbf{f}_{pond.} = -\frac{e^2}{2m_e < \gamma_e >}\nabla < \mathbf{A}^2 >, \tag{1.54}$$

where $\gamma_e = \sqrt{1+ <p>^2 /(m_e c)^2 + e^2 < A^2 > /(m_e c)^2}$. Note that $\mathbf{f}_{pond.}$ basically expels all particles from high intensity regions regardless of their charge. Nevertheless, the lighter electrons experience a much stronger force than that exerted on the heavier ions.

As a general rule the electron momentum and the wave's propagation direction form an angle:

$$\theta = \arctan\left(p_\perp/p_x\right) = \arctan\left(2/a_0\right) = \arctan\sqrt{\frac{2}{\gamma_e - 1}}, \tag{1.55}$$

that diminishes with its energy.

Following Ref. [87], the components of the electron momentum in the laboratory frame write:

$$\begin{aligned} p_x &= \frac{a_0}{4}(1 + \cos 2\Phi) \\ p_y &= a_0 \cos 2\Phi \\ p_z &= 0 \end{aligned} \tag{1.56}$$

while the electron trajectory in the laboratory frame is given by:

$$x = \frac{1}{4}a_0^2 \left(\Phi + \frac{1}{2}\sin 2\Phi \right)$$
$$y = a_0 \sin \Phi \qquad (1.57)$$
$$z = 0$$

Fig. 1.3a represents those trajectories for three different values of the normalized laser amplitude a_0. The electron trajectories are stretched by a factor a_0^2 in the transverse direction and by a factor a_0 in the parallel direction. The drift electron velocity in the laser propagation axis averaged over a laser cycle writes:

$$v_D = \frac{<p_x>}{<\gamma_e> m_c e c} = \frac{a_0^2 c}{4 + a_0^2}. \qquad (1.58)$$

The orbits of the electron trajectories can be calculated in its own frame, where the drift velocity is zero:

$$x = \frac{1}{2}r^2 \sin 2\Phi$$
$$y = 2r \sin \Phi \qquad (1.59)$$
$$z = 0$$

where $r = a_0/(1+a_0^2/2)$. These equations correspond to the eight-shape orbit that is compressed in the transverse direction when the laser intensity increases. Fig. 1.3b shows the electron trajectories in its rest frame for different values of the normalized laser amplitude a_0.
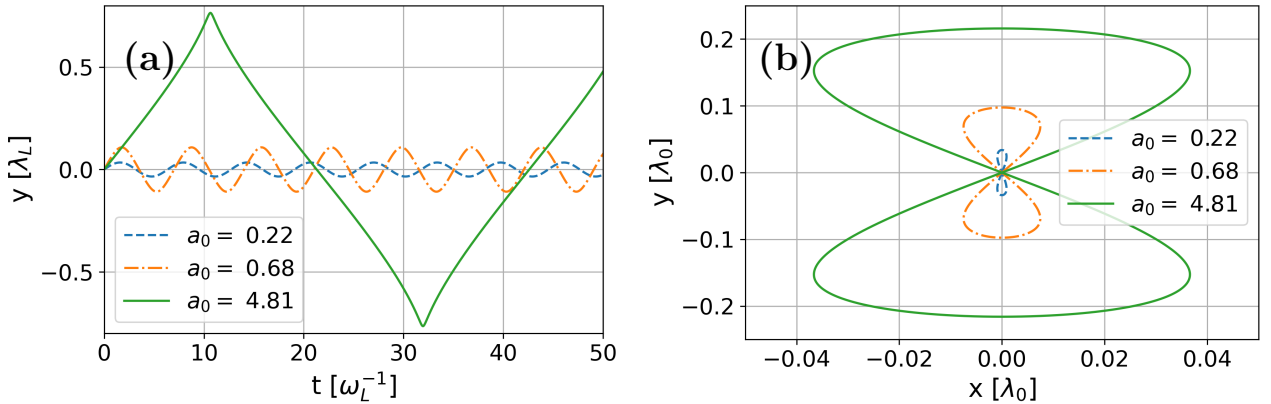
Fig. 1.3: Trajectory of an electron interacting with a linearly polarized laser pulse traveling in the positive x-direction in (a) the laboratory frame and (b) in the average rest frame of the particle. Different values of the normalized laser amplitude are presented: $a_0 = 0.22$ (dashed line), $a_0 = 0.68$ (dashed-dotted line) and $a_0 = 4.81$ (solid line) according to Eqs. 1.57 and 1.59.

1.5.3 Relativistic ponderomotive force in an electron fluid

The so-called *cold-fluid* plasma model is a more complete plasma description that takes into account collective effects. It is based on considering a unmagnetized electron fluid in an immobile ion background. The plasma can be supposed cold since $v_{Te} << v_e$ where $v_{Te} = \sqrt{k_B T_e/m_e}$ is the electrons' thermal velocity and v_e their oscillatory velocity in the laser field. Differing from

Section 1.5.2 the electric field is not only transverse since the longitudinal electron movement will give rise to an electric field in the wave's propagation direction.

Writing the conservation of mass and momentum equations as:

$$\frac{\partial n}{\partial t} + \nabla \cdot \left(\frac{n\mathbf{p}}{\gamma_e} \right) = 0, \tag{1.60}$$

$$\left(\frac{\partial}{\partial t} + \mathbf{v} \cdot \nabla \right) \mathbf{p} = \left(\frac{\partial \mathbf{A}}{\partial t} + \nabla \Phi - \mathbf{v} \times \nabla \times \mathbf{A} \right). \tag{1.61}$$

Note that all quantities have been normalized as $t \equiv \omega_0 t$, $x \equiv \omega_0 x/c$, $\mathbf{A} \equiv e\mathbf{A}/m_e c$, $\Phi \equiv e\Phi/m_e c^2$, $\mathbf{p} = \mathbf{p}/m_e c$ and $n \equiv n/n_c$ where $n_c = m_e \epsilon_0 \omega_0^2/e^2$ is the classical critical density. Knowing that

$$(\mathbf{v} \cdot \nabla)\mathbf{p} = \nabla \gamma_e - \mathbf{v} \times (\nabla \times \mathbf{p}), \tag{1.62}$$

equation 1.61 simplifies as

$$\frac{\partial}{\partial t}(\mathbf{p} - e\mathbf{A}) = \nabla(\Phi - \gamma_e) + \mathbf{v} \times [\nabla \times (\mathbf{p} - \mathbf{A})]. \tag{1.63}$$

Applying the rotational to the last equation we obtain

$$\frac{\partial}{\partial t}[\nabla(\mathbf{p} - \mathbf{A})] = \nabla \times \mathbf{v} \times [\nabla \times (\mathbf{p} - \mathbf{A})]. \tag{1.64}$$

The quantity $\nabla(\mathbf{p} - \mathbf{A}) = 0$ for $t > 0$ if it is null at $t = 0$. Eq. 1.61 can then finally be expressed as:

$$\frac{\partial}{\partial t}(\mathbf{p} - \mathbf{A}) = \nabla(\Phi - \gamma_e), \tag{1.65}$$

where we find the *relativistic ponderomotive factor* $-\nabla \gamma_e$. Supposing an equilibrium between the transverse and the *ponderomotive force*:

$$\frac{\partial}{\partial t}(\mathbf{p} - \mathbf{A}) = 0 = \nabla(\Phi - \gamma_e), \tag{1.66}$$

the potential gradient is then

$$- < \nabla \Phi >=< \mathbf{E}_\perp >= -\nabla_\perp < \gamma_e >, \tag{1.67}$$

Considering that $\gamma_e = \sqrt{1 + p_x^2 + p_\perp^2}$ and $p_\perp << a_0^2$ we obtain $\gamma_e \approx \sqrt{1 + a_0^2}$. Furthermore, for $a_0 >> 1$ and approximating the gradient as $1/R$, where $R \approx \sqrt{\gamma_e} c/\omega_{pe}$ is the *relativistic skin depth*, we can write $\gamma_e \approx a_0/R$ and the relativistic ponderomotive force linear dependence $\mathbf{f}_{pond.} \propto a_0$ on the normalized laser amplitude is unraveled.

1.5.4   Ionization potential

Plasmas are produced by the ionization of a gas by an UHI laser pulse. The final ionization state Z^* of the ions chiefly relies on the strength of the laser electric field. Knowing the ionization potential associated with each shell, Z^* can be estimated with a simple classical model.

Let r be the distance from the electron to the nucleus and E_0 the value of the laser electric field, supposed constant at the atomic scale. The electron is then under the influence of both

the Coulomb potential of the nucleus and of the external field. The total electric potential energy for the last electron tied to the nucleus can be written as:

$$\phi_{tot} = -\frac{Ze^2}{4\pi\epsilon_0 r} - \phi_0, \qquad (1.68)$$

where Z is the atomic number and $\phi_0 = eE_0 r$. Fig. 1.4 shows the potential well in which an electron is placed with (dashed blue line) and without (solid red line) an external field E_0. The horizontal green-dotted line represents the electrons' energy level. The laser electric field diminishes the potential barrier to liberate the electron: $\phi_{max} - E_i$, ϕ_{max} is reached when $r_{max} = \sqrt{Ze/4\pi\epsilon_0 E_0}$ is introduced in Eq. 1.68. If the laser field is intense enough $\phi_{max} < -E_i$, the electron is then no longer tied to its nucleus. This process is known as ionization by electrostatic barrier suppression.
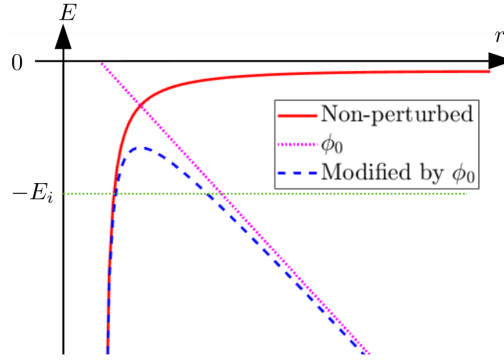
Fig. 1.4: Potential well in which an electron is placed with (dashed line) and without (solid line) an external field E_0. The horizontal green-dotted line represents the electrons' energetic level and the diagonal dotted line the potential created by the laser field ϕ_0.

Knowing that the laser intensity is related to its electric field, $I = \epsilon_0 c E_0^2$ for a circular polarization ($I = 1/2\epsilon_0 E_0^2$ for a linear polarization), one can find the laser intensity needed to completely ionize an atom through the cited electrostatic barrier suppression method. Fig. 1.5 plots the laser intensity needed to tear out each of the electrons of a H, He and N atoms. As the ionization potential rises with Z^2/n^2, where n is the maximum quantum number, extremely intense pulses are required to ionize the deeper shells.
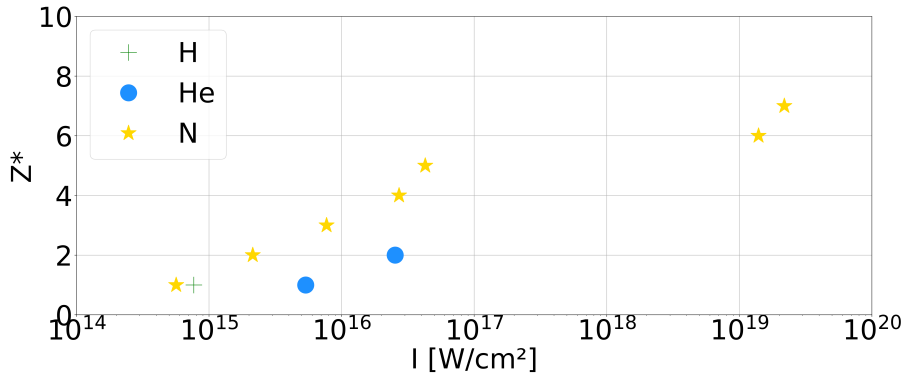
Fig. 1.5: Laser intensity needed to ionize up to Z^* a H, He and N atom.

1.5.5 Propagation of a high-intensity laser pulse through a medium

The propagation of a laser pulse with frequency ω_0 is modified by the medium throughout which it propagates. In a plasma the dispersion relation writes:

$$\omega_0^2 = \frac{\omega_{pe}^2}{<\gamma_e>} + c^2 k_0^2, \tag{1.69}$$

where $<\gamma_e> = (\sqrt{1 - \beta^2})^{-1}$ is the relativistic Lorentz factor for the electrons.

Departing from Eq. 1.69 in the non-relativistic regime, one can identify two regimes: when $\omega_{pe} > \omega_0$, k_0 has a complex value that leads to the presence of an evanescent wave inside the plasma and a reflection of the incident wave. In the contrary case, if $\omega_{pe} < \omega_0$, k_0 is a real number and the laser pulse can propagate through the plasma. The density at which $\omega_0 = \omega_{pe}$ is called the *critical density n_c* equal to:

$$n_c = \frac{m_e \omega_0^2}{4\pi e^2} \tag{1.70}$$

We can rewrite Eq. 1.70 to obtain a more practical expression:

$$n_c = \frac{1.11 \times 10^{21} \text{cm}^{-3}}{\lambda_0^2 [\mu\text{m}]}. \tag{1.71}$$

For a Ti:Sapphire laser whose wavelength $\lambda_0 = 0.8\,\mu\text{m}$ the critical density is equal to $n_c = 1.73 \times 10^{21}$ cm^{-3} while in the case of a $\lambda_0 = 1\,\mu\text{m}$ laser it is equal to $n_c = 1.11 \times 10^{21}$ cm^{-3}. In the relativistic regime where $\gamma_e > 1$ the effective critical density is increased:

$$n_{c,eff.} = \gamma_e n_c, \tag{1.72}$$

and the plasma becomes relativistically transparent at densities $n_e < n_{c,eff.}$. This effect is know as *relativistic induced transparency.*

- In *overdense plasmas* with $n_e > n_{c,eff.}$ the laser wave is reflected from the plasma critical surface and the electron heating occurs either in vacuum or within the so-called plasma *skin layer $l \approx c/\omega_{pe}$*. In this density regime and at laser intensities $I > 10^{18}$ W/cm^2 non-collisional mechanisms dominate the laser absorption. At normal incident angles the so-called $\mathbf{J} \times \mathbf{B}$ mechanism [88] driven by the magnetic term of the Lorentz force dominates the absorption process. The laser-plasma system behaves then as a forced oscillator driven at $2\omega_0$, where ω_0 is the laser's angular frequency. Each time the ponderomotive force $\mathbf{f}_{pond.}$ vanishes, some electrons escape into vacuum where they are subsequently accelerated by the transverse laser's electric field E_y, before being pushed back into the plasma by the combined effects of the laser's magnetic field B_z and the charge separation field E_x.

- In *underdense plasmas* with $n_e < n_{c,eff.}$ the plasma is transparent (yet it can be highly dissipative) and the laser is capable of forming channels within it. In this regime the longitudinal plasma waves driven by the laser's ponderomotive force $\mathbf{f}_{pond.}$ (in a resonant way if the laser FWHM duration is $\approx \pi/\omega_{pe}$) can sustain electric fields $|E_x| \gtrsim E_0 \approx$ TV/m.

- In the intermediate regime we find the *near-critical plasmas* with $n_e \approx n_{c,eff.}$. This regime entails strong electron heating and the acceleration of ions by diverse mechanisms.

1.5.5.1 Laser self-focusing and filamentation

The phase and group velocities of the laser pulse inside the plasma are obtained from the dispersion relation of Eq. 1.69:

$$v_\phi = \frac{\omega_0}{k_0} = \sqrt{1 + \frac{\omega_{pe}^2}{(\omega_0^2 - \omega_{pe}^2)\gamma_e}} \tag{1.73}$$

$$v_g = \frac{d\omega_0}{dk_0} = c \left[\frac{1 + \omega_{pe}^2}{(\omega_0^2 - \omega_{pe}^2)\gamma_e}\right]^{-1/2} \tag{1.74}$$

Contrary to the propagation in vacuum where $v_\phi = v_g = c$, in a plasma $v_\phi > c$ and $v_g < c$. As seen in Eqs. 1.73 and 1.74 the phase and group velocities depend on the electron plasma frequency ω_{pe}, which will be locally modified with the laser passage. To describe the medium response we define the optical index or refraction index of the material:

$$\eta = \frac{c}{v_\phi} \approx 1 - \frac{\omega_{pe}^2 n_e(r)}{2\omega_0^2 n_{e0}\gamma_e(r)}, \tag{1.75}$$

where $n_e(r)$ and $\gamma_e(r)$ the electron density and Lorentz factor as a function of the transverse distance r with respect to the laser axis. The laser pulse is focused if $\frac{d\eta}{dr} < 0$, i.e.the refraction index is maximum in the laser axis and a so-called *plasma lens* is formed.

Both ponderomotive and relativistic effects lead to the relativistic self-focusing of the laser pulse above the critical power threshold $P_c = 17(\omega_0/\omega_{pe})^2$ [GW] [89]. The ponderomotive expulsion of electrons from the laser propagation path locally increases the plasma refractive index η [90]. At the same time, the relativistic mass increase of electrons within the laser field reduces the local plasma frequency ω_{pe}. If the laser focal spot is larger than the relativistic plasma skin depth $D_L >> \sqrt{\gamma_e n_c/n_e}\, c/\omega_0$ [91], the laser will filament into several beamlets rather than self-focus.

1.6 Ion shock wave acceleration

The propagation of solitary waves in plasmas, also called *solitons*, has initially been studied considering cold ions and hot electrons in equilibrium [92, 93]. Refer to Chapter 3 for a detail description of the electron heating process in near-critical plasmas. The plasma region located in front of the *soliton* is called the *upstream* (US) while the region behind it is called the *downstream* (DS). Initially both US and DS have identical temperatures, electron densities and velocities. By placing ourselves in the frame of the electrostatic perturbation (i.e. where the wave is at rest) the incoming ions do so at a velocity v_s, see Fig. 1.6a. Under these assumptions the wave propagation velocity v_s has been found to be limited to $1 \leq M \leq 1.6$ where M is the so-called *Mach number* $M = v_s/C_s$, i.e. the ratio between the wave's velocity v_s and the upstream *ion acoustic speed* $C_s = \sqrt{\gamma Z^* k_B T_e/m_i}$, where γ is the adiabatic index. It has been demonstrated that the profile of the electric potential Φ in a small amplitude *soliton* is similar to the steady solution of the Korteweg-de-Vries (KdV) equation. The latter is called the *Saagdev potential* and it describes the solitary wave structures by comparing them to the equation of a particle moving in a potential [92, 94]. Section 1.6.1 derives the minimum and maximum Mach numbers in these conditions following the Saagdev formalism.

By dropping the equilibrium consideration for electrons and treating them following a kinetic approach, one can distinguish between free electrons and ions with a kinetic energy higher than the electrostatic potential, and electrons that are trapped in the DS region (with a kinetic energy lower than the electrostatic potential) characterized by an undulating potential, see

(a) **(b)**
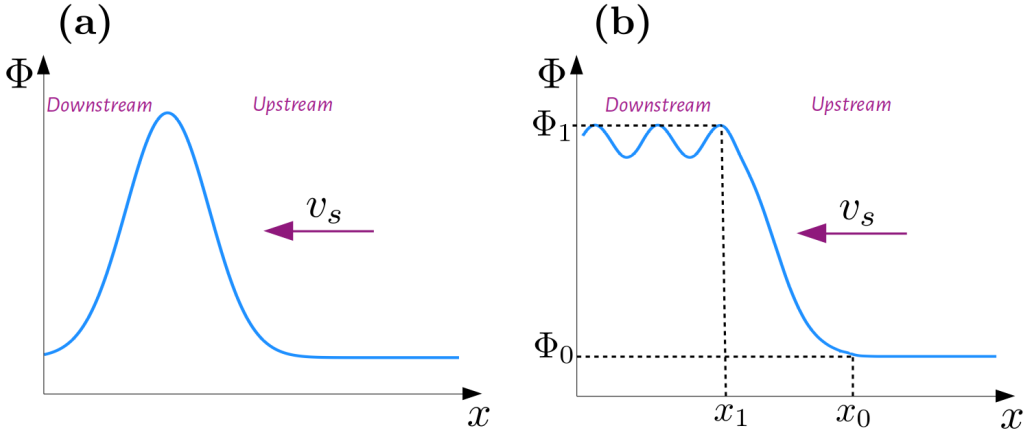
Fig. 1.6: (a) Sketch of a *soliton* wave and (b) of an electrostatic shock structure in the frame of the electrostatic perturbation.

Fig. 1.6b. The cold ions are still treated as a fluid. Considering US and DS plasma slabs with different temperatures, electron densities and/or velocities very large Mach numbers $M \gg 10$ are obtained [46]. Note that such high Mach numbers can not be supported by isothermal plasmas. Depending on the electron temperature the system is described following a classical [46] or a relativistic [95] approach.

In the framework of ion acceleration the interest of the previously described US/DS electrostatic potential structures are the so-called *supercritical shocks* [47, 96], described in Section 1.6.2, where particle reflection provides an additional energy dissipation mechanism. Both laminar and turbulent shocks have been identified [94]. Turbulent shocks exist in many astrophysical scenarios and are characterized by a shock front (SF) where instabilities such as the Weibel instability [97] amplify turbulent electromagnetic fields. Laminar shocks are formed due to the non-linear steepening of ion acoustic waves (IAW) propagating through the plasma. The mechanism is such that the head of the wave propagates faster than the foot forcing the fluid structure to steepen. Kinetic treatment of the fully steepened IAW is needed to describe the subsequent breaking of the wave [98] as well as the overtaking between different waves [99] and particle reflection from the SF. In the case of electrostatic laminar shocks, at the core of this thesis work, the SF is only mediated by the electrostatic potential discontinuity $\Delta\Phi$ [100].

The derivations of Section 1.6.1 are based on Refs. [47, 101].

1.6.1 Soliton wave propagation in a plasma with cold ions and hot electrons

Considering that the wave propagation speed $v_s \ll v_{Te}$, where v_{Te} is the electron thermal speed, and placing ourselves in the wave frame, one can use the ion fluid equations for mass and energy conservation to obtain the ion speed and density as a function of the electrostatic potential Φ

$$v_i(\Phi) = \sqrt{v_s^2 - \frac{2e\Phi}{m_i}}, \tag{1.76}$$

$$n_i(\Phi) = n_0 \left(1 - \frac{2e\Phi}{m_i v_s^2}\right)^{-1/2}, \tag{1.77}$$

where n_0 is the unperturbed plasma density far away from the soliton, and m_i the ion mass. The system closes by considering electrons in equilibrium described by a Maxwell-Boltzmann

distribution

$$n_e(\Phi) = n_0 \exp\left(\frac{e\Phi}{k_B T_e}\right), \tag{1.78}$$

and plugging Eqs. 1.77 and 1.78 into Poisson equation:

$$\frac{d^2\Phi}{dx^2} = -4\pi e(n_i - n_e) = -4\pi e n_0 \left[\left(1 - \frac{2e\Phi}{Mv_s}\right)^{-1/2} - \exp\left(\frac{e\Phi}{k_B T_e}\right)\right]. \tag{1.79}$$

We can now introduce the dimensionless variables

$$\begin{aligned} \phi &= \frac{e\Phi}{k_B T_e} \\ \chi &= \frac{x}{\lambda_{De}} \\ M &= \frac{v_s}{C_s} \end{aligned} \tag{1.80}$$

and rewrite Eq. 1.79 as

$$\frac{d^2\phi}{d\chi^2} = -\frac{d\Psi(\phi)}{d\phi}, \tag{1.81}$$

where $\Psi(\phi)$ is called the *Saagdev potential* and the r.h.s. is defined as

$$\frac{d\Psi(\phi)}{d\phi} = \left(1 - \frac{2\phi}{M^2}\right)^{-1/2} - \exp(\phi). \tag{1.82}$$

Equation 1.81 can be compared with a second harmonic oscillator equation where ϕ can be linked to x and Ψ to a so-called *pseudopotential*, which is a function of the electrostatic potential ϕ. A solitary solution occurs when Ψ is maximum at its origin and comes back to zero at some value ϕ_0 (Fig. 1.7). Making the analogy to an equation of motion, the *pseudo-particle* would describe a trajectory starting at the origin, going to the other zero of the Sagdeev potential and coming back to the origin [47].

Integrating Eq. 1.81 with respect to ϕ one obtains:

$$\frac{1}{2}\left(\frac{d\phi}{d\chi}\right)^2 + \Psi - \Psi_0 = 0, \tag{1.83}$$

with

$$\Psi(\phi) = 1 - \exp(\phi) + M^2\left(1 - \sqrt{1 - \frac{2\phi}{M^2}}\right). \tag{1.84}$$

In Eq. 1.84, Ψ_0 was chosen so that $\Psi(\phi) = 0$ for $\phi = 0$.

The condition for the existence of a soliton solution can be extracted from Eq. 1.83 considering $\Psi(\phi, M) < 0$ for $\phi \ll 1$

$$\Psi(\phi) \approx -\frac{\phi^2}{2} + \frac{\phi^2}{2M^2} < 0, \tag{1.85}$$

which sets the minimum Mach number $M_{min.} = 1$. The potential cannot raise indefinitely, i.e. $\Psi(\phi) > 0$ at the so-called critical potential ϕ_c:

$$\phi_c = \frac{M^2}{2}. \tag{1.86}$$

Introducing $\phi = \phi_c$ in Eq. 1.84 we obtain the maximum Mach number $M_{max.} \approx 1.6$. Fig. 1.7 shows the pseudopotential $\Psi(\phi)$ of Eq. 1.84 for three different Mach numbers. Note the electrostatic potential growing from right to left.
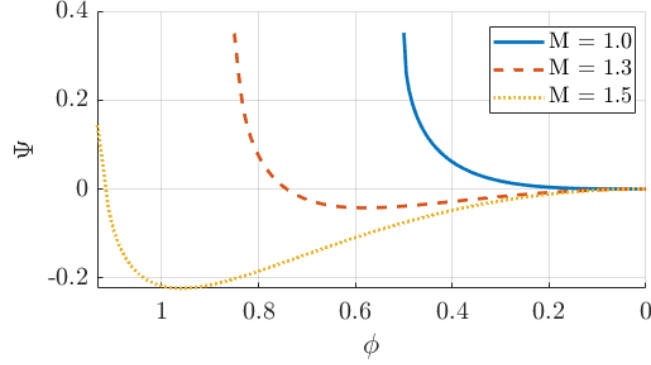
Fig. 1.7: Pseudopotential $\Psi(\phi)$ (Eq. 1.84) for three different Mach numbers.

The shape of the soliton can be obtained from Eq. 1.83:

$$\phi(\chi) = \phi_{max}\cosh^{-4}\left(\frac{\phi_{max}^{1/4}\chi}{\sqrt{15/\pi}}\right), \tag{1.87}$$

where $\phi_{max} = (15/8)^2\pi(M-1)^2$, i.e. the soliton amplitude is proportional to $(M-1)^2$. The soliton potential shapes $\phi(\chi)$, considering M=1.3, 1.5 and 1.7, are plotted in Fig. 1.8.
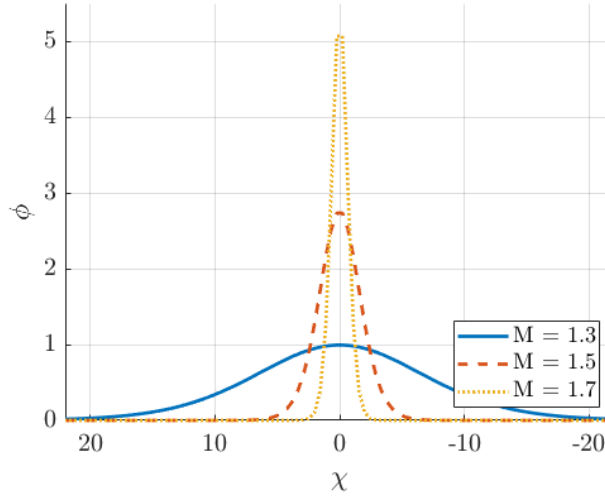
Fig. 1.8: The soliton potential shapes $\phi(\chi)$ considering M=1.3, 1.5 and 1.7.

A shock solution takes place when symmetry of the solitary wave system is broken by e.g., particle reflection. In this case the *pseudo-particle* does not come back to the origin, but it ends in the potential well. In Ref. [47] a shock solution of the system, for the normalized parameters $T = Z^*T_e/T_i = 15$ and $V = v_s/\sqrt{k_B T_i/m_i}$ 4.5, has been found and it is shown in Figs. 1.9a and b.

When $M^2 \gg 1$ and $M^2 \gg \Theta$, where $\Theta = T_1/T_0$ is the temperature ratio between the DS and the US, the maximum Mach number can be written as [46]

$$M_{max.} \approx \frac{3(\Gamma+1)}{\Gamma}\sqrt{\frac{\pi\Theta}{8}}. \tag{1.88}$$
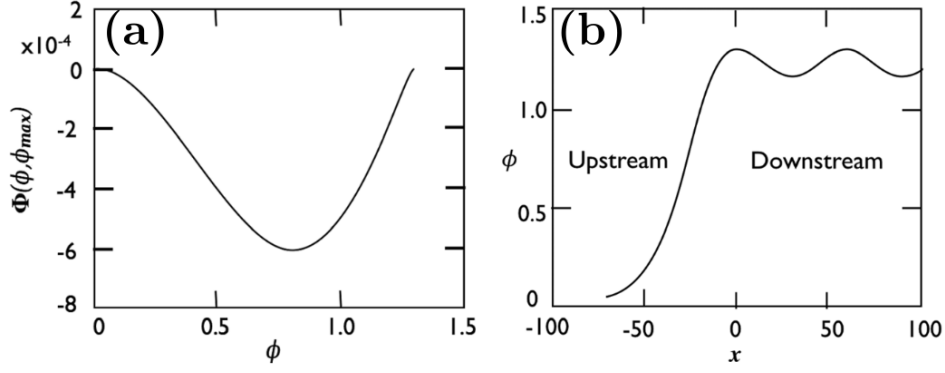
Fig. 1.9: Shock solution found in Ref. [47] for the normalized parameters $T = Z^* T_e / T_i = 15$ and $V = v_s / \sqrt{k_B T_i / m_i}$ 4.5. (a) Sagdeev *pseudopotential* and (b) shape of the potential $\phi(x)$ at the shock region.

Fig. 1.10 shows the prediction of the maximum Mach number according to Eq. 1.88 considering two plasma slabs with density ratio $\Gamma = \mathcal{N}_1 / \mathcal{N}_0 = 1$, 3 and 1/3 and temperature ratios $\Theta = T_1 / T_0$ from 1 to 100.
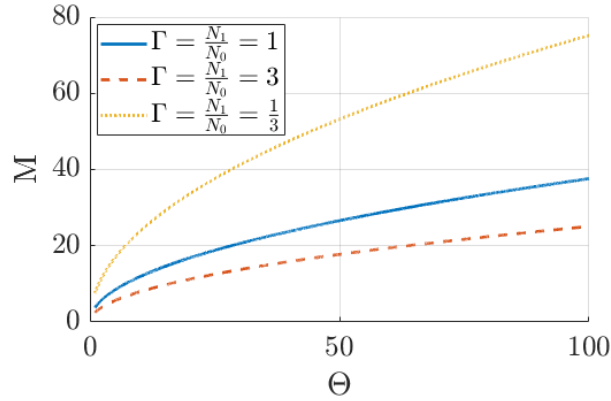
Fig. 1.10: Prediction of the maximum Mach number according to Eq. 1.88 considering two plasma slabs with density ratios $\Gamma = \mathcal{N}_1 / \mathcal{N}_0$ equal to 1, 3 and 1/3 and temperature ratios $\Theta = T_1 / T_0$ from 1 to 100.

The solid blue line represents the case $\Gamma = 1$ where two plasma slabs with equal densities collide and the maximum Mach number $M_{max.} \approx 3$. The minimum Mach number is found imposing that the *Saagdev potential* is negative at its minimum. Considering $\Theta = \Gamma = 1$ one obtains a minimum Mach number $M_{min.} = 1$, i.e. as in the hydrodynamic limit [46].

1.6.2 Collisionless electrostatic shock waves

The interaction of two *collisionless* plasmas with either different densities, temperatures or velocities can lead to the formation of non-linear electrostatic potential structures capable of trapping and/or reflecting charged particles [44–47]. This is depicted in Fig. 1.11, here the DS plasma slab has interacted with a high-intensity laser propagating from left to right that has transferred part of its energy to the electrons heating this plasma region. The US plasma slab has interacted with a highly depleted laser, one can imagine a situation where the laser has been almost completely absorbed inside the DS plasma slab. Hence, the US plasma slab is colder and more rarefied than the DS one. The electrostatic potential $\Delta\Phi$ created in the region located in between both plasma slabs, the so-called *shock region*, will determine, along with the kinetic

energy of the incoming particles, whether the particle is decelerated, accelerated (reflected) or gets trapped in the DS region of the shock. This ion acceleration mechanism, which can trigger partial reflection of background ions at twice the shock velocity, is called *collisionless shock acceleration* (CSA). An ion will be reflected from the SF is its kinetic energy is lower than the electrostatic potential that it experiences in the *shock region*. The shock reflection condition in the shock frame reads:

$$\frac{m_i \left(v_0 - v_s\right)^2}{2} < Z^* e \Delta \Phi, \qquad (1.89)$$

where v_0 is the lab-frame incoming ion velocity, v_s if the lab-frame shock velocity, Z^* is the ionic charge state and e the electron charge. An ion can also cross the *shock region* if it has a high velocity, in which case the electrostatic shock potential $\Delta \Phi$ will slow it down. The slowest electrons can get trapped in the potential wells present in the downstream plasma forming electron vortices.
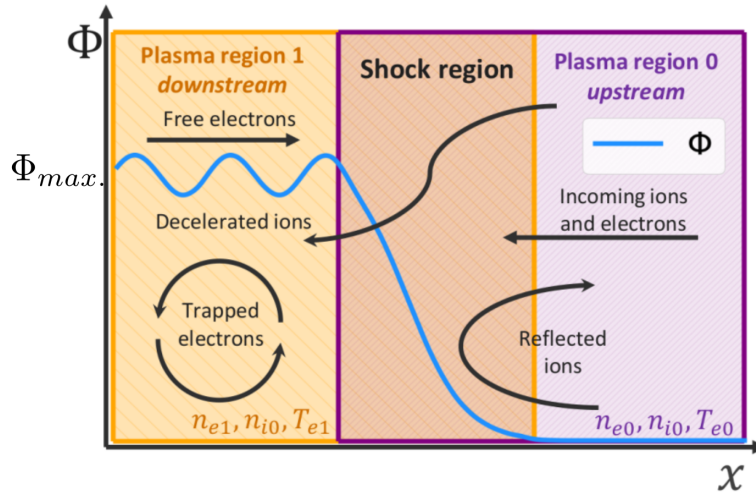
Fig. 1.11: Schematic representation of the interaction of two collisionless plasmas with either different densities, temperatures or velocities which can lead to the formation of non-linear structures capable of trapping and/or reflecting charged particles. The electrostatic potential $\Delta \Phi$ created in the region located in between both plasma slabs, the so-called *shock region*, will determine, along with the kinetic energy of the incoming particles, whether the particle is decelerated, accelerated (reflected) or gets trapped in the downstream region of the shock. Figure inspired from Ref. [23].

Electrostatic shocks can be triggered in several scenarios. Pioneer [48, 49] and more recent [59, 102] works regarding CSA were centered on the generation of electrostatic shocks by applying a laser piston to the boundary of an uniform overcritical plasma. Other studies have considered the shocks triggered from the overcritical boundary of a density decreasing plasma [23, 24, 50]. This thesis work aims at understanding electrostatic shock formation in transparent plasmas, where strong electron pressure gradients accompanied by laser-driven ion pre-acceleration can trigger shock formation [28, 30, 58, 62, 103]. Depending on the gaseous profile, other ion acceleration mechanisms can accompany CSA, e.g. TNSA [23, 24] or magnetic vortex acceleration (MVA) [19, 20, 42, 104–106]. A parametric 1-D PIC study of laminar collisionless electrostatic shock waves excited during the interaction of an UHI laser pulse with a non-uniform gaseous target is described in detail in Chapter 3. An experimental attempt of realizing such scenario is summarized in Chapter 4 and Chapter 2. Finally, Chapter 5 details a 2-D simulation performed to explain the experimental results as well as to direct future experimental research to the generation of forward collisionless electrostatic shocks.

34

Chapter 2

Operation and characterization of pressurized gas target systems

2.1 Introduction

Although gaseous targets constitute a promising path to high-repetition-rate debris-free ultra-high intensity (UHI) laser interaction [107–109], they are still new targetry systems. As so, one must understand how to use them, as well as single out the advantages and possible difficulties that they entail. The present chapter presents the high-pressure gas system (HPGS) used during the experimental tasks of this thesis. The latter is composed of the SL-GT-10 commercial gas compressor developed by SourceLab [110] coupled to diverse shock nozzles. We implemented two shock nozzle models: the J2021 (developed by SourceLab) and the S900 nozzle developed inside our collaboration group with the objective of forming the shock far away from the nozzle's surface to reduce the on-shot laser-induced nozzle damage (LIND). The current nozzle production techniques are not capable of delivering reliable nozzles that produce the same density profile as the one obtained from computational fluid dynamic (CFD) simulations. As a result, one must characterize the HPGS for each nozzle and gas type and manually select the gas density profiles to be targeted during UHI shots. The characterization technique, which is detailed below, is based on interferometric and a strioscopy optical lines.

Section 2.2 and 2.3 summarize the outcome of two HPGS characterization campaigns performed with two different electrovalves, the so-called *rapid valve* (used during the VEGA-2 experiment) and the *microvalve* (used during the VEGA-3 experiment). Refer to Chapter 4 for details on both experimental campaigns. The objective was to locate safe gas-leakage-free operating points where interesting density profiles could be produced. Based on the outcome of the numerical 1-D parametric study, which is presented in Chapter 3, we defined an "interesting profile" as one that exhibits a maximum atomic density $n_{at,max} \approx 10^{20}$ cm^{-3} and that has a visible density peak.

Finally, Section 2.4 describes the performance of the HPGS in UHI shots performed during the VEGA-3 experimental campaign, emphasizing on the LIND. It also discusses the strategy that one found to cope with the damage, in order to increase the experiment's repetition-rate as much as possible. The latter is based on adapting the shock height before each UHI shot.

2.1.1 High-pressure gas system (HPGS)

The gas profile's shape and maximum density depend on several factors: the gas nozzle, the gas electrovalve connected to the gas nozzle, the compressor and gas valve parameters and the gas type. The compressor and gas valve input parameters are: the compressor's backing pressure (P), the gas valve opening time (VOT) and temporal delay between the valve's opening and the laser-gas interaction (CD).

Figure 2.1 shows a scheme of the gas system in which all the mentioned parameters are interconnected. The pressurized gas bottles (normally pressurized between 10 bar for helium and 100 bar for nitrogen) are connected to a gas mixer and regulator system that feeds the gas compressor with a constant pressure. In case of a pure gas, the gas mixer system acts merely as a pressure regulator. As mentioned before, during this thesis work we specifically used the SL-GT-10 gas compressor developed by Sourcelab. This compressor uses pistons to compress the initial gas 75 times with an output nominal pressure between 300 and 400 bar. For this it uses a pressurized air input at 7 bar. An emergency security valve (ESV) is located after the compressor and before entering the interaction chamber. Afterwards a short tube (≈ 1 m) connects the ESV with the main gas electrovalve located inside the vacuum chamber. The gas nozzle is screwed to the exit of the main electrovalve's output, being easily interchangeable. The ESV separates the gas volume that would actually enter the interaction chamber in case the main gas electrovalve fails. This is the reason for the connection between the ESV and the main gas electrovalve to be as short as possible.
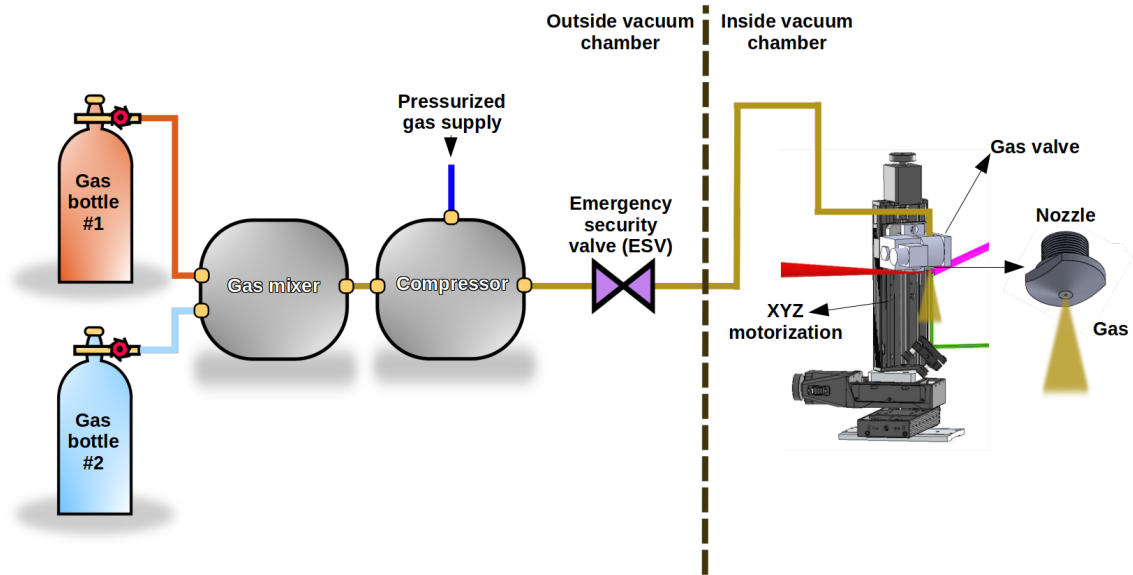
Fig. 2.1: High pressure gas system (HPGS) scheme.

2.1.2 Neutral gas profiles characterization

The characterization of the neutral gas profiles is performed with the SID-4 wavefront sensor sold by the Phasics company. The SID-4 is a plug-and-play modified Hartmann wavefront sensor [107]. A strong continuous diode needs to traverse the neutral gas region of interest and enter perpendicularly to the acquisition CCD. The SID-4 sensor is fielded together with a strioscopy line to analyze the temporal evolution of the density at the shock height. To reduce the number of optical lines a 50/50 beam splitter splits the initial path in two. The reflected light is sent to the SID-4 sensor, and the transmitted one is spatially filtered and directed to a fast photodiode ,connected to an oscilloscope, to acquire time dependent strioscopy signals. The transmitted light also traverses an interferometric filter with central wavelength equal to the diode's one to clean the signal from spurious light coming from the interaction region. The SID-4 plus strioscopy line diagnostic scheme was used during the two characterization campaigns detailed below as well as in the actual VEGA-3 experiment.

The phase charts obtained using the SID-4 wavefront sensor are analyzed using both the Density module of the SID-4 software and a homemade Python routine. Both analysis result on very similar density charts. The advantages of the homemade routine are the possibility to perform batch analysis (the Density module needs to be manually operated analyzing a single-shot at a time) and the fact that the entire phase analysis process is known. The latter includes cropping the phase chart, making the phase chart left border equal to zero so that the density calculation is correct, the symmetrization of the resulting phase chart and the resolution of the inverse Abel equation selecting a numerical method to perform such calculation. The mentioned script makes use of any of the Abel inversion methods included in the PyAbel [111] library. Since there are many different factors that can affect the density calculation, it is interesting to perform the phase charts analysis controlling each step, which is possible by using the cited Python routing. On the contrary, the SID-4 Density module is designed as a "black box", where the user can not modified or access information on the analysis script. Furthermore, the phase charts' analysis was also performed independently by our collaborators from IPPLM using the fast Fourier transformation (FFT) method to solve the Abel equation [112–114], and obtaining very similar density maps.

Fig. 2.2 plots the phase chart corresponding to shot #184 in radians/2π. Fig. 2.3a shows the obtained density map using the homemade routine and the Hansenlaw [111] method, Fig. 2.3b
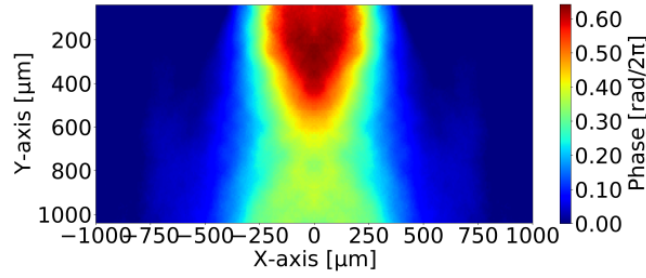
Fig. 2.2: Neutral gas characterization phase chart (in radians/2π) acquired before the UHI shot #184.

the SID-4 density module, Fig. 2.3c the homemade Python routine and the three-point [111] method and Fig. 2.3d the FFT method to solve the Abel equation. Finally, Fig. 2.3e shows transverse lineouts at the shock height of Figs. 2.3a-d. As can be seen all the methods produce a similar density chart and density lineout at the shock height.
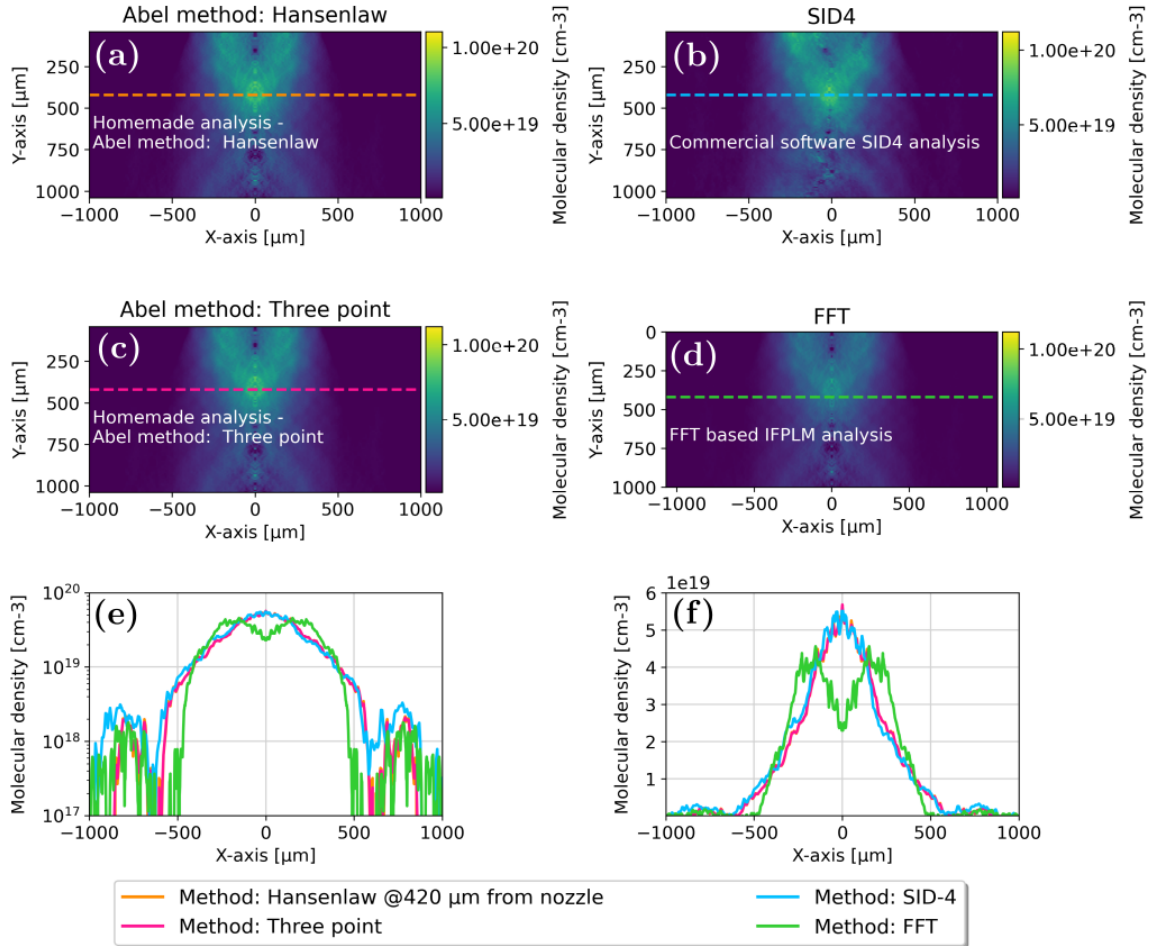
Fig. 2.3: (a) Density map obtained using the homemade routine and the Hansenlaw [111] method, (b) the SID-4 density module, (c) the homemade Python routine and the three-point [111] method and (d) the FFT method to solve the Abel equation. (e) Transverse lineouts at the shock height (plotted in logarithmic scale) extracted from the density charts plotted in (a-d) and (f) same curves as (e) plotted in linear scale.

2.1.3 Design and types of gas nozzles

The design of gas nozzles normally begins by performing CFD simulations either with commercial software such as Fluent [115], or research developed ones such as ARES [116]. Such simulations are based on numerically solving the Navier-Stokes equations on a discrete grid. The code needs a nozzle geometry and a reservoir pressure as inputs. The reservoir pressure translates experimentally into the compressor's backing pressure. Normally, a cylindrically symmetric convergent-divergent geometry is chosen because of its relatively easy fabrication and well known fluid properties [117, 118]. As seen in Fig. 2.4a the cited convergent-divergent nozzle geometry is composed of a gas reservoir, a convergent section, a throat and an expansion section that connects with the laser interaction chamber under vacuum. The main objective of a nozzle is to accelerate a flow throughout the conversion of available pressure and internal energy into kinetic energy. In case of compressible fluids such as gases, it is possible to accelerate subsonic flows up to supersonic speeds v_f (characterized by a Mach number $M = v_f/C_s > 1$, where $C_s = \sqrt{Zk_BT_e/m_i}$ is the ion acoustic speed, k_B the Boltzmann constant, T_e the electron temperature and m_i the ion mass) if the reservoir's pressure is high enough [119]. Hence the common designation of gas nozzles as supersonic nozzles.

Once the nozzle is constructed it is tested to check that the density profiles agree with the CFD simulations. An optical interferometer is used to measure the output density. At the same time, a cylindrical symmetry is imposed to be able to reconstruct the nozzle's output gas density profiles, by applying a numerical Abel inversion to the obtained phase charts, see Appendix A for more details.
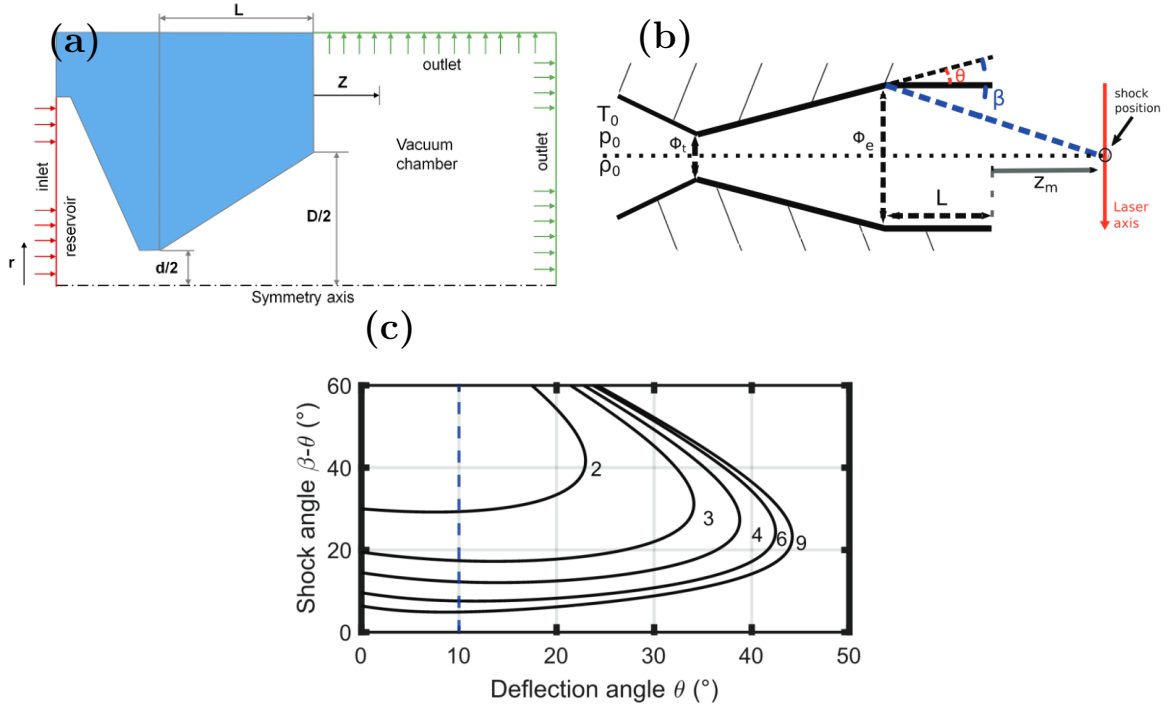
Fig. 2.4: (a) Cylindrically symmetric Laval gas nozzle scheme input into computer aided fluid dynamics (CFD) simulations. Extracted from Ref. [118]. (b) Shock nozzle scheme composed of a Laval nozzle with a straight conduct added at the end of the divergent section. (c) Shock angle $\beta - \alpha$ as a function of the deflection angle θ for different Mach numbers. Fig. (b) and (c) were extracted from Ref. [120].

The most common gas nozzles are those called "Laval nozzles", which produce Gaussian-like gas profiles using convergent-divergent geometries such as the one plotted in Fig. 2.4a. Laval nozzles are normally used in electron wakefield acceleration experiments [121].

Ion acceleration from near-critical transparent gas targets is intrinsically related to the inner charge separation fields that can be created inside the plasma. Therefore, the stronger the initial gas density gradients are, the more will electrostatic longitudinal fields inside the plasma be enhanced. In this scenario, Gaussian-like density profiles extracted from Laval nozzles, are not as interesting as the strong density gradients that can be obtained using the so-called shock nozzles [120]. The present shock nozzle description follows from Ref. [120]. A supersonic flow shock is characterized by a sudden reduction of the flow's Mach number, that has as a consequence the compression of the gas in the shock region. A shock nozzle consists of a Laval geometry with an extra straight conduct attached to its divergent section, see Fig. 2.4b. When the output divergent flow encounters the conduct's walls, it generates a shock wave at the angle β from the original flow direction. The different shock fronts then converge on the nozzle axis at a distance z_m from the nozzle's exit, which is a function of the length of the straight section and of the shock angle $\beta - \alpha$. The relationship between the shock angle $\beta - \alpha$, the deflection angle θ and the shock's upstream Mach number M_1 is

$$\tan \theta = 2 \cot \beta \frac{M_1^2 \sin^2 \beta - 1}{M_1^2(\gamma + \cos 2\beta) + 2}, \tag{2.1}$$

where γ is the specific heat ratio of the gas, equal to 5/3 for a monoatomic gas and 7/5 for a diatomic gas. The solution of Eq. 2.1 for different Mach numbers is plotted in Fig.2.4c. The solutions for $\theta = 10°$ are the intersections of the vertical blue dashed line with the different curves. As can be deduced, two different solutions exist for each deflection angle and upstream Mach number M_1: the low shock angle $\beta - \alpha$ solution, called the *weak shock solution*, where the downstream Mach number is still supersonic $M_2 > 1$; and the high shock angle $\beta - \alpha$ solution, called the *strong shock solution*, with a subsonic downstream shock velocity. The strong shock solution requires high pressures downstream. Since the experimental supersonic flow expands in a chamber in vacuum, the weak shock solution is obtained. The shock front converging distance z_m can be calculated geometrically following Fig. 2.4b

$$z_m = \frac{\phi_e/2}{\tan(\beta - \theta)} - L, \tag{2.2}$$

where ϕ_e is the nozzle exit diameter and L is the length of the straight conduct. z_m is given with respect to the nozzle external surface, which is the natural experimental parameter to use. As a general rule and looking at Eq. 2.2, the shock angle $\beta - \alpha$ must be kept as small as possible to form the shock far away from the nozzle's surface. When the shock is formed close to the nozzle, the laser-gas interaction takes place very close to the nozzle's surface. The laser induces nozzle ablation and melting [70] which alters the gas density profiles, therefore inhibiting high-repetition rate (HRR) operation.

One must take into account that Eqs. 2.1 and 2.2 do not give neither any information regarding the density obtained at the shock point (Fig. 2.4b), nor about the effect of varying the straight conduct's length L. To estimate these parameters CFD simulations must be performed.

2.1.4 Shock nozzles used during this thesis experimental work: S900 and J2021

The experimental work of this thesis was carried out with two different previously designed shock nozzles: the S900 nozzle developed by the LP2i and CELIA laboratories of the University of Bordeaux [108,118] and the J2021 nozzle sold by Sourcelab.

The S900 nozzle was specifically designed to produce a shock further away from the nozzle than in the J2021 case. This was one of the major developments implemented on the VEGA-3
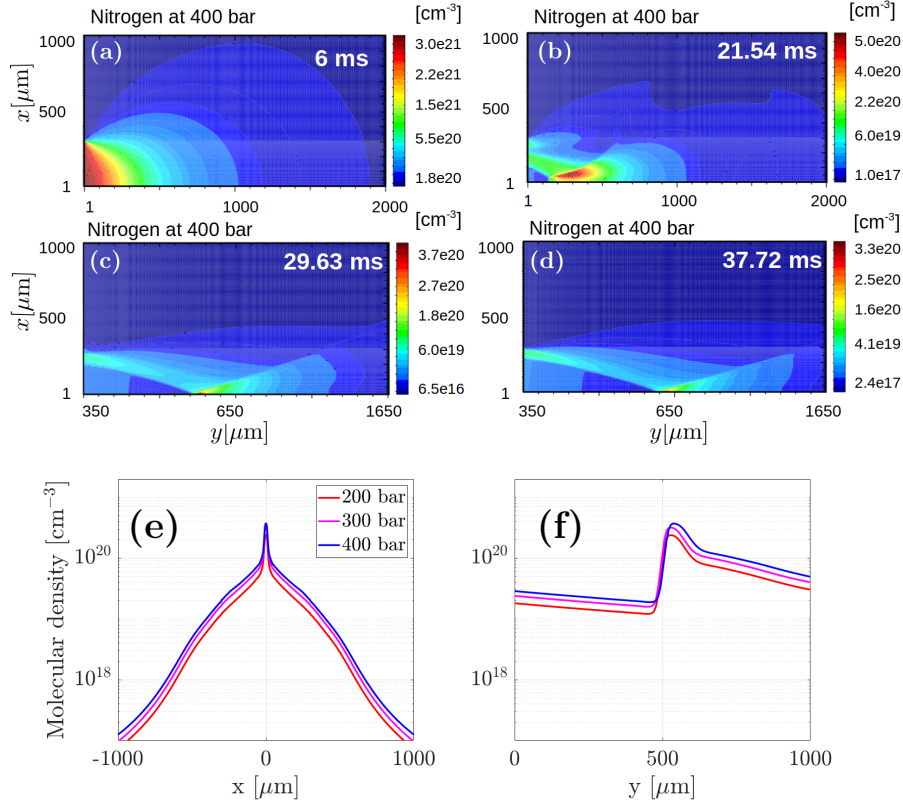
Fig. 2.5: (a-f) ARES code simulation of the gas jet output for the S900 nozzle geometry gas output as a function of the nitrogen reservoir's pressure. (a-d) Molecular density maps in cm^{-3} showing the evolution of the exit flow inputting 400 bar of nitrogen, corresponding to the simulation times 6, 21.54, 29.63 and 37.72 ms, respectively. The (a-d) panels concern the left-side of the cylindrically symmetric exit flow, considering the y axis as the axis of symmetry. The $y = 0$ point is located at the nozzle's surface. (e) Transverse (at $y = 650 \, \mu$m) and (f) longitudinal density profiles (at $x = 0$), respectively (in respect to the gas flow), taken at $t = 37.72$ ms for an input reservoir nitrogen pressure of 200 (red line), 300 (pink line) and 400 bar (blue line, corresponding to a lineout of d at $y = 650 \, \mu$m). The $y = 0$ point in (f) corresponds to the nozzle's surface (note that being nitrogen a diatomic element $n_{at,N_2} = 2 \cdot n_{mol,N_2}$).

campaign. The objective was to interact further away from the nozzle's surface than in the VEGA-2 experiment, diminishing the nozzle ablation rates and improving the HRR operation.

The design and development of gas nozzles was not part of this thesis' work. Dr. Jose Luis Henares and Dr. Thanh-ha Nguyen-bui from the LP2i and CELIA laboratories of the University of Bordeaux, respectively, designed the S900 nozzle in the framework of our collaboration. Nevertheless, the characterization of both nozzles was a fundamental process inside this thesis' experimental tasks.

The ARES code was used to simulate the S900 nozzle geometry gas output as a function of the nitrogen reservoir's pressure, the result is plotted in Figs. 2.5a-f. The CFD ARES simulations were performed by Dr. Thanh-ha Nguyen-bui in the framework of our collaboration.

Figures 2.5a-d are molecular density maps of the exit flow inputting nitrogen at 400 bar and taken 6, 21.54, 29.63 and 37.72 ms after the beginning of the CFD simulation, respectively. The y axis is an axis of symmetry. The $y = 0$ point is located at the nozzle's surface. Fig. 2.5e and f are transverse and longitudinal density profiles, respectively, taken 37.72 ms after the beginning of the simulation with an input reservoir nitrogen pressure of 200 (red line), 300 (pink line) and 400 bar (blue line). The blue transverse and longitudinal profiles correspond to lineouts of (d) along x and y, respectively. In (f) the $y = 0$ point corresponds to the nozzle's

surface as well.

According to the ARES simulations the variation of the reservoir's pressure from 200 bar to 400 bar entails an increase in the maximum molecular density from $2.3 \times 10^{20} \text{cm}^{-3}$ to $3.7 \times 10^{20} \text{cm}^{-3}$, a 25% increment (Fig. 2.5e and f). Such simulations also locate the vertical shock position at 528 µm and 535 µm when inputting a reservoir pressure of 200 bar and 400 bar, respectively (Fig. 2.5b).

Both Fluent [115] and ARES [116] CFD codes were used to simulate the output of the S900 nozzle, obtaining similar density profiles which are plotted in Fig. 2.6 (simulating nitrogen with a reservoir pressure of 400 bar). Dr. Jose Luis Henares performed the Fluent CFD simulations which predict a ≈ 3 times higher maximum density peak than the ARES simulation output. At the same time, the shock is forecast to form at ≈ 650 µm in the Fluent simulation, and at ≈ 535 µm in the ARES simulation (Fig. 2.6d). The distances are given with respect to the nozzle's surface. The study of the vertical shock position discrepancy between both codes lays outside of the scope of this thesis work. Nevertheless, it is an interesting point to work on towards benchmarking both CFD codes, which can be done with loops of simulations and experimental profile characterizations. Since the Fluent results compare better with the experimental data, we will use them hereinafter for successive comparisons.
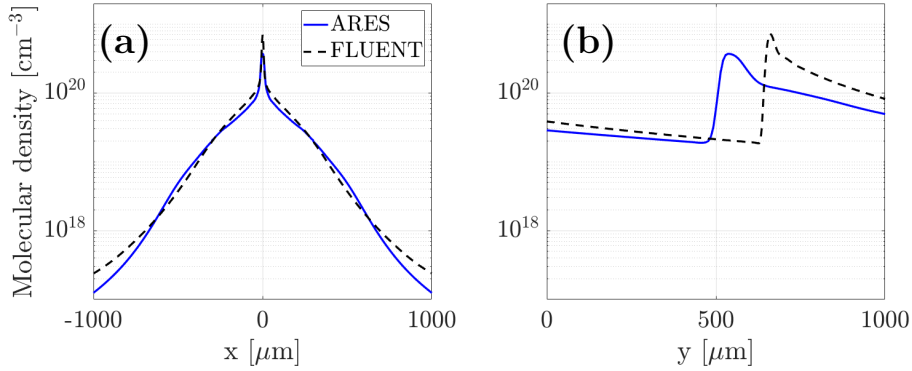
Fig. 2.6: (a) Transverse and (b) longitudinal density profiles obtained after simulating the S900 nozzle using the Fluent [115] and ARES [116] codes inputting a pressure reservoir of 400 bar of nitrogen.

Figures 2.7a and b show the obtained transverse and longitudinal density profiles, respectively, with a 400 bar nitrogen reservoir for both the S900 (dashed line curves) and J2021 (solid line curves) nozzles using the Fluent code. The S900 and J2021 transverse profiles are characterized by density wings with a density scale length $L_n \approx 180$ µm. The difference between both nozzles lays on the density ratio between the background and the peak density. The S900 profile has a density peak that is denser by a factor ≈ 7 than the surrounding gas (considering a background density $n_{N_2,b} \approx 2 \times 10^{20} \text{cm}^{-3}$ in Fig. 2.7a, dashed line). In the J2021 case the density peak is shallower, only four times denser than the background density ($n_{N_2,b} = 7 \times 10^{20} \text{cm}^{-3}$ in Fig. 2.7a, solid line).

Regarding the longitudinal gas profiles of Fig. 2.7b, the S900 nozzle shock forms at $y \approx 650$ µm from the nozzle's surface while the J2021 shock converges at $y \approx 450$ µm. As mentioned before, the S900 nozzle was intentionally designed to produce the shock further away from the nozzle's surface than in the J2021 case. This was done to reduce the nozzle's laser damage encountered in the VEGA-2 campaign (where J2021 nozzle was used, as well as other nozzle designs).
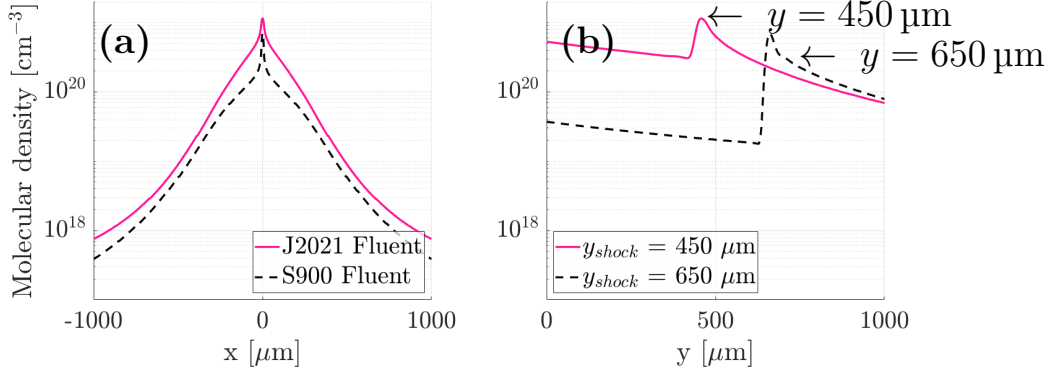
Fig. 2.7: (a) Transverse and (b) longitudinal density profiles obtained by performing computer fluid dynamics (CFD) simulations with the Fluent code for the S900 (dashed line curves) and J2021 (solid line curves) nozzles with a 400 bar nitrogen reservoir.

2.2 *Rapid valve* and *microvalve* characterization campaign

A factor that is normally not taken into account in CFD simulations is the aperture curve of the electrovalve with respect to time, i.e. the fact that the pressure reservoir is not instantly connected with the body of the valve. Experimentally, the connection between the pressure reservoir (the gas compressor output) and the nozzle is done with an electrovalve. The behavior of such electrovalve can affect the output profiles. All the CFD simulations described in Section 2.1.3 were performed considering a perfect step function as the electrovalve's flow vs. stem position curve. A valve's stem is the mechanical axis of the valve which moves longitudinally, along the valve's axis, to open or close it.

During the VEGA-2 experiment the so-called *rapid valve*, developed by Sourcelab, was used. One of the most important problems faced during the VEGA-2 campaign were the gas leakages, occurring when the *rapid valve* was commanded to keep opened for more than ≈ 5 ms. These leakages are very dangerous for the vacuum turbomolecular pumps connected to the interaction chamber, as well as for the laser compressor gratings that must be kept strictly under high-vacuum ($\approx 10^{-6}$ mbar). One of the major improvements for the VEGA-3 campaign was the acquisition of the newly developed Sourcelab electrovalve, called the *microvalve*. This new valve was designed precisely to solve the leakages problem by being more adapted to the small micrometric throats of the shock nozzles that were used in this thesis work, and by having a normally-closed operating valve system. The *rapid valve* used in the VEGA-2 experiment was a normally-opened valve. Figs. 2.8a and b are 3-D CAD renders of both the *rapid valve* and the *microvalve*, respectively.

Fig. 2.9 plots an approximate behavior of the output density with respect to the valve opening time extracted from the characterization of both valves performed during this thesis work. No specific valve curves were delivered by the manufacturer. As can be seen the *rapid valve* reaches a maximum density output at ≈ 5 ms while the *microvalve* reaches such point at ≈ 40 ms.

The electrovalves are characterized by a flow rate with respect to the valve's stem position curve, which is inherent to the device's design, specifically the valve seat and closure member [122]. Figs. 2.10a and b show the quick-opening, linear and equal-percentage flow vs. stem position curves as well as their respective valve seat and closure member designs, respectively. In the case of the *rapid valve*, such curve is an imperfect step function that characterizes the so-called "quick-opening" valves [123]. A quick-opening valve produces a large increase in flow
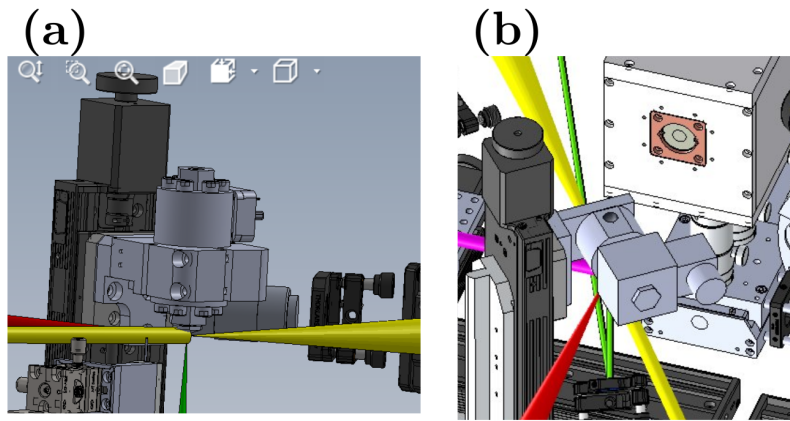
Fig. 2.8: 3-D CAD renders of the (a) *rapid valve* and the (b) *microvalve.*
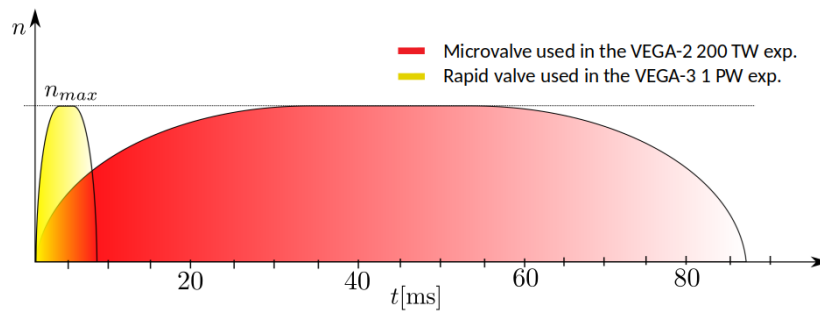
Fig. 2.9: *Microvalve* and *rapid valve* approximate behavior regarding the output density with respect to the valve opening time.

for a small initial change in stem travel distance. The *microvalve* behavior is different and relates more to the so-called "equal-percentage" flow vs. valve stem position curves [123]. For such valves an increment in the stem position produces an equal-percentage increment in exit flow. Such curves can be fitted to an exponential function [122]. There are also the linear valves, in which the exit flow is directly proportional to the stem position.

Rapid valve and *microvalve* characterization campaign

The *rapid valve* and *microvalve* behaviors were studied during a characterization campaign performed in October 2020, two years after the VEGA-2 experiment (detailed in Chapter 4). This characterization campaign was performed using argon and the J2021 nozzle. Argon should behave exactly the same as nitrogen, which gave us confidence towards extrapolating the characterization results to the real experimental conditions (where nitrogen gases were used). The HPGS that was used is the one sketched in Fig. 2.1. The optical path implemented for the characterization of the neutral gas is shown in Fig. 2.11. The SID-4 wavefront sensor developed by Phasics [124] was used.

Both the *microvalve* and the *rapid valve* were characterized with the objective of selecting the safest electrovalve to be used in the VEGA-3 experiment. The characterization outputs were:

I) Gas leakages occurrence as a function of the electrovalve and the valve opening time (VOT).

II) Transverse density profiles at the shock position as a function of the compressor's backing pressure (P), the valve opening time (VOT) and the delay between the opening of the valve and the arrival of the laser (CD).
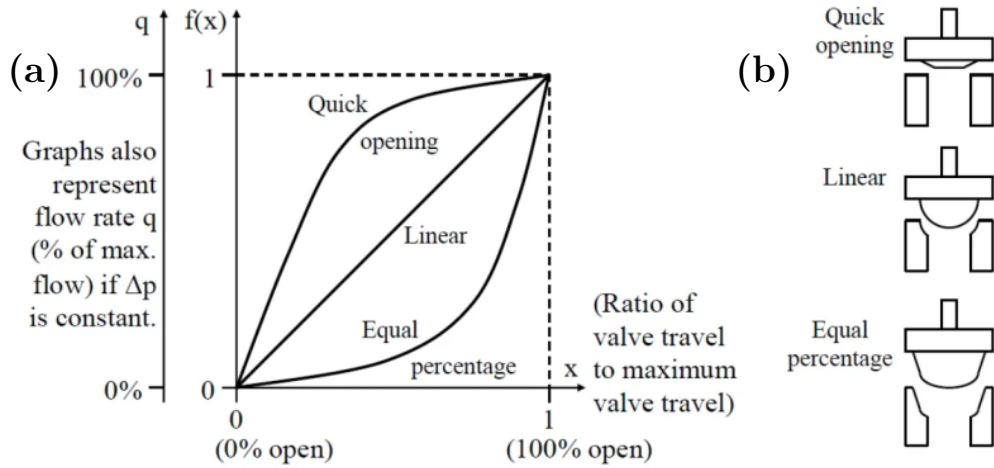
Fig. 2.10: (a) Quick-opening, linear and equal-percentage flow vs. stem position valve opening curves and (b) their respective valve seat and closure member designs. Extracted from Ref. [122].
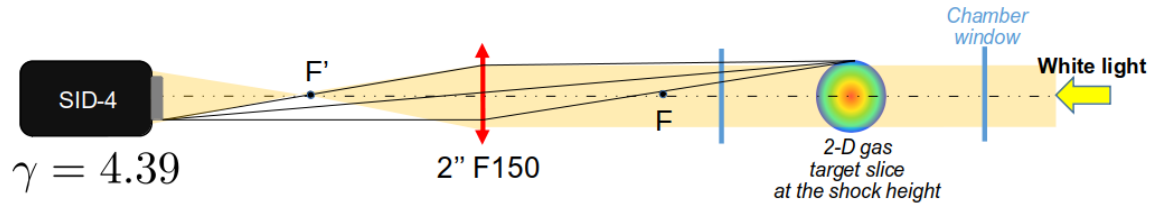
Fig. 2.11: Optical setup used to characterize the phase shifts of the probe beam through the dense gas during the *rapid valve* and *microvalve* characterization campaign.

III) Longitudinal density profiles at the shock position as a function of P, VOT and CD.

The results are summarized bellow.

2.2.1 Gas leakages occurrence as a function of the electrovalve and its opening time

In the cited characterization measurements, P was varied from 300 bar to 400 bar and in each pressure abscissa the minimum and maximum VOTs were found (Figs. 2.12a and b). The minimum VOT has to do with the inner electronics of the normally-opened *rapid valve* and the normally-closed *microvalve*. None of the valves open with VOTs lower than the minimum values.

The maximum VOTs for the *rapid valve* (Fig. 2.12a, purple dots) rise from 4.2 ms to 5.5 ms for backing pressures between 300 bar and 400 bar. The minimum VOTs (Fig. 2.12a, green dots) do not depend on backing pressure, while the maximum values exhibit a linear dependence with respect to P: $VOT[ms] = 0.012 \cdot P[bar] + 0.46$.

The VOTs corresponding to the the *microvalve* are plotted in Fig. 2.12b: maximum VOTs in red dots and minimum VOTs in blue dots. The minimum and maximum VOTs for the *rapid valve* are re-plotted in Fig. 2.12b for comparison purposes. In the *microvalve* case, no gas leakages were observed. The maximum VOT was determined when the measured density profile was quasi-constant. Larger VOTs can be applied without major change in the output gas profile. During the VEGA-3 experiment, VOTs up to 60 ms were input, searching for the most stable operating points, see Section 2.4 for more details.
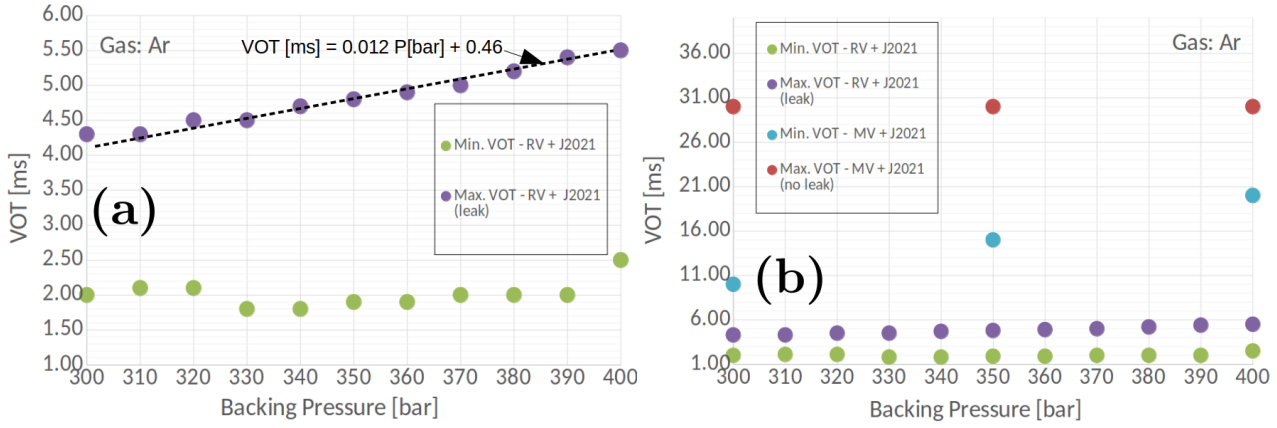
Fig. 2.12: (a) Results of a characterization performed two years after the VEGA-2 experiment using the *rapid valve* (RV, which was used during the VEGA-2 experiment), the J2021 nozzle and argon gas. The maximum VOTs (purple dots) correspond to points were a gas leakage occurs and follow the linear dependence VOT[ms] = 0.012·P[bar]+0.46. The minimum VOTs (green dots) depend on the electronics of the electrovalve, below these VOT values the valve does not open. (b) Results of a characterization performed between the VEGA-2 and the VEGA-3 experiments using the newly developed *microvalve* (MV, used during the VEGA-3 experiment), the J2021 nozzle and argon gas. In the *microvalve* case no gas leakages occurred. The maximum VOTs (red dots) were determined when the obtained density profile was quasi-constant. The minimum VOTs (blue dots) follow the same behavior as (a). The data points plotted in (a) are re-plotted here for comparison purposes.

The *microvalve* was proven to be leakage-free, as expected from its normally-closed design, and the *rapid valve* leakages were localized between VOTs equal to 4.25 ms and 5.50 ms for 300 and 400 bar of backing pressure, respectively. Below the VOT[ms] = 0.012 · P[bar] + 0.46 line, a large range of leakage-free operating points was found. However, the behavior during UHI shots will also be conditioned by the effect of electromagnetic pulses, as seen during the VEGA-2 campaign.

2.2.2 Transverse density profiles at the shock position

Fig. 2.13 shows a 2-D atomic density map obtained using the *rapid valve*, the J2021 nozzle and argon gas. The transverse density lineouts discussed in this section and the longitudinal profiles described in the following section, are obtained by performing lineouts of such density charts at the shock height and transverse position. The longitudinal (transverse) profiles are extracted along the white dashed line (pink dashed line) and are averaged over $\pm 30\,\mu$m. The same process is followed in the *microvalve*-only characterization campaign discussed in Section 2.3. In Fig. 2.13 the $y = 0$ abscissa corresponds to the nozzle's surface, while the $x = 0$ ordinate corresponds to the symmetry axis, see Appendix A for more details. As can be deduced, the gas nozzle (and the valve connected to it) are located upside down. This is done to favor the correct valve's operation, following instructions from the manufacturer.

Fig. 2.14a and Fig. 2.16a show different transverse density lineouts obtained using the *rapid valve* and the *microvalve*, respectively, coupled to the J2021 nozzle and argon gas. P was varied from 300 bar to 400 bar. The VOT was varied from 2.5 ms to 5 ms in the *rapid valve* case and from 20 ms to 30 ms in the *microvalve* case, following each valve's behavior as described in Fig. 2.9. The CD parameter was varied as well between 8 and 20 ms. Hereinafter, each parameter combination of P, VOT and CD will be referred to as PC #x.
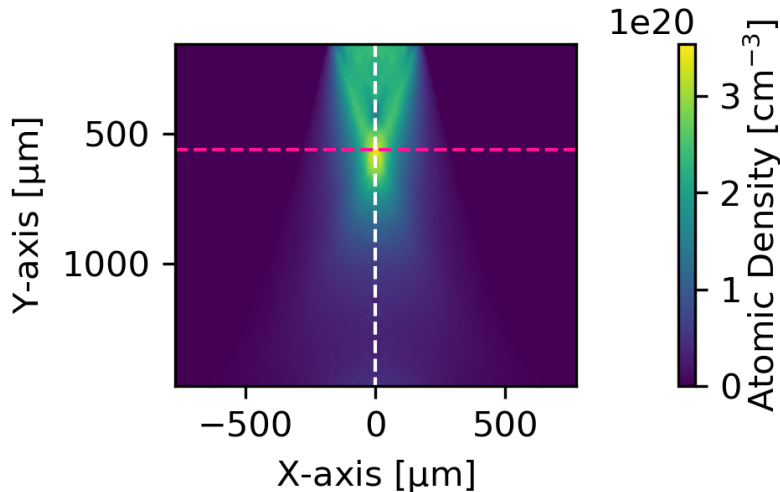
Fig. 2.13: 2-D atomic density map obtained using the *rapid valve*, the J2021 nozzle and argon gas. The nozzle's surface is located at $y = 0$.

The dashed blue curves in Fig. 2.14a and Fig. 2.16a are the transverse density profiles obtained from CFD Fluent simulations inputting the J2021 nozzle geometry, a pressure reservoir of 400 bar and nitrogen gas. The dashed red lines in Fig. 2.14a and Fig. 2.16a mark the maximum atomic density interval where shock formation was seen in the numerical parametric study presented in Chapter 3[a]. The corresponding longitudinal density profiles are plotted in 2.14b and Fig. 2.16b and will be discussed in the next Section 2.3.

As can be seen in Fig. 2.14a, the shape of the measured argon transverse density profiles is different from the nitrogen profile obtained from CFD simulations, and plotted as a blue dashed line. This is due to nozzle manufacturing imperfections, which were observed by acquiring tomography images of the virgin nozzles. A tomography image of a S900 nozzle belonging to the batch used during the VEGA-3 experiment (see Chapter 4) is shown in Fig. 2.15. Several manufacturing imperfections are pointed out with black arrows.

Hereinafter, the measured profiles are compared with the profiles extracted from the Fluent simulation performed inputting the J2021 nozzle geometry and 400 bar of N_2. The profiles' main characteristics are: the wings' density scale length L_n, the ratio between the peak and background density n_{peak}/n_b, the profile's width w_p at the FHWM (obtained by fitting it to a Gaussian-function) and the width l of the density peak at the n_b level. Due to imperfections in the hydrodynamic flow of gas from the nozzle, the density peak can appear shifted from the $x = 0$ ordinate, corresponding to the nozzle's central vertical axis. An important output of the characterization is deducing if the cited displacement compromises the laser interaction with the density peak (LIDP). Note that the Gaussian-like focal spot diameter of the VEGA-3 laser is $D_{FWHM} \approx 15\,\mu m$ (with a negligible shot-to-shot location jitter). The results of the transverse profile's characterization are summarized in Table 2.1 for both the *rapid valve* and the *microvalve*.

In the *rapid valve* case (Fig. 2.14a), the maximum density increases when increasing P and VOT, ranging from $3 \times 10^{19} cm^{-3}$ to $3 \times 10^{20} cm^{-3}$. Some profiles appear shifted from the $x = 0$ positions and LIDP is not ensured for all PCs.

In the *microvalve* case (Fig. 2.16a), the LIDP is ensured in all PCs and the maximum density increases, as well, when increasing P and VOT. However, the range of obtained maximum densities is quite limited: $2.4 \times 10^{20} cm^{-3}$ to $2.7 \times 10^{20} cm^{-3}$.

Comparing Fig. 2.14a and Fig. 2.16a, one can appreciate the potential of the *rapid valve* for

---

[a] Note that this interval is purely indicative since the cited parametric study was performed inputting the S900 nozzle geometry and not the J2021 geometry.

Valve: Rapid valve, Nozzle: J2021, Gas: Ar

- - - J2021 Fluent $n_{at.,max.} = 1.4e21$ cm^{-3} - Nitrogen @400 bar	—— 5) P = 350 bar VOT = 4.0 ms CD = 8 ms
- - - J2021 Fluent $n_{at.,max.} = 1.1e20$ cm^{-3}	—— 6) P = 350 bar VOT = 4.0 ms CD = 20 ms
- - - J2021 Fluent $n_{at.,max.} = 5.4e19$ cm^{-3}	—— 7) P = 400 bar VOT = 2.5 ms CD = 8 ms
—— 1) P = 300 bar VOT = 2.5 ms CD = 20 ms	—— 8) P = 400 bar VOT = 4.0 ms CD = 8 ms
—— 2) P = 300 bar VOT = 4.0 ms CD = 8 ms	—— 9) P = 400 bar VOT = 4.0 ms CD = 20 ms
—— 3) P = 300 bar VOT = 4.0 ms CD = 20 ms	—— 10) P = 400 bar VOT = 5.0 ms CD = 20 ms
—— 4) P = 350 bar VOT = 2.5 ms CD = 20 ms	

Fig. 2.14: (a) Transverse and (b) longitudinal density lineouts extracted at the shock height using the *rapid valve* coupled with the J2021 nozzle and argon gas. The P, VOT and CD parameters corresponding to each density lineouts are summarized in the legend. The dashed blue curve in (a-d) corresponds to the transverse density profile obtained from Fluent simulations inputting the J2021 nozzle geometry, a pressure reservoir of 400 bar and nitrogen gas. The dashed red lines in (a-d) mark the maximum atomic density interval where shock formation was observed in the 1-D particle-in-cell (PIC) parametric study presented in Chapter 3. (c) and (d): zoom of (a) and (b) centered on the density peak.
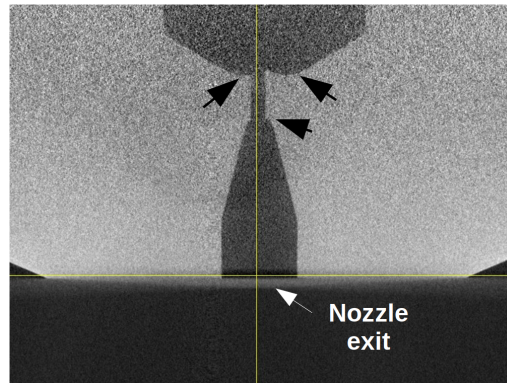
Fig. 2.15: Tomography image of a virgin S900 nozzle belonging to the same manufacturing batch as those used during the VEGA-3 experiment. The image evidences nozzle manufacturing defects pointed out with black arrows. Note that a perfect nozzle should be symmetric with respect to the vertical yellow axis. The nozzle is shown upside down, as located during the experiments. Image courtesy of M. Tarisien.

obtaining profiles with a wide range of maximum densities. Moreover, when applying different PCs to the *rapid valve* one can also indirectly vary the width of the transverse density profile, obtaining density profiles of $w_p \approx 100 - 300\,\mu$m (PC #1 and #7, respectively). The possibility of tuning the gas profile's transverse width can be an interesting tool towards modifying the

Valve: Microvalve, Nozzle: J2021, Gas: Ar
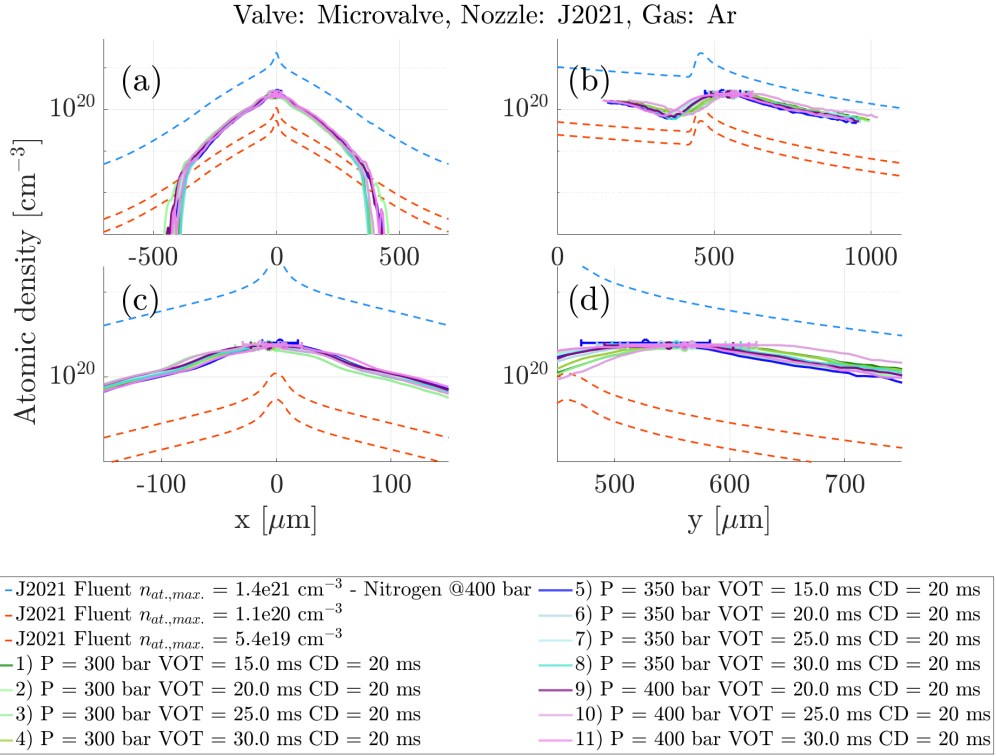
Fig. 2.16: (a-d) As labeled in Fig. 2.14 corresponding to the *microvalve* coupled with the J2021 nozzle and argon gas.

Valve + Nozzle/Gas	$L_{n,wings}$ Sim. [μm]	$L_{n,wings}$ Meas. [μm]	n_{peak}/n_b Sim.	n_{peak}/n_b Meas.	l Sim. [μm]	l Meas. [μm]	w_p Sim. [μm]	w_p Meas. [μm]	Observations	Figures
RV + J2021/Ar	150	110	2	1.3	35	60	300	100-300	Possibility of tuning the profile's transverse dimension Max. density between $3 \times 10^{19} - 3 \times 10^{20}$ cm^{-3} LIDP in PC#4	Fig. 2.14a and c
MV + J2021/Ar	150	160	2	1.7	35	160	300	200	Limited range of densities $2.4 \times 10^{20} - 2.7 \times 10^{20}$ cm^{-3} LIDP in all PCs	Fig. 2.16a and c

Tab. 2.1: Summary of the *rapid valve* characterization campaign, transverse profiles.

laser absorption through the gas.

Finally, the transverse profiles differ from the Fluent simulations regardless of the electrovalve that is used.

2.2.3 Longitudinal density profiles at the shock position

Fig. 2.14b and Fig. 2.16b show the longitudinal density profiles obtained during the characterization campaign using the *rapid valve* and the *microvalve*, respectively. These longitudinal density profiles correspond to the same measurements as the previously described transverse profiles. The blue and red dashed lines are Fluent simulation outputs and are detailed in Section 2.2.2.

The longitudinal profile's main characteristics, i.e. the shock vertical position y_s and whether the LIDP is ensured for all or some PCs are summarized in Table 2.2.

As seen in Fig. 2.14b, in the *rapid valve* case, the shock vertical position moves from $y_s \approx 470\,\mu$m (PC #7) to $y_s \approx 630\,\mu$m (PC #9). As a general trend, larger P and VOT values lead to shocks located further away from the nozzle. For certain PCs, like #1 and #7, the longitudinal density profiles are sharp. The other longitudinal profiles exhibit a soft hump

Valve + Nozzle/Gas	y_s Sim. [μm]	y_s Meas. [μm]	Observations	Figure
RV + J2021/Ar	450	470 - 630	LIDP for PC #7 Sharper profiles for PC #1 and 7	Fig. 2.14b and d
MV + J2021/Ar	450	560	LIDP for all PCs	Fig. 2.16b and d

Tab. 2.2: Summary of the *rapid valve* characterization campaign, longitudinal profiles.

shape. The interaction of the VEGA-3 laser ($D_{FWHM} \approx 15\,\mu m$) is ensured only for some PCs.

In the *microvalve* case plotted in Fig. 2.16b, the shock is almost constantly located at $y \approx 560\,\mu m$, independently of the PC. This value is closer to the predictions of the ARES simulations than the Fluent ones (Fig. 2.7b). LIDP is guaranteed for al PCs.

2.2.4 Conclusions from the *rapid valve* and *microvalve* characterization campaign

The *rapid valve* offers the possibility to tune the maximum gas density in a wide range, while ensuring a reproducible and safe LIDP by working in the leakage-free operating points. However, the facility prioritized the equipment safety and decided to allow only the leakage-free *microvalve* to be used during the VEGA-3 experiment. The main reason was the *rapid valve's* leakage propensity under the influence of the electromagnetic pulses (EMPs) (generated during the laser-plasma interaction [125]), as experienced during the VEGA-2 experiment. Therefore, a *microvalve*-only characterization campaign was performed in preparation for the VEGA-3 experiment. This characterization campaign is summarized in the next Section 2.3.

2.3 *Microvalve*-only characterization campaign

The nozzles that were characterized during this campaign were the six nozzles used during the VEGA-3 experiment, five of the S900-type and one of the J2021-type: S900-1A, S900-2B, S900-3C, S900-4D and S900-5E and the J2021. The characterized gases were helium, nitrogen and a 9/1 N_2/He gas mixture, the same gases used during the VEGA-3 experiment. Hereinafter, the characterization plots of the S900-5E and J2021 nozzles, with both a pure helium gas as well as a 9/1 N_2/He gas mixture are presented. The objective is to portrait the general behavior of both nozzle geometries, as well as the effect of changing from a pure helium gas jet to a gas mixture one.

The setup implemented for the characterization is plotted in Fig. 2.17. The SID-4 wavefront sensor, developed by Phasics [124], was also used. Two optical lines were realized to image the dense gas at low (red line) and high (yellow line) magnifications. The high magnification optical line was used to study in detail the peak of the density profile. A third optical line (blue line) was spatially filtered and shine onto a fast photodiode connected to a digital oscilloscope. This strioscopy line was used to obtain measurements of the temporal evolution of the gas density (as a function of P and VOT) at the shock height during the ms that a gas "puff" lasts. A time-dependent voltage signal proportional to the shock density is obtained. Some examples of such signals are plotted in Figs. 2.18a-d. This diagnostic allows to identify the plateau regions where the output density remains semi-constant, considered the most controlled scenario where the laser-gas interaction can take place. The P and VOT values corresponding to the plateau regions are selected for a full characterization, varying as well the CD parameter and obtaining 2-D density maps.
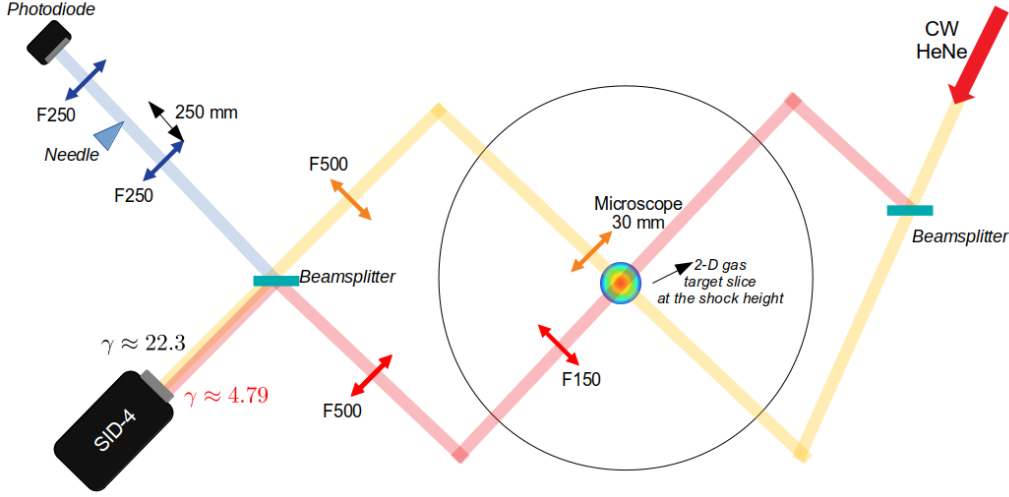
Fig. 2.17: Optical setup used to characterize the phase shifts of the probe beam through the dense gas during the *microvalve*-only characterization campaign.
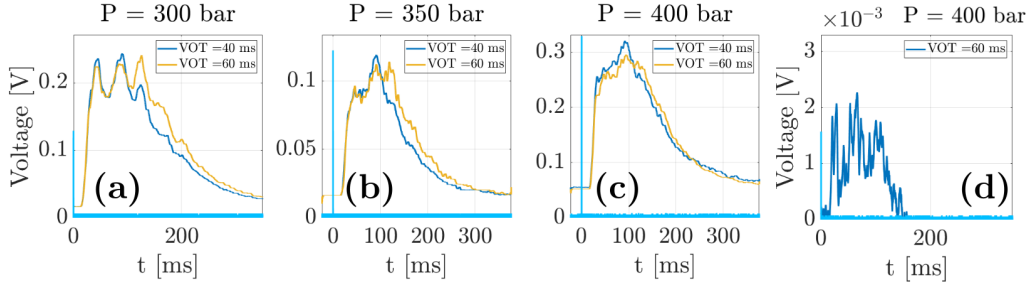
Fig. 2.18: Time-dependent strioscopy voltage signal at the shock height, acquired using a digital oscilloscope, corresponding to the J2021 nozzle and gas mixture (a-c) or helium (d). The voltage level is proportional to the gas density. The different measurements correspond to different P values from 300 bar to 400 bar and VOTs, either 40 ms or 60 ms. The light blue peak corresponds to the oscilloscope's trigger signal.

2.3.1 Nozzle: S900-5E, Gas: mixture and helium

Fig. 2.19a shows three transverse density lineouts obtained using the *microvalve* connected to the S900-5E nozzle and a 9/1 N_2/He gas mixture for different PCs of P, VOT and CD. The CFD simulation outputs plotted as dashed blue and red curves in Figs. 2.19a-d (described in Section 2.2.2) correspond to Fluent outputs inputting the S900 nozzle geometry, a pressure reservoir of 400 bar and nitrogen gas[b]. The main characteristics of the transverse (longitudinal) profiles are summarized in Table 2.3 (Table 2.4).

The measured transverse profile (Fig. 2.19a) are less peaked and have denser wings with similar density scale lengths to the simulated S900 profile. At the same time, the LIDP is secured in all PCs. As mentioned before, when using the *microvalve*, the range of obtained maximum densities is quite limited: $1.15 \times 10^{20} \mathrm{cm}^{-3}$ to $1.35 \times 10^{20} \mathrm{cm}^{-3}$.

Fig. 2.19b shows the longitudinal density profiles corresponding to the same measurements (as the previously described transverse profiles). The shock vertical position moves from $y \approx 900 \,\mu\mathrm{m}$ (PC #2) to $y \approx 1100 \,\mu\mathrm{m}$ (PC #4), very far away from the simulation prediction. As a general trend, larger VOTs lead to shocks located further away from the nozzle. The longitudinal profiles exhibit a flat density plateau for all PCs, and exhibit a sharp up-ramp followed by an exponential decay with a density scale length $L_{long.} \approx 220 \,\mu\mathrm{m}$.

---

[b]Since the gas mixture only contains 10% of He it can be compared with a pure nitrogen simulation.

Fig. 2.19: (a-d) As labeled in Fig. 2.14 corresponding to the *microvalve* coupled with the S900-5E nozzle and a 9/1 He/N$_2$ gas mixture.

Valve + Nozzle/Gas	$L_{n,wings}$ Sim. [μm]	$L_{n,wings}$ Meas. [μm]	n_{peak}/n_b Sim.	n_{peak}/n_b Meas.	l Sim. [μm]	l Meas. [μm]	w_p Sim. [μm]	w_p Meas. [μm]	Observations	Figure
MV + S900-5E/Mix	150	150	2.8	1.9	35	70	300	300	Limited density range between 1.15×10^{20}cm^{-3}-1.35×10^{20}cm^{-3} LIDP in all PCs	Fig. 2.19a and c
MV + S900-5E/He	150	230	2.8	2.3	35	270	300	300	No LIDP guaranteed in PC#1	Fig. 2.20a and c

Tab. 2.3: Summary of the *microvalve*-only characterization campaign S900-5E nozzle, transverse profiles.

Fig. 2.20a corresponds to a transverse density lineout obtained using the *microvalve* connected to the S900-5E nozzle and pure helium gas. The dashed blue and red curves in Figs. 2.20a-d have been detailed in Section 2.2.2 and correspond to CFD Fluent simulations inputting the S900 nozzle geometry, a pressure reservoir of 400 bar and nitrogen gas[c]. The corresponding longitudinal density profile is plotted in Fig. 2.20b.

The measured He transverse profile (Fig. 2.20a) is less peaked and has denser wings with a higher density scale length, in comparison with the simulated S900 profile. It is also more peaked than the mixture profiles, about three times denser (still less dense once both gases are fully ionized) and presents a density peak FWHM width $l \approx 270\,\mu$m, while the simulated profiles value is $l \approx 35\,\mu$m. LIDP is not guaranteed for the PC #1 shown in Fig. 2.20a.

Fig. 2.20b shows the longitudinal density profile corresponding to the previously described transverse profiles. The longitudinal density profile seen in Fig. 2.20b is sharper than in the gas mixture case, closer to the simulated profile than in the gas mixture case. The shock vertical position is centered at $y \approx 640\,\mu$m. The shock forms closer to the nozzle's surface (by about $300\,\mu$m) than in the gas mixture case. However, this feature cannot be considered as a general

_____

[c]This comparison should be consider carefully since nitrogen and helium should not behave in exactly the same way.

Valve + Nozzle/Gas	y_s Sim. [μm]	y_s Meas. [μm]	Observations	Figure
MV + S900-5E/Mix	450	900 - 1100	Flat density plateau	Fig. 2.19b and d
MV + S900-5E/He	450	640	Sharper density profile	Fig. 2.20b and d

Tab. 2.4: Summary of the *microvalve*-only characterization campaign S900-5E nozzle, longitudinal profiles.

trend than can be extrapolated to other nozzles.
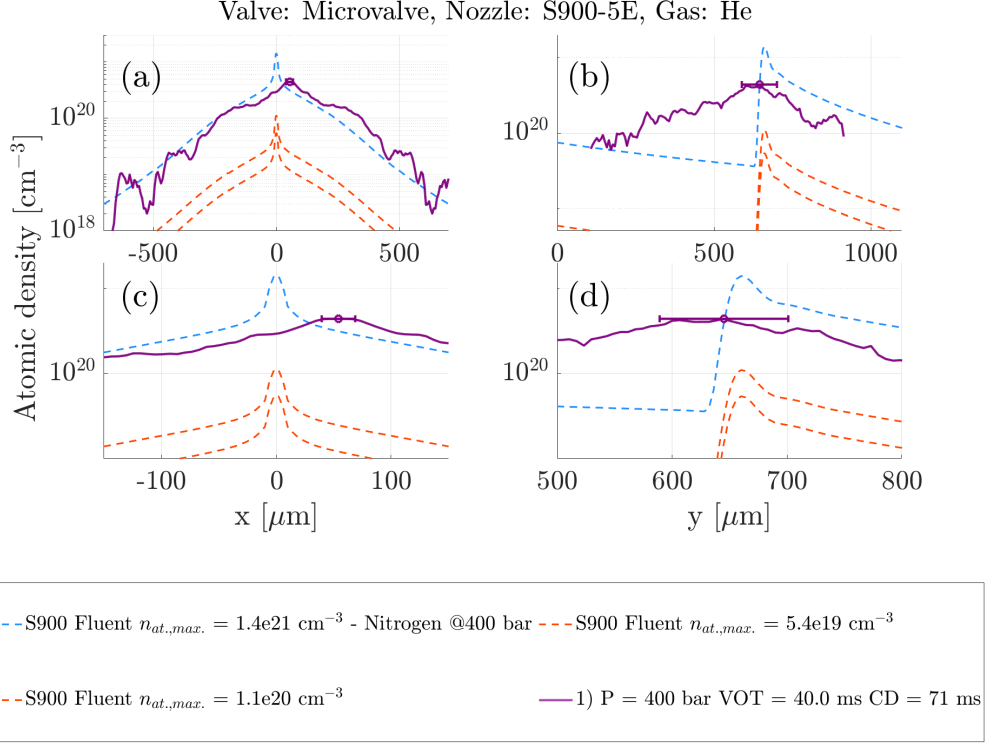
Fig. 2.20: (a-d) As labeled in Fig. 2.14 corresponding to the S900-5E nozzle and He.

2.3.2 Nozzle: J2021, Gas: mixture and He

Fig. 2.21a shows different transverse density lineouts obtained using the *microvalve* connected to the J2021 nozzle and a 9/1 N_2/He gas mixture for different PCs. The dashed blue and red curves in Figs. 2.21a-d have been described in Section 2.2.2 and correspond to density profiles obtained from CFD Fluent simulations inputting the J2021 nozzle geometry, a pressure reservoir of 400 bar and nitrogen gas[d]. The corresponding longitudinal density profiles are plotted in 2.21b. The main characteristics of the transverse (longitudinal) profiles are summarized in Table 2.5 (Table 2.6).

The measured transverse profiles (Fig. 2.21a) are slightly less peaked and have denser wings with higher density scale lengths. The measured profiles' maximum densities are almost equal to the simulated J2021 profile value, and strongly diverge from the simulated ones for $x < -360\,\mu$m and $x > 360\,\mu$m, where the density scale length decreases up to $L_{n,Mix} \approx 60\,\mu$m. The measured profiles exhibit a density peak width $l \approx 50\,\mu$m, almost equal to the simulated profiles' value. The range of maximum achievable densities is quite narrow: 9×10^{20}cm^{-3} to

---

[d]Since the gas mixture only contains 10% of He it can be compared with a pure nitrogen simulation.
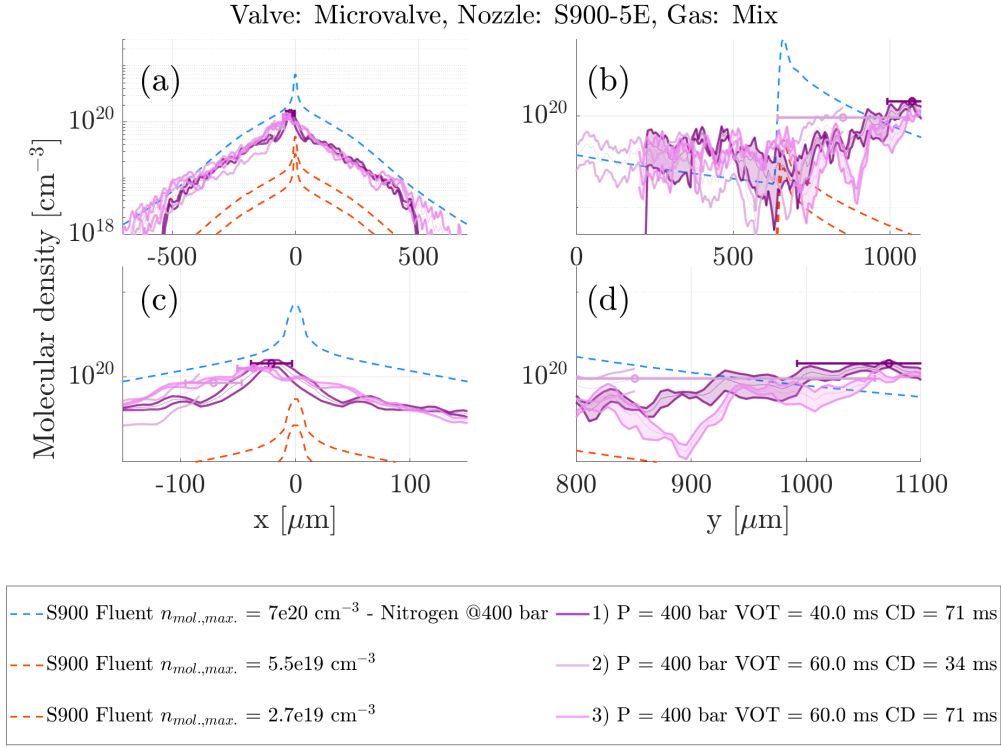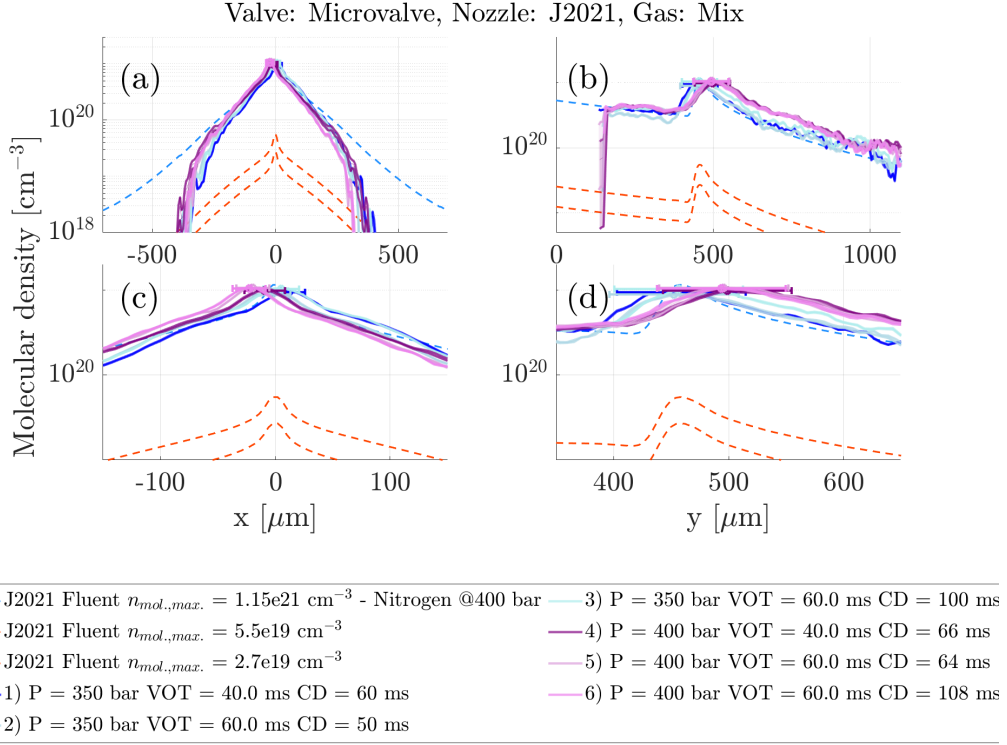
Fig. 2.21: (a-d) As labeled in Fig. 2.14 corresponding to the *microvalve* coupled with the J2021 nozzle and a 9/1 He/N$_2$ gas mixture.

Valve + Nozzle/Gas	$L_{n,wings}$ Sim. [μm]	$L_{n,wings}$ Meas. [μm]	n_{peak}/n_b Sim.	n_{peak}/n_b Meas.	l Sim. [μm]	l Meas. [μm]	w_p Sim. [μm]	w_p Meas. [μm]	Observations	Figure
MV + J2021/Mix	130	90	1.9	1.6	50	50	300	300	Limited density range between 9×10^{20}cm^{-3}-10^{21}cm^{-3} LIDP for all PCs 10 times denser than in the S900 case	Fig. 2.21a and c
MV + J2021/He	130	130	1.9	1.3	50	40	300	300	LIDP in not guaranteed for PC #1	Fig. 2.22a and c

Tab. 2.5: Summary *microvalve*-only characterization campaign J2021 nozzle, transverse profiles.

10^{21}cm^{-3}, almost an order of magnitude higher than in the S900 nozzle and mixture case (Fig .2.19).

Fig. 2.21b shows the corresponding longitudinal density profiles. The density peak shifts from $x = 450\,\mu$m (PC #1) to $x = 500\,\mu$m (PC #4). Higher P and larger VOT values lead to shocks located slightly further away from the nozzle. The longitudinal profiles exhibit a Gaussian-like longitudinal profile for all PCs, characterized by a width at the FWHM $\approx 172\,\mu$m. The simulated longitudinal profile has a sharp up-ramp followed by an exponential decay with a density scale length $L_{n,long} \approx 90\,\mu$m, a much stronger decay than in the S900 nozzle case where $L_{n,long} \approx 220\,\mu$m. Taking into account both the transverse and longitudinal density profiles' characteristics detailed above, the interaction of the VEGA-3 laser ($D_{FWHM} \approx 15\,\mu$m) with the gas density peak is also ensured.

Fig. 2.22a shows a transverse density lineout obtained using the *microvalve* connected to the J2021 nozzle and a pure helium gas. The dashed blue and red curves of Figs. 2.22a-d where extracted from CFD Fluent simulations inputting the J2021 nozzle geometry, a pressure

Valve + Nozzle/Gas	y_s Sim. [μm]	y_s Meas. [μm]	Observations	Figure
MV + J2021/Mix	450	450-550	LIDP for all PCs Flat density plateau	Fig. 2.21b and d
MV + J2021/He	450	550	Flat density plateau	Fig. 2.22b and d

Tab. 2.6: Summary of the *microvalve*-only characterization campaign J2021 nozzle, longitudinal profiles.

reservoir of 400 bar and nitrogen gas[e], see Section 2.2.2. The corresponding longitudinal density profiles are plotted in 2.21b.
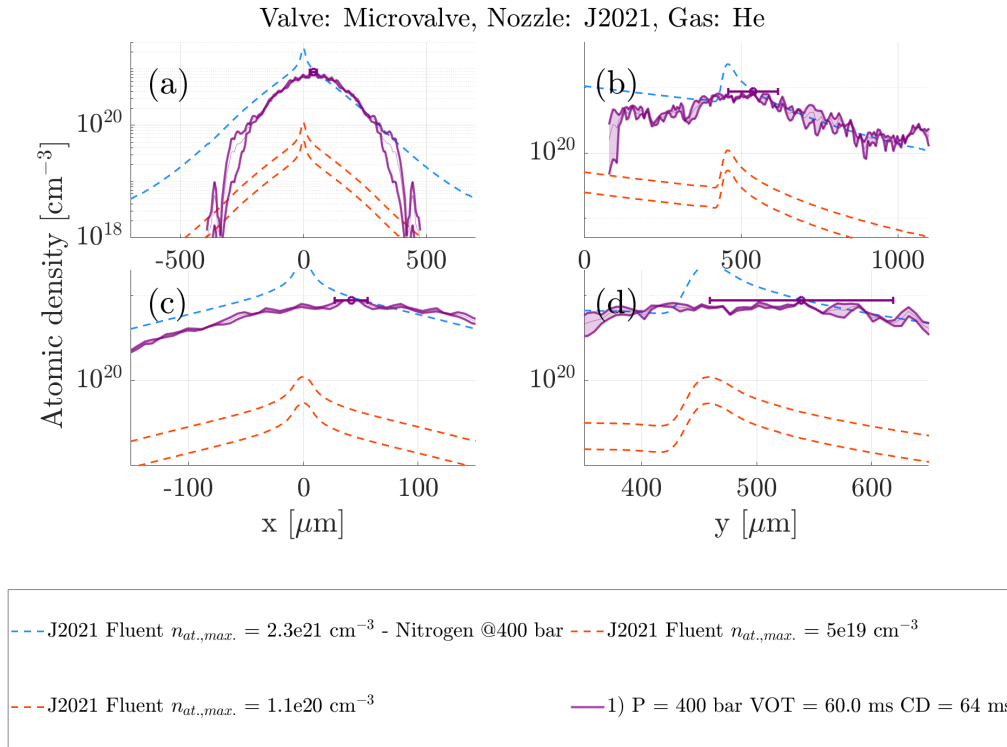
Fig. 2.22: (a-d) As labeled in Fig. 2.14 corresponding to *rapid valve* connected to the J2021 nozzle and helium gas.

The measured transverse profiles are less peaked and have wings with similar density scale lengths and maximum densities as the simulated J2021 profile. The measured transverse profiles strongly diverge from the simulated ones for $x < -430\,\mu$m and $x > 430\,\mu$m, where the density scale length decreases up to $L_{n,Mix} \approx 40\,\mu$m, and have a gas density peak width $l \approx 40\,\mu$m, almost equal to the simulated profiles' value.

Fig. 2.22b shows the longitudinal density profiles corresponding to the previously described transverse profile. The density peak is located at $x \approx 550\,\mu$m and exhibits a maximum atomic density of 8.7×10^{20}cm^{-3} (50% less dense than the simulation) and a density plateau, being the simulated profile much sharper. The interaction of the VEGA-3 laser with the gas density peak is not guaranteed for PC #1.

---

[e] Comparison with the CFD simulations should be consider carefully since nitrogen and helium should not behave in exactly the same way.

2.3.3 Study of the cylindrical symmetry for both nozzle types

Since the high and low magnification (HM and LM) optical lines cross the gas profile forming a 90° angle (Fig. 2.17), a study of the cylindrical symmetry for each nozzle type can be performed.

Note that the Abel inversion phase chart deconvolution needs to start at a point far enough (in the horizontal direction) from the symmetry vertical axis ($x = 0$), where the density can be considered as negligible (see Appendix A for details). Hence, a full analysis of the HM phase charts is not possible, since the density in the chart's borders is not equal to zero. As a result, the maximum density can not be obtained from HM phase charts. However, the profile's shape is correct and the maximum density of the HM density lineout can be extracted from the corresponding LM lineout. This was the analysis procedure followed for the HM phase charts.

Figs. 2.23a and b compare a single measurement corresponding to the S900 and J2021 nozzles, respectively, performed with the HM (dashed lines) and LM (solid lines) optical lines.
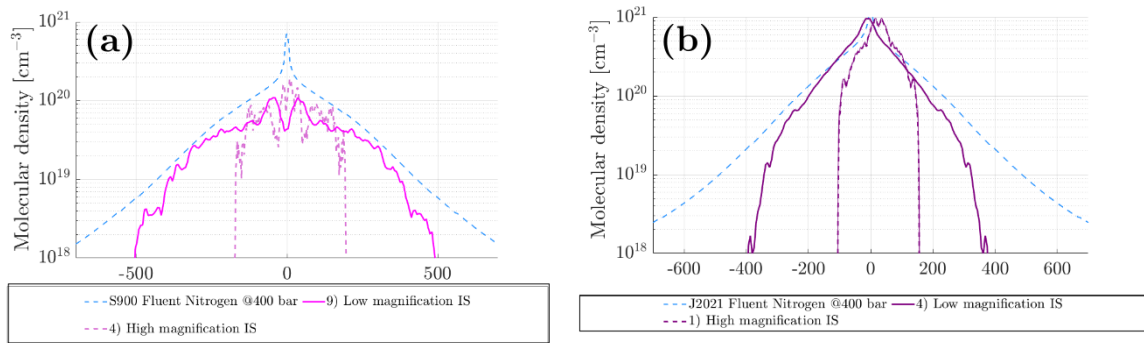
Fig. 2.23: Comparison of the transverse density profile obtained for the (a) S900 and (b) J2021 nozzles with the same gas and PCs (seen in the plot legend) as obtained with both the high magnification (HM) and low magnification (LM) optical lines. See setup of Fig. 2.17.

Both HM and LM transverse profiles can be compared in the $x \approx \pm 200\,\mu\mathrm{m}$ range accessible by the HM optical line. As seen in Figs. 2.23a and b, the cylindrical symmetry of the gas profile seems to be a correct approximation since both HM and LM profiles are quite similar. Nevertheless, the HM system does allow to appreciate some extra details as the exact shape of the density peak (Fig. 2.23a), or the fact the gas profile can appear shifted in both the main IS line as well as in the perpendicular direction, as seen in Fig. 2.23b.

2.3.4 Conclusions from the *microvalve*-only characterization campaign

The S900 nozzle produces a density shock region further away from the nozzle surface regardless of the gas that is being used. The vertical shock position using the S900 nozzle and gas mixture is located at $y \approx 900\,\mu\mathrm{m}$ (Fig. 2.19b) and using helium at $y \approx 650\,\mu\mathrm{m}$ (Fig. 2.20b). When using the J2021 and gas mixture the vertical shock position is located at $y \approx 500\,\mu\mathrm{m}$ (Fig. 2.21b) and when using helium at $y \approx 550\,\mu\mathrm{m}$ (see Fig. 2.22b).

The J2021 nozzle produces thinner and denser transverse density profiles regardless of the gas, compare Fig. 2.21 (J2021 and gas mixture) and Fig. 2.22 (J2021 and helium) with Fig. 2.19 (S900 nozzle and mixture) and Fig. 2.20 (S900 nozzle and helium).

To study the stability of the shock horizontal and vertical positions we center the discussion in the gas mixture measurements, where several data points were acquired for each PC (Fig. 2.19 and Fig. 2.21). One can conclude that the J2021 nozzle produces slightly more stable shocks.

When using helium the transverse density profile's have denser wings and broader density peaks than in the gas mixture case, regardless of the nozzle.

Taking into account both the transverse and longitudinal density profiles' characteristics detailed above for both nozzles and both gas types, the interaction of the VEGA-3 laser ($D_{FWHM} \approx 15\,\mu m$) with the gas density peak is ensured for all the combinations of nozzles and gases in most PCs. This is very important since it guarantees that the density profile "seen" by the laser is known and can be fed to numerical simulations. At the same time, it opens the possibility to high-repetition-rate operation of gas nozzles. Nevertheless, as will discussed in the next Section 2.4, the laser ablation of the nozzle affects the quality of the successive shot-to-shot gas profiles.

The cylindrical symmetry of the gas profile seems to be a correct approximation since both HM and LM profiles (obtained in perpendicular optical axes) are quite similar.

The general behavior seen in the S900-5E nozzle is replicated up to a certain degree in the rest of the S900-type nozzles used during the campaign (S900-1A, S900-2B, S900-3C and S900-4D). However, due to imperfection in the manufacturing processes (Fig. 2.15) the resulting gas profiles are not identical from nozzle-to-nozzle.

2.4 Performance during UHI shots

2.4.1 Shot-to-shot laser-induced nozzle damage in the VEGA-2 experiment

In the VEGA-2 experiment the shock vertical coordinate (or shock "height", see Fig. 2.24a) was kept constant from shot-to-shot. After the experiment, we discovered that the shock vertical position was varying as a result of the laser-induced nozzle damage (LIND). This was done by analyzing neutral density charts acquired before several UHI shots and it is discussed below.
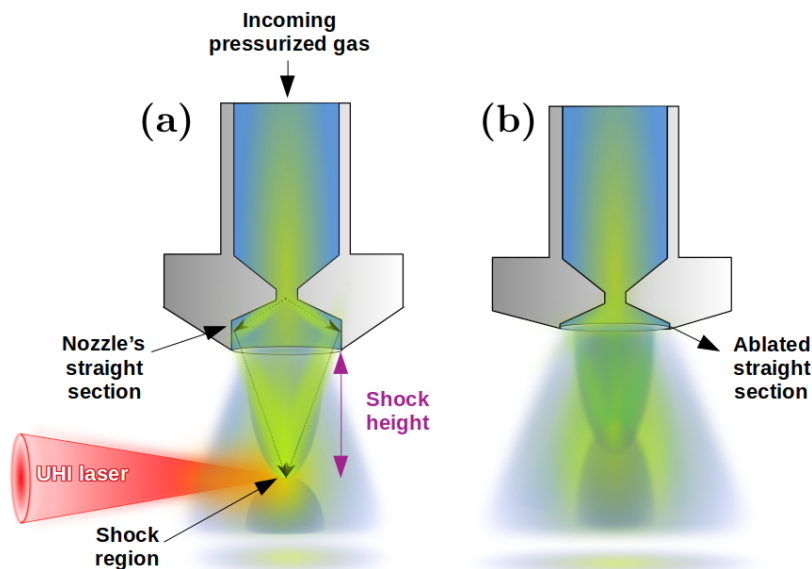
Fig. 2.24: Artist vision of the laser-induced nozzle damage (LIND). (a) Virgin nozzle and (b) same nozzle after the UHI laser interaction has ablated its last straight section.

The LIND is a process in which the plasma expansion from the laser-gas interaction expands and reaches the nozzle surface, melting the material [70]. Figs. 2.24a and b correspond to an artist vision of the LIND. Fig. 2.24a shows a virgin nozzle, in which the exiting gas flow (in light yellow) bounces on the straight section and converges at the shock region (where the

UHI laser-gas interaction takes place). Fig. 2.24b represents the same nozzle once the straight section has been ablated by the UHI laser interaction. The gas flow exits freely, almost without hitting what is left of the nozzle's straight section. As a result, the exit flow does not entirely converge at the shock height and the gas exiting cone widens up.

Figure 2.25a (Fig. 2.25b) shows the neutral density chart corresponding to shot #77 (shot #80) of the VEGA-2 experiment. Figs. 2.26a and b correspond to the transverse and longitudinal lineouts, respectively, of shots #77, #80, #81 and #82. By keeping the shock height constant and not adapting it to the shock vertical position variation, we obtained transverse profiles with a density depletion on axis, as seen in Fig 2.26a in shots #80, #81 and #82.
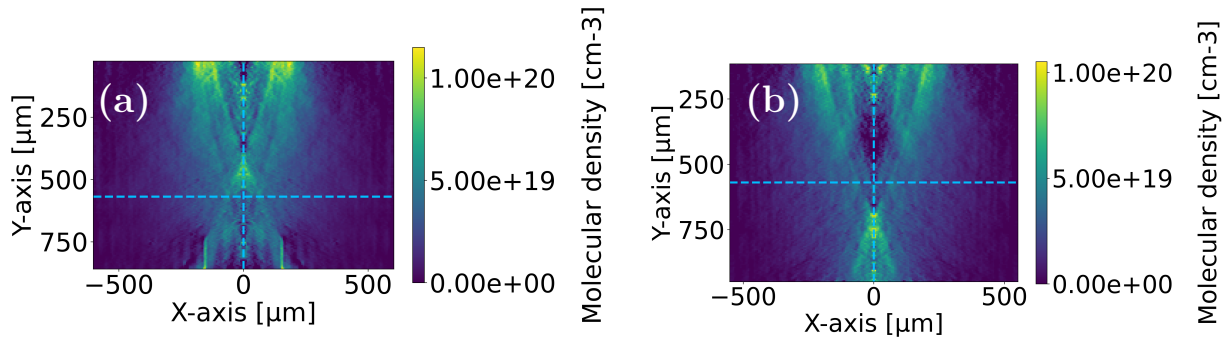
Fig. 2.25: Neutral molecular density charts corresponding to (a) shot #77 and (b) shot #80 of the VEGA-2 experimental campaign.
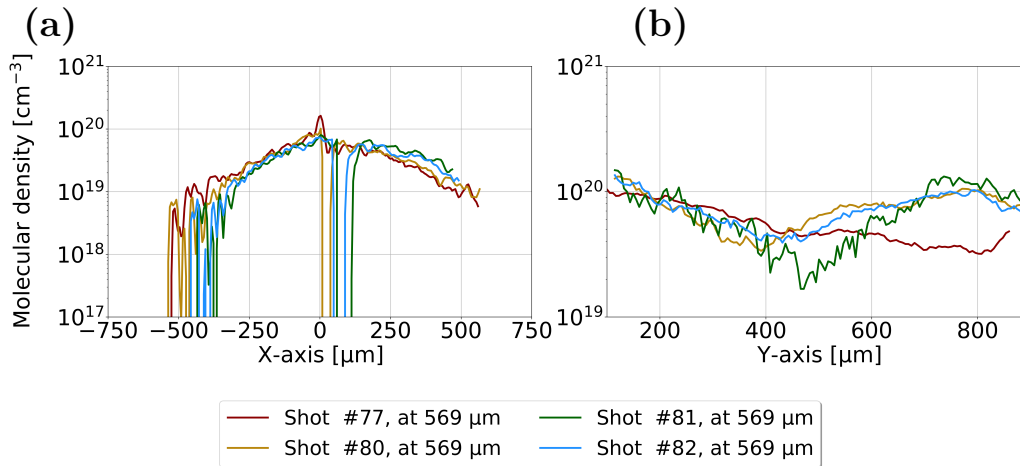
Fig. 2.26: (a) Transverse and (b) longitudinal lineouts of shots #77, #80, #81 and #82 of the VEGA-2 campaign.

If the shock height would have been adapted and moved to $y \approx 705\,\mu m$ (as shown in the neutral density chart of Fig. 2.27a) a transverse density profile of higher quality could have been obtained (Fig. 2.27b). This highlighted the need for neutral gas characterizations to be performed before each UHI shot, in order to re-locate the shock vertical coordinate and ensure that the UHI laser interacts with the shock region (Fig. 2.24a).
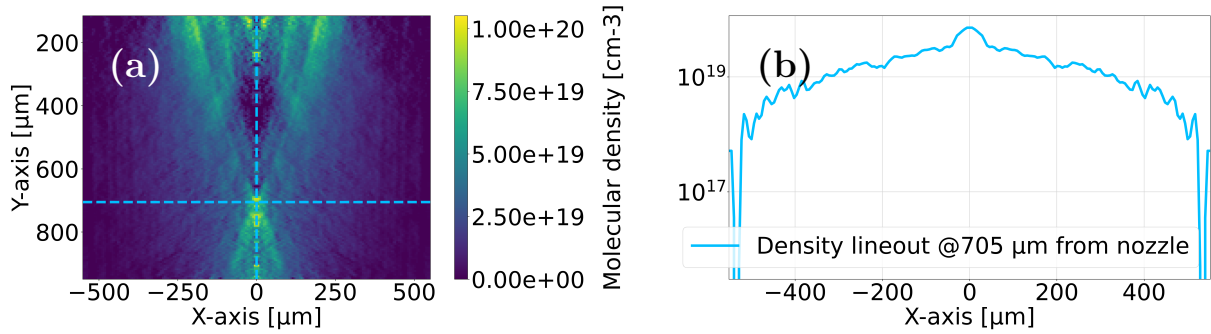
Fig. 2.27: (a) Molecular density chart obtained during the VEGA-2 campaign using the Tucan nozzle and gas mixture. (b) Transverse gas density profile that could have been obtained if the shock height had been correctly adapted following the shot-to-shot laser damage.

Hereinafter, we discuss on the LIND during UHI shots, as observed during the VEGA-3 experimental campaign (see Chapter 4 for details on this experiment).

2.4.2 Shock height selection: towards an automated gas profile selection

The method for locating the shock vertical coordinate was different in the *microvalve*-only characterization camping and in the neutral gas analysis prior to each shot (both in the VEGA-2 and the VEGA-3 experiments). In the first case, a dedicated Python routine automatically converts the phase maps obtained with the SID-4 wavefront sensor into density maps and estimates the shock height. In the second case, before each shot, we use the SID-4 Density module interface to obtain a density chart. Afterwards, we apply the transverse and longitudinal lineouts tool of the SID-4 Density module to manually find the shock height due to its practicability and rapidity, taking into account the limited time while running an experiment. The Python routine could not be used during UHI shots because a system to rapidly import the SID-4 data has not yet been developed. A screen capture of the Density module of the SID-4 is shown in Fig. 2.28.

The SID-4 Density module contains two color maps: the phase chart in radians (left) and the corresponding density chart in cm^{-3} (right). In the left and bottom sides of each color map the transverse and longitudinal lineouts are traced at the height of the yellow thin cross (seen in the corresponding color map), which is manually positioned at any point of the chart. Although this system is useful for a fast inspection of the gas density chart, it is certainly not ideal for selecting the shock height before each shot. Is is not automatized, so it is not repeatable, and depends on the person selecting the best lineouts, a task that is normally done in less than a minute during a laser shot sequence. Furthermore, the transverse lineout is plotted in linear scale so the details of the density peak are hidden and cannot be taken into account when choosing the shock height.

For future experiments, the mentioned automatized Python routine used during the characterizations campaigns could be improved. This could not only ease the process of selecting the shock height but it would also ensure that the targeted transverse and longitudinal profiles are the best ones in terms of maximum density and/or minimum nozzle-to-shock distance (defined by the user). Furthermore, this routine could be linked to an automated XYZ positioning system, as well as to the bottom view system (see Chapter 4), to automatically locate the nozzle
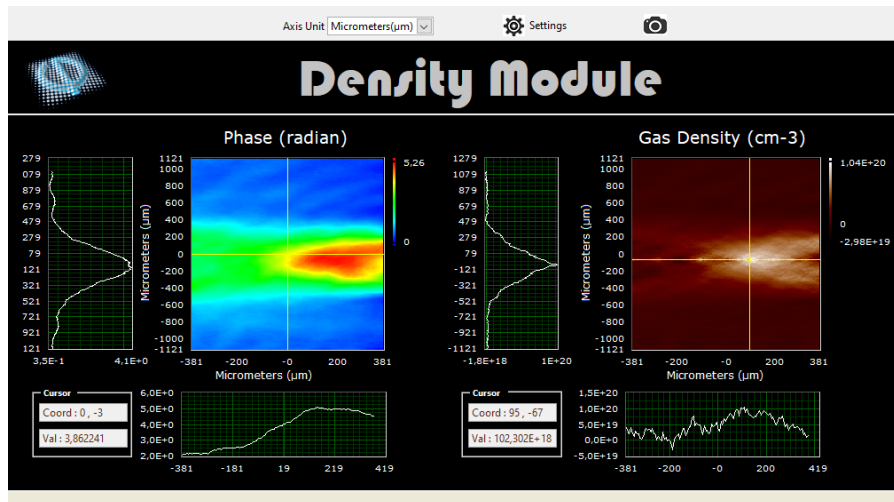
Fig. 2.28: SID-4 Density module interface screenshot used to obtain a density charts from the acquired phase maps.

at the correct coordinates prior to each shot. Improvements to the current routine could also include the selection of the profiles based on the density peak's shape, as well as on the gas wings' density scale length.

2.4.3 Shot-to-shot laser-induced nozzle damage in the VEGA-3 experiment

This section is divided as follows: Section 2.4.3.1 describes the nozzle damage on S900-type nozzles and Section 2.4.3.2 on the single J2021 nozzle.

The procedure for UHI gaseous target shots (for each individual shot) followed during the VEGA-3 experiment was the following:

1. XYZ alignment of the nozzle at TCC. The XY horizontal positioning is done by looking at the bottom view imaging system, the vertical Z positioning is performed looking at the interferometry line imaging system and it is verified by looking at the wavefront imaging system (see Chapter 4, Section 4.3.4).

2. Neutral gas characterization performed using the SID-4 wavefront sensor to select the shock height.

3. Acquisition of a gas-only reference image for the interferometry data analysis process.

4. Acquisition of a gas-and-probe reference image for the interferometry data analysis process.

5. Ultra high-intensity (UHI) laser shot on the gas jet.

The different nozzles and gas combinations (NGCs) implemented during the VEGA-3 experiment were:

- S900 5E nozzle & He gas

- S900 2B nozzle & N_2/gas mixture[f]

---

[f]Both gases behave equally so only N_2 results are presented.

- S900 1A nozzle & gas mixture

- J2021 nozzle & He.

For each NGC the transverse and longitudinal density lineouts corresponding to the *microvalve*-only characterization campaign (Section 2.3), and to the neutral gas characterization performed prior to each shot (obtained during the VEGA-3 experiment), are plotted in Figs. 2.29a-b, 2.30a-b, 2.31a-b and 2.32a-b. All the horizontal shock positions are located in a perpendicular plane with respect to the laser axis, i.e. the 35° formed between the laser and the wavefront sensor optical axes (in the VEGA-3 setup) have been taken into account, see Chapter 4 for details. Note that the displacement along the laser focal axis is much smaller than the laser Rayleigh length ($R_L \approx 300\,\mu\text{m}$).

In the S900 5E nozzle & He case, corresponding to Fig. 2.29, the *microvalve*-only characterization density lineouts were acquired using a gas mixture while the experimental shots were performed using pure He. Hence, the *microvalve*-only characterization campaign lineouts (plotted in dark yellow) are an approximation of what the pure He lineouts would have looked like. Note that when changing from gas mixture to helium we expect higher maximum peak densities and denser gas wings, as evidenced during the *microvalve*-only characterization campaign (see Section 2.3). In all the other NGCs, the *microvalve*-only characterization lineouts were performed with the exact parameter combination of P, VOT and CD and with the same gas as in the experimental conditions.

2.4.3.1 Shot-to-shot laser damage in S900 nozzles

Nozzle damage effect on the transverse density profiles

As can be seen in the transverse profiles of Figs. 2.29a and 2.30a, the laser damage deforms the virgin transverse density profile in three ways.

1. The density peak (seen specially in the transverse profiles) disappears almost completely after the first laser-shot (see shot #138 in dark blue in Fig. 2.29a). This could be due to the laser ablating the straight section of the shock nozzle [70], which inhibits the density peak formation by hindering the convergence of the hydrodynamic output flows (Fig. 2.24), as was previously discussed.

2. Appearance of high-density lobes in the gas wings' extremes (see shots #138 in dark blue and #143 in dark green in Fig. 2.29a).

3. General widening of the profile, which is most dramatic in the S900 2B nozzle & N_2 case shown in Fig. 2.30a. Here the initial transverse profile corresponding to the characterization campaign exhibits a 1 mm width, while the shot #181 (in red) has a transverse lineout width of more than 2 mm.

At the same time, the profiles' maximum density remains almost constant and the shock's horizontal position is not strongly affected by the laser damage. The transverse horizontal positions vary in a similar way as those encountered during the *microvalve*-only characterization campaign (performed with the virgin nozzles).

The laser damage was less intense in the S900 5E (Fig. 2.29a) and the S900 1A (Fig. 2.31a) nozzles. In the S900 2B nozzle the damage was dramatic, deforming completely the transverse density lineouts (Fig. 2.30a).
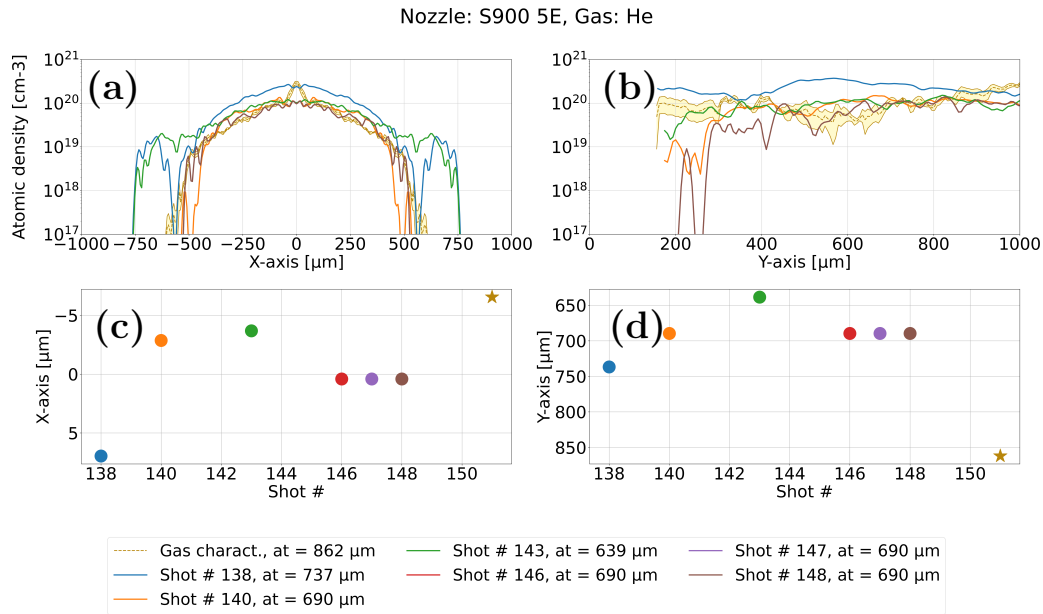
Fig. 2.29: On-shot (a) transverse and (b) longitudinal density lineouts obtained using the S900 5E nozzle & pure He during the VEGA-3 experiment. The dark yellow transverse and longitudinal lineouts in (a) and (b) correspond to measurements obtained during the *microvalve*-only characterization campaign. Shot-to-shot (c) horizontal and (d) vertical shock coordinates, the *microvalve*-only characterization horizontal shock coordinate is plotted as dark yellow stars.

Nozzle damage effect on the longitudinal density profiles

The longitudinal density profiles corresponding to the S900 5E nozzle (Fig. 2.29b) and the S900 1A nozzle (Fig. 2.31b), are originally quite flat and do not suffer strong variations with the laser damage. In the S900 2B nozzle case (Fig. 2.30b), the Gaussian-like peak centered originally at $y \approx 600 \, \mu m$ (yellow line) disappears after the first laser shot, which is also related to the laser ablation of the straight section of the shock nozzle.
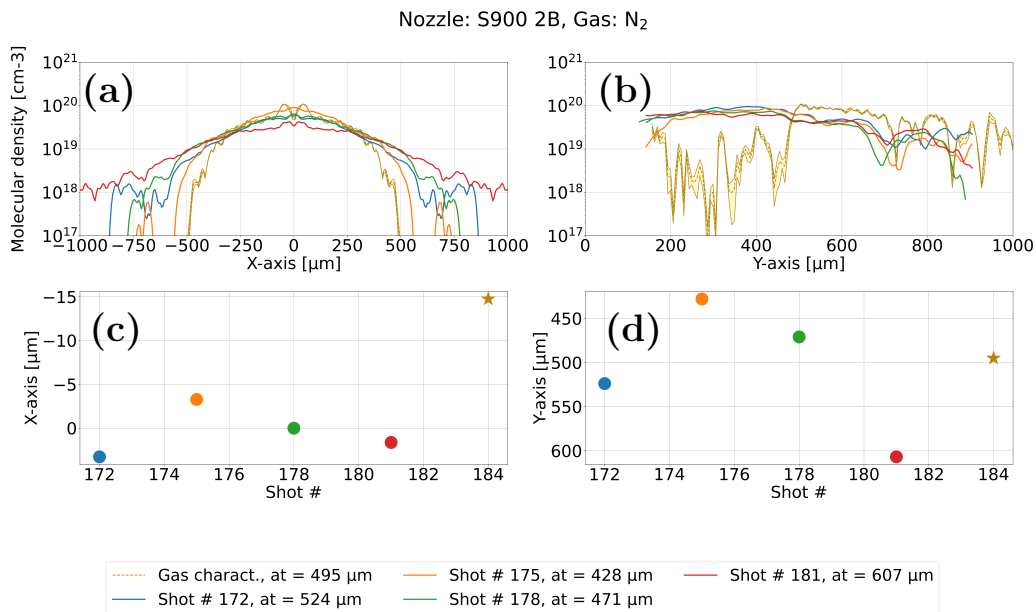
Fig. 2.30: (a-d) As labeled in Fig. 2.29 corresponding to the S900 2B nozzle & pure nitrogen.

In the S900 1A nozzle & gas mixture case, the shock's vertical coordinate moved in a $\Delta y \approx 600\,\mu m$ range (Fig. 2.31d). The shock vertical positions were found to be less stable than in the *microvalve*-only characterization campaign, where the vertical shock varied in a $\Delta y \approx 150\,\mu m$ range.

For the S900-type nozzles, the shock's were found between $y \approx 400\,\mu m$ and $y \approx 1000\,\mu m$ ($y = 0$ corresponds to the nozzle's surface).
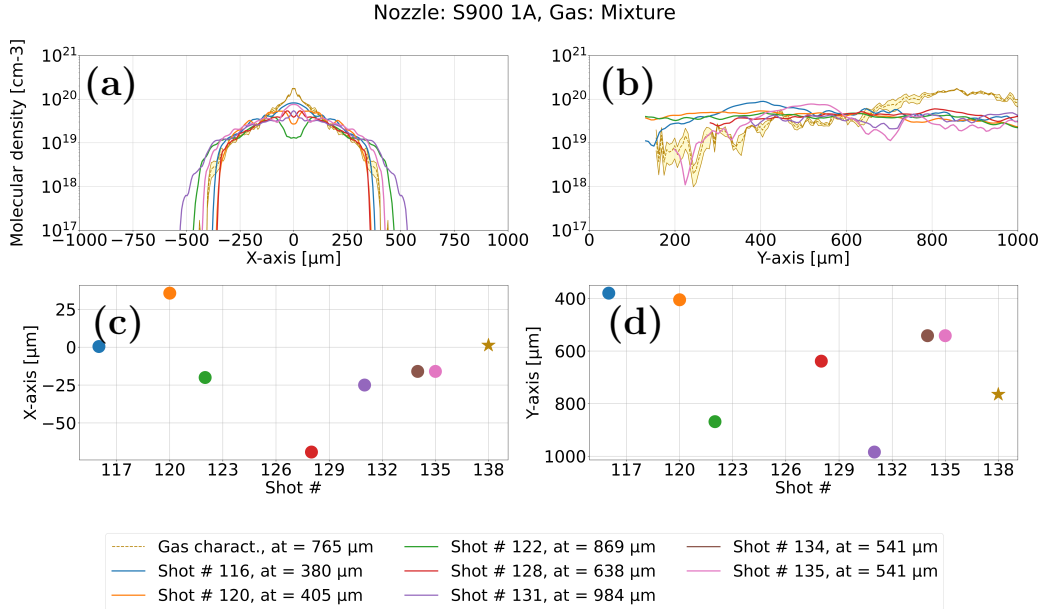
Fig. 2.31: (a-d) As labeled in Fig. 2.29 corresponding to the S900 1A nozzle & gas mixture.

2.4.3.2 Shot-to-shot laser damage in the J2021 nozzles

Nozzle damage effect on the transverse density profiles

The J2021 nozzle laser damage seen in the transverse density lineouts (Fig. 2.32a) is similar to the previously described damage in the S900-type nozzles. The shallow J2021 density peak also disappears after the first shots and the transverse profiles widen-up from shot-to-shot. The shock's horizontal position was located, from shot-to-shot, inside an $\delta x \approx 50\,\mu m$ interval (Fig. 2.32c). The initial $\pm 250\,\mu m$ transverse profile, plotted in dark yellow in Fig. 2.32a, widens up to $\pm 500\,\mu m$ for shot #164 (in purple). However, the transverse profile widening remains much less dramatic than in the S900 nozzles case. The appearance of high-density lobes in the gas wings', linked to laser damage, is also appreciated (see shot #157 in Fig. 2.32a).

Nozzle damage effect on the longitudinal density profiles

The longitudinal gas density profiles plotted in Fig. 2.32b, which are also highly flat, are not strongly altered by the laser damage, as in the S900-type nozzles case. A density depletion region was encountered in shot #167. This density profile resembles the profiles encountered during the VEGA-2 campaign (refer to Chapter 4 for details on this experiment), see the longitudinal lineouts of Fig. 2.26b corresponding to the Tucan nozzle & gas mixture deployed during the VEGA-2 campaign.

The shock's vertical position varied in a $\Delta y \approx 300\,\mu m$ range (Fig. 2.32d). The shock's were found between $y \approx 300\,\mu m$ and $y \approx 600\,\mu m$ ($y = 0$ corresponds to the nozzle's surface), about $300\,\mu m$ close to the nozzle's surface than in the S900-type nozzles.

Both the horizontal and vertical shock positions' variations are slightly higher to those encountered during the *microvalve*-only characterization campaign. However, the laser damage was not deemed extremely critical in this case and was definitely lighter than in the S900-type nozzles, even in the laser-gas interaction took place much close to the nozzle's surface.
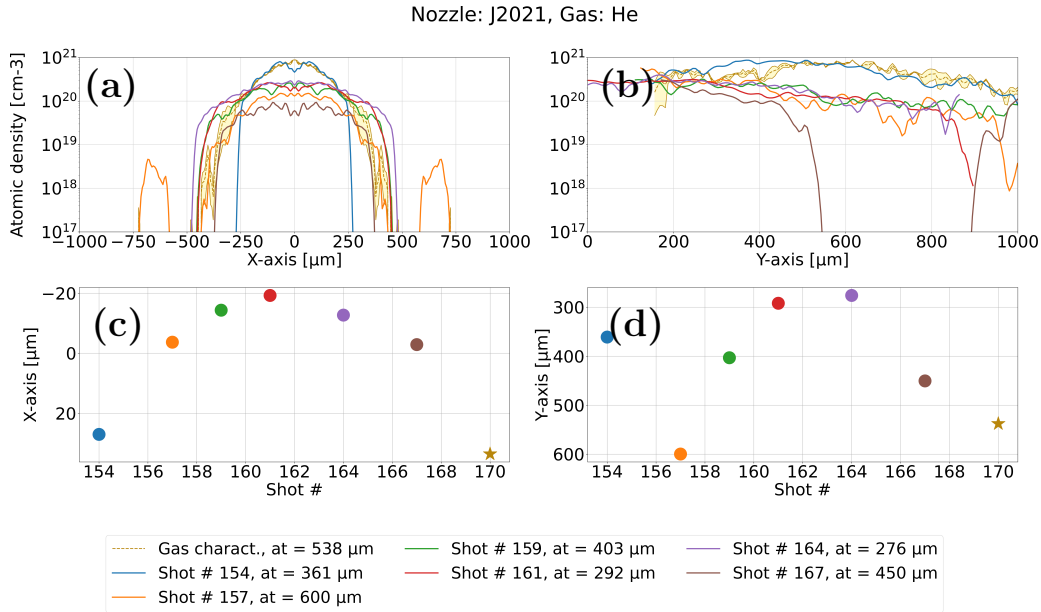
Fig. 2.32: (a-d) As labeled in Fig. 2.29 corresponding to the J2021 nozzle & pure He.

2.4.4 Conclusions from the study of laser-induced nozzle damage during UHI shots

The laser damage specially affects the shock's vertical coordinate, leaving the horizontal one almost unaltered with respect to a virgin nozzle. As a general rule, the more damaged is the nozzle, the closer the shock's vertical position moves towards it. However, when the straight conduct of the nozzle has been fully ablated, the location of the shock becomes quite random.

In the S900 nozzles case, the shock's were located in a $\Delta y \approx 600 \, \mu m$ (from $y \approx 400 \, \mu m$ to $y \approx 1000 \, \mu m$), for the most extreme case, corresponding to the S900 1A & gas mixture (Fig. 2.31d). For the other S900 nozzles, the vertical shock position moved in a less dramatic $\Delta y \approx 200 \, \mu m$ range from the first to the last shot, a value closer to what was encountered during the *microvalve*-only characterization campaign.

The S900 1A nozzle transverse profiles (Fig. 2.31a) are the ones that remained the most unaltered during up to six UHI shots in a row (by adapting the shock height to the LIND). This is probably due to the fact that the shock was produced at $y > 600 \, \mu m$ for most of the UHI shots, which constitutes an interesting hint towards the possibility of producing gas profiles that are not altered by the laser damage in a shot-to-shot basis. Note that the profiles' shot-to-shot widen-up is low compared with the S900 2B nozzle & N_2 profiles (Fig. 2.30) and that no density lateral lobes appear due to the laser damage.

The J2021 density profiles are of better quality and more reproducible from shot-to-shot than those obtained using the S900-type nozzles. The J2021 nozzle seems more resilient to laser damage, even when shooting at $300 \, \mu m$ from the nozzle (Fig. 2.32d). A comparable resilience is only observed in the S900 nozzle when shooting at least at $600 \, \mu m$ from the nozzle's surface (Fig. 2.31).

The virgin nozzles of both types exhibited very flat longitudinal profiles. This could be due to a non-perfect flow of the gas through the non-symmetric nozzle (see manufacturing defects

highlighted in the tomography image of Fig. 2.15), which could inhibit a part of the flow from hitting the straight nozzle section (Fig. 2.24a). As a result, a part of the flow probably exits in a straight direction (Fig. 2.24b) and the longitudinal density profiles become quite flat.

The CFD Fluent simulations, performed for the S900 nozzle and N_2 gas, located the shock vertical position at $y = 650\,\mu m$ (Fig. 2.7b). The actual virgin nozzle shock locations varied from $y \approx 500\,\mu m$ to $y \approx 800\,\mu m$. In the J2021 nozzle case the shock was located at $y = 450\,\mu m$ in the Fluent simulations and was seen to form between from $y \approx 300\,\mu m$ to $y \approx 600\,\mu m$.

The degree of laser-induced nozzle damage seems to depend on the quality of the nozzle manufacturing and, specifically, on its ability to produce the shock at least at $\approx 600\,\mu m$ from the nozzle's surface. In some cases, like in the S900 2B nozzle (Fig. 2.30), the LIND strongly deforms the shot-to-shot density profiles. In other cases, like in S900 5E nozzle (Fig. 2.29) or the S900 1A nozzle (Fig. 2.31), a correction of the shock height in the $100\,\mu m$ to $500\,\mu m$ range allows for an almost constant transverse density lineout to be obtained in a shot-to-shot basis.

Based on the experience gathered during the VEGA-2 and VEGA-3 experimental campaigns, a neutral gas characterization before each UHI shock and corresponding modification of the shock height is definitely an useful tool to prevent the LIND from extremely altering the transverse density profiles. At the same time, the implementation of an automatized routine that selects the shock height, by analyzing the phase charts extracted from the SID-4 wavefront sensor, is a necessary step towards an optimized and repeatable shock height selection system to be implemented during the UHI shots.

Chapter 3

1-D numerical study of the laser-gas interaction

3.1 Introduction

1-D PIC simulations can shed a first light on the physics of laser-gas interaction without resorting to expensive realistic 2-D simulations. Albeit academic, this study further allows to untangle the complex mechanisms at stake by prohibiting multidimensional effects essentially induced by the finite transverse size of the laser pulse. As already discussed in the introduction, collisionless electrostatic shocks (CES) can be triggered in several scenarios. Denavit *et al.* [48] and Silva *et al.* [49] have studied the generation of CES by applying a laser piston to the boundary of an uniform overcritical plasma. Fiuza *et al.*, [23, 126] centered their studies on laser-driven CES triggered from the overcritical boundary of a density decreasing plasma. By contrast, the present study, based on 1-D PIC simulations, aims at understanding CES formation in transparent plasmas as a result of strong electron pressure gradients [30].

We will examine this problem under conditions accessible to the VEGA-3 laser system (I_L=1.7 x 10^{20} W/cm^2, $\lambda_L = 0.8\,\mu$m and $\tau_L = 30\,$fs), and considering as a target the near-critical-density gas jet produced by the non-commercial S900 supersonic nozzle [108], plotted in Fig. 3.1. In the case of a N$_2$ gas, CES are found to occur within quite a narrow electron density n_e range, between 0.35 n_c and 0.7 n_c. The transmission of a significant fraction of the laser pulse across the density peak, while being strongly absorbed (80% - 90%) and creating a hot electron population in the gas up-ramp, is identified as a necessary condition for CES formation. The latter stems from the strong electron pressure gradients located in the density down-ramp. At higher densities, the laser is fully absorbed in the density up-ramp only giving rise to ion acoustic wave (IAW) formation. The direct laser effect on ion acceleration is a strong initial density perturbation that enhances charge separation while electron pressure gradients are identified as the main cause of shock formation. The addition of lighter helium ions to the N$_2$ gas leads to peak in the velocity spectra, which may constitute a signature of CES formation. Finally, the production of a controlled and repetitive gas profile as well as the possibility of performing measurements with statistical meaning are highlighted as fundamental for conducting a thorough experimental study.

3.2 Simulation parameters and initial conditions

The present 1-D simulations describe the interaction of a laser pulse characterized by a normalized field strength a_0=8.8 (I_0=1.7 x 10^{20} W/cm^2), a laser wavelength $\lambda_L = 0.8\,\mu$m and a $\tau_L = 30\,$fs FWHM duration, corresponding to the VEGA-3 laser parameters. The laser is linearly polarized along the y-axis and it is injected along the x-axis from the left-side of the simulation box. This study is restricted to a 1-D geometry because of the large spatial ($\approx$mm) and temporal ($\approx 10\,$ps) considered, and the relatively fine resolution dictated by the n_c maximum density of the fully ionized N$_2$ gas profile. Field and impact ionization together with elastic Coulomb collisions between all charged particles were considered. Absorbing boundary conditions were applied for fields and particles. Each cell initially contained 100 ions of each species. The initial ion temperature was $T_i = 1\,$eV. The temporal and spatial resolutions were Δt= 0.095 ω_0^{-1} (0.05 fs) and Δx= 0.1 c/ω_0 (0.016 µm), respectively. The modeled gaseous targets were composed of either atomic nitrogen or a mixture of 90% atomic nitrogen and 10% helium.

The initial gas density profile was obtained by performing hydrodynamic simulations with the FLUENT code [127]. The reference profile was that predicted with the S900 shock nozzle [108] and a backing N$_2$ gas pressure of 400 bar, and measured far enough from the nozzle to avoid damaging it [70]. This profile plotted in Fig. 3.1, is characterized by a very narrow ($\approx 15\,\mu$m) density peak (up to $n_{at,max} = 1.4\,n_c$) sitting on broad ($\approx 1\,$mm), quasi-exponential

symmetric wings. The chosen gas is nitrogen in order to replicate in a simpler manner the experimental conditions. The actual experimental target is a gas mixture of 90% nitrogen and 10% helium.

In the following and unless explicitly marked differently the density, velocity, time, distance, mass, electron momentum, ion momentum, energy and electric field are normalized to the following quantities, respectively:

$$n_c, c, \omega_0^{-1}, c/\omega_0, m_e, m_e c, m_i c, m_e c^2, m_e \omega_0 c/e, \tag{3.1}$$

where $\lambda_0 = \frac{2\pi}{k_0} = 2\pi\frac{c}{\omega_0}$ is taken to be equal to 1 μm, n_c is the critical density for a 1 μm laser wavelength equal to 1.11×10^{27} m^{-3}, c is the velocity of light in vacuum, ω_0^{-1} is the corresponding inverse laser frequency equal to 0.53 fs, e is the electron charge and m_e and m_i are the electron and ion rest mass, respectively. A table with physical units conversions is found in Appendix B.

Starting from this reference gas profile we will investigate the laser-driven plasma dynamics in uniformly rescaled N$_2$ profiles with $n_{at,max} = 0.3$, 0.1, 0.05 and 0.02 n_c. Additional N$_2$ runs will be performed to examine the role of the sole hot electron to drive the CES, the effect of the stretched laser pulse and the changes brought to the interaction by a gas mixture of 90% N$_2$ and 10% He. Table 3.1 summarizes the simulations' main parameters regarding both the laser and gas target. Note that following the normalization given in Eq. 3.1, $a_0 = 8.8$ for a $\lambda_L = 0.8\,\mu$m transforms into $a_{0,norm.} = 11$ given the normalization for $\lambda_L = 1\,\mu$m, as written in Table 3.1.

Sim. number	$n_{at,max}$ [n_c]	$n_{e,max}$ [n_c]	Gas type	Laser ON/OFF	a_0	τ_L [ω_0^{-1}]
I	1.4	9.8	N$_2$	ON	11	56
II	0.3	2.1	N$_2$	ON	11	56
III	0.1	0.7	N$_2$	ON	11	56
IV	0.05	0.35	N$_2$	ON	11	56
V	0.02	0.14	N$_2$	ON	11	56
VI	0.1	0.7	N$_2$	OFF ($T_e = a_0$)	–	–
VII	0.1	0.7	N$_2$	ON	6.3	169
VIII	0.1	0.7	90% N$_2$+10% He	ON	11	56
IX	0.1	0.7	90% N$_2$+10% H$_2$	ON	11	56
X	0.1	0.7	N$_2$	OFF ($T_e = a_0/2$)	–	–

Tab. 3.1: Main parameters of the 1-D simulations.

3.3 Electron acceleration and plasma heating

3.3.1 Areal density needed for complete laser absorption

To discern between high and low density simulations the criterion of complete laser absorption inside the gas profile is considered. It is important to differentiate between these two interaction regimes since they will trigger different electron acceleration mechanisms, as will be discuss later on. This condition has previously been studied in Ref. [30], where the minimum areal density required for complete laser absorption was found to scale approximately as

$$\sigma_{abs} = \int_{x_0}^{x_{abs}} dx\, n_e(x) \approx \frac{a_0^2 \tau_L}{2\langle\gamma_e\rangle} \tag{3.2}$$

Sim. number	$n_{e,max}$ $[n_c]$	x_{abs} $[c/\omega_0]$
I	9.8	4520
II	2.1	5868
III	0.7	7061
IV	0.35	-
V	0.14	-

Tab. 3.2: X-coordinates where complete laser absorption is met for Sims. I-III considering full ionization of the nitrogen gas in Eq. 3.2. In Sims. IV and V the laser is able to cross the entire profile without being completely absorbed.

where $\langle \gamma_e \rangle \approx a_0$ is the relativistic Lorentz factor corresponding to the mean bulk electron energy.

According to this criterion, the VEGA-3 laser pulse should be fully absorbed before reaching the density peak in the simulations with $n_{e,max} \geq 2.1\ n_c$ (Sims. I-III). In the simulations with $n_{e,max} < 2.1\ n_c$ the laser is able to cross the entire profile. The thicknesses of complete laser absorption x_{abs} in Sims. I-III are indicated as solid lines in Fig. 3.2, and the obtained x_{abs} values are summarized in Table 3.2.
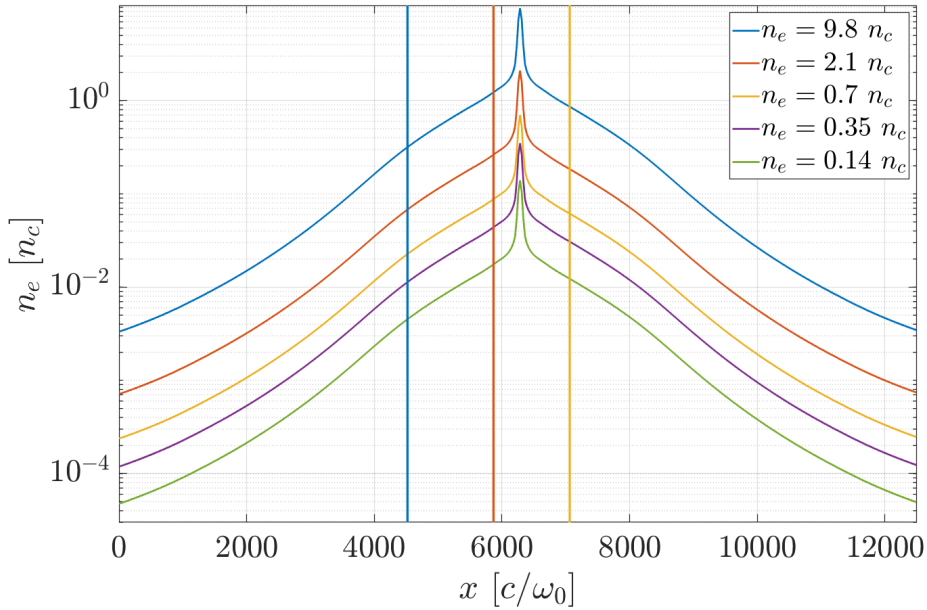
Fig. 3.1: Electron density n_e profiles input in the 1-D PIC simulations.

The (x,t) evolution of the laser field E_y along the y-axis is plotted for various maximum electron densities (9.8 n_c, 2.1 n_c, 0.7 n_c and 0.35 n_c) in Figs. 3.2a-d. The colormaps are saturated to highlight the transmitted fraction of the pulse. The density peak is located at $x = 6432\ c/\omega_0$ and it is marked with pink dashed lines and the positions corresponding to full laser absorption, as predicted by Eq. 3.2, are plotted as solid lines. In the highest density case (Fig. 3.2a) most of the laser has been absorbed or reflected at about 5000 c/ω_0, approximately 100 c/ω_0 ahead of the density peak, a location consistent with Eq. 3.2. Only 0.1% of the laser energy has been transmitted and a few percent of the laser intensity ($I \propto a_0^2$).

In the high density cases, above $n_{at} \geq 0.3\ n_c$ (Figs. 3.2a and b), strong laser reflection takes place possibly as a consequence of backward stimulated Raman scatering (BSRS) [128–131].
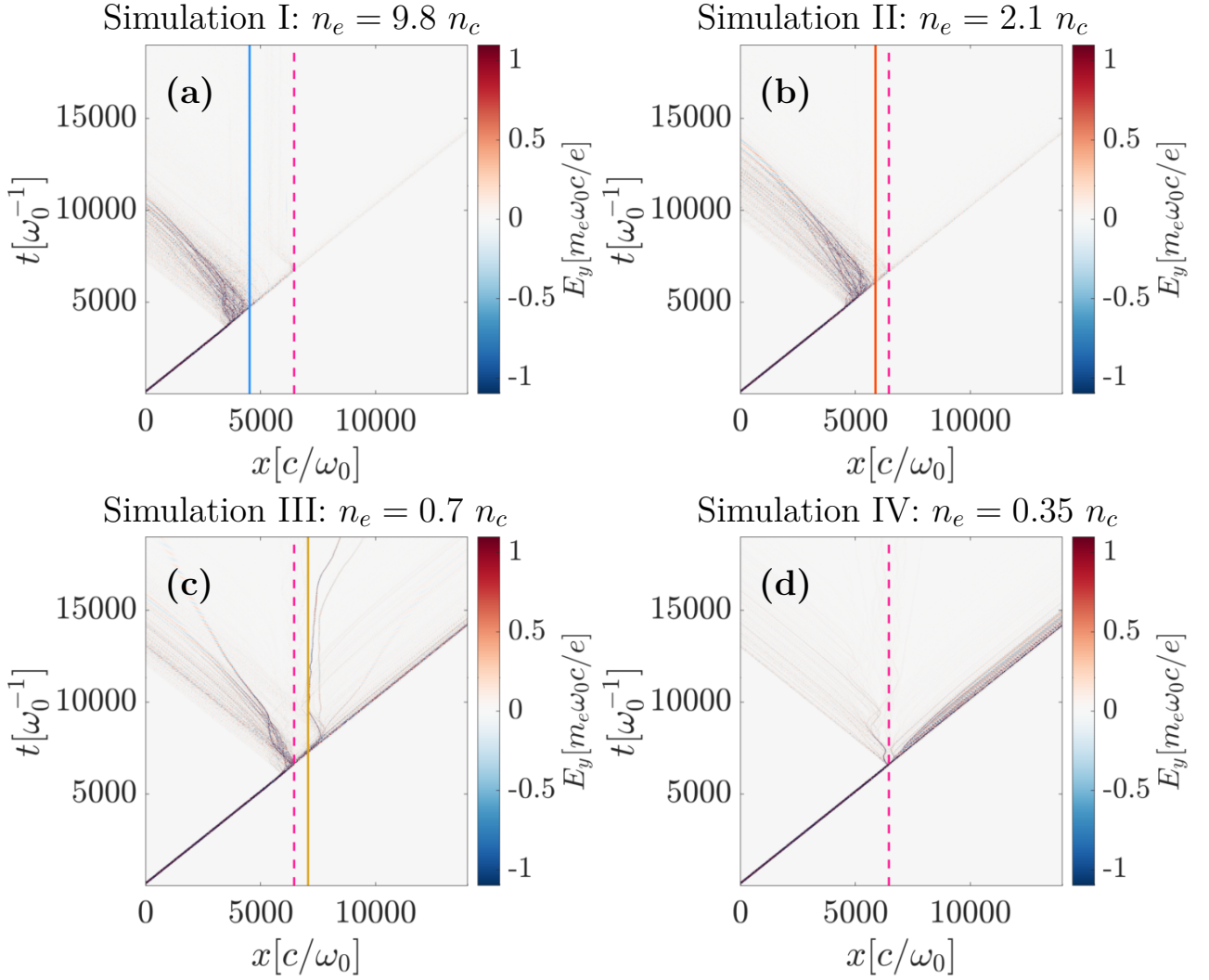
Fig. 3.2: (x,t) evolution of the laser field E_y propagation in the (a) S.I, (b) S.II, (c) S.III and (d) S.IV, see Table 3.1. The theoretical laser absorption positions deduced from Eq. 3.2 are marked with solid lines, and summarized in Table 3.2. The profile's peak density is marked by the pink dashed line at 6432 c/ω_0.

Note that the maximum electron densities in Sims. I and II are $n_{e,max} = 9.8$ and $n_{e,max} = 2.1$, respectively, considering full ionization of the nitrogen gas. The electron density value of strong laser reflection coincides in both high density Sims. I and II: $n_e \approx 1.05\,n_c = 1.16 \times 10^{21}$ cm^{-3}. The latter is greater than $n_{c,\lambda}/4 = 4.35 \times 10^{20}$ cm^{-3}, the lower limit for triggering Raman scattering [131] (where $n_{c,\lambda} = 1.73 \times 10^{21}$ cm^{-3}, i.e. the critical density for a $\lambda_L = 800$ nm laser pulse). In Sims. I, II, III and IV the laser absorption (reflection) coefficients are 94.7% (4.9%), 95.4% (4.1%), 92.7% (2.7%) and 84.1% (1.1%), respectively. When $\omega_0 \gg \omega_{pe}$ the BSRS instability growth rate can be approximated as $\Gamma \approx kc/2(n_e/n_c)^{1/4}a_0$, where k is the wave number of the diffused wave. As a consequence, the instability develops at larger time scales when decreasing the electron density n_e. This could be linked to the diminishing of the percentage of reflected laser energy from high to low densities. Moreover, the density gradients of the gaseous profile impede the instability's development by reducing the wave resonance interaction length with the background plasma [132]. The reflection of a percentage of the laser pulse could also be due to the local variation of the relativistic plasma refractive index $\eta = [1 - \omega_{pe}^2/(\gamma_e^2\omega_0^2)]^{1/2}$, which can give rise to a moving-reflecting wall at the laser front.

Below $n_e \leq 0.7\,n_c$, in the low density regime (Figs. 3.2c and d), the pulse transmitted across the density peak remains intense enough (e.g. $a_0 \approx 3$ at $\omega_0 t = 6500$ in Fig. 3.2c) to

induce a plasma wakefield and thus continue energizing the down-ramp bulk electrons. Several electromagnetic solitons are created as well but are not believed to have a strong effect on the electron acceleration, let alone the ion dynamics.

3.3.2 Stochastic electron heating

All simulations show that, early in the interaction, wakefield-type electron acceleration takes place in the fast-ionized plasma. This fluid stage of electron acceleration is shown in the electron (x, p_x) phase spaces of Figs. 3.3a-d corresponding to Sims. I - IV, see Table 3.1. The wakefield matching condition is met for $\tau_L c \approx 4\pi c/\omega_{pe}$ [133]. Thus, reducing the gas density will shift the resonance condition to a deeper region of the plasma. This is illustrated by the similarity of the electron (x, p_x) phase spaces in Fig. 3.3, for different positions in the plasma while reducing the plasma density.
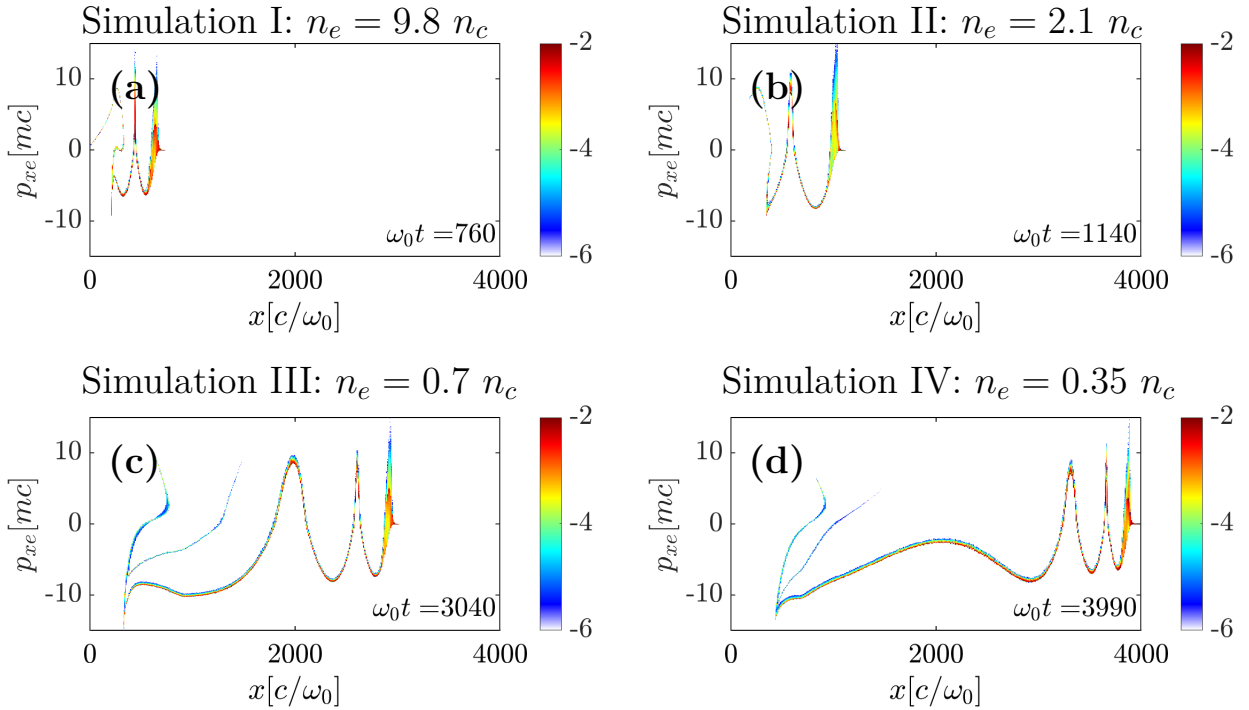
Fig. 3.3: Electron (x, p_x) phase space for (a) S.I, (b) S. II, (c) S. III and (d) S. IV, see Table 3.1, illustrating wakefield-type electron acceleration taking place in the low density part of the gas target up-ramp.

At the beginning of the interaction, the wakefield electron energization stage plotted in Figs. 3.3a-d entails a low laser energy absorption rate. The latter translates into the gentle first section of the laser absorption curves, plotted against time in Fig. 3.4a. Sims. I-IV exhibit a transition from a laminar wakefield stage to a turbulent regime where the laser absorption rate strongly increases. The first stage of electron energization occurs until the times $\sim 3000, 4200, 5000$ and $6000 \; \omega_0^{-1}$ for Sims. I-IV, respectively. The steepening of the laser absorption curves coincides with the instant where the laser reaches the electron density n_e that satisfies the wakefield matching condition $\tau_L c \approx 4\pi c/\omega_{pe}$ [133].

At the same time, since the laser pulse is longer than the local electron plasma wavelength ω_{pe} (e.g. $\tau_L c = 56 \; c/\omega_0 > \omega_{pe} = 3 \; c/\omega_0$, in S.I), the wakefield is generated in the front part of the laser pulse. The front of the laser pulse is then strongly depleted in the process of transferring its energy to the wakefield [134]. This is observed in Figs. 3.4b-d, which correspond to the laser E_y field of S.III plotted at times $\omega_0 t = 3990, 5201$ and 6270. This so-called *optical shock*

increases the ponderomotive force F_p exerted by the laser over the target electrons, since F_p is proportional to the gradient of the laser electric field $F_p \propto -\partial_x \sqrt{1 + p_x^2 + a_0^2}$ [30]. The development of an optical shock could also be linked to the steepening of the laser absorption curves of Fig. 3.4a (see Ref. [30] and references therein).
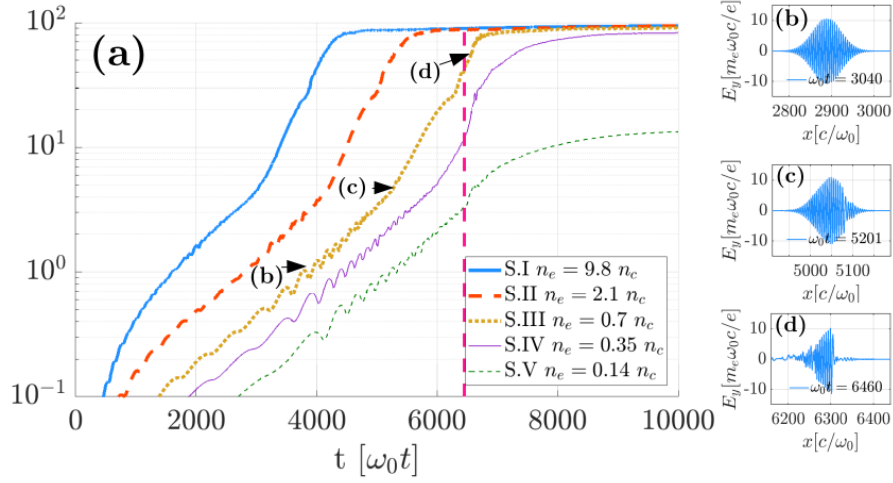
Fig. 3.4: (a) Laser energy absorption with respect to time for S.I (blue solid line), S.II (orange dashed line), S.III (yellow squared-dotted line), S.IV (dark purple thin solid line) and S.V (green thin dashed line), see Table 3.1. The instant when the laser pulse arrives to the density peak $\omega_0 t = 6450$ is marked with a vertical pink dashed line. The insets of the figure correspond to the E_y laser field in S.III at times (b) $\omega_0 t = 3990$, (c) $\omega_0 t = 5201$ and (d) $\omega_0 t = 6460$, marked with black arrows in (a).

Simulation III: $n_e = 0.7 \ n_c$
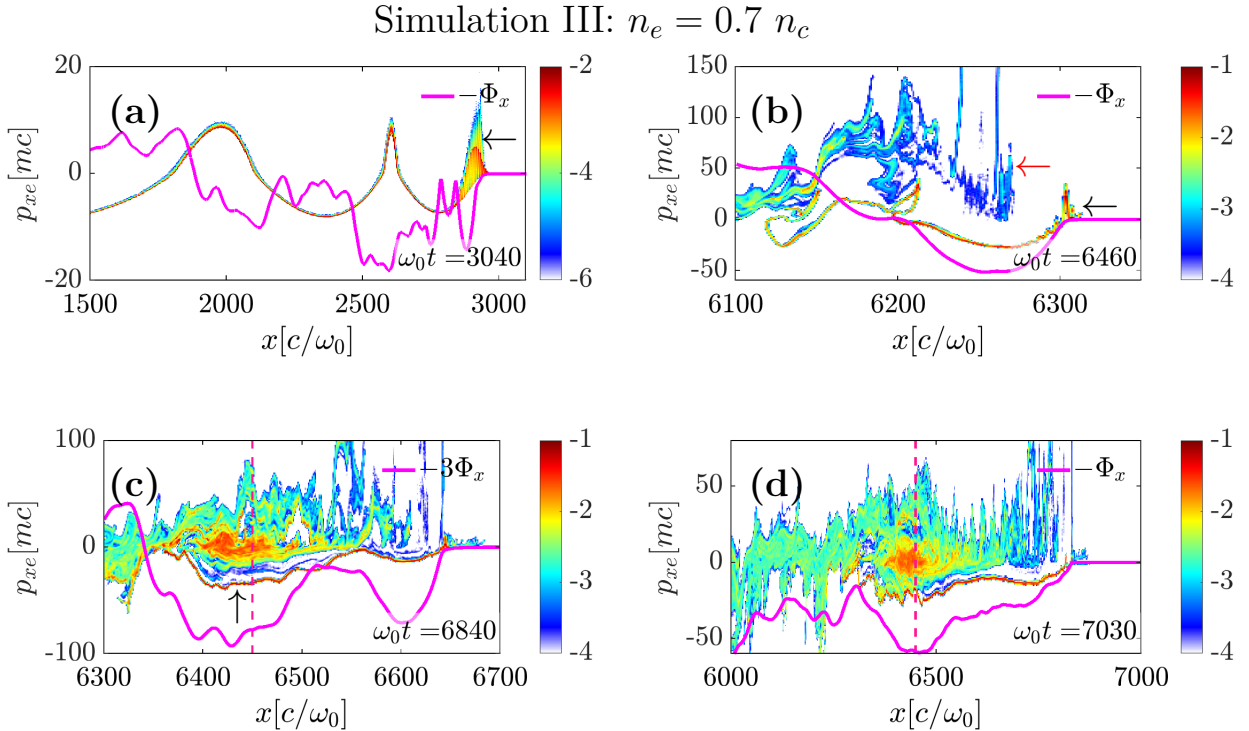
Fig. 3.5: Electron (x,p_x) phase-space (colorscale) extracted at times $\omega_0 t =$ (a) 6270, (b) 6460, (c) 6840 and (d) 7030 corresponding to S.III. The normalized electrostatic potential $-\Phi_x$ is superposed as solid pink lines.

Figures 3.5a-d correspond to the electron (x,p_x) phase spaces of S.III at times $\omega_0 t = 3040$,

6460, 6840 and 7030. The electrostatic potential $-\Phi_x$ is overlaid as solid pink lines.

Fig. 3.5a shows the early stage of electron energization, that takes place when the laser interacts with the low density wing of the target. The nonlinear wakefield has trapped a bunch of electrons that co-move with it, as indicated by the black arrow in Fig. 3.5a. Note that the electrostatic potential $-\Phi_x$ still comes back to zero in the first oscillations wakefield.

Afterwards, at $\omega_0 t = 6460$ (Fig. 3.5b), the laser-plasma interaction gives rise to a two-stream electron distribution resulting from the nonlinear development of the plasma wakefield. Note that the laser front has fully steepened by this point, see Fig. 3.4d. The mentioned electron distribution is composed by a cold electron return current and a hot forward-moving one.

On one hand, the cold return current contains electrons initially accelerated by the laser wakefield and co-moving with it, see black arrows in Figs. 3.5a and b. The laser-induced displacement of these electrons from their initial position gives rise to a strong charge separation E_x field, which drags them back into the plasma core at a negative momentum $p_x \approx -25$, as seen in Fig 3.5b. This charge separation field, which propagates at a velocity close to the speed of light c, is as strong as it is short-lived since the displaced electrons are rapidly pulled back into the plasma. On the other hand, the hot forward electron current is composed of the electrons inside the bulk of the plasma which are already undergoing a heating process in a turbulent regime, as highlighted by the red arrow in Fig 3.5b. At this point, phase mixing between these two electron currents has already started.

At $\omega_0 t = 6840$ (Fig. 3.5c), phase mixing between these high-energy streams continues to develop and results in fast heating of the plasma electrons. The process of breaking of the wakefield and phase mixing between the two cited electron currents is called *beam-loading* [30]. The latter fully develops by $\omega_0 t = 7030$ (Fig. 3.5d). Here the cold return current is re-injected into the target at a negative momentum $p_x \approx 20 \approx \Phi_x/2$, in agreement with the electron heating model in near-critical plasmas developed in Ref. [30]. The electrostatic potential drops strongly behind the laser pulse and oscillates around $-\Phi = 50$ during the interaction between the two electron currents.

Figures 3.6a and b correspond to the late stage of the electron energization of Sims. I and III, as seen in the electron (x,p_x) phase spaces taken at times $\omega_0 t = 12350$ and 12450, respectively. Figs. 3.6c and d are zooms of the gas down-ramp corresponding to Sims. I and III, respectively. The electrostatic potential $-\Phi_x$ is overlaid as a pink solid line in all panels.

In the high-density S.I (Figs. 3.6a and c), the majority of hot electrons are produced at $x \approx 3000\ c/\omega_0$, when the wakefield resonance conditions is satisfied, as was previously discussed. Since the laser is completely absorbed at $\omega_0 t \approx 4500$, this electron population must heat-up all the gas left to its right. The neutralization of this hot electron population is ensured until the point where it reaches a background density similar to that at which it was created (i.e. at $x \approx 9000\ c/\omega_0$, see density profiles of Fig. 3.1). At this point, charge neutralization can no longer be ensured and a charge separation field E_x is created. This field pulls back the hot electrons, obliging them to recirculate around the target (see black arrow in Fig. 3.6a), yielding the broader p_x-extent of its distribution at the right of the density peak.

In the low density S.III (Figs. 3.6b and d), the majority of hot electrons are created at $x \approx 5000\ c/\omega_0$. Hence, charge neutrality is no longer ensured when the hot electrons reach the symmetrical point in the up-ramp, i.e. $x \approx 7800\ c/\omega_0$. The electrostatic fields arising from the strong electron density and pressure gradients cause the electrons to recirculate back and forth (forming a vortex in the phase space) around the maximum density, while triggering TNSA of the local ions located at the density peak, as will be discussed in the following section.

In S.I (S.III) the transmitted percentage of the laser energy is 0.4% (4.6%). The laser can then not be responsible for the electron acceleration seen in the right plasma-vacuum boundary up to momenta $p_x > 60$ in both simulations (see black arrows in Figs. 3.6c and d). This high-energy electron bunch was initially energized in the plasma wakefield, crossed the entire target
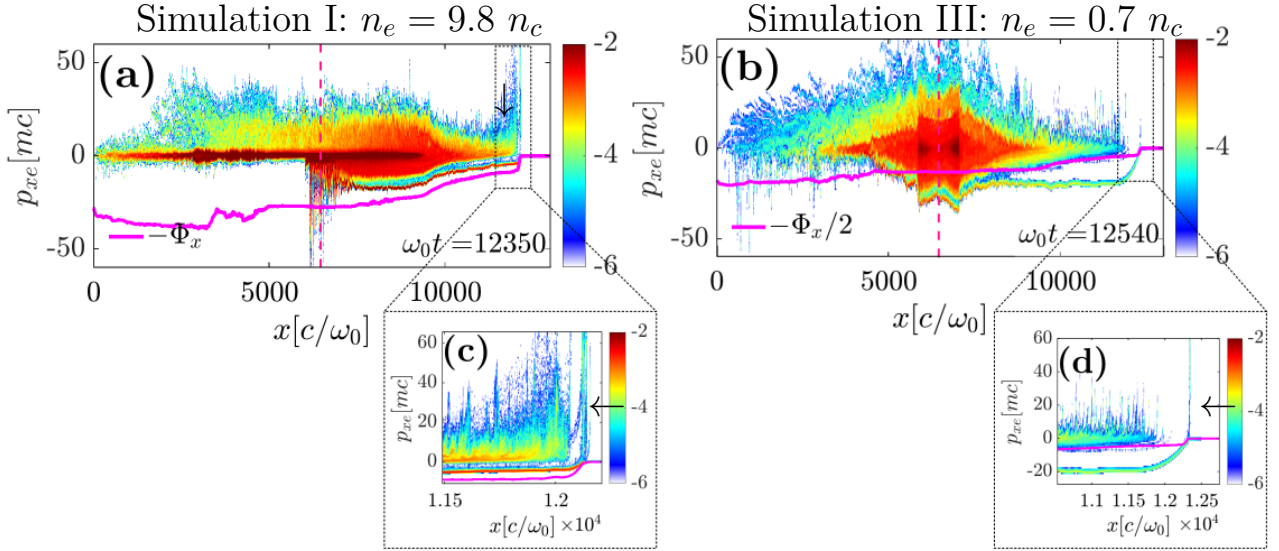
Fig. 3.6: Late stages electron (x,p_x) phase-spaces (colorscale) corresponding to (a) S.I and (b) S.III. The normalized electrostatic potential $-\Phi_x$ is overlaid as solid pink lines.

and exits now into vacuum. The formation of the return current is seen on the fast-ionizing front of the hot electron stream.

3.4 Ion acceleration mechanisms

The subsequent ion acceleration mechanisms and their efficiency chiefly rely on the laser absorption conditions. Three regimes of ion acceleration, illustrated in the (x,t) ion density maps of Fig. 3.7, stem from the 1-D simulations.

- In the high density cases (Sims. I and II), the laser is absorbed in the gas up-ramp. The hot electrons propagate through the gas and trigger IAWs propagating at $\pm C_s$ with equal amplitudes, as observed in Figs. 3.7a and b. The subsequent evolution of these waves into a train of solitons in the TNSA expanding plasma is discussed in Section 3.6.

- For moderate gas densities (Sims. III and IV), the laser drives strong wakefields that trap a large number of electrons, rapidly turn turbulent and heat the plasma. The strong electron pressure triggers an electrostatic shock as illustrated in Fig. 3.7c and d. These cases correspond to the ideal laser absorption regime and are discussed in the Section 3.4.1.

- For low gas densities (S.V), the laser absorption essentially remains in a moderately non-linear wakefield regime. The electron temperature is not strong enough to trigger a shock and only TNSA subsists. This regime is discussed in Section 3.4.2.

Figures 3.7a-d show the ion density n_i charts centered on the target down-ramp for the Sims. I - IV. In the high density Sims. I and II (Figs. 3.7a and b) the ion density charts are cut by several ionic wave pairs that depart from a single point into symmetrical opposite directions all along the target up and down-ramp. In Sims. I and II these soliton trains travel at a velocity $v_{i,w} \approx 0.02\ c \approx C_s$, where $C_s = \sqrt{Z^*T_e/m_i} \approx 0.025\ c$ is the local ion acoustic speed (with $Z^* \approx 5$ and $T_e \approx 3$, the ionic charge and electron temperature, respectively). For
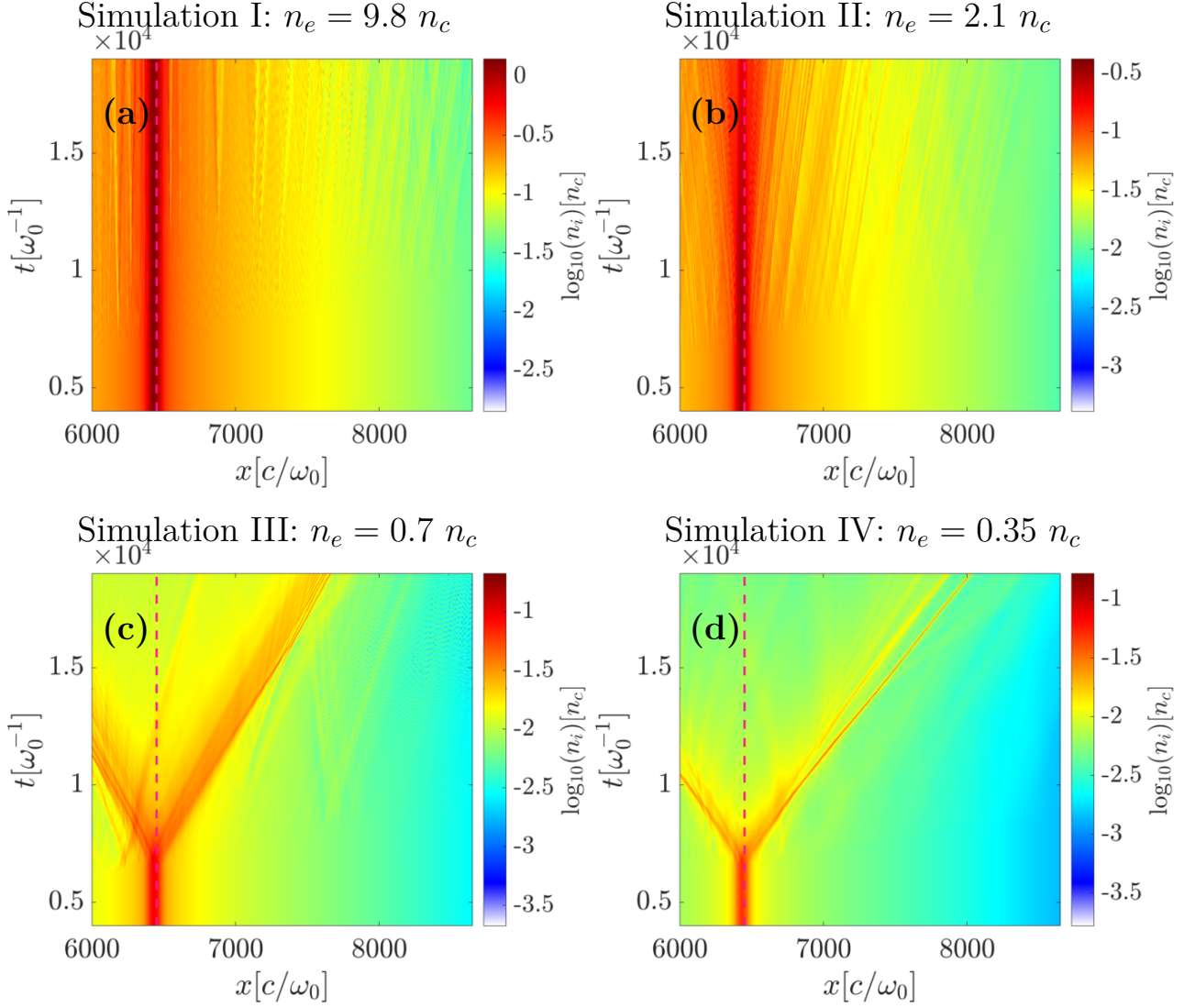
Fig. 3.7: (x,t) maps of the ion density centered on the target down-ramp for the (a) Simulation I with $n_{at,max} = 1.4\ n_c$, (b) Simulation II with $n_{at,max} = 0.3\ n_c$, (c) Simulation III with $n_{at,max} = 0.1\ n_c$ and (d) Simulation IV with $n_{at,max} = 0.05\ n_c$, see Table 3.1. The density peak is marked with a pink dashed line.

more details on the ion wave excitation at high densities see Section 3.6.

In the lower density scenario, corresponding to Sims. III and IV (Figs. 3.7c and d), no IAW formation is seen. In this case, the front of the expanding plasma steepens and triggers a collisionless electrostatic shock that gives rise to background ions reflection at $t \gg \omega_{pi}^{-1}$. In S.III (S.IV) the front of the expanding plasma travels at $v_{i,w} \approx 0.08\ c$, $M \approx 2$ ($v_{i,w} \approx 0.13\ c$, $M \approx 2$), where $M = v_{x,i}/C_s$ is the upstream Mach number. As one can deduce, T_e is higher in S.IV than in S.III.

3.4.1 Ion acceleration in moderate density simulations: collisionless electrostatic shock formation

Figures 3.8a and b plot the ion (x,p_x) phase spaces for the low density Sims. III and IV at the shock formation time, i.e. the onset of ion reflection. At this point, the ion velocity profile has fully steepened. In S.III shock reflection starts at $\omega_0 t \approx 14250$ (7.6 ps), and in the lower

density S.IV it does so at $\omega_0 t \approx 13870$ (7.4 ps). The shock formation time does not satisfy the proportionality $t \propto \omega_{pi}^{-1}$. Shock reflection could be accelerated in S.IV by widening the density profile until achieving optimum plasma heating conditions, i.e. the transition from a laminar to a turbulent electron energization regime while crossing the gas density peak (as in S.III, see absorption curves of Fig. 3.4).
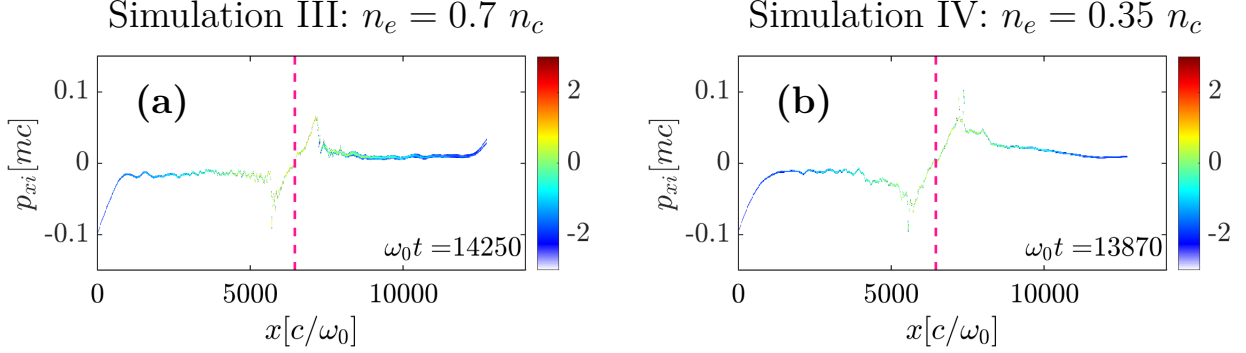
Fig. 3.8: Ion phase-spaces for the (a) simulation III with $n_{at,max} = 0.1\,n_c$ and (b) simulation IV with $n_{at,max} = 0.05\,n_c$ taken at the shock formation instants when background ion reflection is about to start.

Figures 3.9a and b show the ion (x, p_x) phase spaces corresponding to the last time step of the low density Sims. III and IV. CES formation was observed in both simulations.
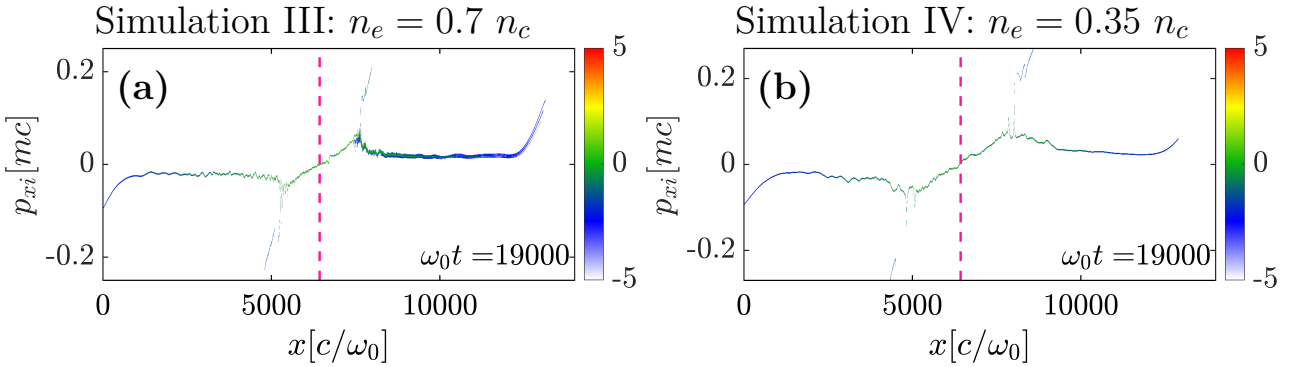
Fig. 3.9: Final ion (x, p_x) phase spaces of the (a) $n_{at,max} = 0.1\,n_c$ and (b) $n_{at,max} = 0.05$ n_c maximum density simulations.

In these cases, the accelerated ion velocity profile continually steepens when moving down the density gradients while the quasi-exponential density "wings" are subject to a uniform slower acceleration in the ambipolar field $E_x \approx T_e/L_n$, where L_n is the quasi-constant density gradient. This process bears resemblance to wavebreaking in TNSA within a pre-expanded plasma profile [135] and has been described as the expansion of a hot plasma into a cold rarefied plasma [136, 137]. The steepening of the ion velocity profile goes along with an increase in the local potential barrier up to the point of reflecting the upstream ions, uniformly accelerated by the ambipolar field. An ion located in front of the shock and moving at a velocity $v_0 - v_s$ in the shock frame, where v_s is the lab-frame shock front velocity and v_0 is the initial lab-frame ion velocity, gets reflected from the shock front if its kinetic energy in the shock frame, E_k, is lower than the electrostatic potential $Z^* e \Delta\phi$ experienced by the particle in the shock region:

$$E_k = \frac{m_i(v_0 - v_s)^2}{2} \; < \; Z^* e \Delta \phi. \tag{3.3}$$

Here, m_i is the ion mass and Z^* the ionization degree. Shock formation was observed in the simulations with peak electron density between 0.35 n_c and 0.7 n_c (Sims. III and IV). Moreover, the uniform slower acceleration of the ions located in the target wings is due to the constant plasma scale length L_n of the density profile, as seen in Fig. 3.9, which gives rise to a constant TNSA derived electrostatic field. The contrary would induce a chirp in the reflected ions, making them lose their CSA characteristic peaked spectra [23]. The shock's Mach number is calculated as $M = (v_0 - v_s)/C_s$, where C_s is the upstream ion sound speed. The CES formed in Sims. III and IV have Mach numbers $M \approx 1.6$ and $M \approx 2.4$, respectively. Mach numbers between $1.6 \le M \le 3$ are characteristic of super-critical shocks, in which ion reflection and plasma heating are the stabilizing energy dissipation mechanisms [23]. The obtained Mach number values agree with the CES conditions in near-critical plasmas studied by F. Fiuza *et al.*, [23, 24] and M.E. Dieckmann *et al.*, [25, 26].

Tab. 3.3: Plasma parameters relative to the shock reflection condition in S.III ($n_e = 0.7 \ n_c$) for the N^{7+} and N^{6+} ion species.

Ion	Time $[\omega_0^{-1}]$	$m_i \ [m_e]$	$v_f \ [c]$	$v_0 \ [c]$	$(v_f - v_0) \ [c]$	$E_k \ [m_e c^2]$	Z^*	$\Delta\phi \ [m_e c^2/e]$	$Z^*\Delta\phi \ [m_e c^2/e]$	$C_s \ [c]$	M
N^{7+}	13945	25704	0.109	0.030	0.079	79.804	7	12	84	0.048	1.642
N^{6+}	13945	25704	0.109	0.020	0.089	101.34	6	12	72	0.048	1.850

The plasma parameters relevant for shock reflection in S.III are summarized in Table 3.3. The shock reflection condition, corresponding to Eq. 3.3, is fulfilled for the N^{7+} ionic species at $\omega_0 t = 13495$. In the case of N^{6+} ions the kinetic energy exceeds the electrostatic potential experienced by the ionic species in the shock region $E_k > Z^* e \Delta\phi$, thus preventing electrostatic reflection.

3.4.1.1   Effect of the ionization degree on shock reflection

In S.III the gas down-ramp has experienced a strongly attenuated laser pulse, and therefore has not been fully ionized. Hence, it is interesting to examine how ionic species of different charge state interact with CES and, in particular, whether they can be reflected by it. Recalling the shock reflection condition of Eq. 3.3, the shock formation is highly sensitive to the ionic species ionization state, since it will determine the electrostatic potential seen by the incoming ions. Figs. 3.10a and b focus on the ion (x, p_x) phase space down-ramp of S.III, corresponding to the N^{6+} and N^{7+} nitrogen ionic species, respectively. The N^{6+} ion species do not see a sufficiently strong electrostatic potential and are consequently not reflected from the shock front, located at $x = 7500 \ c/\omega_0$ in Fig. 3.10a. Instead, they are slightly accelerated and finally cross the shock region. Only the fully ionized N^{7+} ions experience the maximum electrostatic potential and are reflected at twice the shock velocity, see Fig. 3.10b.

3.4.1.2   Early times ion acceleration at the density peak

As was previously mentioned, in the low density Sims. III and IV the laser-induced heating of the plasma electrons around the density peak generates strong electrostatic fields in the neighboring density gradients, which confine the energetic electrons and rapidly accelerated the ambient ions (Fig. 3.6d).

In order to discern between the possible ion acceleration mechanisms that could take place in the density peak for the low density simulation, TNSA of Coulomb explosion, one should
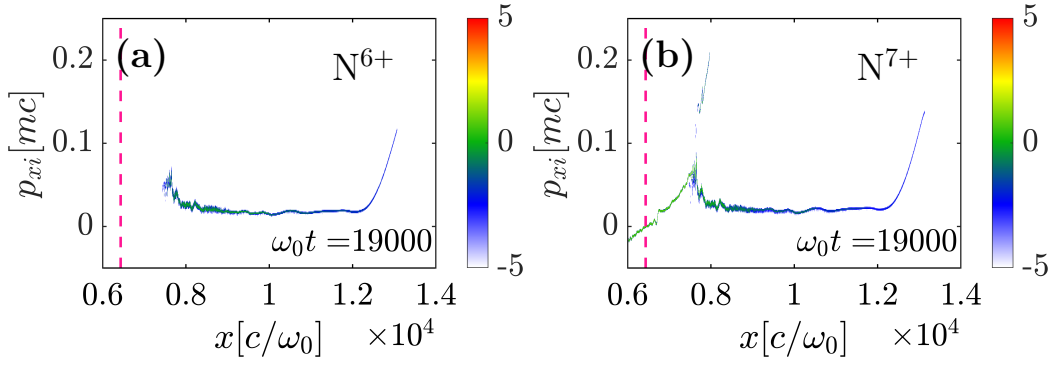
Fig. 3.10: Influence of the ionization state in shock reflection as seen in the ion phase spaces of the (a) N^{6+} and (b) N^{7+} ion charged species phase spaces corresponding to S.III.

compare the local Debye length λ_{De} and density scale length L_n. In this case, $L_n \gg \lambda_{De}$ due to our moderate $a_0 = 11$, which sets an upper limit to the achievable electron temperature T_e ($\lambda_{De} \propto \sqrt{T_e}$). However, Coulomb explosion-dominant ion acceleration scenarios can become important if working with higher intensity lasers.

3.4.1.3 Role of laser-driven ion acceleration combined with the gas profile in shock formation

So far, we have discussed the formation of CES in terms of the slow plasma expansion driven by the uniformly heated bulk electrons, leaving aside the possible influence of shorter-scale velocity of ion density perturbations imparted by the laser.

The direct laser impact on ion acceleration and shock formation was assessed by performing a laser-free simulation with a pre-heated electron population with $T_e = a_0 = 11$ and $n_{at,max} = 0.1\ n_c$ (S.VI). The chosen $T_e = a_0$ value approximately agrees with the mean electronic temperature found in the original laser-on S.III, as seen in Fig. 3.11.
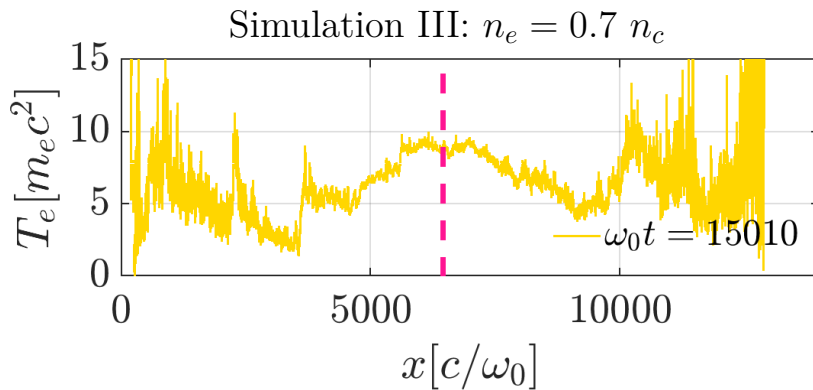
Fig. 3.11: Electron temperature T_e lineout extracted from S.III at $\omega_0 t = 15010$.

Figures 3.12a and b plot the ion (x, p_x) phase spaces corresponding to the last time step of the simulation VI with a pre-heated Maxwellian electron population with $T_e = a_0$ and $n_{at,max} = 0.1\ n_c$ and of the simulation III with $n_{at,max} = 0.1\ n_c$ and $a_0 = 11$, respectively. Figs. 3.12c and d plot the corresponding electron (x, p_x) phase spaces. The longitudinal electrostatic field E_x is overlaid as dark violet lines.
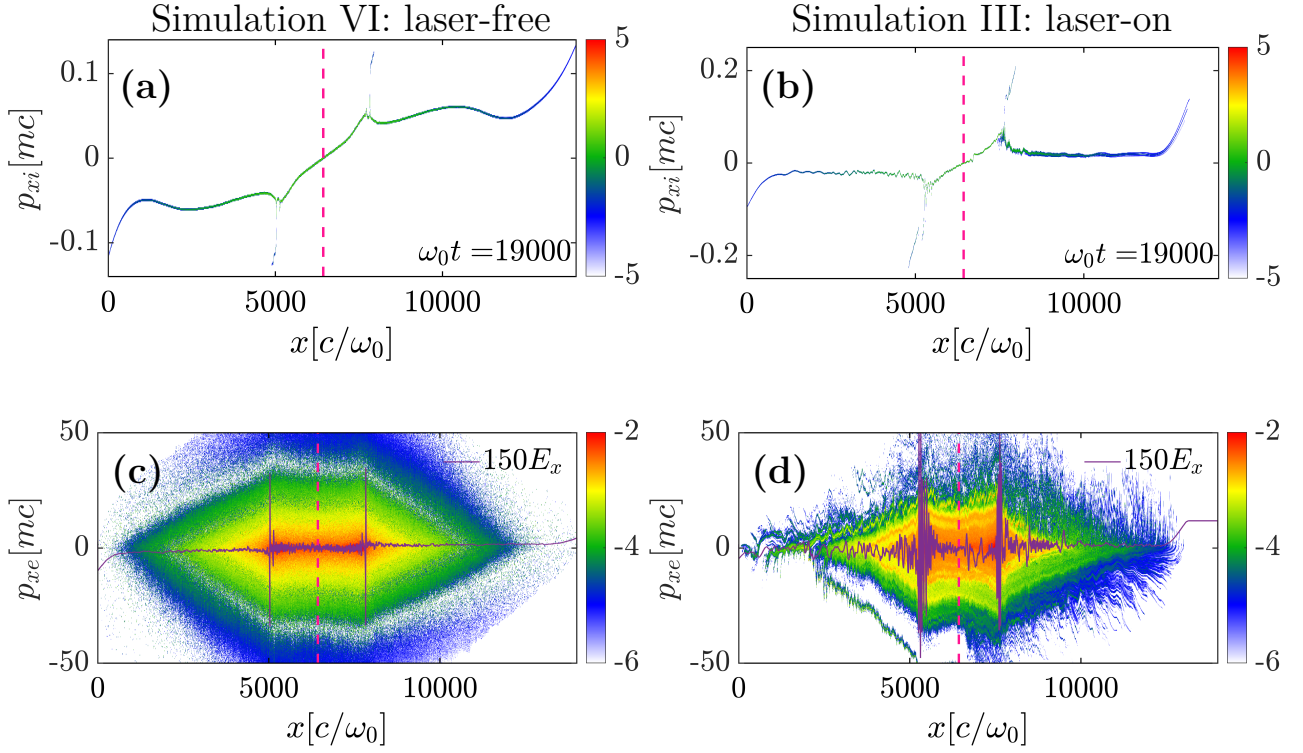
Fig. 3.12: (a) Final ion (x, p_x) phase spaces corresponding to (a) S.VI and (b) S.III. Electrostatic shock barriers in (c) S.VI and (d) S.III, as seen in the electron (x, p_x) phase spaces of the respective simulations. The longitudinal electrostatic field E_x is overlaid in each electron phase space as dark violet lines.

The laser-free simulation produces a shock that is qualitatively similar to the one triggered in the laser-on simulation, as seen by comparing the ion (x, p_x) phase spaces plotted in Figs. 3.12a and b. However, the initial plasma modulations are absent in the laser-free simulation, which confirms their laser-driven nature.

Forcing a uniform electron temperature through the entire profile tends to enhance TNSA in the profile's wings. One can appreciate that in the quasi exponentially decreasing wings, that are subject to a uniform accelerating field, the ion velocity reaches the values $v_i \approx 0.05\ c$ in the laser-free simulation, and $v_i \approx 0.02\ c$ otherwise. In Fig. 3.12a a strong ion acceleration is seen in the gas wings, at $1000\ c/\omega_0 < x < 4000\ c/\omega_0$ and $9000\ c/\omega_0 < x < 12000\ c/\omega_0$. This makes it harder for the fast ions accelerated from the density spike to catch up with and eventually reflect the ions accelerated at the gas wings.

The laser-on electron (x, p_x) phase space is strongly modulated as a consequence of the direct-laser and wakefield-induced electron acceleration [30, 138] (Fig. 3.12d), in comparison with the laser-free simulation (Fig. 3.12c). At the same time, the laser-on electron phase space shows well defined electrostatic shock fronts moving both forward and backward, as seen in Fig. 3.12d at $x = 5000 c/\omega_0$ and $x = 7000 c/\omega_0$. In the laser-free electron (x, p_x) phase space the electrostatic confinement in the downstream region is weaker. As a result, two diluted electron populations centered at $x = 5000 c/\omega_0$ and $x = 8000 c/\omega_0$ travel both forward and backward down the density gradients, as seen in Fig. 3.12c.

A laser free simulation with an initialized hot electron population with $T_e = a_0/2$ (S.X) was performed to investigate whether a weaker target energization could trigger an electrostatic shock in less time. We intended to compare the shock formation time with the value obtained in the laser-free S.VI initialized with $T_e = a_0$, which was previously described, where a shock was triggered at $\omega_0 t = 15171$. However, by the end of S.X no shock reflection was observed.
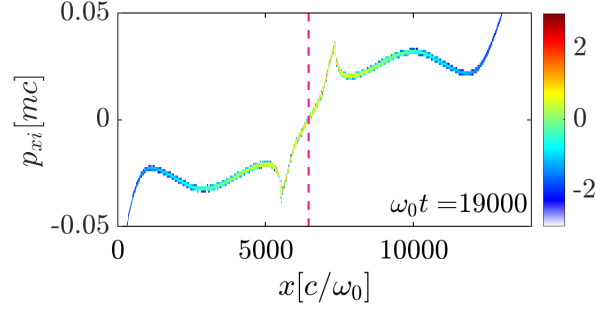
Simulation X: $T_e = a_0/2$

Fig. 3.13: Ion (x, p_x) phase space corresponding to the laser-free Simulation X with $n_{at,max} = 0.1 \, n_c$ and an initialized hot electron population with $T_e = a_0/2$.

The ion (x, p_x) phase space captured at $\omega_0 t = 19000$ is plotted in Fig. 3.13. Hence, the mechanism triggering shock reflection must be linked with the initial density, velocity or electron temperature gradients (Fig. 3.11) imprinted by the laser itself.

One can then conclude that the strong electron pressure gradients are essential for shock formation. Therefore, the same laser interacting with a different density profile with shallower density gradients would not be as effective as it is in this case. This advantage clearly highlights the interest of using shock nozzles, which are precisely designed to produce density profiles with strong density gradients.

3.4.2 Ion acceleration in low density simulations: feeble evolution of the TNSA profile

In the S.V ($n_e = 0.14 \, n_c$), only a 10% of the laser energy is absorbed, see the thin dotted green line in Fig. 3.4. As a result, the electron energization in the target up-ramp is much weaker, attaining a maximum electron momenta $p_{e,max} \approx 0.15$ as seen in the electron (x, p_x) phase space of Fig. 3.14a.

Simulation V: $n_e = 0.14 \, n_c$
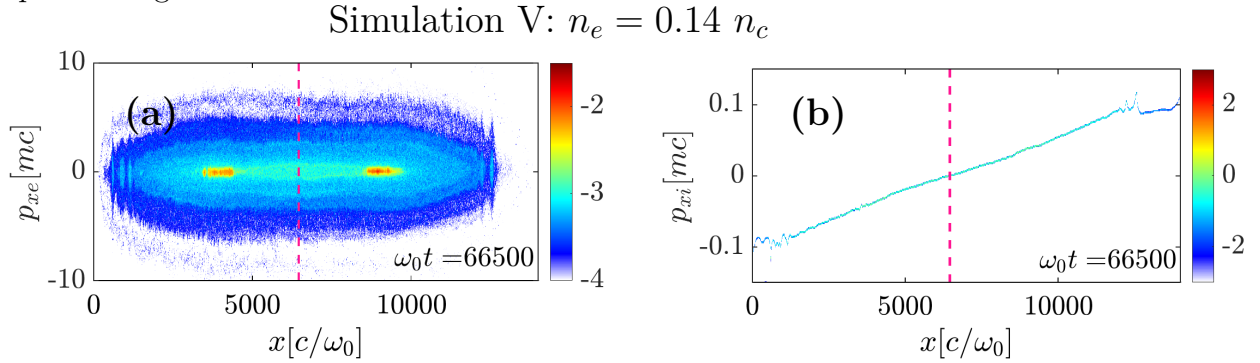
Fig. 3.14: Final (a) electron and (b) ion (x, p_x) phase spaces of Simulation V with $n_{at,max} = 0.02 \, n_c$.

The ion velocity profile formed by TNSA is too slow, with a peak ion velocity $v_{i,peak} \approx 0.1 \, c$, to overtake the ions uniformly accelerated in the wings ($v_{i,wings} \approx 0.1 \, c$), see ion phase space in Fig. 3.14b. In the cases where shock formation was seen, the TNSA triggered at the gas density peak accelerated those ions up to $v_{i,peak} \approx 0.05 \, c$, almost five times the velocity of the ions located on the gas wings ($v_{i,wings} \approx 0.01 \, c$), see Figs. 3.9a and b. By the end of S.V, at $\omega_0 t = 66500$, no shock formation has yet been observed. However, it can not be guaranteed that at large times $t \gg \omega_{pi}^{-1}$ shock formation wouldn't end up occurring from the steepening of the soliton structure located at $x \approx 13000 \, c/\omega_0$. Nevertheless, one should keep in mind that in

a realistic 3-D geometry, the plasma expansion would have already entered a free regime [40] due to a faster decrease in the accelerating field.

3.5 Parametric studies of the laser-matter interaction

3.5.1 Gas mixture effect on ion acceleration

The response time of the ions to the accelerating fields is of the order of ω_{pi}^{-1}, and so ions with the highest Z^*/A ratio will react the fastest. At the same time, recasting equation 3.3 as:

$$E_k = \frac{m_p(v_f - v_0)^2}{2} \quad < \quad \frac{Z^*}{A}e\Delta\phi. \tag{3.4}$$

and considering a similar acceleration of the ionic species located in the shock foot, the existence of ion shock reflection will mostly depend on their Z^*/A ratio. The ions with the highest Z^*/A values will experience a stronger electrostatic barrier at the shock boundary and are more likely to be reflected. However, the shock-reflected ions' velocity $v_{i,r} = 2(v_f - v_0)$, is only dependent on the incoming ions velocity v_0 and the shock front velocity v_f. Once reflected, the different ionic species will do so at the same velocity. Therefore, a gas mixture target provides the opportunity to recognize shock acceleration by looking at coincident peaks in the velocity spectra of the accelerated particles.

A first simulation initiated with the density profile with $n_{at,max} = 0.1\ n_c$ and a composition of 90% nitrogen and 10% hydrogen (see simulation IX in Table 3.1) was performed. Figs. 3.15a and b show the N^{7+} and H$^+$ ion (x, p_x) phase spaces at the onset of H$^+$ shock reflection, respectively. As was previously mentioned, the TNSA for the H$^+$ develops faster ($t \propto \omega_{pi}^{-1}$) triggering the steepening of the ion velocity profile and allowing for an earlier shock reflection. Fig. 3.15c and d show the same ion phase spaces at the onset of N^{7+} shock reflection which occurs must later in time as seen in Fig. 3.15c. In the meantime protons have been almost continuously reflected by the shock as seen in Fig. 3.15d. Fig. 3.15e and f show the final simulation steps for both ionic species. Since the electrostatic shock barrier travels at $v_f \approx 0.1\ c$ the reflected ions do so at $v_{i,r} \approx 0.2\ c$.

A second simulation of the density profile with $n_{at,max} = 0.1\ n_c$ and a composition of 90% nitrogen and 10% helium (see simulation VIII in Table 3.1) was performed and its results compared with the pure atomic nitrogen case (see simulation III in Table 3.1). The selected gas mixture intended to replicate the experimental conditions foreseen at the VEGA-3 facility. The use of hydrogen was forbidden given its explosive nature.

Figures 3.16a and b show the N^{7+} and He^{2+} ion (x, p_x) phase spaces at the onset of shock reflection. Since both fully ionized species share the same Z^*/A ratio the steepening of the TNSA profiles evolves very similarly and the onset of shock reflection occurs simultaneously. Both ion species are accelerated to the same velocity $v_i \approx 0.2\ c$, approximately equal to twice the shock velocity $v_f \approx 0.1\ c$, as seen in Fig. 3.16c and d. The shock Mach numbers $M = (v_0 - v_s)/C_s$ are as well inside the $1.6 \leq M \leq 3$ interval (see Section 3.4.1).

3.5.2 Influence of the laser pulse duration variation

In order to study the effect of the laser pulse duration on shock formation, a simulation with a three times longer laser pulse, with the same energy (keeping $a_0^2\tau$ constant) as the original one was performed. The chosen density profile was the one with $n_e = 0.7\ n_c$ (S.VII). By saturating the color scale on the E_y (x,t) maps visible in Fig. 3.17, one can appreciate the reflection

Simulation IX: 90% N$_2$ + 10% H$_2$
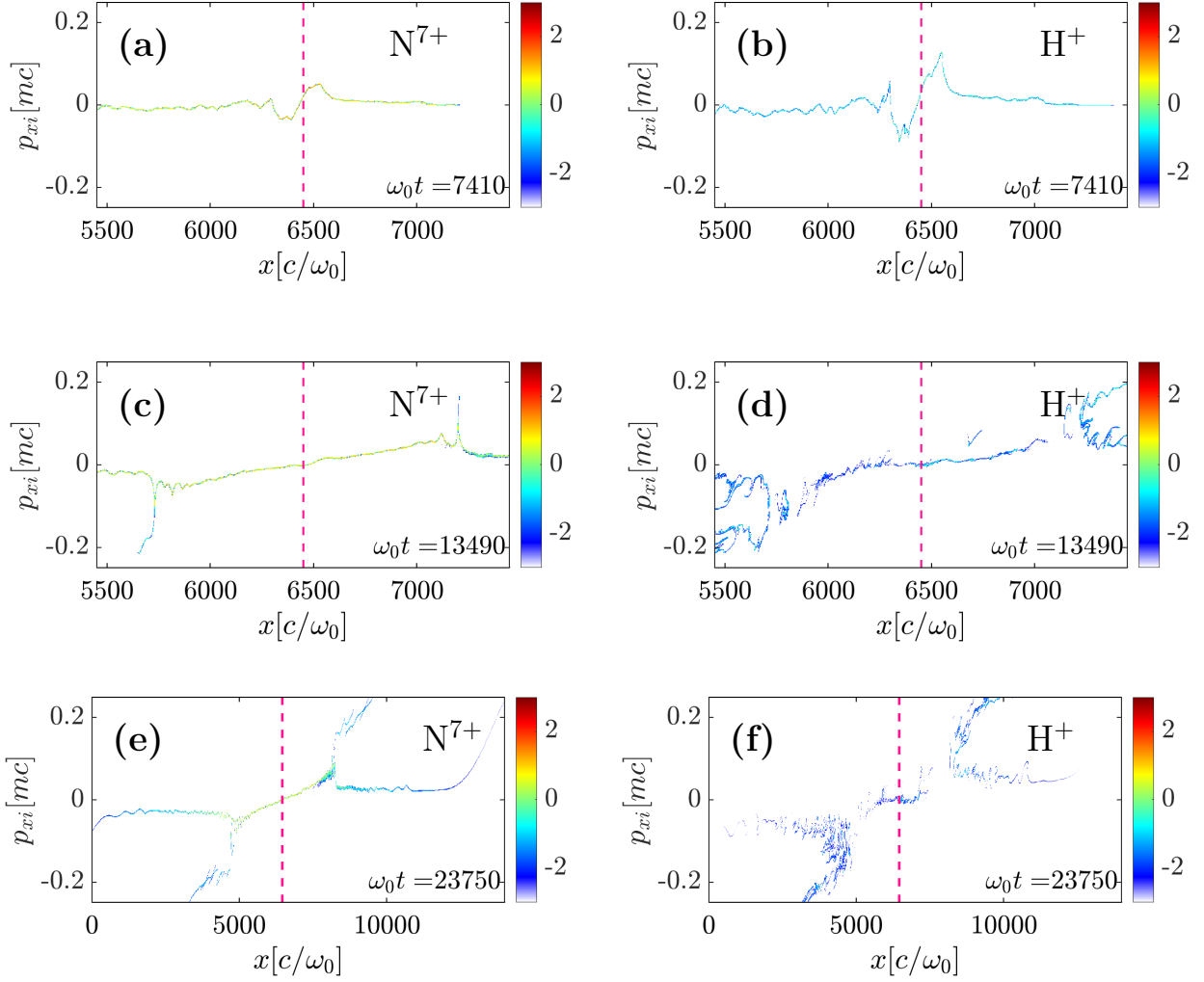
Fig. 3.15: (a), (c), (e) N^{7+} and (b), (d) and (f) ion (x,p_x) phase spaces at different times corresponding to Simulation IX.

and scattering of the laser in the density peak region, marked by the pink dashed line. The transmission coefficient is ten times higher for the longer pulse S.VII (40%), compared to 4% in the original S.III, as seen in the percentage of absorbed, reflected and transmitted laser energy curves, with respect to time, shown below the E_y (x,t) maps. The laser absorption in the longer pulse simulation is equal to 60%, compared to 95% in the original simulation.

Figures 3.18a and b capture the onset of shock reflection for S.VII and S.III, respectively. The onset of shock reflection occurs at $\omega_0 t = 10070$ for the stretched pulse S.VII (Fig. 3.18a) and at $\omega_0 t = 12920$ for the standard pulse S.III. The main difference between both simulations is a less energetic electron population due to the lower laser intensity of the stretched laser pulse.

Therefore, the observed shorter shock formation time in the longer pulse duration simulation is not an obvious result. For instance, it cannot be explained by a lower mean hot electron temperature $\langle T_e \rangle$ (Fig. 3.19) since the latter should lead to a longer wavebreaking time $t_b \approx 4L_n/C_{s0} = \sqrt{16L_n^2 m_i/(Z^* T_e)}$, for $L_n \gtrsim 5\lambda_D$ (a condition which is satisfied for both simulations), where L_n is the local plasma scale length, C_{s0} is the initial ion acoustic speed and λ_{De} is the local Debye length [135].

The laser absorption in the longer pulse duration S.VII is of 60% (see inset of Fig. 3.18c) compared with 95% (see inset of Fig. 3.18d) in the original simulation. Once the shorter laser

Simulation VIII: 90% N_2 + 10% He
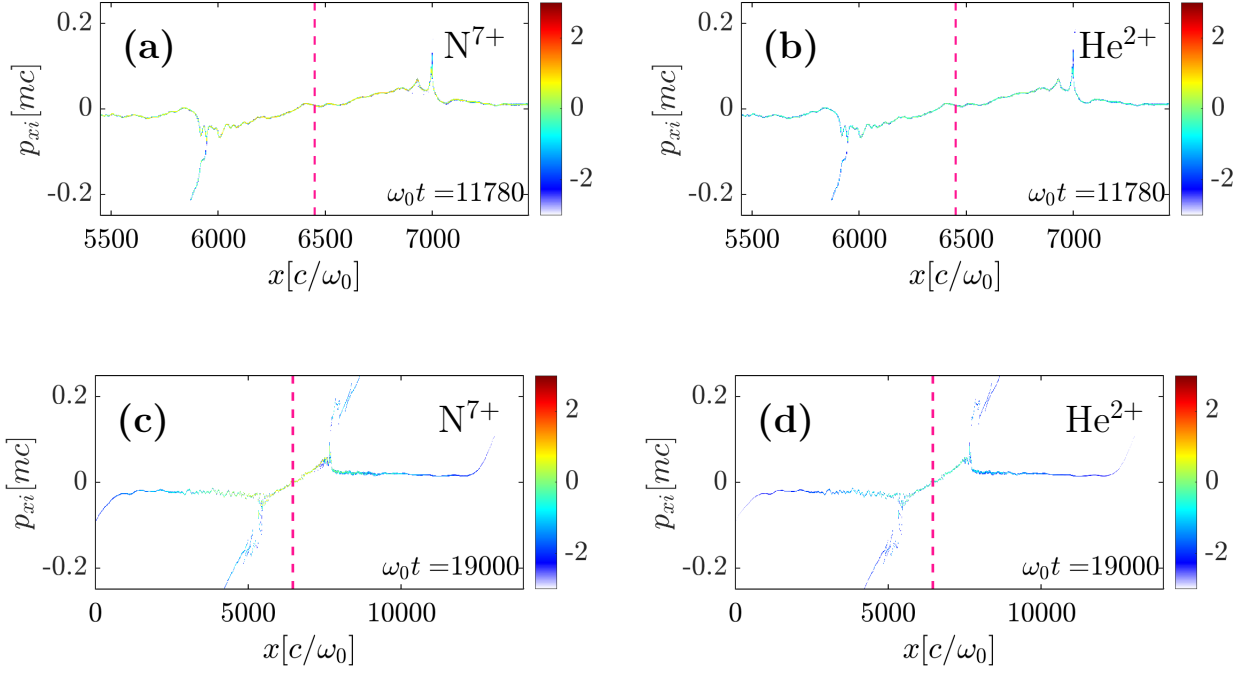
Fig. 3.16: (a-b) Simulation VIII with $n_{at,max} = 0.1$ n_c and a gas composition of 90% nitrogen and 10% helium, see Table 3.1. (a) N^{7+} and (b) He^{2+} ion phase spaces at the last time step of the gas mixture simulation.

Simulation VII: $\tau_L = 169$ ω_0^{-1} Simulation III: $\tau_L = 56$ ω_0^{-1}
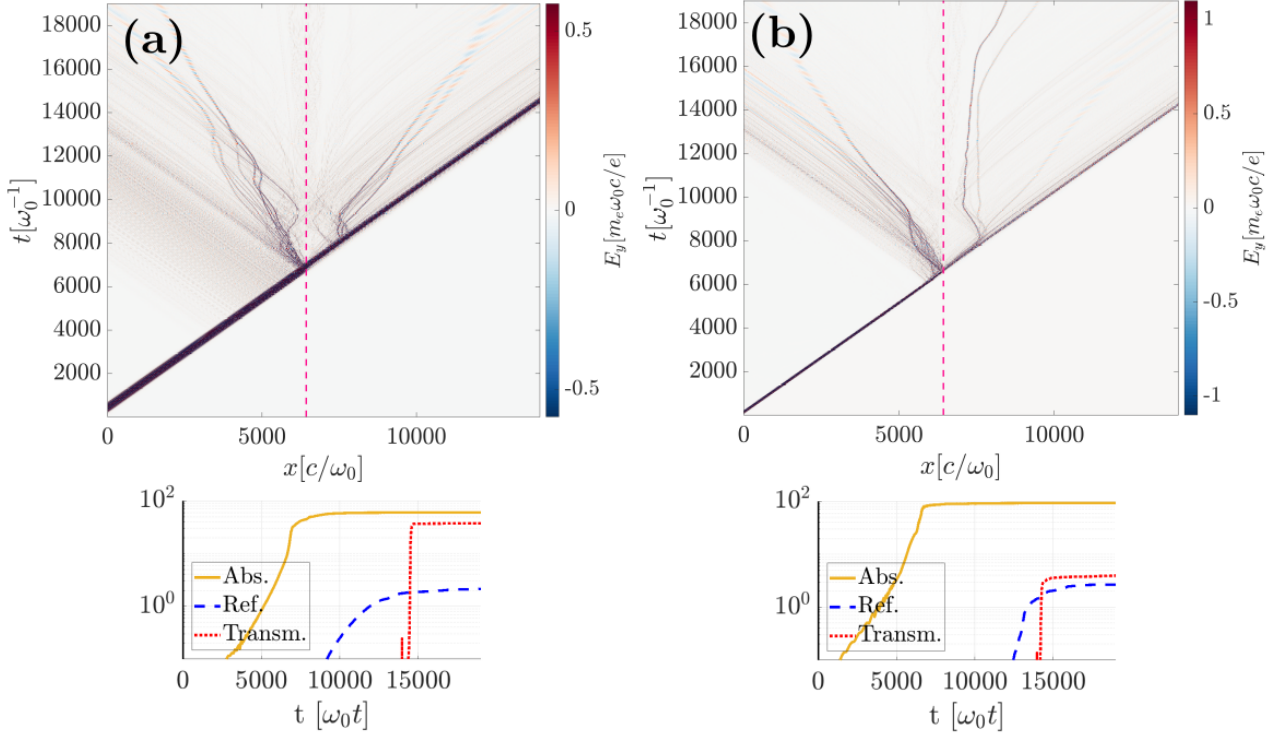
Fig. 3.17: Saturated E_y (x,t) maps for (a) S.VII stretched laser pulse simulation and (b) S.III standard pulse duration simulation. The pink dashed lines mark the location of the gas density peak. The corresponding curves of percentage of absorbed, reflected and transmitted laser energy are plotted below each (x,t) map.

crosses the density peak it transfers its energy to the local electrons giving rise to a charge separation field. In original S.III, the electrostatic field reaches a maximum value $E_{x,max} \approx 2$
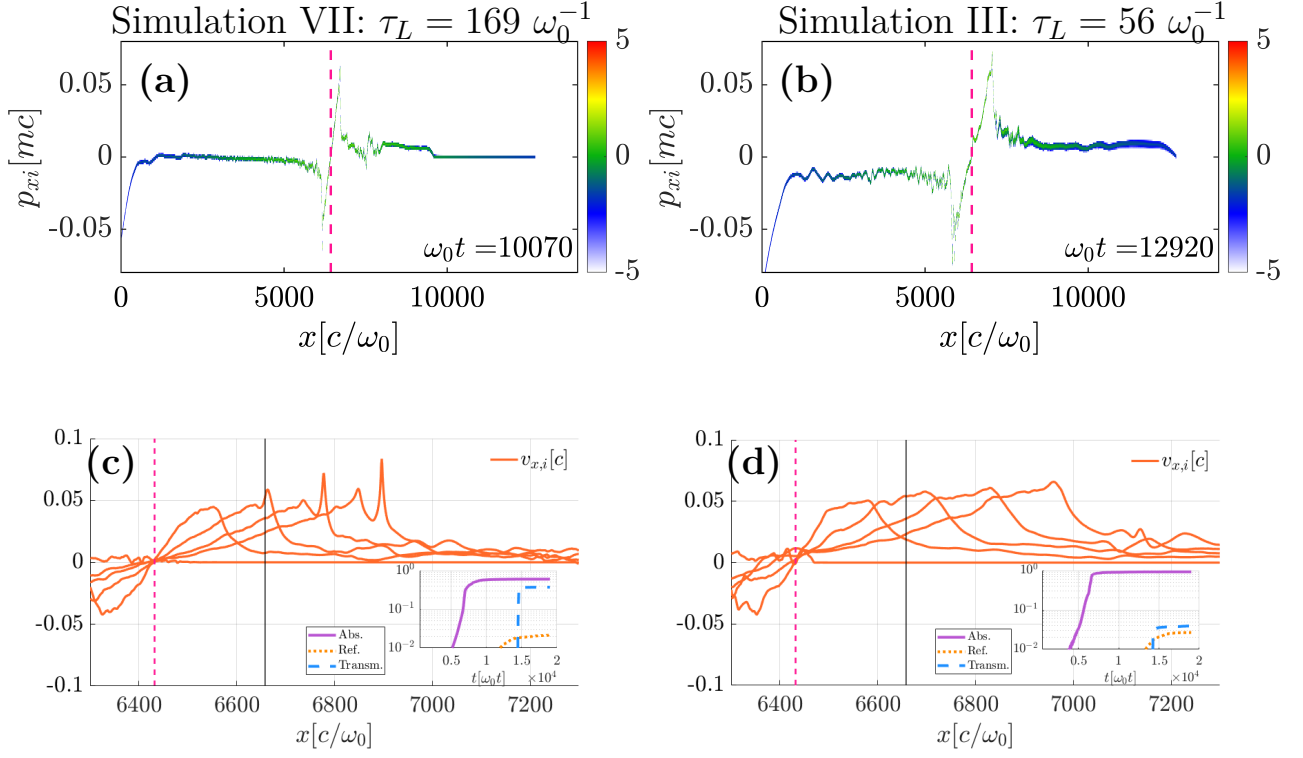
Fig. 3.18: (a and c) S.VII with $\tau_L = 169\ \omega_0^{-1}$ and (b and d) S.III with $\tau_L = 56\ \omega_0^{-1}$, see Table 3.1. Onset of shock reflection seen in the ion phase space of the (a) the stretched laser pulse and (b) the standard duration pulse simulations. Ion velocity profiles at five different times steps plotted in yellow solid lines for (c) S.VII and (d) S.III. The density peak is marked by the dark pink dashed line.

when the laser crosses the density peak. In the stretched pulse S.VII, $E_{x,max} \approx 1$ at $\omega_0 t = 6840$.

In Figs. 3.18c and d, a total of five ion velocity v_i profiles are plotted in solid orange lines for each simulation at five time steps starting when the laser crosses the density peak, and ending approximately at the onset of ion reflection from the shock front. The ion velocity profiles plotted in Fig. 3.18c correspond to $\omega_0 t = 6840, 8170, 9500, 10830$ and 12160. The ion velocity profiles plotted in Fig. 3.18d correspond to $\omega_0 t = 6650, 7980, 9310, 10640$ and 11970.

On the one hand, in S.III the ions from both the density peak and its close surroundings are all equally accelerated to $v_i = 0.05\ c$, which is seen on the ion velocity profile taken at $\omega_0 t = 7980$ in Fig. 3.18d between $6500\ c/\omega_0 < x < 6600\ c/\omega_0$. This makes it harder for the accelerated ions located close to the density peak to catch up and reflect the ions that are further away from the density peak, since those are expanding at the same velocity in the laboratory frame. Shock formation is retarded until the expanding ions reach the ions located in the profile's wings.

On the other hand, in the longer pulse duration S.VII, one observes a chirp in the ion velocity profile. The ions located closer to the density peak expand at $v_i \approx 0.04\ c$ while those further from the peak expand at $v_i \approx 0.01\ c$. This chirp in the ion velocity allows the ions located closer to the density peak to rapidly reach those further from the peak shortening the shock formation time.

However, the scenario is not as simple as this since a higher T_e should entail both a stronger TNSA and a stronger acceleration in the wings. The TNSA ion expansion at the density peak exhibits an ion front velocity $v_{i,f} \propto 2C_s \ln\left(2\omega_{pi}t/\sqrt{2e}\right)$ [40], where e is Euler's number and $\omega_{pi} \propto \sqrt{T_e}$ the ion plasma frequency. At the same time, the self-similar expansion of the bulk ions located in the wings evolves linearly as $v_{i,w} \propto T_e/L_n$, where L_n is the local density scale

85
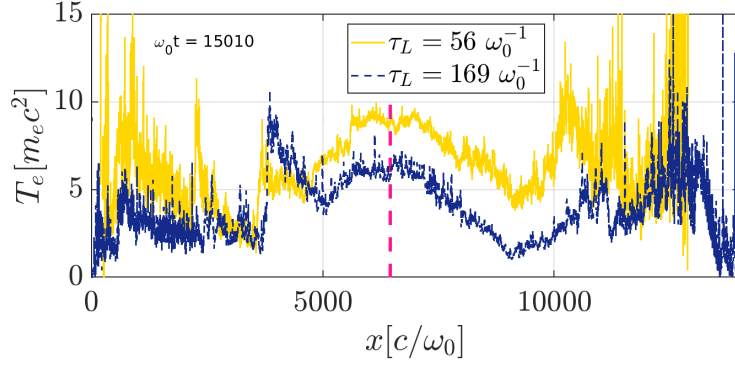
Fig. 3.19: Spatial profile of the mean electron temperature T_e as extracted from the simulations with $\tau_L = 56\ \omega_0^{-1}$ (S.III, solid yellow line) and $\tau_L = 169\ \omega_0^{-1}$ (S.VII, dashed dark blue line).

length. As a result, the ion expansion taking place in the wings of the profile will eventually prevail.

3.6 Ion acceleration in high density simulations

No shock formation was observed in the high-density Sims. I and II. Instead, several nonlinear ion waves eventually emerge in the target wings both in the up and down-ramps, as seen in the ion (x,p_x) of Fig. 3.20 corresponding to S.I. These non-linear ion waves evolve and eventually are able to reflect background ions to velocities $v_i \approx 0.1\ c$ in the gas up-ramp and $v_i \approx 0.05\ c$ in the gas down-ramp, in each case in the direction of the decreasing gradient. Ion acceleration is also observed in the up and down-ramp's extremes, due the TNSA field at the plasma boundary. Ion acceleration triggered by the TNSA fields located in the gas extremes is numerically enhanced due to the abrupt cut of the density profile, introduced in the simulation at a relatively high-density.
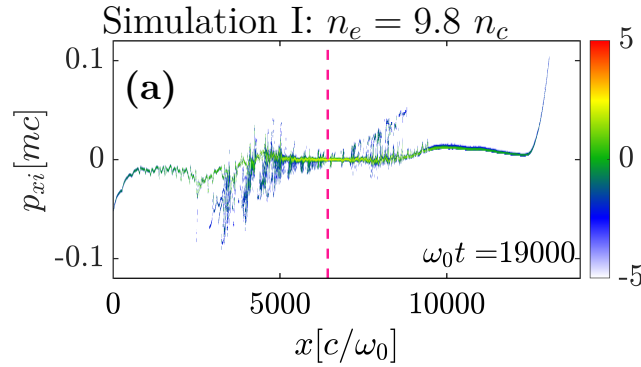
Fig. 3.20: Ion (x, p_x) phase space for the high density simulation I with $n_{at,max} = 1.4\ n_c$.

Such ion density perturbations (IDPs) are seen evolving (both in time and space) into ion acoustic waves (IAWs) travling at $v \approx C_s$ [136, 139], where C_s is the local ion acoustic speed, in the ion density (x,t) charts of Fig. 3.21a and Fig. 3.22a, which zoom on the gas up and down-ramp of S.I, respectively. The corresponding E_x charts are plotted in Fig. 3.21b and Fig. 3.22b. Note that all the figures share the same spatial and temporal x and y-limits, respectively. The IDPs seen in the up-ramp result from the strong laser-driven perturbation on the ions.

86

Such perturbation travels at a velocity $v_{pert.} \gg C_s$. In the down-ramp the laser cannot be the origin of such IDPs since only a 0.1 % of the laser energy is transmitted through the gas density peak. The up-ramp-energized hot electrons, which react in laser-comparable time scales, are most likely the origin of the down-ramp IDPs.
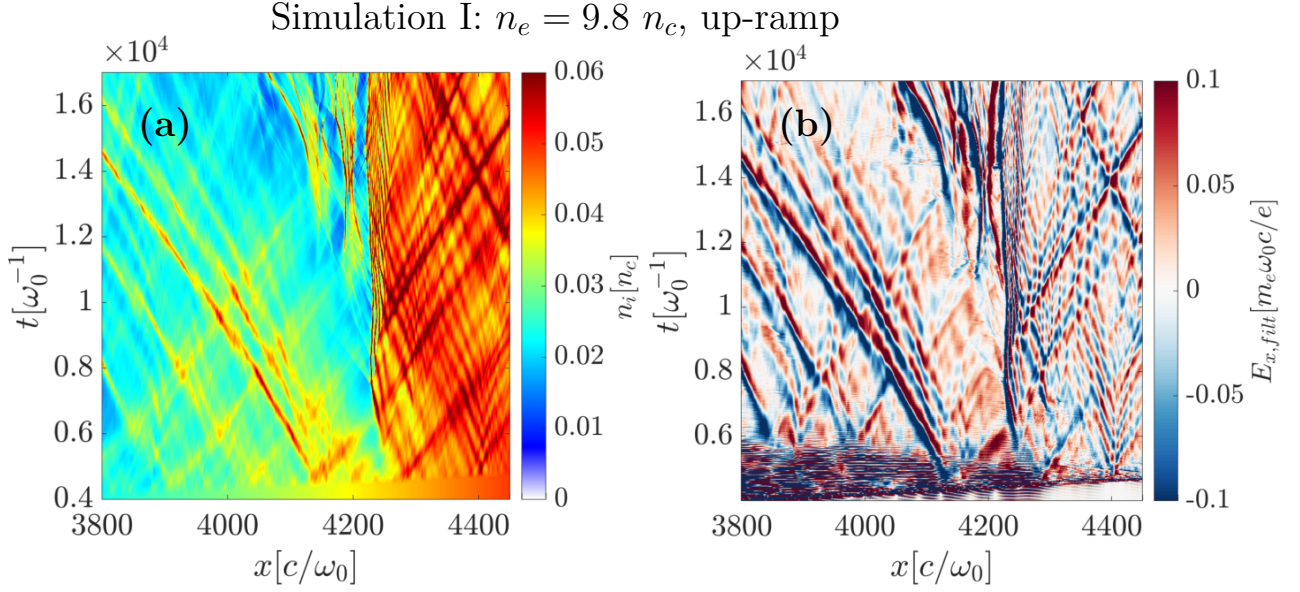
Fig. 3.21: S.I with $n_{at,max} = 1.4 \ n_c$: spatial and temporal evolution in the target up-ramp of the (a) ion density and (b) E_x longitudinal electrostatic field. Note that the density peak is located at $x = 6450 \ c/\omega_0$.
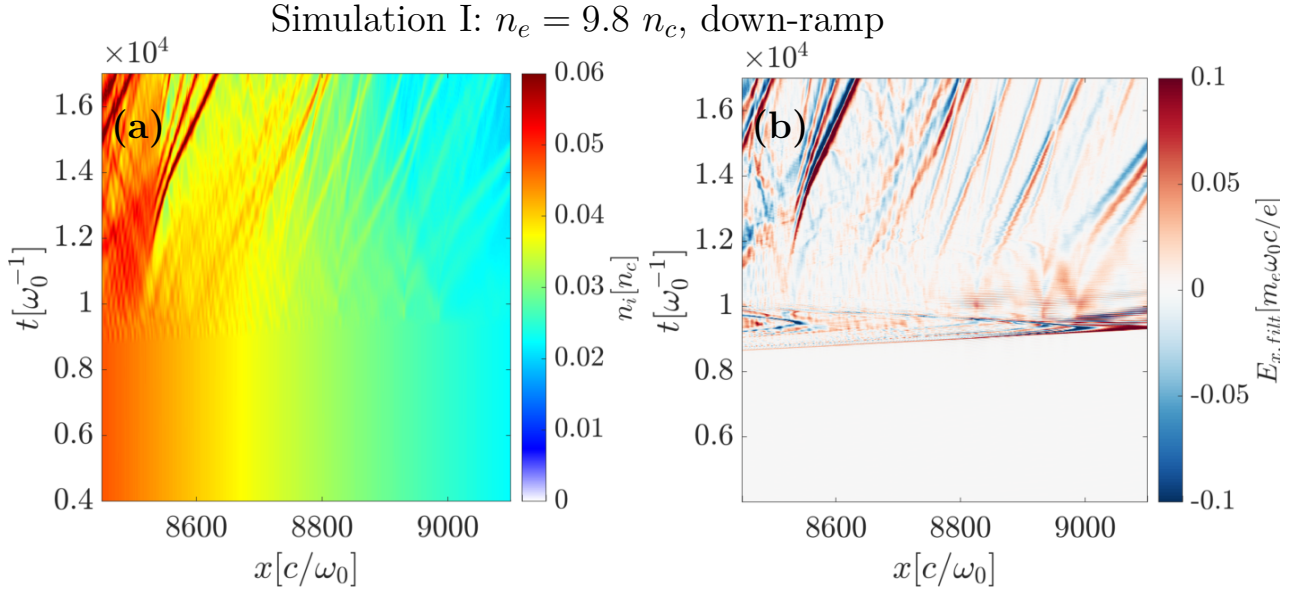
Fig. 3.22: S.I with $n_{at,max} = 1.4 \ n_c$: spatial and temporal evolution in the target down-ramp of the (a) ion density and (b) E_x longitudinal electrostatic field. Note that the density peak is located at $x = 6450 \ c/\omega_0$.

The IDPs descend the density gradients, accelerate and eventually reach a potential $Z^*e\phi > m_i v_i^2/2$ capable of reflecting background ions. This is illustrated in Figs. 3.23a and b, which correspond to the electrostatic potential $-\phi_x$ and ion velocity $v_{x,i}$ of S.IV, extracted at $\omega_0 t = 15010$.

The lineouts correspond to the down-ramp solitary wave seen at $x \approx 8600$ c/ω_0 in Figs. 3.22a and b. In this case, the electrostatic potential seen by the incoming ions $Z^*\phi \approx 17.5$ (with $Z^* = 7$) largely exceeds the ion kinetic energy $E_k \approx 1.85$, enabling background ion reflection from the shock front.

Simulation I: $n_e = 9.8$ n_c, down-ramp
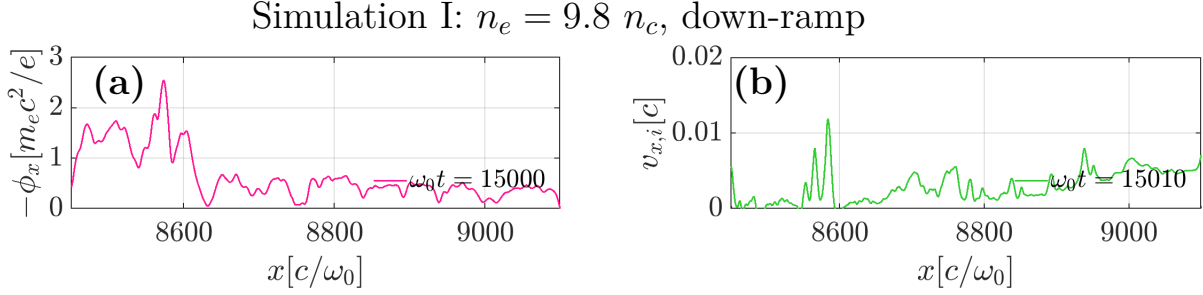
Fig. 3.23: S.I with $n_{at,max} = 1.4$ n_c: (a) ion velocity $v_{x,i}$ and (b) $-\phi_x$ electrostatic potential captured at $\omega_0 t = 15010$ during the solitary wave acceleration observed in Figs. 3.22a and b at $x \approx 8600$ c/ω_0.

The acceleration and steepening of IAWs, seen in the high density Sims. IV and III, is reminiscent of the evolution of a rectangular density disturbance in an homogeneous plasma presented in Ref. [139]. However, the present case is more complex since we treat both density and velocity disturbances in a density gradient, and it lays outside of the scope of this thesis work.

3.7   Conclusions

A parametric study using 1-D PIC simulations has been conducted to derive an optimal set of experimental parameters regarding the interaction of a near-critical non-uniform gas profile, for existent nozzles, with the VEGA-3 laser ($\lambda_L = 0.8$ μm, $a_0 = 8.8$ and $\tau_L = 30$ fs). The gas profile was issued from CFD simulations of the S900 shock nozzle, developed inside our collaboration group. The objective was to simulate realizable experimental conditions. We aimed at understanding the different ion acceleration mechanisms present during the interaction and identifying a range for the density peak in which collisionless electrostatic shock formation occurs. Furthermore we sought to understand the effect on ion acceleration of introducing a small percentage of light ions in the gas as well as to single out the direct laser effect on ion acceleration.

A key factor towards triggering a shock is to have the laser shinning through the profile's density peak while being strongly absorbed (80% - 90%) in the gas up-ramp, where a hot electron population is created. This was achieved with a fourteen times reduction of the S900 nozzle original density profile (Fig. 3.2). Once the correct density is achieved the fast-ion structure originating from TNSA triggered in the density peak evolves into a shock during its propagation across the plasma ramps. This shock can, given the correct conditions, reflect background ions from the down-ramp. Shock formation was achieved in the electron density n_e range between 0.7 n_c and 0.35 n_c (for the profile density peak values). IAW formation and background ion reflection preferentially in the direction of the IAW propagation was seen at higher densities. At lower densities the ion velocity profile formed by TNSA is too shallow to overtake the ions uniformly accelerated in the quasi-exponential target wings. Shock formation is highly sensible to the target density and to the density gradients inherent to the gas profile. Hence, a controlled and repetitive gas profile production is key towards a control of the laser gas interaction.

The direct contribution of the laser to ion acceleration is that of an initial fast and strong perturbation over the ions which modulates both the ion and electron phase spaces. Such modulations create and enhance density perturbations across the profile giving rise to strong charge separation fields inside the plasma. However, the electrostatic shock seed lays elsewhere, with the strong electron pressure gradients, which, linked with the profile's density variations, create plasma slabs of different electronic temperatures and densities. The interaction between these plasma slabs leads to the formation of non-linear trapping structures that can transition into electrostatically-reflecting shocks while traversing the density up and down-ramps. The initial "kick" of the laser acts as a multiplier of charge separation and therefore of the electrostatic barriers, giving rise to stronger shock waves than in the laser-free simulation which will inherently travel faster and hence reflect particles to higher velocities, see ion (x,p_x) phase spaces of Fig. 3.12a and b corresponding to the laser-free and laser-on simulations, respectively.

The times when shock formation and reflection occur are highly sensitive to the laser absorption. A higher laser absorption will strongly heat the plasma electrons giving rise to electron pressure gradients that will create strong charge separation fields. These longitudinal electrostatic fields are enhanced in the density peak due to the natural target density gradients. Such electrostatic fields are capable of homogeneously pre-accelerating the ions present both in the density peak and the gas wings. This will make it more difficult for the ions located closer to the density peak to catch-up with and eventually reflect ions located in the wings, since both ion populations are expanding at the same velocity. On the contrary, a lower laser absorption can actually speed-up ion reflection. The process is such that a less energetic hot electron population creates a weaker and less homogeneous electrostatic field around the density peak. As a result the ions located closer to the density peak will be accelerated at higher velocities than those located in the gas wings. Ion reflection can then readily occur once the fastest ion population reaches the slower expanding ions. Experimentally, when temporally stretching a laser pulse by a factor x the energy contained within it is kept relatively constant, which in return reduces the laser a_0 by a factor $\sqrt{x}$ and the intensity by a factor x. The temporal stretching of the laser pulse becomes then an useful tool for controlling the laser absorption and indirectly the shock formation time without altering the gas profile.

Adding a small percentage of lighter ions (helium) to a pure nitrogen gas does not have a strong effect on the development of the ion acceleration mechanisms already present in the original pure nitrogen simulation. If working in the correct density regime a similar shock is still produced and particle reflection is seen. One must bear in mind that the acceleration mechanisms present during the interaction (Coulomb explosion, TNSA, CSA,...) will occur simultaneously affecting the accelerated particles' spectra in a joint way. Hence, an interesting point lies on the possibility that such gas mixtures offer for recognizing shock acceleration signatures, by looking at the velocity spectra of the accelerated particles. Shock-reflected ion species should translate into peaks in their velocity spectra at the same location whatever the ion species. The observation of such coincident velocity peaks among different ionic species would be consistent with collisionless electrostatic shock particle acceleration. Attention must be paid to the charge-to-mass ratio Z^*/A of the accelerated species in case particle detectors such as Thomson parabolas are being used to avoid ion tracing overlapping. For example, the two fully ionized species N^{7+} and He^{2+} present at the end of the gas mixture simulation share the same charge-to-mass ratio $Z^*/A = 0.5$ and would therefore be difficult to distinguish.

Given the complexity and number of the laser-matter interaction processes the possibility of performing statistical measures in parametric schemes are fundamental for conducting thorough experimental studies. It is then of vital importance to work at high-repetition-rate (HRR) facilities where $\approx$100 shots can be available each day in order to acquire good statistics. Such HRR facilities must combine the high laser repetition rate with data flow and data acquisition software and hardware, as well as laser diagnostics and targetry designed to work at such HRRs.

Chapter 4

Chapter 4

Experimental methods, results and interpretation

4.1 Introduction

The present chapter summarizes the results issued from two experimental campaigns on ion acceleration from near-critical density gaseous targets. Section 4.2 details the experimental setup and diagnostics as well as the main results obtained during the VEGA-2 campaign performed in 2018 in the CLPU facility located in Spain. The VEGA-2 laser, which operates in the 200 TW power level, delivered a maximum intensity of $\approx 10^{20}$ W/cm^2 ($a_0 \approx 6.9$, being a_0 the normalized laser amplitude) and about 3 J on-target. This experiment was the first one conducted by our research group aiming at studying the potential for ion acceleration of relatively new dense gaseous targets. The follow-up experimental effort was performed in the VEGA-3 laser facility (CLPU, Spain) in 2021 and it is detailed in Section 4.3. In this experiment we interacted in the PW regime reaching a maximum intensity of $\approx 10^{20}$ W/cm^2 ($a_0 \approx 6.9$) and about 18 J on-target. I took the leading role in coordinating the design, realization and data analysis of this experiment. The VEGA-3 experiment objectives were (i) understanding the particle acceleration processes triggered by ultraintense femtosecond laser pulses in gases with a near-critical density and (ii) studying the potential for ion acceleration of a state-of-the-art gas jet coupled with shock nozzles in the PW/fs regime. An interesting ion acceleration mechanism that could be triggered in near-critical interactions such as this one is collisionless shock acceleration (CSA) [23, 25]. CSA could produce highly energetic ions with a relatively low energy dispersion [101]. As a complementary objective we wished to seek for experimental conditions where CSA can occur and if possible investigate the lesser-known physics of this ion acceleration scheme. Finally, Sections 4.2.2.3 and 4.2.2.4 draw conclusions and guidelines from both experiments that aim at improving the performance of future experiments.

4.2 VEGA-2 Experiment: 200 TW regime

The experiment presented in this section was carried out in 2018 before I started my Ph.D. thesis. Nevertheless, I was already strongly involved in all the experimental activities including the fielding of diagnostics and the data analysis. The experimental results and discussion are described in detail in the PhD dissertation of Dr. M. Ehret [109] and Dr. Carlos Salgado-López. A brief summary of the outcome of this experiment follows with the purpose of setting the experimental work frame and starting point for the VEGA-3 experiment, which is at the core of my thesis work.

4.2.1 Setup and experimental diagnostics

The experiment was conducted with a pulse energy of 3 ± 0.36 J on target, with pulses of approximately 35(5) fs FWHM duration delivered by the 200 TW VEGA 2 laser at CLPU [140]. This CPA Ti:Sa laser, with a central wavelength of 800 nm, was focused by an $f/4$ off-axis parabolic (OAP) gold coated mirror onto the gaseous target. The focal spot size was regularly measured at low energy by a high magnification imaging system, resulting in a reproducible FWHM of 7 µm from shot to shot. The maximum intensity in the FWHM focal spot was of $1.20 \times 10^{20} \pm 2 \times 10^{19}$ W cm^{-2} ($a_0 = 6.9 \pm 3.1$). The contrast to the ASE level was obtained with a third order autocorrelator system and on the timescale of hundred ps was equal to 5×10^{-12}. The experimental setup is plotted in Fig. 4.1.

The desired near-critical density target was produced with the commercially available SL-GT-10 high pressure gas system (HPGS) manufactured by SourceLab and equipped with supersonic shock nozzles [105]. Note that the HPGS parameters are: the compressor's backing pressure (P), the gas valve opening time (VOT) and the delay between the opening of the
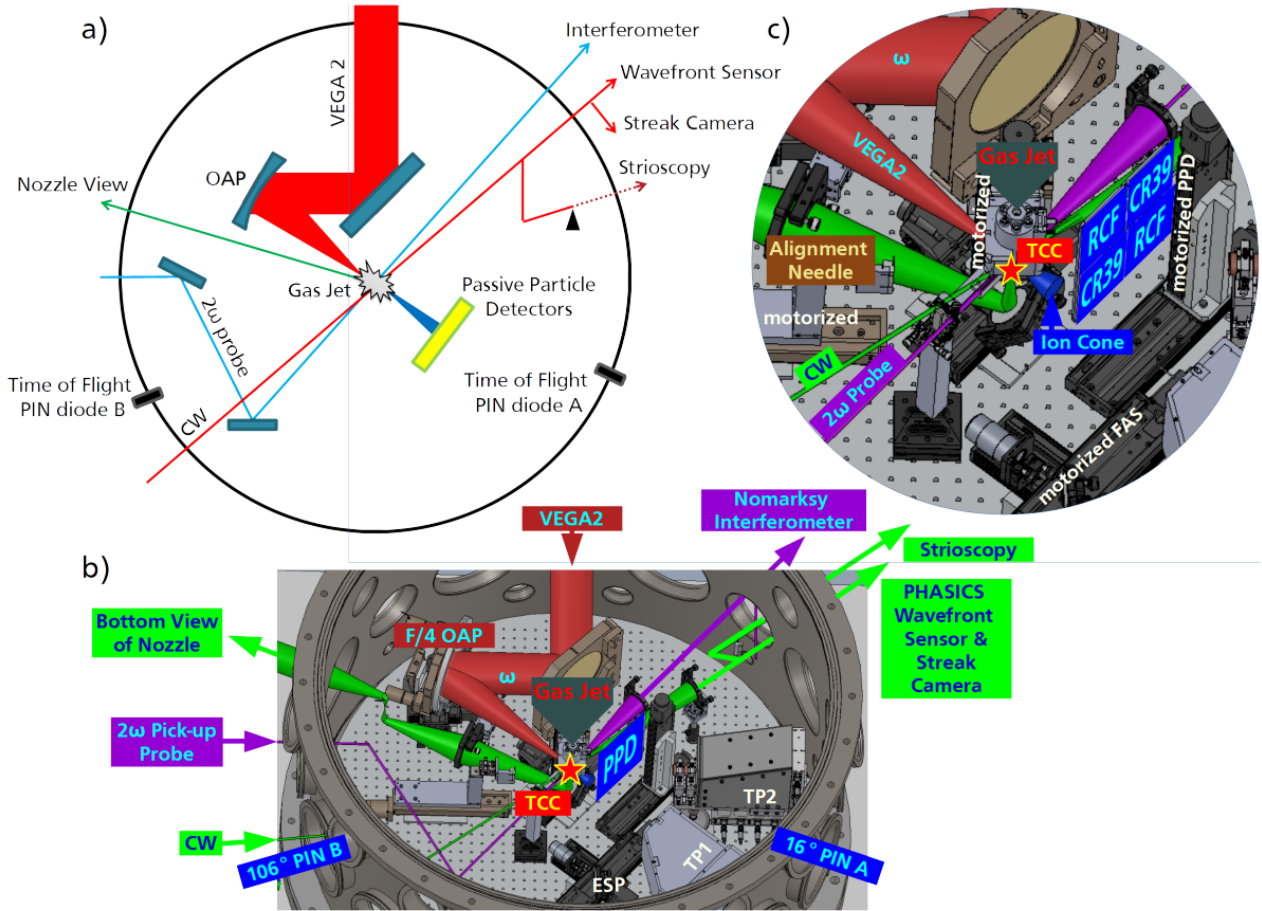
Fig. 4.1: (a) Sketch of experimental setup with axes of main diagnostics. (b) 3-D CAD and (c) zoom on the target chamber centre (TCC).

valve and the laser gas interaction (CD). See Chapter 2 for details on the HPGS system and its operation during ultra-high intensity (UHI) shots. P was set at its maximum value equal to 400 bar. The sub-mm shock nozzles are screwed to a ms-fast electrovalve called *rapid valve* also commercialized by SourceLab. We obtained density profiles of approximately $100\,\mu\text{m}$ FWHM with a peak electron density reaching the critical density of the Ti:Sa laser wavelength after ionization. The gas jet was fully characterized by interferometry using the commercially available SID-4 wavefront sensor from Phasics [141] before and during the experiment. By bottom-view imaging, the nozzle is visually inspected regarding surface damage and perfect cylindrical geometry (note that the nozzle is held up-side-down to facilitate the HPGS operation). The shot-to-shot characterization allows us to evaluate the nozzle's laser damage and its effect on the shot-to-shot variations of the gas jet profile. A three-axis motorization system for the valve holder and two perpendicular imaging systems allowed us to position the density peak at the interaction point, commonly called target chamber centre (TCC). The timing of laser and shocked density is monitored via a strioscopic imaging of the ROI performed using a continuous wave (CW) laser diode backlighter. Like this the VOT and CD parameters of the HPGS are selected targeting the maximum possible density at the shock height.

The gaseous targets were either pure He or mixtures of N_2 and He with a 9/1 ratio. Due to its fluid properties, addition of N_2 is beneficial for proper operation of the gas valve. The He doping yields ions with high charge-to-mass ratio in the bulk of the plasma, expected to be more susceptible to acceleration.

The main diagnostics are on-shot interferometry to determine the driven plasma density, the streaked imaging of plasma self-emission to identify hot plasma regions, and passive particle

detectors as well as time-of-flight (ToF) PiN photodiode detectors to measure ion beam spectra. Note that the Thomson Spectrometers (TP1 and TP2) visible in Fig. 4.1b were not performing during the campaign. The TPs were coupled with Lanex screens imaged with CCD cameras. Very low intensity X-ray spots were seen in the Lanex screens. The Lanex sensitivity was probably too low to detect the number of particles accelerated in the small solid angle of the TP ($\Omega \approx 10^{-6}$ sr).

A frequency-doubled ultra-short pick-up probe was extracted from the edge of the main laser pulse before focusing, and the synchronization with the main beam at TCC is done with the help of a delay line and a streak camera. The probe back-lights the plasma's changing profile perpendicularly to the pump laser axis, with a minimum delay of ≈ 1 ns relative to the pump pulse due to mechanical constraints in the delay line. The probe beam was used in a Nomarski interferometer scheme to acquire on-shot electron density charts.

A fast streak camera (Hamamatsu C7700), with a ps resolution, measured the plasma self-emission under an angle of 82° with respect to the main laser axis in the horizontal plane, protected from scattered laser light and other near-infrared (NIR) photons by using a BG38 filter. We used an opened slit and a sweep range of 2 ns, which allowed us to freeze 2-D images of the prompt self-emission.
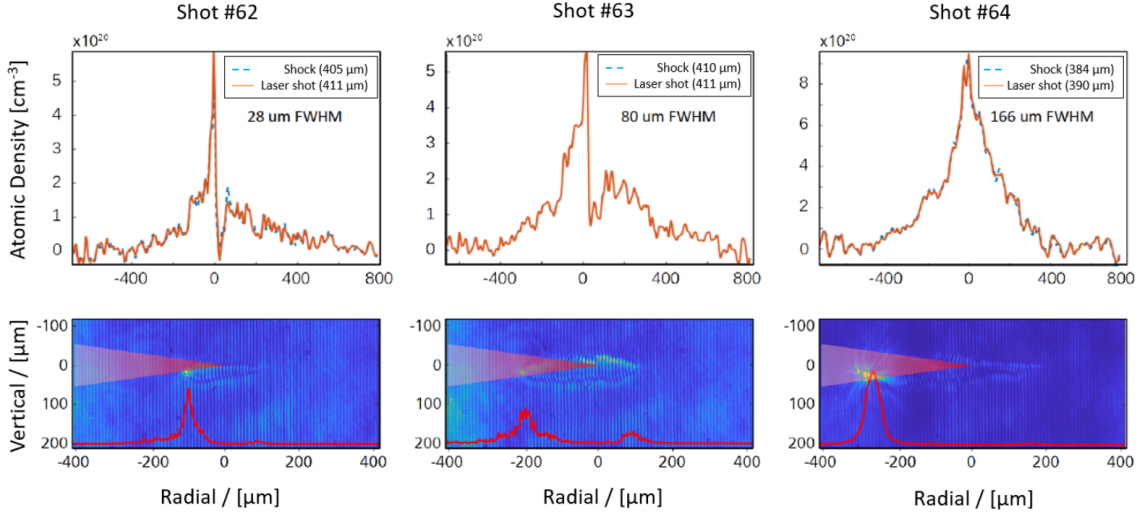
Fig. 4.2: For three consecutive shots varying the pure helium gas jet density profile: (top row) un-driven gas jet longitudinal (along the main laser axis) density profile with indication of the respective distance to the nozzle for the *shock* (dashed line) and the *shot* position (solid line). The solid line profiles correspond to the ones "seen" by the laser. The dashed profiles are taken at the maximum density height. Note that the *shock* and *shot* positions are almost the same, i.e. we targeted the highest density vertical point during shots. (bottom row) Interferometric image superposed to aligned laser beam focusing cone and plasma self-emission longitudinal lineout in arbitrary units (red line), 1 ns after the interaction starts. The laser travels from left to right and it is focused at $x = 0$, $y = 0$, the coordinates of the gas jet's maximum density point.

On-line energy spectra of the accelerated particles were acquired by two silicon (Si) PiN photodiode ToF detectors named PiN A and PiN B. Both photodiodes are located with a 19° vertical inclination at 67 cm from the interaction point. They are positioned at different horizontal angles: (A) 16° and (B) 106° with respect to the main laser propagation axis, see Fig. 4.1. The diode substrate is preceded by a Si layer of 750 nm and extra filtering by Mylar foils with 40 nm thick Al coating, in order to avoid diode saturation by the strong photopeak from the laser-target interaction. mylar foils are (A) 2 µm and (B) 4 µm thick. The temporal resolution

of the ToF diagnostic is 4.5 ns FWHM. 20 dB attenuation is applied to both channels to avoid saturation. The low bias voltage of -60 V is an advantage regarding electrical breakdown risks linked to pressurized gas entering the vacuum chamber.

Solid state passive particle detectors are used to capture the spatial and spectral properties of forward accelerated ion beams in single-shot operation, with stacks of RCF or slaps of CR-39. RCF undergo a color-changing radio-synthesis that allows to retrieve the dose-depth curve from stacked films and an absolute projectile number spectrum, if the projectile species is known. To identify the projectile species, we made use of CR-39 as solid state track detector in alternate shots. Two different types of Gafchromic RCF (Ashland) films were used, the commercially available EBT-3 (batch 10251701) and the especially manufactured U-EBT-3 (batch 06251801). Each RCF stack comprises 4 layers of U-EBT-3 and 2 layers of EBT-3 and is enveloped in a 10 µm-thick Al filter foil. CR-39 are enveloped in an opaque Al-coated 2 µm-thick mylar foil. The passive particle detector surfaces are aligned at 60 mm from TCC and are perpendicular to the laser axis. Active layers of U-EBT-3 face TCC. EBT-3 layers have a symmetric composition so the layer facing TCC is always a plastic protective layer followed by the active layer and a second plastic layer. Technical details on the passive detectors are given in Appendix A.

4.2.2 Summary of main results

Hereinafter, we detail the main experimental results of the VEGA-2 campaign divided in two groups: results obtained shooting on a pure He gas jet and results issued from shots on a gas mixture jet (90% N_2 and 10% He). For each shot group we present: neutral density lineouts corresponding to the density profile seen by the laser compared with on-shot raw interferograms on which we have superposed plasma self-emission lineouts. Each set of results also includes dose deposition maps obtained from the RCF stacks placed at 60 mm from to TCC. Furthermore, in the gas mixture case, the nature of the accelerated species was investigated using a CR-39 particle tracker.

4.2.2.1 Shots on pure helium

Fig. 4.2 plots the neutral gas transverse density profiles (upper row) for shots #62, #63 and #64 using a pure He gas jet. The *shot* profiles (solid line) correspond to the ones "seen" by the laser. The *shock* profiles (dashed lines) are taken at the maximum density height. Note that the *shock* and *shot* positions are almost the same since we targeted the vertical point highest density. The small discrepancy is due to the resolution of the SID-4 density module used to select the shock height during shots (refer to Chapter 2 for details). The vertical distance from the laser interaction point to the nozzle's surface was about 400 µm in this set of shots. In the lower
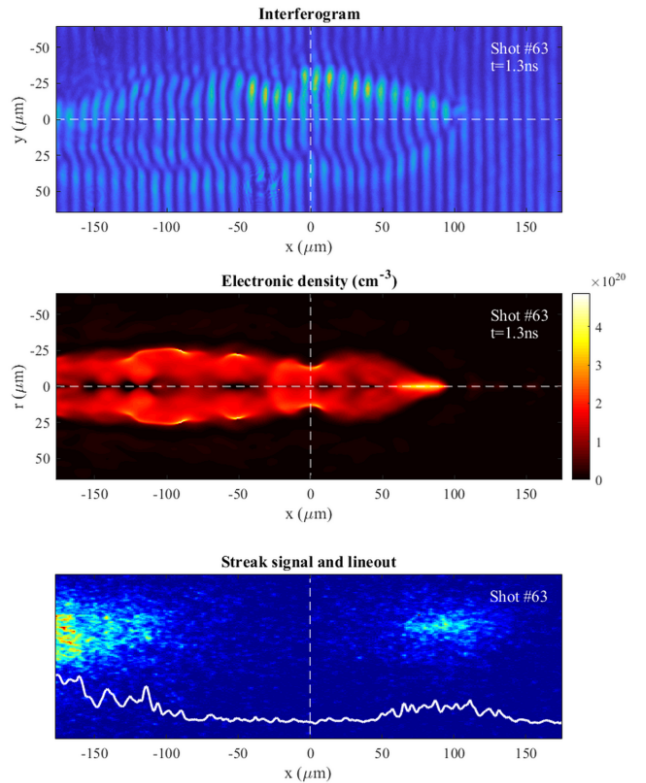
Fig. 4.3: (a) Raw on-shot interferogram, (b) the deconvolved electronic density chart and (c) the acquired on-shot optical self emission corresponding to shot #63. The plasma self-emission signal appears frozen which means that its duration is much shorter than the resolution of the sweep with a 2 ns streak window.

row the on-shot raw interferogram is plotted together with an optical self-emission lineout (red curve). Assuming complete ionization the interaction of shots #62, #63 and #64 took place at a maximum electron density of 0.56 $n_c \leq n_e \leq 0.92$ n_c, where $n_c = 1.73 \times 10^{21}$ cm^{-3} is the critical density for a 0.8 µm laser.

Fig. 4.3 shows the raw interferogram (upper row), the deconvolved electronic density chart (middle row) and the acquired on-shot optical self emission (bottom row) corresponding to shot #63. The plasma self-emission signal appears frozen which means that its duration is much shorter than the resolution of the streak camera's sweep with a 2 ns streak window. Two independent high intensity regions are seen before and after the gas density peak (marked by a vertical dashed line). Intense self-emission arises from strong coupling between the laser and the gaseous target and could be linked to the laser self-focusing during its propagation through the gas [142]. Note that the critical power enabling laser self-focusing $P_c \approx 17 n_c/n_e \approx 170$ GW [43] is largely exceeded here. As can be seen a single ionization region appears at $t \approx 1$ ns crossing the gas density peak located at $x = 0$. The $n_e = 0$ regions are an artifact of the routine used to analyze the data. The fact that no interferograms could be taken at earlier or later times difficults its interpretation. The laser effective ponderomotive force $f_{p,eff.} \propto a_0$ will increase due to the relativistic self-focusing of the laser pulse. If $f_{p,eff.}$ was intense enough as to expel electrons from its path and create a laser ponderomotive channel, we could be looking at the hydrodynamic evolution of such perturbation 1 ns after the beginning of the interaction. Previous experiments [143,144] have observed such ponderomotive channels during the interaction of an UHI ps laser pulse with a pre-expanded solid target. The temporal evolution of the channel radius $R_B(t)$ has been associated to a cylindrical Sedov-Taylor blast wave expansion characterized by $R_B(t) \propto t^{1/2}$ [145]. The transverse expansion of the channel will stop when the pressure behind the radial wave front becomes comparable to the pressure ahead of it [146]. Afterwards, the hydrodynamic evolution of the system would lead to the filling-up of the density depleted region.

RCF results

During these three shots we used RCF stacks located at 60 mm from TCC as particle detectors. Fig. 4.4 shows the obtained dose deposition maps. As can be appreciated a single particle beam is produced with an aperture angle of 9° FWHM and a slight shift from the laser axis for shots #62 and #63. This particle beam does not vanish when traveling throughout the stack and no other particle populations appear except for shot #64 where two small bright spots are seen in the last layer. Analyzing this Gaussian imprint as an α particle beam trace one obtains a maximum energy of 42 MeV yet, as discussed further, it is unlikely that it is an ion trace.

Details on the dose calibration of the RCF layers are given in Appendix A.

ToF results

Two ToF PiN diode detectors were located in the forward (PiN A, 16°) and transverse directions (PiN B, 106°) at 670 mm from TCC. A mylar filter of 2 µm thickness was placed in front of the forward detector while a 4 µm mylar filter was placed in front of the transverse detector. These filters allowed to discard electrons from being the origin of the signal since the times of arrival seen in the oscilloscope data would correspond to low energy electrons that would be stopped in the mylar layer. The distance between TCC and the detectors was not enough as to have the ion peak separate from the photopeak. The photopeak was studied during some shots believed to be particle-free (due to a poor interaction) and an exponential decay with a temporal constant $\tau \approx 21 \pm 6$ ns (that lasts up to 60 ns) was found. This exponential decay temporally overlaps with an α particles' signal of energy higher than 9 MeV, as see in Fig. 4.5, which makes it difficult to conclude on the maximum ion energies that were measured.

Note that the detector's response function is an exponentially modified Gaussian with an
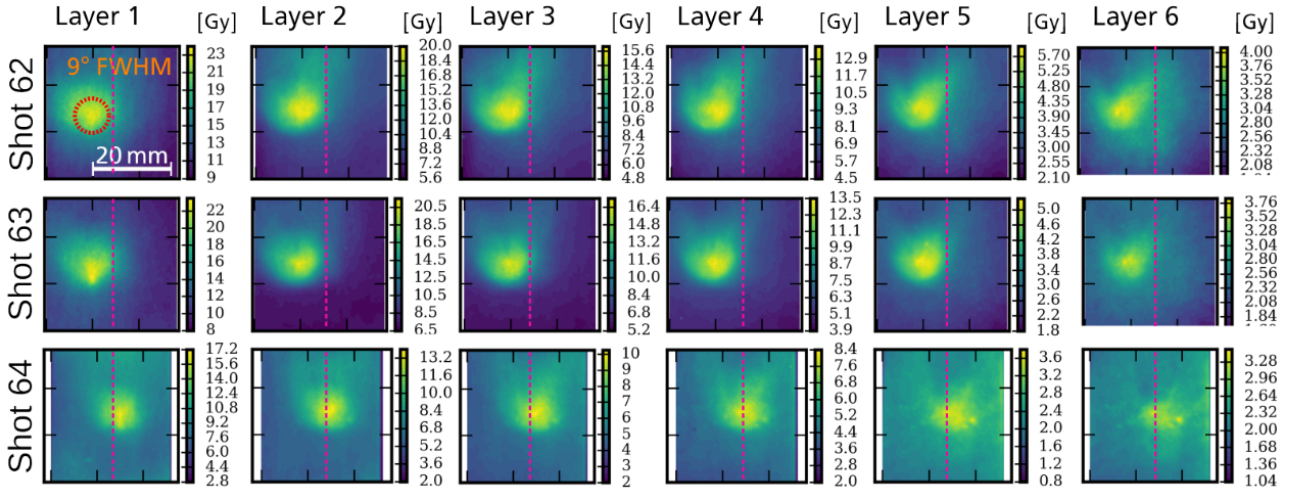
Fig. 4.4: Upper row: RCF imprints converted to dose deposition for the six stack layers corresponding to shot #62, middle row: shot #63 and lower row: shot #64. Layers are numbered in ascending order in direction of particle propagation. The typical FWHM divergence angle of the beam imprint is 9°. The presumed pre-aligned laser axis corresponds to the center of the illustrated frames. In shot #64 the particle beam appears shifted from the supposed laser axis. The approximate position of the laser axis is indicated with vertical dashed lines.
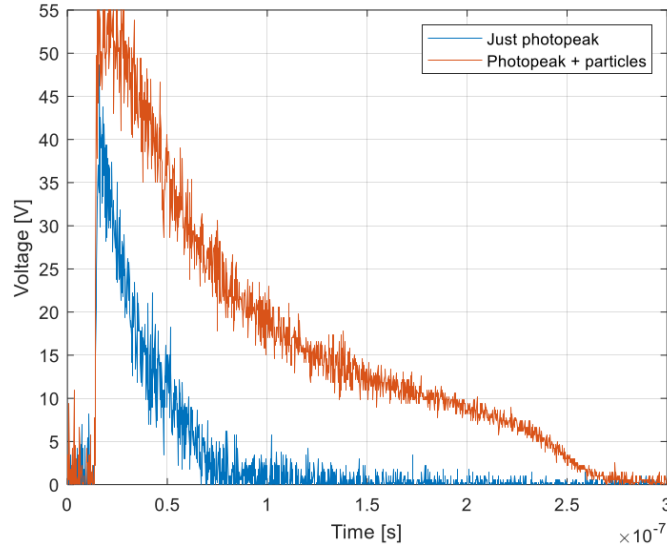
Fig. 4.5: Example of ToF data acquired in a shot believed to be particle-free (blue line) and a normal shot where the photopeak and the ion signal are not separated (orange line).

exponential temporal decay constant $\tau \approx 3\,\text{ns}$ [70]. Hence, the photopeak is not a perfect impulse response since it decays at a slower rate. This means that what was considered a pure photopeak response probably contains as well a low number of high energetic ions, apart from what we already knew: photons and relativistic electrons. Subtracting it from the raw oscilloscope signal may be then a too rough procedure that cannot be use to analyze this data set. Note that this analysis procedure has been successfully used to analyze PiN diode data in other experiment, where the obtained proton spectra were validated with deconvolved spectra from RCF analysis [140].

4.2.2.2   Shots on gas mixture

Fig. 4.6 shows the neutral transverse gas profiles obtained for six different shots performed using a gas mixture of 90% N_2 and 10% He.
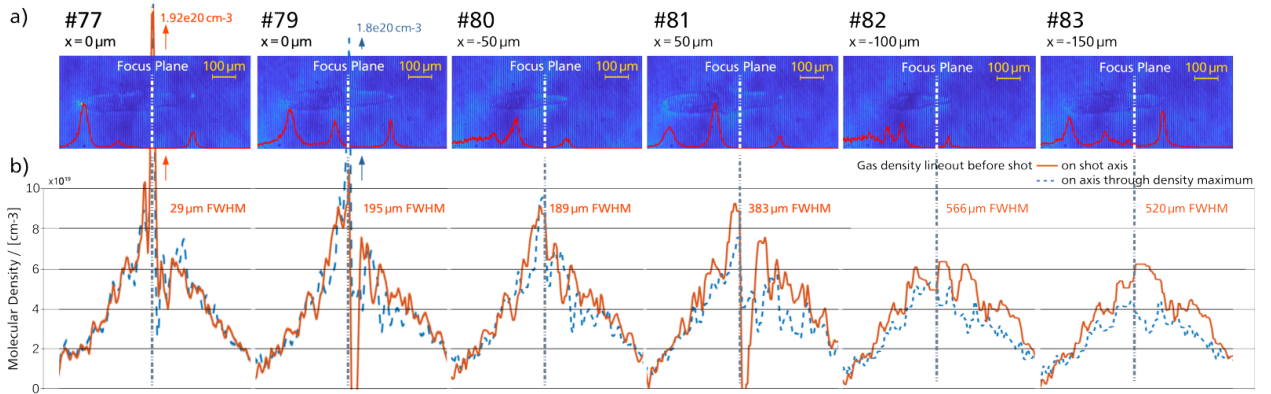
Fig. 4.6:   (a) Interferometric images overlaid by self-emission line-outs in arbitrary units (red line), captured 1 ns after the interaction starts, for shots with variation of the longitudinal position of the laser-gas interaction. (b) Longitudinal un-driven gas density profiles acquired prior to the corresponding high intensity shots show changes from shot-to-shot, indicating progressive damages to the nozzle.

The gas nozzle was changed with respect to the pure helium shots. During these shots the laser transverse plane was displaced from the gas density peak by moving the gas valve in the laser transverse direction. The visible changes of the neutral density profile are due to the successive damage of the nozzle on a shot-to-shot basis and the fact that the profiles are measured at different off-axis transverse distances.

Assuming complete ionization, the maximum electron density was $0.09\,n_c \leq n_e \leq 2\,n_c$ in this shot set. In this case the vertical distance from the laser interaction point to the nozzle's surface was about $570\,\mu m$. The gas nozzle profiles were too damaged as to make conclusions on the effect of translating the laser focal plane. Looking at the raw interferograms a single ionization region is seen traversing the gas density peak, similar to what was seen using pure helium.

RCF results

RCF dose deposition data was acquired for a set of three shots performed afterwards: shot #79, #85 and #87 with a respective transverse nozzle displacement of 0, $-50\,\mu m$ and $50\,\mu m$ (in y-direction), see Fig. 4.7.

Three features are repetitive and clearly pronounced on the RCFs in all shots.

- First and most prominently, a peak-like spot with $3°$ FWHM half-opening angle is located 5 mm right of the laser axis and about 1 mm underneath. The beam is elliptical and the major axis of the ellipse is perpendicular to the laser polarization direction. The feature faints steeply from first to second layer and is barely visible in the third layer. The 4th layer does not allow to distinguish the feature. A longer plasma channel and a higher first self-emission peak coincide with lower doses in the peak feature.

- Second, a wider Gaussian peak with FWHM half-opening angle of $11°$ is visible throughout the RCF stack, with its central position superposing the laser axis. The Gaussian feature has a similar divergence as observed in the pure helium case ($9°$). Also, a dip in its center can be found in proximity of the laser axis for the last two layers, highlighted on the last layer of shot #87 with a white arrow.
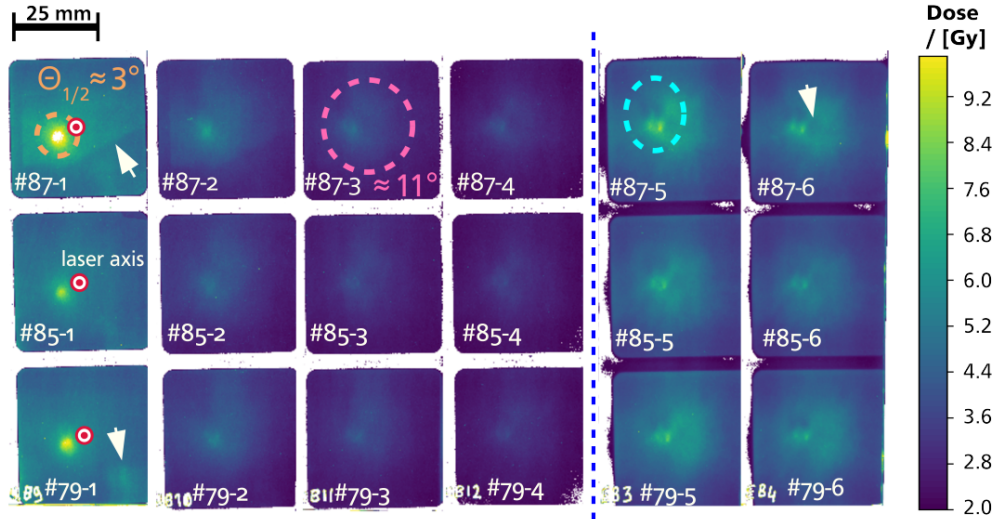
Fig. 4.7: Overview on RCF 2-D dose maps for shots #79, #85 and #87 with a respective transverse nozzle displacement of 0, $-50\,\mu m$ and $50\,\mu m$. For display purposes, the data is averaged over the three color channels. RCF layers are numbered in ascending order in direction of particle propagation. The laser axis is indicated with a white dotted mark, its size represents the alignment uncertainty with respect to the laser axis at air pressure. The EBT-3 films used for both last layers were likely exposed to conditions prior to the experiment that changed their response to dose deposition with respect to the calibrated response.

- Third, four lobes appear on the last layers, highlighted with a cyan circle, two maxima and two minima. Both maxima are horizontally aligned along the laser polarization axis.

CR-39 analysis

In order to resolve the ambiguity regarding the nature of the accelerated species we used a CR-39 particle tracker layer which was located as well at $60\,mm$ from TCC. Ions with doses of several Gy are expected to damage the material in a very specific way, creating bubbles called *pits*. On the contrary, if the beam consists of electrons or photons, such doses are not expected to yield visible damages. The damaged areas are exposed by etching the material in an NaOH solution. We performed etching at $70\,°C$ in a 6.25 N NaOH solution, which was found to yield satisfactory results for this detector type. A huge effort was made by Dr. Michael Ehret in order to analyze a 2 x 2 cm of exposed CR-39 by acquiring and analyzing more than a million images with a motorized electronic microscope. Note that a multi-species gas jet strongly complicates the analysis of this data set.

The chemical etching post-processing unraveled clear etched pits after 15 hours of etching, which indicates the acceleration of ions in the laser forward direction at $\pm 5°$ with respect to the presumed laser axis. The presence of a wide range of crater sizes translates into a broad spectrum of the impacting ion beam.

A first analysis was based on the pit diameter evolution with etching time. We studied the evolution of individual pits at 2, 3, 9 and 15 hours of etching time. Overall, the diameter evolution suggests the presence of multi MeV α particles in a range of 4 to 40 MeV. Particularly α particles of 5.4 MeV were detected. At the same time, N^{7+} from 1.2 MeV to 2 MeV are the only possible cause for a certain group of pits.

A second analysis strategy focused on a scan of the depth of the pits formed in an area containing a wide selection of pit diameters. Note that paired values of diameters and depths measured at a determined etching time can be related to a certain ionic species with a given

energy. The depth-diameter measurements are compared with interpolations of calibration data obtained with the CR-39 plug-in of PySTarT [109]. Fig. 4.8 shows the retrieved depth-diameter measured points in black and calibration curves in false colors linked to the particle energy for α particles (left panel) and N^{7+} ions (right panel).
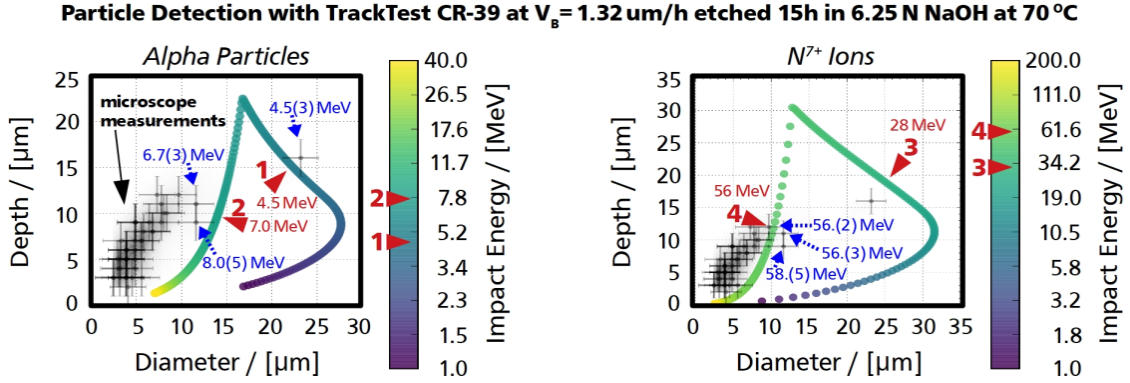
Fig. 4.8: Retrieved depth-diameter measured points in black and calibration curves in false colors linked to the particle energy for α particles (left figure) and N^{7+} ions (right figure).

Taking into account the energy loss in the $2\,\mu m$ mylar filter covering the CR-39 layer, we detected two features representative low energy α particles with energies of $6.7\,MeV$ and $4.5\,MeV$. Nitrogen ions with energies from $3\,MeV$ to $4.5\,MeV$ are also likely to have been measured. Higher energy ions of both kind can not be discarded based on the CR-39 analysis.

4.2.2.3 Conclusions

The interferograms acquired using a He and a gas mixture jet show a single ionization region as well as two successive self-emission peaks located before and after the gas density peak. The maximum electron density n_e obtained in pure He (gas mixture) was $0.9\,n_c$ ($2\,n_c$), supposing complete ionization. The shots were performed at $400\,\mu m$ (pure helium) and $570\,\mu m$ (gas mixture) heights from the nozzle's surface using two different nozzles of identical industrial design (one for the shots on pure helium and one for the shots on gas mixture). Strong laser damage to the nozzle's surface was evidenced in the degradation of the gas density profiles from shot-to-shot as well as in the bottom view nozzle images taken during the shots.

The spatially resolved dose deposition maps obtained by analyzing the RCFs showed an intense single particle beam that stands out over a Gaussian background. This occurred for both pure He and gas mixture shots. The central beam and background appear shifted from the supposed laser axis in some shots. Finally, two bright spots appear in the last layers of the stacks. These spots are horizontally aligned along the laser polarization direction.

CR-39 analysis gave evidence of α projectiles with impact energies that can reach the last layers of the RCF stack, whereas there is no indication for high energy nitrogen acceleration. The Gaussian background registered on the RCF layers might be related to the uniformly distributed ion traces found on CR-39. In parallel, there is no evidence that the spot-like beam or high-dose features seen in the RCF stacks are ion beams. The features visible on the RCF layers have no direct representation on the CR-39 etched pits.

Wakefield electron acceleration may be behind the small-angle peak seen on the first RCF layers. The acceleration of relativistic electrons in the laser-channel can produce *forked* angular distributions of the electron beam [66, 147]. At the same time, the lower dose deposition on-axis could be explained by the deviation of the electrons exiting the plasma by ultra-strong quasistatic B-fields induced by the return current dynamics at the gas target edge.

ToF analysis can only conclude that ion acceleration took place in both the forward and lateral directions, which could be linked to Coulomb explosion as a possible ion acceleration mechanism. It can not be excluded that TNSA triggered at the steep density gradients can also accelerate ions or that electrostatic shock waves descending through the target down-ramp do so as well.

4.2.2.4 Perspectives

In future experiments, it could be worth trying to reduce the maximum electron density of the gaseous target as well as increasing the laser intensity to favor laser channeling. At the same time, one would need to acquire interferometric images at earlier times $t \approx 1\,\mathrm{ps}$ [143] to characterize the channel radial expansion. Note that later probing times $t \approx 4\,\mathrm{ns}$ could also be interesting looking at fitting the late time evolution of the transverse position to a Sedov-Taylor blast wave expansion [144].

The spatial shift from dose peaks in respect to the laser axis seen in the RCF signals could be linked to a tilt of the accelerated particle beam exiting the plasma or to a laser axis error which would direct the accelerated particles along the laser path in a deviated axis. In order to relate such shift to the physics happening inside the plasma one needs to control the laser axis. This procedure is not common. Most of the experiments are performed by aligning the laser focal spot at low energy at a given spatial coordinate. One needs to verify as well that the laser, at least at low energy, follows a given axis.

The identification of the accelerated species using CR-39 needs to be reinforced by locating Thomson parabolas (TPs) as particle detectors or by fielding calibrated ToF detectors with high temporal resolution such as diamond detectors. The fielded TPs must be equipped with high-repetition-rate compatible data acquisition systems, yet of higher sensitivity than the Lanex screens.

The information on the accelerated electron spectra is missing. The latter is fundamental in order to assess the transfer of laser energy to the gaseous target as well as to give a hint on the possible ion acceleration mechanisms at play. Note that a near-critical interaction should yield very high electron temperatures [30].

The horizontal hot spots seen on the RCF could be linked to strong quasistatic magnetic fields generated at the plasma-vacuum border. One would need to measure such fields in future experiments to asses their effect on ion and electron trajectories. They could also be linked to the acceleration of relativistic electrons in the laser-channel through direct laser acceleration (DLA) [148]. To assess the DLA contribution, angular-resolved high energy ($> 50\,\mathrm{MeV}$) electron spectra should be acquired [149].

Extreme nozzle damage was observed after interacting at about $400\,\mu\mathrm{m}$ (in pure He shots) and $570\,\mu\mathrm{m}$ (in gas mixture shots) heights from the nozzle's surface. One should consider developing new nozzles that produce the density peak at larger vertical distances to reduce the nozzle's damage and obtain good quality density profiles for several shots in a row.

The operation of the HPGS in a vacuum chamber was very problematic. We experienced gas leakages coming from failures on the gas valve. These leakages were caused by the strong electromagnetic pulse (EMP) [125] triggered during the laser-gas interaction when opening the gas valve for long times ($\approx 5\,\mathrm{ms}$). As a result the turbomolecular pumps connected to the chamber were strongly disturbed. At the same time, the pressure gauges located at the laser compressor (which is at least $15\,\mathrm{m}$ away from the interaction chamber) detected almost atmospheric pressures during shots. The compressor's gratings are very sensitive and should be kept under high-vacuum at all times. It was seen that an uncontrolled operation of the HPGS could strongly damage the laser system.

High-repetition rate operation was inhibited due to: (i) nozzle damage from shot to shot,

(ii) gas leakages occurring due to the EMP effect on the gas valve and (iii) the fact that the vacuum chamber and pipes leading to the laser compressor were not prepared to deal with high pressure gases entering into the system. Each of these three points should constitute guidelines for future technical developments oriented at maximizing the number of shots per day.

4.3   VEGA-3 Experiment: PW regime

The experiment described in this section was conducted in July 2021. It was conceived as the follow-up of the VEGA-2 experiment (TW regime, $a_0 = 2.5$) in which we aimed at interacting at higher laser intensities using the VEGA-3 laser (PW regime, $a_0 = 6.9$).

For the VEGA-3 experiment we set two clear guidelines for this follow-up experimental effort: (i) the interaction at higher laser intensities aiming not only at ionizing the gas but also at triggering laser-channeling through the density profile and (ii) the production of lower electron density n_e gas targets that allow the laser pulse to penetrate through them.

The production of gas profiles with a lower electron density was achieved by performing a large characterization campaign of the HPGS and studying the neutral density profiles that could be obtained by expanding its input parameters. Note that the HPGS parameters are the compressor backing pressure (P), the gas valve opening time (VOT) and the temporal delay between the opening of the valve and the laser-gas interaction (CD). Note further that up to now the HPGS had only been used setting P equal to its maximum value (400 bar) and the VOT and CD parameters were selected to maximize the peak density of the gas profile. The operation and characterization campaigns of the HPGS are described in detail in Chapter 2, including its operation in UHI interaction conditions.

As concluded in Chapter 3, the near-critical interaction that we aim at studying depends on a high number of variables that regard both the gas targetry and the laser pulse. Consequently, the experiment was designed as a parametric study where three variables were selected for analysis: the gas type, the gas profile and the laser pulse duration.

- The selected gases were pure He, pure N_2 and a 90% N_2 and 10% He gas mixture, as in the VEGA-2 experiment. Note that gas mixtures offer the possibility of recognizing shock acceleration signatures by looking at the velocity spectra of the accelerated particles. At the same time, mass-dependent shock reflection [65] privileges the use of hydrogen. However, neither the facility (at that moment) nor the HPGS were compatible with the use of this gas.

- The gas density profile (GDP) depends on the gas type, the nozzle and the input HPGS parameters. We used two shock nozzle types: the S900 developed inside our collaboration group and the J2021 manufactured by SourceLab. Note that since the measured GDPs differed from the ones issued from fluid dynamics simulations we defined an optimal GDP as one that combines a low maximum atomic density of about 10^{20} cm^{-3} (value issued from the parametric numerical study detailed in Chapter 3) with peaked shapes that account for natural density gradients (refer to Chapter 2 for more details).

- We intended to vary the laser pulse duration between $\tau_L \approx 30$ fs and $\tau_L \approx 100$ fs to assess its effect on ion acceleration. However, we noticed that τ_L increased through the day probably due to temperature and humidity changes in the laser bay. Fig. 4.9 corresponds to several τ_L measurements obtained during the last week of shots. Prioritizing the beamtime over the strict control of the laser pulse length (since correcting it takes about 30 min each time) we decided to let this parameter vary naturally and have short pulse shots in the morning ($\tau_L \approx 50$ fs FWHM) and long pulse ones in the afternoon ($\tau_L \approx 100$ fs FWHM).
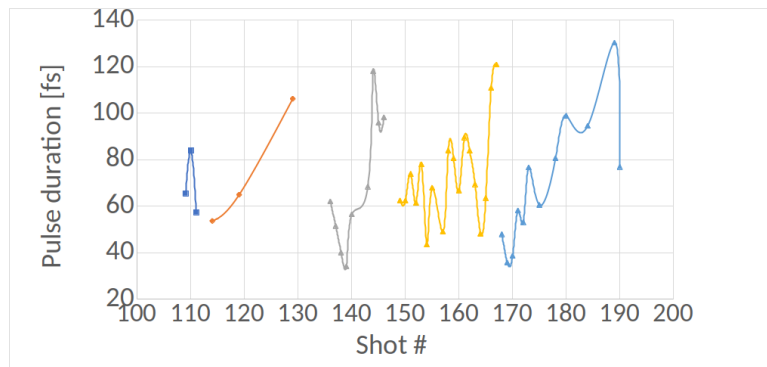
Fig. 4.9: VEGA-3 pulse duration measurements obtained during the last week of shots. Each color corresponds to one day of operation.

The principal *experimental figures of merit* that we aim to obtain are:

- The identification of the accelerated particle species and the possible acceleration mechanisms. In order to do so we deployed two types of ion detectors: Thomson parabolas (located at 0° and 110° from the laser axis) and ToF diamond detectors which were absolutely calibrated for α particles and nitrogen ions. At the same time, we monitored the laser axis to unambiguously link spatial shifts in the dose deposition signals to the particle accelerating physics and not to a laser pointing error.

- The absolute characterization of the electron spectra obtained at diverse angles. The latter should give an insight in the strong electron heating of the target expected from the near-critical laser-gas interaction. Five fully calibrated electron spectrometers were fielded in the interaction chamber.

- As was concluded in the VEGA-2 experiment the magnetic fields (B-fields) present at the plasma-vacuum border could affect the trajectories of the exiting particles. Furthermore, we know that shock structures can be accompanied by azimuthal magnetic fields that move with the expanding plasma [30]. We intended to characterize such B-fields while optimizing the space inside the vacuum chamber by fielding a complex interferometry (CI) diagnostic. CI allows for electron density and B-field retrieval from the same data set. However, the energy of the probe beam was not enough to realize CI and it had to be converted into a Nomarski interferometer line that could only asses the electron density.

Finally, as was previously mentioned the repetition-rate of the VEGA-2 experiment was strongly diminished due to: nozzle damage from shot to shot, gas leakages occurring due to the EMP effect on the gas valve and a vacuum system that was not prepared to deal with high pressure gases entering into the chamber and pipes. A huge effort was done by the facility to prepare for HPGS operation. Specifically they developed an automated system to detect gas leakages in the chamber and to protect the vacuum pipes connecting with the laser compressor from the gas injected into the interaction chamber [150].

In parallel, our collaboration team developed the S900 shock nozzle that produces the high density shock region at about $700\,\mu\text{m}$ from the nozzle's surface, about $200\,\mu\text{m}$ further than the nozzles used during the VEGA-2 experiment. We also acquired a newly developed leakege-free gas valve sold by SourceLab called the *microvalve* which is more resistant to EMPs thanks to its normally-closed operating system. The valve used in the VEGA-2 experiment, called the *rapid valve*, was normally-open so the EMP perturbations opened the valve in an uncontrolled manner leading to gas leakages. Refer to Chapter 2 for more details.

4.3.1 The VEGA-3 laser

The VEGA-3 laser is a Ti: Sapphire laser with a $\lambda_L = 800\,\text{nm}$, capable of delivering a maximum energy on-target $E_{TCC} \approx 18.5\,\text{J}$, a pulse duration $\tau_L \approx 30\,\text{fs}$ at best compression and p-polarized. During the experiment we fielded the HPGS in the VEGA-3 laser target area (TA). A 2-D CAD image of the TA layout can be seen in Fig. 4.10a. The laser is focused using an $f/12$ off-axis parabola (OAP). The interaction chamber (IC) has a rectangular form with dimensions 1.1 x 1.4 x 0.8 m^3 (width x large x height). A 3-D CAD render of the IC can be seen in Fig. 4.10b. Here the VEGA-3 main laser (also called the *pump* beam) enters through a lateral port after being focused. The *probe* beam, which will be presented in detail in Section 4.3.2, enters the chamber perpendicularly to the *pump* beam and intersects it at TCC (see blue beam in Fig. 4.10b).
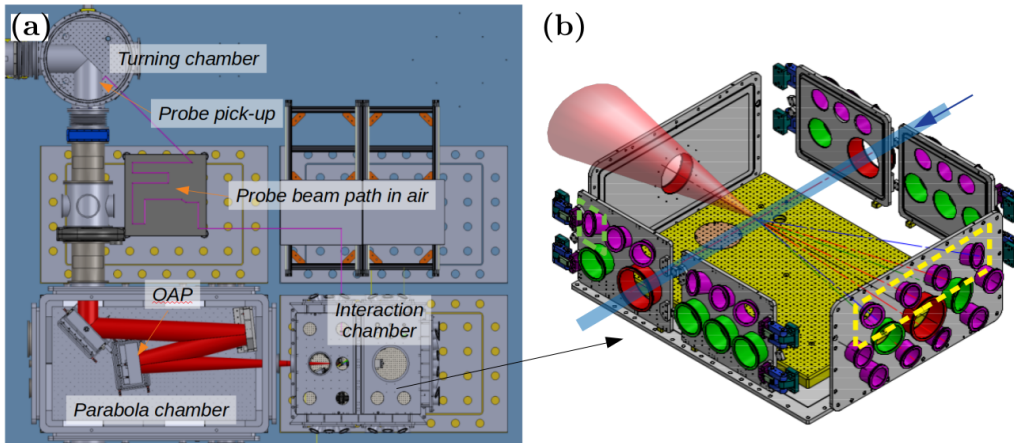
Fig. 4.10: (a) VEGA-3 target area (TA) layout. The main beam enters the interaction chamber (IC) as it is focused using an $f/12$ off-axis parabola (OAP). (b) 3-D CAD render of the VEGA-3 IC. The focused main VEGA-3 pulse is drawn in red and the probe beam in blue. The IC has 1.1 x 1.4 x 0.8 m^3 (width x large x height) dimensions. Images printed with permission of the CLPU.

Focal spot characterization

The optical system implemented to monitor the VEGA-3 focal spot (FS) was composed of two two-lens imaging systems (IS) with magnifications $\gamma = 20$ and $\gamma = 10$ to observe both the laser FS ($D_L \approx 15\,\mu\text{m}$) and the millimetric gas nozzle (for alignment purposes), respectively, see Appendix A for more details. Fig. 4.11a shows a FS image and Figs. 4.11b-e summarize the FS analysis which includes the mean horizontal and vertical profiles as well as encircled energy and radial intensity curves. The mean FWHM FS diameter was reproducibly measured: $D_L \approx 14.1 \pm 1.2\,\mu\text{m}$, yielding a maximum intensity of $8.7 \times 10^{19} \pm 2.1 \times 10^{19}\,\text{W/cm}^2$ ($a_0 = 6.3 \pm 3.1$).

Pulse length characterization

Fig. 4.12 corresponds to the optical system used to measure the high-intensity pulse duration. The latter was monitored on a shot-to-shot basis using the ASF-15M second order autocorrelator [151], refer to Appendix A for more details. A 6% main pulse reflection coming from the parabola shielding (located after the OAP) was conducted through a dedicated optical line drawn in green. All the optics in the line worked in reflection except for the chamber window (light blue rectangle). The stretching of the pulse due to crossing the cited window was taken into account in the final pulse length calculation (see Fig. 4.9).

Laser energy
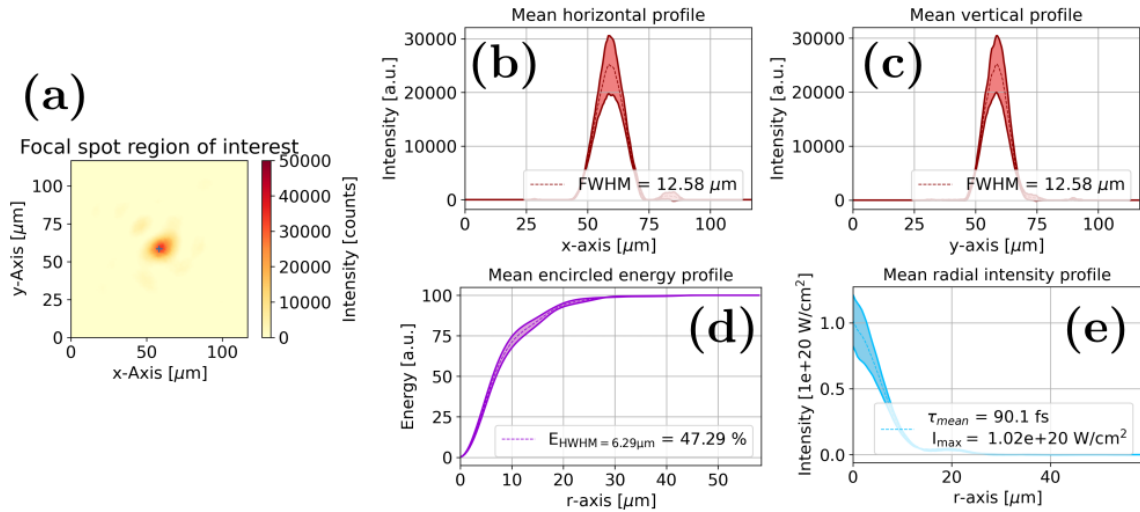
Fig. 4.11: (a) Focal spot (FS) region of interest acquired during the last week of shots. (b) Horizontal FS profile fitted to a Gaussian function to obtain the FS diameter at the FWHM, (c) same analysis as (b) taking as input the vertical profile, (d) encircled energy $\mathcal{E}(r)$ and (e) radial intensity profile $\mathcal{I}(r)$.
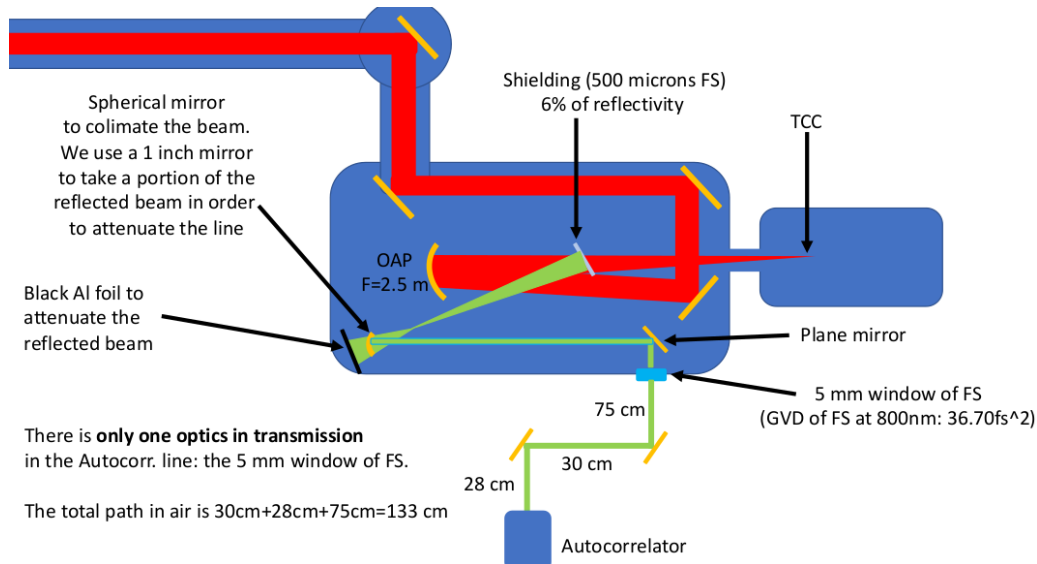
Fig. 4.12: Optical line employed to measure the VEGA-3 main pulse duration on a shot-to-shot basis. A 6% reflection from the parabola shielding (located after the off-axis parabola) was conducted through a dedicated optical line (in green). 2-D setup sketch made by Dr. Carlos Salgado-López from CLPU.

The laser energy is measured by the CLPU laser division in a shot-to-shot basis by analyzing a near-field laser image captured at the main amplifier's output. This measurement is performed for several energy levels to obtain a reliable intensity to energy calibration. The CLPU laser division has observed that the spectral variations of the beam, of the order of $\pm 5\,\text{nm}$ in an spectral bandwidth of $114\,\text{nm}$, have an effect of less than 0.05% on the energy measurement. The energy on target is calculated by multiplying the measurement by an energy loss factor $\eta = 0.72$ obtained as the coefficient of the measured energy at the main amplifier's exit and at TCC. The error in the energy measurement is lower than 1% because the energy noise level (close to 1% of the maximum energy) can be correctly distinguished. Fig. 4.13 corresponds to measurements of the on-target energy during the last week of shots. As can be seen the energy oscillates between 18 and $19.3\,\text{J}$.
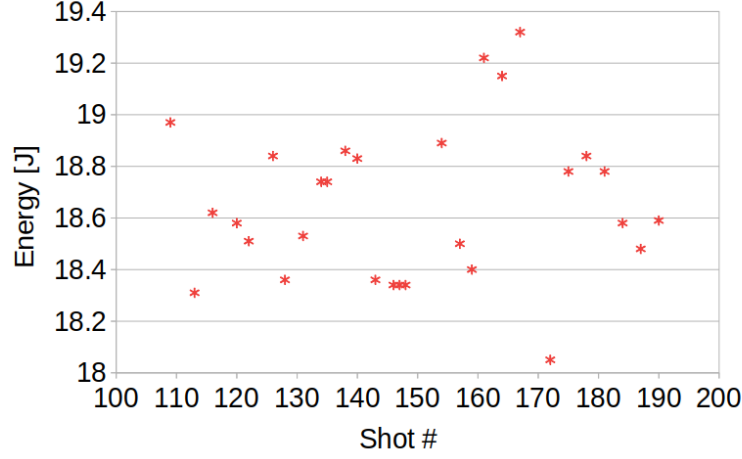
Fig. 4.13: VEGA-3 laser energy on-target measured during the last week of shots.

Laser contrast

The laser contrast was measured before the beginning of the campaign using the Sequoia commercial 3ω autocorrelator (refer to Appendix A for more details). The measurement was performed at maximum energy (23.8 J after the laser compressor), enabling the full amplification of the optical line including the twin amplifiers and locating the compressor gratings' motor at the 0 step position (which corresponds to maximum pulse compression). A laser contrast measurement is plotted in Fig. 4.14a from -460 ps to 190 ps. Here $t = 0$ corresponds to the arrival of the maximum intensity peak. The laser contrast is 10^{12} at $t = -100$ ps and 5×10^8 at $t = -5$ ps, in general recognized as a good quality contrast. Fig. 4.14b, c and d are zooms of Fig. 4.14a.

Fig. 4.14d focuses on the high-intensity peak which is clearly disturbed by peaked oscillations. Note that the Sequoia's temporal step is about 20 fs so the measurement of the ≈ 30 fs main laser pulse is not possible. The device is designed to characterize the laser contrast at tens or hundreds of ps before the main pulse arrival.

Several pre and post pulses are seen in Fig. 4.14a. Due to the nature of the third order autocorrelator, postpulses, i.e. those pulses coming after $(t > 0)$ the main intensity peak, account for a symmetrical replica for $t < 0$ while prepulses do not. The different known pairs of postpulses are marked in Figs. 4.14a-c with the numbers. The laser division of CLPU identified the origin of the pre and postpulses of Figs. 4.14a-c: (1) -454 ps since the Sequoia range is not able to measure up to 454 ps it could be either a pre or post pulse, (2) ±167 ps postpulse regenerative amplifier pockels' cells, (3) 156 ps prepulse regenerative amplifier pockels' cells, (4) ±167 ps postpulse unknown origin, (5) ±40 ps postpulse leak of Ti:Sa preamplifier, (6) ±26 ps postpulse 3 mm beamsplitter, (7) ±20 ps postpulse XPW crystal and (8) ±8.5 ps postpulse 2 mm beamsplitter.

We are mostly worried about prepulses that can interact with the gas target before the arrival of the main pulse and alter the density profile. Lets assess the ionization capabilities of the pulses (1) and (3). Starting from a weak laser intensity, the first atomic shell can be considered to be fully ionized over one laser cycle if the ionization rate is comparable with the laser frequency [152]. The ionization rate $\nu^j(E)$ is defined as (in atomic units):

$$\nu^j(E) = \frac{2^{(8/5)(n_j^*-1)}(2l_j+1)}{n_j^* \Gamma(2n_j^*)} \frac{\left[4(2U_i^j)^{5/2}\right]^{\frac{(6n_j^*-1)}{5}}}{|E|^{2n_l^*-1}} e^{-\frac{2(2U_i^j)^{3/2}}{3|E|}}, \tag{4.1}$$

where $n_j^* = j/\sqrt{2U_i^j}$ is the main quantum number, l_j the orbital quantum number, E the
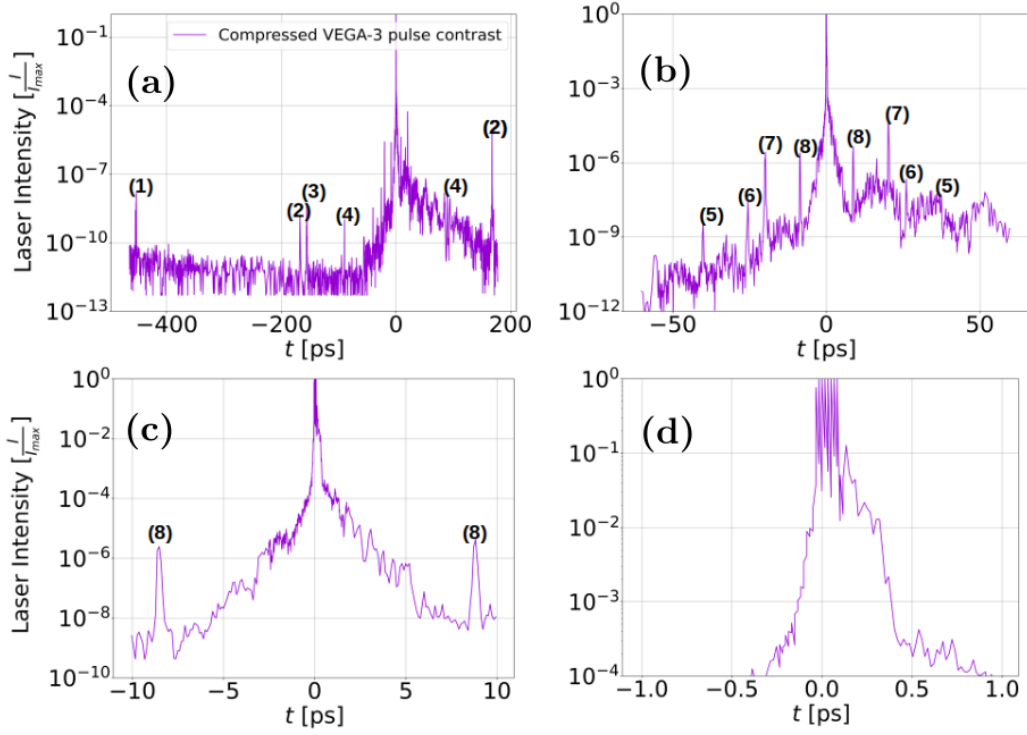
Fig. 4.14: Laser contrast measurement of the VEGA-3 laser performed using the Sequoia commercial 3ω autocorrelator. The laser contrast is $10^{1}2$ at $t = -100\,\mathrm{ps}$ and 5×10^{8} at $t = -5\,\mathrm{ps}$. (a) Full laser contrast measurement from $-460\,\mathrm{ps}$ to $190\,\mathrm{ps}$. Here $t = 0$ corresponds to the arrival of the maximum intensity peak. (b) Zoom of the contrast measurement from $-60\,\mathrm{ps}$ to $60\,\mathrm{ps}$, (c) from $-10\,\mathrm{ps}$ to $10\,\mathrm{ps}$ and (d) from $-1\,\mathrm{ps}$ to $1\,\mathrm{ps}$. The laser division of CLPU identified some pre and postpulses, for details see main text.

electric field and U_i^j the ionization energy of the jth electron obtained from Ref. [153]. The solution $\nu^j(E) = 1/N$, where N is the number of optical cycles, gives the minimum laser amplitude E_j leading to the ionization state $Z^*(E_j) = j$. The corresponding threshold laser intensity is then $I_j = \epsilon_0 c E_j^2/2$. By performing such calculation for nitrogen and 10 laser cycles the minimum laser intensity needed to ionize up to $Z^* = 1$ is $\approx 10^{14}\mathrm{W\,cm^{-2}}$. Therefore, if the pulse (1) was indeed a real prepulse its intensity would not be high enough as to start ionizing the gas before the main pulse arrival. Moreover, the prepulse (3) would not be intense enough to start ionizing the gas neither.

Laser axis monitoring

The laser axis was monitored at low energy by imaging the beam 15 cm after TCC using a motorized in/out mirror as shown in Fig. 4.15.

After analyzing four daily data acquisitions the horizontal and vertical laser axes' tilts were: $\alpha_H = 0.032° \pm 0.026°$ (towards the control room) and $\alpha_V = 0.057° \pm 0.028°$ (upwards, towards the roof), respectively. We consider then that the laser crosses the gaseous target following a known straight path on which detectors like TPs were aligned. Furthermore, we can then unambiguously link shifts in the dose deposition imprints seen on the passive particle detectors to the laser-driven acceleration physics and not to a laser pointing error.

4.3.2 Probe beam

The VEGA-3 probe beam was conceived expressly for this experiment. Our experimental team together with the CLPU scientific division lead by Dr. Carlos Salgado-López designed and implemented this optical line. The probe beam crosses the experimental chamber in an
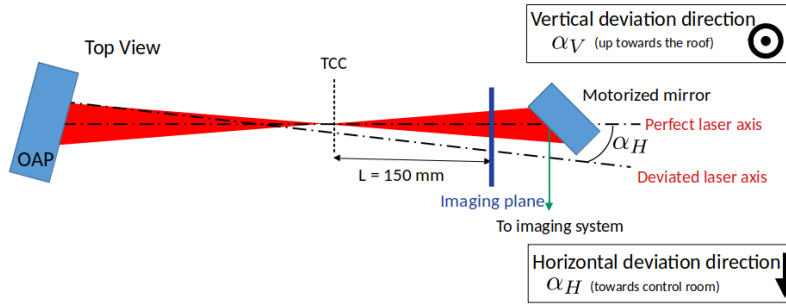
Fig. 4.15: Top view of the experimental setup for laser axis monitoring. The off-axis parabola (OAP) focuses the laser pulse at the target chamber center (TCC). The laser axis was monitored at low energy by imaging the beam 15 cm after TCC using a motorized in/out mirror. By controlling the laser axis we are sure that the laser gas interaction is taking place exactly in the horizontal and vertical planes that we want it to take place in. The mean horizontal and vertical laser axis tilts were: $\alpha_H = 0.032° \pm 0.026°$ (towards the control room) and $\alpha_V = 0.057° \pm 0.028°$ (upwards, towards the roof). 2-D setup cartoon made by Dr. Carlos Salgado-López from CLPU and printed with his permission.

orthogonal axis with respect to the main laser beam, as seen in Fig. 4.16. The probe's frequency was doubled ($\lambda_p = 400\,\text{nm}$) using a beta barium borate (BBO) crystal. The probe beam was built as a pick-up from the main laser using a 6 mm diameter mirror with a Gaussian pattern of reflectivity that yielded about $\approx 6\,\text{mJ}$ of energy before second harmonic conversion and losses on the beam path. The pattern of reflectivity avoids high-intensity regions to be created when cutting a part of the main laser beam, protecting the focusing optics and mirrors downstream. The pick-up mirror was placed in a motorized linear stage. Like this we could perform main-beam-only shots by remotely removing the pick-up mirror from the main beam's path (under vacuum during UHI shots).
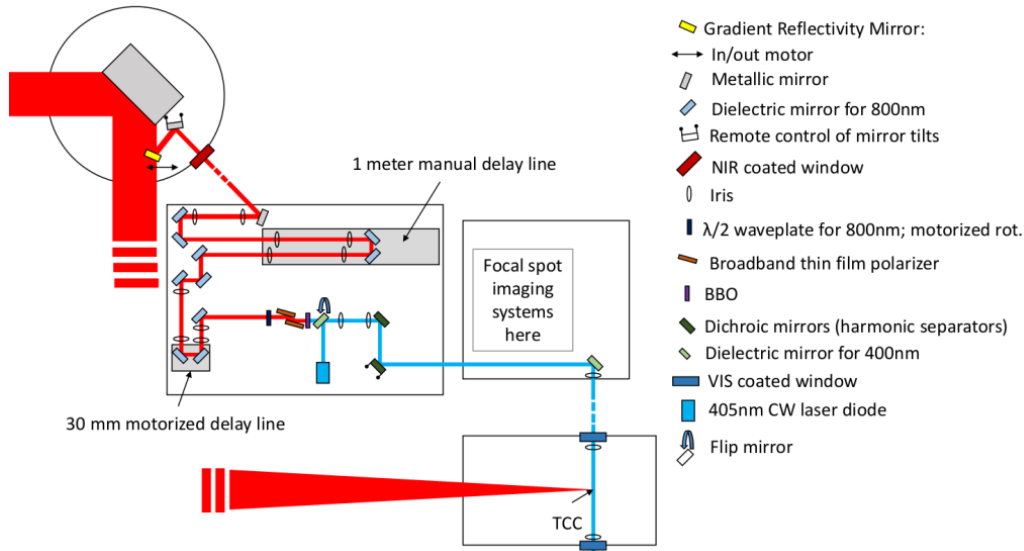
Fig. 4.16: VEGA-3 probe beam with detailed optics and delay lines. The probe design included a delay line composed of a long ($\approx 5\,\mu\text{m}$ resolution) manual delay line and a short ($\approx 1\,\mu\text{m}$ resolution) motorized line providing a total delay of $\pm 700\,\text{ps}$. 2-D setup cartoon made by Dr. Carlos Salgado-López from CLPU and printed with his permission.

Part of the probe beam transport was done in air. Note that when transporting a high-power laser pulse through air and transmissive objects like windows two main phenomena will occur:

(i) temporal stretching of the laser pulse due to the group velocity dispersion (GVD) [154] and (ii) the appearance of non-linear effects that can compromise the laser wavefront. The so-called B-integral is a measure of this non-linear effects:

$$B = \frac{2\pi}{\lambda} \int dz n I(z), \tag{4.2}$$

where $I(z)$ is the optical intensity along the z beam axis and n is the non-linear index of refraction of the medium. The calculated B-integral after $1\,\mathrm{m}$ of air is ≈ 0.006. The path length on air was of about $8\,\mathrm{m}$ for a total B-integral of ≈ 0.048. Regarding the different transmissive objects in the line, the B-integral after $1\,\mathrm{mm}$ of fused silica is ≈ 0.4, which could give rise to an important non-linear phase-shift. For this reason, the amount of transmissive optics in the line was kept as minimum as possible. At the same time, the selected windows were extremely thin, with a $5\,\mathrm{mm}$ thickness. The latter were made of fused silica and had an infrared coating to reduce the main harmonic transmission. We calculated a maximum fluence of $\approx 20\,\mathrm{mJ\,cm^{-2}}$, which is located below the optics' damage threshold.

The probe's design included a delay line composed of a long ($\approx 5\,\mathrm{\mu m}$ resolution) manual delay line and a short ($\approx 1\,\mathrm{\mu m}$ resolution) motorized line providing a total delay of $\pm 700\,\mathrm{ps}$. Both delay lines are visible in Fig. 4.16. Finally, the optical system also included a motorized energy control realized by placing the BBO in a rotation stage as well as a motorized two-dichroic-mirror injection, to allow remote control of the probe injection angle.

4.3.3 Pump and probe synchronization

The pump and probe pulses synchronization consists on obliging the two pulses to arrive at the same time to a given spatial coordinate while characterizing their temporal delay with the highest possible resolution. This procedure is relatively easy when dealing with ns laser pulses, in which case a fast photodiode located at TCC and connected to a digital oscilloscope of enough high sampling frequency is a perfect tool for temporally overlapping such pulses. However, when entering the fs regime such electronic devices are not enough since their temporal resolution is higher than the pulse duration itself. In this regime, more complex synchronization strategies must be adopted, most of the times combining several techniques. The latter include the use of high temporal resolution streak cameras as well as the observation of fast phenomena like probe beam absorption in an expanding plasma in the case of solid targets [140] or prompt gas ionization in the case of gas targets.

A two-stages synchronization procedure was adopted. Firstly, a rough synchronization was carried out by streaking both the pump and probe pulses' signals. The maximum resolution obtained through this method was $\Delta t \approx 760\,\mathrm{ps}$. Afterwards, a fine synchronization based on observing the up-ramp gas ionization triggered by the pump laser at high energy allowed us to achieve a minimum temporal error of $\Delta t \approx 770\,\mathrm{fs}$. In all the stages the probe pulse is translated in time using its delay line with respect to the static main pulse.

4.3.3.1 Rough synchronization

The rough synchronization was performed by looking at the scattered light from TCC using the bottom view IS streak camera. We located a micrometric white microballon at TCC to favor strong light scattering. We acquired pump and probe simultaneously by strongly attenuating the main pulse, which is orders of magnitude more intense than the probe. Fig. 4.17a is the joint acquisition image where the two pulses are roughly visible, the earliest one corresponds to the pump pulse while the latest one corresponds to the probe. Fig. 4.17b is a pump-only acquisition that allowed us to correctly identify the first signal in Fig. 4.17a as the main pulse's signature. The corresponding temporal lineouts are plotted in Fig. 4.17c. Here the intensities

of both signals were modified for comparison purposes. A temporal delay of $\Delta_t \approx 760\,\text{ps}$ (measured between the two vertical dashed lines of Fig. 4.17c) was the maximum temporal resolution that could be obtained through this synchronization method.
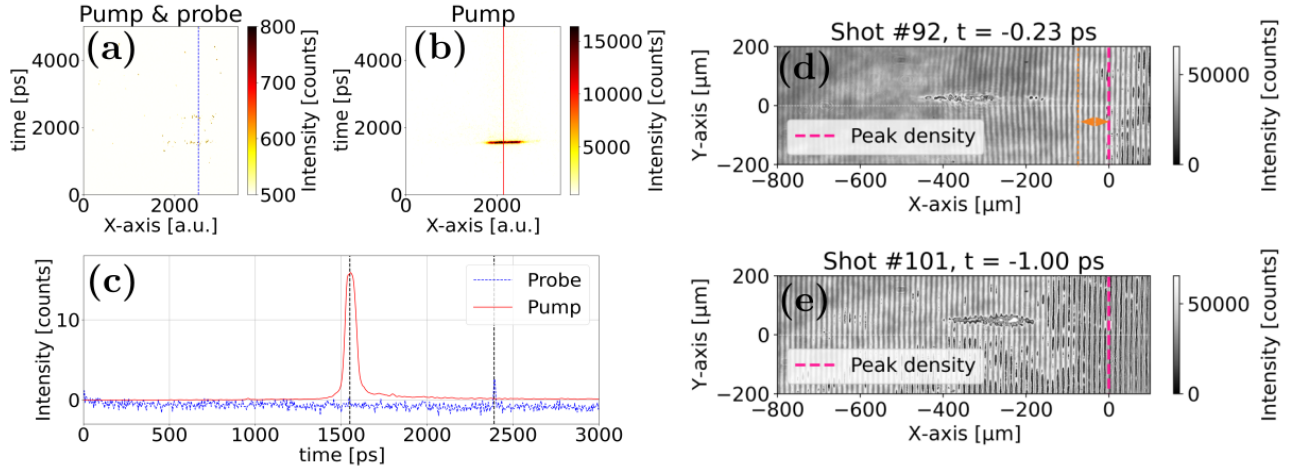
Fig. 4.17: (a-b) Rough synchronization of the VEGA-3 pump and probe pulses. Separate streak camera (a) pump and probe and (b) only-pump acquisitions. (c) Corresponding temporal lineouts of the probe-only (dashed blue line) and pump only (continuous red line) acquisitions with modified intensities of both signals for comparison purposes. (c-e) Fine synchronization of the VEGA-3 pump and probe pulses. (a) Interferogram corresponding to the closest temporal point to $t = 0$ that could be acquired. (b) Closest temporal interferogram to the $t = 0.23\,\text{ps}$ one plotted in (a) that could be acquired were no clear fringe distortion was seen. Therefore, the temporal resolution of the pump and probe synchronization was set at $\Delta t = 770\,\text{fs}$. The worm-like structure seen in both interferograms corresponds to the integrated plasma self emission.

Since probe and pump pulses have such different intensities it can occur that both signals cannot be acquired at the same time. In such cases the measured Δt has a temporal error due to the streak camera jitter of $\approx 250\,\text{ps}$. This jitter is inherent to the way the streak camera is triggered, using an electronically delayed transistor-transistor logic (TTL) signal. This is solved in the most modern version of the Hamamatsu C7700 streak camera that includes an ultra-fast highly-sensitive optical photodiode trigger connection that comes directly from the laser bay.

4.3.3.2 Fine synchronization

The fine synchronization of the pump and probe pulses was performed by looking at the prompt ionization of the up-ramp gas. The temporally-delayed probe beam was used to acquire optical interferograms of the main beam interaction with the gas. We were confident on this synchronization method given the good VEGA-3 laser contrast and the low-intensity of the laser pedestal and prepulses, located under the gas ionization threshold. Note that the gas ionization is seen as the bending of the interferogram's fringes. The synchronization was performed following a dichotomy process were an interferogram with bending fringes and an interferogram with straight fringes are located. Afterwards the corresponding half time is studied and the next temporal interval is selected. Fig. 4.17d and e show two of these interferograms. The first one, plotted in Fig. 4.17d, was the closest to $t = 0$ that could be acquired. Here one can appreciate bent fringes up to $x \approx -70\,\mu\text{m}$ (marked with a vertical orange dashed line), i.e. $70\,\mu\text{m}$ before the gas density peak (located at the vertical dashed pink line). This distance corresponds to $230\,\text{fs}$ at light speed. Therefore, the time of this interferogram was set at $t = -0.23\,\text{ps}$ and the

delay line was corrected by the needed distance to obtain the theoretical $t = 0$ position. The temporal resolution of this synchronization method is the Δt between an interferogram where fringe distortion is seen and an interferogram with straight fringes. The second case is plotted in Fig. 4.17e, this was the closest time to $t = 0.23\,\text{ps}$ that could be acquired where no fringe distortion was seen. Therefore, the temporal resolution was set at $\Delta t = 770\,\text{fs}$. The worm-like structure seen in both interferograms corresponds to the integrated plasma self emission. Its location is not to be mistaken with the main pulse's location. To obtain higher temporal resolutions one could think on increasing the spatial resolution of the interferometry diagnostic to distinguish fainter fringe distortions.
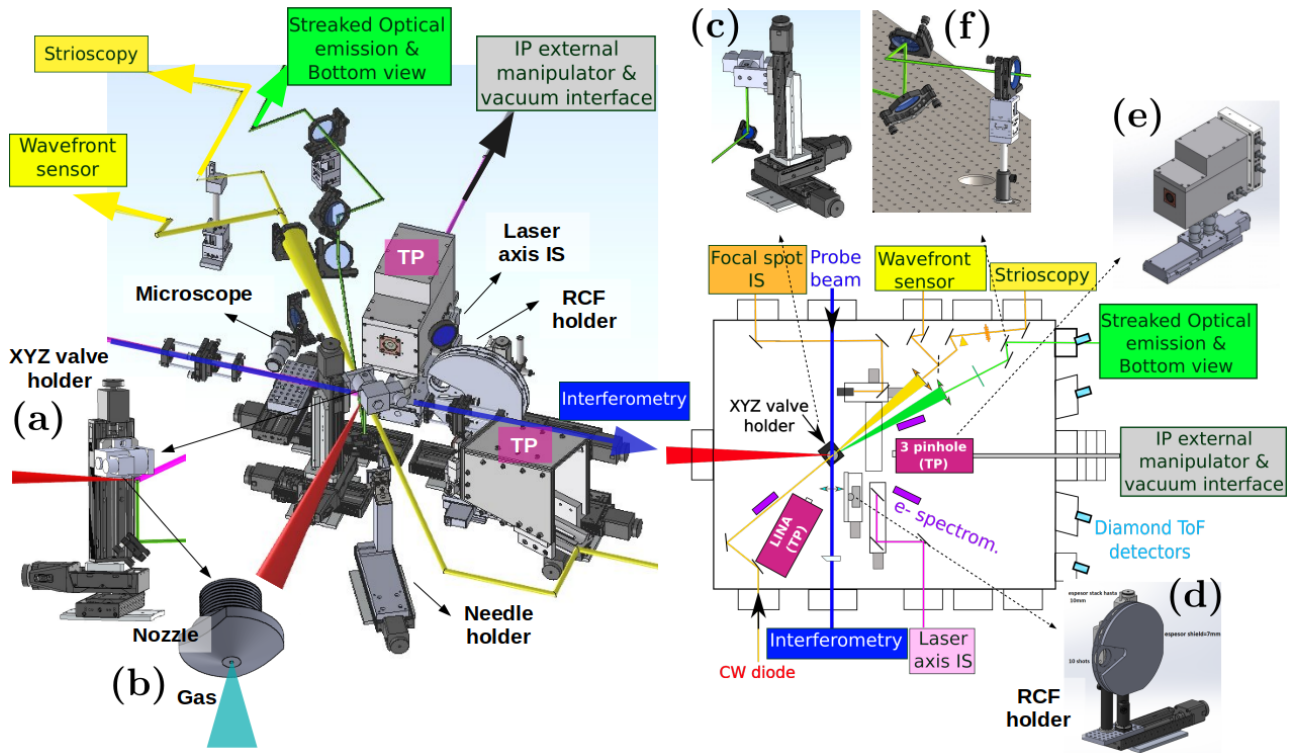
Fig. 4.18: (left) 3-D CAD of the VEGA-3 interaction chamber showing the location of the different optical lines and diagnostics. Figure insets: (a) detail on the XYZ motorized tower that holds the gas valve and (b) detail of the nozzle that is screwed to the output of the gas valve. (right) 2-D schematic cartoon of the interaction chamber. Figure insets: (c) detail on the gas valve holder XYZ motorized tower, (d) RCF rotatory holder, (e) three-pinhole Thomson parabola located over a linear motorized stage to minimize from the TCC to the TP entrance and (f) periscope in the bottom view that rotates the image to allow it to enter in the streak camera slit.

4.3.4 Experimental layout and diagnostics

The different optical lines and diagnostics were located inside the interaction chamber as shown in Figs. 4.18a and b. The main laser beam enters the chamber through a lateral port and intersects the probe beam at TCC forming a 90° angle. The optical lines that were implemented include: an optical interferometry line, a focal spot imaging system line, a wavefront sensor line, a strioscopy line and a bottom view optical imaging system that was used for both image control of the nozzle's surface (and help its realignment) after each shot and through an alternative imaging system to streak the plasma self-emission.

The active particle detectors that were fielded include diamond time-of-flight detectors, permanent magnet spectrometers and Thomson parabolas. The passive detectors were ra-

diochromic film stacks located on the laser axis at 60 mm from TCC. Hereinafter all the optical lines and diagnostics are detailed.

4.3.4.1 Plasma and neutral gas diagnostics

Neutral gas profiles' characterization: interferometry and strioscopy

The characterization of the neutral gas profiles is performed with the SID-4 wavefront sensor [141] using a 10 mJ HeNe diode ($\lambda_d \approx 632$ nm) together with a strioscopy line. The latter serves to analyze the temporal evolution of the density at the shock height. See Appendix A for more details. A 2-D cartoon of the SID-4 plus strioscopy setup implemented during the VEGA-3 experiment is plotted in Fig. 4.19a. A dedicated optical line with a magnification $\gamma \approx 5$ was divided in two using a 50/50 beamsplitter. The transmitted light was spatially filtered and imaged on a fast photodiode connected to an oscilloscope to acquire time resolved measurements of the gas density at the shock height, see Fig. 4.19c. A 632 nm interferometric filter eliminated incoherent light coming from TCC. As can be seen in the top view of Fig. 4.19b the VEGA-3 laser and SID-4 wavefront sensor axes form a 35° angle, which was taken into account to reconstitute the density profiles along the pump laser axis ($\Delta d_t = \Delta \cos 35°$ and $\Delta d_f = \Delta \sin 35°$).
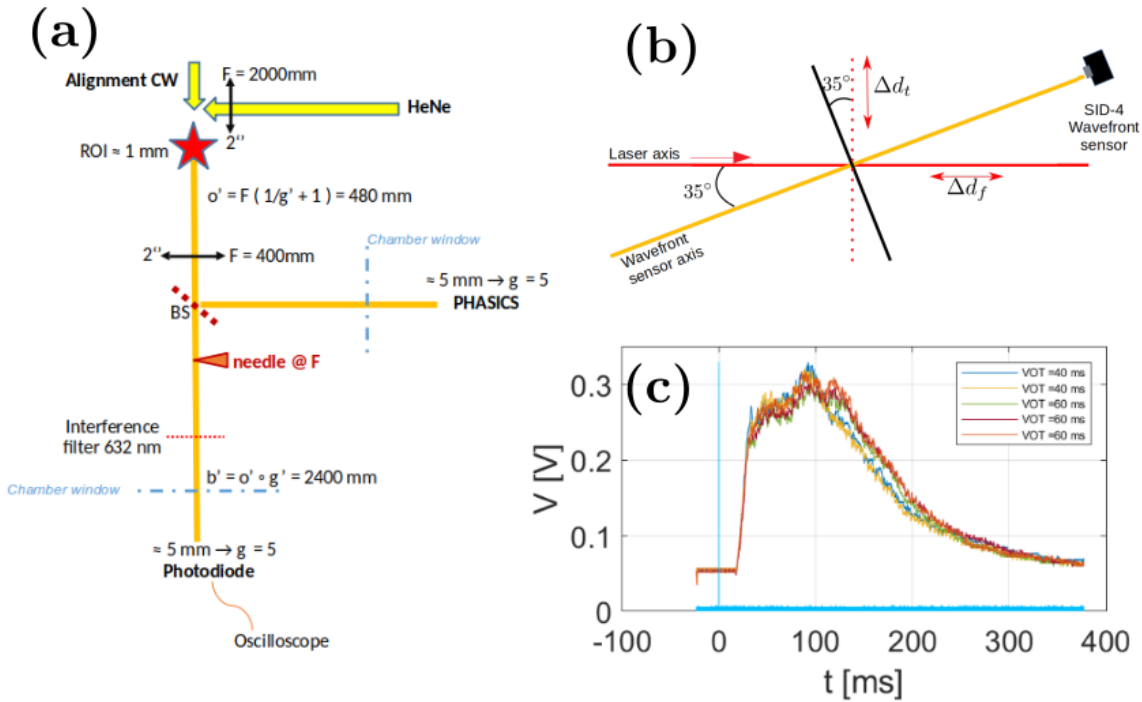
Fig. 4.19: (a) Neutral gas characterization wavefront sensor and strioscopy optical lines implemented during the VEGA-3 experiment. (b) Detail on the angle between both optical lines. (c) Example of a strioscopy time-dependent oscilloscope acquisition.

Chapter 2 contains a detailed description of the high-pressure gas system (HPGS) and the the S900 and the J2021 shock nozzles used during the experiment. Furthermore it details the two HPGS characterization campaigns performed for two different gas valves, including the *microvalve* used during the VEGA-3 experiment. Remind that the gas profile's shape and maximum density depend on several factors: the gas nozzle, the gas electrovalve and the input HPGS parameters: the compressor's backing pressure (P), the gas valve opening time (VOT) and temporal delay between the valve's opening and the laser-gas interaction (CD).

The characterization campaigns served to locate HPGS working points where the system operated safely while producing interesting gas density profiles. Since the measured density profiles differed from the estimations issued from fluid dynamics simulations, we defined an interesting density profile as one that has a visible density peak as well as a maximum atomic density close to $n_{at,max.} \approx 10^{20}$ cm^{-3}, based on the parametric numerical study presented in Chapter 3. Refer to Chapter 2 for details on the measured vs. theoretical gas density profiles for each nozzle type.

On-shot optical interferometry

Using the frequency doubled VEGA-3 probe beam (PB) the on-shot free electron density profiles are characterized up to a $n_e < 10^{20}$cm^{-3}. Given the PB's long delay line a ± 700 ps time interval around the main laser interaction time is accessible for study. At the same time, the pump and probe synchronization allowed to reach a time resolution of $\Delta t = 770$ fs. The implemented Nomarski interferometry setup, which is plotted in Fig. 4.20, had an optical magnification $\gamma \approx 12.2$. We intentionally used the JAI SP-20000M camera that accounts for a large pixel matrix of 5120 x 3840 pixels with a pixel size equal to 0.44 μm/px allowing to obtain a 2.25×1.69 mm field of view.
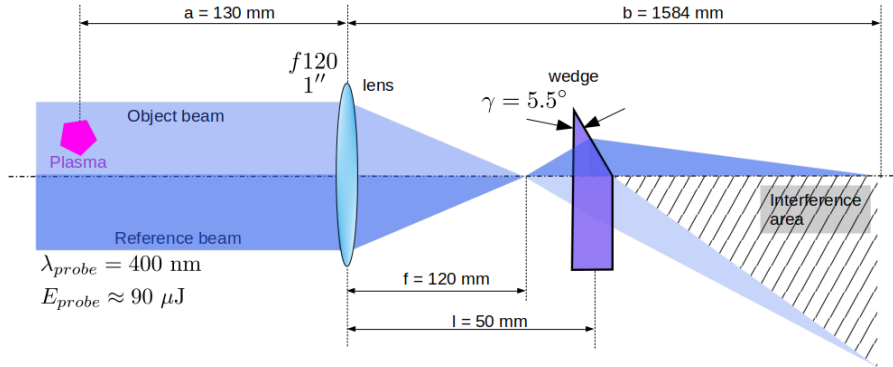
Fig. 4.20: Nomarski interferometry setup implemented during the experiment.

Originally, this interferometry line was designed as a complex interferometry (CI) line to analyze at the same time the electron density and the magnetic fields being created inside the plasma. However, the transport of the probe beam in air caused a strong energy loss (see Figure 4.16). With 5 J of energy in the main beam (propagated in air) the measured probe beam energy at the pick-up position was $E \approx 180$ μJ and after the second dichroic mirror (see Figure 4.16) it had diminished up to $E' \approx 18$ μJ. During full energy shots we estimated $E' \approx 90$ μJ. Moreover, in a CI configuration, after crossing the first polarizer (see details in Appendix A) the probe's intensity diminishes drastically. Ultimately, the probe's injection energy was not enough to acquire complex interferograms. For future experiments one must obtain $E' \approx$ mJ or more to acquire complex interferograms.

Nozzle bottom view and streaked plasma self-emission

The gas electrovalve (called the *microvalve*) and nozzle were held upside down to favor the correct operation of the electrovalve, using a motorized XYZ tower as seen in Fig. 4.18 inset (a). The latter serve for nozzle alignment ans inspection purposes. During this process we noticed that the nozzle moved by tens of µm from shot-to-shot. This was probably due to the EMP effect since this movement was not evidenced during the characterization campaign performed before the experiment and detailed in Appendix A. In any case, this micrometric movement occurs in much larger time scales than the laser-gas interaction so it does not affect the laser-gas pointing, it just obliges us to realign the nozzle at TCC before each shot.

The optical light captured by the bottom view image was streaked to obtain time-resolved

images of the plasma self-emission. This was done via an alternative optical setup out of the same collection lens, as of course, we were now imaging a plane $\approx 500\,\mu m$ below the nozzle's surface. The streak camera was filtered using a BG38 filter to cut the main infrared laser light as much as possible plus an interferometric filter at 532 nm. A periscope in the bottom optical line (see Fig. 4.18 inset (f)) allowed to rotate the bottom view image for imaging the main laser propagation axis along the horizontal slit of the streak camera.

The optical system was composed of three independent optical lines (OL): (i) two two-lens high-magnification OL with $\gamma \approx 5$ to look at a detailed plasma ROI of about 1 mm of diameter and (ii) a single-lens low-magnification OL with $\gamma \approx 2.5$ to image a larger area of about 4 mm of diameter intended for nozzle shot-to-shot realignment.

Joint information from the neutral gas characterization, the streaked plasma self-emission and the on-shot interferometry

Fig. 4.21 shows for one shot the complete data set produced by the plasma diagnostics. The plasma characterization data set is composed of three elements. Fig. 4.21a shows the transverse molecular density lineout at the shock height. This density lineout is obtained using a Python homemade routine to analyze the SID-4 phase maps, detailed in Appendix A. Fig. 4.21b corresponds to the raw on-shot interferogram with the corresponding density lineout superposed. Here the laser focus plane is marked with a green solid line and the gas density peak is marked with a pink dashed line. Note that for some shots we focused the laser not at the density peak but in the gas up-ramp. This was done to try to attenuate laser self-focusing and filamentation, targeting laser channeling through the gas density peak. Fig. 4.21c is a zoom on the interferogram's region of interest (ROI). Finally, Fig. 4.21d shows the streaked plasma self-emission image. During the analysis process the streaked bottom view images are compared with the on-shot interferograms to link the interaction hot spots with features in the electron density charts.

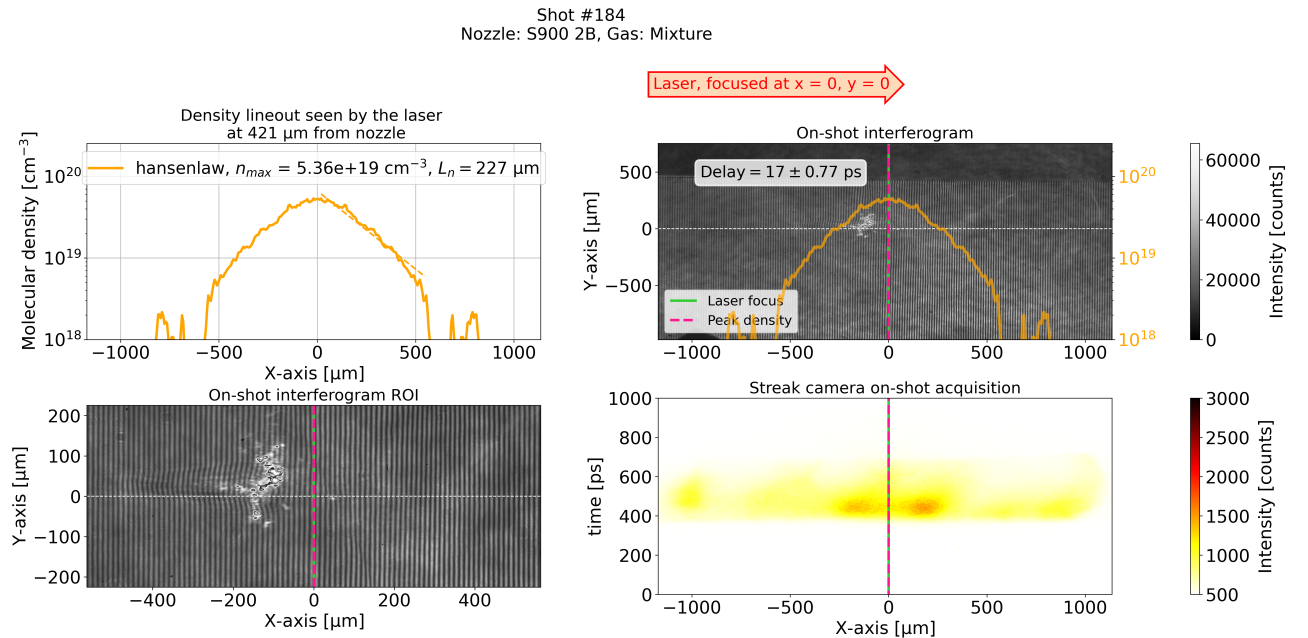Fig. 4.21: Plasma characterization data set composed of (a) the transverse density lineout at the shock height, (b) the raw on-shot interferogram with the corresponding density lineout superposed. Here the laser focus plane is marked with a green solid line and the gas density peak is marked with a pink dashed line, (c) is a zoom on the ROI of the interferogram and (d) the streaked plasma self-emission image.

Tab. 4.1: Diamond detectors used in the VEGA-3 campaign.

Label	Type	τ_{FWHM} [ns]	CCE	Surface [mm^2]	Thickness [µm]	Bias voltage [V]
ToF A	Single crystal, sandwich	0.46	98%	4 x 4	50	+100
ToF B	Single crystal, sandwich	0.46	98%	4 x 4	50	+100
ToF C	Polycrystalline, sandwich	4.10	42%	15 x 15	150	+300
ToF D	Single crystal, interdigitated	0.52	68%	4 x 4	50	+100
ToF E	Single crystal, sandwich	0.46	98%	4 x 4	50	+100

Tab. 4.2: Geometries of the Thomson parabolas used during this thesis work.

TP	$d_{pinh.magn.}$ [mm]	L_m [mm]	D_m [mm]	h [mm]	$B_{th.}$ [T]	$d_{pinh.elect.}$ [mm]	L_e [mm]	d [mm]
LINA	25	75	100	33	0.38	25	102	10
Three pinh.	13.5	75	149.5	16	0.40	13.5	75	10

4.3.4.2   Particle diagnostics

The particle diagnostics fielded during the experiment intended to characterize the energies and number of the accelerated ions and electrons in diverse angles with respect to the laser axis.

Active diagnostics

The active diagnostics for ion energy spectra acquisition included diamond time-of-flight (ToF) detectors and Thomson parabolas (TPs). The diamond ToF detectors were placed at different angles from the laser axis inside a $\pm17°$ cone and located in a 9° inclined plane with respect to the "equator". The exact chamber ports that were used, which all look directly at TCC, are those inside the dashed yellow rectangle in Fig. 4.10b. Five different ToF detectors were fielded at distances ranging from 0.8 m to 1.5 m from TCC. They were named with the letters A to E and their characteristics are summarized in Table 4.1. See Appendix A for details on the diagnostic and data analysis.

Two different TPs were used: LINA (with a single-pinhole entrance) and the so-called three-pinhole TP which had three entrance pinholes aligned horizontally. The objective of a three pinhole TP was to obtain angular-resolved energy spectra, refer to Appendix A for more details on this diagnostic. The TPs' geometries are summarized in Table. 4.2. The three-pinholes TP was located on-axis at 100 mm from TCC to characterize the forward ion emission. The short distance from TCC to the TP entrance was achieved by placing the TP on a motorized linear stage that located the TP in its shot position when other motorized elements in the chamber liberated the axis, see Fig. 4.18 inset (c). The 200 µm diameter entrance pinholes were spaced by 3 mm, obtaining an angular detection cone of $\pm1.1°$ when the TP is located at 100 mm from TCC. The TP LINA was located at 250 mm from TCC and at 110° from the laser axis, as seen in the setup sketch of Fig. 4.18. The single entrance pinhole had a 200 µm diameter as well. The objective of this TP was to characterize lateral ion emission.

The detectors that were used for both TPs were imaging plates (IPs) of the type TR, specially designed for low energy particles' detection. Other detectors such as Lanex screens were not sensitive enough during the VEGA-2 campaign. At the same time, the ≈ 5000 V bias voltages of micro-channel plates (MCPs) could trigger electrical breakdown when pressurized gas enters the chamber. The IPs were covered with 2 layers of 2 µm of aluminized mylar to protect them from background emission. We performed Monte Carlo Geant4 [155] simulations to understand the lower energy detection range. We found that an IP TR covered with 4 µm of aluminized mylar has a minimum detectable energy of 1.5 MeV α particles and 6 MeV nitrogen ions, refer to Appendix A for more details.

To allow several shots without venting the vacuum chamber an external IP manipulator was introduced into the interaction chamber using a small vacuum interface six-ways chamber,

Tab. 4.3: Calibration curves of the five different permanent magnet spectrometers used during this work. The neodymium magnets have a magnetic field $B = 190\,\text{mT}$ while the Ferrite magnets have a $B = 95\,\text{mT}$.

Channel N°	Material	L_c [cm]	E_{min} [MeV]	E_{max} [MeV]	Calibration curve
1	Neodymium	24	0.250	50	$E(x) = -1.17 \cdot 10^{-5}x^4 + 5.81 \cdot 10^{-4}x^3 + 1.53x^2 - 44.83x + 656.72$
2	Neodymium	18	0.250	35	$E(x) = -1.17 \cdot 10^{-5}x^4 + 5.81 \cdot 10^{-4}x^3 + 1.53x^2 - 44.83x + 656.72$
3	Ferrite	18	0.055	21	$E(x) = -2.81 \cdot 10^{-6}x^4 + 1.92 \cdot 10^{-4}x^3 + 0.78x^2 - 24.85x + 295.10$
4	Ferrite	6	0.055	1.5	$E(x) = 0.50x^2 - 7.15x + 80.03$
5	Neodymium	6	0.250	5	$E(x) = -3.07 \cdot 10^{-7}x^4 - 1.25 \cdot 10^{-4}x^3 + 0.34x^2 - 10.64x + 115.4$

see Fig. 4.18b. The manipulator allowed to extract and exchange the three pinholes TP IP in between shots by simply venting this much smaller volume. The IP exchange process took approximately 10 minutes. In the TP LINA case several high-intensity shots were integrated in a single IP.

Passive diagnostics

The passive detectors included permanent magnet electron spectrometers to obtain information on the electron spectra and stacks of radiochromic films (RCFs) to acquire the spatial distribution of the accelerated particles. Five permanent magnet spectrometers were located at different angles from the laser axis and at about 30 cm from TCC, as seen in Fig. 4.18. The five spectrometers were named with numbers from 1 to 5 and their characteristics are summarized in Table 4.3. The detectable electron energies range from 250 keV to 50 MeV. See Appendix A for more details.

The RCF stack was located at 60 mm from TCC perpendicularly and centered on the laser axis and it was composed of a first 10 µm layer of aluminum followed by five layers of Gafchromic unlaminated U-EBT-3 film and ten layers of EBT-3 film. For details on the RCF diagnostic and analysis procedure see Appendix A.

A several-shots operation was ensured by placing ten RCF stacks in a motorized rotatory holder, see Fig. 4.18 inset (b). The latter was also placed in a linear translation stage which allowed to easily switch between shots dedicated to RCF acquisition and shots dedicated to TP measurements. The RCF area exposed during each shot was a 4 cm diameter circle.

4.3.5   Experimental results

The particle diagnostic suite was tested by performing preparatory shots with Al foil targets before moving on to the gaseous targets. Section 4.3.5.1 presents a summary of the test shots' results. Afterwards, Section 4.3.5.2 presents the results on gaseous targets.

4.3.5.1   Preparatory shots on solid target

The solid target shots were performed on Al foils of 6 µm thickness. This material and thickness had been found to be the optimal ones regarding ion acceleration during the VEGA-3 commissioning experiment. The laser energy during these shots was 60% less than the nominal full power energy, about 7 J on-target. This was due to the wrong location of a beam splitter in the laser optical path after the OAP. This was corrected for all the shots on gaseous target performed afterwards. Considering a laser pulse duration $\tau_L \approx 60\,\text{fs}$ and a measured focal spot of $D_L \approx 15\,\text{µm}$ the attained intensity was of about $I_{max} \approx 3.7 \times 10^{19}\text{W/cm}^2$, at normal incidence onto the targets.

Electron acceleration

There were four different electron spectrometers fielded during these shots: channels 1, 2, 4 and 5 located at $-7°$, $21°$, $-21°$ and $-35°$. Note that negative angles correspond to clockwise

rotations. The spectrometers' characteristics are summarized in Table 4.3.

Fig. 4.22a, upper row, shows the acquired electron spectra from an eight-shot integrated acquisition from shot #14 to shot #21. In the bottom row two polar plots, from left to right, correspond to the energy-angle and the electronic temperature-angle (T_e-angle) distributions. The highest energies of $\approx 13\,\mathrm{MeV}$ were obtained at 21° from the laser axis. Lower energies up to 2.5 and 5 MeV were measured at $-21°$ and at a wide angle of $-35°$, respectively. The highest electronic temperatures were of $\approx 1.5\,\mathrm{MeV}$ measured as well at 21° from the laser axis. Channel 1 was the detector located as close as possible to the laser axis, at $-7°$. Maximum energies of $\approx 7.5\,\mathrm{MeV}$ and electronic temperatures of $\approx 800\,\mathrm{keV}$ were measured. The 0° inspection angle was covered by the three-pinhole Thomson parabola (TP) detailed hereafter.
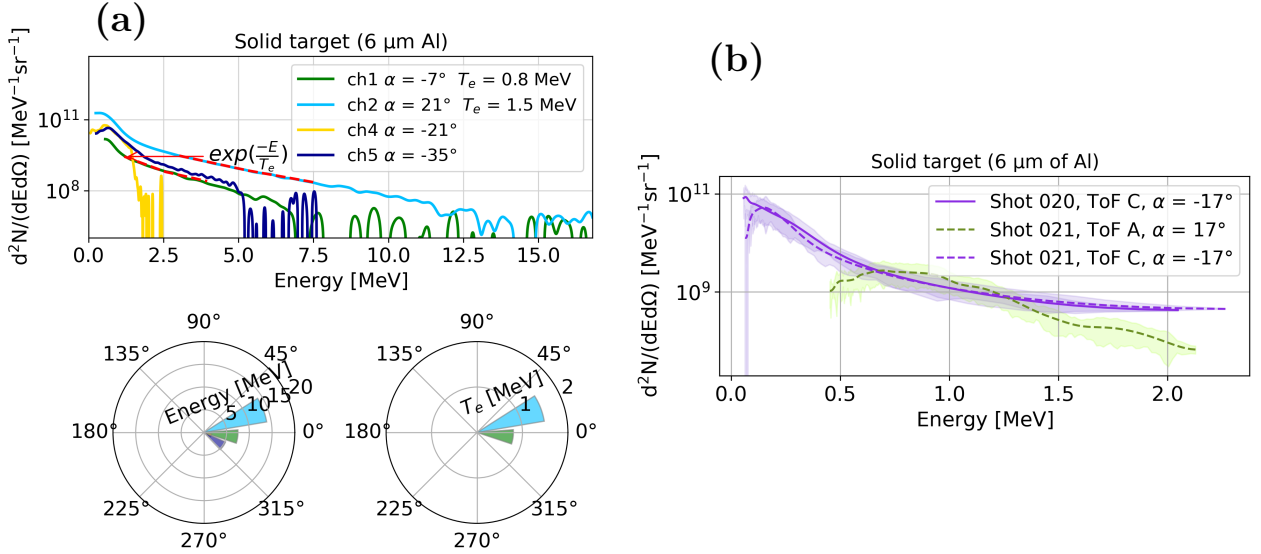
Fig. 4.22: (a) Upper row: acquired electron spectra. Bottom row from left to right: corresponding energy-angle and T_e-angle distributions. The data corresponds to an eight-shot acquisition from shot #14 to shot #21 performed on solid target (6 μm of aluminum). (b) Single-shot proton spectra measured using the ToF A and ToF C detectors in shots #20 and #21.

Ion acceleration

Ion acceleration was characterized using both the three-pinhole TP located at 0° and at 100 mm from TCC and two ToF ion detectors located at ±17° from the laser axis in a 9° inclined plane. Two other ToF detectors (Tof D and E) located at $-110°$ from the laser axis in a 15° inclined plane and the TP LINA located on the laser propagation plane were blocked by the solid target holder. Another ToF detector (Tof B) was located inside the chamber in the laser propagation plane at $-22°$ from the laser axis ye it only acquired noise. Note that ToF detectors are highly sensitive to EMP which is much stronger close to TCC [156].

Fig. 4.22b shows the single-shot proton spectra that was measured using the ToF A and ToF C detectors for shots #20 and #21. Maximum energies of 2.2 MeV were acquired at ±17° from the laser axis. The ion spectra exhibit a TNSA-like decay.

Fig. 4.23a shows the single-shot scanned IP of the 0° three-pinhole TP corresponding to shot #21. Fig. 4.23b shows the deconvolved proton spectra. The spectra doesn't exhibit strong angular asymmetries within the ±1.71° angular positions of the pinholes. We measured maximum proton energies of 12 MeV and 10^{12} particles per sr at 2 MeV.

Figs. 4.24a and b correspond to C^{5+} and C^{4+} energy spectra, respectively, also obtained during shot #21. See the secondary parabolas appearing to the right of the three main parabolas
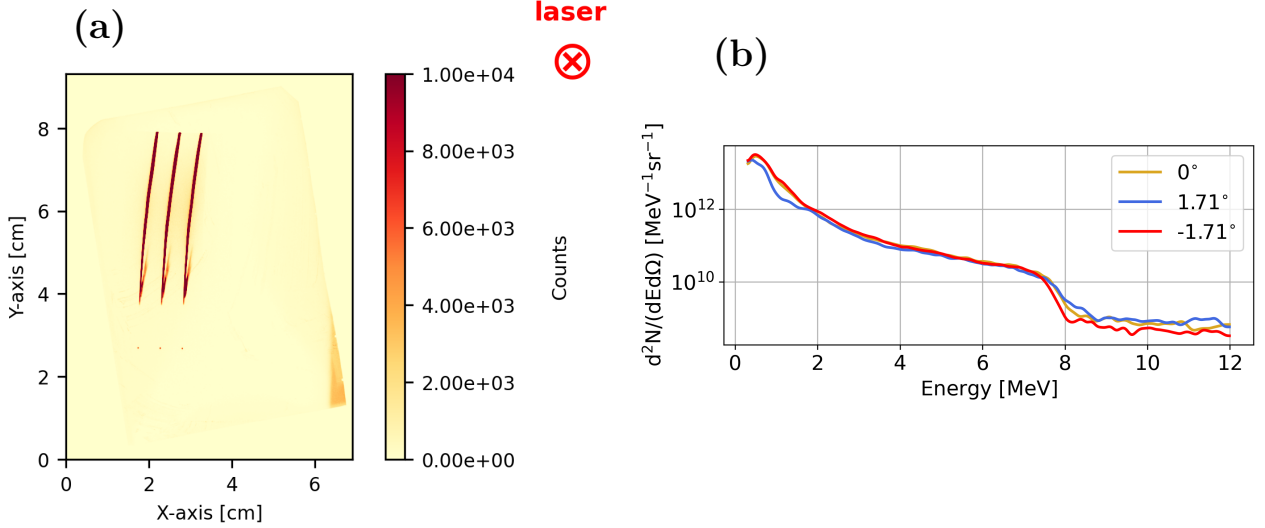
Fig. 4.23: (a) Scanned IP of the 0° three-pinhole TP corresponding to the solid target shot #21. (b) Deconvolved proton spectra at the angles corresponding to each entrance pinhole. When the TP is located at 100 mm from TCC its three pinholes spaced by 3 mm allow the inspection of a ±1.71° cone.

in Fig. 4.23a. Maximum C^{5+} and C^{4+} energies of 13 MeV were measured. The carbon ions spectra do not exhibit strong angular asymmetries neither, within the ±1.71°:
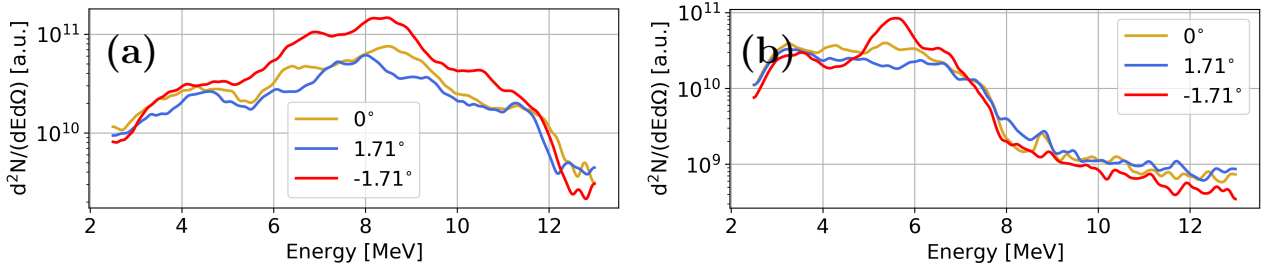
Fig. 4.24: (a) C^{5+} and (b) C^{4+} energy spectra obtained during the solid target shot #21 using the three-pinhole TP located at 100 mm from TCC on the laser propagation 0° axis.

4.3.5.2 Shots on gaseous target

Once the particle diagnostic suite was positively tested with the solid targets we transitioned to gaseous targets. Two shock nozzle designs were deployed during the experiment: the S900 and the J2021. We had five S900 nozzles named S900 1A, S900 2B, S900-3C, S900-4D and S900 5E and a single J2021. For details on the nozzles used during the experiment see Chapter 2. All nozzles were metallic ones manufactured through 3-D printing by SourceLab in the case of the J2021 nozzle and Rolland Bailly in the case of the S900 nozzles.

Measured molecular and atomic density profiles from these nozzles are shown in Fig. 4.25a-d, for the nozzle and gas combinations (NGCs) corresponding to the experimental results detailed below, where the golden profiles correspond to virgin nozzles. Note that the S900 5E and S900 1A nozzles exhibit the thinnest transverse profiles with a longitudinal width of 1000 µm.

The difference between the virgin S900 nozzles (see golden profiles in Figs. 4.25a-c) profiles is due to manufacturing defects. The rest of the profiles are altered due to shot-to-shot nozzle damage [70], which seem to specially affect the S900 2B nozzle (see Fig. 4.25b). Indeed, the
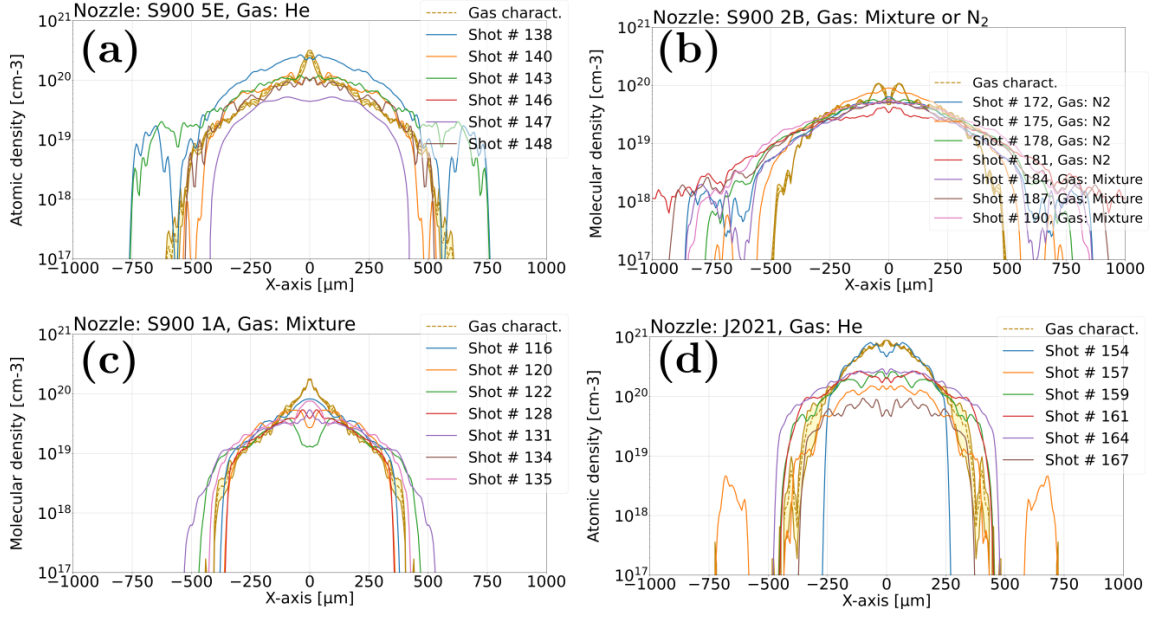
Fig. 4.25: Transverse density lineouts of the nozzle and gas combinations corresponding to the experimental results detailed below. (a) S900 5E nozzle & He, (b) S900 2B nozzle & N_2/gas mixture, (c) S900 1A nozzle & a 9/1 N_2/He gas mixture and (d) J2021 nozzle & He.

S900 2B nozzle produced a twice wider profile of about $2000\,\mu m$ due to shot-to-shot nozzle damage (refer to Chapter 2 for details). At the same time, all the S900 nozzles have a maximum atomic density $n_{at,max.} \approx 10^{20}$ cm^{-3} while the J2021 produces a five times denser gas profile with $n_{at,max.} \approx 5 \times 10^{20}$ cm^{-3}. The P, VOT and CD parameters were directly chosen upon the HPGS *microvalve-only* characterization campaign. As previously mentioned, the HPGS characterization campaign served to locate working points where the system operated safely while producing interesting gas density profiles. Since the measured density profiles differed from the estimations issued from simulations, we defined an interesting density profile as one that has a visible density peak as well as a maximum atomic density close to $n_{at,max.} \approx 10^{20}$ cm^{-3}, based on the parametric numerical study presented in Chapter 3. Refer to Chapter 2 for details on the measured vs. theoretical gas density profiles for each nozzle type as well as on the HPGS *microvalve-only* characterization campaign and the shot-to-shot nozzle damage.

To cope with the laser-induced nozzle damage we had to readjust the shock height on a shot-to-shot basis using the interferometry and strioscopy CW optical lines of Fig. 4.19a.

The main experimental results have been divided into four categories: results on electron acceleration, on ion acceleration, study of the on-axis dose deposition distribution recovered from the RCF stacks and the nature of the interaction as seen in the early ($\approx 10\,ps$) and late ($\approx 100\,ps$) time optical interferograms as well as on the streaked plasma self-emission.

Each result's category is presented for four nozzle-gas combinations (NGCs):

   I. S900 nozzle & He,

  II. S900 nozzle & a 9/1 N_2/He gas mixture,

 III. S900 nozzle & N_2

 IV. J2021 nozzle & He.

Electron acceleration

The electron spectrometers corresponding to channels 1, 2 and 5 (see Table 4.3) were located at $-2°$, $21°$ and $2°$ from the laser axis. Fig. 4.26a-d show the acquired electron spectra (upper row) and the energy-angle and T_e-angle distributions (lower row, from left to right) for the four NGCs. T_e is obtained by fitting an exponential decay $\exp\{-\mathcal{E}/T_e\}$ to the spectra. The maximum electron energies were always below the detectors' maximum limits, detailed in Table 4.3. The data analysis of this diagnostic was performed in collaboration with Dr. J. Dostal, Dr. M. Krupka and Dr. R. Dudzak from the PALS facility (Prague, Czech Republic).
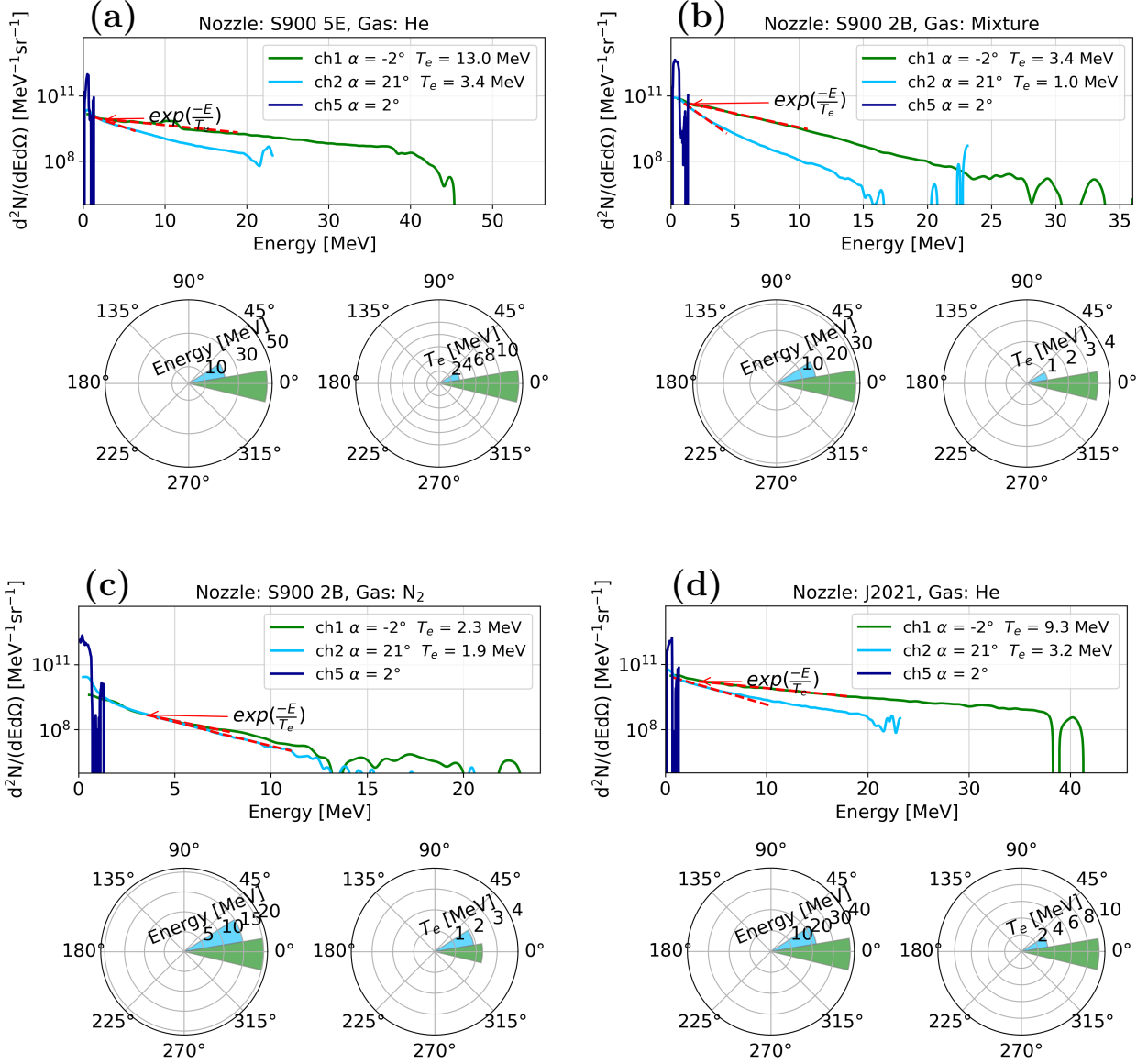
Fig. 4.26: Upper rows: acquired electron energy spectra using electron spectrometers. Bottom rows from left to right: corresponding energy-angle and the T_e-angle distributions. (a) Electron energy spectra obtained using the S900 5E nozzle & He, (b) energy spectra acquired using the S900 2B nozzle & gas mixture, (c) energy spectra acquired using the S900 2B nozzle & N_2 and (d) energy spectra obtained using the J2021 nozzle & He gas.

The presence of He in the gas clearly favors high electronic energies and temperatures on-axis. The maximum energy of $45\,\text{MeV}$ and the maximum temperature $T_e \approx 13\,\text{MeV}$ were obtained with the S900 5E nozzle & He gas, see Fig. 4.26a. The temperature value is six times the *ponderomotive scaling*, i.e. $T_e \approx 6\epsilon_h$, where $\epsilon_h = (\sqrt{1 + a_0^2/2} - 1)m_e c^2 \approx 2\,\text{MeV}$ considering

Tab. 4.4: Diamond detectors used during the VEGA-3 campaign.

Label	Distance from TCC [mm]	Angle [°]	Inclination [°]
ToF A	1590	17°	9°
ToF B	875	0°	9°
ToF C	1680	−17°	9°
ToF D	1624	4.85°	9°
ToF E	1624	5.50°	9°

a normalized laser amplitude $a_0 = 6.9$. This T_e value agrees with the electron heating model presented in Ref. [152] and it is indicative of the strong electron heating of the gaseous target in the near-critical regime.

Using the J2021 nozzle & He gas maximum electron energies of 40 MeV were obtained at −2° from the laser axis. The corresponding electronic temperature was 9.3 MeV.

In the case of the S900 2B nozzle & N_2 (see Fig. 4.26c) the maximum energy, measured on-axis, was 20 MeV. The maximum electron energies measured at 21° from the laser axis were of 15 MeV. The electronic temperatures obtained on-axis and at 21° from it are comparable: 2.3 MeV and 1.9 MeV, respectively.

In all the NGCs the electron energies measured at −2° are drastically higher than the energies measured at 2°. In the S900 5E nozzle & He gas the maximum energies at −2° were of 45 MeV (Fig. 4.26a, ch1) and dropped to 2 MeV at 2° (Fig. 4.26a, ch5). The highly energetic electron beams are also directional and collimated. Finally, in all NGCs the low energy electrons measured at 2° from the laser axis, $\approx 10^{12}$ particles/(MeV · sr) are more numerous by an order of magnitude than those measured at −2° and at 21°, $\approx 10^{11}$ particles/(MeV · sr).

Ion acceleration

Five different ToF diamond detectors were located in the positions and with the inclinations detailed in Table 4.4, inside the chamber ports marked with a dashed yellow rectangle in Fig. 4.10b. The ToF detectors are fully calibrated for α particles and nitrogen ions. The data analysis of this diagnostic was performed in collaboration with Dr. F. Consoli and Dr. M. Salvadori from the ENEA and CNR and Dr. Claudio Verona and Dr. Giuseppe Prestopino from the University of Rome Tor Vergata (Rome, Italy).

Fig. 4.27 shows the acquired absolute ion energy spectra. The particles with energy lower than 100 keV were not included in the

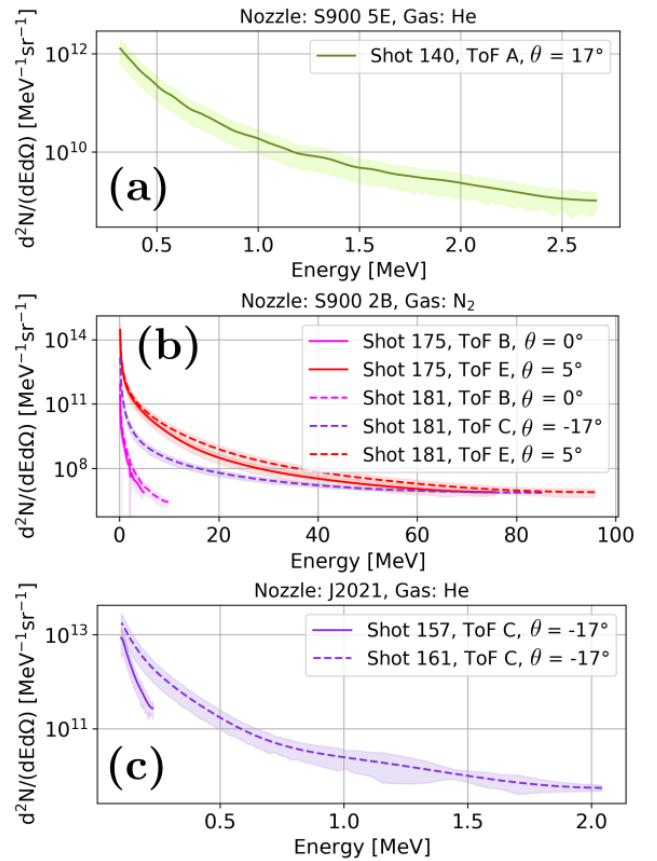Fig. 4.27: Ion energy spectra acquired using ToF diamond detectors. (a) α particles' energy spectra obtained using the S900 5E nozzle & He. (b) Nitrogen ions' energy spectra acquired using the S900 2B nozzle & N_2 and (c) α particles' energy spectra obtained using the J2021 nozzle & He.

analysis since this energy range could be polluted with low energy protons most likely origi-

nated from the nozzle's ablated surface. The analysis of gas mixture shots was not possible due to the temporal overlapping of the different ions. In this case the ionic contributions cannot be treated as parasite signals, i.e. as the protons coming from the ablation of the nozzle surface, since the percentages of He and N_2 in the mixture are non-negligible.

As shown in Fig. 4.27a, using the S900 5E nozzle & He gas we measured up to 2.5 MeV of α particles at 17° from the laser axis with $\approx 10^{11}$ part/(MeV sr) at 500 keV. Using the S900 2B nozzle & N_2 gas we measured maximum energies of 90 MeV at 5° and 17° from the laser axis with $\approx 10^{14}$ part/(MeV sr) at 500 keV (Fig. 4.27b). We also measured nitrogen ions' energies up to 9 MeV on-axis in a 9° inclined plane with $\approx 10^{14}$ part/(MeV sr) at 500 keV. Finally, using the J2021 nozzle & He gas, see Fig. 4.27c, we measured maximum α particles' energies of 2 MeV at −17° from the laser axis with $\approx 10^{11}$ part/(MeV sr) at 500 keV.

The ToF D and ToF E detectors were located during several shot days at −110° from the laser axis in a 15° inclined plane inside the chamber port marked with a dashed green square in Fig. 4.10b. Both ToF detectors were placed at 1480 mm from TCC. The selected chamber port looks directly at TCC and we made sure that nothing was blocking the optical line. However, none of these two detectors acquired ion signals. As mentioned before, once the same detectors were placed in the forward direction at 5° from the laser axis in a 9° inclined plane, the ToF E detector measured nitrogen ions up to 90 MeV.

Absence of signal in both Thomson parabolas (TPs)

We intended to characterize the ion acceleration using both the three-pinhole TP at 0° located at 100 mm from TCC and the LINA TP located at −110° and at 250 mm from TCC, see the sketch of the experimental setup in Fig. 4.18. IPs of type TR, which are the most sensitive ones, were used as TP imagers with two 2 µm layers of aluminized mylar as X-ray filter.

The three-pinhole TP was located on-axis while the LINA TP was placed at −110° from the laser axis. As was previously detailed the three-pinhole TP was tested during shots performed on a solid target (6 µm of Al) measuring protons up to 12 MeV. However, there was no ion signal in none of the two TPs fielded during the gas shots, with none of the NGCs. The only visible signal in the IPs came from the X-ray zero deflection points as seen in Fig. 4.28a for the three-pinhole TP (where the horizontally aligned three zero deflection points correspond to the three entrance pinholes) and in Fig. 4.28b where the single zero deflection point is linked to the unique LINA entrance pinhole. The background signal level was low, around 0.6 PSL.

A Python routine was written to obtain the minimum detectable ion energies considering the TPs' geometries detailed in Table 4.2 and a TP to TCC distance of 100 mm for the three-pinhole TP and of 250 mm for the LINA TP. The minimum detectable energy is calculated by overlapping the parabolic trace over the IP and looking at the curve's intersection point with the IP borders, see Appendix A for details on the calculation. The input voltages (±2000 V for both TPs) and magnetic fields (B-fields) were extracted from experimental values. The three-pinhole TP input B-field was a 2-D measurement of the magnetic field along the magnet's central axis. The maximum value of this B-field is of ≈ 0.4 T. In LINA's case the B-field was constant and equal to 0.3 T. The results are summarized in Table 4.5 for the two fully ionized species He^{2+} and N^{7+}. The minimum He^{2+} detectable energies were 0.390 MeV with the three-pinhole TP and 0.148 MeV with the LINA TP. The minimum N^{7+} detectable energies were 1.370 MeV with the three-pinhole TP and 0.520 MeV with the LINA TP.

Hence, the ionic energies up to 2.5 MeV α particles and up to 90 MeV nitrogen ions measured with the ToF detectors should be detectable with the TPs. The detector's solid angle $\Omega = S/r^2$ is the ratio between its active surface S and the distance between TCC and the detector r squared. Considering 200 µm diameter pinholes for both TPs, the ToF detectors' surfaces detailed in Table 4.1 and the TP to TCC distances of Table 4.4 one obtains the solid angle values summarized in Table 4.6.
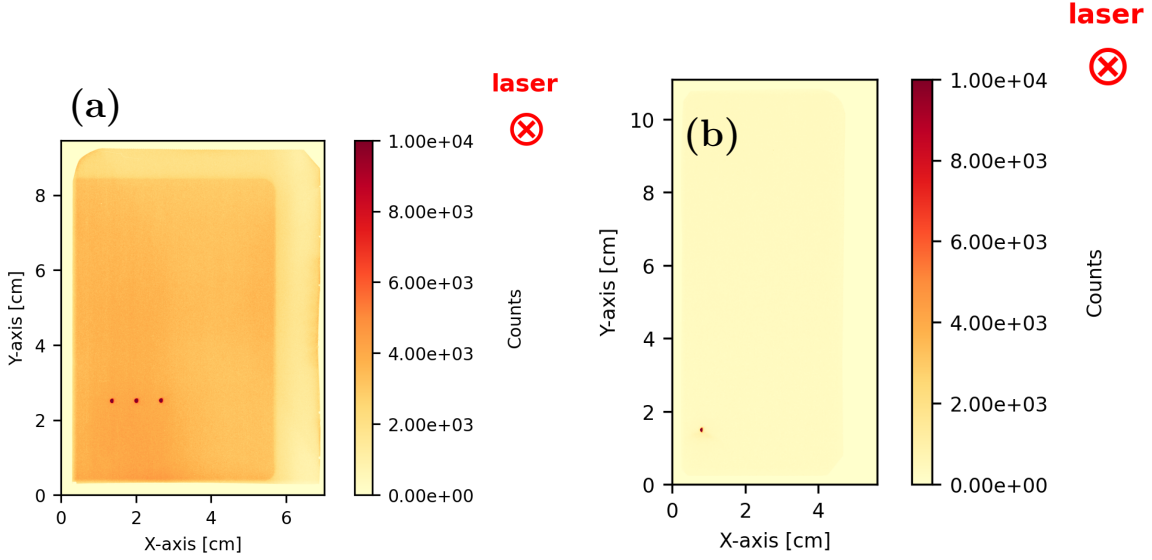
Fig. 4.28: (a) Three-pinhole TP IP scan of shot #109 and (b) LINA TP IP scan of shot #107. In both (a) and (b) the only visible signal in the IPs comes from the X-ray zero deflection points.

Tab. 4.5: Maximum and minimum theoretically detectable ion energies considering each Thomson parabola geometry, distance to TCC, voltage and magnetic field values.

Species	Three-pinhole TP E_{min} [MeV]	LINA TP E_{min} [MeV]
He^{2+}	0.390	0.148
N^{7+}	1.370	0.520

As can be appreciated, the TPs' solid angles are up to two orders of magnitude lower than in the ToF detectors' ones, regardless of being located much closer to TCC. This is due to their very small entrance pinhole diameters, which are needed since they provide the energy resolution of the diagnostic. The ToF detectors active surfaces are millimetric and in particular ToF C has an extremely large diamond layer of 15×15 mm, which increases the possibilities of particle detection with ToF detectors over TPs.

At the same time, the ToF detectors' sensitivity is extremely high, being able to measure a single-particle energy deposition (see Appendix A). On the other hand the TP's sensitivity depends on the imager that is coupled to it. We performed Geant-4 Monte Carlo simulations of the stopping of α particles and nitrogen ions in one IP TR layer covered with 5 µm of aluminized mylar (corresponding to the experimental configuration) and obtained the minimum detectable energies: 1.5 MeV for α particles and 6 MeV for nitrogen ions. The IP's sensitivity is then the major constraint regarding the minimum measurable energies, much more than the electric and

Tab. 4.6: Solid angles calculated for both TPs and for the ToF detectors.

Detector	Surface [mm²]	Distance from TCC [mm]	Solid angle [sr]
3-pinhole TP	3.14×10^{-2}	100	3.14×10^{-6}
LINA TP	3.14×10^{-2}	250	5.03×10^{-7}
ToF A	16	1590	6.32×10^{-6}
ToF B	16	875	2.09×10^{-5}
ToF C	225	1680	7.97×10^{-5}
ToF D	16	1624	6.06×10^{-6}
ToF E	16	1624	6.06×10^{-6}

magnetic deflections.

Fig. 4.29a shows the response curves of an IP TR to electrons [157], photons [158] and α particles [159]. Lets consider the range of energies $\mathcal{E} > 2\,\mathrm{MeV}$ of the α particles spectrum plotted in Fig. 4.27a and re-plotted in purple in Fig. 4.29b. If such spectrum would cross a $5\,\mu\mathrm{m}$ aluminized mylar IP filter, one would obtain the shifted spectrum in red. Integrating the shifted spectrum in an $\Omega = 2.1 \times 10^{-7}$ sr solid angle (considering an IP located at $340\,\mathrm{mm}$ from TCC and a 50 x 50 $\mu\mathrm{m}$ IP pixel) multiplied by the IP response function (plotted in green in Fig. 4.29b) one obtains a signal level of 0.7 PSL/particle. Compared with the noise level measured in a single-shot IP (Fig. 4.29a) one attains a low signal-to-noise level $S/N \approx 1$. Hence, the ionic signature would not be distinguishable from the background noise. To cope with this problem, one could accumulate several shots in a single IP. The noise level in a thirteen-shots-accumulated IP was $\approx$2.3 PSL, which could improve the signal-to-noise level up to $S/N \approx 3.8$. However, no α particles were detected in the accumulative shot intervals neither.
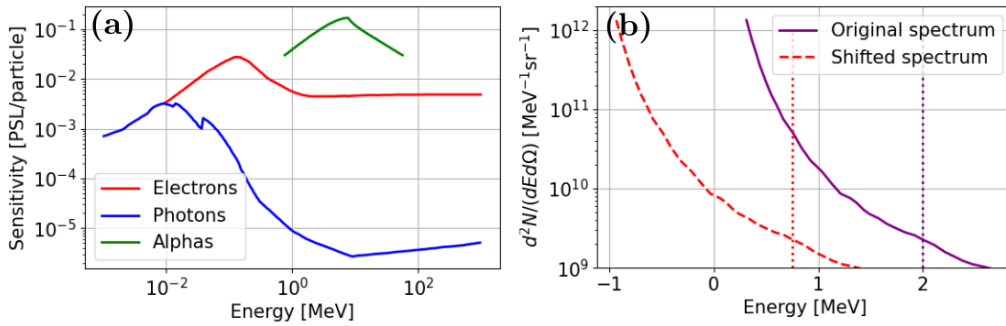
Fig. 4.29: (a) Sensitivity of IPs of the type TR to electrons [157], photons [158] and α particles [159]. (b) α particles spectrum obtained using the ToF A detector, corresponding to shot #140 in pure He.

In summary the TPs energy detection limits were studied by analyzing: (i) their solid angle, (ii) the electric and magnetic deflections of each TP at the specified distances from TCC, (iii) the IP TR energy detection limits taking into account the $5\,\mu\mathrm{m}$ aluminized mylar filter and (iv) the fact that the three-pinhole TP was successfully tested during the solid target shots. The minimum detectable α energy is $1.5\,\mathrm{MeV}$ and in the case of nitrogen ions it is $6\,\mathrm{MeV}$, for both TPs. The energy detection bottle neck arises from the energy loss in the aluminized mylar IP filter.

Taking into account the previously discussed points two possible hypothesis can be made. It could be that there is emission on the laser propagation axis but that it is of particles with energy lower than the minimum energy detectable by the TPs, or that the particle number is too low to be detected by the IP TR plus aluminized filter sensitivity (even when accumulating several UHI shot in a single IP). It must be noted that the IPs of the type TR are the most sensible IPs in the market as they do not have a protective plastic layer (see Appendix A for more details). If this was the case even more sensitive detectors should be used in future experimental campaigns. Other possibility is that there is no emission in the TPs' small solid angles and that the particle acceleration is directed away from the laser propagation axis, reaching the ToF detectors located off-axis.

During the VEGA-2 experiment [109] we encountered a similar situation with TPs located in almost the same positions that used Lanex screens as imagers. As in the VEGA-3 experiment, the ToF detectors (PiN diodes in this case) located at $16°$ and $-106°$ in a $15°$ inclined plane detected ions, see Section 4.2. However, the TPs only detected low intensity zero deflection points and the sensitivity of the Lanex imager was deemed too low.

A similar experiment to the VEGA-3 one is detailed in Ref. [65]. The experiment was car-

ried out with a 30 fs PW laser achieving a maximum intensity on-target of 10^{20} W/cm^2 and a normalized laser intensity $a_0 = 7$. The near-critical gas target composed of He and a small percentage of H_2 had a neutral density of 10^{20} cm^{-3}. The particle diagnostic suite was composed of two TPs located on-axis and at 90°. No ion acceleration was detected in the forward direction. However, ion acceleration was detected in the transverse direction, with a maximum energy of ≈ 500 keV for both α particles and protons using a non-calibrated microchannel plate (MCP) as the TP imager.

On-axis dose deposition

A radiochromic film (RCF) stack composed of a 10 µm layer of aluminized mylar, five layers of U-EBT-3 film and ten layers of EBT-3 film (Gafchromic, Ashland) was placed on-axis at 60 mm from TCC and perpendicular to the laser propagation direction. Refer to Appendix A for details on the RCF counts to dose calibration and analysis procedure. We made sure that the U-EBT3 active layers faced the TCC. The EBT-3 film composition is plastic-active layer-plastic, so any side can face TCC. Each stack was exposed during a single shot. In order to clarify the contribution of ions and electrons to the dose deposition signal we performed Monte Carlo simulations of the energy loss of α particles, nitrogen ions and electrons through the stack.
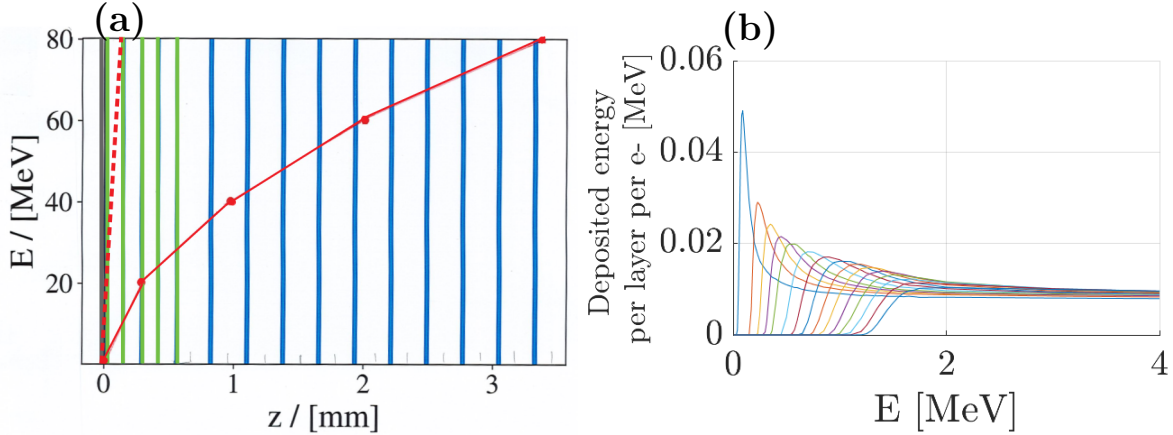
Fig. 4.30: (a) Output of a SRIM [160] simulation using the PySTarT runtime environment [109] of the stopping of α particles (continuous line) and nitrogen ions (dashed line) in an RCF stack composed of a 10 µm layer of aluminum (grey layer) followed by five layers of unlaminated EBT-3 RCF film (green layers) and 10 layers of EBT-3 film (blue layers). (b) Result of a Geant-4 simulation of electrons traversing the same RCF stack. Each curve corresponds to one stack layer, from the 1st to the 15th (from left to right). The abscissa is the energy of the incoming electron and the ordinate the deposit energy per layer and per electron.

Fig. 4.30a corresponds to the output of a SRIM [160] simulation performed using the PySTarT runtime environment [109] of the stopping of α particles (continuous line) and nitrogen ions (dashed line) in the RCF stack. As can be seen α particles of 20 MeV are stopped in the third RCF layer while nitrogen ions of 80 MeV are stopped in the second layer. Fig. 4.30b corresponds to a Geant-4 [155] simulation of electrons traversing the mentioned stack. Electrons of energies between 30 keV and 2 MeV deposited their energy inside the stack. Taking as a reference value the maximum ion energies measured in the ToF detectors: 2.5 MeV for α particles and 90 MeV for nitrogen ions, we expect ionic contributions to be limited to the first three RCF layers. Note that according to the TP results there is no ion emission at 0°.

A. Low energy electron signatures ($\mathcal{E} \approx 500$ keV)

Figures 4.31a-d show the dose deposition signals on the 4th RCF layer for the different

nozzle-gas combinations (NGCs). As detailed before, we expect these signals to be mainly due to electrons of 500 keV and to not have significant ionic dose contributions, see stopping power curves of Figs. 4.30a and b. The VEGA-3 main laser polarization plane coincides with the horizontal dashed lines and the laser was aligned in the intersection point. Note that all figures share the same spatial scale and colorbar limits.
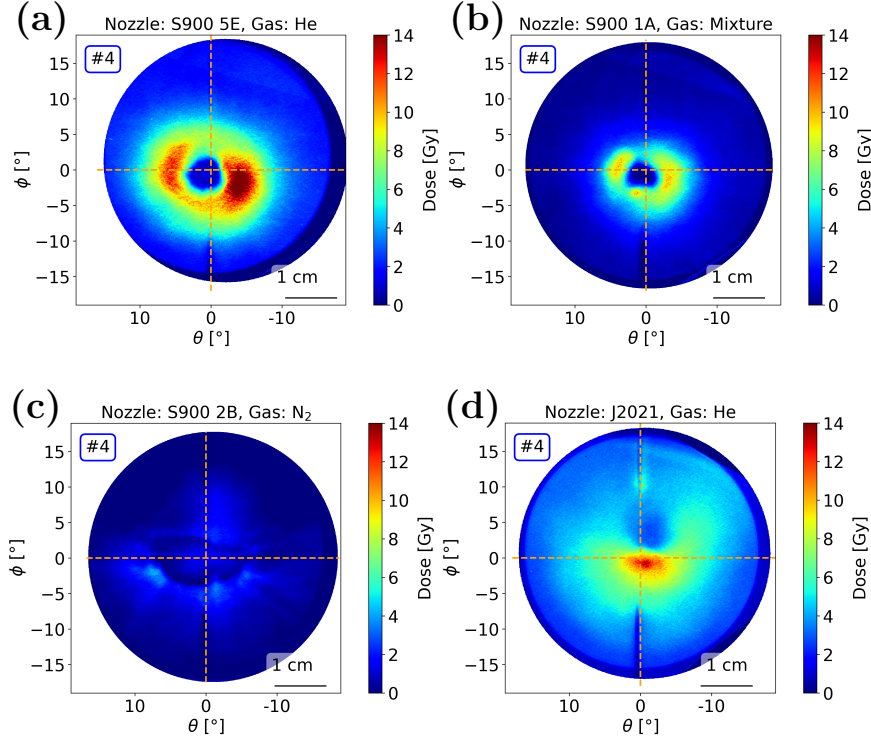
Fig. 4.31: (a) Dose deposition on the 4th layer of the RCF stack corresponding to shot #143 performed using the S900 5E nozzle & He, (b) shot #134 performed using the S900 1A nozzle & gas mixture, (c) shot #172 performed using the S900 2B nozzle & N_2 and (d) shot #167 performed using the J2021 nozzle & He.

Using the S900 nozzle & He (Fig. 4.31a) or gas mixture (Fig. 4.31b) two horizontally aligned hot spots accompanied by a 360° *doughnut*-shaped dose deposition are observed. In the gas mixture case the *doughnut* shape is less symmetrical and tends to divide into two horizontal lobes.

This less symmetrical *doughnut*-shaped was acquired for two other shots using an S900 nozzle & gas mixture. The 4th layers of the RCF stack corresponding to these shots are plotted in Figs. 4.32a and b.

Moreover, either using the S900 nozzle & He or gas mixture, an on-axis dose depletion region is also clearly distinguished, see Figs. 4.31a and b and Figs. 4.32a and b.

In the S900 2B nozzle & pure N_2 case several less intense dose deposition areas appear shifted away from the horizontal and vertical axes, see Fig. 4.31c. Moreover, a dose depletion irregular ellipse is seen around the on-axis dose signal.

Finally, in the J2021 nozzle & He case plotted in Fig. 4.31d a unique elliptical hot spot with an horizontal FWHM of ≈ 5° appears centered in both the longitudinal and vertical directions. The major ellipse axis coincides with the laser polarization plane. The A dose minima is located above the hot spot. This NGC was also shot during the VEGA-2 experiment where a single circular ≈ 9° FWHM beam imprint appeared shifted from the presumed laser axis in shots #62 and #63, see Fig. 4.4. In both experiments the maximum atomic density was approximately $n_{at} \approx 5 \times 10^{20} \mathrm{cm}^{-3}$, see Fig. 4.2 (VEGA-2) and Fig. 4.25d (VEGA-3).

B. High energy electron signatures ($\mathcal{E} \approx 2\,\mathrm{MeV}$)
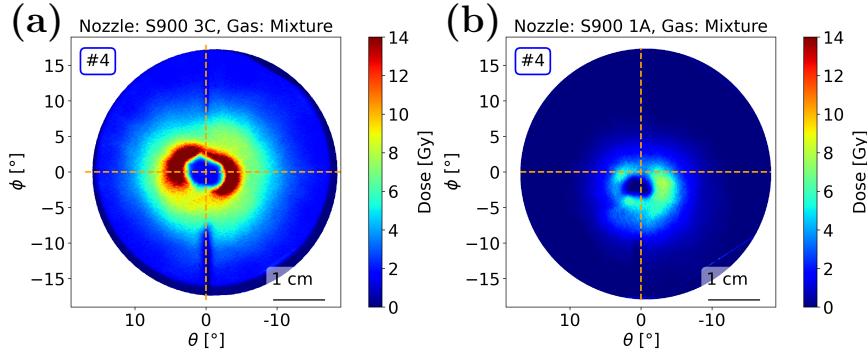
Fig. 4.32: First layer of the RCF stack corresponding to (a) shot #109 and (b) #135 using an S900 nozzle & gas mixture.

The complete RCF stacks corresponding to Figs. 4.31a-d are plotted in Figs. 4.33, 4.34, 4.36 and 4.37. Note that as we travel deeper inside the RCF stack we find traces of more energetic electrons. We aim at distinguishing the dose deposition signatures that correspond to higher energy electrons, i.e. $\mathcal{E} \approx 2\,\mathrm{MeV}$, the maximum electron energy that can be detected with the RCF stack.

In the S900 5E nozzle & He case plotted in Fig. 4.33 the initial hot spots aligned in the RCF horizontal axis and signaled with a red arrows in layer #1 evolve through the RCF stack and are still visible in the last layer (see red arrows in layer #15). They could be linked with an energetic electron population that crossed the entire stack. At the same time, other electron populations located away of the horizontal RCF axis and marked with black arrows are also visible in layer #15. Note that the vertical shadows in all layers correspond to alignment needles that mark the perpendicular axis with respect ot the laser polarization.
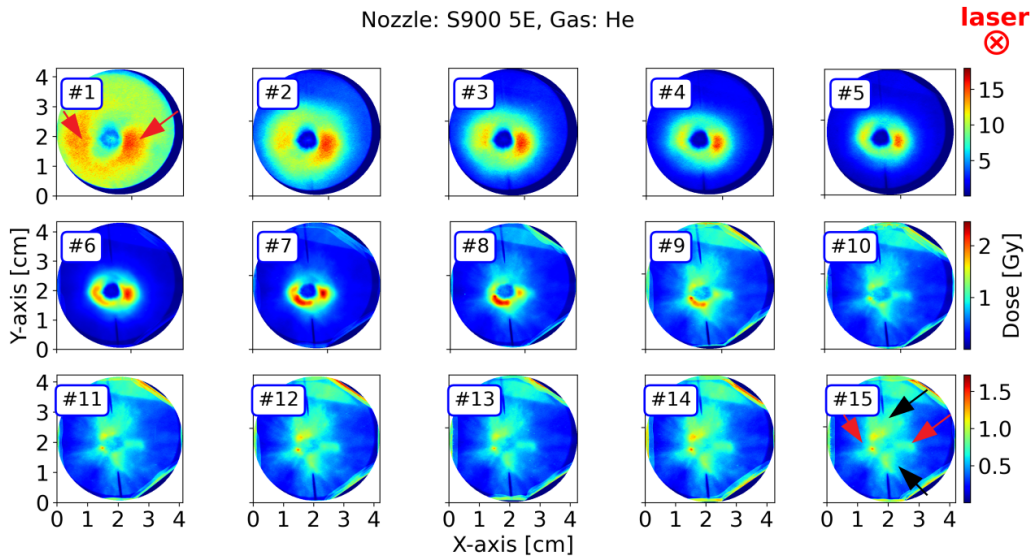
Fig. 4.33: RCF stack of shot #143 performed with the S900 5E nozzle & He.

In the S900 1A nozzle & gas mixture case plotted in Fig. 4.34 the two high intensity lobes aligned on the RCF horizontal axis and marked with red arrows in layer #1 are followed as well through the stack. Both lobes are still visible in the last stack layer where they are marked with red arrows. In this case no strong dose contributions are seen away from the horizontal RCF axis.

Figures 4.35a and b show in more detail the last stack layer of shot #143 using the S900 5E nozzle & He (Fig. 4.33) and shot #135 using the S900 5E nozzle & gas mixture (Fig. 4.34).

127
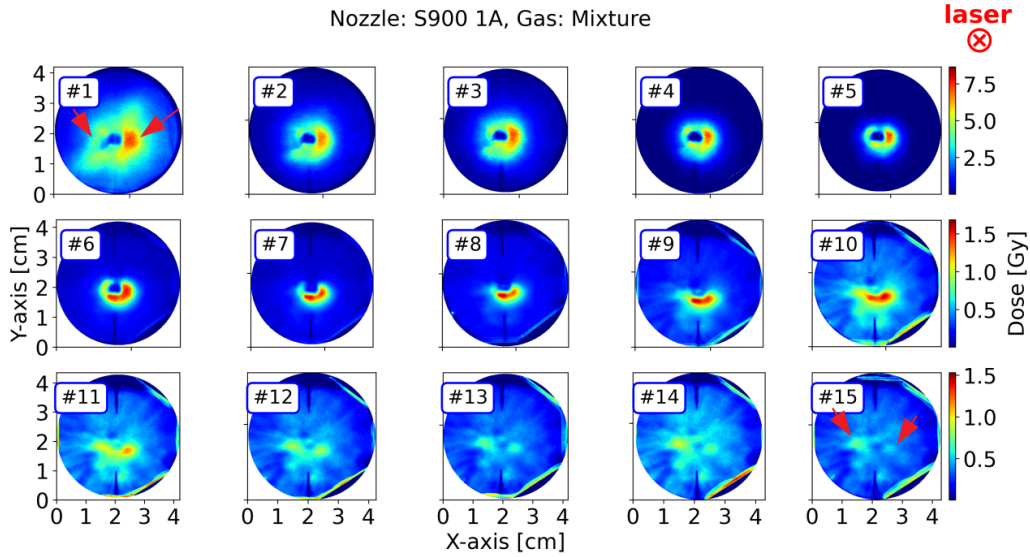
Fig. 4.34: RCF stack of shot #135 performed with the S900 1A nozzle & gas mixture.

The green and blue vertical lines intersections with the RCF horizontal axis mark the position of the ch1 ($-2°$) and ch5 ($2°$) electron spectrometers (see electron spectra of Figs. 4.26a and b). Note that the ch2 ($21°$) spectrometer lays outside of the RCF detection range.
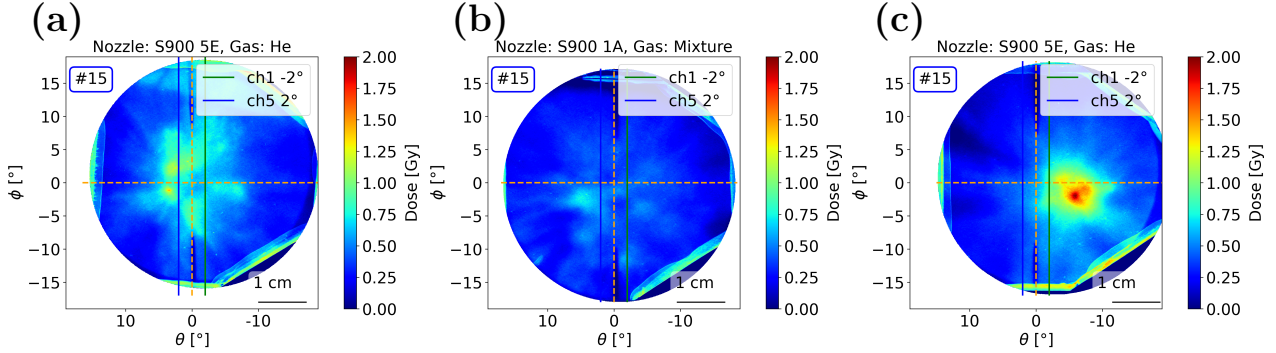
Fig. 4.35: Dose deposition on the 4th layer of the RCF stack for (a) shot #143 using the S900 5E nozzle & He, (b) shot #135 using the S900 5E nozzle & gas mixture and (c) shot #147 using the S900 5E nozzle & He.

The inhomogeneity in the dose distribution seen in Figs. 4.35a and b can be qualitatively linked to the strong angular energy variations observed in the spectra. Fig. 4.35c corresponds to another shot performed with the S900 5E nozzle & He, same as Fig. 4.35a. In this case a shifted hot spot is observed in the last stack layer. Since the laser axis was carefully monitored this shift should be related to physical processes like bending of the laser propagation in high density gas regions.

The RCF stack corresponding to the S900 2B nozzle & N_2 is plotted in Fig. 4.36. In this case the first layer hot spots aligned with the RCF horizontal axis and marked with red arrows quickly vanish through the stack and are no longer visible from layer #13. On the contrary, the hot spot located in the vertical RCF axis (marked with a yellow arrow in layer #1) is still clearly visible in layer #15 (see yellow arrow). Another vertical hot spot which starts to be visible in layer #4 (see green arrow) is also visible in the last RCF layer (see green arrow in layer #15). The low doses seen on the horizontal plane could be correlated with the relatively low and similar energies measured in the ch1 ($-2°$) and ch5 ($2°$) spectrometers, see Fig. 4.26c.

Finally, the RCF stack for the J2021 nozzle & He case is plotted in Fig. 4.37. Here a
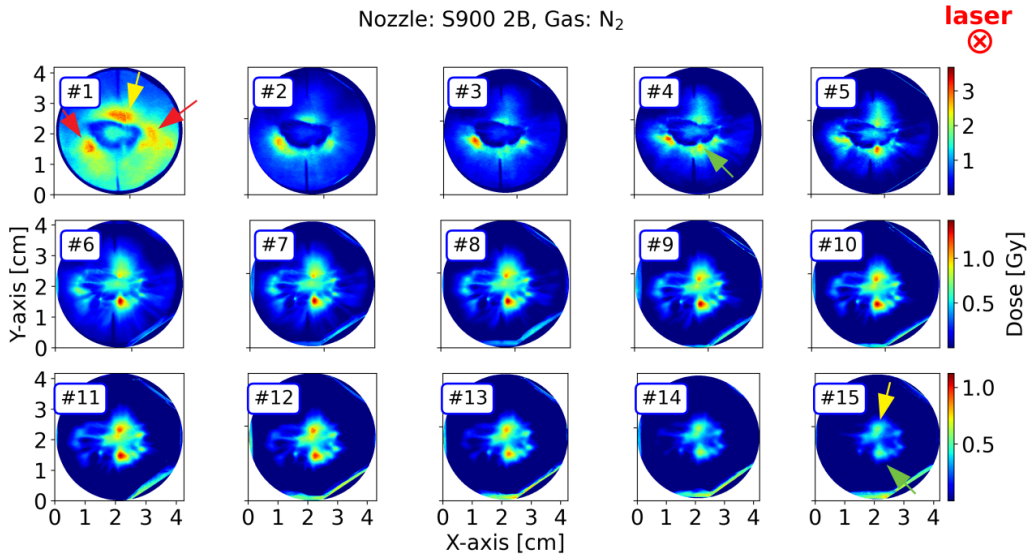
Fig. 4.36: RCF stack of shot #172 performed with the S900 2B nozzle & N_2.

single hot spot centered on-axis vanishes through the stack. A dose minima is seen on top of the hot spot, see white arrows in layer #3. Moreover, an emerging electron population is seen appearing in layer #7, see purple arrow, and by layer #9 two maxima and two minima are distinguishable (see purple and white arrows). These populations are still visible in layer #15 which could associate them with energetic electron beams accelerated in the forward direction.
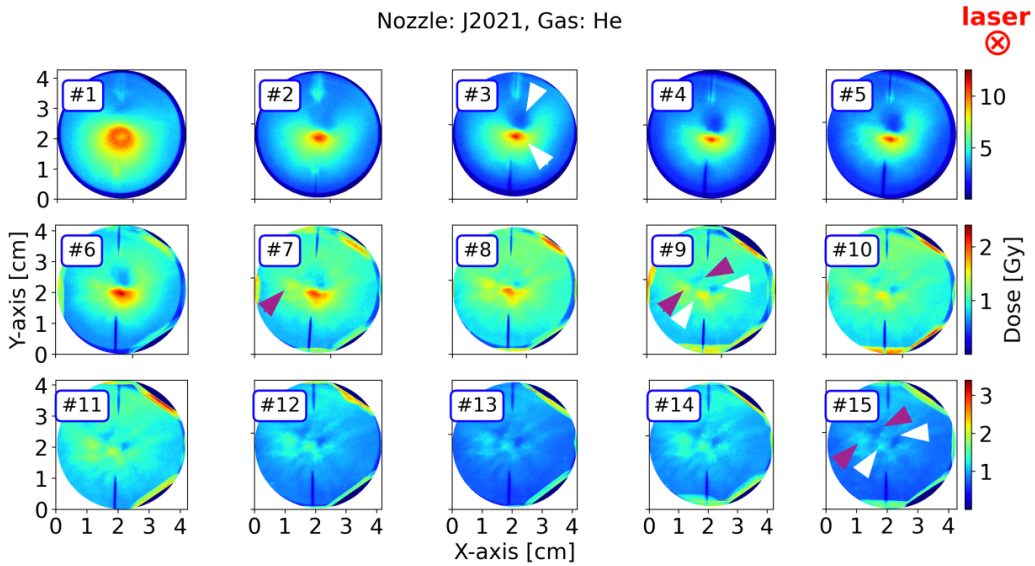
Fig. 4.37: RCF stack of shot #167 performed with the J2021 nozzle & He.

The vertically aligned dose minima and maxima seen in layers #9 and #15 resemble a feature seen in the VEGA-2 experiment, see RCF stack plotted in Fig. 4.7 corresponding to a gas mixture shot. Here the two hot spots are also matched with two dose minima located above them.

Optical interferograms

A. Raw optical interferograms acquired at early times

Fig. 4.38 shows the early time interferograms corresponding to $t < 35\,\text{ps}$. Fig. 4.38a corresponds to the S900 5E nozzle & He, Fig. 4.38b corresponds to the S900 2B nozzle & gas

mixture, Fig. 4.38c to the S900 2B nozzle & N_2 and Fig. 4.38d to the J2021 nozzle & He. The neutral density profiles are overlayed in orange, the laser focus plane is marked with a continuous green vertical line and the gas density peak with a dashed pink vertical line. Note that the laser focus, normally located at the gas density peak, was shifted to the gas up-ramp in some shots. By focusing before the gas density peak one expects the laser to self-focus and filament less during the up-ramp propagation hence increasing the possibilities of laser channeling through the density peak.

Fig. 4.38: Early time interferograms corresponding to probing times $t < 35$ ps corresponding to the (a) S900 5E nozzle & He, (b) the S900 1A nozzle and gas mixture, (c) the S900 2B nozzle & N_2 and (d) the J2021 nozzle & He. In each figure the corresponding neutral gas molecular density profile is overlayed in orange, the laser focus plane is marked with a continuous vertical green line and the gas density peak with a dashed pink vertical line.

In the S900 5E nozzle & He case plotted in Fig. 4.38a, a strong plasma self-emission is seen traversing the gas density peak. The dark region seen in the upper part of Figs. 4.38b-d corresponds to the nozzle's surface. In the S900 2B nozzle & gas mixture case the self-emission spots appear both before and after the gas density peak, see Fig. 4.38b. In the S900 2B nozzle & N_2 case they are only seen before the gas density peak, see Fig. 4.38c. In the J2021 nozzle & He interferogram plotted in Fig. 4.38d a plasma self-emission signal that is seen across the gas density peak. In this case the emission expands vertically and it is much more intense than in the S900 5E nozzle & He interferogram. We observe as well how the expanding plasma reaches the nozzle's surface (in this case the nozzle-shock interaction distance was about 250 µm). The self-emission intensity is certainly correlated with the higher maximum density in the J2021 nozzle & He case, see density profiles of Fig. 4.25d.

B. Raw optical interferograms acquired at late times

Fig. 4.39 plots the late time interferograms corresponding to probing times $t > 90$ ps, Fig. 4.39a corresponds to the S900 5E nozzle & He, Fig. 4.39b to the S900 1A nozzle & gas mixture,

Fig. 4.39c to the S900 2B nozzle & N_2 and Fig. 4.39d to the J2021 nozzle & He. As before, the corresponding neutral density profiles are overlayed in orange, the laser focus plane is marked with a continuous vertical line and the gas density peak with a dashed pink vertical line.
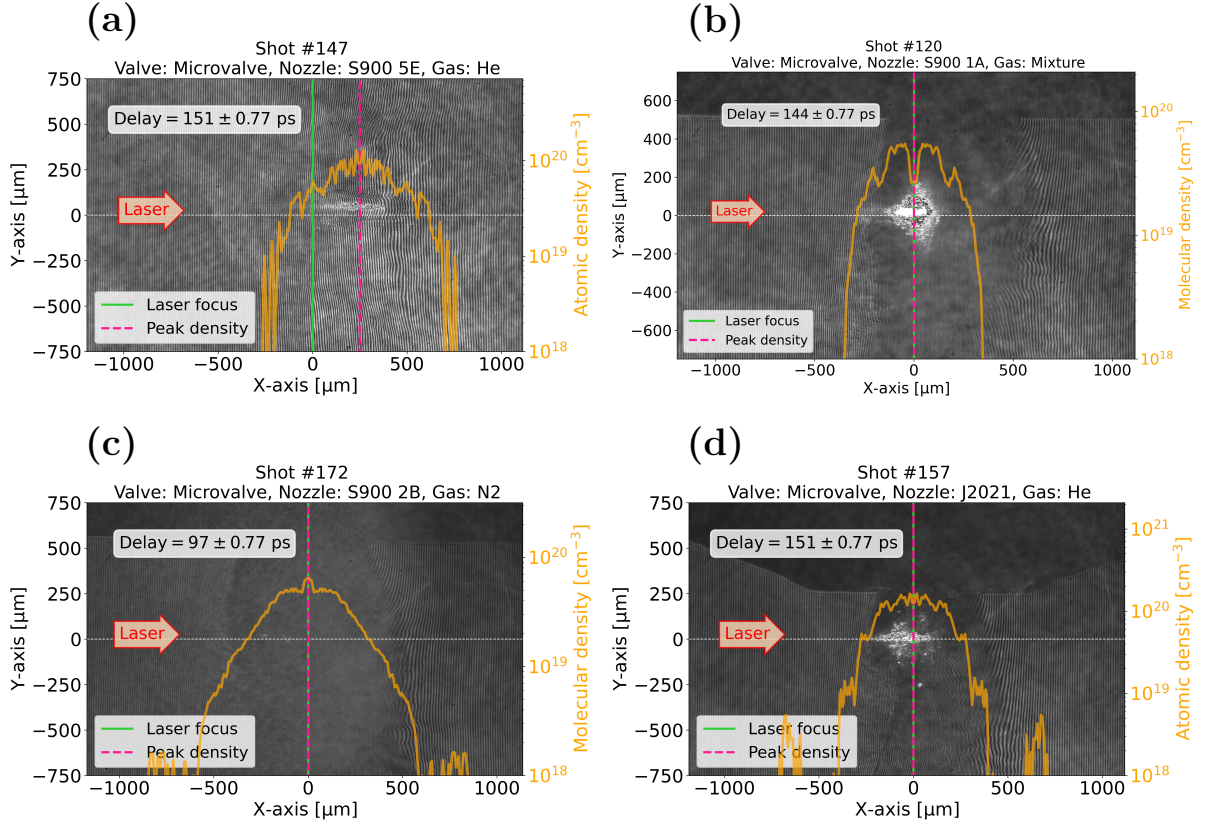
Fig. 4.39: Late time interferograms corresponding to probing times $t > 90\,$ps corresponding to the (a) S900 5E nozzle & He, (b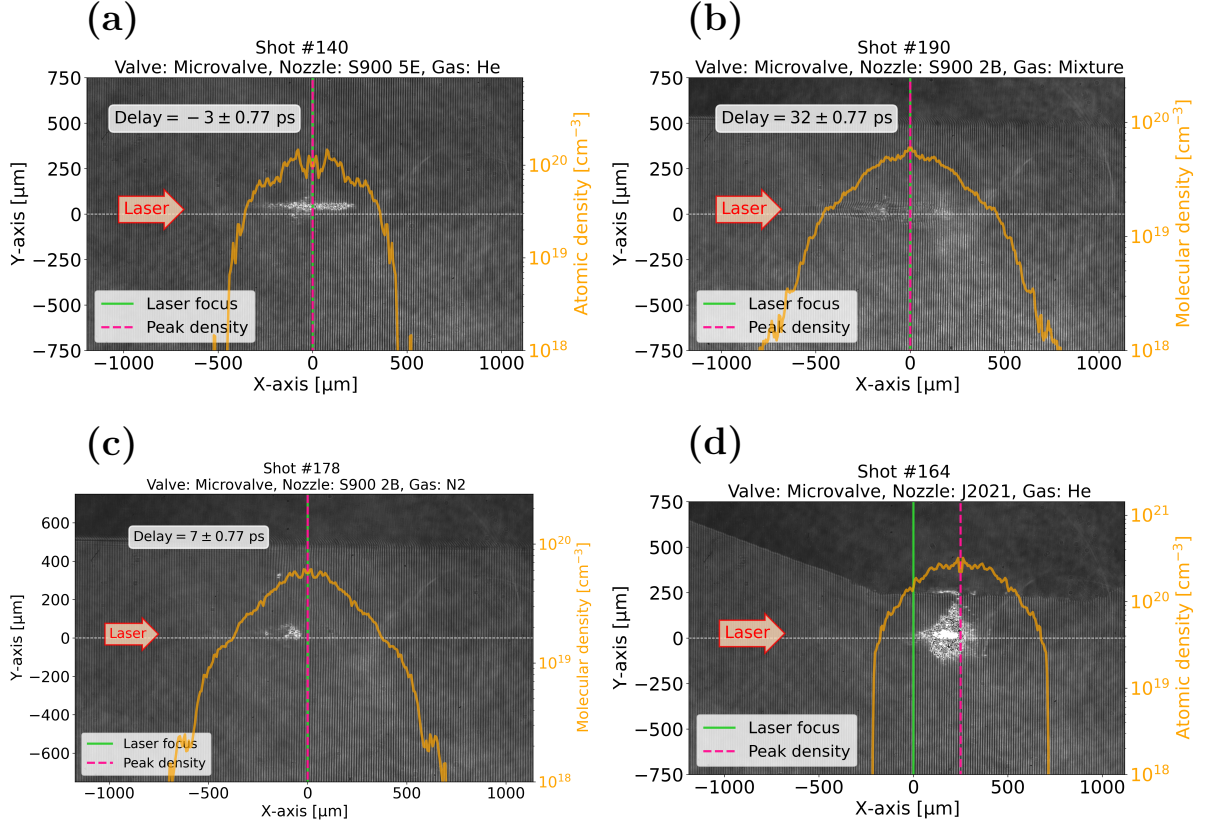) the S900 1A nozzle and gas mixture, (c) the S900 2B nozzle & N_2 and (d) the J2021 nozzle & He. In each figure the corresponding neutral gas transverse profile is overlayed in orange, the laser focus plane is marked with a continuous vertical green line and the gas density peak with a dashed pink vertical line.

In the S900 5E nozzle & He case (Fig. 4.39a) acquired at $t \approx 150\,$ps, two structures are clearly seen. Firstly, a conic shape originating in the top of the figure corresponds to the gas jet exiting the gas nozzle. Secondly, a channel is seen traversing the gas density peak (pink dashed line). The channel is about $200\,\mu$m wide in the vertical direction (y-axis) being the widest in its center ($x \approx 120\,\mu$m). In the x-axis direction it starts at $x \approx -200\,\mu$m and ends at $x \approx 500\,\mu$m for a total approximated channel length of $\approx 700\,\mu$m.

In the other three NGCs we observe a dense plasma column that connects the self-emission region on-axis with the nozzle's surface. We can only estimate this plasma column density to be higher than $\approx 10^{20}$ cm^{-3}, which is the density at which the probe beam will experience strong refraction in the density gradient, since this region is clearly opaque. The self-emission is much more intense in the cases where the gaseous target contains He and the laser-gas interaction took place at less than $500\,\mu$m from the nozzle's surface, i.e. in the S900 1A nozzle & gas mixture and in the J2021 & He cases plotted in Fig. 4.39b and Fig. 4.39d, respectively. In both cases the self-emission extends across the gas density peak. Note that in the S900 5E nozzle & He case of Fig. 4.39a the interaction took place at more than $750\,\mu$m from the nozzle's surface. In the S900 2B nozzle & N_2 case of Fig. 4.39c the on-axis self-emission is much weaker and located only before the gas density peak at $x \approx -250\,\mu$m.

C. Laser channeling across the density peak in low electron density He targets

The interferograms' data analysis was performed in collaboration with Pr. T. Pisarczyk, Dr. T. Chodukowski and Dr. Z. Rusiniak from the IPPLM institute (Warsaw, Poland). To obtain the phase distribution the method of *the maximum fringe* was applied [112–114]. The Fourier analysis could not be used due to the strong self-emission seen in almost all the late time interferograms. The axis of symmetry for the Abel inversion is that of the plasma channel or ionization region that traverses the gas density peak.

The formation of a laser ponderomotive channel that traverses the gas density peak was unraveled by deconvolving the S900 5E nozzle & He interferograms acquired at late probing times ($t > 90$ ps). This was seen for shot #147 and shot #148 plotted in Figs. 4.40a and b, respectively. In both panels we observe two radial expansion regions marked with white arrows in Fig. 4.40a. These regions are a convolution of the actual expansion regions with the conical gas jet (seen in the raw interferogram of shot #147 plotted in Fig. 4.39a). Their "butterfly" figure must then be carefully considered.

Fig. 4.40: Density charts obtained by deconvolving the raw interferograms at $t \approx 147$ ps of (a) shot #147 and (b) shot #147 corresponding to the S900 5E nozzle & He. The laser propagates from left to right.

The highest density regions are located at the expanding channel walls (see fuchsia arrow in Fig. 4.40a) which exhibit a vertical width of about $\Delta y_w \approx 30$ µm and a maximum density $n_{max} \approx 10^{19}$ cm^{-3} for shot #147 and $n_{max} \approx 10^{20}$ cm^{-3} for shot #148. In shot #147 the dense part of the channel walls extends longitudinally from $x \approx 100$ µm to $x \approx 300$ µm. In shot #148 the dense channel walls are shorter extending from $x \approx 200$ µm to $x \approx 300$ µm. This could linked to the more peaked density lineout of shot #148, see Fig. 4.25a.

In shot #147 (see Fig. 4.40a) the channel vertical width is about $y_t =\approx \pm 200$ µm. The latter is not constant being the widest at $x = 0$ which corresponds to the laser focusing plane ($x = 0$). The channel formed in shot #148 is thinner with a width of $y_t \approx \pm 150$ µm, which is maximum as well at the laser focusing plane. An oval density depleted region is observed at the end of the channel, see dashed circle in Fig. 4.40a. Such structure has been linked in other work to a magnetic vortex forming at the head of the channel [20] which expels all the electrons from within it.

Finally, in shot #148 we can distinguish a density structure in the gas down-ramp that has expanded both longitudinally and vertically, see fuchsia dashed circle in Fig. 4.40b. A density depletion area marked with a yellow arrow is also observed at its right side. Such structure could be linked to an electrostatic shell expanding in the gas down-ramp which could be accompanied by a magnetic field [30]. The density depleted longitudinal/bent regions inside the dashed circle could also correspond to magnetic filaments developing in the right plasma-

vacuum border. A polarimetry diagnostic needs to be fielded in future experiments to analyze these magnetic structures.

D. Single or multiple ionization areas appear in high electron density targets

The density charts obtained by deconvolving the raw interferograms of shots #134 and #135 are plotted in Figs. 4.41a and b, corresponding to the S900 1A nozzle & gas mixture at $t \approx 4$ ps. In both cases a single ionization region is seen traversing the gas density peak marked by a vertical pink dashed line. The ionization regions seen in both Figs. 4.41a and b exhibit a transverse width of about $y_t \approx \pm 100 \, \mu$m. In shot #134 the ionization regions are equally divided before and after the gas density peak. The highest density region where $n_{max} \approx 1.5 \times 10^{20}$ cm^{-3} is located about 150 μm after the density peak. In shot #135 the ionized region is located almost completely after the gas density peak with $n_{max} \approx 1.25 \times 10^{20}$ cm^{-3}.
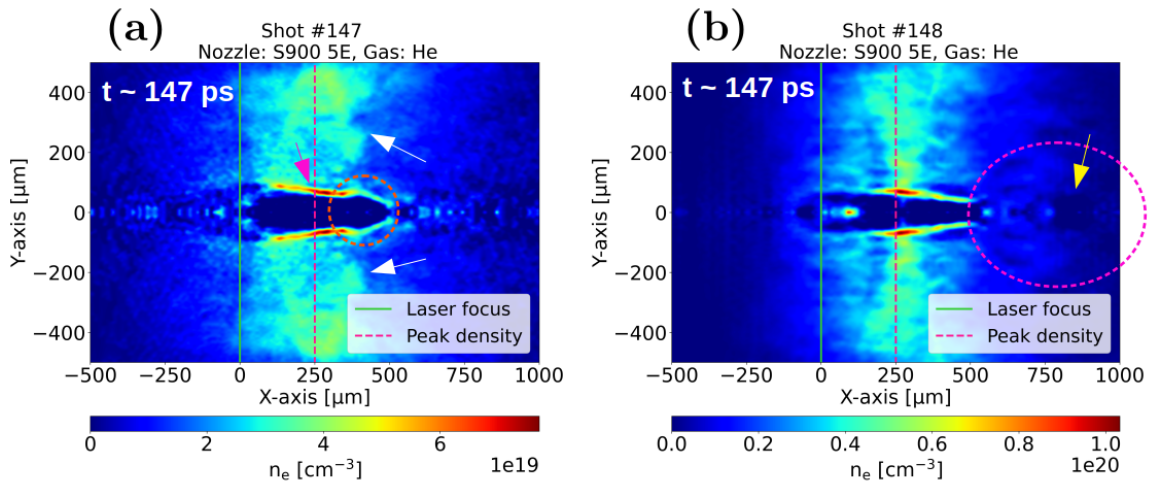

Fig. 4.41: Density charts obtained by deconvolving the raw interferograms $t \approx 4$ ps of (a) shot #134 and (b) shot #135 corresponding to the S900 1A nozzle & gas mixture. The laser propagates from left to right.

The density charts obtained by deconvolving the raw interferograms of shots #184 and #190 are plotted in Figs. 4.42a and b, respectively, at probing times $t = 13$ ps and $t = 28$ ps. In these shots the S900 2B nozzle & gas mixture was deployed. In both cases a large up-ramp ionization region extends from $x = -450 \, \mu$m to $x = -100 \, \mu$m. A second ionization spot is seen about 180 μm after the gas density peak. This ionization region is much smaller than the up-ramp one. The large separation between both ionization regions could link each of them to a different ionization mechanism. A first ionization process could be triggered in the gas up-ramp by the laser itself and be active up to $\approx 100 \, \mu$m before the density peak, where the laser is probably completely absorbed. The second ionization process could be triggered by the hot electron population energized in the up-ramp.

The large up-ramp ionization in the S900 2B nozzle & gas mixture case could be linked to the wider molecular density profile of longitudinal extension $x_t \approx \pm 1000 \, \mu$m (Fig. 4.25d) while the single ionization region of the S900 1A nozzle & gas mixture case occurs in a much thinner molecular density profile with $x_t \approx \pm 500 \, \mu$m (Fig. 4.25a).

These ionization areas are probably precursors of a ponderomotive channel that should form as a result of their transverse expansion.

Streaked plasma self-emission

The plasma self-emission was temporally streaked using the bottom view imaging system and the C7700 Hamamatsu streak camera. In Fig. 4.43 the on-shot raw interferogram (top) and acquired self emission (bottom) are plotted together for the S900 5E nozzle & He (Fig. 4.43a
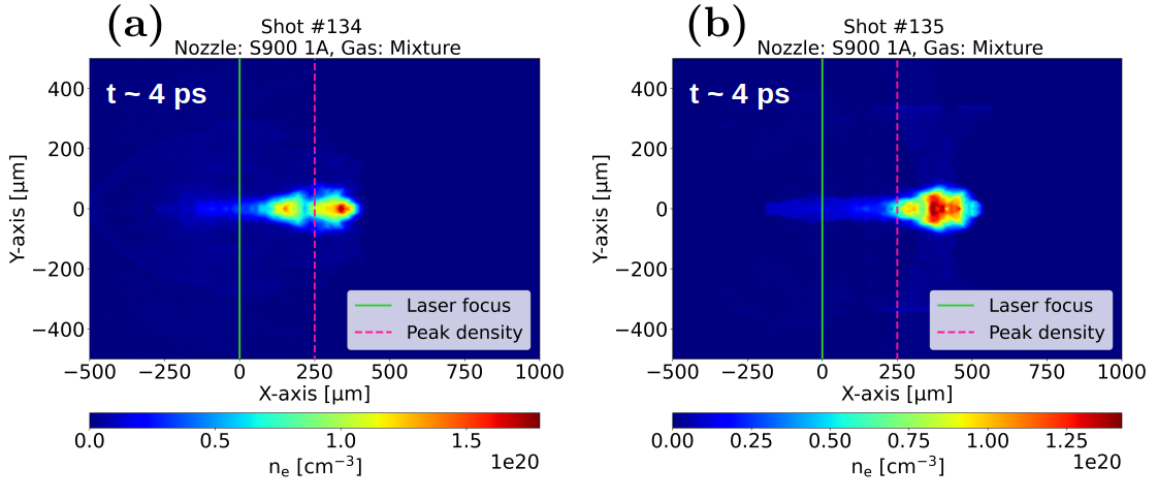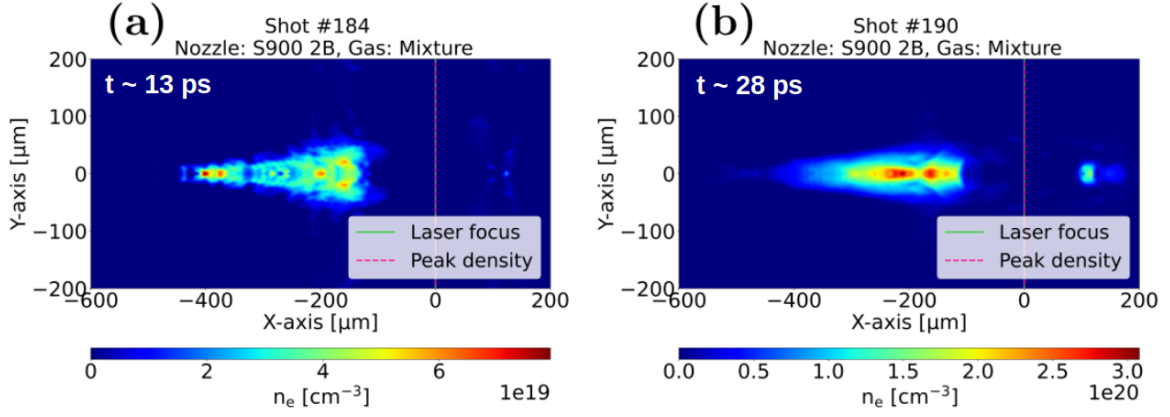
Fig. 4.42: Density charts obtained by deconvolving the raw interferograms of (a) shot #184 and (b) shot #190 performed using the S900 2B nozzle & gas mixture. The laser propagates from left to right.

and c) and for the S900 2B nozzle & N_2 (Fig 4.43b and d). The plasma self-emission signals appear frozen in time which means that their duration is much shorter than the resolution of the sweep with a 1 ns streak window.

In the S900 5E nozzle & He case plotted in Fig. 4.43a a single plasma self-emission hot spot appears at the gas density peak (marked with a vertical dashed pink line). In the S900 2B nozzle & gas mixture plotted in Fig. 4.43b four different hot spots appear both in the gas up and down-ramp.

The self-emission hot spots are correlated with areas of strong laser-gas interaction. Hence, in the S900 5E nozzle & He the strongest laser-gas interaction takes place in the gas density peak. In the S900 2B nozzle & gas mixture case it appears that there are several high-intensity interaction hot spots both before and after the gas density peak.

While propagating through a high density gas up-ramp several non-linear effects including laser self-focusing will occur [142]. The hot spots seen in the S900 2B nozzle & gas mixture case could be interpreted as different laser self-focusing locations. Note that the power threshold for laser self-focusing $P > 17\,\mathrm{GW}$ is largely exceeded here.

4.3.6 Summary of main results

During the gaseous target shots we deployed two different shock nozzles: the S900 and the J2021. The gases that were used were He, N_2 and a 9/1 N_2/He mixture, same as in the VEGA-2 campaign. The shot-to-shot gas profiles of the different nozzle-gas combinations (NGCs) can be seen in Figs. 4.25a-d

The electron acceleration was characterized by fielding three electron spectrometers labeled as channels 1 (ch1), 2 and 5 (see Table 4.3) located at $-2°$, $21°$ and $2°$ from the laser axis, respectively. Note that negative angles correspond to clockwise rotations. It was seen that the presence of He in the gas favors high electronic energies and temperatures on-axis. The highest electronic energies of $45\,\mathrm{MeV}$ and temperatures of $T_e \approx 13\,\mathrm{MeV}$ were obtained with the S900 5E nozzle & He, see electron spectra of Fig. 4.26a. The obtained T_e values are about six times higher than the *ponderomotive scaling* ($\epsilon_h = (\sqrt{1 + a_0^2/2} - 1)m_e c^2$) which is indicative of the strong electron heating of the gaseous target in the near critical regime [30]. The highest electron energies measured at $-2°$ from the laser axis are drastically higher than the energies measured at $2°$ for all NGCs. Hence, the accelerated electron beams are probably highly directional and collimated.

The ion acceleration was characterized using both the three-pinhole Thomson parabola (TP)
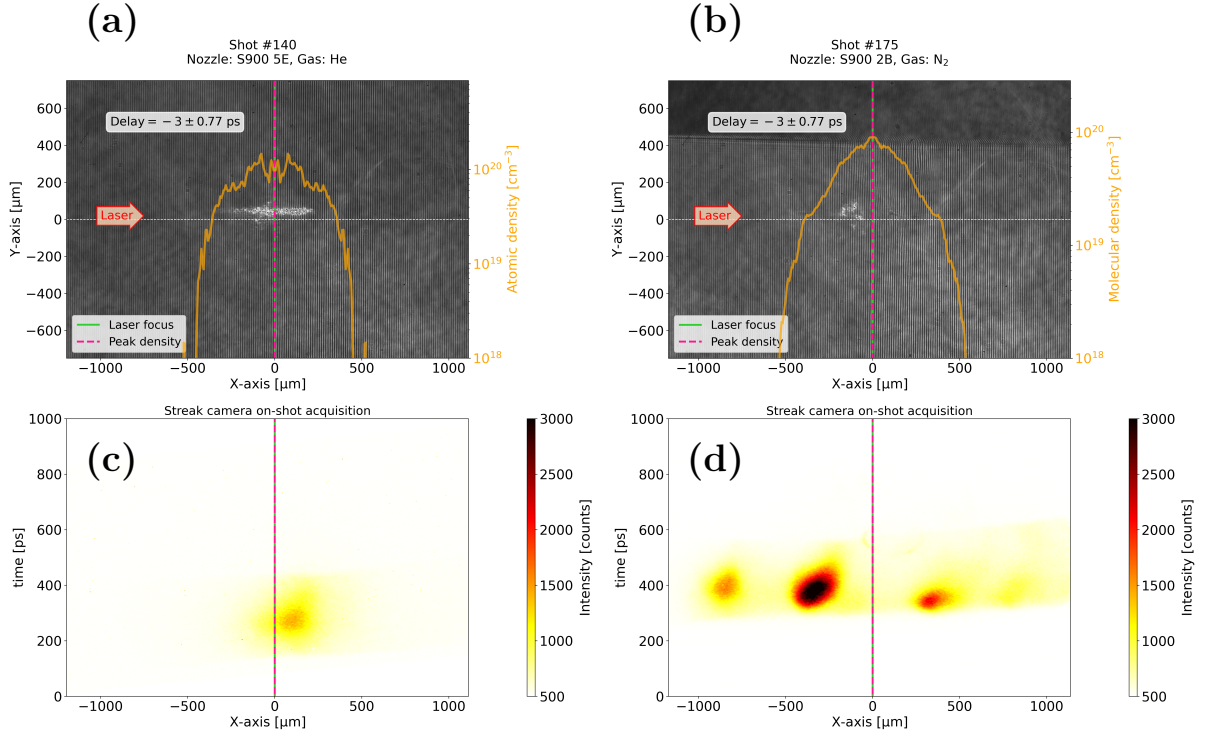
Fig. 4.43: (a) On-shot raw interferogram for the S900 5E nozzle & He and for the (b) S900 2B nozzle & N_2. (c) Corresponding on-shot streak camera acquisition for the S900 5E nozzle & He and for the (d) S900 2B nozzle & N_2.

at 0° located at 100 mm from TCC and the LINA TP located at $-110°$ and at 250 mm from TCC, see the experimental setup of Fig. 4.18. At the same time, five different ToF diamond detectors were located in the forward direction in a $\pm 17°$ cone with respect to the laser axis and in a 9° inclined plane.

There was no ion signal in none of the two Thomson parabolas fielded during the experiment, with none of the nozzles and gas combinations. The only visible signal in the IPs came from the X-ray zero deflection points. The TPs energy detection limits were studied by analyzing: the low background level, the signal-to-noise ratio found to be $S/N \approx 10$, the electric and magnetic deflections of each TP at the specified distances from TCC and the IP TR particle energy detection limits taking into account a 5 μm aluminized mylar filter and the fact that the three-pinhole TP was successfully tested before gaseous shots. The minimum detectable α particles' energy was found to be of 1.5 MeV and for nitrogen ions of 6 MeV, for both TPs. The energy detection bottle neck is the IP TR and its aluminized mylar filter sensitivity. It could be that there is emission on the laser propagation plane but that it is of particles with energy lower than the minimum energy detectable by the TPs or that the particle number is too low to be detected by the IP TR plus aluminized filter sensitivity. Other possibility is that there is no emission in the TPs' small solid angles and that the emission is directed away from the laser propagation plane. The absence of signal in the TPs located on the laser propagation plane was also observed during the VEGA-2 experiment [109] using a Lanex screen as TP imager.

Hereinafter we refer to ToF ion acceleration results. Using the S900 5E nozzle & He we measured up to 2.5 MeV of α particles at 17° from the laser axis with $\approx 10^{11}$ part./(MeV sr) at 500 keV, see ion energy spectra of Fig. 4.27a. With the S900 2B nozzle & N_2 we acquired maximum nitrogen ion energies of 90 MeV away from the laser axis, at 5° and 17° with $\approx 10^{14}$ part/(MeV sr) at 500 keV, see Fig. 4.27b. We also measured nitrogen ions up to 9 MeV on-axis in a 9° inclined plane with $\approx 10^{14}$ part/(MeV sr) at 500 keV. Finally, using the J2021 nozzle & He gas, see Fig. 4.27c, we measured α particles up to 2 MeV at $-17°$ from the laser axis $\approx 10^{11}$

part/(MeV sr) at 500 keV.

The most energetic ion acceleration was seen at $\pm 17°$ for α particles and at 5° for nitrogen ions. On-axis ion acceleration was not measured for α particles while nitrogen ions up to 80 MeV were measured at 0° (in a 9° inclined plane).

A radiochromic film (RCF) stack composed of a 10 μm layer of Al, five layers of U-EBT3 RCF film and ten layers of EBT3 film was placed on-axis at 60 mm from TCC. In order to clarify the contribution of both ions and electrons to the dose deposition signal Monte Carlo simulations of the energy loss of α particles, nitrogen ions and electrons through the stack were performed. Taking as a reference the maximum ion energies measured in the ToF detectors: 2.5 MeV for α particles and 90 MeV for nitrogen ions, and looking at the Monte Carlo simulations' outputs we expect the RCF signal to be mainly due to electrons of energies lower than 2 MeV. The ionic contributions are most likely limited to the first three RCF layers.

In the S900 nozzle & He or gas mixture cases the hot spots located in the horizontal axis, which coincides with the laser polarization one, can be linked to electrons of $\mathcal{E} \approx 2$ MeV. At the same time the inhomogeneity seen in the last layers dose deposition could be qualitatively linked to the angular variations observed in the electron spectra.

In the S900 nozzle & N_2 case the most energetic electrons are located in the vertical axis. At the same time, the low and constant doses seen in the horizontal axis can be correlated with the relatively low energies measured at 2° and $-2°$, see electron spectra of Fig. 4.26c.

In the J2021 nozzle & He case we observe hot spots in the horizontal axis which are accompanied by vertically aligned dose minimums above them. A similar feature was observed in the VEGA-2 experiment, see the RCF image of Fig. 4.7 (corresponding to a gas mixture shots).

Finally, as was detailed in Section 4.3.5.2, both the S900 5E nozzle & He (see Fig. 4.25a) and the S900 1A nozzle & gas mixture (see Fig. 4.25c) exhibit the thinnest transverse gas density profiles among the S900 nozzles of approximately $x \approx 1000$ μm. The S900 2B nozzle transverse profiles (see Fig. 4.25b) exhibit an almost double transverse width of about $x \approx 2000$ μm (due to shot-shot-shot nozzle damage). On one hand, the thinnest transverse profiles seem to favor dose deposition signatures characterized by a dose depletion on-axis and hot spots aligned along the horizontal direction, see Figs. 4.31a and b. On the other hand, wide transverse density profiles like those corresponding to the S900 2B nozzle & N_2 are connected with multiple dose deposition areas of less intensity, see Fig. 4.31c. These imprints are not aligned with the RCF horizontal or vertical axes. Finally, denser gas profiles such as the J2021 nozzle & He ones (see Fig. 4.25d) produce hot spots near the horizontal RCF axis which are accompanied by dose minimums, see Fig. 4.31d.

A strong plasma self-emission signal is seen traversing the gas density peak in the raw optical interferograms acquired at early times $t < 35$ ps for the S900 5E nozzle & He case plotted in Fig. 4.38a. In the S900 2B nozzle & N_2/gas mixture cases (see Figs. 4.38b and c) self-emission spots are also visible although they are isolated and do not form a continuous emission line. In the J2021 nozzle & He interferogram plotted in Fig. 4.38d we observe an intense self-emission signal which crosses the gas density peak while expanding vertically. The self-emission strong intensity could be correlated with the higher maximum density in the J2021 nozzle & He case.

In the S900 5E nozzle & He case the late time ($t > 90$ ps) interferogram plotted in Fig. 4.39a unraveled a laser channel across the gas density peak. In the other three cases: S900 5E nozzle & gas mixture (Fig. 4.39b), S900 2B nozzle & N_2 (Fig. 4.39c) and J2021 nozzle & He (Fig. 4.39d) we observe the formation of a dense opaque plasma column that connects the self-emission region on-axis with the nozzle surface. The self-emission remains much more intense for the cases where He is inside the gaseous target: i.e. in the S900 1A nozzle & gas mixture and in the J2021 & He cases plotted in Fig. 4.39b and Fig. 4.39d, respectively.

The mentioned laser channel was clearly seen in the deconvolved density charts for shot #147 (see Fig. 4.40a) and shot #148 (see Fig. 4.40b) performed with the S900 5E nozzle &

He. The channels are about 200 μm wide and the widest channel transverse section coincides with the laser focus plane. The maximum density regions are located at the channel walls. The channels are 500 μm large. At the front of the channel formed in shot #147 we observe an oval electron depleted structure that could be link with a magnetic vortex, see dashed circle in Fig. 4.40a. In shot #148 the oval shape disappears and in its place we observe an electron density structure that expanded longitudinally and vertically and a density depletion area at its right extreme (see dashed circle and yellow arrow in Fig. 4.40b). This structure could be linked to an electrostatic shell expanding in the gas down-ramp [30]. The density depleted longitudinal areas seen in the right gas boundary could also be traces of magnetic filaments created by the electron return currents. To assess this feature a polarimetry diagnostic must be fielded in future experiments.

When using the S900 1A nozzle & gas mixture a single ionization region is seen traversing the gas density peak marked by a vertical pink dashed line, see density charts of Figs. 4.41a and b. This is probably the same regime encountered in shot #63 performed in pure He in the VEGA-2 campaign, see Figs. 4.3a and b. Using the S900 2B nozzle (which exhibits wide transverse profiles, see Fig. 4.25a) & gas mixture two separate ionization areas are observed. A first large ionization area before the gas density peak and a second much smaller one after the gas density peak. The large separation between both ionization regions of more than 300 μm could be correlated with two different ionization mechanisms giving birth to each region. The first one could be laser-driven and the second one triggered by the up-ramp hot electron population expanding into the colder and more rarefied down-ramp. These ionization regions should precede the formation of a ponderomotive channel form from their transverse expansion.

Finally, the plasma self-emission was temporally streaked using the bottom view imaging system and a streak camera. In the S900 5E nozzle & He case plotted in Fig. 4.43a a single plasma self-emission hot spot appears at the gas density peak (marked with a vertical dashed pink line). In the S900 2B nozzle & gas mixture case plotted in Fig. 4.43b four different self-emission hot spots appear both in the gas up and down-ramp. The self-emission hot spots are linked with areas of strong laser-gas interaction. In the S900 5E nozzle & He plotted in Fig. 4.43a the strongest laser-gas interaction takes place in the gas density peak. In the S900 2B nozzle & gas mixture case plotted in Fig. 4.43b, hot spots located before and after the gas density peak could be correlated with non-linear laser self-focusing occurring while the high intensity laser traverses the gas up-ramp [142].

Chapter 5

2-D PIC numerical simulations for the laser-plasma interaction conditions for the VEGA-3 experiment

5.1   Introduction

The present chapter details a series of 2-D PIC simulations performed with the CALDER code to explain the experimental observations in pure He targets during the VEGA-3 campaign (see Chapter 4 for a comprehensive description of the experiment's results).

Section 5.2 recapitulates the simulation's parameters including the laser intensity profile and longitudinal density profile which were extracted from experimental measurements to reproduce as much as possible the experimental conditions. The physical processes triggered during the laser propagation through the gas up-ramp are explained in Section 5.3 including the strong heating of the plasma, the laser channeling and filamentation and the electron acceleration mechanisms that operate within the ponderomotive channel. Following a chronological order, Section 5.4 describes the expansion of the hot plasma that has been energized in the target up-ramp into the rarefied cold down-ramp. Special attention is paid to the channeling across the gas density peak as well as to the creation of an azimuthal magnetic field (B-field) at the right-side plasma-vacuum interface (PVI). The latter is a result of the interplay between the hot electrons that exit the target and the return currents (partly made of hot electrons) that are dragged back into the plasma core due to the charge separation sheath field formed at the PVI. Section 5.5 details the obtained electron energy-angle distributions. Section 5.6 reviews the transverse and longitudinal ion acceleration mechanisms being triggered at times $t \gg \omega_{pi}^{-1}$, when the ions start to react to the charge separation fields created within the plasma as well as at the PVI. We show that ions can be accelerated to the MeV-range energies by both radial shock and TNSA at the right hand side PVI. We describe as well how the azimuthal B-field created at the PVI can deviate a part of the TNSA-accelerated ions up to $\pm 45°$ exiting angles. The latter process can be linked to the experimental observation of α particles being emitted at $\pm 17°$ from the laser axis in a $9°$ inclined plane. Finally, Section 5.7 summarizes the main features issued from the numerical simulation and Section 5.8 performs a constructive comparison with a similar simulation presented in Ref. [30] with the objective of finding experimental paths prone to forward collisionless electrostatic shock acceleration (CSA) of ions.

5.2   Simulation parameters: Interaction of the VEGA-3 laser pulse with a pure helium gas target

In the following and unless explicitly marked differently, the same normalized units system used in Chapter 3 is applied (a table with physical units conversions is found in Appendix B). The presented 2-D simulation describes the interaction of a laser pulse characterized by a dimensionless laser amplitude $a_0 = 6.9$ ($I_{max.} = 10^{20}$ W/cm^2), a laser wavelength $\lambda_L = 0.8\,\mu$m, a $\tau_L = 100\,$fs FWHM pulse duration and a focal spot diameter $D_L = 15\,\mu$m (FWHM), corresponding to a set of VEGA-3 laser parameters measured during the experiment described in Chapter 2. The laser is linearly polarized along the y-axis and it is injected along the x-axis from the left-hand side of the simulation box and focused at the gas density peak. In the actual experiment the laser was focused in the target up-ramp, $250\,\mu$m before the gas density peak, this configuration was also simulated and it is discussed in Section 5.3.2.
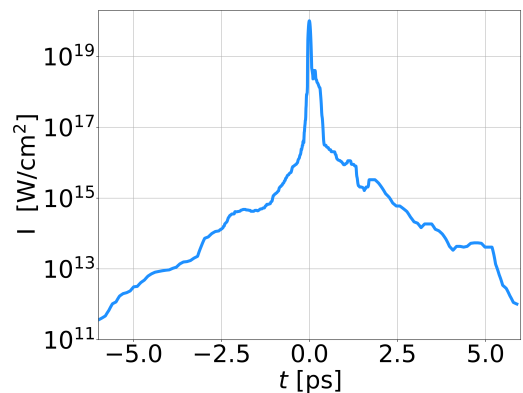
Fig. 5.1: Laser intensity profile used in the 2-D simulation with $I_{max.} = 10^{20}$ W/cm^2 in the ± 6 ps time range extracted from experimental measurements.

The laser intensity profile was extracted from experimental measurements and it is plotted in Fig. 5.1 in a ± 6 ps around the laser peak. It is composed of the main laser pulse starting at $I_L \approx 10^{17}$ W/cm^2 and a prepulse with $I_L < 10^{17}$ W/cm^2. The intensity down-ramp (located at $t > 0$) will interact with an already ionized target.

The temporal and spatial resolutions were 0.285 ω_0^{-1} (0.15 fs) and 0.3 c/ω_0 (0.047 µm), respectively. The modeled gaseous target was pure helium (initially neutral) with maximum atomic density $n_{at.} = 0.1 \ n_c = 10^{20}$ cm^{-3}. Its longitudinal density profile (along x) was extracted from an experimental measurement and kept constant along y. Fig. 5.2a shows the input atomic density profile (see dark red solid line, corresponding to a lineout obtained at $\approx$ 750 µm height from the nozzle's surface) while Fig. 5.2b plots the corresponding 2-D ion density chart, here the gas density peak is marked with a pink dashed line. Both impact field induced ionization and Coulomb collisions between all charged particles were considered. Absorbing boundary conditions were applied for fields and particles. Each cell initially contained 2 particles of each species. The initial ionic temperature was $T_i = 1$ eV.
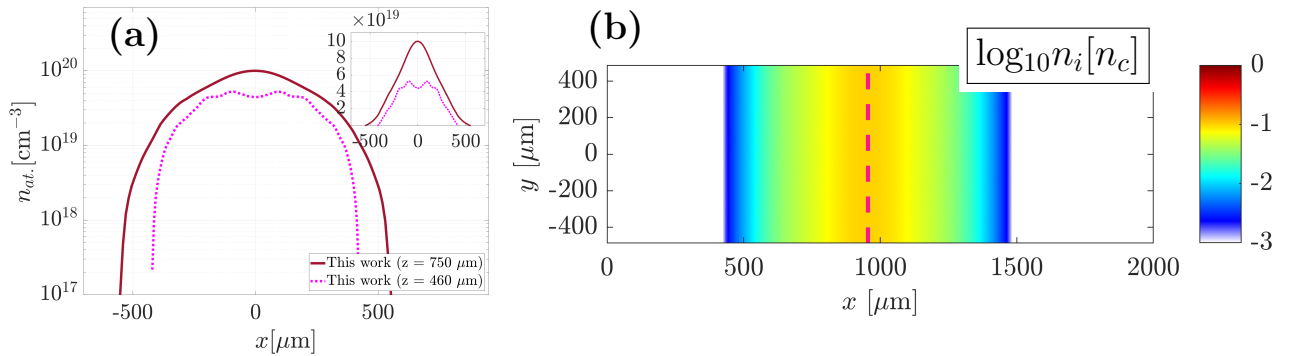
Fig. 5.2: (a, solid line) Atomic density profile of the pure helium target considered in the 2-D simulation. The density scale length at the gas wings is $L_n \approx 100$ µm and close to the gas density peak it is $L_n \approx 340$ µm. This lineout was obtained in the experiment at ≈ 750 µm from the nozzle's surface. (a, squared-dotted line) Longitudinal lineout obtained at ≈ 460 µm from the nozzle's surface. The inset shows the same density profiles plotted using a linear scale in the y-axis. (b) 2-D pure helium ion density chart used in the simulation with maximum atomic density $n_{at} = 0.1 \ n_c$ (10^{20} cm^{-3}). The longitudinal density profile corresponds to the solid line in (a) while the transverse density profile was considered constant.

5.3 Laser propagation through the gas up-ramp

Figures 5.3a-c show 2-D maps of the instantaneous B_z magnetic field (mainly composed of the laser field but also of quasistatic self-induced plasma fields) at times $t = 7.85$ ps, $t = 8.76$ ps and $t = 9.37$ ps and Fig. 5.3d-e the free electron density n_e at the same time steps. The gas density peak is marked with a pink dashed line in all figures. Note that in Fig. 5.3a the main laser pulse is centered at $x \approx 500$ µm and the laser prepulse is located at $x > 500$ µm. According to the 1-D scaling presented in Ref. [30], the laser should be able to cross the helium target.

The gaseous target starts at $x \approx 500$ µm as seen in Fig. 5.2b. Therefore, by $t = 7.85$ ps, the laser prepulse has already partially ionized the gas up-ramp, as seen in Fig. 5.3d. At $t = 8.76$ ps, see Fig. 5.3b and e, two ionization dynamics are distinguishable. A weaker laser-prepulse ionization wave at $x > 800$ µm and a stronger main-pulse-induced ionization wave at $x < 800$ µm.
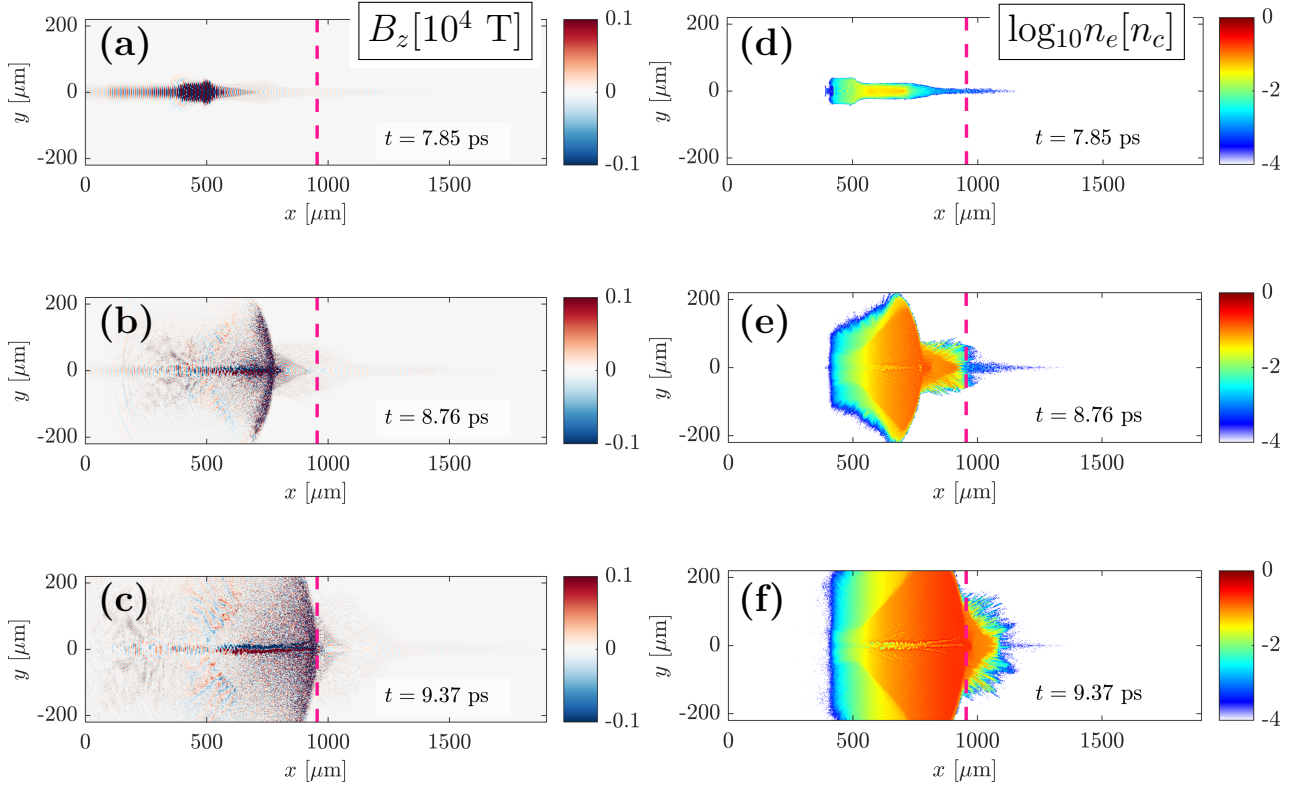
Fig. 5.3: (a-c) B_z instantaneous magnetic field and (d-f) free electron density n_e at successive instants in the laser-gas interaction. The pink dashed lines mark the location of the gas density peak.

5.3.1 Plasma heating: premature laser absorption

Figure 5.4 shows the laser energy absorption with respect to time. The instants when the laser intensity peak reaches the left and right gas boundaries are marked with vertical black solid lines and the instant when it arrives at the gas density peak is marked with a pink vertical dashed line. As can be seen, the absorption curve reaches a 99% when the laser pulse crosses the density peak and stagnates at 98.5% when the pulse exits the gas. The laser is almost completely absorbed by $t \approx 10$ ps, right after crossing the gas density peak.

A non-linear plasma wakefield is triggered in the low density up-ramp of the gaseous target as can be appreciated in the electron density n_e chart of Fig. 5.5a captured at $t = 8.16$ ps. The longitudinal E_x field associated with the plasma wakefield is plotted in Fig. 5.5c and the corresponding E_y laser field chart is depicted in Fig. 5.5b. Since laser pulse is larger than the local plasma wavelength ($c\tau = 30\,\mu\text{m} > 28\,\mu\text{m}$) the wakefield

Fig. 5.4: Absorbed fraction of the laser energy as a function of time (yellow solid line). The instants when the front of the laser pulse arrives to the left and right gas boundaries are marked with vertical black solid lines and the instant when it traverses the gas density peak is marked with a pink vertical dashed line.

is generated at the head of the beam for $n_e > 0.04\,n_c$ [161]. The energy transfer from the laser to the wakefield depletes the laser front, steepening the laser profile into a so-called *optical shock*, thereby increasing its longitudinal ponderomotive force (see Ref. [30] and references therein).

Figure 5.6a shows the electron (x, p_x) phase space integrated in the transverse direction
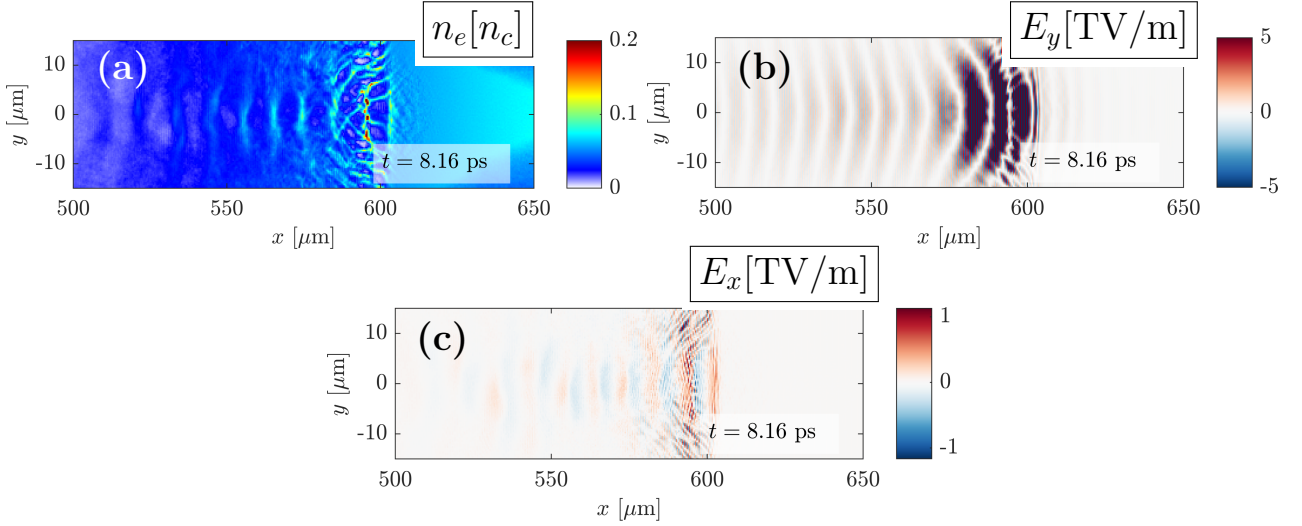
Fig. 5.5: Non-linear plasma wakefield triggered in the low density up-ramp of the gaseous target. (a) Laser-driven wakefield as seen in the electron density n_e chart taken at $t = 8.16\,\text{ps}$, (b) longitudinal E_x field associated to the plasma wakefield is plotted and (c) E_y laser field chart.

at $t = 8.46\,\text{ps}$, while the laser pulse is propagating through the target up-ramp, see laser absorption rate curve of Fig. 5.4. The laser intensity peak is located at $x \approx 690\,\mu\text{m}$. Figure 5.6b is a zoom of Fig. 5.6a centered behind the laser pulse intensity peak ($x \approx 700\,\mu\text{m}$). In Figs. 5.6a and b two electron currents can be distinguished. Firstly, a hot electron current composed of the rightward-moving electrons moving accelerated in the plasma wakefield (Figs. 5.5a-c). Secondly, a cold electron current which is initially accelerated by the laser itself (see black arrow in Fig. 5.6b) and then dragged back by the charge separation field. This return current is accelerated up to $p_x \approx -20\ m_e c$, see Fig. 5.6b. The breaking of the plasma wakefield has occurred earlier in the interaction and hence the two electron streams have already started phase mixing (see Chapter 3). Since the laser has been almost fully absorbed right after the gas density peak, the hot electron population that was energized in the target up-ramp will be in charge of heating all the target down-ramp. This are not optimal conditions for target heating since the up-ramp hot electron population is probably not energetic enough to strongly heat the gas down-ramp. Note that a hot down-ramp would yield a large sound speed C_s and hence fast CSA-driven ions. Lets discuss then how the target heating process could be improved.
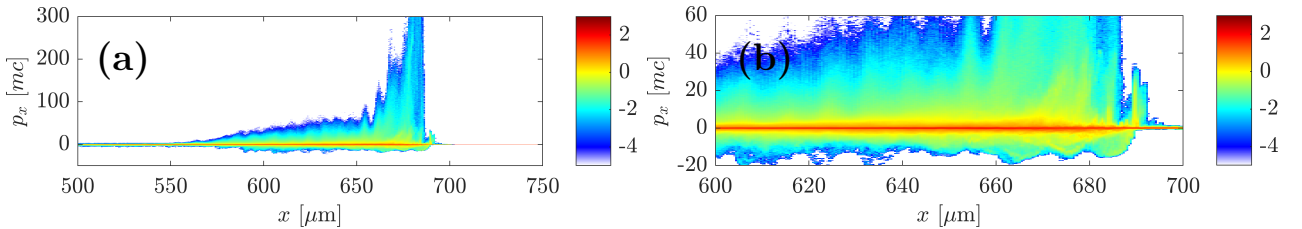
Fig. 5.6: (a) Electron (x, p_x) phase space integrated in the transverse direction at $t = 8.46\,\text{ps}$ and (b) zoom of (a) centered behind the laser pulse intensity peak ($x \approx 700\,\mu\text{m}$).

5.3.1.1 Improving the plasma heating process

To improve the plasma heating process one must deposit the highest amount of laser energy in the gas up-ramp and the beginning of the down-ramp during the laser propagation through the target density peak. This must be done in a turbulent electron energization regime characterized by a steep laser absorption curve. Hence, aiming at an optimal plasma heating scenario one would need the laser pulse to cross the gas density peak before it is completely absorbed.

There are two ways of modifying the gaseous' target density profile so as to allow the laser to reach the gas density peak before it is completely absorbed. One could think of diminishing uniformly the gas density to allow the laser to propagate deeper in the down-ramp. In this case the laser energy absorption curve of Fig 5.4 would be shifted to the right. To obtain a similar outcome one could also shorten the density profile along x.

Since the 3-D density profiles are expected to be created by rotating the 2-D density profile around its symmetry axis ($x = 0$, see Fig. 5.2a), shortening of the gas profile along x, i.e. the laser propagation direction, will translate into a similarly reduced transverse dimension of the profile (along the y direction, perpendicular to the laser propagation axis). Experimentally, the shortening of the gas profile along x could be realized by changing the gas nozzle or by shooting closer to the nozzle's surface. Note that the gas exiting the nozzle has a conic shape so the transverse profiles' dimension increases when increasing the distance from the nozzle's surface to the shot ordinate. However, shooting closer to the nozzle also entails greater nozzle damage and affects the repetition-rate operation of the experiment [70]. The maximum electronic density n_e can be lowered by either changing the gas to one with a lower Z^* or by modifying the gas compressor backing pressure (P), the gas electrovalve opening time (VOT) and/or the temporal delay between the aperture of the gas valve and the laser arrival (CD), as explained in Chapter 4.

In our specific experimental conditions, $n_e \approx 0.2\ n_c$ was the lowest atomic density, at the density peak, achievable with our high-pressure gas system (HPGS) using helium gas. The experimental density profile (plotted in Fig. 5.2a using a solid line) was obtained at $\approx 750\,\mu m$ below the nozzle's surface. During the experiment we had a limited amount of nozzles so we tried to interact as further as possible from the nozzle to diminish its damage per shot. As a consequence the obtained density profile is about $1\,mm$ wide in both x and y directions. Figure 5.2 shows as well the density lineout obtained $\approx 460\,\mu m$ away from the nozzle's surface (squared-dotted line). By shooting at this distance, one would have obtained a density profile with an $\approx 800\,\mu m$ extent along x and y (which entails a 20% reduction in both transverse and longitudinal dimensions with respect to the profile obtained at $\approx 750\,\mu m$ and shot during the experiment) and a $\approx 40\%$ reduction in the maximum density. This could be a fast solution if one considers replacing the nozzle at least every 2 to 3 shots.

Furthermore, the *phase mixing* scenario described in Ref. [30] needs the forward and return electron currents to spatially overlap. The laser focal spot should then be larger that the plasma wavelength. One could either enlarge the laser focal spot by focusing it with a longer focal length parabola or by locating the gaseous target ahead of the focal plane. The other possibility is to work at higher energy facilities that can deliver the same laser intensity with a larger focal spot.

5.3.2 Laser channeling and filamentation

A laser ponderomotive channel begins to form before the laser pulse maximum reaches the gas density peak (Fig. 5.7a). Laser channeling, also referred to as plasma cavitation, occurs due to the ponderomotive expulsion of electrons from the laser propagation path. At this stage, laser filamentation has also started and the initial single central channel has divided into three separate filaments (Fig. 5.7b).
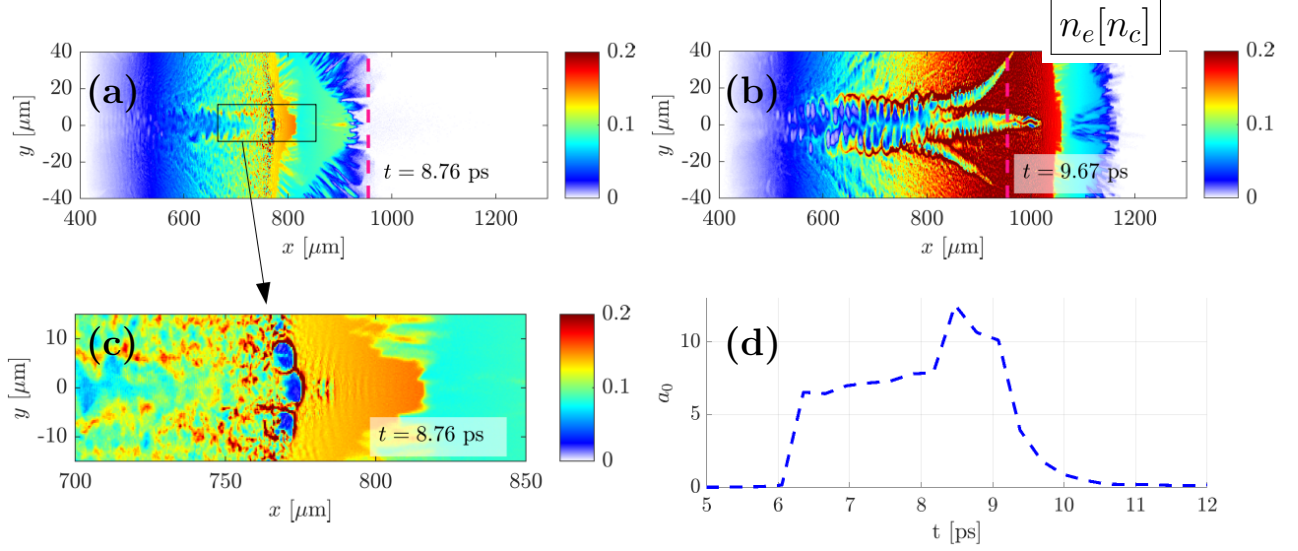
Fig. 5.7: Laser filamentation origin as seen in the electron density n_e charts at (a) $t = 8.76$ ps and (b) $t = 9.67$ ps. (c) Zoom of (a) focused on the laser channel creation region. (d) Maximum normalized laser amplitude a_0 measured in the central filament with respect to time. Note that the a_0 values are normalized to $\lambda = 1\,\mu$m.

The processes of high-intensity laser filamentation and self-focusing in near-critical density plasmas results from the relativistic mass increase of plasma electrons and the ponderomotive expulsion of electrons from the laser channel when exceeding the critical power value $P_{cr} \approx 17(\omega_L/\omega_{pe})^2$ GW (where ω_L is the laser frequency and ω_{pe} the local electron plasma frequency), see Ref. [162] and references therein. In this regime, 3-D processes derived from the finite laser focal spot size can trigger laser filamentation if the focal spot is larger than the relativistic plasma skin depth $D_L \gg 2\pi\sqrt{\gamma_e n_c/n_e}\,c/\omega_0$ [91]. Fig. 5.7a and b are electron density n_e charts zoomed on the laser channel and corresponding to simulation time steps. Fig. 5.7a captures the onset of laser filamentation. Fig. 5.7c is a zoom of Fig. 5.7a that shows the formation of three cavities after the laser ponderomotive force has evacuated the electrons from within them. Note that the laser front is roughly located at $x \approx 775\,\mu$m in Fig. 5.7c. At this point the laser experiences a momentary but strong self-focusing, giving rise to a 40% increase in the laser a_0. This can be see in Fig. 5.7d, which corresponds to the maximum laser amplitude a_0 in the central filament with respect to time. Note that the a_0 values are normalized to $\lambda = 1\,\mu$m. Fig. 5.7b shows the formation of the three laser filaments that departed from the electron depleted cavities. The creation of a dense electron bunch inside the central channel is also evidenced. Here the self-generated magnetic field is sufficiently strong to pinch the relativistic electrons [163].

Let us examine the laser channeling dynamics at later times. Figs. 5.8a and b show the electron density n_e and the transverse electric field E_y at $t = 14.20$ ps. The laser-driven electron expulsion from the channel gives rise to a transverse E_y charge separation field at the channel walls. This field reaches values of $\approx$ TV/m and will be responsible for transverse ion acceleration, which will be discussed afterwards. As can be seen in Fig. 5.8a (and Fig. 5.7b), the laser channel is modulated due to the relativistic non-linear electron currents that flow through it. Furthermore, the currents' propagation along a density gradient entails variations of the local electron plasma wavelength ω_{pe} which will naturally modulate the channel as well.

Figure 5.8c plots the total longitudinal electron flux $n_e v_x$, rightward electron currents appear in red and leftward ones in blue. There are two electron currents created inside the laser channel. A high velocity $v_e \approx c$ laser-driven current moving to the right and a compensating electron
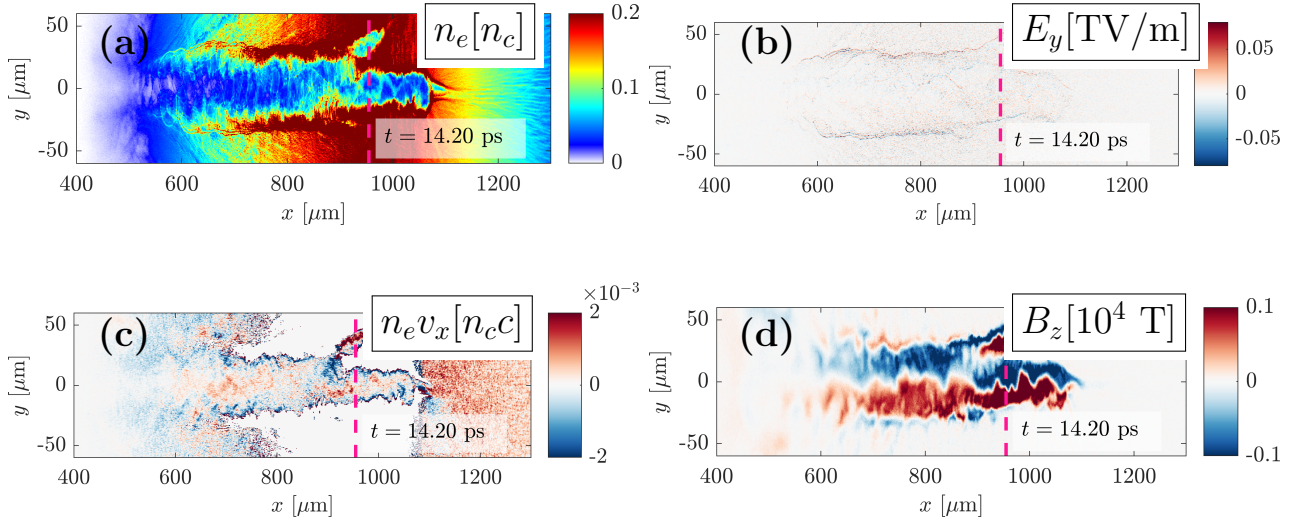
Fig. 5.8: Channel dynamics at $t = 14.20$ ps as seen in (a) the electron density n_e, (b) the E_y transverse electrostatic field, (c) the total electron longitudinal electron flux nv_x and (d) the out-of-plane magnetostatic field B_z. The color scale of B_z is non-saturated; a non-saturated B_z chart in shown in Fig. 5.9.

current flowing to the left. The laser-expelled electrons create a third high density current, which moves to the left through the channel walls. The interplay between the laser-driven forward electron current flowing inside the channel (see red current at $x = 600$ μm, $y = 0$) and return currents flowing through the channel walls gives rise to the azimuthal magnetic field B_z seen in Fig. 5.8d. The net electrical current $J_x = \langle -en_e v_x \rangle$ moves to the left, which explains the sign of the induced magnetic field plotted in Fig. 5.8d.

Fig. 5.9a shows the interplay of these three electron currents in terms of electron density n_e, current **J** and induced transverse magnetic field B_z, with respect to the radial coordinate r. The electron density n_e is maximum at the channel walls. The current **J** is negative in the channel's axis (where laser-driven electrons flow to the right) and positive along the walls. Finally, the induced magnetic field $B_z = \int_0^r 2\pi\mu_0 r' j(r')dr$ evolves as the derivative of the flowing current.

The induced magnetic field reaches a maximum value $\langle B_z \rangle \approx 20$ kT at about 7 μm from the axis of the central current filament, as seen in the B_z non-saturated chart plotted in Fig. 5.9a. This field strength is consistent with the prediction $\langle B_z \rangle \approx \sqrt{a_0 n_e/n_c}\, m_e \omega_0/e$ derived in Refs. [91, 162].

For comparison, Fig. 5.10a plots the electron density n_e map, deconvolved from an optical interferogram acquired during the VEGA-3 campaign at $t \approx 100$ ps after the beginning of the interaction. Fig. 5.10b corresponds to the electron density n_e map extracted from the simulation at $t = 14.80$ ps. The experimental shot was performed in the same conditions as those intended to be replicated in the 2-D simulation, except for the laser focusing plane, which was located 250 μm before the density peak. The experimental laser channel is qualitatively similar to the one observed in the 2-D simulation. It crosses the gas density peak, marked by a vertical dashed line, and exhibits dense channel walls and transverse expansion regions. At the same time, the experimental channel does not cross the entire gas slab, a feature also retrieved in the PIC simulation. The experimentally retrieved channel (Figure 5.10a) is about 100 μm wide in the transverse direction at $t \approx 100$ ps while the channel obtained in the 2-D simulation is about 40 μm wide at $t_{sim} = 9.67$ ps (Figure 5.10b). A direct comparison of the simulation and experimental data is not straightforward, not only because the simulation only captures the first ≈ 10 ps of the interaction but also because of its 2-D reduced geometry that
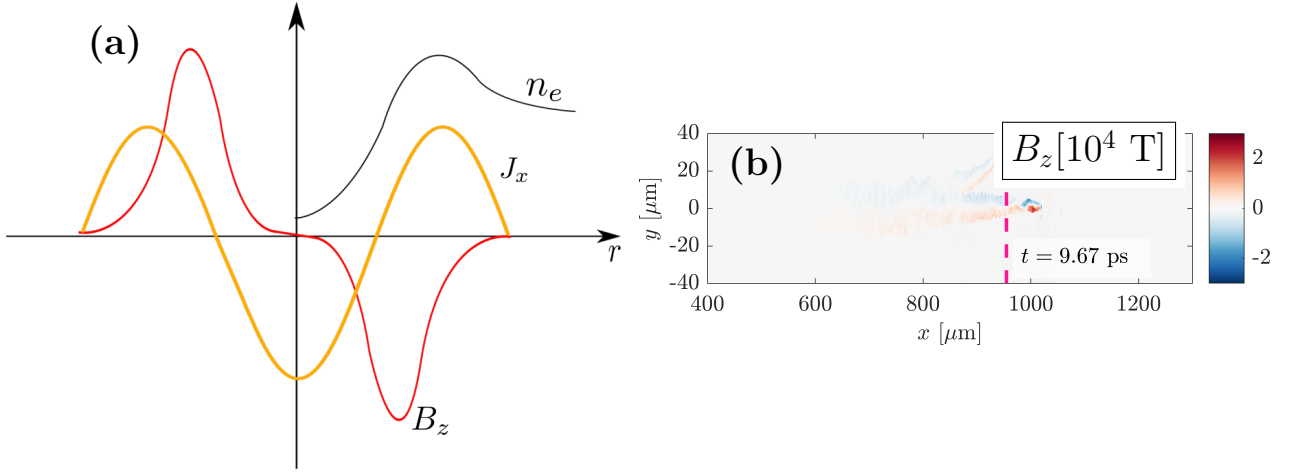
Fig. 5.9: (a) Laser channel dynamics as seen in the electron density n_e (black solid line), total electron flux $n_e v_x$ (orange solid line) and the induced azimuthal magnetic field B_z (red solid line) with respect to the radial coordinate r. (b) Magnetic field B_z chart taken at $t = 9.67$ ps. The magnetic field reaches a maximum value $B_z \approx 20$ kT at about $7\,\mu$m from the axis of the central filament.

is likely to affect the subsequent channel dynamics. In Ref [143] the experimentally retrieved temporal evolution of the channel radius in a near-critical target with $n_e \approx 1.8 \times 10^{20}$ cm^{-3} has been successfully fitted to a cylindrical blast wave (BW) expansion from 10 to 100 ps. Here the channel radius is given by $r_s \propto t^{-2/(\nu+2)}$ [145], where ν is the dimensional index.
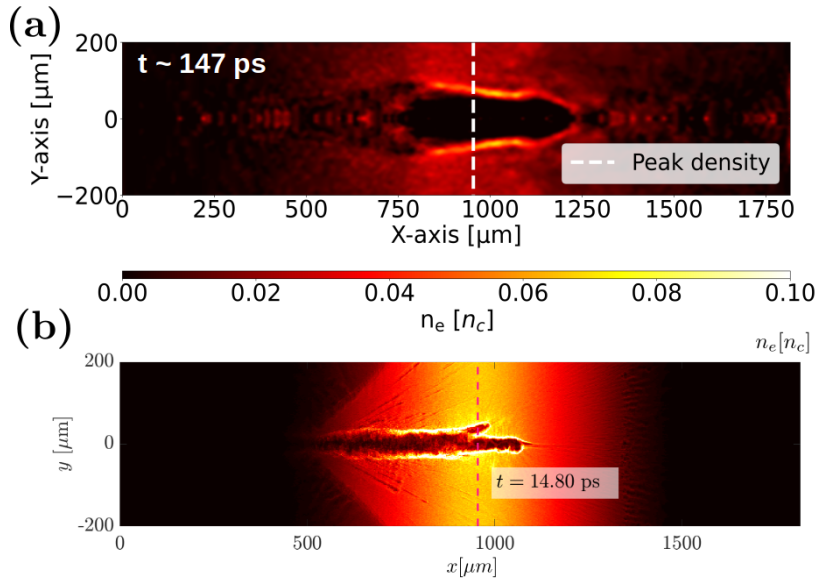
Fig. 5.10: (a) Deconvolved optical interferogram acquired during the VEGA-3 campaign showing the electron density n_e at $t \approx 100$ ps after the beginning of the interaction. The shot was performed in the same conditions as those intended to be replicated in the 2-D simulation. (b) Electron density n_e chart

No laser filamentation is observed in the experimental density chart of Fig. 5.10a. This feature was retrieved by performing a second 2-D simulation where the laser focusing plane was located 250 µm before the gas density peak, as in the experiment. Fig. 5.11a shows the B_z magnetic field corresponding to the simulation where the laser was focused at the density

peak. Fig. 5.11b corresponds to the simulation with the displaced focal plane. In the latter, no laser filamentation was observed and the laser propagation length into the gas down-ramp was shorter. Focusing the laser in the target up-ramp probably diminishes the laser self-focusing and collapsing, preventing it from filamenting, as evidenced in the experiment.
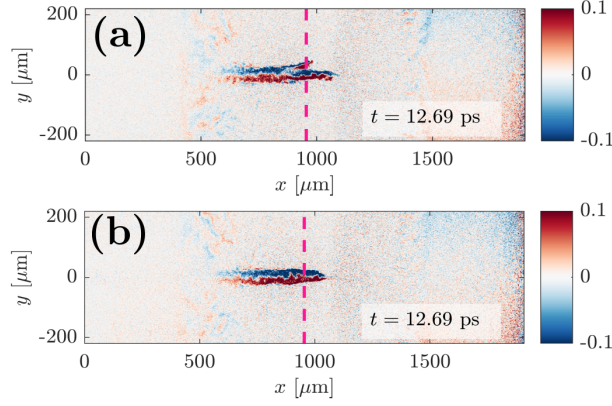
Fig. 5.11: B_z transverse magnetic field at $t = 12.69\,\text{ps}$ corresponding to the simulation where the laser was focused (a) at the density peak and (b) $250\,\mu\text{m}$ before the density maximum.

5.3.3 Electron acceleration inside the laser ponderomotive channel

We are now interested in the electron acceleration mechanisms triggered before complete laser absorption. The electrons located inside the laser channel are subject to both the longitudinal electrostatic fields E_x created by the non-linear plasma wakefield, as well as to the direct effect of the laser transverse field E_y. To discriminate between their respective contributions we plot the electron distribution function f_e in term of the works performed y the longitudinal (W_x) and transverse (W_y) electric fields, namely,

$$W_{x,y} = -e \int_0^t dt'\, E_{x,y}(t',\vec{r}(t'))v_{x,y}(t'). \tag{5.1}$$

The mentioned $f_e(W_x,W_y)$ phase space is plotted at $t = 8.46\,\text{ps}$ in Fig. 5.12a. Here the $W_x = W_y$ line is plotted in red and the $W = W_x + W_y = 0$ line is plotted in blue, where W is the total work exerted over the electrons.

As seen in the B_z-chart of Fig. 5.3b, taken at $t = 8.76\,\text{ps}$, the laser is crossing the target up-ramp at this time step and has been only weakly absorbed, as seen in Fig. 5.4. Fig. 5.12b shows the corresponding mean electron kinetic energy in logarithmic scale. The vast majority of hot electrons are then located inside the channel. Finally, Fig. 5.12c corresponds to the ion density n_i in logarithmic scale. One can see the ions accumulating at the channel walls.

It is worth noticing that the mean energy of the hot electron distribution of Fig. 5.12c $e_h \approx 10$ is at least twice larger than the ponderomotive scaling: $e_h \approx \langle\gamma_e - 1\rangle = \sqrt{1 + a_0^2/2} - 1 \approx 4$, taking into account a normalized laser amplitude $a_0 = 6.9$ and $\lambda_L = 800\,\text{nm}$. This demonstrates the very high electron energization levels characteristic of the near-critical interaction [30].

As seen in the electron $f_e(W_x,W_y)$ phase spaces of Figs. 5.12a and b, the majority of the hot electrons are located in the region where $W_y > W_x$. This means that most of the electrons' energy gain is due to the transverse E_y field, which is characteristic of direct laser acceleration (DLA) [164, 165]. Electrons up to $100\,\text{MeV}$ have been experimentally measured and linked to DLA after shooting at gaseous targets (composed of 99.9% He and 0.1% N_2) with a maximum
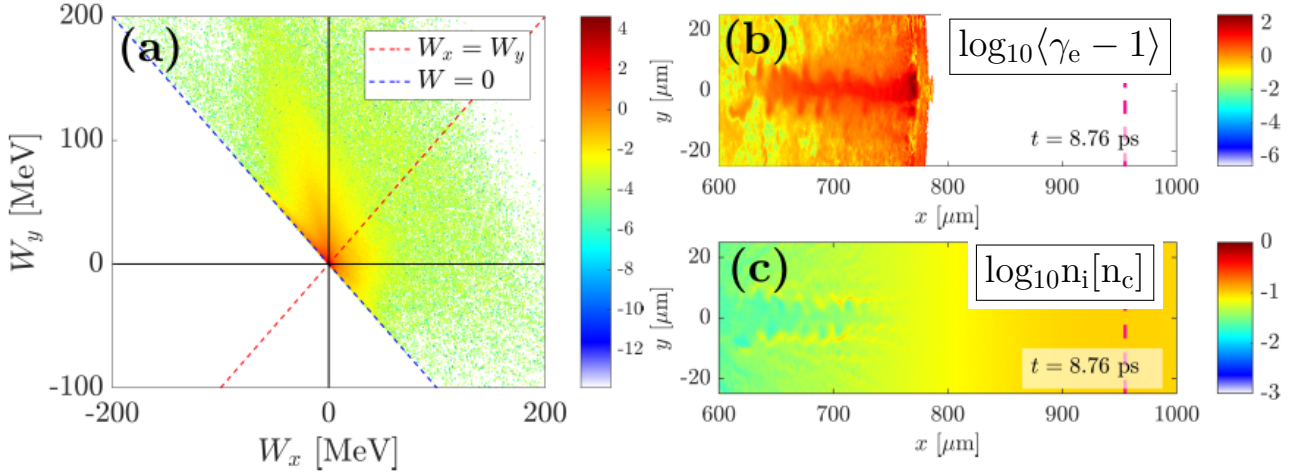
Fig. 5.12: (a) Electron distribution function $f_e(W_x, W_y)$ at $t = 8.46\,\text{ps}$, (b) corresponding mean electron kinetic energy $\langle \gamma_e - 1 \rangle$ and (c) ion density n_i.

electron density $n_e \approx 10^{19}\,\text{cm}^{-3}$ and a normalized laser amplitude $a_0 = 2$. The experimental electron spectra exhibit characteristic *forked* structures at high energies ($\mathcal{E} > 80\,\text{MeV}$) [148,149].

5.4 Late-time plasma dynamics

As seen in Fig. 5.4 the laser has been almost completely absorbed by $t \approx 10\,\text{ps}$, after crossing the gas density peak. Afterwards, the self-generated magnetic field will persist in the channel until the end of the simulation (Figs. 5.13a-c). Figs. 5.13d-f display the free electron density n_e corresponding to the same time steps as in Fig. 5.13a-c. The position of the gas density peak is marked as dashed vertical lines in all figures.

5.4.1 Magnetic field generation at the plasma-vacuum right boundary

Once the electrons energized in the plasma up-ramp reach the plasma-vacuum interface and exit into the vacuum (see n_e chart of Fig. 5.13e) a strong longitudinal charge separation E_x field is created. This field reflects some of the hot electrons into the plasma when the electrostatic potential is greater than the electrons' kinetic energy $-e[\phi(x_2) - \phi(x_1)] \approx -e\Delta\phi > (\gamma_e - 1)m_e c^2$ (where x_1 is located in the plasma bulk and x_2 in the down-ramp). The interplay between the stream of hot electrons exiting the target and the electrons re-injected inside the plasma core acts as a seed for the current filamentation instability (CFI) [162]. CFI is produced by the magnetic repulsion of these counter-propagating electron currents [166].

Figures 5.14a and b visualize the longitudinal electron flux $n_e v_x$ and the B_z-field at $t = 11.48\,\text{ps}$ (same time step as Fig. 5.13b and e) and around the right plasma-vacuum boundary.

The magnetized current filaments can be seen in the region $1350\,\mu\text{m} \leq x \leq 1450\,\mu\text{m}$. At the same time, a right-boundary B-field born from a net current flowing to the left (net electron flux towards the right) appears located at the right side plasma-vacuum interface, as seen in Fig. 5.14b. This magnetic field exhibits the same sign as the one created inside the ponderomotive channel (Fig. 5.13c) with maximum values of $> 1\,\text{kT}$, see Fig. 5.13c, and will be responsible for the deflection of forward acceleration ions, as will be discussed in Section 5.6.1.
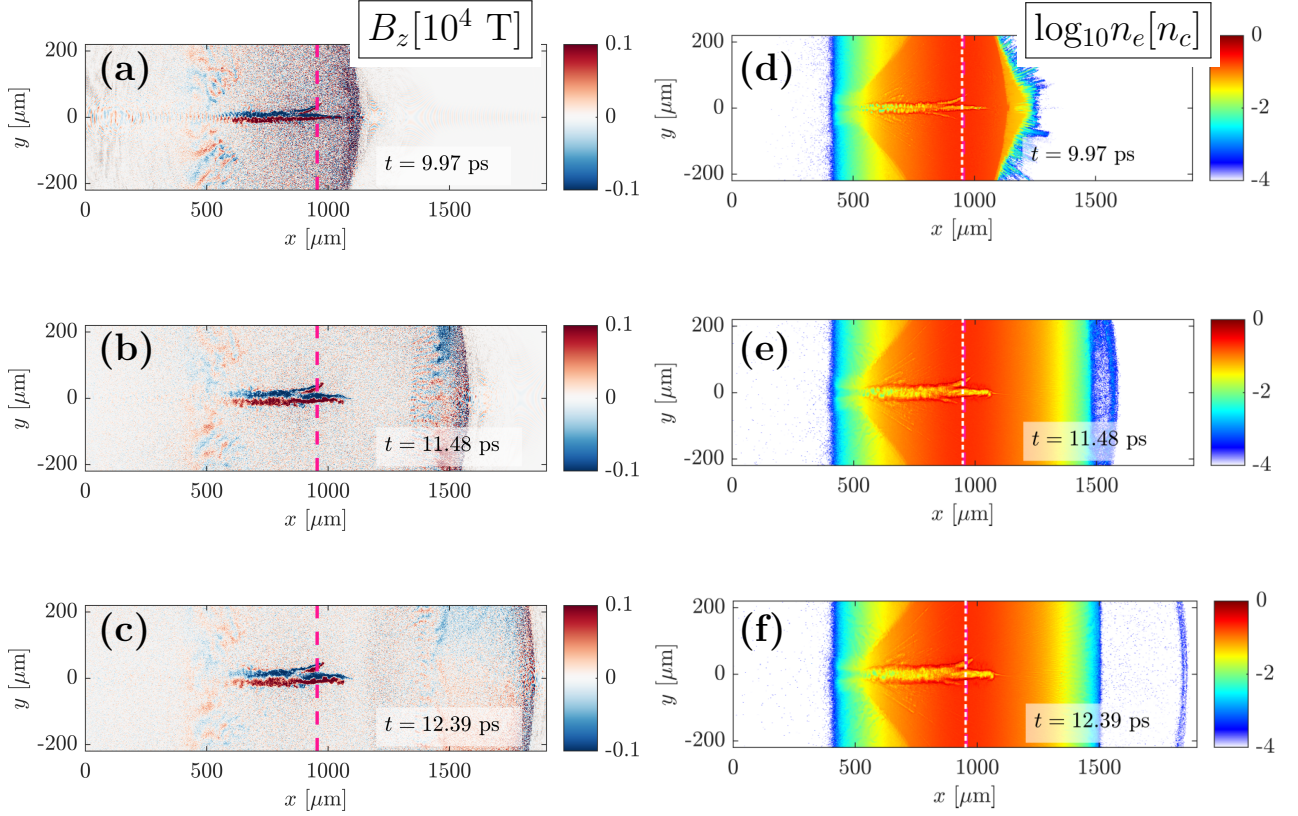
Fig. 5.13: (a-c) B_z laser-associated quasistatic magnetic field. (d-f) Free electron density n_e corresponding to the same time steps as (a-c). The pink and white dashed lines mark the location of the gas density peak.
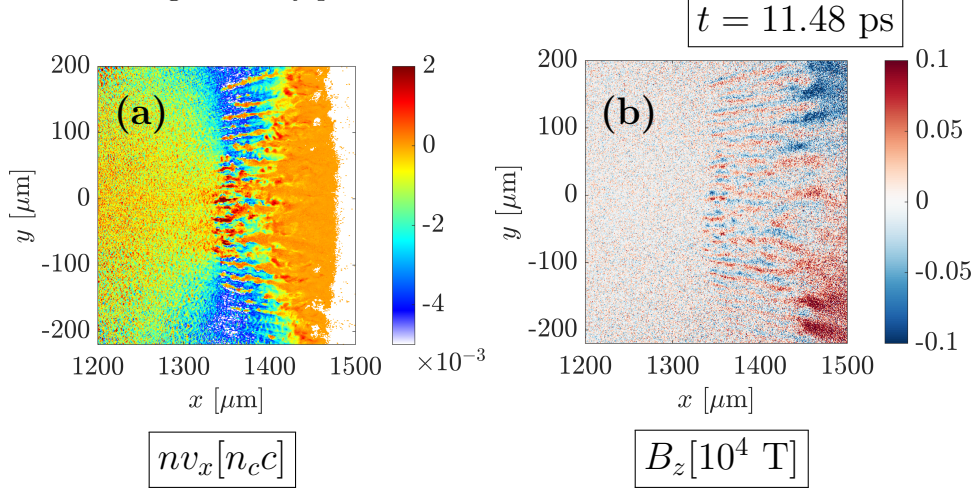
Fig. 5.14: (a) Longitudinal electron flux $n_e v_x$ and (b) B_z magnetic field taken at $t = 11.48$ ps when the hot electrons are traversing the plasma vacuum interface, see Fig. 5.13b and e.

5.5 Angular distribution of the forward accelerated electrons

The energy-angle distribution of the electrons $f_e(\mathcal{E}, \theta)$ was obtained by placing a particle probe at the right boundary of the simulation box. This probe was placed as far as possible from the plasma core to characterize the population of escaping electrons and compare it with the spatially resolved dose deposition maps, extracted from the experimental data (see Chapter 4).

Figs. 5.15a and b show the distribution of electrons with energies below and above 10 MeV, respectively. The colormaps are proportional to the electron density n_e and the laser propagates in the horizontal axis of the plot, from 180° to 0°. The lower energy electrons (Fig 5.15a) exit the simulation box with a *forked* angular distribution with a mean half angle $\theta \approx 15°$ and a FWHM dispersion $\Delta\theta \approx 8°$. The electrons with energies higher than 10 MeV (Fig 5.15b) exhibit a non-homogeneous angular distribution in the interval $\theta \in [-30°,30°]$. An electron beamlet with slightly higher density is visible at $\theta \approx 17°$. These electrons could be linked with the ones accelerated inside the upper laser filament visible in Fig. 5.13c. Note that this laser filament exhibits a final angle of $\approx 25°$ with respect to the main channel's central axis. Note further that all electrons are essentially emitted within the interval $[-30°,30°]$, and that the highest electronic population has an energy $\mathcal{E} > 10$ MeV.
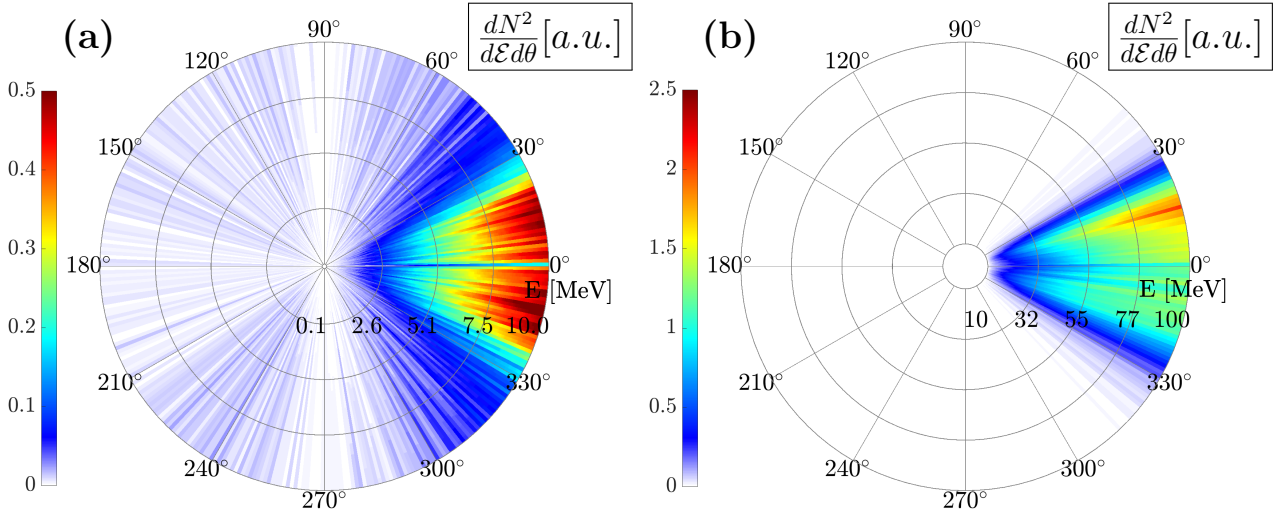
Fig. 5.15: Energy-angle $f_e(\mathcal{E},\theta)$ of electrons crossing the right-hand side boundary of the simulation box. (a) $f_e(\mathcal{E},\theta)$ for electrons of energies lower than 10 MeV and (b) for electrons of energies between 10 MeV and 100 MeV.

The previously described transverse magnetic field B_z, located at the right plasma boundary, can deviate electrons of energies $\mathcal{E} < 50$ MeV. The typical electron deflection is given by

$$\text{atan}\left(\frac{\Delta p_\perp}{p_\parallel}\right) = \text{atan}\left(\frac{Z^* B \Delta t}{m_i}\right), \tag{5.2}$$

where $\Delta t = \Delta x / v_\parallel$. Considering electrons of 50 MeV and a magnetic strength of $B_z \approx 50$ T extending over $\Delta x = 100\,\mu$m (corresponding to the one created at the plasma boundary) $\text{atan}(\Delta p_\perp / p_\parallel) \approx 10°$, i.e. B_z can affect these electrons' trajectories. This is observed in the electron $p_x p_y$ phase spaces of Figs. 5.16a and b obtained before and after the right boundary magnetic field, respectively.

The hot electrons that have been energized inside the plasma channel through DLA exhibit a *forked* angular distribution (Fig. 5.16a). Once these electrons traverse the plasma-vacuum interface, the transverse magnetic field B_z isotropizes the angular electron distribution, as seen in Fig. 5.16b.

The double-peaked angular distribution of the < 10 MeV (Fig 5.15a) electrons bears resemblance to the spatially resolved dose deposition recorded during the experiment (using a radiochromic film stack) and plotted in Fig. 5.17a. Here the laser axis is marked by the intersection of the two dashed lines and the laser polarization axis corresponds to the horizontal
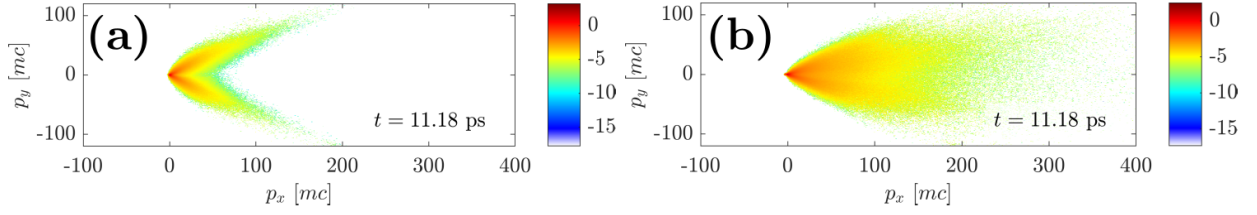
Fig. 5.16: Electron $p_x p_y$ phase spaces obtained (a) before and (b) after the right boundary magnetic field.

dashed line. The RCF layer shown in Fig. 5.17a corresponds to the third layer in the stack, which has contributions from electrons of energies higher than $300\,\text{keV}$ (and especially of energies between $300\,\text{keV} \leq \mathcal{E} \leq 500\,\text{keV}$), and most likely no ionic contributions. The experimental dose deposition exhibits a ring shape with a dose depletion on-axis and hot spots aligned with the laser polarization horizontal axis. The hot spots are located at $\theta_s \approx \pm 7°$ from the dose depletion center. A comparison of the high energy electron energy-angle phase space $f_e(\mathcal{E},\theta)$ of Fig. 5.15b with experimental data is not possible since the radiochromic film stack was not sensitive to high energy electrons.
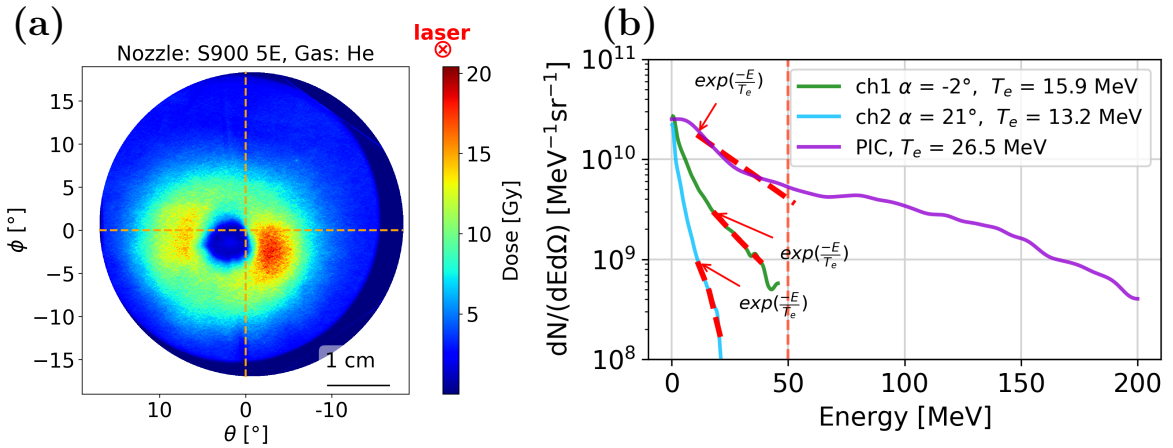
Fig. 5.17: (a) Spatially resolved dose deposition on the third layer of a radiochromic film stack corresponding to a shot on helium from which the 2-D simulation parameters were extracted. The signal in the third RCF layer mainly arises from electrons with energies higher than $300\,\text{keV}$, especially of energies between $300\,\text{keV} \leq E \leq 500\,\text{keV}$, and most likely has no ionic contributions. (b) comparison of two different experimental electron energy spectra acquired during the same set of shots at two different azimuthal angles ($\alpha = -2°$ in green and $\alpha = 4°$ in blue) with an electron spectrum extracted from the simulation plotted in violet. The numerical spectra has been multiplied by a coefficient in order to plot it side-by-side with the absolute experimental energy spectra. The electron spectrometers were placed at the height of the laser propagation plane with no inclination. The orange dashed vertical line marks the maximum energy measurable by the diagnostic. An estimation of the electronic temperature for the three curves is taken from an exponential fit of the energy spectra between 15 and 25 MeV.

Fig. 5.17b compares two experimental electron energy spectra acquired during the same set of shots at two different azimuthal angles ($\alpha = -2°$ in green and $\alpha = 4°$ in blue) with an electron spectrum extracted from the simulation and plotted in violet. Note that the numerical spectrum has been multiplied by a coefficient in order to plot it side-by-side with the absolute

values of the experimental spectra. The electron spectrometers were placed at the height of the laser propagation plane with no inclination. The orange dashed vertical line marks the maximum energy measurable by the diagnostic. An estimation of the electronic temperature T_e is taken from exponential fits of the energy spectra between 15 and 25 MeV. The simulated electron spectrum is harder ($T_e \approx 26.5$ MeV) than the experimentally measured ones ($T_e \approx 14$ MeV) in the detection range of the diagnostic (i.e. up to 50 MeV). Possible explanations for this discrepancy are the reduced 2-D geometry of the simulation and possible experimental uncertainties in the laser or gas parameters.

5.6 Transverse and longitudinal ion acceleration

As was mentioned before, the radial expulsion of electrons from the laser ponderomotive channel entails the creation of transverse charge separation fields at the channel walls. At the same time, longitudinal charge separation electrostatic fields will be created at the plasma right boundary due to the energized electrons escaping into vacuum. At times $t \gg \omega_{pi}^{-1}$, where ω_{pi}^{-1} is the *ion plasma frequency*, the ions will start to react to such fields and different radial and longitudinal acceleration mechanisms will be triggered. Fig. 5.18a shows the ion kinetic energy and Fig. 5.18b the ionic density n_i (for ion energies larger than 100 keV) at $t = 13.56$ ps. As can be seen the most energetic ionic populations are located at the channel walls and at the right gas boundary. Hereafter, we discuss the mechanisms responsible for this ion acceleration.
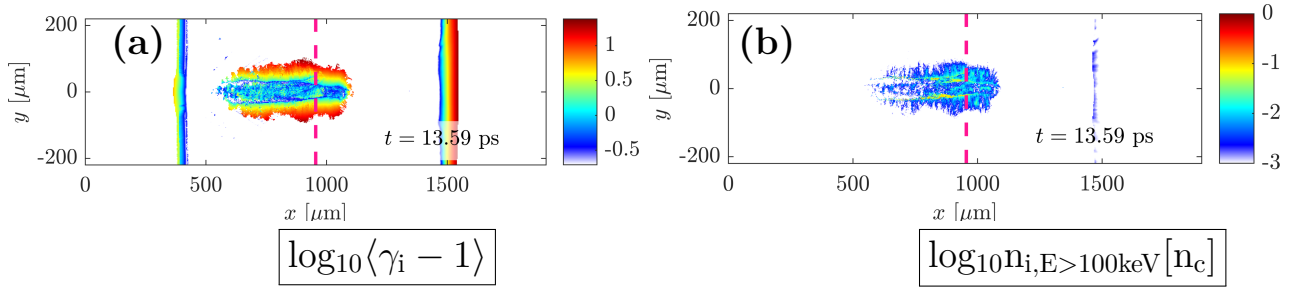
Fig. 5.18: (a) Ion kinetic energy and (b) the ionic density n_i (for ion energies larger than 100 keV) at $t = 13.56$ ps.

5.6.1 Forward target normal sheath acceleration of ions

As it is frequently studied in solid targets, the energized hot electrons exiting into vacuum create a longitudinal charge separation field that accelerates ions present at the right gas boundary at times $t \gg \omega_{pi}^{-1}$, a mechanism known as target normal sheath acceleration (TNSA). Fig. 5.19 corresponds to the ion (x, p_x) phase-space at $t = 13.56$ ps, integrated in the transverse axis. As can be seen, ions are forward-accelerated by the TNSA field up to $v_i \approx 0.06\ c$ corresponding to α particles of about 7 MeV.
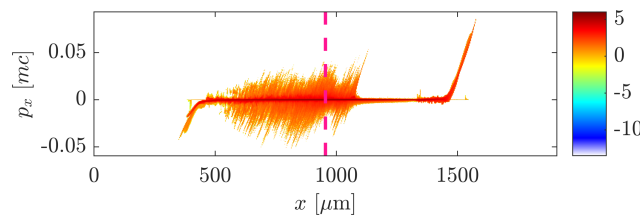
Fig. 5.19: Ion (x, p_x) phase-space at $t = 13.56$ ps, integrated in the transverse axis.

To characterize the forward emission of ions, a probe diagnostic was located after the right plasma-vacuum border, at $x = 1500\,\mu\text{m}$, see Fig. 5.2b. The energy-angle distribution $f_i(\mathcal{E},\theta)$ of the ions having reached this virtual detector is plotted at four different times ($t = 12.08\,\text{ps}$, $t = 12.69\,\text{ps}$, $t = 12.99\,\text{ps}$ and $t = 13.59\,\text{ps}$) in Figs. 5.20a-d. Here the colormap is proportional to the ion density n_i and the laser propagates along the horizontal axis of the plot. At $t = 12.08\,\text{ps}$ we observe a 0° forward acceleration of ions up to $\approx 5\,\text{MeV}$ maximum energies. The mean angle of emission is slightly deviated (by $\approx 2°$) from the laser axis. Afterwards, the angle of the accelerated ions is drastically broadened up to 45°, see Figs. 5.20b-d. By the end of the simulation, the most energetic ions are recorded at ±45° from the laser propagation axis, exhibiting maximum energies of $\approx 5.7\,\text{MeV}$. However, the ions of very low density, about three orders of magnitude less than those accelerated at 0°. Note that the ions plotted in Figs. 5.20a-d are coming from the right plasma-vacuum border since a second probe located inside the plasma (at $x = 1250\,\mu\text{m}$) did not detect any forward ion acceleration.
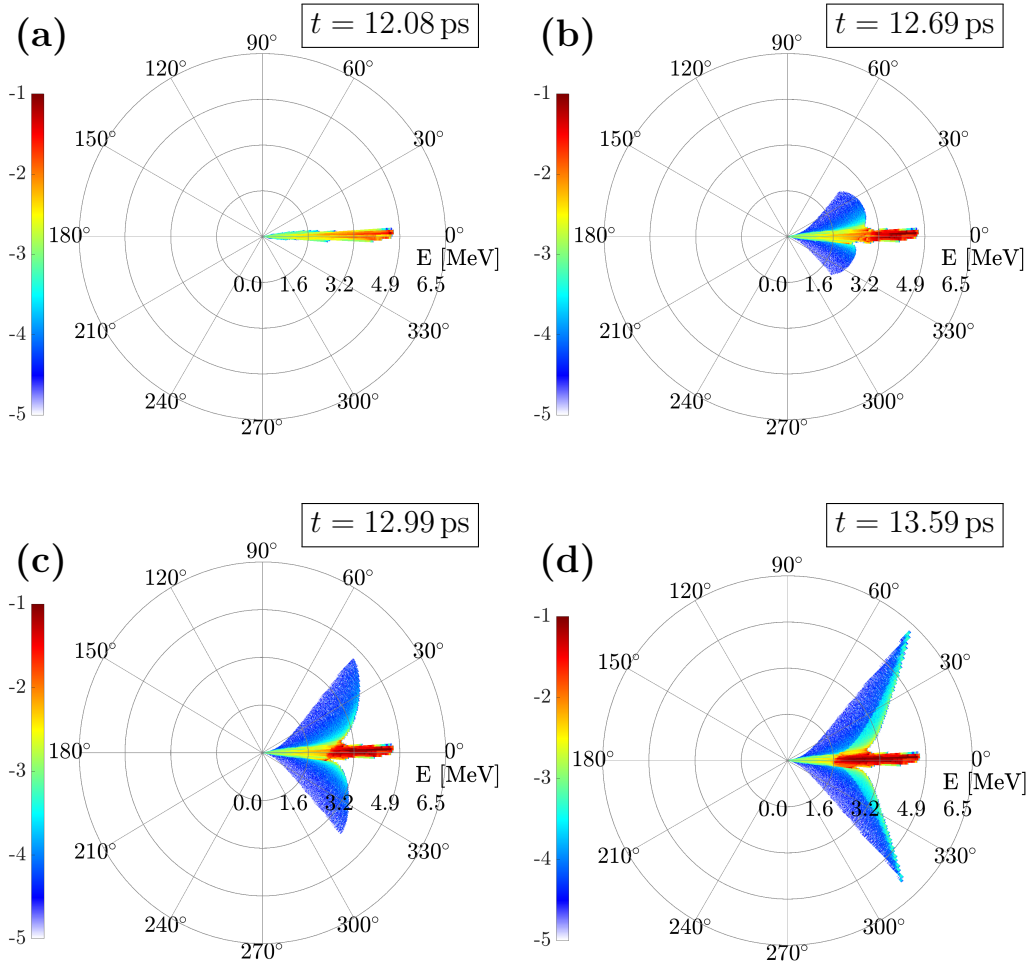
Fig. 5.20: Ion energy-angle $f_i(\mathcal{E},\theta)$ phase space at (a) $t = 12.08\,\text{ps}$, (b) $t = 12.69\,\text{ps}$, (c) $t = 12.99\,\text{ps}$ and (d) $t = 13.59\,\text{ps}$.

Even if the ions accelerated at wide angles represent a minor percentage of the total accelerated ionic population, it is interesting to observe such strong transverse deviation since it was one of the characteristics retrieved from the experimental ion energy spectra. Indeed, using time-of-flight diamond detectors we measured α particles at ±17° from the laser axis in an 5° inclined polar plane.

Taking a look at the different processes occurring at the right plasma-vacuum boundary one

could think that the transverse magnetic field discussed in Section 5.4.1 could be the source the ion deviation. Following Eq. 5.2 one obtains a typical ion deflection $\mathrm{atan}(\Delta p_\perp/p_\parallel) \approx 10°$, where $\Delta t = \Delta x/v_\parallel$, for α particles of 5 MeV and a magnetic field value of $B_z \approx 50\,\mathrm{T}$ over $\Delta x = 100\,\mu\mathrm{m}$ (as the one created at the plasma boundary). Hence, such magnetic field can have significant effect on the α particle trajectories. To test this theory we computed the mean B_z magnetic field (see Fig. 5.21a) and the mean ion transverse flux $n_i v_y$ (see Fig. 5.21b) values at the right upper gas boundary (1450 μm $\leq x \leq$ 1550 μm, $y > 0$, see Figs. 5.13b and c) with respect to time.
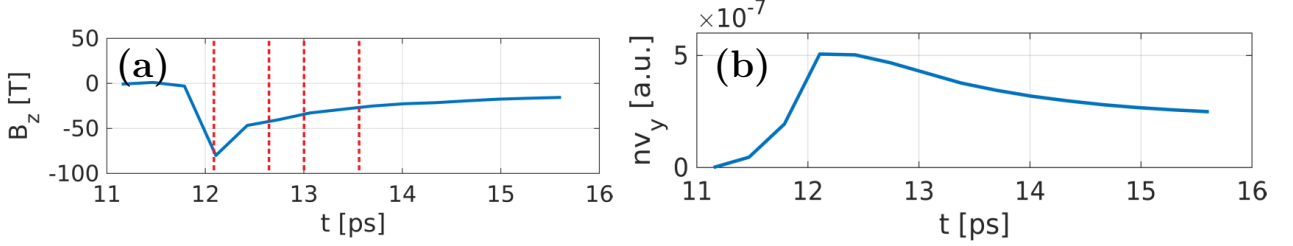
Fig. 5.21: (a) B_z magnetic field (see Fig. 5.21a) and (b) ion transverse flux $n_i v_y$ (see Fig. 5.21b) mean values computed at the upper right gas boundary (1450 μm $\leq x \leq$ 1550 μm, $y > 0$, see Figs. 5.13b and c) with respect to time.

As can be seen in Fig. 5.21a, the B_z magnetic field created at the plasma-vacuum border reaches its maximum value $B_z \approx 75\,\mathrm{T}$ at $t \approx$ 12.20 ps, which is strong enough as to significantly deviate 5 MeV α particles. The transverse ion flux $n_i v_y$ reaches its maximum value at the same time and decays at a similar rate than the B_z magnetic field. The four instants plotted in Figs. 5.20a-d are marked with red dashed lines in Fig. 5.21a. We can then confirm that the ions accelerated after $t = 12.08$ ps (see Fig. 5.20a) experience the B_z magnetic field created at the plasma-vacuum boundary by the exiting hot electron current and are deviated at large angles, see Figs. 5.20b-d, giving rise to the transverse ion flux $n_i v_y$ of Fig. 5.21b.

Figure 5.22 shows a comparison of the experimental and numerical

Fig. 5.22: Comparison of the experimental and numerical ion spectra at different azimuthal angles. The experimental ion spectra were acquired at $\pm 17°$ from the laser axis (see green and violet spectra). Numerical ion spectra are obtained by integrating the energy-angle ion phase space $f_i(\mathcal{E},\theta)$ of Fig. 5.20d (corresponding to the last time step of the simulation) in 2° cones centered at 0° (light purple curve), 17° (cyan curve) and 45° (light salmon curve). Note that the numerical spectra has been multiplied by a coefficient in order to plot it side-by-side with the absolute experimental energy spectra.

ion spectra at various azimuthal angles. The experimental ion spectra were measured at $\pm 17°$ from the laser axis with $\approx 0.2°$ collection angles (see green and violet spectra of Fig. 5.22). Numerical ion spectra are obtained by integrating the energy-angle ion distribution $f_i(\mathcal{E},\theta)$ of Fig. 5.20d (corresponding to the last time step of the simulation) in 2° aperture cones centered at 0° (light purple curve), 17° (cyan curve) and 45° (light salmon curve). Note that

the numerical spectra has been multiplied by a coefficient in order to plot it side-by-side with the absolute experimental energy spectra.

Although the maximum experimental and numerical ion energies at 17° ($\approx 2.5\,\mathrm{MeV}$) are comparable, the numerical spectra do not decay exponentially as the experimental ones. Furthermore, the lower energy part of the numerical spectra (for example the ion energies $E_i < 2.5\,\mathrm{MeV}$ of the 17° cyan spectrum) probably needs larger simulation times to exit the plasma, most likely after the transverse B_z magnetic field of Fig. 5.21 is weak enough. The maximum numerical ion energies of $\approx 6.3\,\mathrm{MeV}$ were obtained at 45° while the spectrum on-axis exhibits a maximum energy of $\approx 4.7\,\mathrm{MeV}$ and about two orders of magnitude more particles.

5.6.2 Transverse ion acceleration: formation of radial collisionless electrostatic shocks

Figures 5.23a and b are zooms, taken at $t = 9.67\,\mathrm{ps}$, of the ion density n_i and the transverse electric field E_y, centered on the upper channel wall. As before, the gas density peak is marked with a vertical pink dashed line. Figs. 5.23c and d are transverse lineouts of the ion density n_i and electrostatic potential ϕ taken at four different times from $t = 9.37\,\mathrm{ps}$ to $t = 10.27\,\mathrm{ps}$. These lineouts are obtained at $x = 955\,\mathrm{\mu m}$, i.e. at the gas density peak. In Fig. 5.23c one can see how the ion density profile steepens during the transverse channel expansion. Reflection from the ion front at $y = 7\,\mathrm{\mu m}$ occurs at $t = 9.67\,\mathrm{ps}$ when the transverse electrostatic potential is equal to $\phi \approx 1.25 m_e c^2/e$. At this instant the lab-frame shock velocity is equal to $v_f \approx 0.025\,c$, which can be seen in the ion (y, p_y) phase space (integrated in the $925\,\mathrm{\mu m} \leq x \leq 975\,\mathrm{\mu m}$ interval) plotted in Fig. 5.23e. Taking into account the ion velocity v_f and the electrostatic potential ϕ_y, the ionic kinetic energy is about $E_{k,i} \approx 2.3\,m_e c^2$ and the electrostatic potential energy of the fully ionized He^{2+} species is approximately $Z^* \Delta\phi_y \approx 2.5\,m_e c^2$. The electrostatic potential seen by the ions at the channel wall is higher then their kinetic energy which allows them to be reflected. As seen in the ion (y, p_y) phase space of Fig. 5.23f, recorded when th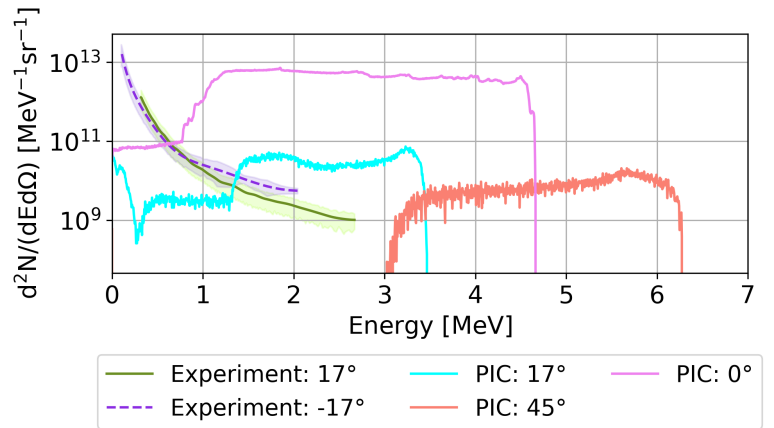e reflection is already taking place, the ions are reflected from the shock front at approximately twice the shock velocity: $v_r = 2v_f \approx 0.05\,c$. Notice that the momentum structures centered at $y \approx 25\,\mathrm{\mu m}$ in both Figs. 5.23e and f are a result of the ion acceleration at the walls of the upper filament seen in Fig. 5.23a.

Fig. 5.24a shows the transverse y-position of the shock barrier as a function of time, as measured at the density peak located at $x = 955\,\mathrm{\mu m}$ (blue dashed line with circle marks) and at $x = 700\,\mathrm{\mu m}$ (pink dashed line with cross marks), see ion density n_i chart of Fig. 5.23a. Accurate shock transverse positions were obtained from the consecutive locations of the E_y electric field discontinuity seen in Fig. 5.23b. As can be seen in Fig. 5.24a the E_y discontinuities located at the channel walls and at the two different longitudinal x positions travel approximately at the same velocity $v_f \approx 0.018\,c$. Figs. 5.24b and c correspond to ion (y, p_y) phase spaces integrated in the $925\,\mathrm{\mu m} \leq x \leq 975\,\mathrm{\mu m}$ (i.e. at the density peak) and in the $675\,\mathrm{\mu m} \leq x \leq 725\,\mathrm{\mu m}$ (i.e. at the gas up-ramp) intervals. The maximum reflected ion velocity is $v_i \approx 0.05\,c$ in both cases, which is twice the shock velocity v_f plus an extra acceleration probably coming from transverse ambipolar fields located in the shock upstream. Note that the reflection taking place at the expanding upper filament wall at $x = 955\,\mathrm{\mu m}$ gives rise to less energetic ions (up to a velocity $v_i \approx 0.02\,c$), as seen in Fig. 5.24b. Since the filament is expanding following an oblique axis (perpendicular to the expansion direction) the accelerated ions have a non-negligible longitudinal momenta p_x. Fig. 5.24d shows the ion (y, p_y) phase space integrated in the entire x domain where the ion reflection taking place at various transverse locations along the plasma channel for in the gas up-ramp and around density peak create a wide spectra of accelerated particles.

In order to characterize the ion spectra resulting from the channel expansion around the
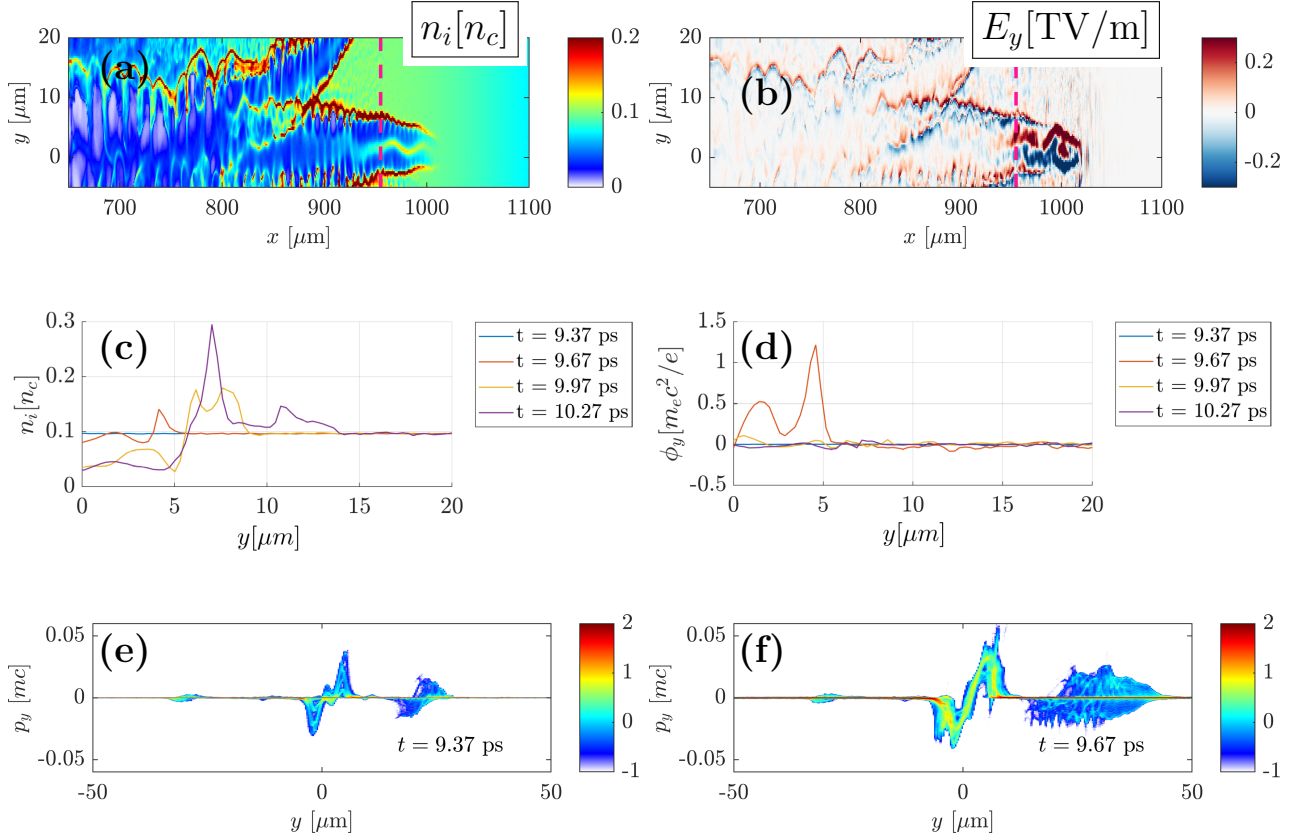
Fig. 5.23: (a) Ion density n_i and (b) transverse electric field E_y charts centered on the upper channel wall taken at $t = 9.67$ ps. Here the gas density peak is marked with a vertical pink dashed line. (c) Transverse lineouts of the ion density n_i and (d) transverse electrostatic potential ϕ_y taken at four different times from $t = 9.37$ ps to $t = 10.27$ ps. These lineouts are obtained at $x = 955\,\mu$m, i.e. at the gas density peak. (e-f) Ion (y, p_y) phase spaces captured when the shock reflection is already taking place. Ions are reflected from the shock front at approximately twice the shock velocity: $v_r = 2v_f \approx 0.05\,c$. Notice that the momenta structures centered at $y \approx 25\,\mu$m in (e) and (f) are a result of the ion acceleration at the walls of the upper filament seen in (a).

gas density peak a rectangular probe centered in both x and y coordinates with dimensions $\Delta x = 80\,\mu$m and $\Delta y = 30\,\mu$m was placed in the simulation box. The obtained ion energy-angle phase space $f_i(\mathcal{E},\theta)$ is plotted in Fig. 5.25a. Here the colormap is proportional to the ion density n_i. and the laser propagates in the horizontal axis of the plot, from $180°$ to $0°$. As can be seen ions are accelerated in the radial opposite directions. The upward and downward ions are reflected in a cone of approximate $\theta \approx 15°$ half-angle. The upward ion acceleration is slightly stronger with maximum α particle energies of about $E_\alpha \approx 5$ MeV compared with 4 MeV in the downward direction. Fig. 5.25b shows the ion spectra extracted at three different angles by integrating the energy-angle phase space of Fig. 5.25a in $\pm 2°$ cones. The spectra centered at $\theta = 80°$ and $\theta = 90°$ plotted in yellow and green, respectively, exhibit an exponential decaying shape with a flat low energy region between 1 and 3 MeV. The spectrum along $\theta = 70°$, plotted in pink in Fig. 5.25b, shows a small bump at slight peaked energy distribution, which hints collisionless shock acceleration (CSA) of a percentage of the accelerated ions. Indeed a peak centered at 5 MeV.

A similar simulation performed in Ref. [107] shows transverse proton acceleration at the beginning of the target up-ramp. This ion acceleration has been linked to the Coulomb explosion of light protons being expelled from the laser path. Fig. 5.26a shows a comparison between the
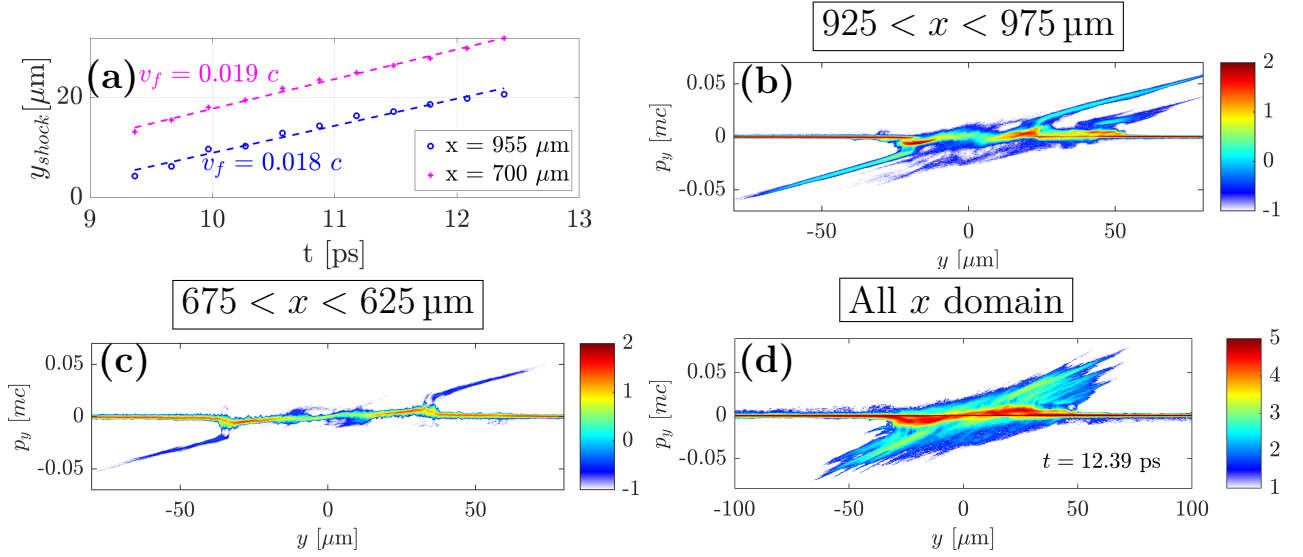
Fig. 5.24: (a) Transverse y positions of the shock barrier with respect to time taken at the density peak located at $x = 955\,\mu m$ (blue dashed line with circle marks) and at $x = 700\,\mu m$ (pink dashed line with cross marks), see ion density n_i chart of Fig. 5.23a. Accurate shock transverse positions were obtained from the consecutive locations of the E_y electric field discontinuity seen in Fig. 5.23b. (b) Ion (y, p_y) phase space integrated in the $925\,\mu m \leq x \leq 975\,\mu m$ (i.e. at the density peak) and (c) in the $675\,\mu m \leq x \leq 725\,\mu m$ (i.e. at the gas up-ramp) intervals. (d) Ion (y, p_y) phase space integrated in the entire x domain where the different ion reflections taking place in the gas up-ramp and density peak as well as in the different filament's walls create a wide spectra of accelerated particles.
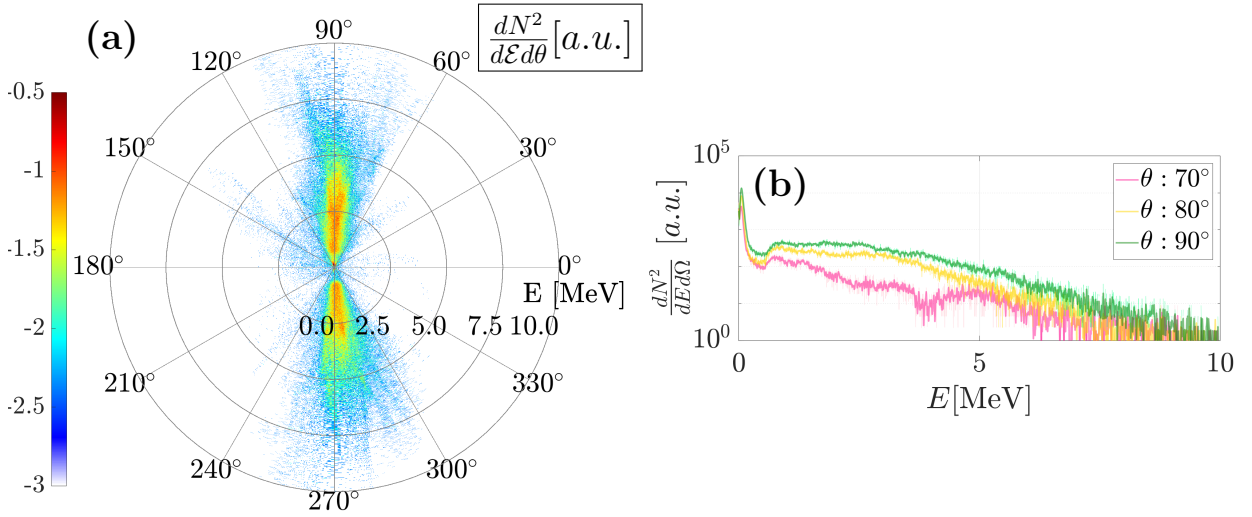
Fig. 5.25: (a) Ion energy-angle $f_i(\mathcal{E}, \theta)$ phase space and (b) numerical spectra obtained at three different angles by integrating a $\pm 1°$ cone.

pure helium gas profile simulated in this work (solid line) and the 99% helium and 1% hydrogen profile of Ref. [107] (dotted line). The profile of Ref. [107] has a similar maximum atomic density $n_{at} = 0.12\ n_c \approx 1.3 \times 10^{20}$ cm^{-3}. The laser amplitude was of $a_0 = 4$ in Ref. [107] while in this work it is $a_0 = 6.9$. Figs. 5.26b and c are electron density charts taken at $t = 1.26$ ps and $t = 1.68$ ps obtained in Ref. [107]. Here the position and dynamics of the 150 more energetic

protons accelerated by Coulomb explosion are plotted in colors. Note that in this configuration the laser pulse is completely absorbed before reaching the gas density peak as well. Transverse Coulomb explosion of α particles is not likely to be observed in our simulation conditions since the laser pulse length is larger than the local plasma wavelength ($c\tau = 30\,\mu m > 28\,\mu m$) [167] for $n_e > 0.04\,n_c \approx 4.4 \times 10^{19}$ cm^{-3} and the ion mass is significantly higher.
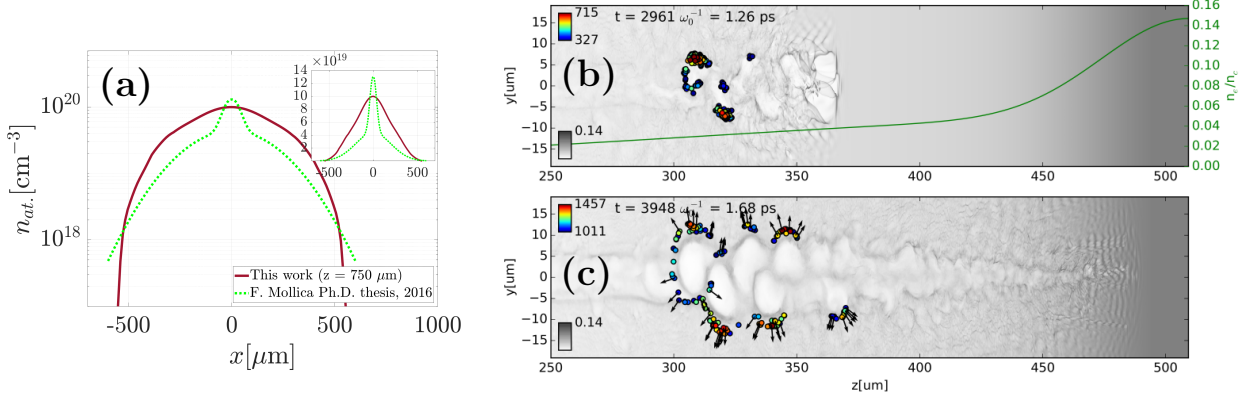
Fig. 5.26: (a) Comparison between the pure helium gas profile simulated in this work (solid line) and the 99% helium and 1% hydrogen profile of Ref. [107] (dotted line). Electron density charts taken at (b) $t = 1.26$ ps and (c) $t = 1.26$ ps extracted from Ref. [107]. Here the position and dynamic of the 150 more energetic protons accelerated by Coulomb explosion are plotted in colors.

5.7   Conclusions

We performed a 2-D PIC simulation of the interaction of the VEGA-3 laser pulse characterized by an $a_0 = 6.9$ ($I_{max.} = 10^{20}$ W/cm^2), a laser wavelength $\lambda_L = 0.8\,\mu m$ and a laser pulse duration $\tau_L = 100$ fs with a pure helium near-critical density profile with maximum atomic density $n_{at.} = 0.1\,n_c \approx 10^{20}$ cm^{-3}. Both the longitudinal density profile and the laser intensity profile were extracted from experimental measurements in order to replicate as much as possible the real experimental conditions. The laser intensity profile was composed of the $\tau_L = 100$ fs intensity peak and a ≈ 6 ps prepulse with maximum intensity $\approx 10^{17}$ W/cm^2.

The propagation of the laser prepulse followed by the laser intensity peak through the target up-ramp triggers a two-staged ionization of the gas. In the laser prepulse case, this ionization process is weak and restricted to its propagation path. On the contrary, the laser intensity peak strongly ionizes the ensemble of the gas, see electron density n_e charts of Figs. 5.3e and f. Looking at the early time electron (x, p_x) phase space (integrated in the transverse direction, see Figs. 5.6a and b) one observes that the turbulent electron heating phase starts very early, when the laser is still crossing the gas up-ramp. This process is characterized by the phase mixing of hot forward-moving and cold return electron currents. A premature laser absorption follows as seen in the absorption rate curve of Fig. 5.4, leaving the up-ramp energized electrons as the main heating source of the gas down-ramp.

The strongly depleted laser pulse manages to still expel electrons from its path, probably aided by the ponderomotive force increase due to the *optical shock* at the laser pulse front [30], as well as by the laser self-focusing (see Fig. 5.7d), and creates a channel visible in the electron density n_e charts of Figs. 5.7a and b. The laser-created channel does not traverse the entire gas slab, which is consistent with the experimental observation (Figs. 5.10a and b). It was

seen that focusing the laser pulse in the target up-ramp can favor the formation of a single non-filamented laser channel, as observed during the experiment.

The electrons within this channel are mainly energized through direct laser acceleration (DLA) up to mean energies about two times larger than the ponderomotive potential scaling. DLA was singled out as the main electron acceleration mechanism within the laser channel by plotting the electron distribution function in the W_x, W_y phase space. W_x and W_y are the work performed by the longitudinal and transverse electric fields computed following Eq. 5.1. As seen in the phase spaces of Fig. 5.12c and d a large fraction of the hot electrons are located in the triangular region where $W_y > W_x$. Hence most of the electrons' energy gain is related to the E_y electric field which is mainly due to the laser itself.

The forward electron energy-angle distribution $f_e(\mathcal{E}, \theta)$ was obtained by placing a probe diagnostic at the right boundary of the simulation box. The lower energy electrons ($\mathcal{E} <$ 10 MeV) exhibit a *forked* angular distribution (see Fig. 5.15a) that qualitatively agrees with the experimental dose deposition horizontal hot spots seen in the experimental data (and plotted in Fig. 5.17a). The angular distribution of the electrons between 10 and 100 MeV exhibit a more homogeneous angular distribution inside the cone $[-30°, 30°]$. The latter cannot be compared with experimental data since the radiochromic film stack was not sensitive to high energy electrons. Fig. 5.17b shows a comparison between experimental and numerical electron spectra. The simulated electron spectrum is harder ($T_e \approx 26.5$ MeV) than the experimentally measured ones ($T_e \approx 13$ MeV) in the detection range of the diagnostic (i.e. up to 50 MeV). Possible explanations for this discrepancy are the reduced 2-D geometry of the simulation and possible uncertainties in the laser or gas parameters.

The expulsion of electrons from the channel creates transverse E_y fields at the channel walls that drive ion acceleration at times $t \gg \omega_{pi}^{-1}$. The transverse channel expansion triggers collisionless electrostatic radial shocks that accelerate α particles up to ≈ 5 MeV all along the channel walls. The transverse ion spectra of Fig. 5.25b exhibit maximum energies of ≈ 7.5 MeV and the spectrum centered at 70° shows an energy peak at ≈ 5 MeV corresponding to the reflection from the shock front. Transverse particle emission is seen in $\pm 15°$ cones centered at the gas density peak, see ion energy-angle phase space of Fig. 5.25a. The measurement of transverse ion energy spectra is left as a challenge for future experiments.

TNSA forward acceleration of ions is driven by the charge separation fields created at the plasma-vacuum boundary once the hot electron current exits the plasma. The maximum ion energies measured at 0° were also ≈ 5 MeV. A lower density ion population exits the target at symmetric large angles up to 45°. This large deviation in the ion trajectories was found to be linked to the setup of an azimuthal magnetic field at the plasma-vacuum border once the hot electrons exit into vacuum. During the experiment we measured up to ≈ 2 MeV of α particles at $\pm 17°$ from the laser axis in a 5° inclined polar plane. This ions could be exiting away from the laser axis due to the magnetic field created at the plasma-vacuum interface. A comparison of experimental and numerical ion spectra is plotted in Fig. 5.22. Although the maximum experimental and numerical ion energies at 17° (≈ 2.5 MeV) are comparable, the numerical spectra do not decay exponentially as the experimental ones. The maximum numerical ion energies of ≈ 6.3 MeV were obtained at 45° while the spectrum on-axis exhibits a maximum energy of ≈ 4.7 MeV and about two orders of magnitude more particles.

5.8 Perspectives

Hereinafter, a comparison with a similar 2-D simulation described in Ref. [30] is performed. The cited simulation is based on experimental conditions that resemble the ones detailed in this chapter with the difference that it does spawn a forward collisionless electrostatic shock.

We aim at performing a constructive comparison in order to deduce possible experimental paths leading to interaction conditions that are more favorable to forward collisionless shock acceleration of ions. The main simulation parameters are summarized in Table 5.1 for both simulations.

The 2-D simulation of Ref. [30] was performed with a normalized laser amplitude $a_0 = 15.68$, obtained at full compression of the laser pulse ($\tau_L = 30\,\text{fs}$). The cited simulation did not include any laser prepulse in the laser intensity profile, which is supposed to have Gaussian spatial and temporal shapes. The laser pulse is focused down to $D_L = 6\,\mu\text{m}$ FWHM and the transverse dimension of the gaseous target is $\Delta y = 67\,\mu\text{m}$. The pure helium longitudinal density profile input of Ref. [30] is plotted using a blue dashed line in Fig. 5.27. Its maximum density is $n_{at,max} = 0.08\ n_c \approx 8.8 \times 10^{19}\ \text{cm}^{-3}$. Note that this density profile is a Gaussian fit of a density lineout extracted at $50\,\mu\text{m}$ from the nozzle's surface. In this case a Laval-type nozzle was used. The pure helium longitudinal density profile input in this work (obtained at $\approx 750\,\mu\text{m}$ from the nozzle) is plotted using a solid line in Fig. 5.27 and has a maximum density $n_{at,max} = 0.1\ n_c \approx 10^{20}\ \text{cm}^{-3}$, 25% higher than the simulation of Ref. [30]. Both simulations start with an initially neutral gas. In Ref. [30] the ratio $\Delta y/D_L = 53$ and in this work $\Delta y/D_L = 65$, where Δy is the gaseous target transverse dimension and D_L the laser

Fig. 5.27: (solid line) Pure helium longitudinal lineout input in the 2-D simulation. The density scale length at the gas wings is $L_n \approx 100\,\mu\text{m}$ and close to the gas density peak it is $L_n \approx 340\,\mu\text{m}$. This lineout was obtained at $\approx 750\,\mu\text{m}$ height from the nozzle's surface. (squared-dotted line) Pure helium longitudinal lineout obtained at $\approx 460\,\mu\text{m}$ from the nozzle's surface. This density lineout was extracted from the same density 2-D chart as the one plotted using a solid line. (blue dashed line) Pure helium longitudinal lineout input in a similar 2-D PIC simulation detailed in Ref. [30]. The figure inset shows the same density profiles in linear scale.

focal spot diameter at the FHWM. Finally, the gaseous target longitudinal dimension in this work ($\Delta x = 1000\,\mu\text{m}$) is more than twice the one of Ref. [30] ($\Delta x = 400\,\mu\text{m}$).

Tab. 5.1: Main simulation parameters of (upper row) a 2-D simulation described Ref. [30] and (lower row) the simulation presented in this chapter.

Extracted from:	$a_0 (\lambda_L = 0.8\,\mu\text{m})$	τ_L	Laser prepulse	$D_L[\mu\text{m}]$	$\Delta y[\mu\text{m}]$	$\Delta x[\mu\text{m}]$	$\Delta y/D_L$	Gas	$n_{at,max}[n_c]$
A. Debayle *et al.*,, NJP **19**, 2017 [30]	15.68 (5.3×10^{20} W/cm²)	30 fs	No	$6\,\mu\text{m}$	318	400	53	He	0.08
This work	6.90 (10^{20} W/cm²)	100 fs	$\pm 6\,\text{ps}$, 10^{17} W/cm²	$15\,\mu\text{m}$	974	1000	65	He	0.1

Figures 5.28a-f are a comparison of the main results extracted from both simulations. The left column corresponds to results from Ref. [30] and the right column to results from this work. The locations of the maximum density peak are marked with pink vertical dashed lines. Figures 5.28a and b show the electron (x, p_x) phase spaces extracted during the turbulent energization phase. Figures 5.28c and d are the mean electron kinetic energy $\langle \gamma_e - 1 \rangle$ charts. Finally, Figs. 5.28e and f correspond to electron density n_e charts at the last time step of each simulation.

In Ref. [30] the laser is not completely absorbed in the target up-ramp. On the contrary, it manages to cross the gas density peak while triggering a turbulent electron energization regime and efficiently energizing the up-ramp electrons. This can be seen in the electron (x, p_x) phase

Fig. 5.28: (a-f) Comparison of the two simulations' results: the left column corresponds to results from Ref. [30] and the right column to results from this work. The locations of the density profiles' peaks are marked with pink vertical dashed lines (in the images where it is visible given the x-axis limits, $x_{n_{max}} = 1500\ c/\omega_0$ in Ref. [30] and $x_{n_{max}} = 6000\ c/\omega_0$ in this work). (a-b) Electron (x, p_x) phase spaces captured during the turbulent energization phase. (c-d) Mean electron kinetic energy $\langle\gamma_e - 1\rangle$ charts. (e-f) Electron density n_e charts taken at the last time step of each simulation.

space of Fig. 5.28a taken at $t = 0.8\,\mathrm{ps}$. Here, the hot electrons initially trapped inside the laser wakefield have a very high longitudinal momenta $p_x > 200\ m_e c$. At the same time, the

electrons first pushed by the laser front and then pulled back into the plasma core exhibit a negative momenta $p_x \approx -45 \ m_e c$. The same interaction moment, corresponding to this work, is plotted in the electron (x, p_x) phase space of Fig. 5.28b. Notice that the y-axis limits are the same as in Fig. 5.28a. In this case, the premature laser absorption forces the turbulent electron energization regime to occur before the density peak (located at $x = 1000 \ \mu m$). The hot electrons have maximum momenta $p_x \approx 100 \ m_e c$ and the cold backward-accelerated electrons are re-injected into the target with a negative momenta $p_x \approx -20 \ m_e c$. Two factors play a key role in the shallower electron energization seen in Fig. 5.28b:

- The lower laser $a_0 = 6.9$ (compared to $a_0 = 15.68$ in Ref. [30]) which entails a weaker ponderomotive laser push ($f_p \propto a_0/2\pi$ [30]) on the target electrons. As a result the cold return electrons exhibit relatively moderate negative electron momenta since $p_{x,c} \approx -\Delta\phi/2$ [30], where $\Delta\phi \approx 20 \ m_e c^2/e$ is the local electrostatic potential departing from the cold return current $x \approx 800 \ \mu m$ position.

- The larger, yet experimentally realistic, longitudinal gaseous target dimension $\Delta x = 1000 \ \mu m$ (compared to $\Delta x = 400 \ \mu m$ in Ref. [30]), which gives rise to a premature laser absorption.

Figures 5.28c and d are mean electron kinetic energy $\langle \gamma_e - 1 \rangle$ charts taken at key instants in both simulations. Note that the y-axis limits in both figures are the same. Fig. 5.28b, corresponding to the simulation of Ref. [30] is taken at $t = 2 \ ps$, after the laser has crossed the gas profile. Here we can observe that the mean electron energy inside the laser channel ($y \approx \pm 30 \ \mu m$) is approximately $\langle \gamma_e \rangle \approx 60$, four times higher than the ponderomotive scaling. This value is consistent with the theoretical prediction of the simple model for electron heating model (EHM) as a function of n_e and a_0 obtained in Ref. [30]. Fig. 5.28d corresponds to the electron kinetic energy at $t = 3.34 \ ps$, after the laser pulse has been completely absorbed in the gas up-ramp. Here $\langle \gamma_e \rangle \approx 10$, which is two times higher than the ponderomotive potential, and does not follow the EHM detailed in Ref. [30]. The latter is probably due to the lack of volumetric target heating. The main aspects of the electron energization scenarios seen in the two simulations are:

- In the simulation presented in Ref. [30] the laser crosses the gas density peak and energizes the electrons within the channel at the gas down-ramp edge.

- On the contrary, in the simulation presented in this work the laser is prematurely absorbed in the target up-ramp. As a result the electron energization is quite shallow (although still twice the ponderomotive scaling) as seen in Fig. 5.28d. The electron heating is also confined to a transverse region of the order of the laser focal spot D_L. No volumetric heating of the target is achieved.

Figures 5.28e and f correspond to electron density n_e charts obtained at the last time step of each simulation. Fig. 5.28e is taken at $t = 3.6 \ ps$ and Fig. 5.28f at $t = 9.7 \ ps$, much later than Fig. 5.28e. Fig. 5.28e evidences partial transmission of the laser pulse through the He gas. Note that the thin electron density shell that extends up to $x \approx 480 \ \mu m$ has been singled out as a possible signature of an *electrostatic shock* accompanied by a *magnetic dipole vortex* [18, 20, 104]. The ionization dynamics seen in both electron density n_e charts are quite different.

Figure 5.28f has been re-plotted in Fig. 5.29 using the same y-axis limits as Fig. 5.28e and a 1:1 ratio between both axes to allow better visual comparison of the channel dynamics. Here we can appreciate that the transverse length of the channel in Fig. 5.28e is actually comparable to our simulation results $\Delta y \approx 30 \ \mu m$. However, the longitudinal dimension of the gas, which is

twice long in our simulation, inhibits the laser propagation after $x \approx 1080\,\mu$m. On the contrary, in Ref. [30] the laser crosses the entire gas, which has a longitudinal dimension $\Delta x \approx 400\,\mu$m, without being completely absorbed.
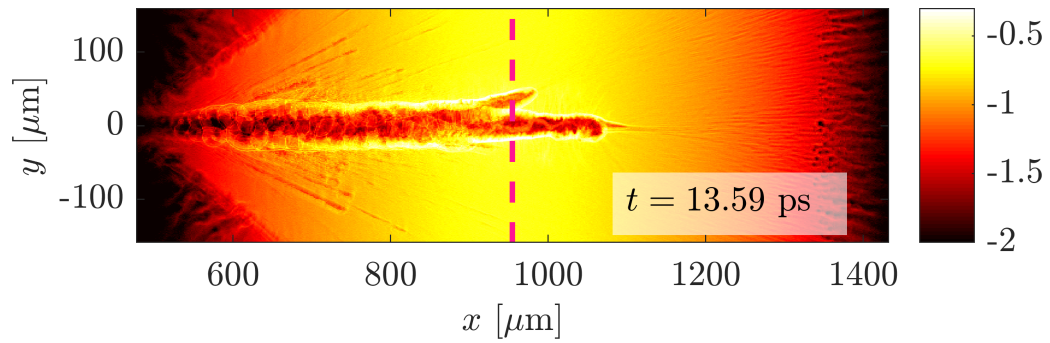
Fig. 5.29: Electron density n_e chart taken at $t = 13.59\,$ps corresponding to the simulation presented in this chapter.

Conclusions and perspectives

Over the course of this thesis we have investigated laser-driven ion acceleration from near-critical transparent gas jets. The research was conducted both from the numerical and the experimental sides.

From the experimental side, two experimental campaigns were performed: VEGA-2 (200 TW) in 2018 and VEGA-3 (1 PW) in 2021. The VEGA-2 experiment was performed before this thesis work started. However, the author was already strongly involved in all the experimental activities as fielding of diagnostics and data analysis. During the VEGA-3 experiment, at the center of this thesis work, the author was the effective PI who coordinated the design, realization and data analysis, which was conducted together with an international group of collaborators.

The maximum laser intensity achieved in both campaigns was approximately 10^{20} W cm^{-2}, corresponding to a normalized laser amplitude $a_0 \approx 6.9$. Nevertheless, the VEGA-3 laser delivered about 18.5 J on-target while the VEGA-2 laser's maximum energy on-target was of 3 J. An important effort was dedicated to field the most complete diagnostic suite as possible to extract a meaningful picture of the laser-matter interaction. At the same time, an important effort was dedicated to the characterization of high pressure gas target systems (HPGS), which are a naturally debris-free target, well suited for high-repetition-rate (HRR) operation. The objective was to understand the current advantages, as well as point out the technical difficulties that they entail. The author performed and analyzed the two HPGS characterization campaigns performed as part of this thesis' work.

The numerical efforts performed during this thesis included a comprehensive 1-D particle-in-cell (PIC) parametric study, which aimed at understanding the physical mechanisms at play during the interaction of an ultra-high intensity laser with a near-critical transparent plasma. Furthermore, 2-D PIC simulations were also performed to shed light on the experimental results issued from the VEGA-3 experiment. The PIC code Calder developed at CEA was used. The author conducted and analyzed all the PIC simulations presented in the 1-D parametric study as well as all the 2-D simulations.

The results obtained during this thesis contribute to expand the knowledge on the highly unexplored regime of ultra-high intensity (UHI) lasers interacting with near-critical targets. Furthermore, they provide an insight into particle acceleration from the interaction of fs-laser pulses with high density gas jets, as well as point out the technical advantages and challenges of state-of-the-art high density gas targetry.

1-D particle-in-cell parametric study

We conducted a parametric study based on 1-D PIC simulations with the objective of understanding the interaction of intense lasers with near-critical, non-uniform density transparent gas targets. Specifically, we aimed to find an optimal set of experimental parameters regarding the interaction of the VEGA-3 laser ($\lambda_L = 0.8\,\mu$m, $a_0 = 8.8$ and $\tau_L = 30$ fs) with the near-critical, non-uniform pure nitrogen gas profile produced by the S900 non-commercial gas nozzle design. The mentioned density profile was extracted from computational fluid dynamics simulations using the the Fluent code. Several parameters where studied including varying the

peak gas density, the direct laser contribution to ion acceleration, the effect of interacting with a temporally stretched laser pulse and of including a small percentage of lighter ions in the gas mixture.

In the case of a pure N_2 gas jet, shock formation was achieved for a peak electron density ranging between 0.35 n_c and 0.7 n_c. In this interval, the survival of a percentage of the laser pulse until the gas density peak, while being strongly absorbed (80% - 90%) and creating a hot electron population in the gas up-ramp, is singled out as a necessary condition for shock formation. Moreover, the laser absorption must give rise to a super ponderomotive heating of the target electrons in order to launch an electrostatic shock inside the plasma. At higher densities, ion acoustic waves (IAWs) are triggered, accelerate while descending through the density gradients and reflect background ions to modest velocities. At lower densities, the TNSA profile gently develops and no shock is launched.

The direct laser effect on ion acceleration was singled out by performing a laser-free simulation initialized with a hot electron population with $T_e = a_0 \approx 5\,MeV$. Shock formation was indeed achieved in the laser-free simulation and the direct laser-effect was identified as a strong initial density perturbation that enhances charge separation. Hence, the electron pressure gradients were pointed out as the main ingredient for shock formation, emphasizing on the advantage of interacting with shock-nozzle-produced density profiles, that exhibit strong density gradients.

The addition of lighter ions to the gas mixture provides a collisionless electrostatic shock (CES) experimental signature in the means of equally placed peaks in the velocity spectra of the different species. At the same time, lighter ions favor CES acceleration by reducing the ion kinetic energy $E_{k,i} \propto m_i$, recalling that the shock reflection condition reads: $Z^* e \Delta \Phi \geq m_i v_i^2 / 2$, where the l.h.s is the electrostatic potential seen by an ion of charge state Z^* crossing the shock region, and the r.h.s. is the ion's kinetic energy.

Finally, the production of a controlled and repetitive gas profile, as well as the possibility of performing measurements with statistical meaning, are highlighted as fundamental for conducting a thorough experimental study.

Despite reduced to a 1-D geometry, the presented study shed some light on the complex UHI laser interaction with near-critical targets. Guided by the outcome of this study we decided to interact at lower electron densities, with respect to those targeted during the VEGA-2 experiment, as well as to vary the laser pulse duration from 30 to 100 fs. However, the density profile extracted from CFD simulations ended up being quite different from the actual density profiles measured before the experiment. This occurred due to nozzle manufacturing imperfections. Consequently, the 1-D parametric study can not be directly related to the VEGA-3 experimental conditions. Yet, it still highlighted important aspects of the interaction.

Particle acceleration from near-critical gas jets

Ion acceleration

During the VEGA-3 experiment, we demonstrated forward acceleration of α particles up to $0.7\,MeV\,u^{-1}$ with 10^9 particles/sr and of nitrogen ions up to $5.7\,MeV\,u^{-1}$ with 10^7 particles/sr, from a pure He and a pure N_2 gas jet, respectively, using to the S900 shock nozzle. We also measured α particles up to $0.5\,MeV\,u^{-1}$ with 10^{10} particles/sr in the forward direction using the J2021 shock nozzle. Time-of-flight (ToF) detectors were used to obtain ion spectra, which proved to be an excellent tool for particle characterization from near-critical gas targets. All ToF measurements were performed in a 9° inclined plane with respect to the chamber "equator" and inside a $\pm 17°$ cone centered in the laser axis. These results can be compared with Chen *et al.* [62], that reported measuring on-axis protons up to $1\,MeV$ with 10^{12} particles/sr, from

a pure hydrogen gas jet[a]. The only difficulty encountered regarding the ToF detectors was their sensitivity to EMP when installed close to the TCC, inside the chamber, and not in a chamber flange. Future experiments should make use of signal filtering techniques such as those described in Ref. [156].

The ions were accelerated through TNSA arising in the plasma-vacuum border and afterwards deflected by the B-field of $\approx 50\,\text{T}$ created by the electron return currents, as seen in the 2-D simulations. Numerical and experimental ion spectra approximately agree on the maximum α particles energy. Moreover, the 2-D simulations indicate that a small population of α particles ($\mathcal{E} \approx 0.7\,\text{MeV}\,\text{u}^{-1}$) are accelerated off-axis, as was experimentally demonstrated. However, they also suggest that most of the particles are emitted close to the laser axis with a small tilt, probably linked to the bending of the laser pulse at the high density peak of the gas target. Consequently, in future experiments, Thomson parabolas should be placed inside the experimental chamber with enough space as to relocate the diagnostic in the particles' emission line.

The repetition-rate (RR) of the experiment was impacted by the security systems fielded to protect the laser pipes from the pressurize gas. Furthermore, the RR was also conditioned by the nozzle realignment procedure in between shots as well as by the need to acquire two reference images before each UHI shot (for the analysis of the interferometry diagnostic). We managed to perform one UHI shot each thirty minutes. Improvements on the RR could include acquiring a single reference image (as needed in standard interferometry) as well as simplifying the laser pipes security system, profiting from the leakage-free against EMP effects microvalve.

Previous ideas [109] regarding the application of α particles to the production of isotopes for cancer treatment require high energies of α particles $\mathcal{E} \approx 20\,\text{MeV}$. Recent studies [168] have pointed out that $63\,\text{MeV}$ α particles could be used in radiotherapy to produce Tb^{149}. These energies are slightly far away from nowadays gas jet laser-driven ion acceleration capabilities and clearly motivate the improvement of the ion yields. However, we did achieve very high currents, in the order of the mA, which is comparable to modern cyclotrons [169].

The fusion reaction of deuterium and tritium produces one neutron of $14.1\,\text{MeV}$ and an α particle of $3.5\,\text{MeV}$. The subsequent stopping of these α particles can condition the obtention of a self-sustained heating of the fuel in ICF implosion experiments. Once slightly higher energies are obtained particle selectors, such as the one developed in Ref. [170], could be used to select the central energy and bandwidth of a particle beam. The latter can be implemented to study the stopping of α particles in conditions representative of the cold fuel surrounding the hot spot in a fusion target [171].

Regarding the use of nitrogen ions, the industrial process of hardening surfaces through nitriding needs about 10^{18} particles/sr and energies between 50-500 keV [172]. One could also make use of particle selectors in order to adapt the measured nitrogen ions spectra to those needs and adapt the RR to produce enough particles.

The absence of ion signal in the TPs could be due to their very small solid angles linked with a low signal-to-noise ratio S/N. At the same time, the ions seem to be accelerated off-axis (and outside the "equator" plane) as measured by the ToF diagnostics. Future experiments should approach TP acquisition by firstly locating the ion emission, and only afterwards positioning the diagnostic. This can be done by placing passive detectors such as RCFs around TCC and shooting several times, as to have an statistically valid idea of the preferential ion acceleration direction. Accumulating several UHI shot in a single IP could improve the S/N ratio.

We intended to characterize the transverse ion acceleration fielding a Thomson parabola in the "equator" plane at $110°$ from the laser axis, and two ToF detectors (as well at $\theta = 110°$ from the laser axis, in a $\varphi = 15°$ inclined plane) without success. It would be interesting to

---

[a]Facility: TITAN, $\lambda_L = 1054\,\text{nm}$, $I_{max} \approx 2.2 \times 10^{19}\,\text{W.cm}^{-2}$ ($a_0 = 4.2$), $E \approx 210\,\text{J}$, $\tau_L \approx 5\,\text{ps}$, $D_L \approx 10\,\mu\text{m}$ FWHM, Laval gas nozzle, H_2 gas jet, $n_e \simeq 0.2 n_c$

explore the $\theta = 90°$ angle as well as intermediate angles in future experiments. Note that the interferometry axis can be tilted some degrees without compromising the diagnostic. In any case, a cylindrical gas symmetry is imposed during the data analysis process (see Appendix A). The 2-D simulations evidenced transverse ion acceleration in the symmetrical angle intervals $\theta \in [60°, 120°]$ and $\theta \in [-60°, -120°]$.

Electron acceleration

The fully calibrated electron spectrometers delivered valuable data on the electron heating of the gaseous target. We measured a maximum electronic temperature $T_e = 13\,\text{MeV}$ which is six times higher than the normally assumed *ponderomotive scaling*. Such temperature is in agreement with the electron heating model in near-critical targets developed in Ref. [30]. The highest electron temperature $T_e = 13\,\text{MeV}$ and energy values $\mathcal{E} = 45\,\text{MeV}$ were obtained at $\theta = -2°$ from the laser axis, using pure He targets. The measured electron beams are most likely highly collimated and directional since the spectrometer located at $\theta = 2°$ measured much lower energies ($\mathcal{E} \approx 1\,\text{MeV}$).

Thanks to the careful control of the laser axis, the spatial shifts seen in the dose deposition maps in the RCF stacks can now be unambiguously linked to processes taking place inside the plasma (an not to a laser pointing error). An example of such processes could be laser bending in high density gas regions. Furthermore, by conducting Monte Carlo simulations of the stopping of electrons, α particles and nitrogen ions in the RCF stack, we could conclude that the signals that are seen are mostly coming from low energy ($\mathcal{E} < 2\,\text{MeV}$) electrons.

Since the RCF stack could only measure electron energies up to $\mathcal{E} \approx 2\,\text{MeV}$, linking the horizontal dose deposition areas (aligned with the laser polarization plane) with electron acceleration mechanisms such as DLA is not possible. To do so, one would need to obtain electron spectra resolved in angle for high energy electrons ($> 50\,\text{MeV}$ [149]). Future experiments could field higher energy electron spectrometers as well as RCF stacks that are sensitive to such energies.

Laser channeling

The interaction at lower electron densities, with respect to the VEGA-2 experiment, allowed the triggering of laser channeling through the gas density peak, as revealed by deconvolving late time interferograms ($t \approx 150\,\text{ps}$). This feature was observed in the 2-D PIC simulations, where it gave rise to transverse CSA of α particles up to $0.7\,\text{MeV}\,\text{u}^{-1}$.

The on-shot interferograms revealed electron density structures departing from the laser channel, that could be linked to a magnetic vortex expanding in the gas down-ramp, or to magnetic filaments created by the return electron currents in the right plasma-vacuum border. Due to the limited amount of energy available in the probe beam, our complex interferometry diagnostic failed to characterize the B-fields created inside the plasma. The interesting features appearing in the electron density charts need to be further examined with a polarimetry diagnostic in future experiments.

In addition to a low enough electron density, laser channeling could also be observed due to the fact that the density profiles in the S900 nozzle & He case were thin ($x \approx 1000\,\mu\text{m}$). Thicker profiles, like those resulting from the S900 nozzle & N_2, triggered laser self-focusing in the target down-ramp, as deduced by the multiple hot spots seen in the plasma self-emission acquisition. Hence, if the production of strongly non-uniform profiles issued from nozzles that resist the laser damage is too difficult, one could also opt for producing thin low density profiles in a controlled and repetitive manner. The advantages of interacting with strongly non-uniform profiles remain experimentally unexplored. Nevertheless, the 1-D parametric study presented

in Chapter 3 highlighted their capability of triggering CSA, benefiting from the natural density gradients.

Further steps towards forward collisionless shock acceleration (CSA) of ions

The current analysis of the VEGA-3 laser focusing capabilities concludes that there is about a 47% of the laser energy inside the focal spot (FWHM), that the laser system is capable of delivering about 18.5 J on-target (considering all the losses in the optical path) and that a good quality 15 µm focal spot (FWHM) is achievable with the current $f/12$ long focal parabolic mirror. Regarding the laser pulse compression, 30 fs pulses (FWHM) were measured using a 2ω on-shot autocorrelator. However, the laser pulse length was seen to increase through the day up to ≈ 100 fs. In order to achieve an $a_0 = 16$ (comparable to Ref. [30], where forward CSA was observed) one would need to improve the focal spot quality and obtain at least a 50% of the laser energy inside the focal spot. The current on-target energy is adequate if one achieves a 10 µm focal spot (FWHM) and a constant 30 fs pulse compression. A smaller focal spot could be achieved making use of the future short focal length parabola to be installed at VEGA-3.

A reduction in the gas profile transverse dimension can be obtained, in the short term, by shooting closer to the nozzle, see squared-dotted profile in Fig. 5.27 corresponding to a lineout taken at ≈ 460 µm from the nozzle's surface. New nozzle designs should target hydrodynamic shock formation at least ≈ 600 µm away from the nozzle's surface (see Chapter 2) to cope with nozzle damage [70, 109] while producing a thinner gas transverse profile. Disposable nozzle operation could be a path to HRR operation if one develops a cheaper way to manufacture them and an automatic nozzle exchange system. Sub-µm high precision 3-D printing of ceramic structures could massively produce robust nozzles at a relatively cheaper price [109, 173]. However, the present metallic and the newly-developed ceramic nozzles are currently sold at similar prices (≈ 1000 EUR per nozzle) since nozzle 3-D printing is still in development phase. It would be worth contacting the manufacturers (see Ref. [173]) and trying to establish a mid-term academic collaboration so that one can advance on nozzle manufacturing techniques as well on the physical understanding of the interaction processes. At the same time, the experimental efforts should make use of different nozzle types, including Laval and shock nozzles, that allow to characterize both the target electron heating and the ion acceleration mechanisms that are triggered. Both forward and lateral ion acceleration mechanisms are to be studied. A reproducible density profile should be the priority and only then one should think on producing strongly non-uniform profiles. The use of hydrogen would decrease the electrostatic potential needed in order to trigger background ion reflection through CSA.

The role of the laser prepulse is not clear. From the 2-D simulations conducted in this work it seems that the ionization dynamics that it triggers are weak and restricted to the laser path. It could be interesting to perform shots with and without a laser prepulse to assess the experimental outcome. This can be done at facilities like the new Bella iP2 target area (Berkeley, USA) where a motorized double plasma mirror is located before the short focal parabola. Finally, the advent of the new 10 PW facilities like the F1 beam of Apollon (Palaiseau, France), the Corels laser (Gwangju, Republic of Korea) or the L4 Aton beam at ELI Beamlines (Dolni Brezany, Czech Republic) opens exciting experimental paths regarding the study of laser-gas interaction at very high laser intensities and with large focal spots, targeting an efficient volumetric heating of the target and the possible forward (longitudinal) acceleration of ions by *electrostatic shocks* triggered inside the plasma.

Operation of high pressure gas target systems

The S900 nozzles developed for the VEGA-3 experiment are more resilient to laser damage than those used during the VEGA-2 experiment. It was seen that the production of the shock at more than 600 µm from the nozzle's surface strongly reduces the laser-induced nozzle damage. We achieved an almost-constant gas density profile for up to six UHI shots in a row. Nevertheless, the density peak does disappear after the first shot, and it is replaced by a smooth peak. This occurs because the laser ablates the straight final section of the shock nozzle, hindering the hydrodynamic exit flows from converging and forming the shock region.

A procedure based on thorough characterization of the HPGS coupled to each nozzle, through interferometry and strioscopy optical lines, was used to locate stable operating points. The latter were selected during UHI shots to ensure maximum reproducibility of the gas profiles from shot-to-shot. Furthermore, the laser-induced nozzle damage was tracked on a shot-to-shot basis and a strategy to cope with it was developed. If the shock is produced at least at ≈ 600 µm from the nozzle's surface, the laser damage will be restricted to an ablation of the last section of the shock nozzle. As a result, the gas profile is not extremely altered, but its vertical position will shift. One must acquire neutral gas density charts before each shot and adapt the shock height correspondingly. Thoroughgoing HPGS characterization campaigns as the ones detailed in Chapter 2 must be performed before future experiments to select the HPGS working points until one can rely on the reproducibility of the nozzle manufacturing process.

The operation of the HPGS was greatly improved with respect to the VEGA-2 experiment. The newly developed *microvalve* proved to be leakage-free even under the effect of EMPs. Furthermore, the automated system for leakages detection and protection of the vacuum pipes [150] worked correctly. However, taking into account that the *microvalve* did not leak (contrary to the *rapid valve* used during the VEGA-2 experiment) the vacuum protection automated system did diminish the repetition-rate of the experiment. The automated system must be only used if the *rapid valve* is fielded in future experiments. Note that the *rapid valve's* interest lays on the possibility of tuning the neutral profile's maximum density in a much larger range than the *microvalve* allows to.

Experimental experience

Conducted

Ion acceleration from near critical density gas targets
07/2021 (4 weeks) VEGA 3 (1 PW), CLPU (Salamanca, Spain)
Experiment design and implementation, effective experimental PI and leader of the data analysis process

Zeeman splitting in the UV range for characterization of laser-driven magnetic fields in the 100 Tesla range
05/2021 (4 weeks) PICO2000, LULI (Palaiseau, France)
Experiment design and implementation, effective experimental PI

Participated

Ion stopping power measurements in coupled and degenerate plasma
05/2022 2 weeks ALEPH, CSU Fort Collins, Colorado, USA
Setup of the streaked optical pyrometry optical line, operation of the optical streak camera

Ion stopping power measurements in coupled and degenerate plasma
01/2020 (4 weeks) VEGA 2 (200 TW), CLPU (Salamanca, Spain)
Setup of the streaked optical pyrometry optical line, operation of the optical streak camera and data analysis

Plasma magnetization by interaction with chiral targets for laboratory astrophysics
11/2019 (3 weeks) GSI (Darmstadt, Germany)
Target alignment, interferometry setup and probe beam alignment

Complex interferometry and Faraday rotation measurements of laser-driven B-fields
10/2019 (2 weeks) PALS (Prague, Czech Republic)
B-dot probe and capacitor coil targets mounting and alignment

High resolution measurements of laser-driven magnetic fields with application to isochoric heating and ion acceleration
09/2019 (4 weeks) Pico2000, LULI (Palaiseau, France)
Target alignment, streaked optical pyrometry alignment and operation

Ion acceleration by ultra-intense laser interaction with a high density gas jet
10/2018 (4 weeks) VEGA 2 (200 TW), CLPU (Salamanca, Spain)
Time-of-flight diagnostics, alignment and management of the optical streak camera

Correlated study of parametric instabilities and hot electron generation
09/2018 (4 weeks) PALS (Prague, Czech Republic)
K-alpha emission imaging with a Bragg crystal and an x-ray streak camera and management of a Bremsstrahlung cannon

Proton stopping power measurements in coupled and degenerate plasma
05/2018 (4 weeks) VEGA 2 (200 TW), CLPU (Salamanca, Spain)
Alignment and operation of optical systems and time-of-flight diagnostics Data acquisition and development of Matlab scripts for time-of-flight and radiochromic films data analysis

Proton acceleration from solid target: commissioning experiment of the VEGA 2 system
09/2017 – 02/2018 (6 months) VEGA 2 (200 TW), CLPU (Salamanca, Spain)
Set up of imaging systems for target and laser pulse alignment, transport and focusing of laser pulses, set up and analysis of radiochromic films

Scientific contributions

Publications

- V. Ospina-Bohórquez *et al.*, **Ion and electron acceleration from near-critical density gas targets using fs-laser pulses**, to be submitted to Phys. Rev. Res.

- V. Ospina-Bohórquez *et al.*, **Parametric study on ion acceleration from the interaction of ultra-high intensity laser pulses with near-critical density gas targets**, to be submitted to Phys. Plasmas

- V. Ospina-Bohórquez *et al.*, **Experimental and numerical investigations of ion acceleration by ultraintense laser pulses in near-critical transparent gas jets.**, APS Division of Plasma Physics Meeting Abstracts (Vol. 2021, pp. NO05-001)

- M. Ehret, C. Salgado-López,V. Ospina-Bohórquez *et al.*, **Ion acceleration by an ultra-short laser pulse interacting with a near-critical-density gas jet**, arXiv :2012.09455

- S. Malko, W. Cayzac, V. Ospina-Bohórquez *et al.*, **Proton stopping measurements at low velocity in warm dense carbon**, Nat Commun **13**, 2893, 2022

- G. Pérez-Callejo *et al.*, **Cylindrical implosion platform for the study of highly magnetized plasmas at Laser MegaJoule**, Phys. Rev. E **106**, 035206, 2022

- T. Pisarczyk *et al.*, **Influence of the magnetic field on properties of hot electron emission from ablative plasma produced at laser irradiation of a disc-coil target**, Plasma Phys. Control Fusion **64**, 115012, 2022

- F. Mirani *et al.*, **Integrated quantitative PIXE analysis and EDX spectroscopy using a laser-driven particle source**, Sci. Adv. **7**, eabc8660, 2021

- J.I. Apiñaniz *et al.*, **A quasi-monoenergetic short time duration compact proton source for probing high energy density states of matter**, Sci. Rep. **11**, 6881, 2021

- K. Nelissen *et al.*, **Characterisation and modelling of ultrashort laser-driven electromagnetic pulses**, Sci. Rep. **10**, 9108, 2020

- L. Volpe *et al.*, **Generation of high energy laser-driven electron and proton sources with the VEGA 2 200 TW system at the Centro de Laseres Pulsados**, High Power Laser Sci. Eng. **7**, 25, 2019

- G. Cristoforetti *et al.*, **Time evolution of stimulated Raman scattering and two-plasmon decay at laser intensities relevant for shock ignition in a hot plasma**, High Power Laser Sci. Eng. **7**, E51, 2019

- S. Malko *et al.*, **Stopping power measurements of ions in a moderetaly coupled and degenerate plasma**, Bulletin of the American Physical Society, 2019

Oral presentations & posters

- V. Ospina-Bohórquez *et al.*, **Experimental and numerical investigations of ion acceleration by ultraintense laser pulses in near-critical transparent gas jets** 30/06/2022 48th EPS Conference on Plasma Physics
Mastricht, Netherlands (on-line)

- V. Ospina-Bohórquez *et al.*, **Numerical and experimental investigations of ion acceleration by ultraintense laser pulses in high-density gas jets** 11/2021 APS DPP Meeting
Early career scientist oral presentation
Pittsburgh, USA

- V. Ospina-Bohórquez *et al.*, **Numerical and experimental investigations of ion acceleration by ultraintense laser pulses in high-density gas jets** 05/2021 PhD seminar
Univ. of Salamanca, Spain

- V. Ospina-Bohórquez *et al.*, **Near-critical plasmas from supersonic gas jets for laser-driven ion acceleration** 10/2019 Poster at the Forum Interaction Laser Plasma 2019
Frejus, France

- V. Ospina-Bohórquez *et al.*, **Near-critical plasmas from supersonic gas jets for laser-driven ion acceleration** 09/2020 Oral presentation at the LaPlass school
CLPU, Spain

- V. Ospina-Bohórquez *et al.*, **Charged particle detectors: time-of-flight technique** 03/2019 Oral presentation at the PowerLaPs 2019 school
CLPU, Spain

Submitted proposals

- **Collisionless shock formation in high-density transparent gas jets interacting with PW femtosecond laser pulses** PI: V. Ospina-Bohórquez
  BELLA iP2 facility
  LaserNetUS cycle 4 2021 (no beamtime granted)

- **Parametric studies on ion acceleration in relativistic laser-gas interactions, towards a high-repetition-rate** PI: V. Ospina-Bohórquez
  Apollon SFA target area
  SFA first user call 2021 (no beamtime granted)

- **Influence of the gas density profile and laser duration on ion acceleration in relativistic laser-gas interactions** PI: L. Gremillet
  VEGA-3 laser facility
  2021 call for proposals (no beamtime granted)

Appendix

Laser, plasma and particle diagnostics

A.1 Introduction

This Appendix is dedicated to summarize the main experimental diagnostics that were used during this thesis or that could be used in future experiments. The diagnostics are divided in laser, plasma and neutral gas characterization and particle detection. Section A.2 describes the laser pulse diagnostics including pulse duration measurements, laser contrast and energy and focal spot analysis. Afterwards, Section A.3 makes a brief introduction to plasma and neutral gas characterization through optical interferometry, polarimetry and complex interferometry techniques. This section describes as well the strioscopy spatial filtering technique as well as the acquisition of time resolved plasma self-emission. Finally Section A.4 discusses on particle detectors dividing them into active and passive detectors. The latter are much more resilient to electromagnetic pulse (EMP) disturbances triggered during the laser-gas interaction. The active detectors include time-of-flight diamond detectors as well as Thomson parabolas. The passive detectors were electron spectrometers, CR-39 particle tracker, imaging plates and radiochromic film stacks.

A.2 Laser pulse characterization

In the framework of this thesis ultraintense ($I_L > 10^{18}\,\mathrm{W\,cm^{-2}}$) and ultrashort ($\tau_L < 100\,\mathrm{fs}$) laser pulses focused on gas targets are used to create plasma conditions prone to various acceleration processes. Low-intensity laser pulses (in general collimated) can also probe the fast-evolving density or magnetic field distributions inside the plasmas, as resulting from irradiation by a higher-intensity (or *pump*) laser beam. In such pump-probe configurations, the probe beam is delayed increasing or decreasing its optical path with respect to the static pump beam. In this way, time-framed resolved density or magnetic field maps are acquired. The pump and probe beams can either be obtained by splitting the main beam or by using, if available, two separate laser beams. The beam splitting assures known delays (no jitter) between the probe and pump lasers.

The full characterization of a laser pulse intensity includes the measurement of both its temporal profile and 2D spatial distribution through the analysis of 2w autocorrelator signals and high-resolution focal spot images acquired at low energy. It includes as well the measurement of the energy delivered at the target chamber center (TCC). Laser pulses of femtosecond duration are accompanied by non-perfect intensity ramps before or after the main pulse arrival with intensities that can be more than ten orders of magnitude lower than the main pulse intensity. Pre and post-pulses also arise due to elements in the laser oscillator or the beam transport. The laser contrast, that is, the ratio of the laser intensity (as measured at a given time) to the peak laser intensity, is characterized using a 3ω autocorrelator that allows one to measure the intensity in temporal intervals of $\pm 500\,\mathrm{ps}$ centered on the laser peak.

A.2.1 2ω autocorrelator: Pulse length duration

An accurate, systematic measurement of the laser pulse duration τ_L is of vital importance to evaluate the peak laser pulse intensity, which determines the strength of the laser-plasma interaction.

The principle of operation of a second order autocorrelator [151] is based on recording the cross distribution of the second harmonic (SH) energy produced in a nonlinear crystal under non-collinear interaction of two beams with a determined angular aperture Ψ, see Fig. A.1a. The main idea of the method is depicted in Fig. A.1a for an ideal case where the initial pulse has a rectangular temporal shape and a uniform intensity cross distribution. As seen in Fig.

A.1 b, an initial single pulse is divided into two identical pulses using a beam splitter (BS). The cross size Dz of the second harmonic (SH) beam depends on the pulse duration τ_L of the 1ω pulse:
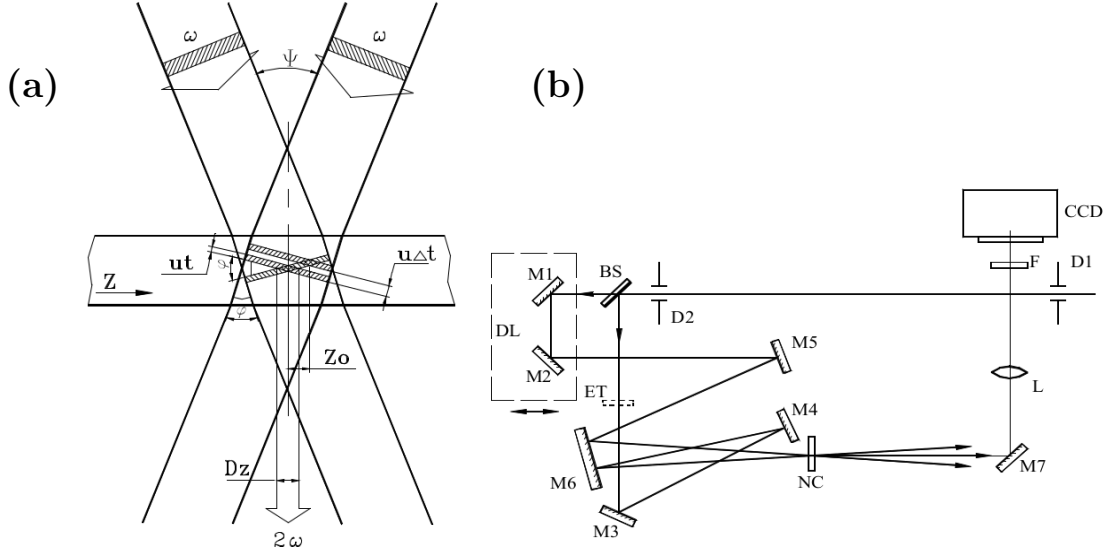
Fig. A.1: (a) Principle of operation of a second order autocorrelator based on recording the cross distribution of the second harmonic energy produced in a nonlinear crystal under non-collinear interaction of two beams with a determined aperture Ψ and (b) optical system of the second order autocorrelator. Varying Δt using a delay line modifies the location of the center of the SH energy distribution, Z_0. Panels a and b have been extracted from Ref. [151].

$$Dz = \frac{vt}{\sin\left(\frac{\varphi}{2}\right)},\tag{A.1}$$

where v is the 1ω beam group velocity inside the crystal and φ is the angle formed by the combination of both 2ω beams inside the crystal, see Fig. A.1b. If the two pulses are delayed by Δt the center of the SH cross distribution shifts by Z_0 (see Fig. A.1a):

$$Z_0 = \frac{v\Delta t}{2\sin\left(\frac{\varphi}{2}\right)}.\tag{A.2}$$

From Eqs. A.1 and A.2 one can obtain an expression for the 1ω beam duration:

$$\tau_L = \frac{Dz\Delta t}{2Z_0}.\tag{A.3}$$

Equation A.3 is correct for a rectangular shaped pulse with a uniform intensity cross distribution. For Gaussian (in time and space) pulses Eq. A.3 is rewritten as:

$$\tau_L = \frac{Dz\Delta t}{\sqrt{2}\,Z_0},\tag{A.4}$$

considering that $Nvt << D\tan\left(\frac{\Psi}{2}\right)$ where N is the refractive index of the nonlinear crystal and D the FWHM beam diameter.

Since measuring Δt and Z_0 with enough precision is quite difficult, a delay line (DL) is introduced in the optical system, see Fig. A.1b. The DL permits one to vary Δt and hence the

location of the center of the SH distribution, Z_0, following Eq. A.2. If two centers of the SH energy distribution Z_{01} and Z_{02} correspond to the micrometric head positions L_1 and L_2 one can rewrite Eq. A.4 as:

$$\tau_L = \sqrt{2}\, Dz \frac{(L_1 - L_2)}{(Z_{01} - Z_{02})c},$$ (A.5)

with c the speed of light in vacuum.

The VEGA-3 pulse length was monitored on a shot-to-shot basis using the ASF-15M second order autocorrelator model [151] sold by the Avesta company. The spectral range of the ASF-15M second order autocorrelator ranges from 700 to 900 nm, it can measure temporal pulses from 15 to 200 fs for $D > 3\,\mathrm{mm}$ and from 100 to 200 fs for $D > 6\,\mathrm{mm}$, where D is the laser pulse diameter at the FHWM. The second harmonic generator crystal has a thickness of 150 μm and it is made of Potassium Dideuterium Phosphate or KDP.

A.2.2   3ω autocorrelator: Laser contrast

In order to measure the laser contrast at the VEGA laser facility, we have employed the SE-QUOIA system developed by Amplitude Technologies [174], a widely used diagnostic for temporal characterization of ultrashort laser pulses over a temporal range of $\pm 500\,\mathrm{ps}$ around the laser maximum. The general principle of the measurement is summarized in Fig. A.2, extracted from Ref. [174]. As can be seen, the main pulse is separated in two lines one of which is delayed and frequency doubled in a second harmonic generator (SHG) crystal. The two pulses are recombined into a third harmonic generator (THG) crystal. The fact that the wavelength of the cross-correlation signal is different than the two beams' wavelengths makes it easy to identify, since the wavelength selection is done via dichroic mirrors. The evolution of the signal with respect to the time delay gives the pulse temporal profile. The delay line is controlled by software as well as an inner photomultiplier to automatically adjust the signal-to-noise (S/N) ratio. The dynamic range is strongly increased by neutral filters that are automatically positioned in the optical line.

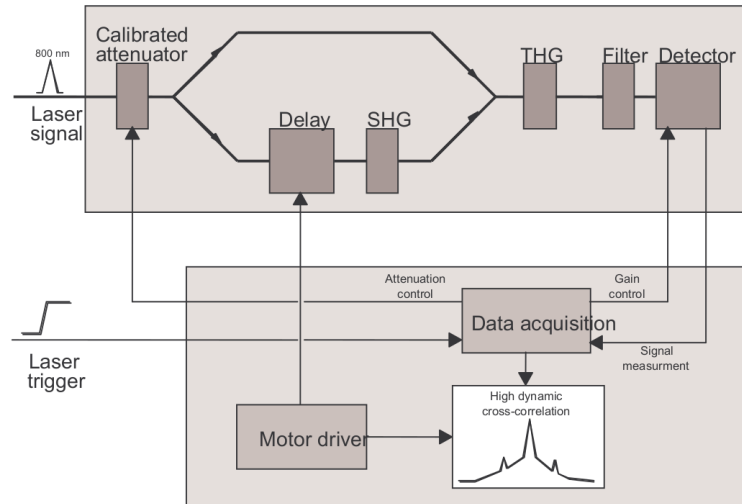Fig. A.2:   General principle of the Sequoia third order autocorrelator for laser contrast measurements. Extracted from Ref. [174].

Using such system the VEGA-3 temporal laser contrast was measured before the VEGA-3 experimental campaign began in 2021. The results of such measurements are plotted in Fig. A.2. Figure A.2a shows the entire laser contrast measurement over the [-500 ps, + 200 ps] time

window, while Fig. 3.3b zooms in on the $\pm 8\,\text{ps}$ range around the intensity peak. In both figures the compressed VEGA-3 laser contrast is plotted in purple while the uncompressed VEGA-3 pulse contrast is plotted in blue. The compressed pulse measurment is the most important one as it is the pulse the one that will interact with the near-critical gas target. As can be seen in Fig. A.3a the contrast of the compressed VEGA-3 pulse ranges from 10^{-11} at $-100\,\text{ps}$ to 10^{-8} at $-10\,\text{ps}$. Note that the contrast values of the uncompressed laser pulse are worse than those of the compressed pulse, namely 10^{-9} at $-100\,\text{ps}$ to 10^{-6} at $-10\,\text{ps}$. For more details on the VEGA-3 laser contrast measurement during the experiment, see Chapter 4.
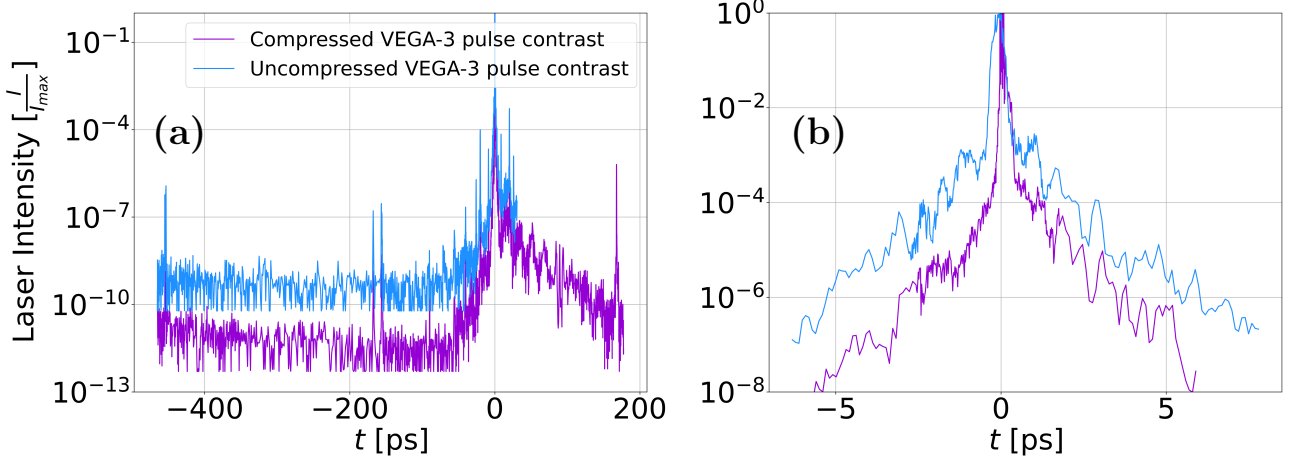
Fig. A.3: (a) Temporal intensity profile of the VEGA-3 pulse over the [-500 ps, +200 ps] range. (b) Same as (a) but over the $\pm 8\,\text{ps}$ range. The purple and blue curves correspond, respectively, to the compressed and uncompressed VEGA-3 pulse.

The low-intensity laser pedestal and prepulses can strongly affect a gaseous target before the arrival of the main pulse, which makes their characterization of vital importance. According to hydrodynamic simulations, besides preionizing the target (thus increasing the free electron density seen by the main laser pulse), they can cause a significant steepening or even expansion of the irradiated gas boundary or launch hydrodynamic shock waves.

A.2.3 Focal spot analysis

Laser pulses are focused on-target to attain high intensities $I \propto \frac{1}{S}$ where S is the focal spot surface. For short $\text{fs} - \text{ps}$ pulses reflective optics like off-axis parabolas (OAPs) or spherical mirrors are used. For longer ns pulses, where the temporal stretching of the laser pulse inside the focusing optics material can be neglected, convex lenses are implemented. The laser pulses can be focused until reaching the diffraction limit:

$$D_L \approx f\frac{\lambda_L}{a}, \tag{A.6}$$

where D_L is the minimum focal spot diameter measured at the full-width at half-maximum (FWHM) attainable with a focal length f system, a laser wavelength λ_L and a beam diameter a. The so-called numerical aperture is the fraction f/a.

Normally, the focal spot is monitored on a daily basis using a microscope objective located at the microscope's focal distance F and a refocusing lens close to the acquisition camera. In order to not damage the microscope objective the laser is used at low energy ($\approx$ mJ). A background image must be saved as well and subtracted from the focal spot image for correct analysis. The essential information to extract is: the horizontal and vertical FWHM diamaters, the encircled

energy and the radial intensity with respect to r, the radial coordinate. The horizontal and vertical FWHM diameters are obtained by fitting a Gaussian function $f(x) = a \cdot e^{-\frac{(x-x_0)^2}{2\sigma^2}}$ to the horizontal and vertical focal spot profiles. The focal spot diameter at the FWHM is $D_L = 2\sigma\sqrt{2\ln 2}$. The encircled energy $\mathcal{E}(r)$ is calculated as:

$$\mathcal{E}(r) = \frac{E_{L,TCC}}{\int_0^{R_{max}} dr\, F(r,\theta)} \int_0^r dr\, F(r) \int_0^{2\pi} r\, d\theta, \tag{A.7}$$

where $E_{L,TCC}$ is the laser energy delivered at the target chamber center (TCC), R_{max} is the maximum radius of the analyzed region of interest (ROI) and $F(r)$ is the signal intensity distribution in counts. $E_{L,TCC}$ is normally measured using a calorimeter in dedicated shots. The radial intensity profile has the expression [175]:

$$I(r) = \frac{I_{L,max}}{R_{max}} \mathcal{E}(r) \int_0^\infty dr\, F(r,\theta) \int_0^{2\pi} r\, d\theta, \tag{A.8}$$

where R_{max} is the maximum coordinate along the radial axis, $E(r)$ the encircled energy as a function of the radius and $I_{L,max}$ the maximum attained intensity that can be calculated supposing spatial and temporal laser pulse Gaussian profiles:

$$I_{L,max} \int_0^{D_L/2} 2\pi dr\, r\, e^{-4\ln 2 \left(\frac{r}{D_L}\right)^2} \int dt\, e^{-4\ln 2\left(\frac{t}{\tau_L}\right)^2} = \alpha E_L. \tag{A.9}$$

Simplifying Eq. A.9 one obtains:

$$I_{L,max} \approx 1.658 \frac{\alpha E_{L,TCC}}{D_L^2 \tau_L}, \tag{A.10}$$

where D_L is the focal spot diameter taken at the FWHM, τ_L is the pulse duration and α is the percentage of energy encircled in the focal spot radius taken at the half-width at half-maximum (HWHM) that is extracted from the encircled energy curve $E(r)$ following Eq. A.7.

Fig. A.4 shows the optical system implemented to monitor the focal spot during the VEGA-3 experiment. Two images with magnifications $\gamma = 20$ and $\gamma = 10$ capture the focal spot ($D_{FWHM} \approx 15\,\mu\text{m}$) and the gas nozzle edges (for nozzle alignment purposes), respectively. The nozzle's diameter is $D_{nozzle} \approx 1.15 - 3\,\text{mm}$ for the J2021 and the S900 nozzles, respectively. An alignment diode is also sent in contra-propagation through the optical line.

The first shots of the campaign were performed on a solid target (6 μm of Al) to test the particle diagnostic suite before gaseous target shots. A backlighter torch focused with an f2300 achromatic illuminates the surface of the solid foil for target prealignment.

Rayleigh length

The Rayleigh length [176] z_R of a beam is the distance from the beam best focus position where the beam radius is equal to w_0 (called beam waist) to the location where the radius equals $\sqrt{2}\,w_0$ and the transverse section is doubled. For a Gaussian beam with wavelength λ_L the Rayleigh length is defined as:

$$z_R = \frac{\pi w_0^2}{\lambda_L} = \frac{\pi D_L^2}{4\lambda_L}, \tag{A.11}$$

A sketch of a Gaussian beam width varying with the longitudinal distance is plotted in Fig. A.5.

Geometrically, when focusing a Gaussian beam using a long focal focusing optic the Rayleigh length will be much longer than in the case where the beam is focused with a short focal optic. In other words, the beam remains focused for a long distance which eases the constraints
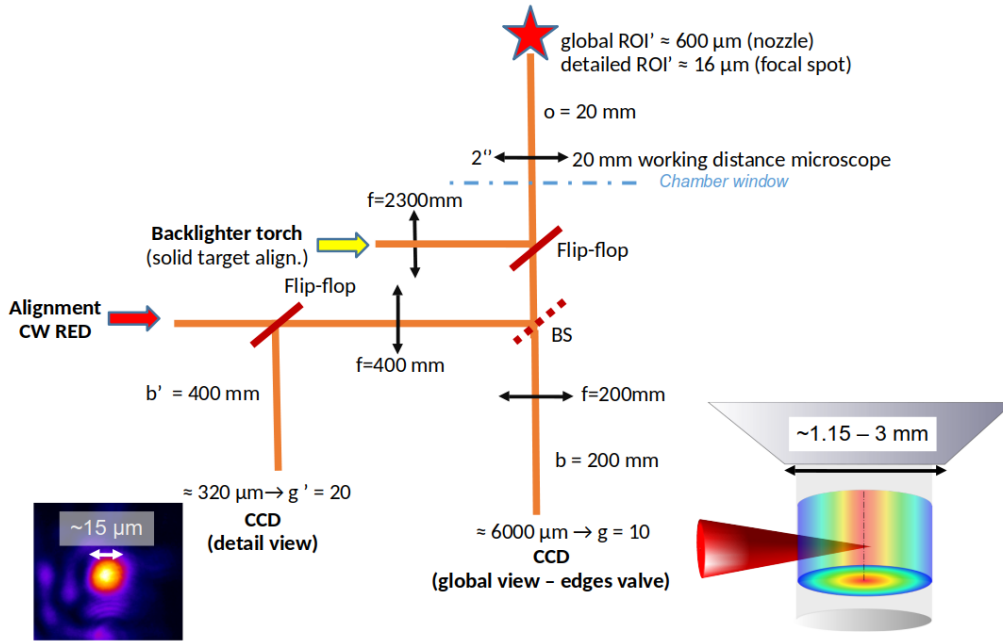
Fig. A.4: Optical system implemented to monitor the VEGA-3 focal spot.
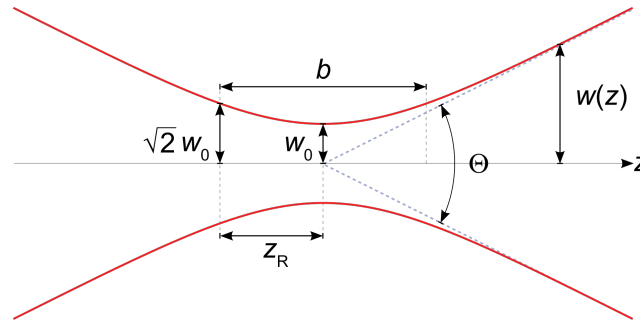
Fig. A.5: Sketch of a Gaussian beam width varying with the longitudinal distance. Extracted from Ref. [176].

regarding laser focus alignment. The beam waist w_0 will be of course smaller when focusing using a short focal optic which will increase the maximum laser intensity.

A.3 Plasma and neutral gas characterization

Once the laser pulse has been fully characterized the same must be done with the gaseous target (prior to the laser-gas interaction) and with the near critical plasma that is created. To obtain a high temporal resolution short laser pulses ($\approx 100\,\text{fs}$) are used as probes. The measurement of time resolved electronic density and magnetic fields in the plasma interior give hints on the physical processes that are occurring.

A.3.1 Optical interferometry

Interferometric techniques are based on measuring a phase shift $\Delta\Phi$ between two beams: the object beam and the reference beam. The object beam traverses the region of interest (ROI) while the reference beam traverses a plasma-free region. Such phase shift is related to the difference between the optical paths that is traversed by each of the two beams and is used to obtain the plasma or neutral gas density traversed by the object beam. This diagnostic

can be used to characterize electronic or neutral densities below the critical density n_c at the wavelength of the probe beam. Density gradients tend to reduce the maximum density that can be probed by a laser of a given wavelength, due to beam refraction out of the optical aperture of the imaging system.

Interferometry is based on the undulatory nature of light and on the linearity of its electric field, e.g. the electric fields coming from two different beams are added creating high and low-intensity regions called fringes. Taking two waves of same wavelength λ with non-orthogonal linear polarizations and a small intersection angle: $E_1 \ e^{i(\omega t+\phi_1)}$ and $E_2 \ e^{i(\omega t+\phi_2)}$ with E the amplitudes of both waves, ω the laser angular frequency and ϕ the phase. Adding these two waves one obtains:

$$E_t = (E_1 + E_2 e^{\Delta\phi})e^{i(\omega t+\phi_1)} \tag{A.12}$$

where $\Delta\Phi = \phi_2 - \phi_1$ is the phase shift between the two waves. The observed intensity is proportional to the square root of the electric field module:

$$I_L\alpha|E_t|^2 = (E_1^2 + E_2^2)\left(1 + \frac{2E_1E_2}{E_1^2 + E_2^2}\cos\Delta\Phi\right). \tag{A.13}$$

As seen in Eq. A.13 the intensity is composed of a constant term $E_1^2 + E_2^2$ and a varying one, function of the cosinus of the phase shift, which periodically creates intensity variations that range from $I_{min} = (E_1 - E_2)^2$ to $I_{max} = (E_1 + E_2)^2$. In the case that $E_1 = E_2$, the interferometry pattern from $I_{min} = 0$ to $I_{max} = 4E_1^2$.

Plasma characterization: electronic density

The experimentally obtained phase shift $\Delta\phi$ depends on the plasma parameters as [177–179]:

$$\Delta\Phi(y) = \frac{1}{\lambda}\int_0^L (\eta(x) - 1)dx = \frac{-\lambda[\text{cm}]e^2}{2\pi c^2 m_e}\int_0^L n_e(x)dx = 4.49 \times 10^{-14}\lambda\int_0^L n_e(x)dx, \tag{A.14}$$

where $\eta = \sqrt{1 - n_e/n_c}$ ($\sim 1 - n_e/2n_c$ in vacuum for $n_e/n_c \ll 1$) is the refractive index of the plasma, λ is the probing laser wavelength, e is the electron charge, c is the speed of light, m_e is the electron rest mass, x is the coordiante along the beam propagation direction, y is the coordinate perpedicular to the beam propagation (see Fig. A.6), L is the geometrical path inside the plasma and n_e is the electron density. The latest expression is in cgs units.

In the case of an axisymmetric distribution with an axis orthogonal to the probing direction (as sketched in Fig. A.6) a new cylindrical coordinate system can be introduced and Eq. A.14 can be expressed as:

$$\Delta\Phi(y) = 2 \times 4.49 \cdot 10^{-14}\lambda\int_y^R \frac{n_e(r)r dr}{\sqrt{r^2 - y^2}}, \tag{A.15}$$

where r is the distance from the symmetry axis and R is a sufficiently long radius to be able to neglect phase contributions outside of it and giving the highest accuracy to the Abel inverted distribution. The Abel transform of a function $f(r)$ is defined as:

$$F(y) = \mathcal{A}(f(r)) = 2\int_y^R \frac{f(r)r}{\sqrt{r^2 - y^2}}dr. \tag{A.16}$$

Then Eq. A.15 results in:

$$f(r) = 4.49 \cdot 10^{-14}\lambda n_e(r) \tag{A.17}$$
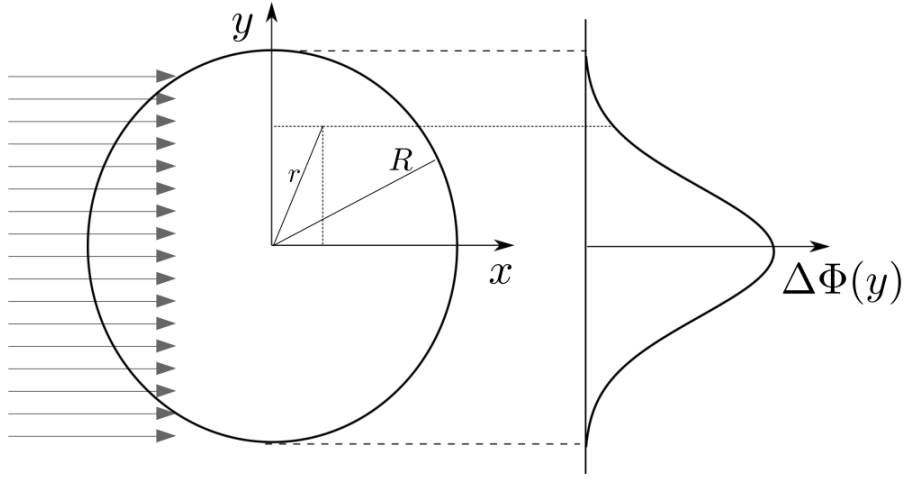
Fig. A.6: Scheme of the Abel transformation. The probing beam propagates along x and accumulated a phase displacement $\Delta\phi$ proportional to the refractive index and density of the medium assumed to be cylindrically symmetric.

$$F(y) = \Delta\Phi(y) \tag{A.18}$$

By inverting Eq. A.16, once a cylindrical symmetry has been supposed, one obtains:

$$f(r) = \mathcal{A}^{-1}(F(y)) = \frac{F(R)}{\pi\sqrt{R^2 - r^2}} - \frac{1}{\pi}\int_y^R \frac{\left(\frac{dF}{dy}\right) dy}{\sqrt{r^2 - y^2}}. \tag{A.19}$$

There are several numerical methods of obtaining the Abel inversion which can be divided into interpolation and approximation methods.

Neutral gas characterization: atomic or molecular density Since the laser beam samples the gas in one direction, the accumulated phase shift $\Delta\Phi$ corresponds to a projection of the gas density along the beam propagation direction [117]:

$$\Delta\Phi(y) = \frac{4\pi}{\lambda}\int_y^R \frac{(\eta(r) - 1)r\,dr}{\sqrt{r^2 - y^2}}. \tag{A.20}$$

Once again, under the assumption that the object or phase distribution has a cylindrical symmetry, Eq. A.20 can be inverted using the Abel inversion:

$$\frac{2\pi}{\lambda}(\eta(r) - 1) = -\frac{1}{\pi}\int_y^R \frac{d}{dy}\frac{\Delta\Phi(y)}{\sqrt{y^2 - r^2}}dy, \tag{A.21}$$

$$\frac{2\pi}{\lambda}(\eta(r) - 1) = \mathcal{A}^{-1}(F(y)). \tag{A.22}$$

The relationship between the refractive index and the atomic or molecular density (n) in a gas is the so-called Gladston-Dale relationship:

$$(\eta(r) - 1) = Kn, \tag{A.23}$$

where η is the gas refractive index and K is known as the Gladstone-Dale constant that writes, in cgs units:

$$K[\text{cm}^3] = 10^6\frac{\alpha}{4\pi\epsilon_0}, \tag{A.24}$$

Tab. A.1: Polarizability α of different gases. Extracted from Ref. [180].

Gas	α [F m²]
H₂	$9.143 \cdot 10^{-41}$
N₂	$19.620 \cdot 10^{-41}$
He	$2.300 \cdot 10^{-41}$
Ne	$4.421 \cdot 10^{-41}$
Ar	$18.520 \cdot 10^{-41}$

where α is the gas polarizability in SI units (F m²) and ϵ_0 is the vacuum permittivity in SI units (F m⁻¹). Table A.1 extracted from Ref. [180] summarizes the values of the gas polarizability (α) for different gases including helium and nitrogen, the two gases used during the experimental work of this thesis. A expression for the neutral atomic or molecular density can then be obtained taking into account that the left-hand side of Eq. A.21 is given in units of 1/px and therefore both the system magnification and the charged coupled device's (CCD's) μm/px conversion must be taken into account. The final expression for the density in cgs units is:

$$n(r)[\text{cm}^{-3}] = 10^{-6}\frac{\lambda}{\xi}\frac{1}{\alpha}2\epsilon_0 \mathcal{A}^{-1}(F(y)), \tag{A.25}$$

where $\mathcal{A}^{-1}(F(y))$ is obtained from Eq. A.21 and $\xi = \frac{\mu\text{m}}{\text{px}}/\gamma$ where γ is the system's optical magnification. In Eq. A.25 α is expressed in F m², ϵ_0 in F m⁻¹ and λ in μm.

Nomarski interferometer

The Nomarski interferometer diagnostic used in this work was realized using a wedge prism of angle $\gamma = 1.9°$, which deflects light by an angle $\delta = (\eta-1)\gamma$ where η is the index of refraction of the prism material. A part of the wedge input and output surfaces remain parallel to each other so as to not change the light propagation direction. In this way, the object and the reference beams are made to interfere. A scheme of the optical path is depicted in Fig. A.7.
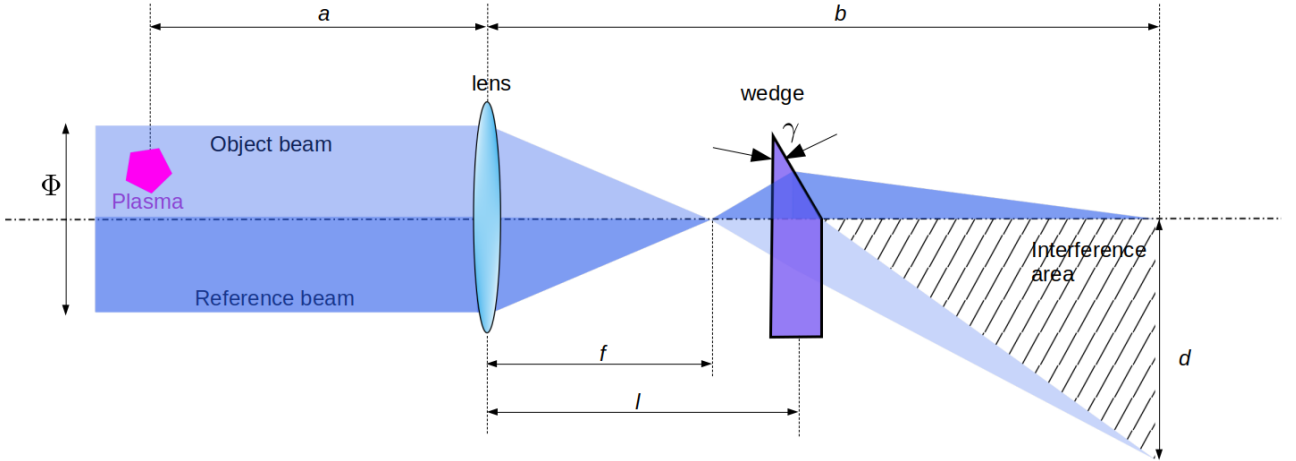
Fig. A.7: Scheme of the optical path of a Nomarski interferometer realized using a wedge prism (in purple).

The interferogram is obtained by separation, inversion and folding of the front phase of the probing wave. The diameter of the probe beam Φ must be at least twice as large as the investigated plasma dimension. The width of the interference fringes Δd and the distance between the object and the reference beam in the detection plane d are given by these formulas:

$$\Delta d = \frac{(b-f)\lambda}{2\eta f\gamma}, \tag{A.26}$$

$$d = \frac{1}{2}\left(b - \left(\frac{b}{f} - 1\right)l\right)\eta\gamma \tag{A.27}$$

where f is the objective's focal length and l is the distance between the objective and the wedge, with $l > f$. The distances a and b are governed by the thin lens equation:

$$\frac{1}{f} = \frac{1}{a} + \frac{1}{b}. \tag{A.28}$$

so that the detector plane corresponds to the image of the plasma produced by the lens. The two images formed at the CCD plane will have an interference area where fringes will appear as schematized in Fig. A.8.
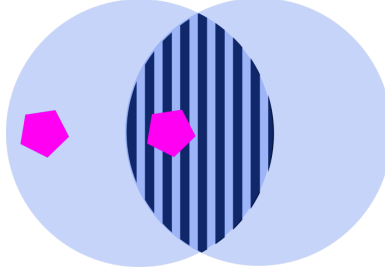
Fig. A.8: Two images interference fringes as seen at the CCD plane of the Nomarski interferometer optical path of Fig. A.7. The plasma region is located inside the pink pentagon.

Attention must be paid to the fact that the interfringe width Δd must be larger by at least a factor ξ than the resolution of the optical system and to the fact than no element in the line must cut the initial diameter of the beam Φ. Temporal resolution can be achieved using ultra-short laser pulses as probe beam or by the means of gated optical imagers (GOIs).

A.3.2 Polarimetry

The propagation of an ultra-intense laser pulse through a near-critical plasma slab creates non-linear wakefields that accelerates electrons from the inner propagation channel. A double current system is then formed by a forward current composed by the laser-accelerated electrons and a backward electron current flowing through the channel walls once the displaced electrons are made to recirculate due to the electrostatic fields form at the right edge of the described plasma channel. Such current system is the origin of strong azimuthal magnetic fields inside the plasma that have been already measured in previous experiments [181, 182] and that may affect considerably the ion acceleration mechanisms that take place. Although in this work a polarimetry diagnostic was not implemented it should be part of the main diagnostic suite for future experiments.

A polarimetry diagnostic can be used to characterize such magnetic fields (B-fields) by the means of magneto-optical effects. Magneto-optical materials suffer changes in their permittivity ϵ_r in the presence of a magnetic field. During the propagation of an electromagnetic (EM) wave through such medium, circularly polarized light of positive and negative rotating polarizations (from the point of view of the source) exhibit a different phase velocity, which can be described as a difference in the medium's refractive index $\Delta\eta$. The Faraday effect discovered by Michael Faraday in 1845 [183] refers to cases where the B-field is parallel to the wave propagation direction and the Cotton-Mouton [184] effect to cases where the B-field is parallel to the wave polarization direction and orthogonal to its propagation direction.

The proposed polarimetry setup intends to measure the Faraday effect by the means of a magneto-optical Terbium Gallium Garnet (TGG) crystal (or other birefringent crystal) located in the vicinity of the B-field in between two polarizers, as shown in Fig. A.9.
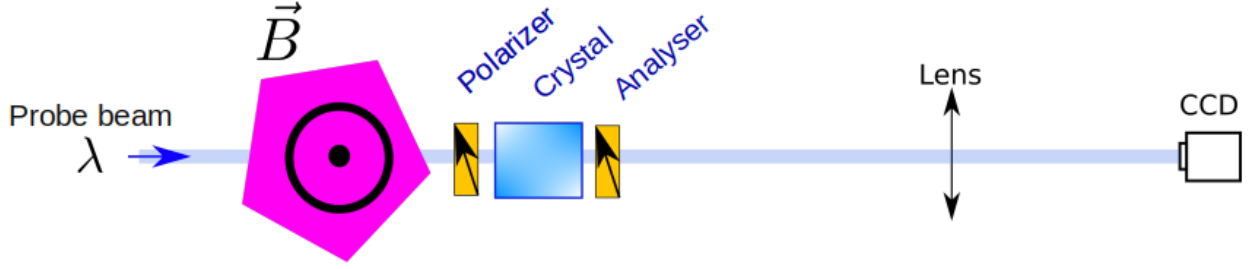

Fig. A.9: Polarimetry setup intended to measure the Faraday effect by the means of a magneto-optical Terbium Gallium Garnet (TGG) crystal located in the vicinity of the B-field in between two polarizers.

The linearly polarized probe beam is guided through the TGG crystal where its polarization will suffer a rotation due to magneto-optical effects. This can be understood by decomposing the linearly polarized wave into two circularly polarized waves of negative and positive circular polarization, whose superposition is always a linearly polarized wave. The difference in the phase velocity $v_\phi^- - v_\phi^+$ of both virtual circularly polarized waves yields a rotating polarization. The polarization rotation angle Φ is equal to half of the phase difference measured at the back of the crystal of length L_C along the optical axis. The polarization rotation angle Φ can be expressed as:

$$\Phi = \frac{\Delta\Theta}{2} = \frac{\omega_P \cdot L_C}{2} \cdot \left(\frac{1}{v_\phi^-} - \frac{1}{v_\phi^+} \right) = \frac{\omega_P \cdot L_C \cdot \Delta\eta}{2c}, \tag{A.29}$$

where ω_P is the angular frequency of the probe beam and c is the speed of light. $\Delta\eta$ depends on the longitudinal component of the magnetic field and on ω_P. Following Ref. [185] Φ can be expressed as:

$$\Phi = \frac{\omega_P}{2c} \int_{-\infty}^{+\infty} \Delta\eta \, dz, \tag{A.30}$$

z being the probe beam propagation axis. We can now introduce a frequency dependent constant called the Verdet constant V_B expressed in $\mathrm{rad\,T^{-1}\,m^{-1}}$ and rewrite Eq. A.30 as:

$$\Phi = -V_B \cdot \int_{-\infty}^{+\infty} B_z \, dz. \tag{A.31}$$

The probe beam crosses a linear polarizer (in red) to adjust its polarization before traversing the plasma that will be diagnosed. The probe's intensity diminishes after crossing the polarizer following Malu's law: $I = I_0 \cos^2(\phi)$. Here I_0 is the probe beam's intensity after the polarizer and ϕ is the angle between the probe's initial polarization direction and the polarizer axis. The plasma affects both the phase and the polarization of the probe beam, which are detected by an analyser (in orange) and an optical wedge (in purple) located after the plasma region of interest (ROI), respectively.

The polarization rotation is measured with a polarizer-analyser configuration. The polarizer adjusts the probe beam polarization before traversing the plasma that will be diagnosed. The probe's intensity diminishes after crossing the polarizer following Malu's law: $I = I_0 \cos^2(\phi)$. Here I_0 is the probe beam's intensity after the polarizer and ϕ is the angle between the probe's

initial polarization direction and the polarizer axis. $\beta = (\pi/2) - \phi$ is the complementary angle of ϕ. Adding the magneto-optically induced polarization rotation, the expression for small rotation angles is derived:

$$\Phi = -\beta + \arcsin\left(\sqrt{\frac{I_S}{I_A}} \cdot \sin(\beta)\right) \cdot \text{sgn}(V_B), \tag{A.32}$$

where $\text{sgn}(V_B)$ is the sign of the Verdet constant. Following a standard convention, in paramagnetic media a negative Verdet constant corresponds to an anti-clockwise rotation when $\vec{k} \upuparrows \vec{B}$ (parallel vectors) and vice versa. In the case of diamagnetic materials with a positive Verdet constant the direction of polarization is inverted.

The TGG crystal plus polarizer and analyser may be positioned inside the interferometry line plotted in Fig. A.7, before the focusing object, and should be motorized to be able to perform shots to asses the plasma density and shots to asses the azimuthal magnetic field. If the probe beam energy is enough a 50/50 beam splitter can be used to split the probe beam and perform both measurements at the same time using two slightly tilted optical axes. Attention must be paid to reflections coming from the different beam splitter surfaces which produce interfering beams.

A.3.3   Complex interferometry

Complex interferometry combines conventional interferometry and polarimetry in a single diagnostic tool recording two sets of independent data from a single data object called a complex interferogram (CI) [178]. As in a conventional interferogram, in a CI the interference pattern distortion represents the phase distribution. The distribution of the polarization plane rotation angle is coded in the intensity distribution of the interference fringes. Some advantages of the complex interferometry technique over standard interferometry and polarimetry are the setup's compactness and the natural superposition of electron density and magnetic field charts avoiding data interpretation errors due to incorrect matching of the coordinates of the data from different physical charts.

The experimental setup of this diagnostic, schematized in Fig. A.10, is based on an initially linearly polarized ultra short probe beam and follows a Normarki interferometer design (see Section A.3.1). The plasma region is located inside the pink pentagon.

If the expanding plasma exhibits a reasonable axial symmetry, good approximation of the Faraday rotation angle ϕ and the phase shift Θ are [186] (in cgs units):

$$\phi(x,y) = 5.24 \times 10^{-17} \cdot \lambda^2[\text{cm}] \cdot \int_x^R dr \frac{B_\phi(r,y)n_e(r,y)}{\sqrt{r^2 - x^2}}, \tag{A.33}$$

$$\Theta(x,y) = 8.92 \times 10^{-14} \cdot \lambda[\text{cm}] \cdot \int_x^R dr \frac{n_e(r,y)r}{\sqrt{r^2 - x^2}}. \tag{A.34}$$

where $r^2 = z^2 + x^2$ is the radial cylindrical symmetry coordinate around the plasma axis y and $B_\phi(r,y)$ is the azimuthal SMF at the plasma plane cut at the y ordinate with radius R. The azimuthal B-field and electron density distributions [186] can be obtained by performing an Abel inversion as previously described in Section A.3.1:

$$\frac{B_\phi(r,y) \cdot n_e}{r} = -\frac{5.24 \times 10^{-17}\lambda^2}{\pi} \cdot \int_r^R dx \frac{\partial_x \phi(x,y)}{\sqrt{x^2 - r^2}}, \tag{A.35}$$

$$n_e(r,y) = -\frac{8.92 \times 10^{-14}\lambda}{\pi} \cdot \int_r^R dx \frac{\partial_x \Theta(x,y)}{\sqrt{x^2 - r^2}}, \tag{A.36}$$
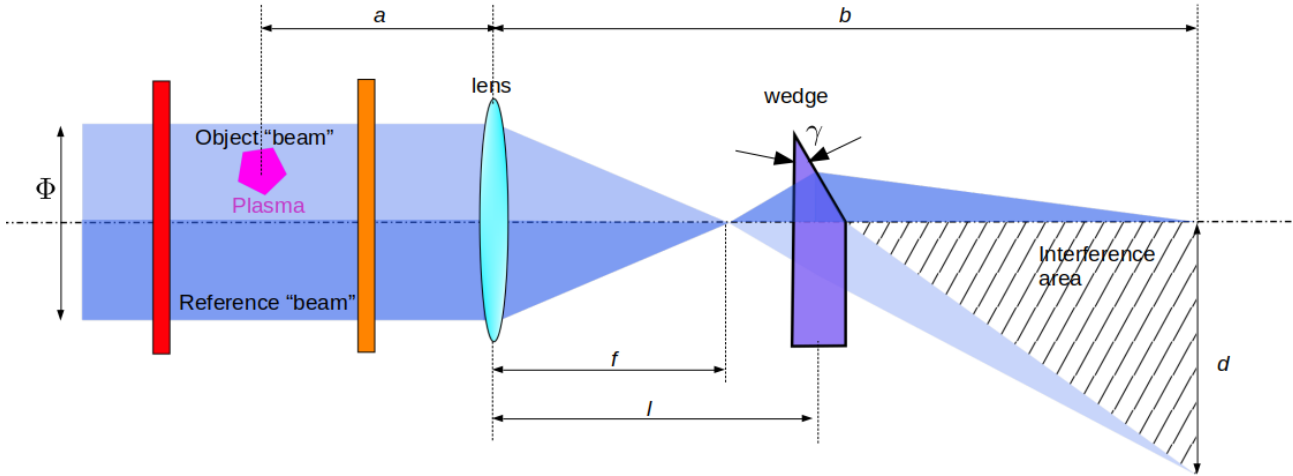
Fig. A.10: Experimental setup of a complex interferometry line. The diagnostic's experimental setup is based on an initially linearly polarized ultra short probe beam that crosses a linear polarizer (in red) to adjust its polarization before traversing the plasma that will be diagnosed. The plasma affects both the phase and the polarization of the probe beam, which are detected by an analyser (in orange) and an optical wedge (in purple) located after the plasma region of interest (ROI), respectively. The plasma region is located inside the pink pentagon.

A.3.4 Spatial filtering techniques: Strioscopy

When focusing an image by means of a focusing optic the Fourier spatial transform of the object image appears at the focusing plane. The introduction of needles, which act as high-band filters, or irises, which act as low-band filters, allows for spatial filtering of the image that is then formed at the detection plane (optically conjugated to the object by the use of optics).

Strioscopy or *schlieren* imaging relays on imaging a back-lighted object using a collimated beam and locating a high-band filter needle at the focusing optic focal distance, as seen in Fig. A.11. This system is used to visualize areas with gradients of refractive index.
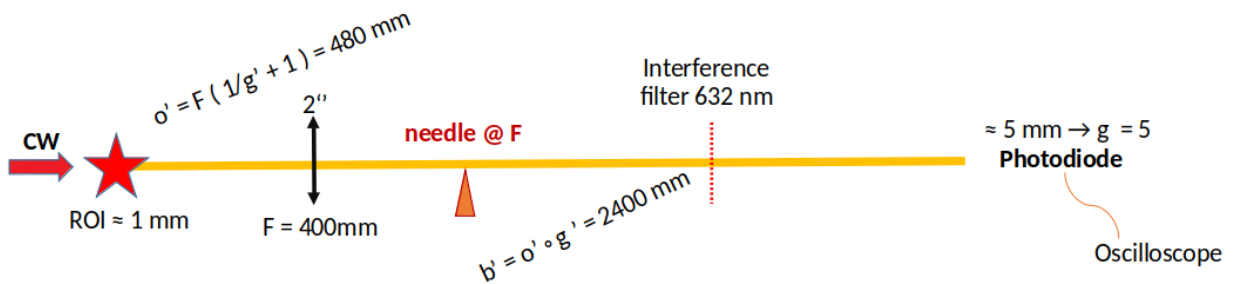
Fig. A.11: Strioscopy optical path that relays on imaging a back-lighted object using a collimated beam and locating a high-pass filter needle at the focusing optic focal distance optical path to spatially filter low-frequency modes.

A.3.5 Streaked optical self-emission

Figure A.12 shows an schematic view of a streak camera [187] composed of an entrance slit, a photocathode that converts the incident light into electrons, electronic focusing optics that guide the electron bunch, E and B-field deflection plates, an image intensifier micro-channel plate, a phosphor screen that converts the electron bunch into photons once again and finally

a charged coupled device (CCD) that forms a digital image of the streaked input light pulses (schematized as the blue, red and yellow Gaussian-like peaks entering the streak camera's slit through a given optical system). Short duration light pulses can then be measured by transforming the temporal information into a spatial one using a photocathode to transform the entering light into an electron bunch and deflecting fields to obtain temporal-to-spatial information conversion. Note that the three Gaussian-type pulses entering the slit translate into the yellow, red and blue signals in the image formed by the CCD.

By streaking the optical plasma self-emission coming from the TCC one can identified the laser-plasma interaction hot spots as a function of time. This information can be useful for comparison with the free electron density charts obtained from optical interferometry.

During this thesis work the C7700 streak camera model (see inset (a) of Fig. A.12) manufactured by Hamamatsu Photonics was used. This streak camera has a $\approx 10\,\mathrm{ps}$ resolution, a $6.45\,\mu\mathrm{m/px}$ pixel size and an internal demagnification $\gamma = 0.5$.
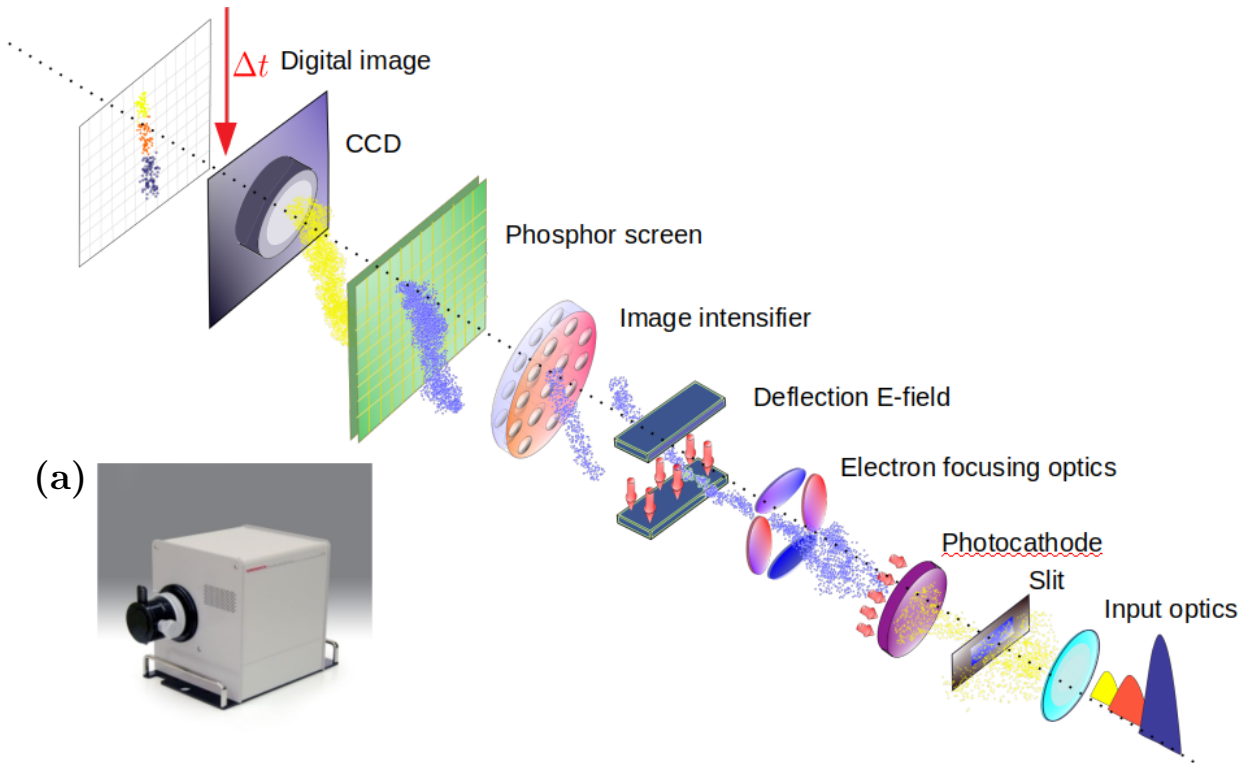
Fig. A.12: Schematic view of a streak camera composed of an entrance slit, a photocathode that converts the entering light into electrons, electronic focusing optics that guide the electron bunch, E-field deflection plates, an image intensifier micro-channel plate, a phosphor screen that converts the electron bunch into photons once again and finally a charged coupled device (CCD) that forms a digital image of the streaked input light pulses (schematized as the blue, red and yellow Gaussian-like peaks entering the streak camera's slit through a given optical system). (a) C7700 streak camera model sold by Hamamatsu Photonics used during this thesis' experimental work. This streak camera has a ps resolution, a $6.45\,\mu\mathrm{m/px}$ pixel size and an internal demagnification $\gamma = 0.5$.

A.4 Particle diagnostics

The production of high-energy particles is a major output of relativistic laser-plasma interaction. The particle diagnostics fielded in our experiments are called active or passive, depending on

whether they are electrically biased or not. This difference can be important in harsh laser-plasma interaction environments where strong electromagnetic pulses (EMP) are created and are known to disturb biased devices [125].

A.4.1 Active diagnostics

A.4.1.1 Time-of-flight detectors

The time-of-flight (ToF) technique is suited to characterizing the velocity distribution of non-relativistic particles, and is therefore well adapted to measuring the ion emission from the laser-plasma interaction. In our experiments, it was implemented by placing a semiconductor detector at a known distance from TCC. The principle of detection relies on the creation of free electron-hole pairs when charged particles and/or ionized radiation interacts with the detector's substrate. A bias voltage, ranging from tens to hundreds of volts is provided to overcome the electrostatic potential barrier of the doped layers' junction, allowing a signal current to flow through the circuit. This fast oscillating current must be then acquired and sampled with a high-bandwidth oscilloscope. The oscilloscope's impedance must be of about $1\,\text{M}\Omega$ to protect the oscilloscope and the circuit must be closed with an external $50\,\Omega$ impedance connected using a T connector to reduce electrical reflections in the signal due to impedance imbalance between the signal cable (the commonly used RG58 coaxial cable has a 50 $50\,\Omega$ impedance) and the internal oscilloscope measurement circuit. A scheme of the detector and acquisition circuit can be seen in Fig. A.13.

The acquired signal is normally divided in two parts: i) a first peak corresponding to the arrival of the x-rays and relativistic electrons (propagating at or near the speed of light) emitted from the laser-plasma interaction and ii) a second or multiple peak signals which is due to the ions emitted from the interaction, see Fig. A.14. From the knowledge of the distance d at which the detector is located and the particle mass, one can predict the kinetic energy of the particle impinging onto the detector's active surface. Note that the detector must be located far enough from the particle source so that the first and second signals are well separated in time.
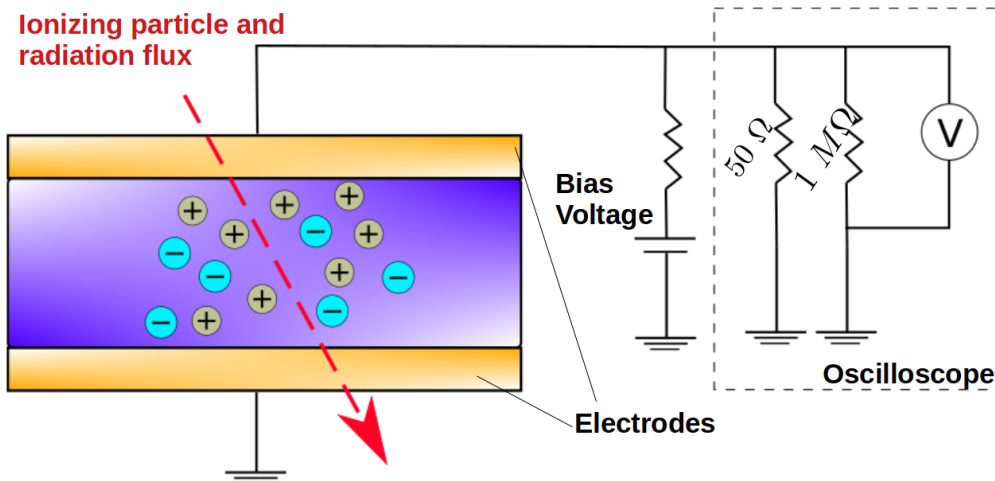

Fig. A.13: Schematic representation of a ToF detector and acquisition circuit.

The photopeak occurs at a time

$$t_{p,abs} = \frac{d}{c} \tag{A.37}$$
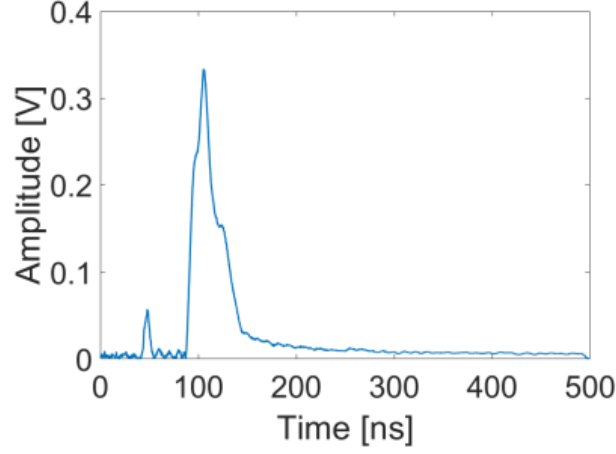
Fig. A.14: (a) Example of a raw time-of-flight (ToF) signal.

which is selected as the time origin where c is the speed of light.

The absolute time of arrival of an ion group of given energy (assuming an instantaneous emission) is given by

$$t_i = \Delta t_i + t_p \tag{A.38}$$

where Δt_i is the time relative to the photopeak.

The ion kinetic energy is then obtained following Eqs. A.39 and A.40

$$\mathcal{E}_i = \frac{m_i v_{d,i}^2}{2} \tag{A.39}$$

$$\gamma = 1/\sqrt{1 - \beta^2} \; ; \beta = \frac{d}{t_i} \cdot \frac{1}{c} \tag{A.40}$$

where the ion drift velocity $v_{d,i} = d/t_i$ and m_i is the ion mass.

Retrieval of the number of particles

The charge collection at the detector's electrodes, due to production of free electron-hole pairs by the incoming particles, is characterized by the energy-dependent charge collection efficiency parameters $CCE(\mathcal{E}_i)$ inherent to each detector. This parameter is a function of the energy (ϵ_g) needed to generate a free electron-hole pair in the crystalline structure forming the detector's active surface. $\mathcal{E}_g = 13.1$ eV [188] for the diamond detectors used in this thesis work. Such parameter is equivalent to the energy needed to generate a free electron-hole pair inside the detector's substrate. The collected charge associated with N_i particles of kinetic energy $\mathcal{E}_i$ is then

$$Q_i = N_i \frac{\mathcal{E}_i e}{\mathcal{E}_g} CCE(\mathcal{E}_i) \tag{A.41}$$

where e is the elementary charge. It is possible to retrieve the number of particles N_i generating the voltage signal from its amplitude. For each time step, defined by the temporal resolution of the system Δt, N_i writes:

$$N_i = Q_i \frac{\mathcal{E}_g}{\mathcal{E}_i \cdot e \cdot CCE(\mathcal{E}_i)} = \frac{1}{R} \int_{t_1}^{t_2} dt V(t) \frac{\mathcal{E}_g}{\mathcal{E}_i \cdot e \cdot CCE(\mathcal{E}_i)} \tag{A.42}$$

where R is the system impedance and $t_2 - t_1 = \Delta t$.

Fig. A.15: (a) Enegy dependent charge correction factor CF, extracted from Ref. [189], and (b) its effect on the calculation of the accumulated charge in the detector's electrodes. Image courtesy of M. Salvadori.

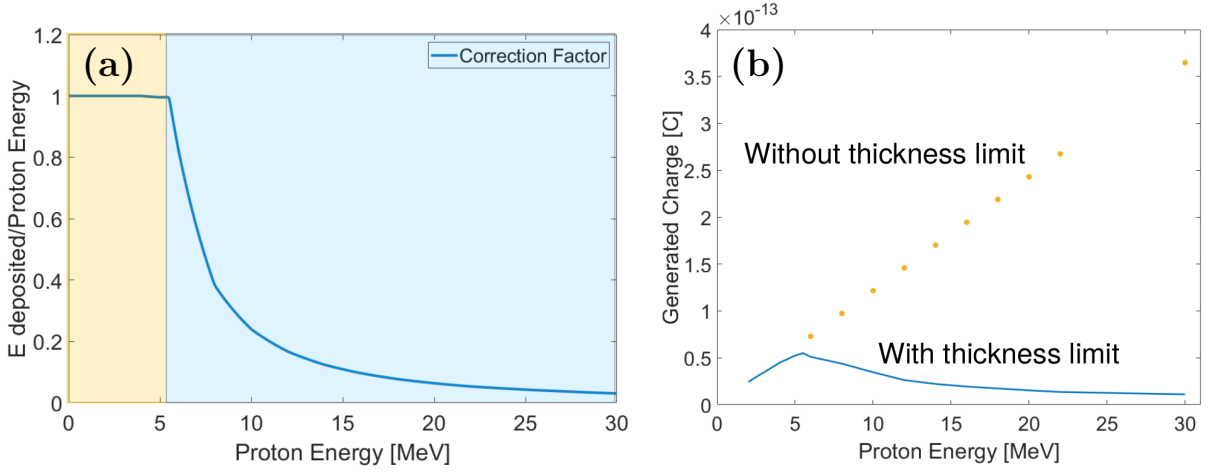Since the actual detector has a limited thickness, high-energy particles are able to cross the detector depositing only a fraction of their energy in the detector's active surface. Hence, a correction factor CF is introduced in Eq. A.42:

$$N_i = \frac{1}{R} \int_{t_1}^{t_2} dt V(t) \frac{\mathcal{E}_g}{\mathcal{E}_i \cdot e \cdot CCE(\mathcal{E}_i) \cdot CF}. \tag{A.43}$$

This correction factor is obtained from Monte Carlo simulations of the particle transport and energy deposition inside the detector's substrate. CF equals 1 for particles of energy low enough to be stopped inside the detector. For higher energies $CF < 1$, see Fig. A.15a. Without this correction factor the accumulated charge would grow infinitely with increasing particle energy, see Fig. A.15b.

Types of time-of-flight detectors

Two types of ToF detectors have been used during this thesis experimental work. PiN diodes during the VEGA-2 experiment (October 2018) and diamond detectors during the VEGA-3 experiment (June 2021).

PiN diodes have an extra neutral layer "I" in the middle of the doped electrode layers "P" and "N", which allows for a quantum efficiency enhancement by increasing the interaction volume of ionizing radiation with the diode substrate, and a faster response in absence of a minority carriers current that delays the signal current formation. The temporal resolution of the PiN diodes used during the VEGA 2 campaign is τ_{FWHM} is $\Delta t = 4.5$ ns [109]. Such detectors have only been calibrated for X-ray linear energy deposition obtaining a calibration coefficient of $0.282 \, \text{J} \, \text{C}^{-1}$ [190].

Single crystal diamond detectors are characterized by their high purity and crystalline quality which leads to a high charge collection efficiency (CCE) up to 98%. This results in high-time-resolution ToF measurements and the retrieval of highly resolved energy spectra [189]. Five different diamond ToF detectors were used during the VEGA-3 campaign. Their main characteristics are summarized in Table A.2.

The type of detector is characterized by the crystalline structure of its substrate, either composed of single or multiple crystalline species and by the electrodes layout which can be interdigitated or sandwich-like [191], see Fig. A.16a and b respectively, where the electrical contacts are shown in gold, the substrate over which the crystalline structure is grown is shown

Tab. A.2: Diamond detectors used in the VEGA-3 campaign.

Label	Type	Δt [ns]	CCE	Surface [mm^2]	Thickness [µm]	Bias voltage [V]
ToF A	Single crystal, sandwich	0.46	98%	4 x 4	50	+100
ToF B	Single crystal, sandwich	0.46	98%	4 x 4	50	+100
ToF C	Polycristaline, sandwich	4.10	42%	15 x 15	150	+300
ToF D	Single crystal, interdigitated	0.52	68%	4 x 4	50	+100
ToF E	Single crystal, sandwich	0.46	98%	4 x 4	50	+100

in blue and the crystalline diamond structure in purple. The crystalline structure is normally grown using a Chemical Vapor Deposition (CVD) technique, which is why diamond detectors are also commonly referred to as CVD detectors. In a sandwich configuration the diamond substrate is located in between the two doped metal contacts. A constant CCE is obtained through the entire detector thickness. On the other side, the interdigitated electrode layout has superficial contacts. Hence, the region of efficient charge collection is limited to the detector's surface. However, thanks to its inherent low capacity, due to a lower electrode surface, the smaller CCE is compensated and the final temporal resolution is not strongly affected, see penultimate row of Table A.2.

The detector's temporal resolution is characterized by sending single 5.486 MeV α particles produced by an ^{241}Am radioactive source, which is considered as an impulse signal from which the system's impulse response can be retrieved [191]. The detector's impulse response has the shape of an exponentially modified Gaussian pulse [109].

Two-channel oscilloscope connection

The oscilloscope connection for the ToF C and ToF D detectors was done by splitting the input signal into two oscilloscope channels. The first channel is optimized with respect to the temporal resolution by decreasing the voltage and temporal oscilloscope scales. The second channel is optimized with respect to the dynamic range needed to correctly acquire the ion signal. Like this, the first channel will acquire a highly resolved photopeak signal steep up-ramp while the second channel will acquire the ion signal with highest possible voltage and temporal resolutions [156].

Electrical breakdown and electromagnetic pulse (EMP) coupling risks

With pressurized gas entering the vacuum chamber, both PiN diodes and diamond CVD detectors are advantageous due to their low bias voltages on the order of tens of volts. Other ToF detectors (such as micro-channel plates - MCPs) are polarized with bias voltages of the order of kV, thereby posing risks of electrical breakdown.

By using long cables, the data acquisition oscilloscopes can be positioned far away from the interaction chamber, reducing the possiblities of the EMP fields coupling with the scopes' circuits. EMP fields outside the chamber attenuate as $1/r$ where r is the distance from TCC. At the same time, those cables filter out the high-frequency component of the EMP pulses [156,192]. The acquired signal must be convolved with the frequency response function of the cables for a correct analysis.

Discrimination between different particles impinging onto the detector

ToF detectors do not discriminate between the different particles that interact with its active surface. However, there are different techniques to avoid some particles from hitting the detector and contributing to its signal. For example, one can locate thin filters of materials like aluminium or mylar in order to cut low energy electrons and ions from the signal [109]. Sophisticated ToF detectors can also apply an electric field at their entrance in order to repel electrons [189].

A more complex picture should take into account that the expanding plasma cloud traveling
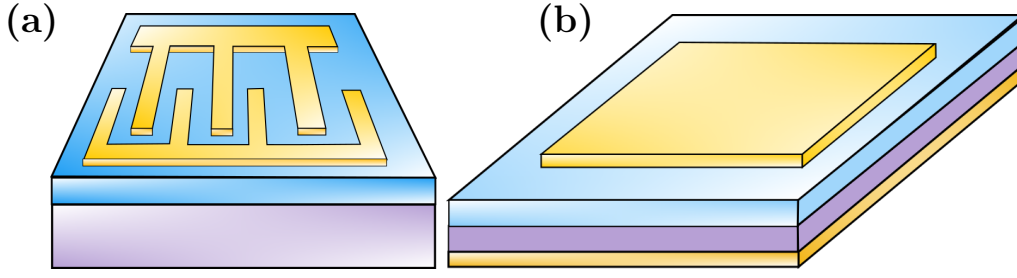
Fig. A.16: (a) Schematic representation of a chemical vapor deposition (CVD) diamond detector with an interdigitated electrode layout and (b) a sandwich-like electrode layout. The electric contacts are shown in gold, the substrate over which the crystalline structure is grown is shown in blue and the crystalline diamond structure in purple. Figures inspired from Ref. [191].

from the interaction point to the detector is composed of ions with a drift velocity $v_{d,i}$ and electrons revolving around the ion cloud. These energetic electrons are characterized by a drift velocity $v_{d,e} \approx v_{d,i}$ and a thermal velocity $v_{t,e} \gg v_{d,e}$. A correct measurement requires the detector to be located far enough from the interaction point so that the ion-electron expanding cloud thermalizes before reaching the detector. A good point is that such thermalization should occur over a ≈ 100 µm spatial scale [193] and ToF detectors are normally located at roughly >1 m from the TCC. It is to be noticed that neutrons are not expected to interfere with the ToF measurements since, to yield a significant signal, higher-absorption-efficiency materials like lithium fluoride or boron and amplification circuits should be used.

If a particle beam is composed of several types of ions the ToF signal analysis becomes complex. Supposing that all ion species undergo the same electric field (a questionable assumption), those with the largest charge-to-mass (Z/m_i) ratio will arrive the first on the detector. Yet given the velocity dispersion characterizing all species, it is possible that a given fraction of the ToF signal is due to distinct ion species with different energies.

A.4.1.2 Thomson parabolas

Thomson parabolas (TPs) are a type of particle spectrometers capable of resolving both the particle's energy and its charge-to-mass $\frac{Z}{A}$ ratio. In order to do so they rely on both magnetic and electric deflections. The magnetic deflection is implemented using permanent magnets with constant magnetic fields of the order of 1 T. The electric deflection is caused by two charged capacitor plates which are biased with voltages in the kV range. The particle enters the TP through a small pinhole with a diameter of the order of hundreds of µm. A scheme of a Thomson parabola with both magnetic and electric deflection plates can be seen in Fig. A.17. Most of the times the magnetic dipole plates and the electrodes are overlapped in space to make the TP more compact. This however does not affect the particle spatial deflection calculations that follow.

The functioning of the Thomson parabola can be modeled as follows [194–196]. Considering the geometry of the diagnostic and the second law of Newton $F = \frac{d\rho}{dt}$ where $F = e\vec{E} + e\vec{v} \times \vec{B}$ is the Lorentz force, it is possible to determine the X component of the position of a particle of mass m_i and kinetic energy $\mathcal{E}k,i$ as:

$$X^2 = \frac{Z^2 e^2 B_y^Z L_m^2}{2 m_i E_{k,i}} \left(D_m + \frac{L_m}{2} \right)^2, \tag{A.44}$$

where Z^* is the ion charge state, e is the elementary charge, B_y is the module of the magnetic field in the y axis, L_m is the length of the magnet and D_m the distance between the end of
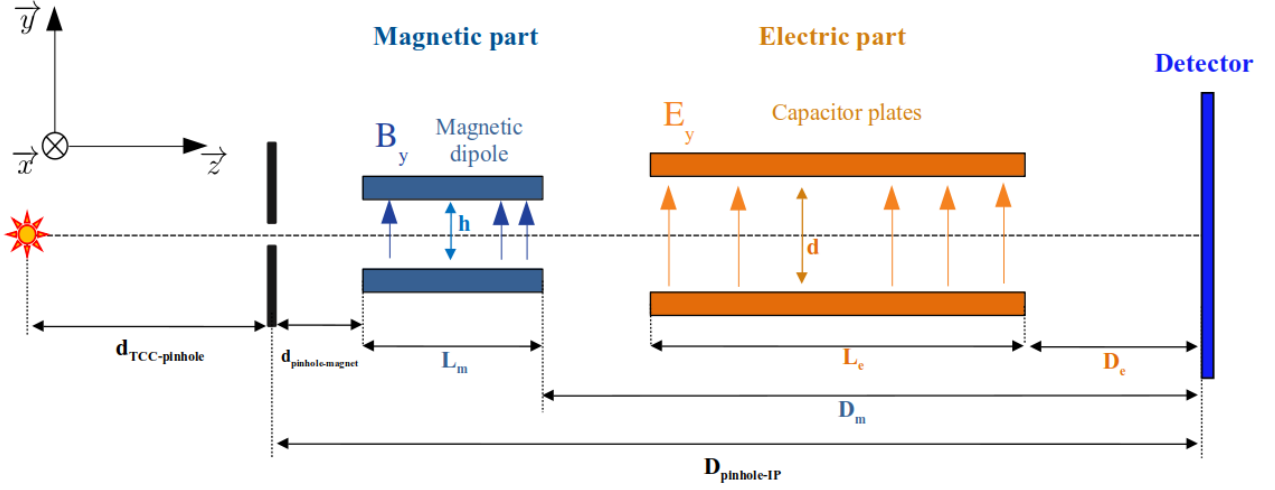
Fig. A.17: Scheme of a Thomson parabola particle spectrometer.
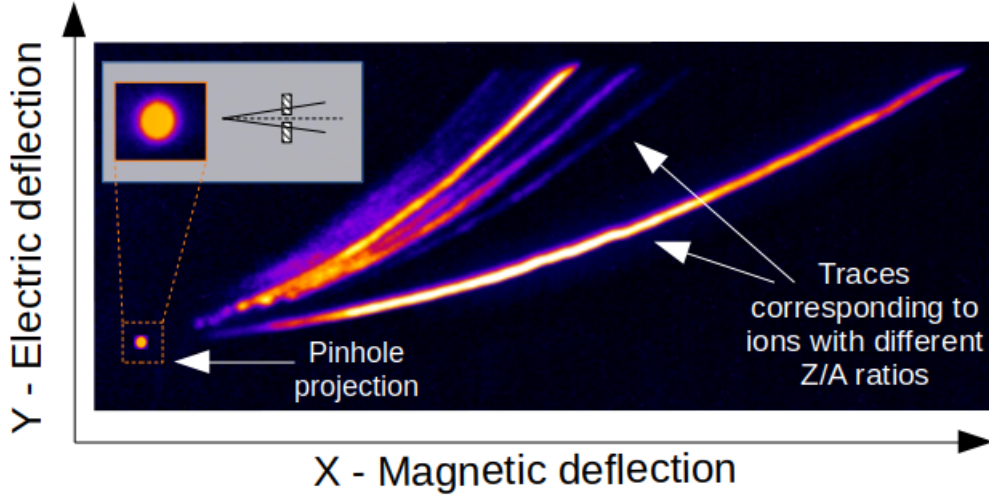
Fig. A.18: Proton and carbon ions' traces on a Thomson parabola detector (imaging plate, IP) obtained after a laser shot on solid aluminium.

the magnet and the detector (see Fig. A.17). No relativistic correction is applied here. The expression is correct for ion energies up to a few tens of MeV, as those typically encountered in our experiments.

Similarly, one can obtain the electric y-axis deviation Y that the particle experiences inside a parallel capacitor due to the electric field E_y:

$$Y = \frac{ZeE_yL_e}{2\mathcal{E}_{k,i}}\left(D_e + \frac{L_e}{2}\right), \tag{A.45}$$

where L_e is the electrodes' length and D_e the distance between the end of the electrodes and the detector (see Fig. A.17). One can combine Eqs. A.44 and A.45 to yield:

$$Y = \frac{m_iE_yL_e\left(D_e + \frac{L_m}{2}\right)}{ZeB_y^2L_m^2\left(D_m + \frac{L_m}{2}\right)^2}X^2. \tag{A.46}$$

showing that particles of fixed Z/A follow a parabolic trajectory on the detector plane.

Thomson parabolas can be coupled with different detectors including imaging plates (IPs), micro-channel plates (MCPs), scintillators or 2-D localization detectors based on CMOS technology. The chosen detector will determine the repetition-rate of the diagnostic.
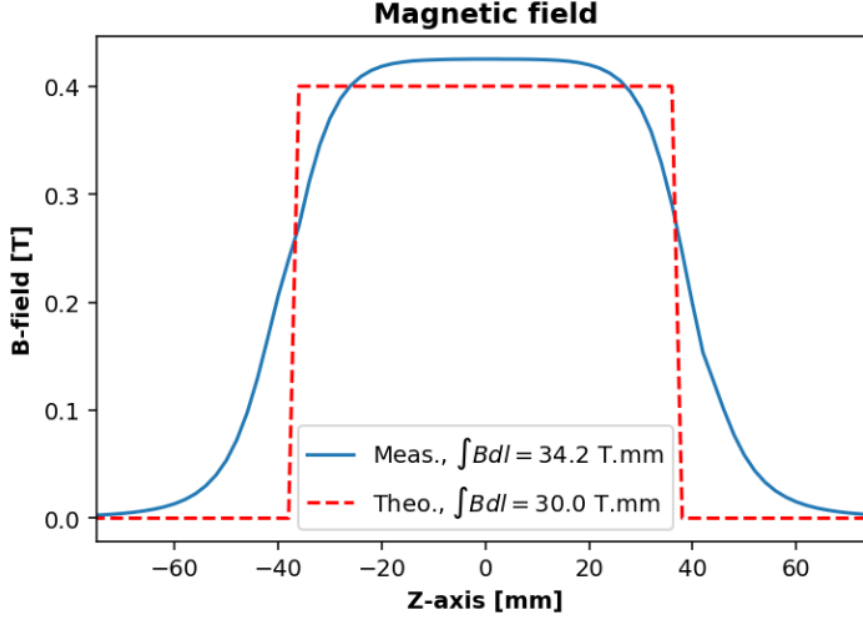
Fig. A.19: B-field inside a TP magnet supposed constant along the magnet's length (dashed red line) and measurement along the magnet's central axis (blue solid line).

Magnetic deflection

As was shown before, the electric and magnetic deflections can be dissociated and studied separately. From Eq. A.44 one can obtain the ion's kinetic energy:

$$\mathcal{E}_{k,i} = \frac{Z^2 e^2 B_y^2 L_m^2}{2 m_i X^2} \left(D_m + \frac{L_m}{2} \right)^2 = \frac{A_m}{X^2}. \tag{A.47}$$

The coefficient A_m can be interpreted as a magnetic deflection coefficient expressed in MeVmm²:

$$A_m = \frac{Z^2 e^2 B_y^2 L_m^2}{2 m_i} \left(D_m + \frac{L_m}{2} \right)^2. \tag{A.48}$$

A_m only depends on the physical parameters of the Thomson parabola and on the charge-to-mass Z/m_i ratio of the incident particle. The magnetic field along the y-axis B_y in Eq. A.48 can be assumed ideal, e.g. constant throughout the magnet's length. However, if experimental and analytical traces do not match a nonconstant magnetic field must be assumed. Its spatial distribution needs to be characterized, either along the central axis (see Fig. A.19) or by obtaining a 3-D magnetic field chart.

Electric deflection

In the case of the electrical deflection Eq. A.45 is rewritten as:

$$\mathcal{E}_{k,i} = \frac{Z e E_y L_e}{2 Y} \left(D_e + \frac{L_e}{2} \right) = \frac{A_e}{Y}, \tag{A.49}$$

where the coefficient A_e is defined by:

$$A_e = \frac{Z e E_y L_e}{2} \left(D_e + \frac{L_e}{2} \right). \tag{A.50}$$

A_e is the electric deflection parameter and it is expressed in MeVmm units. As A_m, it only depends on the TP's geometry.

Energy resolution and energy limit

200

Tab. A.3: Thomson parabolas' geometries used during this thesis experimental work.

TP	$d_{pinh.magn.}$ [mm]	L_m [mm]	D_m [mm]	h [mm]	$B_{th.}$ [T]	$d_{pinh.elect.}$ [mm]	L_e [mm]	d [mm]
LINA	25	75	100	33	0.38	25	102	10
Three pinh.	13.5	75	149.5	16	0.40	13.5	75	10

The point projection of the pinhole taken from TCC determines the energy and $\frac{Z}{A}$ resolutions at the detector's plane, see Fig. A.18. The energy resolution can be expressed as a function of the particle's energy and the value of the magnetic or electric field by derivating Eqs. A.44 and A.45, respectively. The magnetic resolution for protons can be expressed as:

$$\Delta\mathcal{E}_B = \frac{2\mathcal{E}_k^{3/2}\Delta X}{\sqrt{A_m(B_y)}} \tag{A.51}$$

where $A_m(B_y)$ is given by Eq. A.48 written only as a function of the magnetic field B_y and ΔX is the pinhole projection diameter at the detector's plane measured along the magnetic deflection direction (see Fig. A.18).

The electric resolution for protons is:

$$\Delta\mathcal{E}_E = \frac{\mathcal{E}_k^2\Delta Y}{\sqrt{A_e(E_y)}} \tag{A.52}$$

where $A_e(E_y)$ is given by Eq. A.50 written only as a function of the electric field E_y and ΔY is the pinhole projection diameter at the detector's plane measured along the electric deflection direction (see Fig. A.18).

The lowest energy particles will be the most deflected ones both in the magnetic and electric directions, see Eqs. A.44 and A.45. Hence, the minimum energy that can be detected can be calculated from the intersection of the analytical deflection curves with the physical borders of the detector by knowing its surface and location. On the contrary, the highest energy particles will be only slightly deflected. As a consequence, their traces will be close to the pinhole projection on the detector's plane. The maximum detectable energies can be then deduced by the cut of the pinhole projection and the high-enegy part of the parabola. In reality, the pinhole projection will not be a perfect circle but a circle with a halo around it due to the particle's interaction with the pinhole's substrate, see inset in Fig. A.18. Therefore, the maximum detectable energy will be the cut of the parabola trace with the mentioned halo.

Angularly resolved spectra

A clever way to obtain an angular resolution is to replace a single-pinhole entrance with a multi-pinhole one. Several pinholes can be placed horizontally or vertically to obtain particle spectra at different angles from the laser axis in a $\phi \approx 1°$ aperture cone. By adding a motorized axis to the TP along the TCC - pinhole direction the ϕ cone aperture angle can be easily modified.

Geometries of the TPs that where used during this thesis

Two different Thomson parabolas where used during this thesis experimental work: LINA belonging to CEA-Saclay and a three-pinhole TP belonging to CLPU. Their geometries are summarized in Table. A.3 according to the scheme of Fig. A.17.
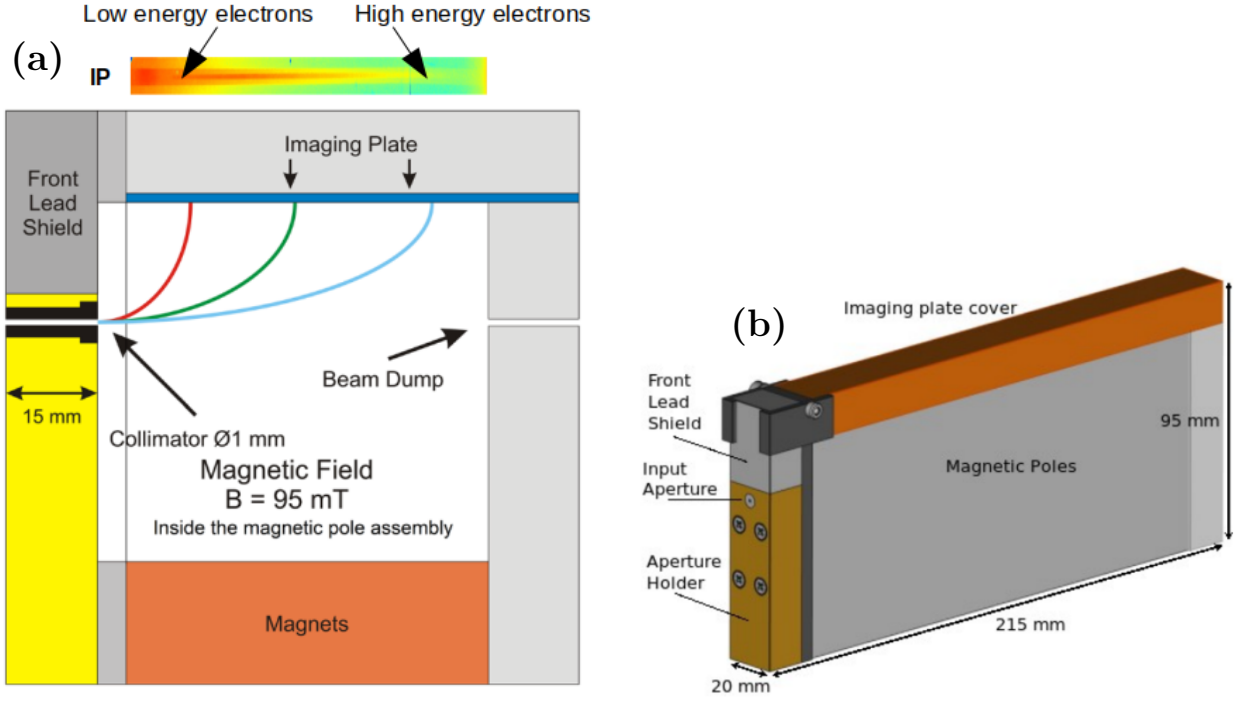
Fig. A.20: (a) Cross section view of the electron spectrometer with an example of an electron beam signal on an IP on top and (b) 3D view of the electron spectrometer. Both figures have been extracted from Ref. [198].

Tab. A.4: Calibration curves of the five different permanent magnet spectrometers used during this work. The neodymium magnets have a magnetic field $B = 190\,\mathrm{mT}$ while the Ferrite magnets have a $B = 95\,\mathrm{mT}$.

Channel N°	Material	L_c [cm]	E_{min} [MeV]	E_{max} [MeV]	Calibration curve
1	Neodymium	24	0.250	50	$E(x) = -1.17 \cdot 10^{-5}x^4 + 5.81 \cdot 10^{-4}x^3 + 1.53x^2 - 44.83x + 656.72$
2	Neodymium	18	0.250	35	$E(x) = -1.17 \cdot 10^{-5}x^4 + 5.81 \cdot 10^{-4}x^3 + 1.53x^2 - 44.83x + 656.72$
3	Ferrite	18	0.055	21	$E(x) = -2.81 \cdot 10^{-6}x^4 + 1.92 \cdot 10^{-4}x^3 + 0.78x^2 - 24.85x + 295.10$
4	Ferrite	6	0.055	1.5	$E(x) = 0.50x^2 - 7.15x + 80.03$
5	Neodymium	6	0.250	5	$E(x) = -3.07 \cdot 10^{-7}x^4 - 1.25 \cdot 10^{-4}x^3 + 0.34x^2 - 10.64x + 115.4$

A.4.2 Passive diagnostics

A.4.2.1 Permanent-magnet electron spectrometers

To obtain electron energy spectra several electron spectrometers were used during this thesis work. Such spectrometers are composed of sets of permanent magnets that deviate electrons proportionally to their energy. Their displacement on the detector plane is given by a relativistic extension of Eq. A.44:

$$X^2 = \frac{Z^2 e^2 B_y^Z L_m^2}{2\gamma m_e E_{k,i}} \left(D_m + \frac{L_m}{2} \right)^2 . \qquad (A.53)$$

The electron spectrometers are sketched in Fig. A.20. They were calibrated using particle tracking simulations. Table A.4 summarizes the calibration curves of the five different spectrometers (called "channels") used during this work can be found in Table A.4. The types of IPs used were MS and their response to electrons have been extracted from Ref. [197] for electron spectra deconvolution (Fig. A.21).
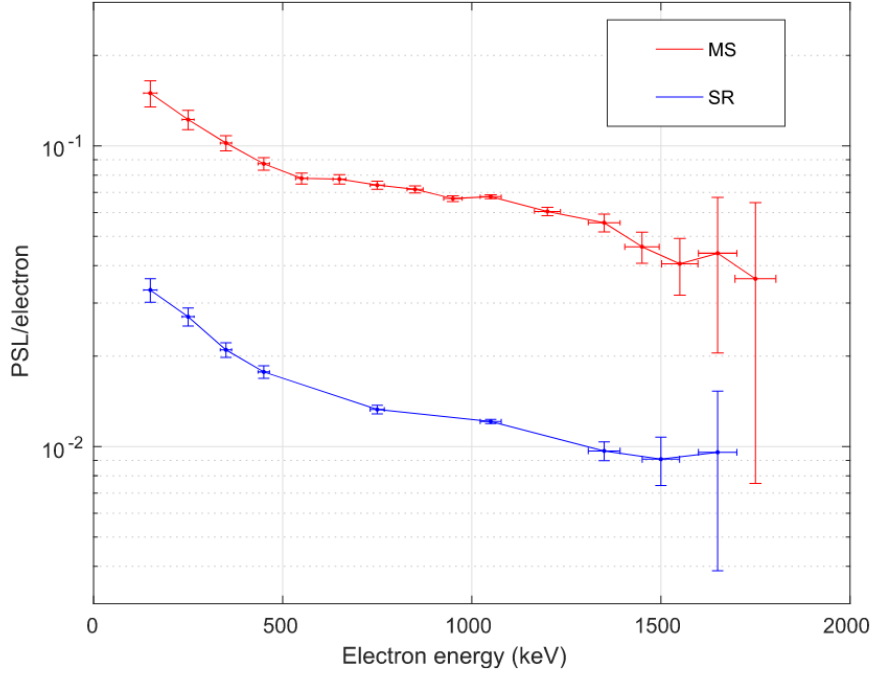
Fig. A.21: Sensitivity curve for IPs of the type MS and SR to electrons. Extracted from Ref. [197].

A.4.2.2 CR-39 solid-state nuclear track detector

CR-39 or Columbia resine #39 is a polycarbonate plastic (whose chemical formula is $C_{12}H_{18}0_7$) commonly used in laser-plasma experiments to characterize beams of neutrons and diverse ions, taking profit of their low sensitivity to photons and electrons [199]. CR-39 is a transparent plastic at visible wavelengths and it is used in industry for the fabrication of glasses.

A detailed section dedicated to CR-39 can be found in Ref. [109]. When exposed to ionizing radiation the CR-39 polymer breaks following a decarboxylation process [200] that produces CO_2 and a residual. When ion projectiles deposit energy inside CR-39 the polymer's chains break and leave tracks, or zones where damage was induced. This explains why CR-39 is called a solid-state track detector (SSTD) [201]. To infer the particle number, the radiation-exposed CR-39 must be etched in a sodium hydroxide NaOH alkali distilled water solution which will remove the outer layer of the material leaving the tracks exposed. Care must be taken since the ablation rate will only be constant under constant etching solution concentration and temperature. The hydroxide ions will ablate the polymer at a higher rate when it has already been broken, e.g. along tracks. The crater that develops is usually called an etched pit. The material's etching rate v_B depends on the CR-39 properties. The etching rate along tracks v_T will also depend on the plastic's response to the irradiation.

The etch pits are characterized using a microscope in terms of diameter and length with respect to time in order to obtain etching rates. The direction of the projectiles that impinged onto the material can also be retrieved by measuring the crater axis inclination with respect to the material's surface [202]. The standard process consists of comparing the time-varying etch pits' diameters with calibration curves of etching rate available in literature to obtain the particle energy. Following Ref. [201] and supposing a constant material (v_B) and track (v_T) etching rate and a particle normal incidence with respect to the detector's surface, the etch pit length as a function of time can be written as:
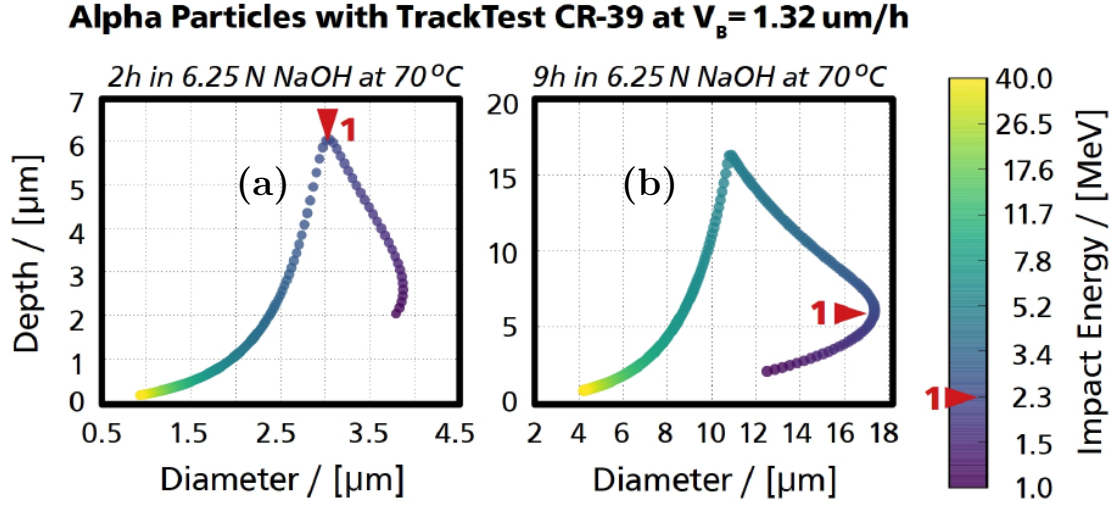
$$L(t) = t \cdot (v_T - v_B). \tag{A.54}$$

Fig. A.22: Simulated etch pit L/D ratio for varying α particle impact energies considering a (a) 2 hours etching and a (b) 9 hours etching in a 6.25 N (normal solution concentration) NaOH distilled water solution at 70°. The 2.3 MeV energy is marked with a red arrow in the two panels to highlight how the same energy level is better resolved after 2 hours of etching. The CR-39 plug-in of the PySTarT code [109] was used. Figure extracted from Ref. [109].

This will cause the growth of a cone-like crater with a semi-cone angle $\delta = \arcsin \frac{v_B}{v_T}$. The pit diameter D is then:

$$D = 2L \tan(\delta) = 2t v_B \sqrt{\frac{v_T - v_B}{v_T + v_B}} . \tag{A.55}$$

By dividing Eq. A.54 and A.55 an $\frac{L}{D}$ ratio is obtained

$$\frac{L}{D} = \frac{1}{2} \cdot \sqrt{\left(\frac{v_T}{v_B}\right)^2 - 1} . \tag{A.56}$$

When the track etching rate is much higher than the bulk's material etching rate $v_B \ll v_T$, a narrow pit cone with diameter $lim_{v_t \to \inf} D = 2 v_B t$ is obtained. When $v_B \approx v_T$ no pit is formed. Track rates can be measured using Eq. A.56 and compared to calibration data to derive projectile energies. Moreover, the number of approximately similar craters will be equal to the number of particles. As an example, the $\frac{L}{D}$ ratio is plotted in Figs. A.22a and b for varying α particle impact energies considering a 2 hours etching and a 9 hours etching, respectively, in a 6.25 N (normal solution concentration) NaOH distilled water solution at 70°. As can be seen, the two etching times considered resolve the energy spectra with different energy resolutions, i.e. curve slopes. The 2.3 MeV energy is marked with a red arrow in Figs. A.22a and b to highlight how the same energy level is better resolved after 2 hours of etching. Optimum NaOH concentrations and solution temperatures depend on the ion species and on its energy [109].

A.4.2.3 Imaging plates

Imaging plates (IPs) are particle detectors widely used in laser-plasma experiments to characterize particle and X-ray beams both in particle/photon number and position. They were developed in the 1980s by the Japanese company Fujifilm, who still produces them nowadays, targeting mainly medical applications. The selling has been transferred to General Electric (GE) Healthcare Life Sciences.

Tab. A.5: Layers and compositions of commonly used IPs of type SR, MS and TR.

Layer	SR	MS	TR
Protective			
Composition	C_2H_2O	C_2H_2O	No layer
Density [$g\,cm^{-3}$]	1.273	1.66	0
Thickness [µm]	6	9	0
Phosphoric			
Composition	BaFBr	$BaFBr_{0.85}I_{0.15}$	$BaFBr_{0.85}I_{0.15}$
Density [$g\,cm^{-3}$]	3.1	3.31	2.85
Thickness [µm]	120	115	50
Support			
Composition		C_2H_2O	
Density [$g\,cm^{-3}$]	1.273	1.66	1.66
Thickness [µm]	188	190	250
Magnetic			
Composition		$ZnMg_2Fe_5NO_{40}H_{15}C_{10}$	
Density [$g\,cm^{-3}$]	3.1	2.77	2.77
Thickness [µm]	160	160	160

Imaging plates are based on the principle of photo-stimulated luminescence (PSL) [203] which is basically the storage of information in the form of excited atomic states that decay while emitting photons. IPs are made of phosphors which allow energy to be stored for a long time until being stimulated by photons of a suitable wavelength. The interaction of a particle or X-ray beam with the active IP phosphor layer substrate excites its inner electrons to a higher energy level. The number of excited electrons is proportional to the number of incident particles or photons. The spatially distributed intensity information is read with a specialized scanner that makes use of the PSL effect. The scanner uses a red laser that triggers the trapped electrons' decay which leads to the emission of the so-called PSL (3 eV photons). A PSL is defined as the IP intensity unit of measurement.

Fujifilm sells different types of IPs: the multipurpose standard IPs (MS), the super resolution (SR) screens and the Tritium (TR) ones, among others. Note that MS type IPs are no longer produced by Fujifilm since 2009. IPs are composed of different layers, notably a protective plastic layer, a phosphor layer, a mechanical support and a magnetic layer. TR IPs are the only ones that don't have a protective layer, which makes them more sensitive to low energy particles. The purpose of the magnetic layer is to hold the IP still to the scans' magnetized surface while scanning. The layers' compositions and thicknesses of the IPs of type SR, MS and TR commonly used in laser-plasma experiments are summarized in Table. A.5 (extracted from Ref. [159]). Advantages of IPs include their very high dynamic range, above 10^{18} [204], high-sensitivity and reusability. Furthermore, IPs are also electromagnetic pulse (EMP) insensitive passive detectors.

IPs have an spatial resolution of 119 µm, 150.8 µm and 200.4 µm for the TR, SR and MS IP types, respectively [158]. Absolute resolution values vary slightly for different calibrations [205]. SR IPs are supposed to have a higher spatial resolution ($\approx 50\,\mu m$) than the other IP types. However, it turns out that the scattering, diffusion and reflection processes of the scanner light in the phosphor layer can affect the final screen resolution [205].

Calibration data for IPs (giving the energy-dependent PSL per incident particle or photon) are available in the literature for X rays, electrons, protons and different ion species, as summarized in Table. A.6.

Imaging plates' calibration using CR-39 stripes and a Thomson parabola spec-

Tab. A.6: Summary of imaging plates calibrations for electrons, protons, X-rays and other ions.

| Calibration	IP type	Particle and energy range	Instrumentation & Methods
Bonnet et al. [159]	MS, SR, TR	photons (0.01 - 1 MeV) electrons (0.01 - 1 MeV) α particles (1 - 100 MeV)	Exposure to radioactive source.
Doria et al. [206]	TR	carbon ions (3 - 300 MeV)	TNSA produced C^+ ions measured with a TP over CR-39 stripes.
Boutoux et al. [158]	MS, SR, TR, MP, ND	photons (0.001 - 1 MeV)	Laser produced relativistic electrons interact with Al target. K_α and K_β lines are acquired with the IP and X-ray spectra is obtained using an X-ray CCD.
Izumi et al. [207]	SR	neutrons (0.001 - 100 MeV)	Exposure to radioactive source.
Boutoux et al. [157]	MS, SR, TR, MP, ND	electrons (0.01 - 1000 MeV)	Linear electron accelerator ELSA (CEA-DIF).
Rabhi et al. [208]	MS, SR, TR	protons (1 - 200 MeV)	ALTO tandem accelerator (IPN Orsay).
Won et al. [209]	TR	aluminum ions (40 - 222 MeV)	TNSA produced Al^+ ions measured with a TP over CR-39 stripes.
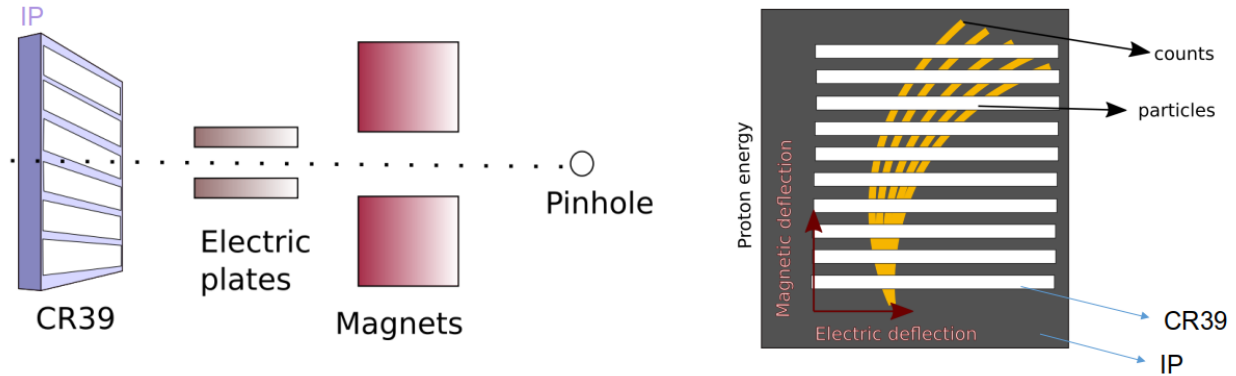
Fig. A.23: IP calibration scheme using CR-39 stripes and a Thomson parabola spectrometer.

trometer

To diagnose ionic emissions, IPs are commonly calibrated by coating them with CR-39 stripes and using the resulting multilayer structure as the detector of a Thomson parabola spectrometer. Protons as well as carbon or aluminum ions are produced through TNSA and measured using a TP. The parabolic traces that will be left in the IP can be correlated to the pits damages in the CR-39 structure (visible after proper etching), see Section. A.4.2.2. The particle energy is given by the electric and magnetic deflections (see Section. A.4.1.2) and particle number resolution can be deduced by comparison with available CR-39 calibration data. A scheme of the calibration setup is shown in Fig. A.23.

Detection of low-energy α particles and nitrogen ion with imaging plates

Detecting low-energy α particles with IPs is generally difficult due to the thick protective surface plastic layer that most of them include. Such layer serves as water protection in biology applications. IPs of the type TR do not have such plastic layer and are therefore much more sensitive to low-energy particles. Additionally, during high-intensity laser-plasma experiments IPs are normally covered by a protective layer filtering out the strong X-ray emission from the target, which further complicates low-energy particle detection

Figures A.24 a and b shows the energy deposition of α particles and nitrogen ions, respectively, in both IPs of type TR and MS as predicted by Monte Carlo Geant-4 [155] simulations. Energy depositions for both ions are plotted as well when using a TR IP and an aluminized mylar filter of varying thickness. As can be seen, IPs TR are needed to detect α particles of energies lower than 3 MeV or nitrogen ions of less than 6 MeV. Adding a filter in front of the IP increases the minimum detectable energy values.
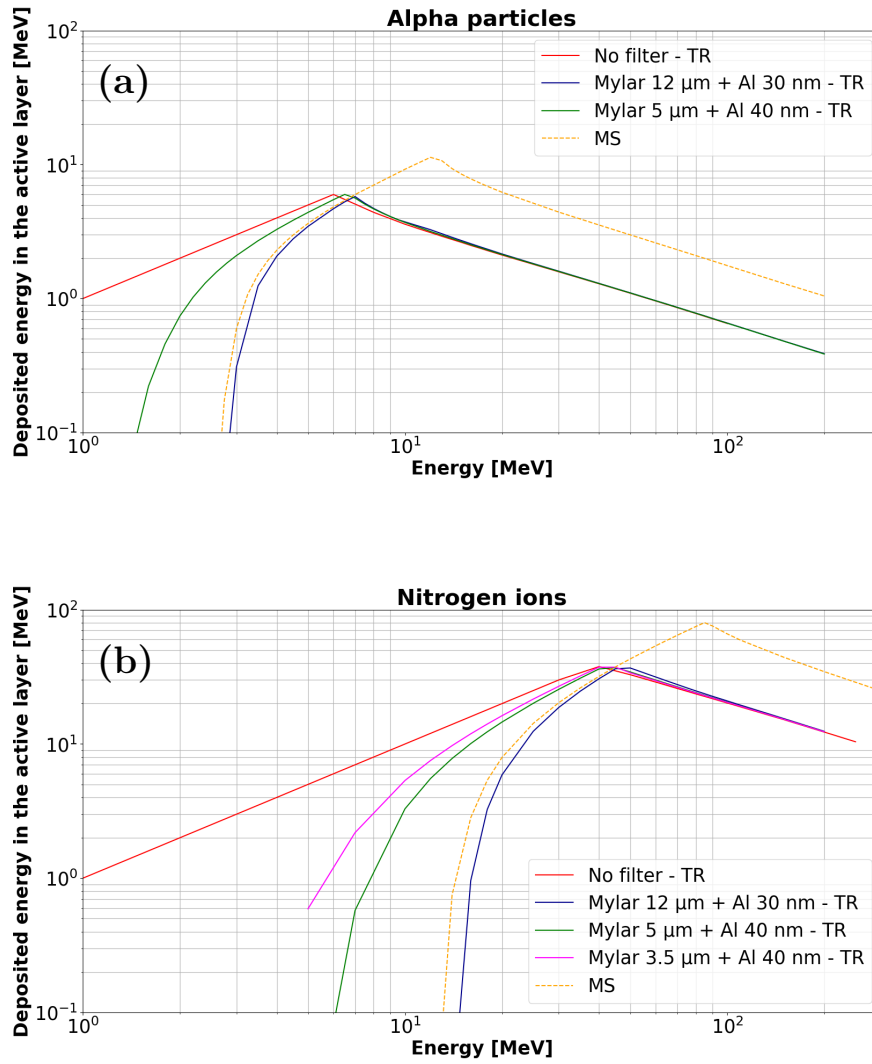
Imaging plate signal deconvolution

Fig. A.24: Energy deposition of (a) α particles and (b) nitrogen ions in MS- and TR-type IPs (with an aluminized Mylar coating of varying thickness) as simulated by the Geant-4 Monte Carlo code.

To obtain the number of projectiles hitting the IP the screen must be scanned. The transportation of the irradiated screen to the scanner must be performed in the darkness and a light-tight box must be used to avoid extra loss of signal. Recent scanners produce a .gel file with information in counts. The information must be then converted to PSL. This transformation is not at all trivial and depends on the scanner and on the IP type. In Ref. [210] the GE Typhoon 7000 used at the National Ignition Facility was calibrated using a ^{14}C impregnated polymethyl-methacrylate plastic disc sealed source with a known PSL/mm^2 value. In Ref. [211] the same scanner GE Typhoon 7000 belonging to PETAL [212] was calibrated using a Fe^{55} radioactive source and an absolute calibrated scanner Fujifilm belonging to CELIA. The following conversion formula was obtained:

$$\text{PSL} = a\,b\,\text{counts}^2 \tag{A.57}$$

with

$$a = \frac{4000}{S} \cdot 10^{\frac{L}{2}} \cdot \left(\frac{R}{100}\right)^2$$

$$b = \left(\frac{1}{(2^D - 1)}\right)^2 \tag{A.58}$$

$$S = 10^{-15.845 + 6.861 \cdot 0.4343 \cdot \ln(V)},$$

Here, L is a scanner parameter called latitude generally set to 5, R is the scanner resolution in µm which can be set to 25, 50 or 100 µm, normally it is set to 50 µm. D is the number of bits of the output data that should be set to 16. V is the scanner's photo-multiplier voltage, which can be set between 500 and 1000 V. If the signal level is low it should be increased. Finally, S is called the sensibility scanner function which only depends on the photo-multiplier voltage V. While the above conversion formula is independent of the IP type, it strongly depends on the scanner being used, which must therefore be calibrated.

During the time passed between the irradiation (or exposure) and scanning of the IP (from minutes to hours depending on the facility) the spontaneous recombination of electron/hole pairs inside the IP's sensitive layer leads to a signal loss. This signal loss is a function of the IP type and of the time and can be fitted with double exponential functions:

$$f(t) = A_1 e^{\left(\frac{-t}{B_1}\right)} + A_2 e^{\left(\frac{-t}{B_2}\right)}. \tag{A.59}$$

The parameters of Eq. A.59 extracted from the calibration performed in Ref. [157] are summarized in Table. A.7 for IPs of type MS, TR and SR and the respective functions are plotted in Fig. A.25. These fading functions can be considered as independent from the incident particle type if a 10% systematic error is included in the calculations [157].

Tab. A.7: Imaging plates' fading time equation parameters.

IP type	A_1	B_1 [min]	A_2	B_2 [min]
MS	0.334 ± 0.011	107.320 ± 9.661	0.666 ± 0.010	33974 ± 11235
TR	0.535 ± 0.016	23.812 ± 2.201	0.465 ± 0.012	3837.2 ± 498.1
SR	0.579 ± 0.021	15.052 ± 1.580	0.421 ± 0.013	3829.25 ± 650.9

Finally, the correct calibration (see Table. A.6) and the detector's solid angle should be taken into account to obtain a number of particles per sr value.
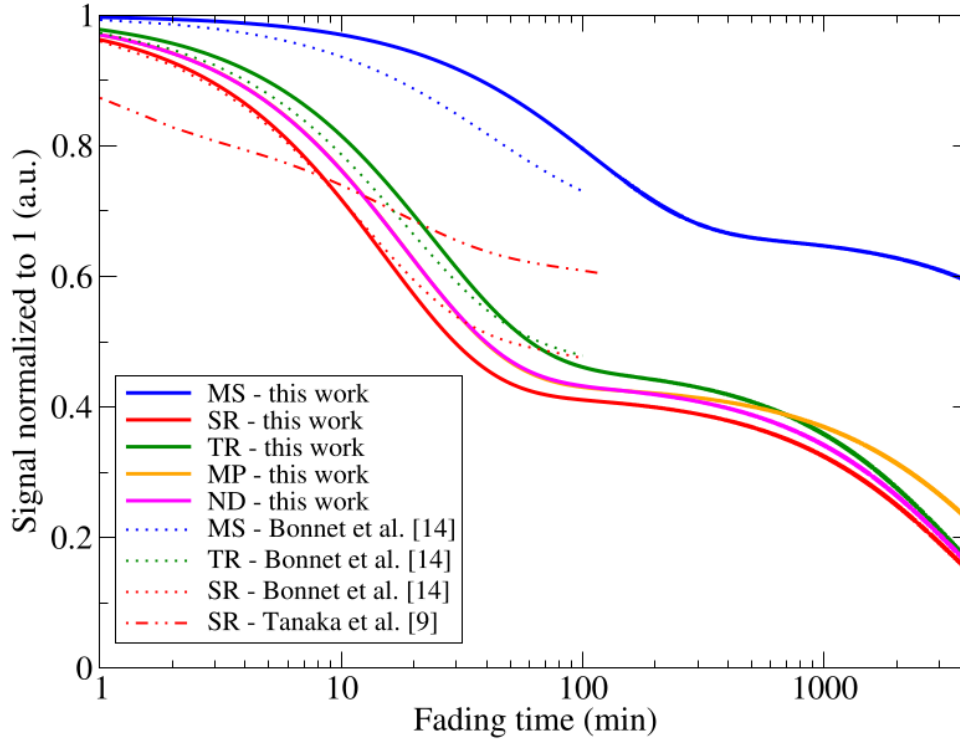
Fig. A.25: Normalized fading functions with respect to time for different IP types. Extracted from Ref. [157].

A.4.2.4 Radiochromic film stacks

Radiochromic films developed by the American chemical company Ashland^TM through their brand Gafchromic^TM provide accurate dose measurements for radiotherapy applications. Meditest company is their French reseller. Radiochromic films are a versatile 2-D dosimeter for many clinical tasks in radiation oncology. Their main characteristics include a high spatial resolution (less than $5\,\mu m$ for the HD-V2 films according to the manufacturer), near-water equivalent composition and consistent response in an extended range of doses [213]. Radiochromic films may also be immersed in water for short time periods, cut into any wanted shape and are relatively cheap.

Stacks of radiochromic films (RCFs) are commonly used to characterize laser-driven ion beams [214, 215]. The acquired 2-D maps of dose deposition can be analyzed to obtain spatial and energy resolved ion distributions [214]. A radiochromic film (RCF) consists of a plastic layer of about $100\,\mu m$ to $200\,\mu m$ thickness composed of one or two polyester layers and an active layer in a sandwich-like configuration were the active layer is located in the middle of the two polyester layers. When non-irradiated, RCFs are semi-transparent films of a light yellow color.

The RCF's active layer contains a special dye (made of lithium-10,12-penta-cosdiynoate – LiPCDA of chemical formula $C_{25}H_{41}LiO_2$ [216]). When exposed to radiation, a solid-state, polymerization process [217] turns the irradiated areas into a dark blue color. Although 90% of the dyeing appears milliseconds after irradiation, the complete film dyeing can take up to 24 hours. Hence, film scanning should happen at least 24 hours after exposure [214]. The change in color of the RCF can be related to the dose deposition through calibration data.

Gafchromic films

During this thesis work two types of Gafchromic^TM films have been used: EBT-3 [218] and unlaminated EBT-3, the composition of which is detailed in Figs. A.26a and b, respectively. Unlaminated EBT-3 films are EBT-3 films without the top polyester layer, thus leaving exposed the active layer and making them more sensitive to lower doses.
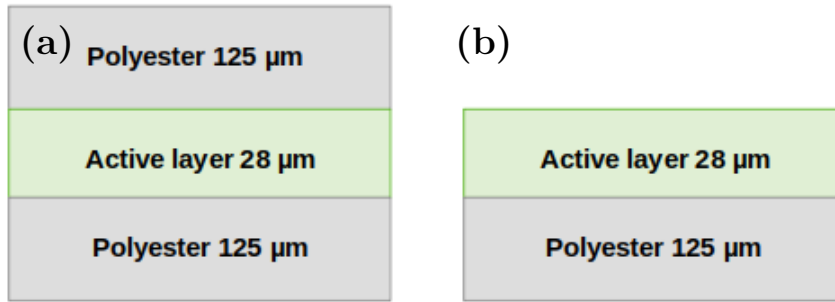
Fig. A.26: (a) EBT-3 and (b) unlaminated EBT-3 Gafchromic^{TM} films' layers.

The absorption spectrum of Gafchromic^{TM} EBT-3 films exposed to doses up to 20 Gy is plotted in Fig. A.27. The absorption curves up to 4 Gy have two peaks centered at 580 µm and 640 µm. For higher doses from 4 Gy up to 10 Gy three absorption maxima are visible at 580 µm, 630 µm and 650 µm. For 20 Gy the 650 µm peak is shifted at 660 µm and only one other absorption peak is found at 600 µm. Hence, doses below 10 Gy can be characterized with red or green light wavelengths while doses above 10 Gy should be characterized using red wavelengths only to optimize both the dynamic range and the measurement's resolution. This translates into the correct RBG scanned data slice to use for OD and consequent deposited dose extraction.

Fig. A.27: Absorption spectrum of Gafchromic^{TM} EBT-3 films exposed to doses up to 20 Gy. Extracted from Ref. [219].

Films must be kept at temperatures below 25° and not be exposed to sunlight to avoid darkening [109].

Scanning procedure
During this thesis work the EPSON EXPRESSION11000XL flat-bed scanner was used, the

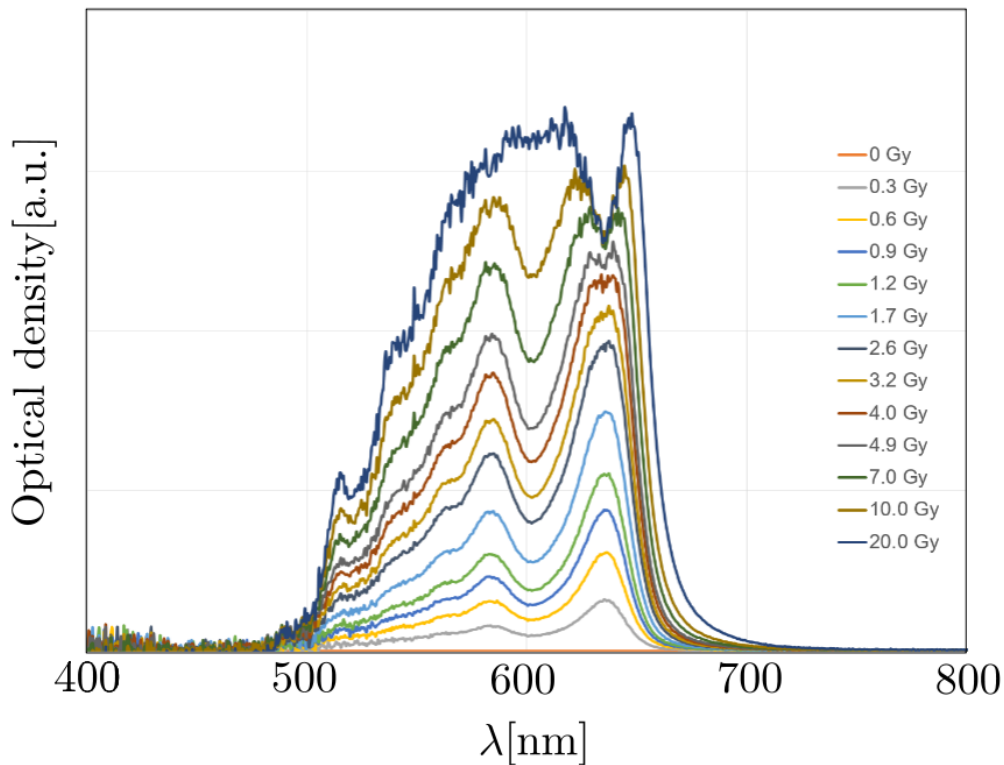emission spectrum of which is plotted in Fig. A.28. Note that the scanner correctly detects the 630 µm and specially the 580 µm absorption peaks seen in Fig. A.27 which lay in the red and green detection bands, respectively.
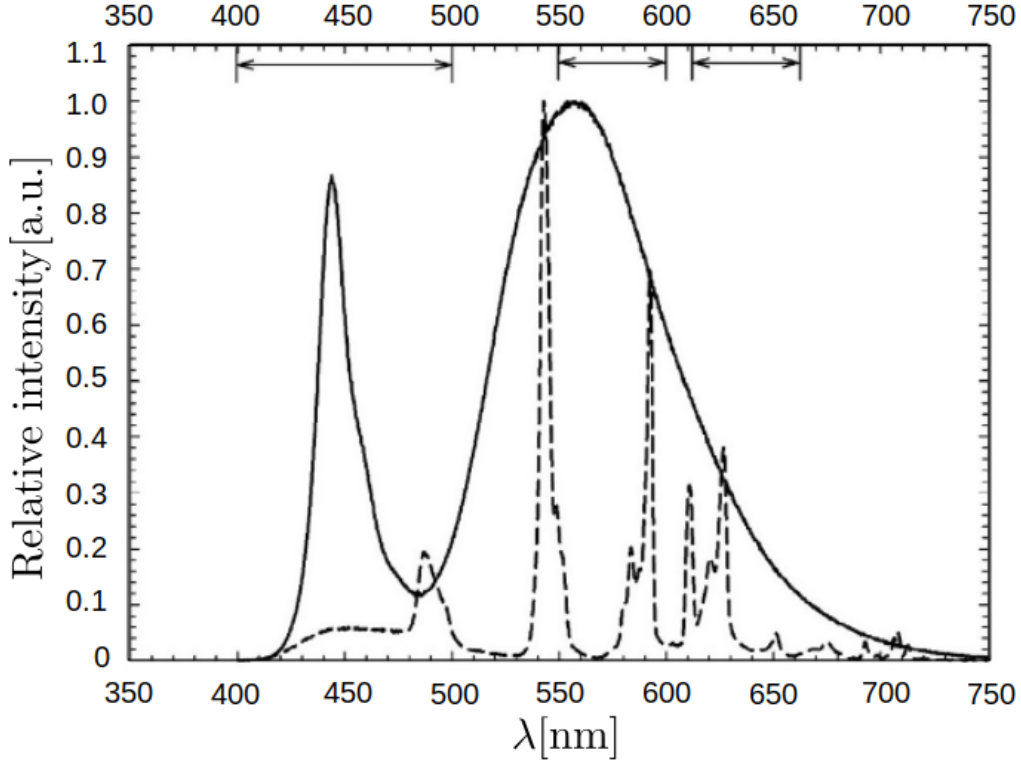

Fig. A.28: Emission spectrum of the EPSON EXPRESSION11000XL flat-bed scanner in dashed line. The detection bands of the RGB color channels are indicated with arrows. Extracted from Ref. [220].

We have followed the scanning procedure detailed in Ref. [109] to ensure reproducibility of the measurements and their consistency with previously published data. The scanner should heat before starting the operation and an initial blank scan must be performed to start operation with a warm lamp. No image correction tools must be applied and a 48 bit RGB multi-exposure scan option is to be selected. Scans can be performed in reflection or in transmission. All the scans in this work were performed in transmission. The scanner central axis must be prioritized and scanning coordinates should not vary since the scanner function depends on the flat bed (x,y) coordinates, see Fig. A.29a. Due to possible polarization effects of the active layer dye the orientation of the RCF during scan is important. When a new batch of RCFs is open the large and short sides of the original RCF rectangle must be marked and such marks must be transferred to all the cut slices as seen in Fig. A.29b. This ensures the comparability of all films in a batch whatever their manufacturing procedure. Finally, the scanning angle measured between the short side of a non-cut RCF and the long side of the scanner must be logged and kept constant, see Fig. A.29c.

Transformation of greyscale data to optical density

In order to transform greyscale data to optical density (OD) defined as:

$$\text{OD} = \log_{10} \frac{I_0}{I} \tag{A.60}$$

where I_0 is the greyscale value obtained for a scanning without any film, a scanner calibration must be performed. Kodak WRATTEN filters of known optical density (OD) are scanned and
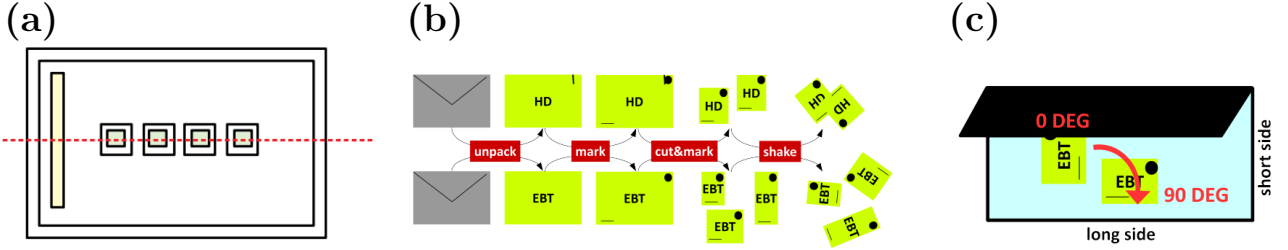
Fig. A.29: (a) Scanner central axis (red dashed line) perpendicular to the scanner lamp (yellow filled rectangle) to be prioritized and scanning frames to be respected and kept constant as much as possible (b) marks on the large and short sides of the orignal RCF rectangle and (c) scanning angle to be respected measured between the short-side of a non-cut RCF and the longside of the scanner, (b) and (c) have been extracted from Ref. [109].

a fitting function of the type:

$$\ln(\mathrm{OD_{ch}}) = \mathrm{B_{ch}} \cdot (\mathrm{C_{ch}} - \mathrm{I_{ch}}) \tag{A.61}$$

is obtained for each color channel. The RGB fitting parameters found in Ref. [109] for the EPSON EXPRESSION11000XL used during this thesis work are summarized in Table A.8.

Tab. A.8: Fitting parameters of Eq. A.61 found in Ref. [109] for the EPSON EXPRESSION11000XL used during this thesis work.

Parameter	Value	Standard deviation	Parameter	Value	Standard deviation
$\mathrm{B_R}$	2.254	0.012	$\mathrm{C_R}$	4.922	0.022
$\mathrm{B_G}$	2.320	0.020	$\mathrm{C_G}$	4.766	0.034
$\mathrm{B_B}$	2.339	0.012	$\mathrm{C_B}$	4.740	0.022

Transformation of optical density to deposited dose values: dose deposition calibration

The RCF calibration with respect to dose deposition was performed at the Medical Accelerator Unit (MAU) of the cancer treatment center in Institut Bergonié in Bordeaux, France. Here either electrons or photons with variable energies can be used to deposit dose in the RCFs. The deposited dose has a 1% precision. For the calibration performed during this thesis work only electrons with initial energy equal to 9 MeV where used.

A uniform irradiation is achieved by a flat-top beam with a 15 x 15 cm aperture for electrons and a 10 x 10 cm for photons. During our calibration performed with 9 MeV electrons small RCF rectangles of 2 x 3 cm where positioned inside the constant dose deposition area, see Fig. A.30a not further than 4 cm from the central axis. The dose deposition in the MAU is calibrated for medical applications with respect to depth in water. Although RCF films can be immersed in water we performed the calibration in a dry environment with the help of water-equivalent RW3 slab phantoms delivered by PTW Freiburg GmbH.

The RCF cut rectangles were irradiated at a 100 cm source-to-RCF distance. They were located on top of a pile of 10 RW3 plates of 1 cm of thickness each. This avoids extra dose deposition coming from secondary electrons generated by the interaction of the main electron beam with the diagnostic table. Additionally, 2 x 2 cm and 1 x 1 mm RW3 slab phantoms were located over the RCF rectangles in order to irradiate them at the maximum dose percentage relative to the depth, see Fig. A.30b. The dose is delivered in bunches of 1 cGy with a rate of 10 Gy min^{-1}. A macro-bunch maximum dose is set at 50 Gy, after each macro-bunch the MAU operator is requested to continue as part of the facility security system.
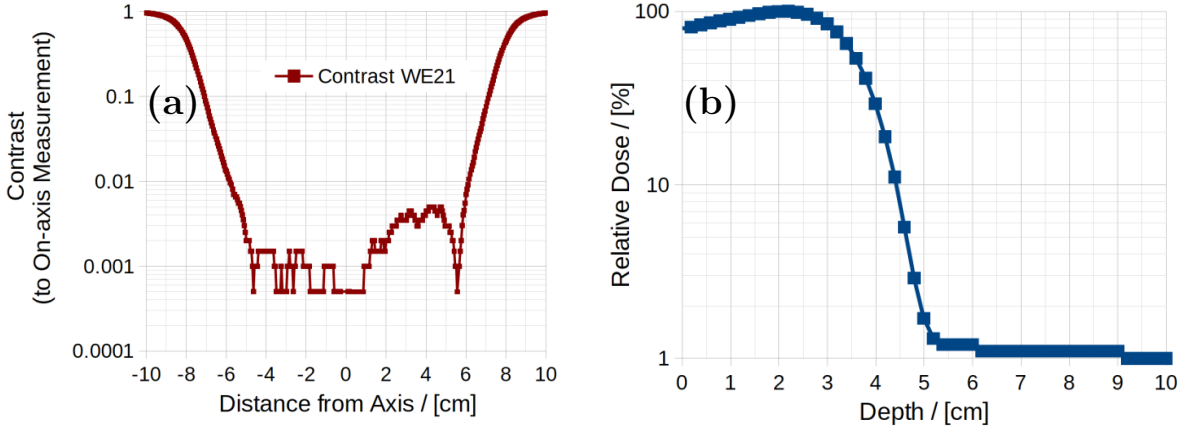
Fig. A.30: (a) Contrast of dose measurements of the transverse dose profile with respect to the dose deposited on axis. The MAU is adjusted to a 100 cm source distance and doses are deposited in a water-equivalent depth of 2.1 cm, shaped by a 15 cm x 15 cm aperture and (b) dose percentage variation as a function of depth on the central axis of 9 9 MeV electrons in water-equivalent material. A plateau is obtained for a water equivalent depth of 2.1 cm. (a) and (b) have been extracted from Ref. [109].

Once several data points have been collected a greyscale to dose calibration curve of the type:

$$Dose_{ch} = C_{ch} + \frac{B_{ch}}{I - A_{ch}} \qquad (A.62)$$

can be fitted to the data, where I is the greyscale value and A_{ch}, B_{ch} and C_{ch} are fitting coefficients which depend on the RFC batch and on the scanner. One curve is generated for each of the three RGB color channels. The A_{ch}, B_{ch} and C_{ch} fitting coefficients for the RCF batches used during this work are summarized in Table A.9. The described calibration curves are plotted in Fig. A.31.

Tab. A.9: Fitting parameters of Eq. A.62 for the unlaminated EBT-3 11181901P1 and the EBT-3 5081902 RCF batches used during this work.

Batch / RCF type	A_R	A_G	A_B	B_R	B_G	B_B	C_R	C_G	C_B
11181901P1 / U-EBT-3	412.52	-38.32	1684.75	127395.84	1961166.92	380267.16	-3.88	-5.46	-13.98
5081902 / EBT-3	114.08	-228.28	-329.59	39797.31	40633.41	110077.8014	-1.50	-0.71	-6.62

RCF calibration results may vary within 10% from batch to batch according to the manufacturer. A new calibration must then be performed for each new batch.
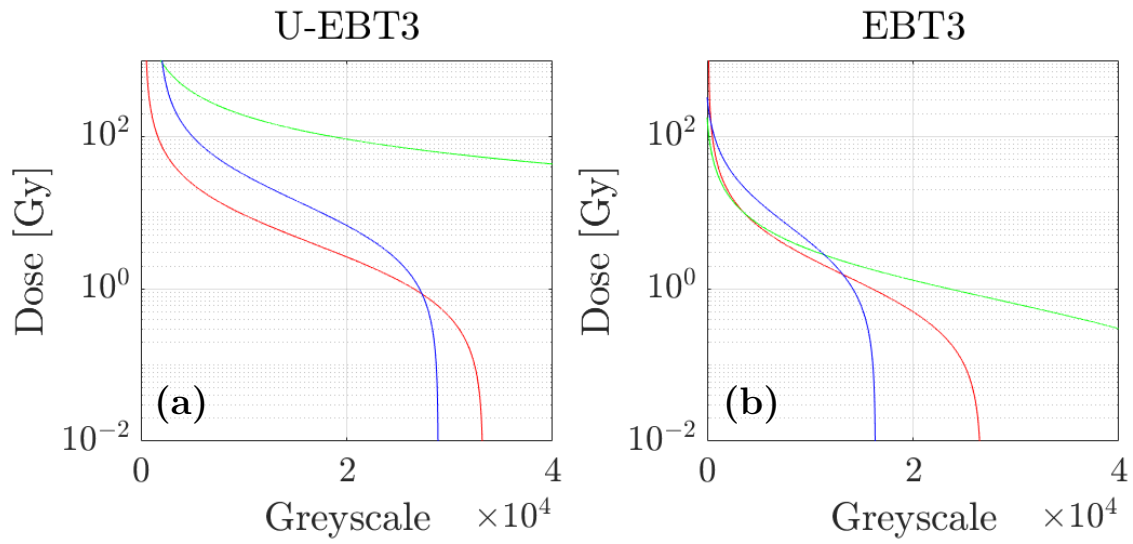
Fig. A.31: (a) Unlaminated EBT-3 (batch number 11181901P1) and (b) EBT-3 (batch number 5081902) RCFs greyscale to dose calibration curves obtained at the MAU.

Appendix B

Calder normalization

	Variable	**Value** ($\lambda_0 = 1\,\mu\mathrm{m}$)
Density	n_c	$1.11 \times 10^{27}\,\mathrm{m}^{-3}$
Velocity	c	$3.00 \times 10^{8}\,\mathrm{m/s}$
Distance	c/ω_0	$1.59 \times 10^{-7}\,\mathrm{m}$
Time	ω_0^{-1}	$5.31 \times 10^{-16}\,\mathrm{s}$
Mass	m_e	$9.11 \times 10^{-31}\,\mathrm{kg}$
Momentum	$m_e c$	$2.73 \times 10^{-22}\,\mathrm{kg.m/s}$
Energy	$m_e c^2$	$8.20 \times 10^{-14}\,\mathrm{J}$
Current density	$n_c e c$	$5.34 \times 10^{16}\,\mathrm{A/m}^2$
Magnetic field	$B_0 = m_e \omega_0 / e$	$1.07 \times 10^{4}\,\mathrm{T}$
Electric field	$E_0 = m_e \omega_0 c / e$	$3.21 \times 10^{12}\,\mathrm{V/m}$

.

Bibliography

[1] M. D. von Ehrenfried, *Ingenuity* (Springer International Publishing, 2022). — Cited in page 2.

[2] D. Strickland and G. Mourou, Optics communications **55**, 447 (1985). — Cited in pages 2 and 4.

[3] L. Evans and P. Bryant, Journal of instrumentation **3**, S08001 (2008). — Cited in page 2.

[4] R. Dendale *et al.*, International Journal of Radiation Oncology* Biology* Physics **65**, 780 (2006). — Cited in page 3.

[5] M. Borghesi *et al.*, Review of Scientific Instruments **74**, 1688 (2003). — Cited in page 3.

[6] M. Borghesi *et al.*, Physical Review Letters **92**, 055003 (2004). — Cited in page 3.

[7] J. J. Santos *et al.*, New J. Phys. **17**, 083051 (2015). — Cited in page 3.

[8] M. Ehret *et al.*, GSI Scientific Report 2016 **GSI-2017-1**, 227 (2017). — Cited in page 3.

[9] M. Roth *et al.*, Plasma Physics and Controlled Fusion **51**, 124039 (2009). — Cited in page 3.

[10] S. Fritzler *et al.*, Applied physics letters **83**, 3039 (2003). — Cited in page 3.

[11] I. Spencer *et al.*, Nuclear Instruments and Methods in Physics Research Section B: Beam Interactions with Materials and Atoms **183**, 449 (2001). — Cited in page 3.

[12] K. W. D. Ledingham *et al.*, Appl. Sci. **4**, 402 (2014). — Cited in page 3.

[13] A. Macchi, M. Borghesi, and M. Passoni, Rev. Mod. Phys. **85**, 751 (2013). — Cited in pages 3 and 4.

[14] H. Daido, M. Nishiuchi, and A. S. Pirozhkov, Reports on Progress in Physics **75**, 056401 (2012). — Cited in pages 3, 4, and 8.

[15] V. Malka *et al.*, Science **298**, 1596 (2002). — Cited in page 3.

[16] V. Y. Bychenkov and V. F. Kovalev, Quantum Electronics **35**, 1143 (2005). — Cited in page 4.

[17] S. V. Bulanov and T. Z. Esirkepov, Physical Review Letters **98**, 049503 (2007). — Cited in page 4.

[18] S. V. Bulanov, D. V. Dylov, T. Z. Esirkepov, F. F. Kamenets, and D. V. Sokolov, Plasma Physics Reports **31**, 369 (2005). — Cited in pages 4, 7, and 163.

[19] J. Park *et al.*, Physics of Plasmas **26**, 103108 (2019), 1904.03281. — Cited in pages 4 and 33.

[20] T. Nakamura, S. V. Bulanov, T. Z. Esirkepov, and M. Kando, Physical Review Letters **105**, 135002 (2010). — Cited in pages 4, 7, 33, 132, and 163.

[21] L. Willingale *et al.*, Physical Review Letters **96**, 245002 (2006). — Cited in page 4.

[22] L. Romagnani *et al.*, Physical Review Letters **101**, 025004 (2008). — Cited in pages 4, 9, and 10.

[23] F. Fiuza *et al.*, Physical Review Letters **109**, 215001 (2012), 1206.2903. — Cited in pages 4, 33, 68, 78, and 92.

[24] F. Fiuza *et al.*, Physics of Plasmas **20**, 056304 (2013), 1301.4262. — Cited in pages 4, 33, and 78.

[25] M. E. Dieckmann *et al.*, Physics of Plasmas **20**, 042111 (2013), 1304.6523. — Cited in pages 4, 78, and 92.

[26] M. E. Dieckmann, G. Sarri, D. Doria, M. Pohl, and M. Borghesi, Physics of Plasmas **20**, 102112 (2013), 1310.1740. — Cited in pages 4 and 78.

[27] Z. Lécz and A. Andreev, Physics of Plasmas **22**, 043103 (2015). — Cited in page 4.

[28] M. Liu *et al.*, Physics of Plasmas **23**, 113103 (2016), 1611.06616. — Cited in pages 4 and 33.

[29] B. Liu, J. Meyer-ter-Vehn, and H. Ruhl, Physics of Plasmas **25**, 103117 (2018), 1803.06358. — Cited in page 4.

[30] A. Debayle *et al.*, New J. Phys. **19**, 123013 (2017). — Cited in pages 4, 8, 33, 68, 69, 73, 74, 80, 101, 103, 132, 134, 137, 140, 141, 142, 144, 148, 159, 160, 161, 162, 163, 164, 168, and 169.

[31] S. Gitomer *et al.*, The Physics of fluids **29**, 2679 (1986). — Cited in page 4.

[32] Y. Kishimoto, K. Mima, T. Watanabe, and K. Nishikawa, The Physics of fluids **26**, 2308 (1983). — Cited in page 4.

[33] F. Beg *et al.*, Physics of plasmas **4**, 447 (1997). — Cited in page 4.

[34] A. Gurevich, L. Pariiskaya, and L. Pitaevskii, Sov. Phys. JETP **22**, 449 (1966). — Cited in page 4.

[35] J. Crow, P. Auer, and J. Allen, Journal of Plasma Physics **14**, 65 (1975). — Cited in page 4.

[36] F. Wagner *et al.*, Physical Review Letters **116**, 205002 (2016). — Cited in pages 4 and 6.

[37] A. Higginson *et al.*, Nat. Commun. **9**, 1 (2018). — Cited in page 4.

[38] S. Wilks *et al.*, Physics of plasmas **8**, 542 (2001). — Cited in page 4.

[39] M. Borghesi, Nuclear Instruments and Methods in Physics Research Section A: Accelerators, Spectrometers, Detectors and Associated Equipment **740**, 6 (2014). — Cited in page 4.

[40] P. Mora, Physical Review Letters **90**, 185002 (2003). — Cited in pages 5, 6, 82, and 85.

[41] K. Matsukado *et al.*, Physical Review Letters **91**, 215001 (2003). — Cited in page 7.

[42] S. S. Bulanov *et al.*, Physics of plasmas **17**, 043105 (2010). — Cited in pages 7 and 33.

[43] C. E. Max, J. Arons, and A. B. Langdon, Physical Review Letters **33**, 209 (1974). — Cited in pages 7 and 96.

[44] S. S. Moiseev and R. Z. Sagdeev, Journal of Nuclear Energy **5**, 43 (1963). — Cited in pages 8 and 32.

[45] D. W. Forslund and C. R. Shonk, Physical Review Letters **25**, 1699 (1970). — Cited in pages 8 and 32.

[46] G. Sorasio, M. Marti, R. Fonseca, and L. O. Silva, Physical Review Letters **96**, 045005 (2006), physics/0512231. — Cited in pages 8, 29, 31, and 32.

[47] R. A. Cairns, R. Bingham, P. Norreys, and R. Trines, Physics of Plasmas **21**, 022112 (2014), 1402.2804. — Cited in pages 8, 29, 30, 31, and 32.

[48] J. Denavit, Physical Review Letters **69**, 3052 (1992). — Cited in pages 8, 33, and 68.

[49] L. O. Silva *et al.*, Physical Review Letters **92**, 015002 (2004). — Cited in pages 8, 33, and 68.

[50] E. Boella, F. Fiúza, A. S. Novo, R. Fonseca, and L. Silva, Plasma Physics and Controlled Fusion **60**, 035010 (2018). — Cited in pages 8 and 33.

[51] J. H. Bin *et al.*, Physical Review Letters **115**, 064801 (2015). — Cited in pages 9 and 10.

[52] J. H. Bin *et al.*, Physical Review Letters **120**, 074801 (2018), 1710.09855. — Cited in pages 9 and 10.

[53] W. J. Ma *et al.*, Physical Review Letters **122**, 014803 (2019), 1801.10338. — Cited in pages 9 and 10.

[54] A. Pazzaglia, L. Fedeli, A. Formenti, A. Maffini, and M. Passoni, Communications Physics **3**, 133 (2020). — Cited in page 9.

[55] T. Esirkepov, M. Borghesi, S. Bulanov, G. Mourou, and T. Tajima, Physical Review Letters **92**, 175003 (2004). — Cited in page 9.

[56] C. Hooker *et al.*, Commissioning the astra gemini petawatt ti: sapphire laser system, in *Conference on Lasers and Electro-Optics*, p. JThB2, Optica Publishing Group, 2008. — Cited in page 9.

[57] J. H. Sung, S. K. Lee, H. W. Lee, J. Y. Yoo, and C. H. Nam, High-contrast 0.1-hz 4-pw laser at corels, in *2016 IEEE Photonics Conference (IPC)*, pp. 456–457, IEEE, 2016. — Cited in page 9.

[58] P. Antici *et al.*, Scientific Reports **7**, 16463 (2017), 1708.02539. — Cited in pages 9, 10, and 33.

[59] A. Pak *et al.*, Physical Review Accelerators and Beams **21**, 103401 (2018), 1810.08190. — Cited in pages 9, 10, and 33.

[60] D. Haberberger *et al.*, Nature Physics **8**, 95 (2012). — Cited in pages 9, 10, and 11.

[61] F. Sylla *et al.*, Physical Review Letters **110**, 085001 (2013), 1206.6329. — Cited in pages 10 and 11.

[62] S. N. Chen *et al.*, Scientific Reports **7**, 13505 (2017), 1708.02492. — Cited in pages 10, 11, 33, and 166.

[63] P. Puyuelo-Valdés *et al.*, Physics of Plasmas **26**, 123109 (2019). — Cited in pages 10 and 11.

[64] S. Wilks, W. Kruer, M. Tabak, and A. Langdon, Physical Review Letters **69**, 1383 (1992). — Cited in pages 10 and 11.

[65] P. K. Singh *et al.*, Scientific reports **10**, 1 (2020). — Cited in pages 10, 11, 102, and 124.

[66] O. N. Rosmej *et al.*, New Journal of Physics **21**, 043044 (2019). — Cited in pages 9 and 100.

[67] E. d'Humières *et al.*, Plasma Physics and Controlled Fusion **55**, 124025 (2013). — Cited in page 9.

[68] O. Tresca *et al.*, Physical Review Letters **115**, 094802 (2015), 1503.06180. — Cited in page 9.

[69] F. Tsung, S. Y. Tochitsky, D. J. Haberberger, W. B. Mori, and C. Joshi, Journal of Plasma Physics **78**, 373 (2012). — Cited in page 9.

[70] M. Ehret *et al.*, arXiv e-prints , arXiv:2012.09455 (2020), 2012.09455. — Cited in pages 11, 40, 57, 61, 68, 97, 118, 144, and 169.

[71] D. R. Nicholson, *Introduction to plasma theory* (Wiley New York, 1983). — Cited in page 14.

[72] J. D. Huba, *NRL plasma formulary* (Naval Research Laboratory, 1998). — Cited in page 16.

[73] P.-A. Raviart, *Modeling of collisions* (Masson, 1997). — Cited in page 16.

[74] B. Lapeyre, E. Pardoux, and S. Rémi, *Méthodes de Monte-Carlo pour les équations de transport et de diffusion* (Springer, 1998). — Cited in page 16.

[75] T. Z. Esirkepov, Computer Physics Communications **135**, 144 (2001). — Cited in page 17.

[76] K. Yee, IEEE Transactions on antennas and propagation **14**, 302 (1966). — Cited in page 17.

[77] E. Lefebvre *et al.*, Nuclear Fusion **43**, 629 (2003). — Cited in page 18.

[78] L. Clarke, I. Glendinning, and R. Hempel, The mpi message passing interface standard, in *Programming environments for massively parallel distributed systems*, pp. 213–218, Springer, 1994. — Cited in page 18.

[79] R. Nuter *et al.*, Physics of Plasmas **18**, 033107 (2011). — Cited in page 19.

[80] G. L. Yudin and M. Y. Ivanov, Physical Review A **64**, 013409 (2001). — Cited in page 19.

[81] F. Pérez, L. Gremillet, A. Decoster, M. Drouin, and E. Lefebvre, Physics of Plasmas **19**, 083104 (2012). — Cited in page 19.

[82] T. Takizuka and H. Abe, Journal of computational physics **25**, 205 (1977). — Cited in page 19.

[83] K. Nanbu and S. Yonemura, Journal of Computational Physics **145**, 639 (1998). — Cited in page 19.

[84] Y.-K. Kim, J. P. Santos, and F. Parente, Physical Review A **62**, 052710 (2000). — Cited in page 19.

[85] W. Kruer, *The physics of laser plasma interactions* (crc Press, 2019). — Cited in pages 19 and 20.

[86] B. Quesnel and P. Mora, Physical Review E **58**, 3719 (1998). — Cited in page 23.

[87] P. Gibbon, *Short pulse laser interactions with matter: an introduction* (World Scientific, 2005). — Cited in page 23.

[88] W. Kruer and K. Estabrook, The Physics of fluids **28**, 430 (1985). — Cited in page 27.

[89] P. Sprangle, C.-M. Tang, and E. Esarey, IEEE transactions on plasma science **15**, 145 (1987). — Cited in page 28.

[90] K. Krushelnick *et al.*, Physical Review Letters **83**, 737 (1999). — Cited in page 28.

[91] H. Wang *et al.*, Physical Review Letters **107**, 265002 (2011). — Cited in pages 28, 145, and 146.

[92] R. Saagdev, *Reviews of Plasma Physics* (Consultants Bureau, 1966). — Cited in page 28.

[93] H. Washimi and T. Taniuti, Physical Review Letters **17**, 996 (1966). — Cited in page 28.

[94] D. Tidman and N. Krall, (1971). — Cited in pages 28 and 29.

[95] A. Stockem, E. Boella, F. Fiuza, and L. Silva, Physical Review E **87**, 043116 (2013). — Cited in page 29.

[96] H. Schamel, Plasma Physics **14**, 905 (1972). — Cited in page 29.

[97] M. Tatarakis *et al.*, Physical Review Letters **90**, 175001 (2003). — Cited in page 29.

[98] D. Forslund, J. Kindel, K. Lee, and B. Godfrey, The Physics of Fluids **22**, 462 (1979). — Cited in page 29.

[99] S. Hosseini Jenab and F. Spanier, Physics of Plasmas **24**, 032305 (2017). — Cited in page 29.

[100] A. Grassi, L. Fedeli, A. Sgattoni, and A. Macchi, Plasma Physics and Controlled Fusion **58**, 034021 (2016). — Cited in page 29.

[101] E. Boella, *Ion acceleration driven by intense laser pulses*, Phd thesis, Politecnico di Torino, 2014. — Cited in pages 29 and 92.

[102] Y.-K. Kim *et al.*, Phys. Rev. E **94**, 033211 (2016). — Cited in page 33.

[103] P. Puyuelo-Valdés *et al.*, Physics of Plasmas **26**, 123109 (2019). — Cited in page 33.

[104] T. Nakamura and K. Mima, Physical Review Letters **100**, 205006 (2008). — Cited in pages 33 and 163.

[105] F. Sylla *et al.*, Physical Review Letters **108**, 115003 (2012). — Cited in pages 33 and 92.

[106] M. Helle *et al.*, Physical Review Letters **117**, 165001 (2016). — Cited in page 33.

[107] F. Mollica, *Interaction laser-plasma ultra-intense à densité proche-critique pour l'accélération d'ions.*, PhD thesis, Université Paris Saclay (COmUE), 2016. — Cited in pages 36, 37, 157, 158, and 159.

[108] P. Puyuelo-Valdés, *Laser-driven ion acceleration with high-density gas-jet targets and application to elemental analysis*, Phd thesis, Université de Bordeaux ; Institut national de la recherche scientifique (Québec, province), 2020. — Cited in pages 36, 40, and 68.

[109] M. Ehret, *Charged particle beam acceleration and strong discharge currents' fields generation by laser : a study on laser-driven ion sources and beam transport suited for application in high-energy-density physics experiments*, Phd thesis, Université de Bordeaux ; Université de sciences appliquées de Darmstadt, 2021. — Cited in pages 36, 92, 100, 124, 125, 135, 167, 169, 196, 197, 203, 204, 210, 211, 212, and 213.

[110] Sourcelab, Sl-gt-10, the ultra thin high density gas jet for near-critical regime. — Cited in page 36.

[111] D. D. Hickstein, S. T. Gibson, R. Yurchak, D. D. Das, and M. Ryazanov, Review of Scientific Instruments **90**, 065115 (2019). — Cited in pages 37 and 38.

[112] T. Chodukowski, Parameters and dynamics of the pf-1000-facility-generated plasma in the plasma column formation/disintegration phase using the multi-frame laser interferometry method. — Cited in pages 37 and 132.

[113] T. Pisarczyk *et al.*, Journal of Instrumentation **14**, C11024 (2019). — Cited in pages 37 and 132.

[114] A. Zaraś-Szydłowska *et al.*, AIP Advances **10**, 115201 (2020). — Cited in pages 37 and 132.

[115] Ansys, (2018). — Cited in pages 39 and 42.

[116] N.-H. Nguyen-Bui and G. Duffa, Journal of spacecraft and rockets **43**, 919 (2006). — Cited in pages 39 and 42.

[117] K. Schmid and L. Veisz, Review of Scientific Instruments **83**, 053304 (2012). — Cited in pages 39 and 187.

[118] J. Henares *et al.*, Review of Scientific Instruments **90**, 063302 (2019). — Cited in pages 39 and 40.

[119] Springer, Supersonic micro-nozzles. — Cited in page 39.

[120] L. Rovige *et al.*, Review of Scientific Instruments **92**, 083302 (2021). — Cited in pages 39 and 40.

[121] S. Lorenz *et al.*, Matter and Radiation at Extremes **4**, 015401 (2019). — Cited in page 39.

[122] Instrumentationtools, Valve characteristics. — Cited in pages 43, 44, and 45.

[123] Instrumentationtools, Different control valve flow characteristics, 2022. — Cited in pages 43 and 44.

[124] Phasics, Sid4. — Cited in pages 44 and 50.

[125] K. Nelissen *et al.*, Scientific Reports **10**, 1 (2020). — Cited in pages 50, 101, and 194.

[126] F. Fiuza *et al.*, Physics of Plasmas **20**, 056304 (2013). — Cited in page 68.

[127] Fluent, Ansys fluent Academic Research Release **14** (2015). — Cited in page 68.

[128] S. Guérin *et al.*, Physics of Plasmas **2**, 2807 (1995). — Cited in page 70.

[129] S. Guerin, P. Mora, J. Adam, A. Héron, and G. Laval, Physics of Plasmas **3**, 2693 (1996). — Cited in page 70.

[130] J. Moreau, E. d'Humières, R. Nuter, and V. Tikhonchuk, Physical Review E **95**, 013208 (2017). — Cited in page 70.

[131] J. Moreau, *Interaction d'une impulsion laser intense avec un plasma sous dense dans le régime relativiste*, PhD thesis, Université de Bordeaux, 2018. — Cited in pages 70 and 71.

[132] L. Yin *et al.*, Physics of Plasmas **26**, 082708 (2019). — Cited in page 71.

[133] D. Teychenné, G. Bonnaud, and J.-L. Bobin, Physical Review E **48**, R3248 (1993). — Cited in page 72.

[134] J. Vieira, F. Fiúza, L. O. Silva, M. Tzoufras, and W. B. Mori, New Journal of Physics **12**, 045025 (2010). — Cited in page 72.

[135] T. Grismayer and P. Mora, Physics of Plasmas **13**, 032103 (2006). — Cited in pages 77 and 83.

[136] M. Perego, P. D. Howell, M. D. Gunzburger, J. R. Ockendon, and J. E. Allen, Physics of Plasmas **20**, 052101 (2013). — Cited in pages 77 and 86.

[137] A. A. Nechaev, M. A. Garasev, A. N. Stepanov, and V. V. Kocharovsky, Plasma Physics Reports **46**, 765 (2020). — Cited in page 77.

[138] A. Robinson, R. Trines, J. Polz, and M. Kaluza, Plasma Physics and Controlled Fusion **53**, 065019 (2011). — Cited in page 80.

[139] Y. V. Medvedev, Plasma Physics and Controlled Fusion **56**, 025005 (2014). — Cited in pages 86 and 88.

[140] L. Volpe *et al.*, High Power Laser Science and Engineering **7** (2019). — Cited in pages 92, 97, and 109.

[141] J. Primot, S. Velgue, N. Guerineau, R. Haïdar, and J. Chanteloup, Photoniques (Orsay) , 57 (2005). — Cited in pages 93 and 112.

[142] J. Bonvalet *et al.*, Physics of Plasmas **28**, 113102 (2021). — Cited in pages 96, 134, and 137.

[143] M. Borghesi *et al.*, Physical Review Letters **80**, 5137 (1998). — Cited in pages 96, 101, and 147.

[144] K. S. Budil *et al.*, The Astrophysical Journal Supplement Series **127**, 261 (2000). — Cited in pages 96 and 101.

[145] J. A. Nicholls, M. Sichel, R. Fry, and D. R. Glass, Acta Astronautica **1**, 385 (1974). — Cited in pages 96 and 147.

[146] I. B. Zeldovich and Y. P. Raizer, *Physics of Shock Waves and High-temperature Hydrodynamic Phenomena. Volume i* (Academic Press New York and London, 1966). — Cited in page 96.

[147] L. Pugachev, N. Andreev, P. Levashov, and O. Rosmej, Nuclear Instruments and Methods in Physics Research Section A: Accelerators, Spectrometers, Detectors and Associated Equipment **829**, 88 (2016). — Cited in page 100.

[148] J. Shaw *et al.*, Physical Review Letters **118**, 064801 (2017). — Cited in pages 101 and 149.

[149] J. Shaw, N. Lemos, K. Marsh, D. Froula, and C. Joshi, Plasma Physics and Controlled Fusion **60**, 044012 (2018). — Cited in pages 101, 149, and 168.

[150] A. Martín-López, *Safety system automation for gaseous targets experiments and real-time leak detection in the vacuum system*, master thesis, universidad de salamanca, 2021. — Cited in pages 103 and 170.

[151] A. Ltd., *Femtosecond Single Shot Autocorrelator - Model: ASF-15M. User's manual.*, Avesta Ltd. — Cited in pages 104, 180, 181, and 182.

[152] A. Debayle, P. G. de Alaiza Martínez, L. Gremillet, and L. Bergé, Physical Review A **91**, 041801 (2015). — Cited in pages 106 and 121.

[153] M. Berger, J. Coursey, M. Zucker, and J. Chang, Estar, pstar, and astar: Computer programs for calculating stopping-power and range tables for electrons, protons, and helium ions (version 1.2.3). — Cited in page 107.

[154] Wikipedia, Rayleigh length. — Cited in page 109.

[155] S. Agostinelli *et al.*, Nuclear Instruments and Methods in Physics Research Section A: Accelerators, Spectrometers, Detectors and Associated Equipment **506**, 250 (2003). — Cited in pages 115, 125, and 206.

[156] M. Salvadori *et al.*, Scientific Reports **11**, 3071 (2021), 2003.01442. — Cited in pages 117, 167, and 197.

[157] G. Boutoux *et al.*, Review of Scientific Instruments **86**, 113304 (2015). — Cited in pages 124, 206, 208, and 209.

[158] G. Boutoux *et al.*, Review of Scientific Instruments **87**, 043108 (2016). — Cited in pages 124, 205, and 206.

[159] T. Bonnet *et al.*, Review of Scientific Instruments **84**, 103510 (2013). — Cited in pages 124, 205, and 206.

[160] J. F. Ziegler, M. D. Ziegler, and J. P. Biersack, Nuclear Instruments and Methods in Physics Research Section B: Beam Interactions with Materials and Atoms **268**, 1818 (2010). — Cited in page 125.

[161] S. Bulanov, I. Inovenkov, V. Kirsanov, N. Naumova, and A. Sakharov, Physics of Fluids B: Plasma Physics **4**, 1935 (1992). — Cited in page 142.

[162] A. Pukhov and J. Meyer-ter Vehn, Physical Review Letters **76**, 3975 (1996). — Cited in pages 145, 146, and 149.

[163] B. Liu *et al.*, Physical Review Letters **110**, 045002 (2013). — Cited in page 145.

[164] A. Arefiev *et al.*, Physics of Plasmas **23**, 056704 (2016). — Cited in page 148.

[165] A. E. Hussein *et al.*, New Journal of Physics **23**, 023031 (2021). — Cited in page 148.

[166] P. McKenna, D. Neely, R. Bingham, and D. Jaroszynski, *Laser-plasma interactions and applications* (Springer, 2013). — Cited in page 149.

[167] L. Gorbunov, P. Mora, and A. Solodov, Physical Review Letters **86**, 3332 (2001). — Cited in page 159.

[168] R. Aliev *et al.*, Atomic Energy **129**, 337 (2021). — Cited in page 167.

[169] J. Grillenberger, C. Baumgarten, and M. Seidel, SciPost Physics Proceedings , 002 (2021). — Cited in page 167.

[170] J. Apiñaniz *et al.*, Scientific Reports **11**, 1 (2021). — Cited in page 167.

[171] S. Malko *et al.*, Nature Communications **13**, 1 (2022). — Cited in page 167.

[172] P. Phadke, J. M. Sturm, R. W. van de Kruijs, and F. Bijkerk, Applied surface science **505**, 144529 (2020). — Cited in page 167.

[173] L. Jonušauskas *et al.*, Optics express **27**, 15205 (2019). — Cited in page 169.

[174] A. Technologies, *High dynamic third order cross correlator. User's manual.*, Amplitude Technologies. — Cited in page 182.

[175] P. J. Brannon, J. P. Anthes, G. L. Cano, and J. E. Powell, Journal of Applied Physics **46**, 3576 (1975). — Cited in page 184.

[176] Wikipedia, Group velocity dispersion. — Cited in pages 184 and 185.

[177] A. Kasperczuk and T. Pisarczyk, Optica Applicata **31**, 571 (2001). — Cited in page 186.

[178] I. Kochetkov *et al.*, Physics of Plasmas **28**, 102110 (2021). — Cited in pages 186 and 191.

[179] T. Pisarczyk, A. Rupasov, G. Sarkisov, and A. Shikanov, Journal of Soviet Laser Research **11**, 1 (1990). — Cited in page 186.

[180] T. Wolterink, University of Twente, Master of Science Thesis, Faculty of Science and Technology, Laser Physics and Nonlinear Optics (2011). — Cited in page 188.

[181] A. Buck *et al.*, Nature Physics **7**, 543 (2011). — Cited in page 189.

[182] A. Flacco *et al.*, Nature Physics **11**, 409 (2015), 1503.04696. — Cited in page 189.

[183] P. Schatz and A. McCaffery, Quarterly Reviews, Chemical Society **23**, 552 (1969). — Cited in page 189.

[184] A. A. Cotton and H. Mouton, Comptes Rendus heb- domadaires des Séances de l'Académie des Sciences Paris **145** (1907). — Cited in page 189.

[185] V. L. Ginzburg and A. A. Rukhadze, Moscow Izdatel Nauka (1975). — Cited in page 190.

[186] T. Pisarczyk *et al.*, Plasma Physics and Controlled Fusion **62**, 115020 (2020). — Cited in page 191.

[187] H. P. K. K., *Guide to Streak Cameras.*, Hamamatsu Photonis K. K. — Cited in page 192.

[188] R. S. Sussmann, *CVD diamond for electronic devices and sensors* (John Wiley & Sons, 2009). — Cited in page 195.

[189] M. Salvadori *et al.*, High Power Laser Science and Engineering **10**, e6 (2022). — Cited in pages 196 and 197.

[190] D. M. Corallo, D. M. Creek, and G. M. Murray, J. Phys. E: Sci. Instrum. **13**, 623 (1980). — Cited in page 196.

[191] C. Verona *et al.*, Journal of Instrumentation **15**, C09066 (2020). — Cited in pages 196, 197, and 198.

[192] F. Consoli *et al.*, Plasma Physics and Controlled Fusion **60**, 105006 (2018). — Cited in page 197.

[193] S. Chen *et al.*, Physics of Plasmas **21**, 023119 (2014). — Cited in page 198.

[194] A. Alejo *et al.*, Review of Scientific Instruments **87**, 083304 (2016). — Cited in page 198.

[195] J. E. Ducret *et al.*, Review of Scientific Instruments **89**, 023304 (2018). — Cited in page 198.

[196] F. Schillaci *et al.*, Journal of Instrumentation **9**, T10003 (2014). — Cited in page 198.

[197] S. Singh *et al.*, Review of Scientific Instruments **88**, 075105 (2017). — Cited in pages 202 and 203.

[198] M. Krupka *et al.*, Review of Scientific Instruments **92**, 023514 (2021). — Cited in page 202.

[199] Y. He *et al.*, Calibration of CR-39 solid state track detectors with monoenergetic protons from 0.3 MeV to 2.5 MeV, in *European Physical Journal Web of Conferences*, , European Physical Journal Web of Conferences Vol. 239, p. 07006, 2020. — Cited in page 203.

[200] N. X. Thang and T. T. Doan, Radiation Measurements **25**, 185 (1995). — Cited in page 203.

[201] S. A. Durrani and R. K. Bull, *Solid state nuclear track detection: principles, methods and applications* (Elsevier, 2013). — Cited in page 203.

[202] F. Ingenito *et al.*, Directional track selection technique in cr39 ssntd for lowyield reaction experiments, in *EPJ Web of Conferences* Vol. 167, p. 05006, EDP Sciences, 2018. — Cited in page 203.

[203] H. von Seggern, Nuclear Instruments and Methods in Physics Research A **322**, 467 (1992). — Cited in page 205.

[204] M. A. True, J. R. Albritton, and E. A. Williams, Physics of Fluids **24**, 1885 (1981). — Cited in page 205.

[205] G. Fiksel, F. J. Marshall, C. Mileham, and C. Stoeckl, Review of Scientific Instruments **83**, 086103 (2012). — Cited in page 205.

[206] D. Doria *et al.*, Review of Scientific Instruments **86**, 123302 (2015). — Cited in page 206.

[207] N. Izumi *et al.*, X-ray and neutron sensitivity of imaging plates, in *Target Diagnostics Physics and Engineering for Inertial Confinement Fusion II*, edited by P. M. Bell and G. P. Grim, , Society of Photo-Optical Instrumentation Engineers (SPIE) Conference Series Vol. 8850, p. 885006, 2013. — Cited in page 206.

[208] N. Rabhi *et al.*, Review of Scientific Instruments **88**, 113301 (2017). — Cited in page 206.

[209] J. Won *et al.*, Applied Sciences **11** (2021). — Cited in page 206.

[210] G. J. Williams, B. R. Maddox, H. Chen, S. Kojima, and M. Millecchia, Review of Scientific Instruments **85**, 11E604 (2014). — Cited in page 208.

[211] G. Boutoux and D. Raffestin, CDEA/CESTA/DLP/SEIL Report No. PTW-20000-ZV1-4NT-PTP001798A, 2017 (unpublished). — Cited in page 208.

[212] N. Blanchot *et al.*, Overview of PETAL, the multi-Petawatt project in the LMJ facility, in *European Physical Journal Web of Conferences*, , European Physical Journal Web of Conferences Vol. 59, p. 07001, 2013. — Cited in page 208.

[213] A. Niroomand-Rad Chair *et al.*, Medical Physics **25**, 2093 (1998). — Cited in page 209.

[214] F. Nürnberg *et al.*, Review of Scientific Instruments **80**, 033301 (2009). — Cited in page 209.

[215] J. Kaufman *et al.*, Radiochromic film diagnostics for laser-driven ion beams, in *Research Using Extreme Light: Entering New Frontiers with Petawatt-Class Lasers II* Vol. 9515, pp. 174–181, SPIE, 2015. — Cited in page 209.

[216] T. Santos, T. Ventura, and M. d. C. Lopes, Radiation Physics and Chemistry **179**, 109217 (2021). — Cited in page 209.

[217] M. Al-Sheikhly *et al.*, Solid state polymerization reactions for passive and active guided-wave components, in *Optoelectronic Interconnects and Packaging IV*, edited by R. T. Chen and P. S. Guilfoyle, , Society of Photo-Optical Instrumentation Engineers (SPIE) Conference Series Vol. 3005, pp. 184–192, 1997. — Cited in page 209.

[218] L. Porter, Gafchromic^{TM} ebt3 dosimetry film. — Cited in page 209.

[219] P. Casolaro, Applied Sciences **11**, 2132 (2021). — Cited in page 210.

[220] J. M. Lárraga-Gutiérrez, O. A. García-Garduño, C. Treviño-Palacios, and J. A. Herrera-González, Physica Medica **47**, 86 (2018). — Cited in page 211.